# ADVANCES IN OPTICAL IMAGING FOR CLINICAL MEDICINE

*Edited by*

**NICUSOR IFTIMIA**
**WILLIAM R. BRUGGE**
**DANIEL X. HAMMER**

WILEY

A JOHN WILEY & SONS, INC., PUBLICATION

Copyright © 2011 by John Wiley & Sons, Inc. All rights reserved.

Published by John Wiley & Sons, Inc., Hoboken, New Jersey.
Published simultaneously in Canada

No part of this publication may be reproduced, stored in a retrieval system, or transmitted in any form or by any means, electronic, mechanical, photocopying, recording, scanning, or otherwise, except as permitted under Section 107 or 108 of the 1976 United States Copyright Act, without either the prior written permission of the Publisher, or authorization through payment of the appropriate per-copy fee to the Copyright Clearance Center, Inc., 222 Rosewood Drive, Danvers, MA 01923, (978) 750-8400, fax (978) 750-4470, or on the web at www.copyright.com. Requests to the Publisher for permission should be addressed to the Permissions Department, John Wiley & Sons, Inc., 111 River Street, Hoboken, NJ 07030, (201) 748-6011, fax (201) 748-6008, or online at http://www.wiley.com/go/permission.

Limit of Liability/Disclaimer of Warranty: While the publisher and author have used their best efforts in preparing this book, they make no representations or warranties with respect to the accuracy or completeness of the contents of this book and specifically disclaim any implied warranties of merchantability or fitness for a particular purpose. No warranty may be created or extended by sales representatives or written sales materials. The advice and strategies contained herein may not be suitable for your situation. You should consult with a professional where appropriate. Neither the publisher nor author shall be liable for any loss of profit or any other commercial damages, including but not limited to special, incidental, consequential, or other damages.

For general information on our other products and services or for technical support, please contact our Customer Care Department within the United States at (800) 762-2974, outside the United States at (317) 572-3993 or fax (317) 572-4002.

Wiley also publishes its books in a variety of electronic formats. Some content that appears in print may not be available in electronic formats. For more information about Wiley products, visit our web site at www.wiley.com.

***Library of Congress Cataloging-in-Publication Data:***

Advances in optical imaging for clinical medicine / [edited by] Nicusor Iftimia, William R. Brugge, Daniel X. Hammer.
p. ; cm.—(Wiley Series in Biomedical engineering and multidisciplinary integrated systems)
Includes bibliographical references.
ISBN 978-0-470-61909-4 (cloth)
1. Diagnostic imaging. 2. Clinical medicine. I. Iftimia, Nicusor. II. Brugge, William R. III. Hammer, Daniel X. IV. Series: Wiley series in biomedical engineering and multidisciplinary integrated systems.
[DNLM: 1. Diagnostic Imaging–trends. 2. Clinical medicine–methods. 3. Diagnostic Imaging–methods. 4. Optical devices–trends. WN 180 A2445 2010]
RC78.7.D53A3887 2010
616.07′54–dc22

2010008434

Printed in Singapore

10 9 8 7 6 5 4 3 2 1

*To my parents, family, colleagues, and friends*
*Nicusor Iftimia*

*To my father, a physicist, and my wife, Joan Brugge, for their inspiration*
*William R. Brugge*

*To Owen*
*Daniel X. Hammer*

# CONTENTS

**Contributors** xi

**Preface** xv

1 **Introduction to Optical Imaging in Clinical Medicine** 1
*Nicusor Iftimia, Daniel X. Hammer, and William R. Brugge*

2 **Traditional Imaging Modalities in Clinical Medicine** 11
*Ileana Iftimia and Herbert Mower*

3 **Current Imaging Approaches and Further Imaging Needs in Clinical Medicine: A Clinician's Perspective** 47
*Gadi Wollstein and Joel S. Schuman [Section 3.1]; Cetin Karaca, Sevdenur Cizginer, and William R. Brugge [Section 3.2]; Ik-Kyung Jang and Jin-Man Cho [Section 3.3]; Peter K. Dempsey [Section 3.4]*

4 **Advances in Retinal Imaging** 85
*Daniel X. Hammer*

5 **Confocal Microscopy of Skin Cancers** 163
*Juliana Casagrande Tavoloni Braga, Itay Klaz, Alon Scope, Daniel Gareau, Milind Rajadhyaksha, and Ashfaq A. Marghoob*

6 **High-Resolution Optical Coherence Tomography Imaging in Gastroenterology** **187**

*Melissa J. Suter, Brett E. Bouma, and Guillermo J. Tearney*

7 **High-Resolution Confocal Endomicroscopy for Gastrointestinal Cancer Detection** **205**

*Jonathan T. C. Liu, Jonathan W. Hardy, and Christopher H. Contag*

8 **High-Resolution Optical Imaging in Interventional Cardiology** **233**

*Thomas J. Kiernan, Bryan P. Yan, Kyoichi Mizuno, and Ik-Kyung Jang*

9 **Fluorescence Lifetime Spectroscopy in Cardio- and Neuroimaging** **255**

*Laura Marcu, Javier A. Jo, and Pramod Butte*

10 **Advanced Optical Methods for Functional Brain Imaging: Time-Domain Functional Near-Infrared Spectroscopy** **287**

*Alessandro Torricelli, Davide Contini, Lorenzo Spinelli, Matteo Caffini, Antonio Pifferi, and Rinaldo Cubeddu*

11 **Advances in Optical Mammography** **307**

*Xavier Intes and Fred S. Azar*

12 **Photoacoustic Tomography** **337**

*Huabei Jiang and Zhen Yuan*

13 **Optical Imaging and Measurement of Angiogenesis** **369**

*Brian S. Sorg*

14 **High-Resolution Phase-Contrast Optical Coherence Tomography for Functional Biomedical Imaging** **413**

*Taner Akkin and Digant P. Davé*

15 **Polarization Imaging** **431**

*Mircea Mujat*

16 **Nanotechnology Approaches to Contrast Enhancement in Optical Imaging and Disease-Targeted Therapy** **455**

*Nicusor Iftimia, Lara Milane, Amy Oldenburg, and Mansoor Amiji*

**17 Molecular Probes for Optical Contrast Enhancement of Gastrointestinal Cancers 505**

*Jonathan W. Hardy, Anson W. Lowe, Christopher H. Contag, and Jonathan T. C. Liu*

**Index 529**

# CONTRIBUTORS

**Taner Akkin**, Department of Biomedical Engineering, University of Minnesota, Minneapolis, Minnesota

**Mansoor Amiji**, Department of Pharmaceutical Sciences, School of Pharmacy, Northeastern University, Boston, Massachusetts

**Fred S. Azar**, Siemens Corporate Research, Inc., Princeton, New Jersey

**Juliana Casagrande Tavoloni Braga**, Hospital A. C. Camargo, São Paulo, Brazil

**Brett E. Bouma**, Harvard Medical School and Wellman Center for Photomedicine at the Massachusetts General Hospital, Boston, Massachusetts

**William R. Brugge**, Department of Gastroenterology, Massachusetts General Hospital, Boston, Massachusetts

**Pramod Butte**, Cedars–Sinai Medical Center, Los Angeles, California

**Matteo Caffini**, Dipartiménto di Fisica, Politècnico di Milano, Milan, Italy

**Jin-Man Cho**, Department of Cardiology, Massachusetts General Hospital, Boston, Massachusetts

**Sevdenur Cizginer**, Department of Gastroenterology, Massachusetts General Hospital, Boston, Massachusetts

**Christopher H. Contag**, Department of Pediatrics and of Microbiology and Immunology, Stanford University School of Medicine, Stanford, California

**Davide Contini**, IIT Research Unit and Dipartiménto di Fisica, Politècnico di Milano, Milan, Italy

**Rinaldo Cubeddu**, IIT Research Unit and Dipartiménto di Fisica, Politècnico di Milano, Milan, Italy

**Digant P. Davé**, Bioengineering Department, University of Texas–Arlington, Arlington, Texas

**Peter K. Dempsey**, Department of Neurosurgery, Lahey Clinic, Burlington, Massachusetts; Tufts University School of Medicine, Boston, Massachusetts

**Daniel Gareau**, Department of Biomedical Engineering, Oregon Health and Science University, Portland, Oregon

**Daniel X. Hammer**, Medical Technologies Department, Physical Sciences, Inc., Andover, Massachusetts

**Jonathan W. Hardy**, Department of Pediatrics and of Microbiology and Immunology, Stanford University School of Medicine, Stanford, California

**Ileana Iftimia**, Radiation Oncology Department, Lahey Clinic, Burlington, Massachusetts; Tufts University School of Medicine, Boston, Massachusetts

**Nicusor Iftimia**, Medical Technologies Department, Physical Sciences, Inc., Andover, Massachusetts

**Xavier Intes**, Biomedical Engineering Department, Rensselaer Polytechnic Institute, Troy, New York

**Ik-Kyung Jang**, Department of Cardiology, Massachusetts General Hospital, Harvard Medical School, Boston, Massachusetts

**Huabei Jiang**, Department of Biomedical Engineering, University of Florida, Gainesville, Florida

**Javier A. Jo**, Texas A&M University, College Station, Texas

**Cetin Karaca**, Department of Gastroenterology, Massachusetts General Hospital, Boston, Massachusetts

**Thomas J. Kiernan**, Division of Cardiology, Massachusetts General Hospital, Harvard Medical School, Boston, Massachusetts; Nippon Medical School, Tokyo, Japan

**Itay Klaz**, Dermatology Service, Memorial Sloan–Kettering Cancer Center, New York, New York

**Jonathan T. C. Liu**, Department of Biomedical Engineering, State University of New York at Stony Brook, Stony Brook, New York

**Anson W. Lowe**, Department Gastroenterology, Stanford University School of Medicine, Stanford, California

**Laura Marcu**, Department of Biomedical Engineering, University of California–Davis, Davis, California

**Ashfaq A. Marghoob**, Dermatology Service, Memorial Sloan–Kettering Cancer Center, New York, New York

**Lara Milane**, Department of Pharmaceutical Sciences, School of Pharmacy, Northeastern University, Boston, Massachusetts

**Kyoichi Mizuno**, Division of Cardiology, Massachusetts General Hospital, Harvard Medical School, Boston, Massachusetts; Nippon Medical School, Tokyo, Japan

**Herbert Mower**, Radiation Oncology Department, Lahey Clinic, Burlington, Massachusetts; Tufts University School of Medicine, Boston, Massachusetts

**Mircea Mujat**, Medical Technologies Department, Physical Sciences, Inc., Andover, Massachusetts

**Amy Oldenburg**, Department of Physics and Astronomy, University of North Carolina at Chapel Hill, Chapel Hill, North Carolina

**Antonio Pifferi**, IIT Research Unit and Dipartiménto di Fisica, Politècnico di Milano, Milan, Italy

**Milind Rajadhyaksha**, Dermatology Service, Memorial Sloan–Kettering Cancer Center, New York, New York

**Joel S. Schuman**, UPMC Eye Center, Eye and Ear Institute, Ophthalmology and Visual Science Research Center, Department of Ophthalmology, University of Pittsburgh School of Medicine; Department of Bioengineering, Swanson School of Engineering, University of Pittsburgh; Center for the Neural Basis of Cognition, Carnegie Mellon University and University of Pittsburgh; Pittsburgh, Pennsylvania

**Alon Scope**, Dermatology Service, Memorial Sloan–Kettering Cancer Center, New York, New York

**Brian S. Sorg**, J. Crayton Pruitt Family Department of Biomedical Engineering, University of Florida, Gainesville, Florida

**Lorenzo Spinelli**, Istituto di Fotonica e Nanotecnologie–Sezióne di Milano, Milan, Italy

**Melissa J. Suter**, Harvard Medical School and Wellman Center for Photomedicine at the Massachusetts General Hospital, Boston, Massachusetts

**Guillermo J. Tearney**, Harvard Medical School and Wellman Center for Photomedicine at the Massachusetts General Hospital, Boston, Massachusetts

**Alessandro Torricelli**, IIT Research Unit and Dipartiménto di Fisica, Politècnico di Milano, Milan, Italy

**Gadi Wollstein**, UPMC Eye Center, Eye and Ear Institute, Ophthalmology and Visual Science Research Center, Department of Ophthalmology, University of Pittsburgh School of Medicine, Pittsburgh, Pennsylvania

**Bryan P. Yan**, Division of Cardiology, Massachusetts General Hospital, Harvard Medical School, Boston, Massachusetts; Nippon Medical School, Tokyo, Japan

**Zhen Yuan**, Department of Biomedical Engineering, University of Florida, Gainesville, Florida

# PREFACE

Clinical medicine lies at the nexus of the perspectives of physicians, researchers, engineers, physicists, technicians, philanthropists, insurers, administrators, venture capitalists, entrepreneurs, and, most of all, those afflicted with a health-related condition. Anyone who has worked in a field even remotely related to clinical medicine realizes that even with the vast expenditure of effort on the part of communities that comprise the first groups listed above, the results are sometimes unsatisfactory to all, and especially to the patients and their relatives. There are many reasons for the challenge in moving a potentially promising technology from laboratory bench to bedside, despite the best intentions of all involved. One of them is that no matter how much money and labor are behind an idea in a medically related field, it will always be a difficult prospect to reach full realization of that idea in a manner that is safe, efficacious, cost-effective, and easy to use.

The impact of new advances in clinical medicine can be observed easily by analyzing the trends in life expectancy. Up until the early twentieth century, life expectancy rarely exceeded 40 years, even in the most developed countries (see Figure P.1a). Today we can reasonably assume that a large percentage of us, and the majority of our children, will become octogenerians. However, the asymptotical trend means that it will be more difficult to achieve an increase in life expectancy of 0.1 year today than it was to achieve an increase of 10 years in the twentieth century. This is in part related to stress-related diseases in a modern society, and to the ease in spreading new viruses or new forms of cancer in a globalized society. Fortunately, many accomplishments in medical research in the last 30 years, such as the development of monoclonal antibodies and other targeted therapies, the identification of cancer-associated genes, and the introduction of computer-assisted imaging, have contributed significantly to the

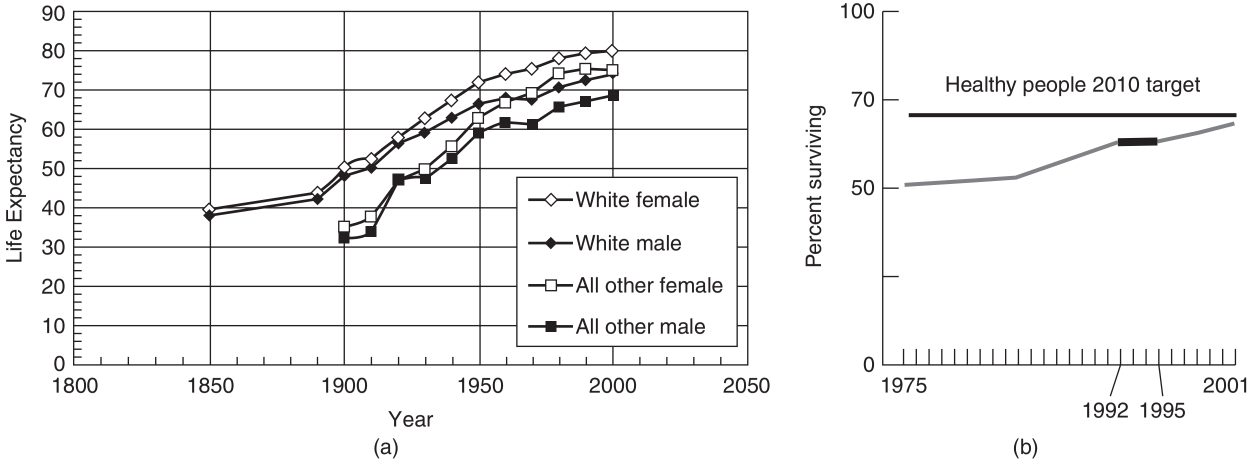

(a)

(b)

**FIGURE P.1** (a) Life expectancy at birth in the United States (1850 data for Massachusetts only). (From U.S. Department of Commerce, Bureau of the Census, *Historical Statistics of the United States*. (b) Cancer survival rates. (From: http://progressreport.cancer.gov/summary-tables_lac.asp.)

development of new tools that have helped control some of these life-expectancy impacting factors. For example, a very clear trend has been observed in increasing cancer survival rates (see Figure P.1b), due in part to new advances in gene therapy, as well as to the development of new tools that allow for early diagnosis of cancer at the cellular level. Since the complete mapping of the human genome in 2003, the field of biological science has flourished, and the prospect of the eradication of inherited or transmitted diseases using viral vectors and other gene therapies has started to become a reality.

The future of medical technologies will be impacted, on one hand by the biotech-driven trend of elucidating natural processes of health, disease, and healing in order to exploit understanding of the natural sciences to solve medical problems, and on the other, by the technology-centric trend of developing hardware, largely surgical or at least interventional technology, that may achieve dramatically better surgical/interventional endpoints. If today it takes more than ten years for a technology or drug to become widely available clinically, in the future it is expected to take significantly less time. The new pace, while challenging for researchers striving to remain at the forefront of their respective fields, is exciting for all to behold.

*Advances in Optical Imaging for Clinical Medicine* was written to provide a fragment of this perspective to students, researchers, and clinicians. It is designed to educate those who are new to the field of biomedical optics, and to provide a snapshot of the current technologies for the rest of us. Biomedical optics and biomedical imaging lie at the nexus of several fields, including biology, optics, physics, mechanical engineering, electrical engineering, and computer science. It is not uncommon; in fact, the converse is now rare that a system soon to be deployed in the clinic has custom optical, electrical, and mechanical components all managed and controlled with specialized software, firmware, and user interface. This requires more extensive collaboration and coordination between researchers, clinicians, and engineers in fields that may not have previously communicated so extensively with one another. It also requires the individual researcher to become familiar with the fundamental concepts, jargon, and current research trends in fields outside their own. We hope that this text will aid in such knowledge transfer and communication.

A book on optical imaging, even one restricted to fields related to clinical medicine, is bound to be incomplete. We have sought to highlight many fields where the pace of technical advancement has been particularly rapid, with the recognition that some areas outside our own limited scope may be experiencing or will soon experience similar great progress. We regretfully leave to other authors coverage of fields that we have omitted.

We would like to thank all the contributors, especially Mircea Mujat, who provided valuable assistance in the editing process, as well as to our publishers for very good feedback throughout the editing process. We would also like to thank all of our teachers, mentors, fellow researchers, and collaborators, who are too numerous to list individually.

Nicusor Iftimia
William R. Brugge
Daniel X. Hammer

*August 2010*

# 1

# INTRODUCTION TO OPTICAL IMAGING IN CLINICAL MEDICINE

NICUSOR IFTIMIA AND DANIEL X. HAMMER
*Physical Sciences, Inc., Andover, Massachusetts*
WILLIAM R. BRUGGE
*Massachusetts General Hospital, Boston, Massachusetts*

1.1 Brief history of optical imaging 1
1.2 Introduction to medical imaging 2
1.3 Outline of the book 4
References 9

## 1.1 BRIEF HISTORY OF OPTICAL IMAGING

Throughout history, as soon as a piece of optical apparatus was invented, human beings have used it to gaze both outward and inward. The refractive power of simple lenses made from quartz dates back to antiquity. The modern refractive telescope was invented in the Netherlands by Lippershey in 1608 and refined and used widely by Galileo in Italy during the Renaissance to discover the satellites of Jupiter, among other extraterrestrial objects. The modern microscope was also invented in the Netherlands several years earlier, in 1595, by the same lens and eyeglass makers (Lippershey, Sacharias Jansen, and his son, Zacharias). Soon thereafter it was used to probe the microarchitecture of the human cell. Both

---

*Advances in Optical Imaging for Clinical Medicine*, Edited by Nicusor Iftimia, William R. Brugge, and Daniel X. Hammer
Copyright © 2011 John Wiley & Sons, Inc.

telescopes and microscopes have evolved considerably over the years, guided by the elegantly simple fundamental physical laws that govern optical image formation by refraction proffered mathematically by Willebrord Snellius in 1621. Indeed, the principles of optics can simultaneously seem exceedingly simple and irreducibly complex. The early work in the Renaissance on the theory of diffraction and dispersion was led by Descartes, Huygens, and Newton, and was followed by the famous double-slit experiment of Young, which was subsequently supported by theory and calculations by Fresnel. The end of the nineteenth century saw the application of interferometry (Michelson) followed by the rise of quantum optics in the twentieth century. These scientific giants and their work provide the framework upon which all the fields and applications discussed in this book are built.

## 1.2 INTRODUCTION TO MEDICAL IMAGING

The dawn of the modern era of medical diagnosis can be traced to 1896, when Wilhelm Roentgen captured the first x-ray image, that of his wife's hand [1]. The development of radiology grew rapidly after that. Many noninvasive radiologic methodologies have been invented and applied successfully in clinical medicine and other areas of biomedical research. For the first 50 years of radiology, the primary examination involved creating an image by focusing x-rays through the body part of interest and directing them onto a single piece of film inside a special cassette. Later, modern x-ray techniques have been developed to significantly improve both the spatial resolution and the contrast detail. This improved image quality allows the diagnosis of smaller areas of pathology than could be detected with older technology. The next development involved the use of fluorescent screens and special glasses so that the physician could see x-ray images in real time. This caused the physician to stare directly into the x-ray beam, creating unwanted exposure to radiation. A major development along the way was the application of pharmaceutical contrast agents (dyes) to help visualize, for the first time, blood vessels, the digestive and gastrointestinal systems, bile ducts, and the gallbladder. The discovery of the image intensifier in 1955 has also contributed to the further blossoming of x-ray-based technology. Digital imaging techniques were implemented in the 1970s with the first clinical use and acceptance of the computed tomography (CT) scanner, invented by Godfrey Hounsfield [2].

Nuclear medicine (also called *radionuclide scanning*) also came into play in the 1950s. Nuclear medicine studies require the introduction into the body of very low-level radioactive chemicals. These radionuclides are taken up by the organs in the body and then emit faint radiation signals which are detected using special instrumentation. Imaging techniques that derive contrast from nuclear atoms, such as positron emission tomography (PET) and single-photon emission computed tomography (SPECT), reveal information about the spatiotemporal distribution of a target-specific radiopharmaceutical, which in turn yields information about various physiological processes, such as glucose metabolism and blood volume and flow [3–5]. Magnetic resonance imaging (MRI) provides structural and functional information from concentration, mobility, and chemical bonding of hydrogen [6,7]. All this information is essential for the early detection, diagnosis, and treatment of disease.

In the 1960s the principles of sonar (developed extensively during World War II) were applied to diagnostic imaging. The process involves placing a small device called a *transducer* against the skin of a patient near the region of interest, such as the kidneys. The transducer produces a stream of inaudible high-frequency sound waves that penetrate the body and bounce off the organs inside. The transducer detects sound waves as they bounce off or echo back from the internal structures and contours of the organs. These waves are received by an ultrasound machine and turned into live pictures through the use of computers and reconstruction software. For example, in ultrasonography, images reveal tissue boundaries [6].

In addition to these traditional imaging modalities, optical imaging began to play a significant role in clinical medicine in early 1960. Optical imaging at both the macroscopic and microscopic levels is used intensively these days by clinicians for diagnosis and treatment. New advances in optics, data acquisition, and image processing made possible the development of novel optical imaging technologies, including diffuse tomography, confocal microscopy, fluorescence microscopy, optical coherence tomography, and multiphoton microscopy, which can be used to image tissue or biological entities with enhanced contrast and resolution [8]. Optical imaging technologies are more affordable than conventional radiological technologies and provide both structural and functional information with enhanced resolution. However, the optical techniques still lack sensitivity and specificity for cancer detection. Within the past few years, there has been increased interest in improving the clinical effectiveness of optical imaging by combining two or more optical imaging approaches (or integrating optical imaging technologies into traditional imaging modalities) [9–11].

Emerging optical technologies are now combined with novel exogenous contrast agents, including several types of nanovectors (e.g., nanoparticles, ligands, quantum dots), which can be functionalized with various agents (such as antibodies or peptides) that are highly expressed by cancer receptors [12–15]. These techniques provide improved sensitivity and specificity and make possible in situ labeling of cellular proteins to obtain a clearer understanding of the dynamics of intracellular networks, signal transduction, and cell–cell interactions [16–20]. Ultimately, the combination of these new molecular and nanotechnology approaches with new high-resolution microscopic and spectroscopic techniques (e.g., optical coherence tomography, optical fluorescence microscopy, scanning probe microscopy, electron microscopy, and mass spectrometry imaging) can offer molecular resolution, high sensitivity, and a better understanding of the cell's complex "machinery" in basic research. The resulting accelerated progress in diagnostic medicine could pave the way to more inventive and powerful gene- and pharmacologically based therapies.

## 1.3 OUTLINE OF THE BOOK

The desire for powerful optical diagnostic modalities has motivated the development of powerful imaging technologies, image reconstruction procedures, three-dimensional rendering, and data segmentation algorithms. In particular, the overwhelming problem of light scattering that occurs when optical radiation propagates through tissue and severely limits the ability to image internal structure is discussed. The broad range of methods that have been proposed during the past decade or so to improve imaging performance are presented. The relative merits and limitations of the various experimental methods are discussed. We consider whether the new advanced approaches will contribute further to the likelihood of successful transition from benchtop to bedside. A brief presentation of each chapter follows.

Chapter 2 outlines traditional clinical imaging modalities and their use in therapy planning and guidance, including ultrasound (US), x-ray imaging, computed tomography (CT), magnetic resonance imaging (MRI), positron emission tomography (PET), and single-photon emission computed tomography (SPECT). Although these imaging technologies provide good structural and functional information, they have inherent safety issues (especially x-ray/CT and those used in nuclear medicine—PET/SPECT), and their resolution is limited. Future advances in medical imaging may be possible by combining these traditional imaging modalities with novel optical, molecular, and nano-imaging approaches. The advantages of these multimodal approaches enable higher-resolution structural and functional imaging and disease detection in its early stage when the therapy success rate is relatively high.

Chapter 3 outlines the current imaging approaches in clinical medicine and is authored by leading clinicians from several prestigious teaching hospitals in the United States. This chapter is organized in four independent sections dealing with ophthalmic imaging, imaging of the gastrointestinal mucosa, cardioimaging, and neuroimaging. Current technological approaches, their limitations, and further needs are presented in detail.

Because the eye is the only transparent organ in the body accessible to in vivo *and* noninvasive examination, it is often the first and best venue for the application of new optical imaging techniques. Optical coherence tomography (OCT) is a prime example. Before this technique spread rapidly to other fields of inquiry, it was perfected in ophthalmology. The optics of the eye can be limiting in terms of theoretical achievable resolution (i.e., ocular aberrations, numerical aperture, etc.) compared to conventional or confocal microscopy. These limitations have, however, provided opportunities for the development of tools to overcome them (e.g., adaptive optics). Chapter 4 is a monograph of the optical-based imaging modalities for ophthalmic use, including conventional fundus imaging, OCT, and scanning laser ophthalmoscopy, and also new technologies such as adaptive optics and polarization imaging.

Confocal microscopy, invented by Minsky in 1957, is an elegant and simple method for achieving high image contrast by reduction of light scatter from adjacent (lateral and axial) voxels. Chapter 5 focuses on reflectance confocal microscopy (RCM) for skin cancer detection. RCM enables real-time in vivo visualization of nuclear and cellular morphology. The ability to observe nuclear and cellular details clearly sets this imaging modality apart from other noninvasive imaging technologies, such as MRI, OCT, and high-frequency ultrasound. The lateral resolution of RCM, typically 0.2 to 1.0 μm, enables tissue imaging with a resolution comparable to that of high-magnification histology. As a result, RCM is being developed as a bedside tool for the diagnosis of melanoma and nonmelanoma skin cancers. The development and testing of advanced RCM instrumentation by the Memorial Sloan–Kettering cancer microscopy group is discussed in detail in this chapter.

Chapter 6 is devoted to the clinical applications of OCT in gastroenterology, including the esophagus, stomach, colon, duodenum, and the pancreatic and biliary ducts. OCT is an attractive tool for the interrogation of gastrointestinal tissue because it rapidly acquires optical sections at resolutions comparable to those of architectural histology, is a noncontact imaging modality, does not require a transducing medium, relies on endogenous contrast, and unlike the collection of forceps biopsies, is nonexcisional. Traditional assessment of gastrointestinal tissues is typically performed by endoscopy with accompanying forceps biopsy in organs with a larger-diameter lumen (esophagus and colon) or with brush cytology in the pancreatic or biliary ducts. OCT has shown promise for targeting premalignant mucosal lesions, grading and staging cancer progression, and reducing the risks and sampling error associated with biopsy acquisition. Although biopsy has traditionally been considered the gold standard for the diagnosis of gastrointestinal pathology, in many cases this assessment suffers greatly from sampling errors, with only a small percentage of the involved tissue being imaged. This is especially evident in cases where the disease may be focally distributed. Recent use of high-speed Fourier-domain OCT in the gastrointestinal tract has made significant strides toward comprehensive imaging, which may help to reduce the sampling error associated with the current assessment.

The most recent advances in confocal endomicroscopy for gastrointestinal (GI) cancer diagnosis are presented in Chapter 7. Confocal endomicroscopy is a rapidly emerging optical imaging modality that is currently being translated to routine clinical use. Advances in miniaturization have led to the development of numerous fiber optic–based confocal microscopes which may be deployed through the instrument channel of a conventional endoscope, or permanently packaged within the tip of a custom endoscope. Confocal endomicroscopes can enable real-time, high-resolution, three-dimensional visualization of epithelial tissues for improved early detection of disease and for image-guided interventions such as physical biopsies and endoscopic mucosal resection. Current research effort has focused on overcoming the limitations of confocal microscopy. For example, its limited field of view is now overcome by real-time generation of a mosaic of stitched images. The application of confocal microscopy for the interrogation of epithelial surfaces in the GI tract presents unique design challenges.

Therefore, this chapter focuses on clinical motivation, challenges, design parameters, and other fundamental aspects of GI endomicroscopy. Also discussed are the latest efforts to develop miniature confocal microscopes that are compatible with those of GI endoscopy.

Chapter 8 presents recent progress in minimally invasive approaches in interventional cardiology (IC). The diagnosis of vulnerable plaques occupies an important part of this chapter. The structure of these plaques (i.e., hard core, fluid-filled lesions accessible only with depth-resolved techniques) makes them the most difficult to diagnose, yet they seem to be responsible for most deleterious coronary events. Identification and visualization of high-risk plaques are key to designing customized therapeutic approaches. The ultimate goal is to accurately categorize high-risk patients, target therapy to appropriate areas of vulnerable plaque, and thus prevent or reduce the probability of adverse events. A number of minimally invasive imaging modalities currently in use are presented, including intravascular ultrasound (IVUS) and angioscopy. Also presented are promising new investigational methodologies, including OCT, intracoronary thermography, near-infrared spectroscopy, and intracoronary MRI. OCT in particular uniquely enables excellent resolution of coronary architecture and precise characterization of plaque morphology.

An overview of time-resolved (lifetime) laser-induced fluorescence spectroscopy (TR-LIFS) is presented in Chapter 9. TR-LIFS instrumentation, methodologies for in vivo characterization, and diagnosis of biological systems are presented in detail. Emphasis is placed on the translational research potential of TR-LIFS and on determining whether intrinsic fluorescence signals can be used to provide useful contrast for the diagnosis of high-risk atherosclerotic plaque and brain tumors intraoperatively.

Chapter 10 outlines the use of near-infrared spectroscopy (NIRS) for noninvasive monitoring of brain hemodynamics and oxidative metabolism (i.e., oxygenation status). This technology is capable of monitoring cerebral activity in response to various stimuli (motor, visual, and cognitive) and therefore is currently being used to study functional processes in the brain, to diagnose mental diseases, and more precisely, to localize brain injuries. Clinical demonstration and widespread use of this technology is expected to increase in the coming years because of its promise for functional imaging. In particular, major breakthroughs are expected in cutting-edge techniques such as time-domain functional near-infrared spectroscopy. Current research systems employ low-power pulsed diode lasers and complex, efficient detection instrumentation. Future prototype clinical instruments will achieve higher signal/noise ratios through the use of ultrafast (picoseconds), high-power ($>1$ W) broadband fiber laser and miniaturized, sensitive, and fast photonic crystal devices combined with high-throughput photodetection electronics.

Chapter 11 describes the application of NIRS to mammography. In optical mammography, diagnosis is based on the detection of local differential concentrations of endogenous absorbers and/or scatterers between normal and diseased breast tissue. Various implementation approaches in conjugation with MR imaging are discussed in detail. The prevalence and implication of age, hormonal status, weight, and demographic factors on complex structural changes in the breast are discussed as well. Such intra- and interpatient variations affect the effectiveness of these imaging modalities adversely and to date have restricted wide clinical use to a specific demographic or time window. As clinical optical mammography matures, its potential impact on cancer management will become more clearly defined. The main applications of this optical technology, as proposed by the Network for Translational Research in Optical Imaging, are monitoring of neoadjuvant chemotherapy response, screening for subpopulations of women in which mammography does not work well, and optical imaging as an adjunct to x-ray mammography.

A promising new optical technology called *photoacoustic tomography* (PAT) is introduced in Chapter 12 for breast imaging. Research interest in laser-induced PAT is growing rapidly, largely because of its unique capability of combining high-contrast optical imaging with high-resolution ultrasound in the same instrument. Recent in vivo studies have shown that the optical absorption contrast ratio between tumor and normal tissues in the breast can be as high as 3 : 1 in the near-infrared region, due to significantly increased tumor vascularity. However, optical imaging has low spatial resolution, due to strong light scattering. Ultrasound imaging can provide better resolution than optical imaging due to less scattering of acoustic waves. However, the contrast for ultrasound imaging is low, and it is often incapable of revealing diseases in early stages. In a single hybrid imaging modality, PAT combines the advantages of optical and ultrasound imaging while avoiding the limitations of each. PAT imaging can penetrate to a depth of about 1 cm with an axial resolution of less than 100 $\mu$m at a wavelength of 580 nm. PAT has shown the potential to detect breast cancer, to probe brain functioning in small animals, and to assess vascular and skin diseases.

Chapter 13 focuses on the application of optical imaging to tissue angiogenesis monitoring. Angiogenesis is a process fundamental to several normal tissue physiological functions and responses as well as to many pathological conditions. The ability to monitor and quantify angiogenesis clinically could aid in the management of certain diseases, healing responses, and therapies. While several methods for measurement of angiogenesis are under development and are being implemented using conventional medical imaging modalities, optical techniques have also shown potential. To properly design and evaluate optical techniques to measure angiogenesis, an appreciation of the complex physiology of the process is necessary. Methodology to quantify angiogenesis and independent test optical measurements are also needed. The fundamental characteristics of angiogenesis, measurement methods, and the current state of optical techniques are reviewed briefly in this chapter.

Chapter 14 introduces a relatively new technology, called phase-contrast optical coherence tomography. This technique can detect subwavelength changes in optical pathlength (OPL) by measuring the phase of an interference signal. Although phase information is readily available in any interferometric setup, environmental noise corrupts the phase information, rendering it difficult to use.

Robust phase measurement requires interferometer designs that cancel common-mode noise. This can be achieved with common path and differential phase interferometric implementations. Measurement of depth-resolved subwavelength changes in OPL is now possible for novel optical imaging applications. Phase-sensitive low-coherence interferometry in both time- and spectral-domain implementation, as well as their potential for biomedical applications (including surface profilometry, quantitative phase-contrast microscopy, and optical detection of neural action potentials), are described in this chapter.

Polarization is a fundamental property of light that can be harnessed to provide additional contrast without staining or labeling. Imaging technologies that detect and visualize the interaction of tissue with polarized light, revealing structural or chemical characteristics not visible with standard intensity imaging, are described in Chapter 15. The anisotropic real and imaginary parts of the refractive index of tissue are fundamental properties that can be quantified through the detection of transmitted or reflected polarized light. The linear and circular birefringence and dichroism also calculated with polarimetric techniques can help to differentiate normal and diseased tissue. Currently, linear birefringence is most often measured because it is related to the highly organized structure of collagen. Circular birefringence and linear and circular dichroism, which are related to other structural and chemical anisotropies, are generally not explored. Whereas traditional light-scattering techniques normally probe only size distribution and concentration of particles, polarized light scattering is sensitive to shape, orientation, and internal structure of the particles, as well as to structural characteristics of the global system. Applications of this technology to the fields of biomedicine, materials science, and industrial and military sensors are presented in this chapter.

Chapter 16 covers the use of various nanotechnologies for contrast enhancement in optical imaging. Optical imaging technologies are more affordable than traditional radiological technologies and provide both structural and functional information with enhanced resolution. However, they still lack sensitivity and specificity for cancer detection. Therefore, in the past few years there has been increasing interest in improving clinical effectiveness of optical imaging by combining emerging optical technologies with novel exogenous contrast agents, including several types of nanovectors (e.g., nanoparticles, ligands, quantum dots), which can be functionalized with various agents (such as antibodies or peptides) that are expressed highly by cancer receptors. In this way, it becomes possible to label proteins in live cells and obtain a clearer understanding of the dynamics of intracellular networks, signal transduction, and cell–cell interactions in addition to improving sensitivity and specificity. Use of the enhanced sensitivity and specificity of molecular imaging approaches in medicine has the potential to affect positively the prevention, diagnosis, and treatment of various diseases, including cancer. These new molecular and nanotechnology approaches with new developments in microscopic and spectroscopic techniques toward high spatial resolution (i.e., optical coherence tomography, optical fluorescence microscopy, etc.) are presented to some extent in this chapter. Implications of the various nanotechnologies for more efficient drug delivery and tissue regeneration are discussed as well.

Chapter 17 focuses on the use of molecular probes for optical contrast enhancement of GI cancers. The surface of the GI tract is accessible to direct examination via endoscopy. The most common GI cancers originate in the superficial mucosa, where unscattered ballistic photons can penetrate to depths that are relevant for interrogating tissue properties and detecting cellular markers. Improvements in instrumentation now permit the detection of these photons to depths that were not possible previously. In addition, molecular probes whose binding characteristics are verified by microscopy facilitate rapid wide-field detection of precancerous lesions over large areas, followed by closer inspection with endomicroscopy. Probes that detect GI cancer have been identified and the clinical application of both contrast-enhancing agents and specific molecular diagnostic reagents capable of revealing early disease markers is on the horizon. The effort ongoing toward the development of GI cancer probes and detection reagents is presented in detail in this chapter.

A broad cross section of optical imaging research and clinical technology development for early disease detection and therapy guidance is described in the book. We recognize that the broadness of the biomedical optical imaging field makes it likely that we have omitted many important investigations in our sampling. Moreover, the rapid pace of discovery, although exciting for all the authors, also provided the challenge of trying to hit a moving target. We hope that the book will provide a foundation of knowledge upon which future technological developments in optical imaging will materialize.

## REFERENCES

1. Stanton, A., Wilhelm Conrad Röntgen on a new kind of rays: translation of a paper read before the Würzburg Physical and Medical Society, 1895 *Nature*, Vol. 53, No. 1896, pp. 274–276.
2. Ambrose, J., and Hounsfield, G., Computerized transverse axial tomography, *Br. J. Radiol*., Vol. 46, No. 542, 1973, pp. 148–149.
3. Terpogossian, M.M., et al., Positron-emission transaxial tomograph for nuclear imaging (Pett), *Radiology*, Vol. 114, No. 1, 1975, pp. 89–98.
4. Nutt, R., The history of positron emission tomography, *Mol. Imaging Biol*., Vol. 4, No. 1, 2002, pp. 11–26.
5. Patton, J.A., and Budinger, T.F. (eds.), *Single Photon Emission Computed Tomography*, 4th ed., *Diagnostic Nuclear Medicine*, M.P. Sandler et al. (eds.), Lippincott Williams & Wilkins, Philadelphia, 2003.
6. Lauterbur, P.C., Image formation by induced local interactions: examples employing nuclear magnetic resonance, *Nature*, Vol. 242, No. 5394, 1973, pp. 190–191.
7. Shung, K.K., *Diagnostic Ultrasound: Imaging and Blood Flow Measurements*, Taylor & Francis Group, CRC Press Book, Boca Raton, FL, 2005.
8. Fujimoto, J.G., and Farkas, D., *Biomedical Optical Imaging*, Oxford University Press, New York, 2009.

9. Nahrendorf, M., Sosnovik, D.E., and Weissleder, R., MR-optical imaging of cardiovascular molecular targets, *Basic Res. Cardiol*., Vol. 103, No. 2, 2008, pp. 87–94.
10. Cherry, S.R., Multimodality in vivo imaging systems: Twice the power or double the trouble? *Annu. Rev. Biomed. Eng*., Vol. 8, 2006, pp. 35–62.
11. Serganova, I., and Blasberg, R.G., Multi-modality molecular imaging of tumors, *Hematol. Oncol. Clin. North Am*., Vol. 20, No. 6, 2006, pp. 1215+.
12. Licha, K., Schirner, M., and Henry, G., Optical agents, *Handb. Exp. Pharmacol*., Vol. 185, Pt. 1, 2008, pp. 203–222.
13. Zhang, L.M., et al., Molecular imaging of Akt kinase activity, *Nat. Med*., Vol. 13, No. 9, 2007, pp. 1114–1119.
14. Medintz, I.L., et al., Quantum dot bioconjugates for imaging, labelling and sensing, *Nat. Mater*., Vol. 4, No. 6, 2005, pp. 435–446.
15. Weissleder, R., and Ntziachristos, V., Shedding light onto live molecular targets, *Nat. Med*., Vol. 9, No. 1, 2003, pp. 123–128.
16. Kumar, S., and Richards-Kortum, R., Optical molecular imaging agents for cancer diagnostics and therapeutics, *Nanomedicine*, Vol. 1, No. 1, 2006, pp. 23–30.
17. Morgan, N.Y., et al., Real time in vivo non-invasive optical imaging using near-infrared fluorescent quantum dots, *Acad. Radiol*., Vol. 12, No. 3, 2005, pp. 313–323.
18. Wang, H.Z., et al., Detection of tumor marker CA125 in ovarian carcinoma using quantum dots, *Acta Biochim. Biophys. Sin*., Vol. 36, No. 10, 2004, pp. 681–686.
19. Jaiswal, J.K., et al., Long-term multiple color imaging of live cells using quantum dot bioconjugates, *Nat. Biotechnol*., Vol. 21, No. 1, 2003, pp. 47–51.
20. Brigger, I., Dubernet, C., and Couvreur, P., Nanoparticles in cancer therapy and diagnosis, *Adv. Drug Deliv. Rev*., Vol. 54, No. 5, 2002, pp. 631–651.

# 2

# TRADITIONAL IMAGING MODALITIES IN CLINICAL MEDICINE

ILEANA IFTIMIA AND HERBERT MOWER

*Lahey Clinic, Burlington, Massachusetts; Tufts University School of Medicine, Boston, Massachusetts*

2.1 Introduction 11
2.2 Diagnostic imaging technologies 12
  2.2.1 Ultrasound 12
  2.2.2 X-rays, fluoroscopy, and computed tomography 17
  2.2.3 Magnetic resonance imaging 22
  2.2.4 Nuclear medicine 26
2.3 Imaging for radiation therapy planning 32
  2.3.1 Ultrasound, CT, and MR imaging in brachytherapy 32
  2.3.2 CT, MR, and PET imaging in external beam radiation therapy 35
2.4 Image-guided radiation therapy 38
2.5 Conclusions 43
References 44

## 2.1 INTRODUCTION

In this chapter we present a brief overview of the most important traditional imaging modalities currently used in clinical medicine for diagnosis and treatment. The human body is an incredibly complex system. A real challenge for

---

*Advances in Optical Imaging for Clinical Medicine*, Edited by Nicusor Iftimia, William R. Brugge, and Daniel X. Hammer
Copyright © 2011 John Wiley & Sons, Inc.

researchers and physicians is acquiring and processing information about the human body with the purpose of using these data for diagnosis and treatment. The use of imaging to interpret biological processes is in continuous expansion, not only in clinical medicine but also in the biomedical research field. For example, in ultrasonography, images reveal tissue boundaries. X-ray films and computed tomography (CT) images reveal the intrinsic properties of the regions of the body through which they are transmitted, such as atomic number, physical density, and electron density. Nuclear medicine images, such as positron emission tomography (PET) and single-photon emission computed tomography (SPECT), reveal information about spatial or spatiotemporal distribution of a target-specific radiopharmaceutical, which in turn yields information about various physiological processes, such as glucose metabolism and blood volume and flow. Magnetic resonance imaging (MRI) gives information about the structure and function of the body, using data such as concentration, mobility, and the chemical bonding of hydrogen. All this information is essential for the early detection, diagnosis, and treatment of disease.

Contrast agents are media often used during medical imaging examinations to highlight specific parts of the body and make them easier to see. They can be used with many types of imaging examinations, including x-ray exams and CT and MRI scans, and can be administered in various ways (i.e., as a drink, injected, or delivered through an intravenous line or an enema). The contrast agents used for CT imaging are high-atomic-number substances such as iodine or barium sulfate, while paramagnetic substances such as gadolinium are most often used for MRI.

An ideal imaging modality should be noninvasive and safe for the patient and technician, should provide anatomical, functional, and metabolic information, and should have a good spatial resolution, sensitivity, and specificity. (Sensitivity and specificity are statistical quantities used to describe a diagnostic test. A sensitivity of 100% means that a test recognizes all sick people as sick, and a specificity of 100% means that a test recognizes all healthy people as such.) Neglecting the safety issues, CT images fused with magnetic resonance (MR) images can be considered a good approximation of such a concept. Future advances in medical imaging (optical, molecular, nanoimaging) and computer technology should eventually resolve many of the current issues.

## 2.2 DIAGNOSTIC IMAGING TECHNOLOGIES

### 2.2.1 Ultrasound

Ultrasound imaging (US) is one of the most widely used diagnostic modalities in medicine, mainly because of its low cost, safety, and efficacy. Ultrasounds simply refer to sounds above the highest audible frequency, about 20 kHz. The US signal is a wave whose propagation through soft tissue is governed by the standard wave equation [1],

$$\nabla^2 P - \frac{1}{c^2}\frac{\partial^2 P}{\partial t^2} = 0 \tag{2.1}$$

where $P$ is the pressure and $c$ is the speed of sound. The speed of sound depends on the density ($\rho$) and volumetric compressibility ($\kappa$) of a medium as follows:

$$c^2 = \frac{1}{\rho\kappa} \tag{2.2}$$

The volumetric compressibility ($\kappa$) is given by the product of isothermal specific heat ($c_T$) and isothermal bulk modulus ($B_T$), $\kappa = c_T B_T$. Since both $c_T$ and $B_T$ are nearly constant for the medical US frequency range (2 to 10 MHz), the ultrasound speed in a medium is almost constant, so the US wavelength ($\lambda$) is almost inversely proportional to US frequency ($f$):

$$\lambda = \frac{c}{f} \tag{2.3}$$

The US speed varies from 1450 m/s for fat to 4080 m/s for bones [2] (this is about 50 to 200 times higher than, for example, a car's speed of 50 mph = 22.2 m/s). At the interface of two media with different density and compressibility, the US beam undergoes reflection and refraction. The reflection and transmission coefficients are determined by the acoustic impedance ($Z$) of the two media, defined as $Z = \rho c$.

As a US beam advances through tissue, it loses energy by absorption and scattering. The attenuation coefficient, $\alpha$, is given by the sum of the scatter and absorption coefficients. The frequency dependence of the attenuation coefficient varies with tissue type and is usually described as a power function:

$$\alpha(f) = \alpha_0 f^n \tag{2.4}$$

For many soft tissues $n \approx 1$ and $\alpha_0 = 0.5$ dB cm$^{-1}$ MHz$^{-1}$, so the range for the soft tissue attenuation coefficient is 0.1 to 0.6 dB cm$^{-1}$ MHz$^{-1}$. The attenuation coefficient is high for lung (30 dB cm$^{-1}$ MHz$^{-1}$) and bone (22 dB cm$^{-1}$ MHz$^{-1}$) [3]. For a plane US wave propagating a distance $x$ in an attenuating medium, the peak pressure varies exponentially:

$$P(x, f) = P_0 e^{-\alpha(f)x} \tag{2.5}$$

*Operation Principle* US imaging employs a transducer, which is a piezoelectric device used to generate pulses of high frequency (usually, 2 to 10 MHz) and to detect the returning echo signals. Echoes are produced at any tissue interface where a change in acoustic impedance occurs. The time between the transmission of a pulse and the arrival of an echo is used to estimate the depth to a reflecting tissue surface located below the transducer. The US images reveal the positions of tissue boundaries within the body.

The transducer is a part of the system serving as a transmitter and a receiver, where electrical and acoustic signals are converted back and forth. The transformation between electrical and mechanical pulses can be explained based on the piezoelectric effect. When voltage is applied across a piezoelectric plate, the permanently polarized molecules are realigned, leading to a change in plate thickness. Conversely, mechanical stress on the plate can cause a variation in the internal electric field sensed as a voltage fluctuation. Resonance occurs when the plate thickness is half the US wavelength in the material. At resonance the mechanical and electrical oscillations are reinforcing each other. Two-dimensional phased-array transducers that can sweep the beam in three dimensions have been developed. These can image faster and can even be used to make live three-dimensional images [4]. Ultrasound is basically a radar or sonar system, but it operates at speeds that differ from these by orders of magnitude. Ultrasound designers have adopted ideas from radar systems and have expanded on the principle of steering beams using phased arrays.

A high-voltage (HV) multiplexer/demultiplexer is used in some arrays to reduce the complexity of transmitting (Tx) and receiving (Rx) hardware, but at the expense of flexibility. On the Tx side, the Tx beamformer determines the delay pattern and pulse train that set the desired transmitting focal point. The outputs of the beamformer are then amplified by HV transmitting amplifiers that drive the transducers. These amplifiers might be controlled by digital-to-analog converters (DACs) to shape the transmitted pulses for better energy delivery to the transducer elements. Typically, multiple transmitter focal regions (zones) are used; that is, the field to be imaged is deepened by focusing the energy transmitted at progressively deeper points in the body. The main reason for multiple zones is that the energy transmitted needs to be greater for points that are deeper in the body, because of the attenuation of the signal as it travels into the body and as it returns. On the receiving side, there is a Tx/Rx switch, generally a diode bridge, which blocks the HV Tx pulses transmitted. It is followed by a low-noise amplifier (LNA) and one or more variable-gain amplifiers (VGAs), which implement time gain compensation (TGC). Time gain control, which provides increased gain for signals originating from deeper parts in the body and therefore arriving later, is under operator control and used to maintain image uniformity [1,3].

After amplification, beamforming is performed, implemented in either analog or digital form. Finally, the beams received are processed to show either a gray-scale image, color flow overlay on the two-dimensional image, and/or a Doppler output. The US image density is proportional to the intensity of the echo, which is determined by the magnitude of the change in the acoustic impedance at the echoing interface, the characteristics of the intervening tissue, and the normality (perpendicularity) of the interface to the transducer. The appearance of the echo on the image is also determined by the degree of amplification (gain) applied after the echo has been received by the transducer.

US devices have several modes of operation: amplitude (A)-mode, brightness (B)-mode, and motion (M)-mode. A detailed presentation of US modes of operation and instrumentation can be found elsewhere [1,3]. The A-mode gives information about the scatterers that lie along a single scanline, the amplitude being proportional to the echo signal. The B-mode is a two-dimensional approach, creating an image from a set of closely spaced scanlines. For each scanline the amplitude of an echo signal is displayed on the screen with pixel brightness proportional to the signal amplitude. Early B-mode US systems used a mechanically scanned transducer. By contrast, modern B-mode systems use transducers whose core is an array of hundreds or more piezoelectric elements. In the M-mode the images are created from echo amplitude information along a single scanline through tissue, but the information is displayed as the brightness of the light point, as in the B-mode. The M-mode is designed to record motion, such as in monitoring cardiac valves.

The US waveform is a short pulse, characterized by the peak frequency and the bandwidth. The US beamwidth at the focal point of the transducer and the depth of focus are linearly proportional to the US wavelength. If the US frequency increases, the wavelength decreases, so the beamwidth and pulse duration decrease; consequently, the US axial and lateral resolutions, assessed by the minimum separation of two point targets when their images could just be distinguished, improve. Axial resolution is the minimum separation between two interfaces located parallel to the beam so that they can be imaged as two different interfaces. Lateral resolution is the minimum separation of two interfaces aligned along a direction perpendicular to the ultrasound beam. It depends on the beamwidth. As an example, the axial resolution for a linear array transducer with parallel beams varies from about 1 mm at 3-MHz to about 0.3 mm at 10-MHz peak frequency. The lateral resolution varies from about 2.8 mm at 3-MHz to about 1 mm at 10-MHz peak frequency. Unfortunately, the depth of focus decreases if frequency increases. The US wave spectrum varies with depth because the attenuation in tissue is frequency dependent. The axial resolution worsens as the beam penetrates deeper because the peak frequency and the bandwidth decrease with depth [5].

The image quality can be improved by using intravenously administered contrast agents. They usually consist of a gaseous suspension in a fluid. The big difference in acoustic impedance between the gas and surrounding blood or tissue will improve the image contrast. US is an efficient image modality and it is universally considered to be safe. The potential biophysical effects can be divided into thermal (US energy absorption) and nonthermal (acoustic streaming of cell content) [3]. Even though there may be little evidence for biological harm done by US, the practitioners should be aware of and follow the U.S. Food and Drug Administration (FDA) safety rules.

*Medical Applications* Ultrasound imaging is used largely in clinical medicine because it provides a reasonably good resolution and imaging depth at affordable

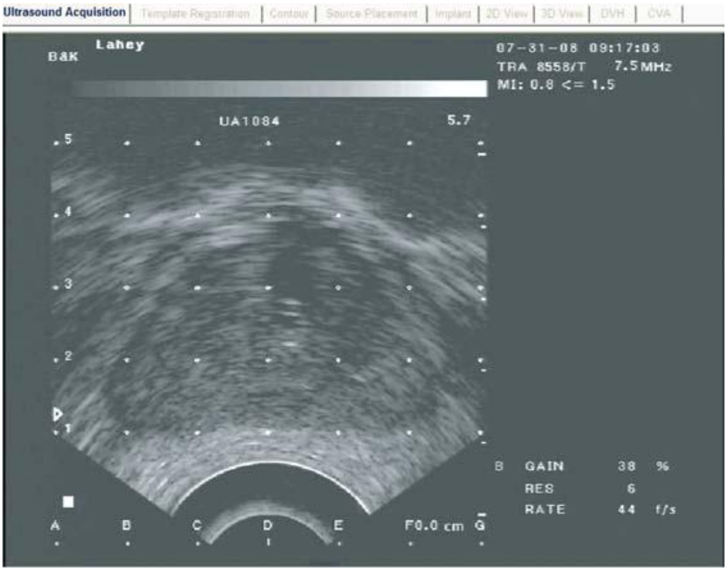
Ultrasound Acquisition
Template Registration
Contour
Source Placement
Implant
2D View
3D View
DVH
CVA
B&K
Lahey
07-31-08 09:17:03
TRA 8558/T 7.5MHz
MI: 0.8 <= 1.5
UA1084
5.7
5
4
3
2
1
B GAIN 38 %
RES 6
RATE 44 f/s
A
B
C
D
E
F0.0 cm
G

**FIGURE 2.1** Axial US image of a prostate gland. (Courtesy of Radiation Oncology Department, Lahey Clinic.)

costs. The soft tissue is in general well delineated, as shown in Figure 2.1, which depicts an axial US image of a prostate gland.

Among the US imaging strengths, one can consider the following:

- It images muscle and soft tissue well and is particularly useful for delineating the interfaces between solid and fluid-filled spaces.
- It renders “live” images, often enabling rapid diagnoses.
- It shows the structure of organs.
- It has no known long-term side effects and rarely causes any discomfort to the patient.
- Equipment is widely available, including portable scanners.
- Examinations can be performed at the bedside.
- US imaging is inexpensive compared to o ther modes of investigation.

However, like any other technology, US imaging also has some weaknesses:

- US imaging has poor resolution and sensitivity compared to other approaches.
- US devices have trouble penetrating bone (e.g., sonography of the adult brain is very limited).
- Ultrasonography performs very poorly when there is a gas between the transducer and the organ of interest, due to the extreme differences in acoustic

impedance (e.g., overlying gas in the gastrointestinal tract often makes ultrasound scanning of the pancreas difficult, and lung imaging is not possible, except for pleural effusion).

- Even in the absence of bone or air, the US penetration depth is limited, making it difficult to image structures deep in the body, especially in obese patients.
- US imaging is operator dependent.
- There is no scout image; therefore, once an image has been acquired, there is no exact way to tell which part of the body was imaged.

Despite these weaknesses, the US imaging modality has numerous applications in such medical fields as echocardiography, endocrinology, gastroenterology, gynecology and obstetrics, ophthalmology, urology, musculoskeletal, and intravascular. The acoustic Doppler effect, applicable to US pulses, can be used to evaluate blood flow, vessel wall motion, and cardiac valves. A source and an observer experience the same frequency when they are stationary, but a frequency shift appears when they move relative to each other. This frequency shift is a measurable quantity, proportional to the observer velocity. Assuming that the observer is a blood cell, the Doppler frequency shift will give information about its motion [6]. At higher frequencies, the US waves can be used for therapeutic purposes (e.g., dental hygiene, physical therapy, cancer treatment, kidney stone fragmentation by lithotripsy, cataract treatment by phacoemulsification).

Many developments in the diagnostic US field have taken place over the past few years. To name a few: real-time three-dimensional imaging, promising results for four-dimensional imaging, elastic imaging, miniaturized piezoelectric transducers, and US systems using higher frequency to image small targets [7–10]. For example, the coronary arteries can be seen using 10 to 40-MHz US pulses, and at higher frequencies (hundreds of megahertz) US imaging can be used in ophthalmology, dermatology, and perhaps even for cellular-level imaging [11].

### 2.2.2 X-rays, Fluoroscopy, and Computed Tomography

***X-rays*** Radiography has played a central role in diagnostic imaging since Roentgen's discovery of x-rays. Projection x-ray films still comprise more than half of all clinical examinations, despite the rapid evolution of more sophisticated three-dimensional imaging modalities. Compared to other types of images, film radiography provides the higher resolution/cost ratio. Digital x-ray imaging has evolved rapidly in recent decades, enhancing image display and storage.

*Technique Description* X-rays are generated using an x-ray tube in which electrons accelerated at high voltage hit the anode. The anode is made by a high-atomic-number material, usually tungsten or molybdenum. The photons emitted from the anode atoms predominantly through the bremsstrahlung mechanism have a continuous energy spectrum, with maximum energy in the keV range.

This photon beam exiting from the x-ray tube is collimated and directed toward the patient. The photon beam is attenuated in tissue mainly through photoelectric absorption and Compton scattering. The differential attenuation through different types and thicknesses of tissues gives rise to image contrast. The exit beam from the patient is captured using a detector [either a film, a film-intensifying screen combination to increase the detection efficiency, or a photoconductor (amorphous selenium) flat-panel imager, as in digital radiography]. The traditional x-ray film consists of a transparent film base (0.2 mm thick), coated on one or both sides with a silver bromide granulated emulsion. The silver ions are neutralized after exposure to radiation and deposited in the emulsion. This will create a latent image, which serves as a catalyst for the deposition of metallic silver on the film base during the developing process. The degree of blackening of the processed region of the film depends on the amount of silver deposited in that area, and therefore on the number of x-rays absorbed in that area. A detailed description of the interaction mechanisms in tissue, detector types, and image quality may be found elsewhere [1,3].

*Medical Applications* Bony tissue and metals are denser than the surrounding tissue, and thus by absorbing more of the x-ray photons they prevent the film from getting exposed as much, so it will appear translucent blue, whereas the black parts of the film represent lower-density tissues such as fat, skin, and internal organs, which cannot stop the x-rays. This is used to see bony fractures, foreign metallic objects, and to find bony pathology such as osteoarthritis, osteomyelitis, and cancer (osteosarcoma) as well as growth problems (leg length, achondroplasia, scoliosis, etc).

Soft tissues commonly imaged with x-rays include the lungs and heart shadow in a chest x-ray, the air pattern of the bowel in abdominal x-rays, the soft tissues of the neck, and the orbits by a skull x-ray to check for foreign metallic objects. X-rays are also used extensively in dental radiography and in mammography. The breast contains only soft tissue, so relatively low-energy x-rays (e.g., those emitted by a molybdenum target) are appropriate to create good image contrast.

### *Fluoroscopy*

*Technique Description and Medical Applications* Fluoroscopy is an imaging technique commonly used to obtain real-time moving images of the internal structures of a patient. In its simplest form, a fluoroscope consists of an x-ray source and a fluorescent screen between which a patient is placed. However, modern fluoroscopes couple the screen to an x-ray image intensifier and charge-coupled device (CCD) video camera, which allows the images to be played and recorded on a monitor.

The use of x-rays, a form of ionizing radiation, requires that the potential risks from a procedure be carefully balanced with the benefits of the procedure to the patient. Although physicians always try to use low-dose rates during fluoroscopy procedures, the length of a typical procedure often results in a relatively high absorbed dose to the patient. This depends greatly on the size of the patient as well as the length of the procedure, with typical skin dose rates quoted as 20 to 50 mGy/min. [The *absorbed dose*, defined as the energy deposited per unit mass, is measured in SI in gray units (1 Gy = 1 J/kg). The most used subunit is the rad (1 rad = 0.01 Gy).] Because of the long duration of some procedures, in addition to standard cancer-inducing stochastic radiation effects, deterministic radiation effects have also been observed, ranging from mild erythema to more serious burns. Modern fluoroscopes use cesium iodide screens and produce noise-limited images of acceptable quality. Digitization of the images captured, improvements in screen phosphors and image intensifiers, and the use of flat-panel detectors have allowed for increased image quality while minimizing the radiation dose to the patient. Flat-panel detectors have increased sensitivity to x-rays, improved contrast and temporal resolution, and reduced motion blurring [1,3].

There are various medical applications for fluoroscopy. They include investigations of the gastrointestinal tract, orthopedic surgery, angiography, urological surgery, placement of a feeding tube, and implantation of pacemakers or defibrillators.

***Computed Tomography*** X-ray computed tomography (CT) was introduced clinically in the early 1970s [12] as a new medical imaging method. The term *tomography* is derived from the Greek *tomos* (slice) and *graphein* (to write). A three-dimensional image of an object is generated from a large series of two-dimensional x-ray images taken around a single axis of rotation. Although the images generated are in the axial plane, modern scanners allow this volume of data to be reformatted in various planes or even volumetrically. A scout image is used in planning the exam and to establish where the target organs are located.

*CT Scanner Construction and Operation* Five generations of CT scanners were designed in the last few decades. The first generation used a pencil beam of x-rays and a pair of detectors that acquired simultaneous views of two adjacent axial slices across the patient. The second generation of scanners used a wider fan beam and multiple (ca. 30) detectors. In the third generation the x-ray source and the detectors rotate together around the patient. The third-generation systems are the basis of modern multislice CT scanners, which have more than one detector ring (currently, up to 64). The major benefit of multislice CT is the increased speed of volume coverage. The fourth generation uses a wide fan beam and a stationary bank of detectors. The fifth generation of CT scanners uses a very large nonstandard stationary x-ray source and a stationary detector ring, each partially surrounding the patient. A focused electron beam is swept rapidly around a semicircular tungsten target positioned below the patient: hence the name *electron beam CT*. This new type of scanner is not yet in widespread use.

There are three different modes of CT image acquisition: axial, helical, and cine. In the *axial* acquisition mode, each CT slice is taken and then the table is incremented to the next location. The *helical* scan is the most popular. Here a gantry holding the source and detector array rotates as the patient is translated along the axis of rotation. The volume is scanned very quickly because the table is in constant motion as the gantry rotates continuously. The major advantages of helical scanning compared to the traditional axial approach are speed, reduced-motion artifacts, and more optimal use of intravenous contrast enhancement. *Cine* scan consists of a time sequence of axial images. In a cine acquisition the cradle is stationary and the gantry rotates continuously, while x-rays are delivered at a specified interval and duration. A cine acquisition is used when the temporal nature is important, such as in perfusion applications to evaluate blood flow and volume.

X-ray slice data are generated using an x-ray source and x-ray detectors. The earliest sensors were scintillation detectors, with photomultiplier tubes excited by sodium iodide crystals. Modern detectors are filled with low-pressure xenon gas. Many data scans are taken progressively as the object is passed gradually through the gantry. The scans are combined by tomographic reconstruction. Data are arranged in a matrix in memory, and each data point is convolved with its neighbors using the fast Fourier transform technique. Using a backprojection method, the acquisition geometry is reversed and the results are stored in memory. The data can then be displayed, photographed, or used as input for further processing, such as multiplanar reconstruction.

CT imaging has multiple advantages:

- Very good spatial resolution.
- Complete elimination of the superimposition of images of structures outside the area of interest.
- High contrast (because of the inherent high-contrast resolution of CT, differences between tissues that differ in physical density by less than 1% can be distinguished).
- Data from a single CT imaging procedure consisting of either multiple contiguous scans or one helical scan can be viewed as images in the axial, coronal, or sagittal planes, depending on the diagnostic task (i.e., multiplanar reformatted imaging).

Although CT imaging is relatively accurate, it is liable to produce artifacts, such as the following:

1. *Aliasing artifacts or streaks* (due mainly to motion). These appear as dark lines that radiate away from sharp corners.
2. *Partial volume effect*. This appears as “blurring” over sharp edges. It is due to the scanner being unable to differentiate between a small amount of high-density material (e.g., bone) and a larger amount of lower-density material (e.g., cartilage).
3. *Noise artifact*. This appears as graining on the image and is caused by a low signal/noise ratio. This occurs most commonly when a thin slice is used.
4. *Motion artifact*. This is seen as blurring and/or streaking, which is caused by movement of the object being imaged.

5. *Beam hardening*. This can give a "cupped" appearance. It occurs when there is more attenuation in the center of the object than around the edges. This is easily corrected by filtration and software.

*Medical Applications* Since its introduction in the 1970s, CT has become an important tool in medical imaging to supplement x-rays and medical ultrasonography. Although quite expensive, it is the gold standard in the diagnosis of a large number of diseases. For example, Figure 2.2 shows a CT image of a lung tumor.

CT has more recently begun to be used for preventive medicine or disease screening. An example is the CT colonography of patients with a high risk of colon cancer. CT is used frequently for cancer staging in both diagnosis and follow-up procedures. It is also a useful test to investigate acute abdominal pain. Renal stones, appendicitis, pancreatitis, diverticulitis, abdominal aortic aneurysm, and bowel obstruction are conditions that are readily diagnosed and assessed with CT. CT is also the first line for detecting solid organ injury after trauma. Oral (usually, barium sulfate or iodinated contrast) and/or rectal contrast may be used, depending on the indications for the scan. Other agents are usually required to optimize the imaging contrast of specific organs, such as rectally administered gas (air or carbon dioxide) or fluid (water) for the colon, or oral water for stomach imaging. CT is also used in osteoporosis studies, to image complex fractures, especially those around joints, because of its ability to reconstruct the area of interest in multiple planes. Fractures, ligamentous injuries, and dislocations can

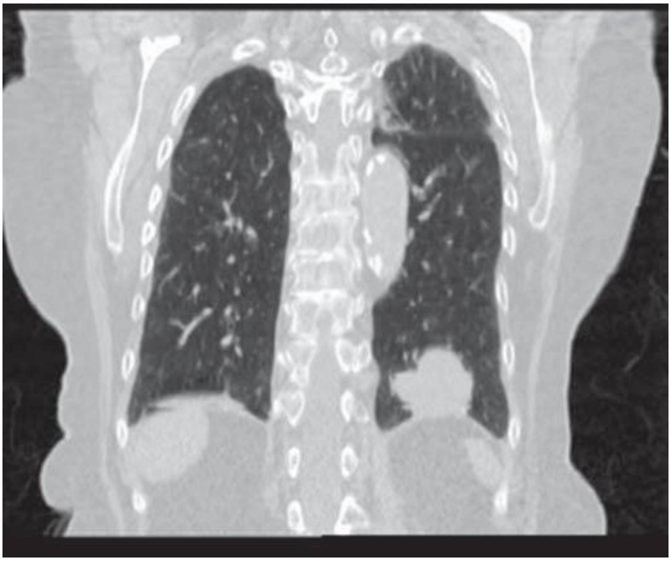

**FIGURE 2.2** Coronal chest CT image showing a lung tumor. (Courtesy of Radiation Oncology Department, Lahey Clinic.)

easily be recognized with 0.2-mm resolution. CT has limited application in evaluation of the female pelvis. For this, US and magnetic resonance are the imaging modalities of choice.

CT angiography of the chest is also becoming the primary method for detecting pulmonary embolism and cardiac problems. Cardiac CT angiography (CTA) results in a relatively high effective dose equivalent of about 12 mSv [13]. Methods are available to decrease this dose, but at the risk of compromising image quality. For comparison, the effective dose equivalent from a chest x-ray is less than 0.2 mSv, from a chest CT it is about 6 mSv, and from natural background it is about 0.01 mSv/day [14]. The *effective dose equivalent* is defined as the sum of the weighted dose equivalents for irradiated tissues or organs, where the *dose equivalent* is the product of the absorbed dose and the quality factor of the radiation. The SI unit for the effective dose equivalent is the sievert (1 Sv = 1 J/kg). The common unit is the rem (1 rem = 0.01 Sv) [15].

The significance of radiation doses in the diagnostic imaging range has not been proven, although the possibility of inducing an increased cancer risk across a population is a source of significant concern. This potential risk must be weighed against the competing risk of not performing a test and potentially not diagnosing a significant health problem. The radiation dose for a particular study depends on volume scanned, patient build, number and type of scan sequences, and desired resolution and image quality. CT imaging of children has been estimated to produce nonnegligible increases in the probability of lifetime cancer. It has been proposed that the current settings (voltage and current) for CT scans of children should be reduced [16,17]. US scanning and MRI are safer alternatives that lack the risk of radiation exposure. An important issue in radiology today is to reduce the radiation dose during CT examinations without compromising the image quality. A high radiation dose results in high-quality images, while a lower dose leads to increased noise and blurriness. Unfortunately, the radiation-induced cancer risk increases with radiation dose. Several methods to lower the patient exposure during a CT scan have been developed; for example, image filtering can be used to reduce noise [18].

### 2.2.3 Magnetic Resonance Imaging

Magnetic resonance imaging (MRI) is a relatively new technology, most commonly used in radiology to visualize the structure and function of the body. It can provide detailed images of the body in any plane. The first magnetic resonance (MR) image was published in 1973 [19], and the first study performed on a human being took place in 1977. MRI uses a powerful magnetic field to align the nuclear magnetization of (usually) hydrogen atoms in water in the body. Radio-frequency (RF) fields are used to modify the alignment of this magnetization, causing the hydrogen nuclei (i.e., protons) to produce a rotating magnetic field detectable by the scanner. This signal can be manipulated by additional magnetic fields to build up enough information to reconstruct an image of the body.

*MRI Scanner Construction and Operation* The magnet is the largest and most expensive component of the scanner, and the remainder of the scanner is built around it. The magnetic field within the center of the magnet needs to be very homogeneous. Fluctuations in the field strength within the scan region should be less than 3 parts per million. Three types of magnets have been used: a permanent magnet (up to 0.4 T), a resistive electromagnet, and a superconducting electromagnet (niobium–titanium alloy cooled to 4 K by liquid helium). Despite their cost, helium-cooled superconducting magnets are the most common type found in MRI scanners today.

Magnetic field strength is an important factor in determining image quality. Higher magnetic fields increase the signal/noise ratio, permitting higher resolution and faster scanning. However, higher field strengths require more costly magnets with higher maintenance costs and have increased safety concerns. Field strengths of 1.0 to 1.5 T are a good compromise between cost and performance for general medical use. However, for certain specialist uses (e.g., brain imaging), field strengths up to 3.0 T may be desirable.

The RF transmission system consists of an RF synthesizer, a power amplifier, and a transmitting coil. This is usually built into the body of the scanner. The receiver consists of a coil, a preamplifier, and a signal processing system. A variety of coils are available which fit around parts of the body (e.g., the head, knee, wrist, breast) or internally (e.g., the rectum). A recent achievement in MRI technology has been the development of sophisticated multielement phased-array coils which are capable of acquiring multiple channels of data in parallel [20,21]. Another interesting new technology used mainly in neurosurgery is intraoperative MRI [22].

During MRI scanning, protons found in abundance in the human body in water molecules align with the strong main magnetic field. A second electromagnetic field, perpendicular to the main field, is then pulsed to force some of the protons out of alignment with the main field. These protons then drift back into alignment with the main field, emitting a detectable RF signal. Since protons in different tissues of the body realign at different speeds, the different structures of the body can be revealed.

In the static magnetic fields commonly used in MRI, the energy difference between the nuclear spin states corresponds to a photon at RF wavelengths. Resonant absorption of energy by the protons due to an external RF oscillating magnetic field will occur at the Larmor frequency for the particular nucleus. The Larmor frequency represents the precession frequency of nuclear magnetization around the direction of the static magnetic field. For protons, the Larmor frequency is 42.58 MHz in a magnetic field of 1 T.

The net magnetization vector has two components. The longitudinal magnetization is due to a small excess of protons in the lower-energy state. This gives a net magnetization parallel to the external field. Use of an RF pulse can destroy or even reverse this magnetization vector. The transverse magnetization is due to coherences formed between the two proton energy states following an RF pulse. This gives a net magnetization perpendicular to the external field in the transverse plane. The recovery of longitudinal magnetization, called *longitudinal* or $T_1$ *relaxation*, occurs exponentially with a time constant $T_1$. The loss of phase coherence in the transverse plane is called *transverse* or $T_2$ *relaxation*. When the RF pulse is turned off, the transverse vector component produces an oscillating magnetic field which induces a small current in the receiver coil. Ideally, this signal decays approximately exponentially with a time constant $T_2$, but in practice, small inhomogeneities in the static magnetic field cause the Larmor frequency to vary across the body, creating destructive interference, which shortens the signal. The time constant for the observed decay is called the $T_2^*$ *relaxation time*; it is always shorter than $T_2$.

Gradient coils are used to spatially encode the positions of protons by varying the magnetic field linearly across the imaging volume. Typical gradient systems are capable of producing gradients from 20 to 100 mT/m. Scan speed is dependent on the performance of the gradient system. Stronger gradients allow for faster imaging and for higher resolution; similarly, gradient systems capable of faster switching can also permit faster scanning. Application of a field gradient destroys the MRI signal, but this can be recovered and measured by refocusing the gradient (to create a *gradient echo*) or by an RF pulse (to create a *spin echo*). The entire process can be repeated when some $T_1$ relaxation has occurred and the thermal equilibrium of the spins has been more or less restored. Typically, in soft tissues $T_1$ is around 1 s, while $T_2$ and $T_2^*$ are a few tens of milliseconds, but these values vary widely between different tissues (and different external magnetic fields), giving MRI its tremendous soft tissue contrast.

A number of methodologies have been devised for combining field gradients and RF excitation to create an image. The majority of MR images today are created by either the two-dimensional Fourier transform (2DFT) technique with slice selection or by the three-dimensional Fourier transform (3DFT) technique.

*Medical Applications* In MR $T_1$-weighted images of the brain, the nerve connections of white matter appear white and the congregations of neurons of gray matter appear gray, while cerebrospinal fluid appears dark. The contrast of white matter, gray matter, and cerebrospinal fluid is reversed using $T_2$ or $T_2^*$ imaging. In some situations it is not possible to generate enough image contrast to adequately show the anatomy or pathology of interest by adjusting the imaging parameters alone. In this case a contrast agent may be administered. A contrast agent may be as simple as water, taken orally, for imaging the stomach and small bowel. However, most contrast agents used in MR are selected for their specific magnetic properties. Most commonly, a paramagnetic contrast agent (usually, a gadolinium compound) is given [23]. Gadolinium-enhanced tissues and fluids appear extremely bright on $T_1$-weighted images. This provides high sensitivity for detection of vascular tissues (e.g., tumors) and permits assessment of brain perfusion (e.g., in stroke). Concerns have been raised recently regarding the toxicity of gadolinium-based contrast agents and their impact on persons with impaired kidney function. More recently, superparamagnetic contrast agents (e.g., iron oxide nanoparticles) have become available [24]. These agents appear very dark on

$T_2^*$-weighted images and may be used for liver imaging, as normal liver tissue retains the agent, but abnormal areas (e.g., scars, tumors) do not. They can also be taken orally to improve visualization of the gastrointestinal tract and to prevent water in the gastrointestinal tract from obscuring other organs (e.g., pancreas). Diamagnetic agents such as barium sulfate have also been studied for potential use in the gastrointestinal tract, but are used less frequently.

The blood–brain barrier is a complex defensive mechanism that prevents many substances circulating in the bloodstream (including some germs) from invading the brain. The blood–brain barrier is disrupted in patients with brain tumors or multiple sclerosis. MRI contrast agents cannot penetrate this barrier in normal brain tissue. This absence of contrast agent uptake in normal brain tissue provides the basis for differentiation from pathological brain tissue. MR probes (receiver coil) can be engineered with various shapes to improve the image efficiency for certain applications, such as intravascular MRI. Recently, MR probes utilizing iron oxide nanoparticles targeted to an engineered transferrin receptor have been used successfully to image gene expression [25].

MRI provides much greater contrast between the various soft tissues of the body than does CT, making it especially useful in neurological conditions, disorders of the muscles and joints, for evaluating tumors, and to show abnormalities in the heart and blood vessels. MRI is best suited for cases when a patient is to undergo the exam several times successively in the short term, because unlike CT it does not expose the patient to the hazards of ionizing radiation. While CT provides good spatial resolution, MRI provides comparable resolution with far better contrast resolution. The basis of this ability is the complex library of *pulse sequences* [26] that the modern medical MRI scanner includes, each of which is optimized to provide *image contrast* based on the chemical sensitivity of MRI:

- *Diffusion MRI* measures the diffusion of water molecules in biological tissues. This has multiple applications, such as in examining areas of neural degeneration and demyelination in diseases such as multiple sclerosis and ischemic stroke [27].
- *Magnetic resonance angiography* (MRA) is used to generate pictures of the arteries in order to evaluate them for stenosis or aneurysms [28].
- *Magnetic resonance spectroscopy* is used to measure levels of various metabolites in body tissues [29].
- *Functional MRI* measures signal changes in the brain that are due to changing neural activity. Increases in neural activity cause changes in the MR signal via $T_2^*$ changes [30].
- *Interventional MRI*. The lack of harmful effects on the patient and the operator make MRI well suited for interventional radiology, where the images produced by an MRI scanner are used to guide minimally invasive procedures [31].

For purposes of tumor detection and identification in the brain, MRI is generally superior to CT. Fine details of the human brain can be better visualized using

MRI, as can be seen in Figure 2.3. However, in the case of solid tumors of the abdomen and chest, CT is preferred, due to fewer motion artifacts. Furthermore, CT usually is more widely available, faster, much less expensive, and may be less likely to require that a person be sedated or anesthetized.

Pacemakers are generally considered an absolute contraindication toward MRI scanning, although highly specialized protocols have been developed to permit scanning of select pacing devices. Other electronic implants have varying contraindications, depending on scanner technology and implant properties, scanning protocols, and the anatomy being imaged. These may include vagus nerve stimulators, implantable cardioverter-defibrillators, loop recorders, insulin pumps, cochlear implants, deep brain stimulators, and many others. Ferromagnetic foreign bodies (e.g., shell fragments), or metallic implants (e.g., surgical prostheses, aneurysm clips) are also potential risks, and safety aspects need to be considered on an individual basis.

A powerful radio transmitter is needed for excitation of proton spins. This can heat the body to the point of risk of hyperthermia in patients, particularly in obese patients or those with thermoregulation disorders. Also, the rapid switching on and off of the magnetic field gradients is capable of causing nerve stimulation. Rapidly switched magnetic gradients interact with the main magnetic field to cause minute expansions and contractions of the coil itself, resulting in loud noises and vibrations. Appropriate use of ear protection is essential for anyone inside the MRI scanner room during the examination. Because scan times on older machines may be long (occasionally, up to 40 minutes for the entire procedure), people with even mild claustrophobia are sometimes unable to tolerate an MRI scan without management. Modern scanners have short bores and scan times are much quicker (e.g., 10 to 15 minutes for a brain scan, depending on the MR sequences used). No harmful effects of MRI on the fetus have been demonstrated. However, as a precaution, current guidelines recommend that pregnant women undergo MRI only when essential.

### 2.2.4 Nuclear Medicine

***Positron Emission Tomography*** Positron emission tomography (PET) is a nuclear medicine imaging technique that produces a three-dimensional image or map of functional processes in the body [32]. The system detects pairs of gamma rays emitted indirectly by a positron-emitting radionuclide (tracer), which is introduced into the body on a biologically active molecule. Images of tracer concentration in three-dimensional space within the body are then reconstructed by computer analysis.

*PET Scanner Operation Principle* Radionuclides used in PET scanning are typically isotopes with short half-lives, such as carbon-11 (ca. 20 min), nitrogen-13 (ca. 10 min), oxygen-15 (ca. 2 min), and fluorine-18 (ca. 110 min). The positron-emitting radioactive isotope, incorporated chemically into a biologically active molecule, is injected into the patient (usually, into blood circulation). These

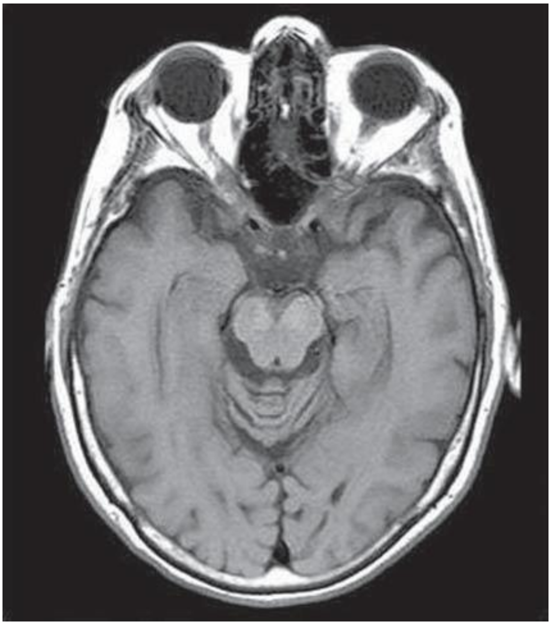

(a)

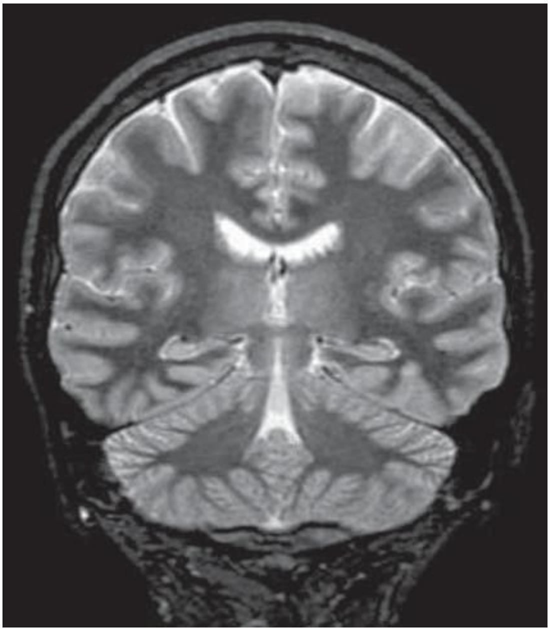

(b)

**FIGURE 2.3** Brain MR images: (a) axial plan; (b) coronal plan; (c) sagittal plan. (Courtesy of Radiation Oncology Department, Lahey Clinic.)

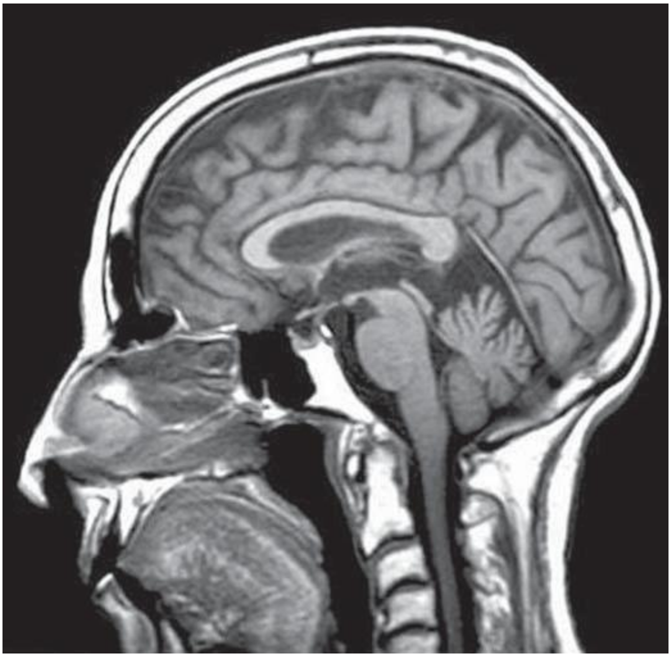

(c)

**FIGURE 2.3** (*Continued*)

radionuclides are incorporated either into compounds (radiotracers) normally used by the body, such as glucose, water, or ammonia, or into molecules that bind to receptors or other sites of drug action. Due to the short half-lives of most radioisotopes, the radiotracers must be produced using a cyclotron and radiochemistry laboratories that are in close proximity to the PET imaging facility. The half-life of fluorine-18 is long enough such that fluorine-18-labeled radiotracers can be manufactured commercially at an off-site location. There is a waiting period while the active molecule becomes concentrated in tissues of interest; then the patient is placed in the imaging scanner.

The molecule most commonly used for PET is fluorodeoxyglucose (FDG), for which the waiting period is typically 1 hour. The concentration of tracer imaged gives tissue metabolic activity in terms of regional glucose uptake. The radioisotope concentrated in tissues of interest undergoes positive beta decay. After traveling up to a few millimeters, the positron emitted encounters an electron and is annihilated, producing simultaneously a pair of annihilation photons moving in opposite directions. These are detected when they reach a scintillator material in the scanning device, creating a burst of light that is detected by photomultiplier tubes or silicon avalanche photodiodes. The detection technique, termed the *coincidence technique*, depends on coincident detection of the pair of photons; photons that do not arrive in pairs (i.e., within a few nanoseconds) are ignored. The most significant fraction of electron-positron decays result in two 511-keV gamma photons being emitted at almost 180° to each other; hence, it is possible to localize their source along a straight line of coincidence. Early PET scanners had only a single ring of detectors; hence, the acquisition of data and subsequent reconstruction was restricted to a single transverse plane. Modern scanners now include multiple rings, essentially forming a cylinder of detectors.

The raw data collected by a PET scanner are a list of *coincidence events* representing nearly simultaneous detection of annihilation photons by a pair of detectors. Each coincidence event represents a line in space connecting the two detectors along which positron emission occurred. Coincidence events can be grouped into projection images called *sinograms*, which are analogous to the projections captured by CT scanners and can be reconstructed similarly. However, the statistics of the data are much worse than those obtained through transmission tomography. In practice, considerable preprocessing of the data is required: correction for random coincidences, estimation and subtraction of scattered photons, detector dead-time correction, and detector-sensitivity correction [33,34]. Filtered backprojection has often been used to reconstruct images from the projections. This algorithm has the advantage of being simple while having a low requirement for computing resources. Iterative expectation-maximization algorithms are now the preferred method of reconstruction. The advantage is a better noise profile and fewer streak artifacts, but the disadvantage is higher computer resource requirements.

The photons are attenuated differentially by traversing different thicknesses of tissue. Contemporary scanners can perform attenuation correction using integrated x-ray CT equipment. PET scans are read increasingly alongside CT or MRI scans, the combination (*co-registration*) giving both anatomic and metabolic information. Because PET imaging is most useful in combination with anatomical imaging, such as CT, modern PET scanners are now available with integrated high-end multiple-detector-row CT scanners. Because the two scans can be performed in immediate sequence during the same session, with the patient not changing position between the two types of scans, the two sets of images are registered more precisely (see Figure 2.4), so that areas of abnormality on the PET imaging can be better correlated with anatomy on the CT images.

*Medical Applications* While some imaging scans such as CT and MRI isolate organic anatomical changes in the body, PET scanners are capable of detecting areas of molecular biology detail, even prior to anatomical change. PET is both a medical and a research tool, used, for example, in mapping normal human brain and heart function. It is used frequently in clinical oncology and for clinical diagnosis of certain diffuse brain diseases (such as dementia). FDG-PET is used for diagnosis, staging, and monitoring treatment of cancers, particularly Hodgkin's disease, non-Hodgkin's lymphoma, and lung cancer. PET neuroimaging (see Figure 2.5) is based on the assumption that areas of high radioactivity are associated with brain activity.

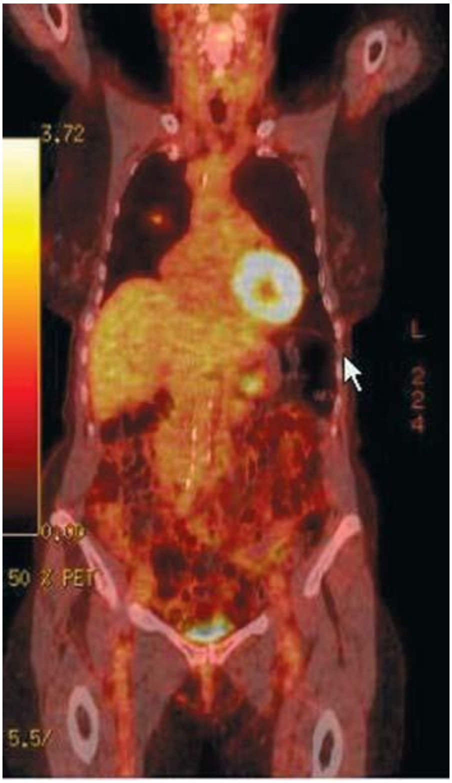

**FIGURE 2.4** Coronal full-body PET-CT image. (Courtesy of Radiation Oncology Department, Lahey Clinic.)

What is actually measured indirectly is the blood flow to various parts of the brain, which is generally believed to be correlated and has been measured using the tracer oxygen-15. Standard FDG-PET of the brain may also be used for early diagnosis of Alzheimer's disease [35]. In clinical cardiology, FDG-PET can identify hibernating myocardium and atherosclerosis. PET scanning is noninvasive, but it does involve exposure to ionizing radiation. The total dose of radiation is small, however, usually around 7 mSv. Patients with small children may be advised to limit proximity to them for several hours following completion of the test.

***Single-Photon Emission Computed Tomography*** Single-photon emission computed tomography (SPECT) is a nuclear medicine tomographic imaging technique using gamma rays. The gamma-ray emitter is an intravenous injected radioisotope, usually thallium-201 or technetium-99m, coupled to a pharmaceutical. This technique provides three-dimensional information presented as cross-sectional slices through the patient.

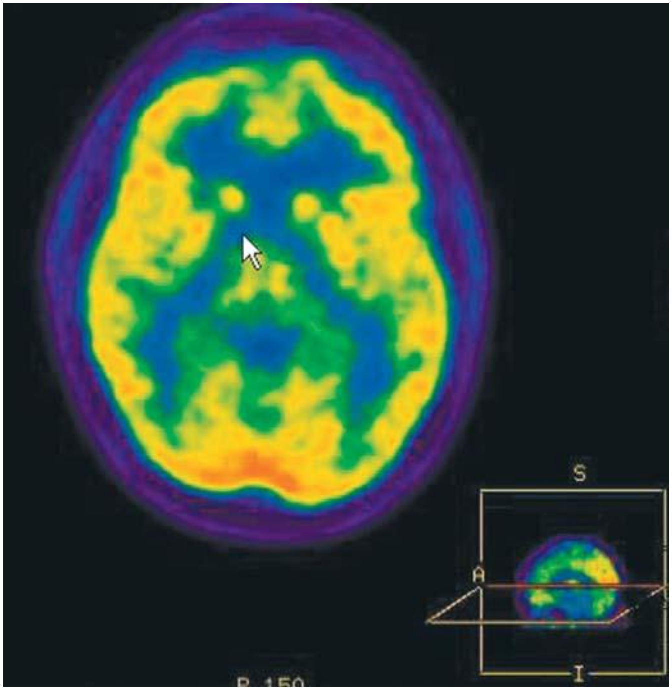

**FIGURE 2.5** Axial brain PET-CT image. (Courtesy of Radiation Oncology Department, Lahey Clinic.)

*SPECT Scanner Operation Principle and Medical Applications* SPECT imaging is performed using a gamma camera to acquire multiple two-dimensional images, from multiple angles. Projections are acquired typically every 3 to 6°. In most cases, a full 360° rotation is used to obtain an optimal reconstruction. A gamma camera is a device used to image gamma radiation–emitting radioisotopes. It consists of one or more flat crystal detectors, coupled optically to an array of photomultiplier tubes, mounted on a gantry. The gantry is connected to a computer system that controls both operation of the camera and acquisition and storage of images acquired.

The system accumulates events (counts) of gamma photons that are absorbed by the crystal (sodium iodide with thallium doping) in the camera. The crystal scintillates in response to incident gamma radiation. The light emitted is detected by the photomultiplier tubes, located behind the crystal. Multiheaded gamma cameras can provide accelerated SPECT acquisition. A computer is used to apply a tomographic reconstruction algorithm (filtered backprojection) to the multiple projections, yielding a three-dimensional data set. This reconstructed image reflects the distribution and relative concentration of radioactive tracer elements present in the organs and tissues imaged. The pixel size ranges from 3 to 6 mm. Movement can cause significant degradation of the reconstructed images. Modern SPECT equipment is available with an integrated x-ray CT scanner. Molecular imaging with SPECT/CT seems to be a complete reversal of traditional SPECT imaging, because newly developed SPECT tracers are target specific. SPECT can be used to complement any gamma imaging study, where a true three-dimensional representation can be helpful [e.g., for tumor imaging, infection (leukocyte) imaging, thyroid imaging, bone imaging, cardiac imaging, brain imaging] [36].

It is interesting to compare briefly the two main techniques used in nuclear medicine. PET offers imaging characteristics substantially superior to those of SPECT, resulting in higher diagnostic accuracy. In addition, the examination time using PET is shorter. The PET procedure in general has a higher sensitivity and specificity than SPECT, but also a higher cost [37]. Over the last few years the SPECT technique has improved. Recently, it was found that bone SPECT is superior to FDG PET in detecting bone metastases in breast cancer, having a higher sensitivity and a comparable specificity [38].

## 2.3 IMAGING FOR RADIATION THERAPY PLANNING

Radiation therapy is an essential tool in the cancer treatment arsenal. More than 1 million patients undergo radiation therapy in the United States each year, and recent improvements in instrumentation have increased the clinical utility of this treatment modality. The traditional imaging modalities described in previous sections have multiple applications in various subfields of radiation oncology, such as brachytherapy and external beam radiation therapy.

### 2.3.1 Ultrasound, CT, and MR Imaging in Brachytherapy

Brachytherapy is a treatment modality used in radiation oncology in which sealed radioactive sources are employed to deliver a localized radiation dose by interstitial, intracavitary, or surface application. The radioactive sources can have a low dose rate (LDR) or a high dose rate (HDR). The LDR (dose rate $\sim$0.5 to 2 cGy/min) implants can be temporary or permanent. The most common radioisotopes used for LDR treatments are iodine-125 radioactive seeds for permanent implants; and cesium-137 and iridium-192 ribbons for temporary implants. The HDR (dose rate>20 cGy/min) implants are done using automatic afterloaders, the source (high-activity iridium-192) being inserted into the tumor only for a very short time (minutes).

Multiple imaging modalities may be necessary to visualize the area to be treated and to deliver the radiation. With the patient in an operational room under general or local anesthesia, catheters or needles (for interstitial treatments) and special intracavitary applicators (for intracavitary treatments) are inserted into the tumor. The applicator insertion is usually performed using image-guided techniques (US or C-arm fluoroscopy). In traditional brachytherapy the applicators placed into the tumor are visualized by fluoroscopy. Dummy wires containing metallic seeds which can be visualized easily on the x-ray films are used to simulate the real radioactive source positions. X-ray films are taken with the dummy wires placed inside the applicators and the dummy dwell positions are digitized in treatment planning software. The dose prescribed at a certain distance from the applicator is achieved by varying source location, source activity, or dwell times [15,39].

In modern brachytherapy, US, CT, or MR images are used to visualize the tumor and to perform the treatment planning. For example, real-time US imaging is used for LDR permanent radioactive seed implant for prostate carcinoma. Metallic needles are inserted intraperineally into the prostate via a template using US and C-arm fluoroscopy guidance. Low-activity iodine-125 seeds are inserted permanently into the tumor through these needles. The real-time US images are transferred to treatment planning software, contours are drawn for the prostate and urethra, and the seed distribution is replicated on the images to estimate the dose delivered to the prostate (see Figure 2.6). The physicist estimates on the fly the dose to the prostate, and this feedback aids in establishing the number of needles, seeds, and seed location needed to achieve the dose prescribed.

HDR treatments for prostate cancer are usually performed using CT images. The needles are inserted into the prostate similar to the method used for LDR implants, and then CT images are acquired and imported into the treatment planning computer. Contours are usually drawn for tumor (prostate) and critical structures (urethra and rectum). Optimized distribution of the radioactive sources is generated in the treatment planning, with the purpose of covering the tumor

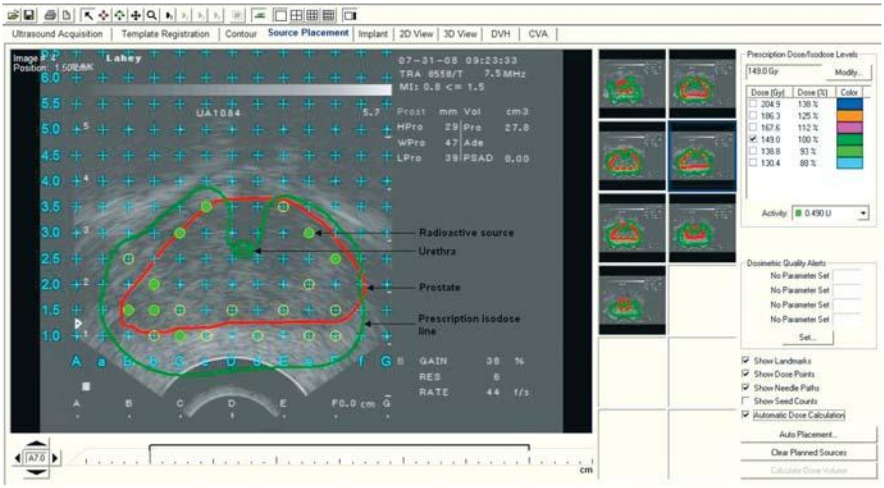
Ultrasound Acquisition
Template Registration
Contour
Source Placement
Implant
2D View
3D View
DVH
CVA
Lahey
UA1084
Radioactive source
Urethra
Prostate
Prescription isodose line
A a B b C c D d E e F f G
A B C D E F0.0 cm G
6.0 5.5 5.0 4.5 4.0 3.5 3.0 2.5 2.0 1.5 1.0
cm
A7.0
Modify...
Set...
Auto Placement...
Clear Planned Sources
Calculate Dose Volume

07-31-08 09:23:33
TRA 8558/T 7.5MHz
MI: 0.8 <= 1.5

Prost mm Vol cm3
HPro 29 Pro 27.8
WPro 47 Ade
LPro 39 PSAD 0.00

GAIN 38 %
RES 6
RATE 44 f/s

Prescription Dose/Isodose Levels: 149.0 Gy

| Dose (Gy) | Dose (%) | Color |
|---|---|---|
| ☐ 204.9 | 138 % | 🟦 |
| ☐ 186.3 | 125 % | 🟧 |
| ☐ 167.6 | 112 % | 🟪 |
| ☑ 149.0 | 100 % | 🟩 |
| ☐ 138.8 | 93 % | 🟩 |
| ☐ 130.4 | 88 % | 🟦 |

Activity: 0.490 U

Dosimetric Quality Alerts
No Parameter Set
No Parameter Set
No Parameter Set
No Parameter Set

☑ Show Landmarks
☑ Show Dose Points
☑ Show Needle Paths
☐ Show Seed Counts
☑ Automatic Dose Calculation

**FIGURE 2.6** Brachytherapy US axial image. Prostate and urethra are contoured. Circles represent the needles (which are placed in the tumor using a template). They are loaded with seeds (filled circles) to provide the prescribed dose at the periphery of the prostate while sparing the urethra. (Courtesy of Radiation Oncology Department, Lahey Clinic.)

with the prescribed dose and reducing the dose to critical structures and normal tissue. Figure 2.7a shows an axial cut through the prostate and the corresponding coronal and sagittal projections. The arrows drawn on the coronal plan indicate the prostate (color wash), the prescription isodose line, and a needle loaded with radioactive sources. For HDR treatment of vaginal carcinoma, a dummy wire is placed inside the intracavitary applicator (vaginal cylinder) inserted into the vagina under local anesthesia. CT images are taken and used for treatment planning to optimize the source dwell times and deliver the desired dose to the vaginal wall (Figure 2.7b). Cervical carcinomas can be treated using either LDR

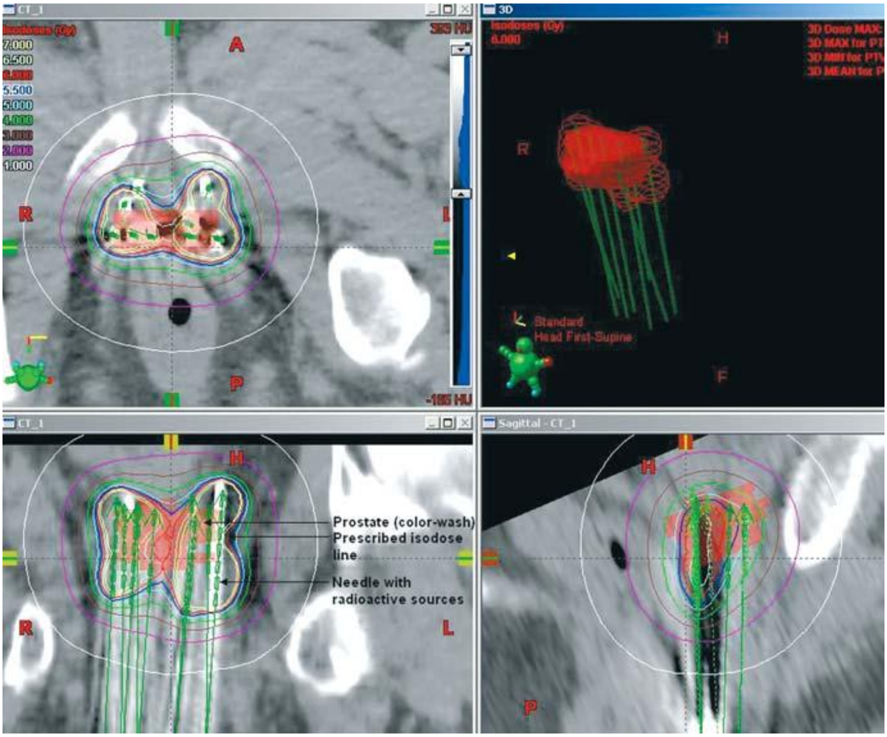
CT_1
Isodoses (Gy)
7.000
6.500
6.000
5.500
5.000
4.000
3.000
2.000
1.000
A
R
L
P
369 HU
-185 HU
3D
Isodoses (Gy)
6.000
H
3D Dose MAX:
3D MAX for PT
3D MIN for PTV
3D MEAN for P
R
Standard
Head First-Supine
F
CT_1
H
Prostate (color-wash)
Prescribed isodose line
Needle with radioactive sources
R
L
Sagittal - CT_1
H
P

(a)

**FIGURE 2.7** Brachytherapy CT images. (a) Prostate cancer treatment planning. Arrows drawn on the coronal plan indicate the prostate (color wash), the prescription isodose line, and a needle loaded with radioactive sources. The dwell positions and dwell time of the radioactive source in each needle are simulated in the plan to achieve the prescribed dose to the tumor while sparing critical structures such as the urethra and rectum. (b) Vaginal cancer treatment planning. The vaginal insert (cylinder) is in place. The dwell positions and dwell time of the radioactive source are simulated to achieve the prescribed dose distribution around the vaginal wall. (Courtesy of Radiation Oncology Department, Lahey Clinic.)

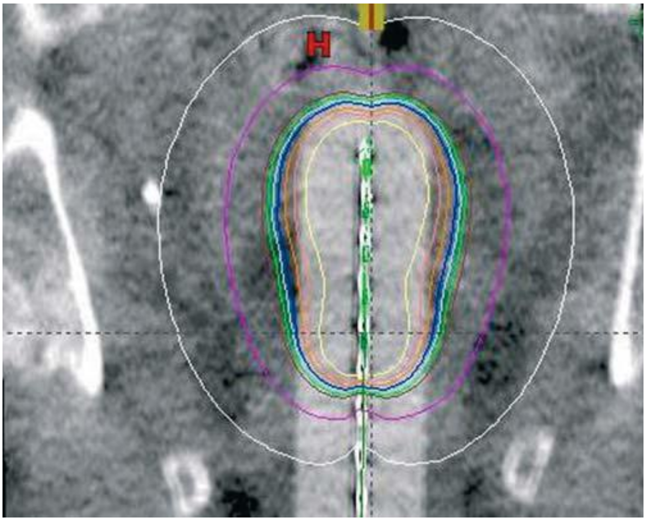

(b)

**FIGURE 2.7** (*Continued*)

or HDR techniques. US images are taken to estimate the length of the uterus prior to intracavitary applicator insertion. An MR-compatible dummy insert is placed inside the intracavitary applicator and then MR images are acquired and used for treatment planning. MR images are preferred since they can better visualize soft tissues. MR-CT fusion should be used to enhance the image contrast for both soft tissue (tumor and organs of risk) and the applicators.

### 2.3.2 CT, MR, and PET Imaging in External Beam Radiation Therapy

External beam radiation therapy is a treatment approach that has been used in the radiation oncology field since the discovery of x-rays. The radiation beams (electrons or photons) are currently generated in linear accelerator (LINAC) machines. Electrons are extracted from a metallic filament by thermionic emission and then accelerated in a waveguide up to a desired energy. Magnetic fields are used for beam stirring. In modern multienergy machines, the electron beam that exits the horizontal waveguide is bent vertically down (90 or 270°) in a magnetic field, then hits a *scattering foil* used to flatten the cross-sectional beam profile, which otherwise will have a Gaussian-like shape. This flattened beam is then collimated using special collimation systems and directed toward the patient for treatment delivery. The photon beams are created through a *bremsstrahlung* process: the electron beam created as described above hits a target made from a high-atomic-number material. Photons with a continuous energy spectrum are emitted as a result of electronic interactions in the target material. The photon beam is flattened using a *flattening filter*, collimated, and used for treatment [15,40,41].

Modern treatment machines can deliver multiple electron and photon energies. The most common energies for electron beams are in the range 4 to 20 MeV. Electron fields are used primarily to treat superficial tumors or as a boost to treat scar tissue after the tumor or tumor bed have been treated using photon beams. The maximum distance (in centimeters) the electrons can travel in tissue is given approximately by the electron energy (in MeV) divided by 2. The penetration depth increases with energy and is much larger for photon beams than for electron beams. The most common photon energies used for radiotherapy treatments are 6, 10, and 15 MeV. The photon energy of 10 MeV is approximately the threshold for a photon–neutron nuclear reaction. The probability for neutron production increases rapidly with energy for photon energies higher than 10 MeV. Since the neutrons are very dangerous for patients and personnel, it is not a good practice to perform treatments using photons with energy higher than 15 MeV. LINAC machines are accommodated in shielded rooms to reduce the personnel dose to a safety limit [15]. The wall thickness, and consequently the shielding cost, increase with energy. Also, more costly shielding materials must be used if neutrons are involved.

The radiotherapy treatment is delivered in multiple fractions (usually, 25 to 35) to allow radiation-induced normal tissue damage to be repaired [14]. The prescribed dose is usually in the range 180 to 200 cGy per fraction. Another treatment technique, called *stereotactic radiosurgery*, used initially only for brain lesions, has been expanded to treat extracranial tumors. This technique uses mostly a 6-MeV photon beam. The treatment is delivered in only a few fractions (1 to 5), with a high dose per fraction (6 to 20 Gy) and a high dose rate (6 to 10 Gy/min). Also, protons and heavy ions can be used for radiotherapy treatments, but these techniques are not yet in widespread use [15].

A few steps are required for radiotherapy treatment. First, the patient is imaged for diagnosis. If the physician decides that the disease (malignant or benign) can be treated using radiation, the patient is *simulated* to create a treatment plan. The simulation process involves acquisition of a new set of images (CT, or CT in combination with MR or PET), acquired using the same setup as the one that will be used for treatment. A flat couch top similar to the one used for treatment is used when these images are acquired and the patient is immobilized in the same way that she or he will be during treatment. Using these images the physician draws the tumor volume. A point called an *isocenter* is placed inside the tumor. The coordinates of this point are exported to the CT external laser system, and the patient receives permanent tattoos in three points, where two perpendicular laser beams intersect each other on the patient's skin. These tattoos will help in daily treatment setup. The images are then used by physicists or dosimetrists to create a treatment plan. The images acquired are imported into treatment planning software and a virtual simulation is performed, during which beam orientation and field size are defined. The treatment is delivered in one or multiple fractions using static (coplanar or noncoplanar) beams or arcs. Figure 2.8 shows a Varian LINAC machine. The patient is placed and immobilized on the machine couch in "treatment position." The radiation produced in the machine head is collimated

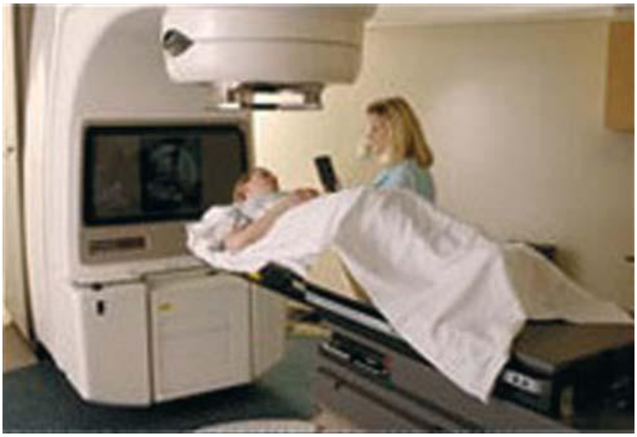

**FIGURE 2.8** Varian LINAC machine. The patient is placed and immobilized on the machine couch in "treatment position." The radiation produced in the machine head is collimated and directed toward the area to be treated. The beam field size is shaped as simulated in the treatment plan using special blocks (see the text for details). (Courtesy of Radiation Oncology Department, Lahey Clinic.)

(using a primary and a secondary collimator) and directed toward the area to be treated. The beam field size is shaped as simulated in the treatment plan using special blocking. For Varian machines, this special blocking system is a "tertiary" collimator, also located in the machine head. Because of its design, this is called a multileaf collimator (MLC). The MLC leaves are motorized so that they can move independently and help to collimate and fit the beams around the tumor, even for unusual tumor shapes. The medical LINAC design and functions are described elsewhere in detail [15,40,41].

The goal of each treatment protocol is to deliver a prescribed dose to the tumor while sparing the critical structures and normal tissues. Besides the tumor, the physician and the physicists/dosimetrists will contour some organs of risk. The physician draws the gross tumor volume (GTV), and then some margins are added to account for microscopic disease. The new structure is called the *clinical target volume* (CTV). To account for setup and dosimetric uncertainties, and also roughly for tumor motion, new margins are added to the CTV, generating the *planning target volume* (PTV). Many tumors (located primarily in the chest and abdomen) are prone to motion, which is caused mainly by breathing. New methodologies were developed to take the tumor motion into consideration during treatment delivery (intrafraction motion) or between fractions (interfraction motion). One way to deal with this problem is to acquire three sets of CT images (free breathing, exhale, and inhale) and fuse them together. The tumor defined using these fused images will generate the *internal target volume* (ITV), which gives the envelope of tumor location during a respiratory cycle. Tumor motion is a very complicated problem that can drastically affect the treatment outcome. If the target localization is uncertain, the dose conformality is meaningless. Another way to take the tumor motion into account is to use a four-dimensional CT scanner in cine mode. The respiratory cycle is recorded using a tracking system and divided in phases. At a certain couch position, images are acquired for all phases of the respiratory cycle. The images can be played as a cine loop and the physician can visualize the tumor motion. Using this movie, an ITV can be drawn and used for treatment. Alternatively, the physician may decide to gate the treatment (i.e., to treat the patient only during that portion of the respiratory cycle when the tumor is most stable) [42,43].

The use of CT to define and localize anatomical structures for radiotherapy simulation and treatment planning has become standard practice over the past decade. CT has played a revolutionary role in establishing *three-dimensional conformal radiotherapy* by providing a three-dimensional geometry model of the patient for target and critical structures delineation, beam placement, dose calculations, and plan evaluation (see Figure 2.9). In three-dimensional conformal radiotherapy, multiple (coplanar or noncoplanar) beams are aimed toward the same point in the tumor (the isocenter). Using blocks, the field size for each beam is shaped to fit around the tumor. The dose delivered to the tumor through all beams can be sculpted in three-dimensions to cover the tumor with certain margins, which are included to take into account the uncertainties for setup, dosimetry, and eventually tumor motion, as described above.

Often, CT images alone are not sufficient for cancer delineation. PET has added biological and metabolic information to the radiotherapy process to facilitate target definition and treatment assessment (Figure 2.10). Unfortunately, the spatial resolution for PET images is poor. These images can be used qualitatively for staging and nodal assessment, but not for a very accurate delineation of the tumor. PET imaging in radiation oncology has been performed so far exclusively with FDG, being effective in evaluation of tumors in lung, colon and rectum, breast, head and neck, esophagus, pancreas, and melanoma and lymphoma [44].

MR images provide superior image quality for soft tissue delineation compared with CT images (see Figure 2.11). MR-CT fusion has been widely adopted for accurate anatomical delineation (using MRI) and dose calculation (using CT). Special MR sequences such as functional MRI and MR spectroscopy can provide information about vasculature change, blood flow, and oxygen use, which can be used in target definition and treatment assessment.

## 2.4 IMAGE-GUIDED RADIATION THERAPY

Despite significant progress in radiation oncology treatment, there are still situations where patient or organ motion limits the dose that can be delivered safely to the tumor without damaging adjacent radiosensitive organs such as bladder, heart, spinal cord, and others. There have been significant recent advances in this area, such as the development of implantable markers, introduction of respiratory gating, and advances in image-guided radiation therapy [42,43]. Guiding

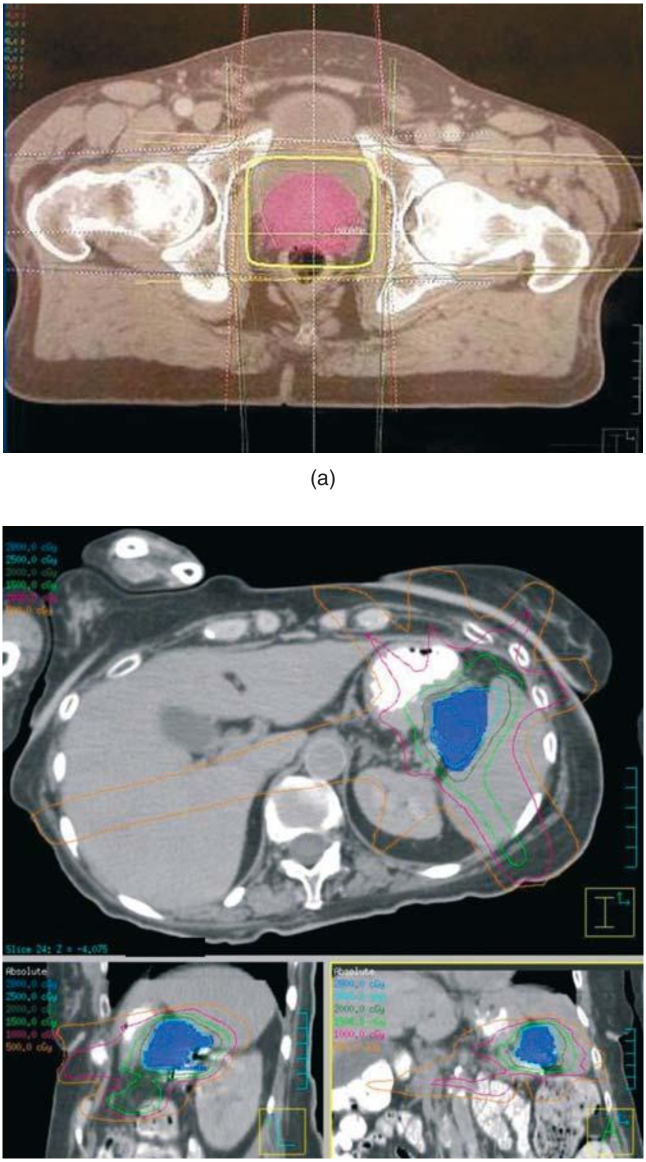

(a)

(b)

**FIGURE 2.9** External beam radiation therapy CT images. (a) Three-dimensional conformal treatment planning for prostate cancer. Four coplanar beams were used for this treatment. The prostate (color wash) was covered with the prescribed dose. (b) Three-dimensional conformal stereotactic body radiation therapy treatment planning for pancreatic cancer. Beam arrangement and weight are simulated in the plan to deliver the prescribed dose to the tumor while sparing the critical structures. Multiple noncoplanar beams were used for this treatment. (Courtesy of Radiation Oncology Department, Lahey Clinic.)

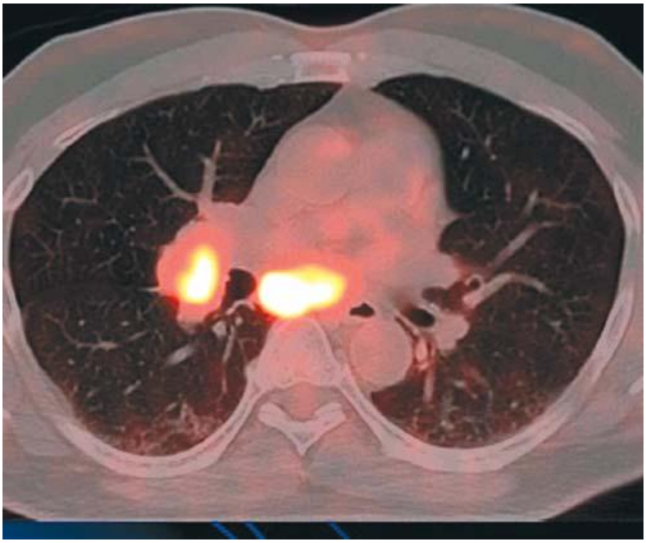

**FIGURE 2.10** Axial PET image showing the FDG intake for a lung tumor. (Courtesy of Radiation Oncology Department, Lahey Clinic.)

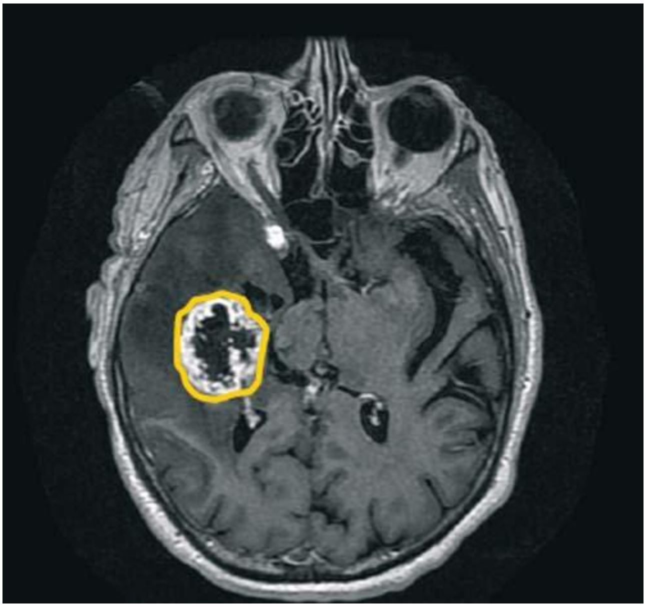

**FIGURE 2.11** Axial MR image showing brain metastases. (Courtesy of Radiation Oncology Department, Lahey Clinic.)

the placement of the treatment field is not a new concept. Since the advent of fractionated radiation therapy for the treatment of disease, techniques have been employed to help ensure the accurate placement of a treatment field. In the past, the treatment setup was performed using the patient tattoo, done during the simulation. Portal films were taken for each beam to verify the correctness of treatment position. Today, using advancements in digital imaging devices, the use of electronic portal imaging has developed into both a tool for accurate field placement and as a quality assurance tool for review by radiation oncologists during check film reviews. Electronic portal imaging (EPI) is the process of using digital imaging, such as a CCD video camera, liquid ion chamber, and amorphous silicon flat-panel detectors to create a digital image with improved quality and contrast over traditional portal imaging. The benefit of the system is the ability to capture images, for review and guidance, digitally. The same x-ray source (MeV energy range), located in the LINAC head, can be used for both treatment and portal films/EPI setup verification.

Image-guided radiation therapy (IGRT) can reduce the setup uncertainties, allowing for further tumor dose escalation and conformality and decreased dose to surrounding healthy tissues, which will lead to improved treatment outcome. IGRT is the process of frequent two- and/or three-dimensional imaging during a course of radiation treatment. The patient is localized in the treatment room in the same position as planned from the reference imaging data set (images used for treatment planning). The IGRT images are compared with the images taken for treatment planning. The patient shifts (in the $x$, $y$, and $z$ directions) needed for a perfect match are calculated by the software. Two basic correction strategies are used in determining the most beneficial patient position and beam structure: online and off-line correction. The online strategy makes adjustment to patient and beam position during the treatment process, based on continuously updated information throughout the procedure. The off-line strategy determines the best patient position through data gathered during treatment sessions.

Recently, the EPI was complemented with megavoltage (MV) or kilovoltage (kV) images, either CT, cone-beam computed tomography (CBCT), or kV fluoroscopic images. CBCT-based IGRT systems have been integrated with medical linear accelerators to great success. An additional x-ray source (kV energy range) is engaged to acquire kV and CBCT images. With improvements in flat-panel technology, CBCT has been able to provide volumetric imaging and allows for radiographic or fluoroscopic monitoring throughout the treatment process [43]. An example of three-dimensional IGRT would include localization of a CBCT data set with the treatment planning CT data set. Similarly, two-dimensional IGRT would include matching planar kV radiographs or MV images with digital reconstructed radiographs (DRRs) from the planning CT. (A DRR is a simulation of a conventional two-dimensional x-ray image, created from CT data.) The matching for CT-CT or CBCT-CT images is based on either soft tissue or bony structures (Figure 2.12), while high-atomic-number implanted fiducials can be used for kV–kV image matching (Figure 2.13).

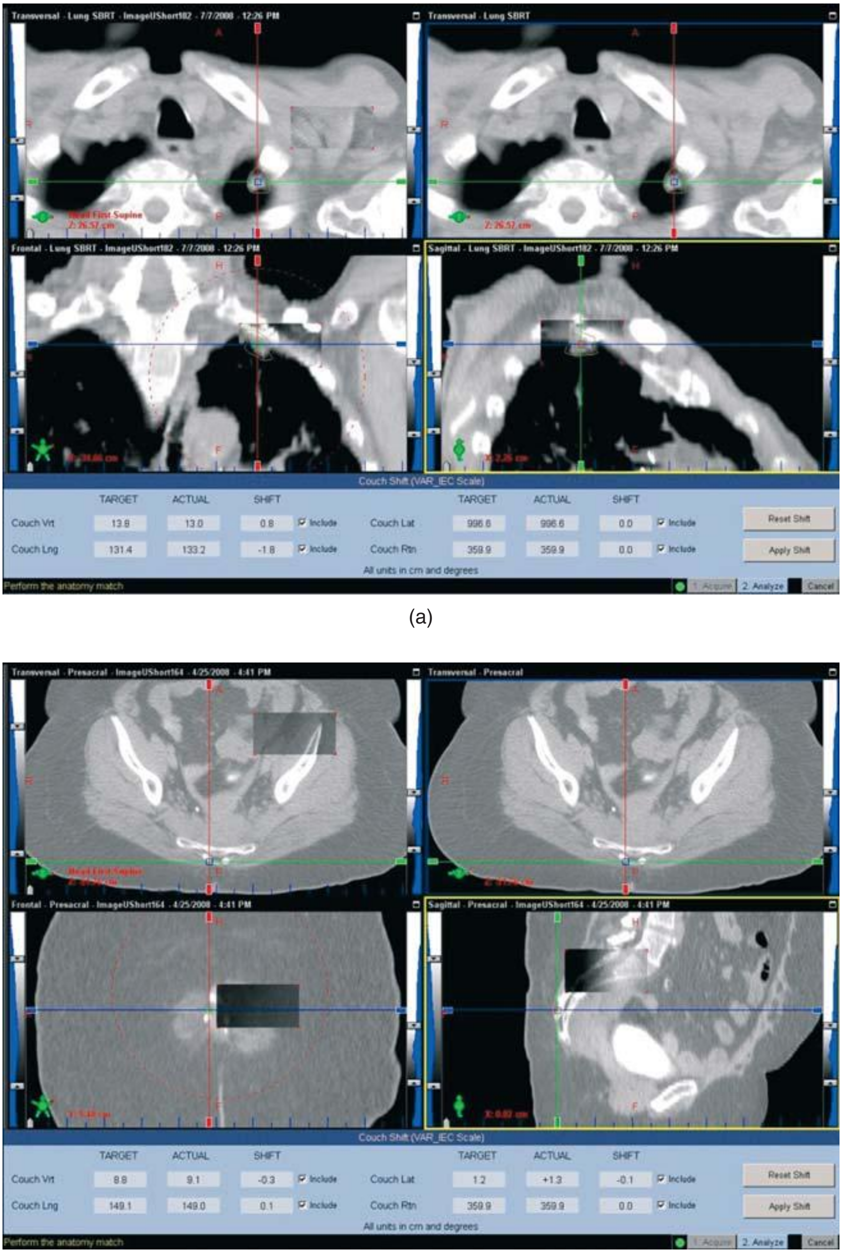
Transversal - Lung SBRT - ImageUShort182 - 7/7/2008 - 12:26 PM
Transversal - Lung SBRT
Head First Supine
Z: 26.57 cm
Frontal - Lung SBRT - ImageUShort182 - 7/7/2008 - 12:26 PM
Sagittal - Lung SBRT - ImageUShort182 - 7/7/2008 - 12:26 PM
A
R
P
H
F
Transversal - Presacral - ImageUShort164 - 4/25/2008 - 4:41 PM
Transversal - Presacral
Head First Supine
Frontal - Presacral - ImageUShort164 - 4/25/2008 - 4:41 PM
Sagittal - Presacral - ImageUShort164 - 4/25/2008 - 4:41 PM
X: 0.02 cm
Reset Shift
Apply Shift
1. Acquire
2. Analyze
Cancel

Couch Shift (VAR_IEC Scale)

|  | TARGET | ACTUAL | SHIFT |  |  | TARGET | ACTUAL | SHIFT |  |
|---|---|---|---|---|---|---|---|---|---|
| Couch Vrt | 13.8 | 13.0 | 0.8 | ☑ Include | Couch Lat | 996.6 | 996.6 | 0.0 | ☑ Include |
| Couch Lng | 131.4 | 133.2 | -1.8 | ☑ Include | Couch Rtn | 359.9 | 359.9 | 0.0 | ☑ Include |

All units in cm and degrees

Perform the anatomy match

(a)

Couch Shift (VAR_IEC Scale)

|  | TARGET | ACTUAL | SHIFT |  |  | TARGET | ACTUAL | SHIFT |  |
|---|---|---|---|---|---|---|---|---|---|
| Couch Vrt | 8.8 | 9.1 | -0.3 | ☑ Include | Couch Lat | 1.2 | +1.3 | -0.1 | ☑ Include |
| Couch Lng | 149.1 | 149.0 | 0.1 | ☑ Include | Couch Rtn | 359.9 | 359.9 | 0.0 | ☑ Include |

All units in cm and degrees

Perform the anatomy match

(b)

**FIGURE 2.12** CBCT-CT matching. The CBCT images are superimposed on the CT images used for treatment planning. (a) Soft tissue (tumor) or (b) bony anatomy (backbone) are used as reference. The software calculates patient shifts in the $x$, $y$, $z$ directions to achieve the match desired. (Courtesy of Radiation Oncology Department, Lahey Clinic.)

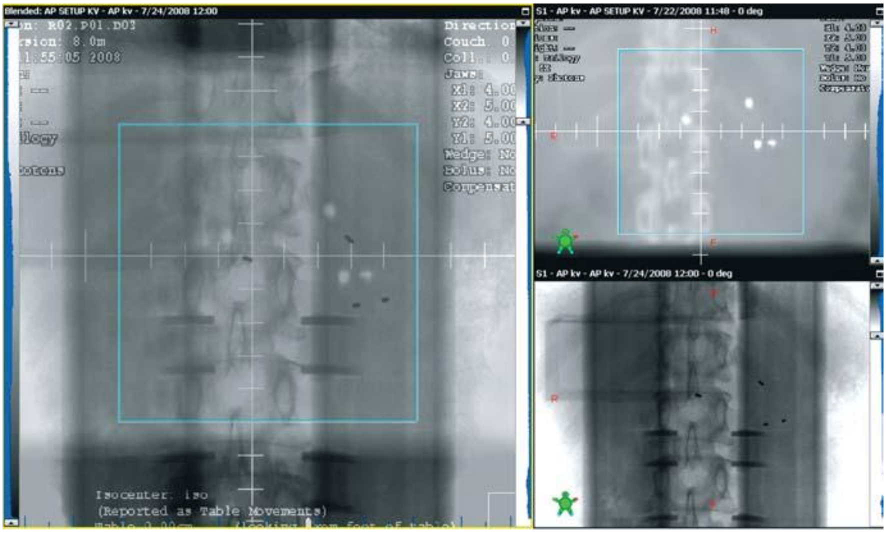
Blended: AP SETUP KV - AP kv - 7/24/2008 12:00
S1 - AP kv - AP SETUP KV - 7/22/2008 11:48 - 0 deg
S1 - AP kv - AP kv - 7/24/2008 12:00 - 0 deg
Direction
Couch
Coll
Jaws
X1: 4.00
X2: 5.00
Y2: 4.00
Y1: 5.00
Wedge: No
Bolus: No
Isocenter: iso
(Reported as Table Movements)

**FIGURE 2.13** kV–kV image matching using high-atomic-number implanted fiducials. Two orthogonal kV images taken prior to treatment are superimposed on the corresponding DRRs obtained from the CT images used for treatment planning. The fiducials are seen on both sets of images (white dots on the DRR images, black dots on the kV images). The software calculates patient shifts in the $x$, $y$, and $z$ directions to achieve the desired match. (Courtesy of Radiation Oncology Department, Lahey Clinic.)

As discussed in a previous section, the main disadvantage of using CT imaging is patient irradiation. The patient exposure increases even further if the IGRT technology is used for treatment setup. To justify the use of IGRT, the benefit should overcome this negative aspect. The IGRT clinical benefit for the patient is the ability to monitor and adapt to changes that may occur during the course of radiation treatment. Such changes can include tumor shrinkage or expansion, or changes in the shape of the tumor and surrounding anatomy. Alternatively, to reduce patient exposure, the fiducials can be replaced with magnetic transponders, detectable with an external ac (alternating current) magnetic array. This would allow for continuous monitoring of the target position without the need of x-rays [1].

## 2.5 CONCLUSIONS

CT is currently the main imaging modality used in traditional clinical medicine. Other imaging technologies, such as MR and PET, complement the anatomical information with functional and metabolic details. Medical technologies have undergone a rapid change in the last few years, especially based on new advances in imaging and computer technology. The latest imaging modalities, such as molecular imaging and nanoimaging, novel ideas and devices imported into the medical field from other disciplines, and new software, may drastically change the diagnosis and treatment procedures. Undoubtedly, the future will lead to more advanced imaging modalities in terms of spatial resolution, sensitivity, specificity, and patient safety.

## REFERENCES

1. Wolbarst, A.B., Zamenhof, R.G., and Hendee, W.R., *Advances in Medical Physics*, Medical Physics Publishing, Madison, WI, 2006.
2. Duke, F.A., *Physical Properties of Tissue*, Academic Press, San Diego, CA, 1990.
3. Hendee, W.R., and Ritenour, E.R., *Medical Imaging Physics*, 4th ed., Wiley, Haboken, NJ, 2002.
4. Smith, S.W., et al., Feasibility study: real-time 3D ultrasound imaging of the brain, *Ultrasound Med. Biol*., Vol. 30, 2004, pp. 1365–1371.
5. Shung, K.K., *Diagnostic Ultrasound: Imaging and Blood Flow Measurements*, Taylor & Francis Group, CRC Press Book, Boca Raton, FL, 2005.
6. Cathignol, D.N., Fourcade, C., and Chapelon, Y., Transcutaneous blood flow measurement using pseudorandom noise Doppler system, *IEEE Trans. Biomed. Eng*., Vol. 27, 1980, pp. 30–36.
7. Acar, P., et al., Real time 3D echocardiography in congenital heart disease, *Arch. Mal. Coeur Vaiss*., Vol. 97, 2004, pp. 472–478.
8. Espinoza, J., et al., Novel algorithm for comprehensive fetal echocardiography using 4D ultrasound and tomographic imaging, *J. Ultrasound Med*., Vol. 25, No. 8, 2006, pp. 947–956.
9. Bercoff, J., Tanter, M., and Fink, M., Supersonic shear imaging: a new technique for soft tissue elasticity mapping, *IEEE Trans. Ultrason. Ferroelectr. Freq. Control*, Vol. 51, No. 4, 2004, pp. 396–409.
10. Carson, P.L., and Fenster, A., Anniversary Paper: Evolution of ultrasound physics and the role of medical physicists and the AAPM and its journal in that evolution, *Med. Phys*., Vol. 36, No. 2, 2009, pp. 411–428.
11. Goertz, D.E., et al., High-frequency Doppler ultrasound monitors the effect of antivascular therapy on tumor blood flow, *Cancer Res*., Vol. 62, No. 22, 2002, pp. 6371–6375.
12. Hounsfield, G., Computerized transverse axial scanning (tomography): I. Description of system, *Br. J. Radiol*., Vol. 46, 1973, p. 1016.
13. Boyd, D.P., and Lipton, M.J., Cardiac computed tomography, *Proc. IEEE*, Vol. 71, 1983, pp. 298–307.
14. Hall, E.J., *Radiology for the Radiologist*, 5th ed., Lippincott Williams & Wilkins, Philadelphia, 2000.
15. Khan, F.M., *The Physics of Radiation Therapy*, 3rd ed., Lippincott Williams & Wilkins, Philadelphia, 2003.
16. Brenner, D.J., and Hall, E.J., Computed tomography: an increasing source of radiation exposure, *N. Engl. J. Med*., Vol. 357, No. 22, 2007, pp. 2277–2284.
17. Brenner, D.J., et al., Estimated risks of radiation-induced fatal cancer from pediatric CT, *Am. J. Roentgenol*., Vol. 176, 2001, pp. 289–296.

18. Donnelly, L.F., et al. Minimizing radiation dose for pediatric body applications of single-detector helical CT, *Am. J. Roentgenol.*, Vol. 176, No. 2, 2001, pp. 303–306.
19. Lauterbur, P.C., Image formation by induced local interactions: examples of employing nuclear magnetic resonance, *Nature*, Vol. 242, 1973, pp. 190–191.
20. Pruessmann, K.P., et al., SENSE: sensitivity encoding for fast MRI, *Magn. Reson. Med.*, Vol. 42, No. 5, 1999, pp. 952–962.
21. Griswold, M.A., et al., Generalized autocalibrating partially parallel acquisitions (GRAPPA), *Magn. Reson. Med.*, Vol. 47, No. 6, 2002, pp. 1202–1210.
22. Seifert, V., Intraoperative MRI in neurosurgery: technical overkill or the future of brain surgery? *Neurol. India*, Vol. 51, 2003, pp. 329–332.
23. Weinmann, H. J, et al., Characteristics of gadolinium-DTPA complex: a potential NMR contrast agent, *Am. J. Roentgenol.*, Vol. 142, No. 3, 1984, pp. 619–624.
24. Weissleder, R.G., et al., Ultrasmall superparamagnetic iron oxide: characterization of a new class of contrast agents for MR imaging, *Radiology*, Vol. 175, No. 2, 1990, pp. 489–493.
25. Liu, C.H., et al., Noninvasive delivery of gene targeting probes to live brains for transcription MRI, *FASEB J.*, Vol. 22, 2008, pp. 1193–1203.
26. Haacke, E.M., et al., *Magnetic Resonance Imaging: Physical Principles and Sequence Design*, Wiley, New York 1999.
27. Huppi, P. S, Maier, S.E., and Peled, S.S., Microstructural development of the human newborn cerebral white matter assessed in vivo by diffusion tensor MRI, *Pediatr. Res.*, Vol. 44, No. 4, 1998, pp. 584–590.
28. Saloner, D., MRA: principles and display, in *Magnetic Resonance Imaging of the Body*, 3rd ed., pp. 1345–1368, C. B Higgins, H. Hricak, and C.A. Helms (eds.), Lippincott-Raven, Philadelphia, 1997.
29. Stadlbauer, A., et al., Proton magnetic resonance spectroscopy in pituitary macroadenomas: preliminary results, *J. Neurosurg.*, Vol. 109, No. 2, 2008, pp. 306–312.
30. Logothetis, N.K., Neurophysiological investigation of the basis of the fMRI signal, *Nature*, Vol. 412, 2001, p. 150.
31. Kahn, T., Jolesz, F.A., and Lewin, J.S., Special Issue: Interventional MRI update, *J. Magn. Reson. Imaging*, Vol. 27, No. 2, 2008, p. 252.
32. Ter-Pogossian, M.M., Phelps, M.E., and Hoffman, E.J., A positron-emission transaxial tomograph for nuclear imaging (PETT), *Radiology*, Vol. 114, No. 1, 1975, pp. 89–98.
33. Cherry, S.R., Meikle, S.R., and Hoffman, E.J., Correction and characterisation of scattered events in three-dimensional PET using scanners with retractable septa, *J. Nucl. Med.*, Vol. 34, 1993, pp. 671–678.
34. Badawi, R.D., and Marsden, P.K., Developments in component-based normalization for 3D PET, *Phys. Med. Biol.*, Vol. 44, No. 2, 1999, pp. 571–594.
35. Klunk, W.E., et al., Imaging brain amyloid in Alzheimer's disease with Pittsburgh Compound-B, *Ann. Neurol.*, Vol. 55, No. 3, 2004, pp. 306–319.
36. Frankle, W.G., et al., Neuroreceptor imaging in psychiatry: theory and applications, *Int. Rev. Neurobiol.*, Vol. 67, 2005, pp. 385–440.
37. Chen, E., et al., Myocardial viability studies using fluorine-18 FDG SPECT: a comparison with fluorine-18 FDG PET, *J. Nucl. Med.*, Vol. 38, No. 4, 1997, pp. 582–586.
38. Uematsu, T., et al., Comparison of FDG PET and SPECT for detection of bone metastases in breast cancer, *Am. J. Roentgenol.*, Vol. 184, 2005, pp. 1266–1273.

39. Devlin, P.M., *Brachytherapy: Applications and Techniques*, Lippincott Williams & Wilkins, Philadelphia, 2007.
40. Greene, D., and Williams, P.C., *Linear Accelerators for Radiation Therapy*, 2nd ed., Taylor & Francis, New York, 1997.
41. Dyk, J.V., *The Modern Technology of Radiation Oncology: A Compendium for Medical Physicists and Radiation Oncologists*, Medical Physics Publishing, Madison, WI, 1999.
42. Keall, P.J., et al., *The Management of Respiratory Motion in Radiation Oncology*, Report of AAPM Task Group 76, American Association of Physicists in Medicine, College Park, MD, July 2006.
43. Meyer, J., *IMRT, IGRT, SBRT: Advances in the Treatment, Planning, and Delivery Radiotherapy*, S. Karger, Basel, Switzerland, 2007.
44. Hoh, C.K., et al., PET in oncology: Will it replace the other modalities? *Semin. Nucl. Med*., Vol. 27, 1997, pp. 94–106.

# 3

# CURRENT IMAGING APPROACHES AND FURTHER IMAGING NEEDS IN CLINICAL MEDICINE: A CLINICIAN'S PERSPECTIVE

Gadi Wollstein [Section 3.1]

*University of Pittsburgh School of Medicine, Pittsburgh, Pennsylvania*

Joel S. Schuman [Section 3.1]

*University of Pittsburgh School of Medicine, Swanson School of Engineering, University of Pittsburgh and Carnegie Mellon University, Pittsburgh, Pennsylvania*

Cetin Karaca, Sevdenur Cizginer, and William R. Brugge [Section 3.2]

*Massachusetts General Hospital, Boston, Massachusetts*

Ik-Kyung Jang and Jin-Man Cho [Section 3.3]

*Massachusetts General Hospital, Boston, Massachusetts*

Peter K. Dempsey [Section 3.4]

*Lahey Clinic, Burlington, Massachusetts; Tufts University School of Medicine, Boston, Massachusetts*

3.1 Ophthalmic imaging 48
  3.1.1 Ocular malignant melanoma 49
  3.1.2 Glaucoma 49
  3.1.3 Slit lamp and ophthalmoscope 50
  3.1.4 Fundus photography 50
  3.1.5 Ultrasound 52
  3.1.6 Computerized tomography and magnetic resonance imaging 52

---

*Advances in Optical Imaging for Clinical Medicine*, Edited by Nicusor Iftimia, William R. Brugge, and Daniel X. Hammer
Copyright © 2011 John Wiley & Sons, Inc.

3.1.7 Optical coherence tomography 52
3.1.8 Confocal scanning laser ophthalmoscopy 56
3.1.9 Scanning laser polarimetry 56
3.1.10 Summary 58
3.2 Imaging of the gastrointestinal mucosa 58
3.2.1 Gastrointestinal conditions 61
3.2.2 Imaging modalities 65
3.2.3 Summary and conclusions 69
3.3 Cardioimaging 70
3.3.1 Current imaging modalities in interventional cardiology 70
3.3.2 Clinical need for high-resolution imaging in interventional cardiology 71
3.3.3 Conclusions and future directions 71
3.4 Neuroimaging: current technologies and further needs 72
3.4.1 Neuroimaging history 72
3.4.2 Computed tomography 72
3.4.3 Magnetic resonance imaging 73
3.4.4 Positron emission tomography 75
3.4.5 Optical imaging 77
3.4.6 Conclusions 77
References 78

## 3.1 OPHTHALMIC IMAGING

Ocular examination and diagnosis rely substantially on direct observation of the eye. This takes advantage of the excellent optical properties of the eye, allowing the examiner to have a clear and direct view. To visualize the internal structures of the eye, one must use illumination and magnification devices. The most basic ophthalmic examination devices, the slit lamp and the ophthalmoscope, provide exactly these properties and are widely in use by ophthalmic care providers. However, some of the ocular structures are transparent (e.g., cornea and retina), while others are located in regions that are difficult to visualize or are hidden from view (anterior chamber angle, ciliary body). Moreover, qualitative assessment is prone to interobserver and intervisit variation, which limits the use of the information gleaned. Further complicating the yield of clinical examination is the natural path of many ocular abnormalities (e.g., glaucoma), which progress slowly over the years, and detection of these minute changes can be challenging. These were the main drive in exploring innovative methods to image the eye and provide reliable, accurate, detailed, and preferably quantitative information. In the last 15 years an array of ocular imaging devices has been developed, and these instruments are now playing a substantial role in ophthalmic clinical evaluation.

In this section we present two examples of ocular pathologies where imaging has become the cornerstone of clinical evaluation, followed by a description of common ocular imaging devices currently in use. We also identify current and further imaging needs in ophthalmology.

### 3.1.1 Ocular Malignant Melanoma

Malignant melanoma is a solid cancerous tumor originating from melanocytes. These pigmented cells are located predominantly in the skin but also exist elsewhere in the body, including the eye. Although the incidence of malignancy in the eye is relatively low, it is still the most common primary malignant ocular tumor in adults. Most lesions appear initially as raised pigmented areas in the fundus that resemble nevi, although occasionally the lesion may be nonpigmented, further hindering detection. While nevi themselves do not require intervention, melanoma has a high mortality rate and requires multimodal treatment, depending on the stage of the tumor. Early detection and treatment are the key to achieving survival in managing this disease. However, the only concrete way to determine the malignant nature of a suspicious ocular mass is through tissue biopsy, which is generally obtainable only through a major invasive procedure. This has led to a substantial number of cases where eyes with nevi were enucleated or malignant tumors misdiagnosed as nevi, with predictably bad outcomes. The introduction of ocular ultrasound revolutionized the diagnosis paradigm for ocular melanoma when it was realized that nevi and melanoma have a marked difference in their acoustical reflectivity pattern. The ultrasound scan demonstrates peaks in interface between structures, such as aqueous humor and lens, lens and vitreous, and vitreous and retina. An ultrasound beam crossing through nevi will demonstrate a high peak in the anterior interface, followed by a rapid descent in the signal. A beam through melanoma will show a high anterior peak followed by a high "internal reflectivity" signal. This allows for simple and noninvasive diagnosis with high accuracy that substantially reduces the false positive and negative assessments. Ocular ultrasound has become a routine part of evaluating suspicious nevi and is instrumental in following the lesions for growth and the response to treatment of malignancies.

### 3.1.2 Glaucoma

Glaucoma is the second leading cause of blindness worldwide, characterized by gradual loss of the neural tissue in the eye accompanied by visual field loss. Several types of glaucoma exist, and the one prevalent in the Western world is mostly asymptomatic until a late stage of the disease. Since the neural damage is irreversible, much effort has gone into detecting the disease at an early stage, allowing for the initiation of treatment and possibly maintaining functional sight. Conventional methods for diagnosing glaucoma depend on clinical examination of the eye and visual field testing. Clinical examination is highly dependent on the professional skills of the observer and is prone to interobserver variability. Visual field examination depends on the response of the subject when a light stimulus is detected, resulting in significant short- and long-term variability. In addition, the disease usually is slowly progressing, and detection of these changes over time can be difficult. Taken together, detection of early glaucoma and disease progression can be clinically challenging, and in most cases delay in diagnosis and treatment causes significant and irreversible neural loss. The incorporation of ocular imaging devices in the assessment of these subjects allows for quantitative and reproducible measurements of structures in the eye. Optical coherence tomography, scanning laser ophthalmoscopy, and scanning laser polarimetry are the three main imaging devices that are commonly in use in assessing glaucoma. The devices quantify structures in the retina and optic nerve head and have been shown to be valuable in discriminating between healthy and glaucomatous eyes [1–7]. Several studies that investigated their use in longitudinal follow-up have shown potential benefit in the use of these devices in identifying change over time [8,9].

### 3.1.3 Slit Lamp and Ophthalmoscope

The basic ocular examination devices are the ophthalmoscope and the slit lamp, which allows eye-care professionals to view in detail the external and internal structures of the eye. The slit lamp includes a chin rest for the subject, a light source that illuminates the eye, and a magnifying binocular microscope. The ophthalmoscope provides coaxial light and viewing pathways, lighting the fundus and magnifying the structure for assessment of the posterior pole. The slit lamp and ophthalmoscope allow the examiner to extract detailed visual information from both the anterior and posterior segments of the eye. This information is either recorded subjectively by the examiner or recorded by connecting the device to a camera or video system. This enables snapshot recording of visible findings, but this must still be evaluated subjectively.

### 3.1.4 Fundus Photography

Fundus photography is a common way of recording ocular information. The device was specifically customized to provide high-quality photographs of the eye using optimized optics. The device is coupled with a camera that provides photographs either recorded on film or, more recently, digitally. Pairs of photographs can be acquired (either simultaneously or consecutively) to provide stereoscopic three-dimensional views of the area of interest (Figure 3.1). This method is commonly used for assessment of the optic nerve head region in glaucoma, where gradual changes appear over time, and comparison of the photographs provides a snapshot record for comparison. However, this comparison is influenced markedly by observer skills and is prone to high variability between visits and between observers [10]. Nonetheless, numerous studies have demonstrated good discriminating ability between healthy and glaucomatous eyes when evaluated by expert observers in a disk photograph reading center [11]. A few programs allow for quantification of optic nerve head structures (planimetry) such as disk and cup area, but most programs require human input in defining

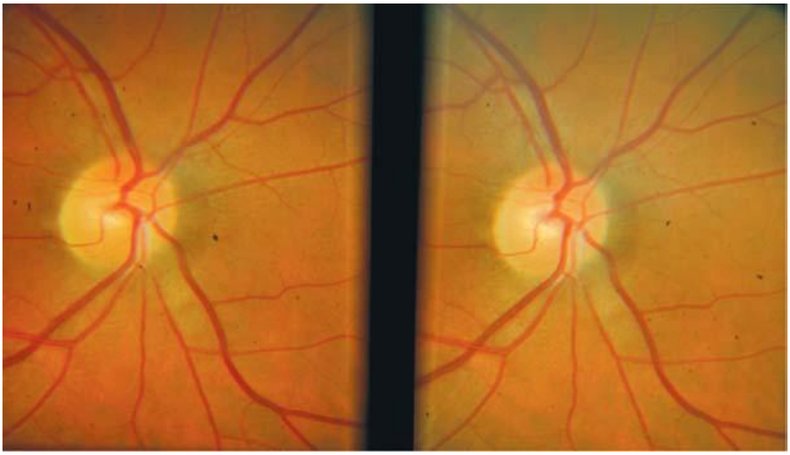

**FIGURE 3.1** Stereoscopic optic nerve head photography of the right eye of a healthy subject.

the boundaries of these structures in order to perform an analysis. Because of the human input requirement, these assessments are still prone to variability related to subjective user definitions. Another limitation is that the markings cannot be exported from one visit to another, and therefore limit the ability to detect small changes over time. Fundus photography is also widely used to document retinal diseases such as diabetic retinopathy, macular degeneration, retinal detachment, optic neuropathy, and others. In most of these cases, gross comparison between consecutive photographs is sufficient for clinical decision making.

Incorporation of certain filters has expanded the utility of fundus photography. Red-free photography enhances the user's ability to visualize the retinal nerve fiber layer, which is part of glaucoma assessment. Fluorescein dye injected intravenously can be observed inside the ocular vasculature using specific filters. This procedure uses the physical phenomenon of fluorescence, where susceptible molecules absorb electromagnetic energy, temporarily exciting them to a higher-energy state. As the molecules return to their original energy level they emit light at a different wavelength. The ocular application of this method is to use fluorescein sodium with an exciter filter that transmits blue–green light at a wavelength of 465 to 490 nm and a barrier filter that transmits yellow light with a wavelength of 520 to 530 nm. This imaging method has become a cornerstone for diagnosing vasculature abnormalities such as retinal artery or vein occlusion, anterior ischemic optic neuropathy, or diabetic retinopathy. In the latter situation, the underlying diabetes causes small vessel abnormalities that can leak and the formation of new and abnormal blood vessels. Both situations can be detected using fluorescein angiography, which can be highly effective in demonstrating disease and can be crucial for clinical decision making and monitoring of the disease and treatment.

### 3.1.5 Ultrasound

Ultrasound has been widely accepted for imaging in various regions of the body, including the eye and orbit. This technology provides noninvasive, real-time, and interactive imaging with a resolution and penetration depth which are dependent on the sound beam frequency that is used. The acoustic echo can discern between structures based on their resonance properties, such as the anterior and posterior interface of the lens with the aqueous humor, and the interface between vitreous and retina. A few common uses of ultrasound in ophthalmology are for measuring the axial length or the distance between the corneal surface and the retina, corneal thickness (pachimetry), and assessing the gross integrity of the posterior part of the eye in the presence of media opacities that preclude viewing of this region. The role of ultrasound in ocular melanoma assessment was discussed above.

Another important application of this technology is ultrasound biomicroscopy of the anterior segment. This device, with high resolution but low penetration into the tissue, allows for detailed imaging of the anterior segment of the eye. This is valuable primarily in assessing the region of the anterior chamber angle (between the cornea and iris), where the drainage of the aqueous humor occurs, and the ciliary body. This modality is used currently to discern between various types of glaucoma. Anterior chamber ultrasound also allows for viewing of structures inside the iris (such as cysts or tumors) or behind it.

Some of the ultrasound devices can record Doppler signals and can be used to evaluate the blood flow in the optic nerve head region inside the eye or in ocular vessels outside the eyeball.

While ultrasound has been shown to be of value in diagnosis and monitoring disease, the main limitations are technician dependence, the requirement for direct contact by the use of a coupling solution to transmits the acoustic waves from and to the transducer, and the limited ability of conventional ultrasound to quantify observed structures reproducibly.

### 3.1.6 Computerized Tomography and Magnetic Resonance Imaging

Computerized tomography (CT) and magnetic resonance imaging (MRI) are commonly used imaging methods throughout the body, with scan utility in intraocular evaluation [12]. Due to the limited in vivo resolution of these devices, their clinical utility for assessing intraocular pathologies is limited and their main use is to visualize intraorbital structures such as the extraocular muscles, tumors, and ocular or orbital foreign bodies. Another common application of these methods is in neuro-ophthalmic evaluation. In this case the devices allow for visualization of the entire visual pathway from the optic nerve through the lateral geniculate body to the visual cortex in the occipital lobe of the brain. Both CT and MRI have a fundamental role in detection of infarcts, tumors, vascular anomalies, and other causes of visual morbidity of neurologic origin.

### 3.1.7 Optical Coherence Tomography

Optical coherence tomography (OCT) is a noncontact, real-time, high-resolution cross-sectional imaging technology that has became widely used in the eye, in particular for glaucoma and retina diagnostics. The device is currently experiencing a major technological evolution that is improving its performance substantially. OCT is similar to ultrasound, but instead of using sound, the OCT uses light echoes to provide an image of the area of interest [13].

Time-domain OCT (TD-OCT) uses near-infrared (center wavelength: ca. 820 nm) broad-bandwidth light originating from superluminescent diodes. The light is split such that one beam is projected toward the eye and the other toward a reference arm containing an oscillating mirror. An interference signal is created when the pathlengths of the backreflected light from the eye and the reference arm reflection meet at the detector and are closely matched to within the coherence length of the light. By matching each scanned point (each pixel) with the actual location of the oscillating mirror, the device can determine the precise location of the ocular reflection. By moving the light across the scanned region, multiple adjacent samples are collected, which result in a two-dimensional optical cross-sectional tomogram. OCT is particularly beneficial in areas with layered structures with unique time-delay signatures from the various tissue components, such as the retina or the cornea.

The commercially available device for TD-OCT scanning of the posterior segment of the eye (Stratus OCT; Carl Zeiss Meditec, Dublin, California) has an in vivo axial resolution of 8 to 10 μm and a transverse resolution of about 20 μm, a scanning depth in the tissue of approximately 2 mm, a scanning speed of 400 axial scans per second, and a typical time for most scan patterns of approximately 1 to 1.5 s. TD-OCT provides detailed cross-sectional maps and automatically computes various retinal layer thicknesses and optical nerve head topography parameters. Among the most clinically useful information that can be quantified by OCT automatically is the thickness of the retinal nerve fiber layer (RNFL). This layer is composed by axons that transmit the signal from photoreceptors in the retina toward to the brain's visual cortex. Quantification of this layer provides a robust indicator of the structural integrity of the intraocular neural system. Stratus OCT includes a normative database allowing for age-matched comparison of the measurements in a given person to that of the healthy population (Figure 3.2). TD-OCT has been shown to provide reproducible ocular measurements [14,15] with substantial ability to differentiate between healthy and glaucomatous eyes as well as detection of other ocular abnormalities [1,16–19].

The anterior segment version of TD-OCT uses a longer wavelength (1310 nm) than that of the posterior segment device, with an in vivo axial resolution of 18 μm. This device provides a detailed view of the cornea, anterior chamber, and the surface of the iris with quantitative structural measurements. Longer wavelength better penetrates through the sclera, allowing full visualization of the anterior chamber angle, a crucial component in the comprehensive evaluation of this region that is obscure by most other anterior segment imaging methods.

Recent technological improvements in OCT have lead to a substantial increase in the scanning speed and improved resolution. These newly released commercially available devices are known as spectral-domain OCT (SD-OCT) [20]. In this iteration of the device, the light source is broad bandwidth near infrared and

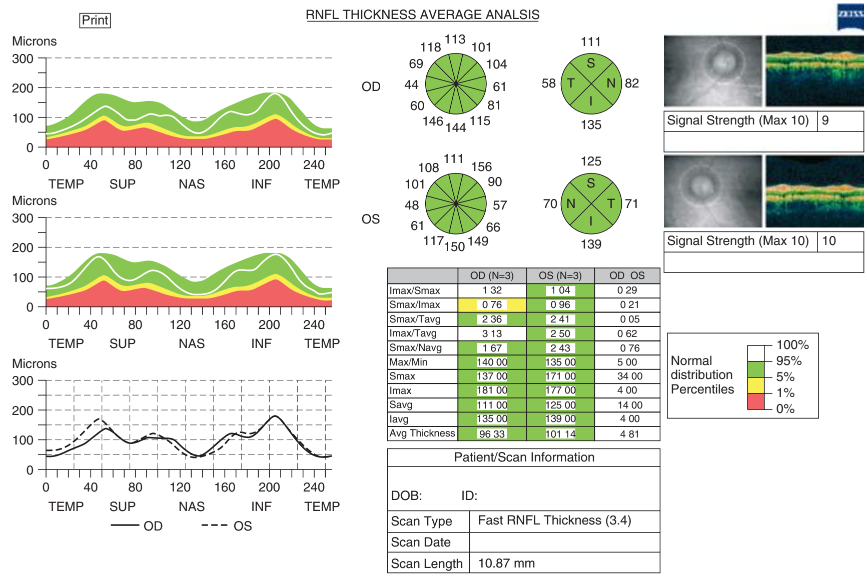
Print
RNFL THICKNESS AVERAGE ANALSIS
ZEISS
Microns
300
200
100
0
0 40 80 120 160 200 240
TEMP SUP NAS INF TEMP
Microns
300
200
100
0
0 40 80 120 160 200 240
TEMP SUP NAS INF TEMP
Microns
300
200
100
0
0 40 80 120 160 200 240
TEMP SUP NAS INF TEMP
OD
OS
OD
118 113 101
69 104
44 61
60 81
146 144 115
111
S
58 T N 82
I
135
OS
108 111 156
101 90
48 57
61 66
117 150 149
125
S
70 N T 71
I
139
Normal distribution Percentiles
100%
95%
5%
1%
0%

| Signal Strength (Max 10) | 9 |
|---|---|

| Signal Strength (Max 10) | 10 |
|---|---|

| | OD (N=3) | OS (N=3) | OD OS |
|---|---|---|---|
| Imax/Smax | 1 32 | 1 04 | 0 29 |
| Smax/Imax | 0 76 | 0 96 | 0 21 |
| Smax/Tavg | 2 36 | 2 41 | 0 05 |
| Imax/Tavg | 3 13 | 2 50 | 0 62 |
| Smax/Navg | 1 67 | 2 43 | 0 76 |
| Max/Min | 140 00 | 135 00 | 5 00 |
| Smax | 137 00 | 171 00 | 34 00 |
| Imax | 181 00 | 177 00 | 4 00 |
| Savg | 111 00 | 125 00 | 14 00 |
| Iavg | 135 00 | 139 00 | 4 00 |
| Avg Thickness | 96 33 | 101 14 | 4 81 |

Patient/Scan Information

DOB: ID:

| | |
|---|---|
| Scan Type | Fast RNFL Thickness (3.4) |
| Scan Date | |
| Scan Length | 10.87 mm |

**FIGURE 3.2** Time-domain optical coherence tomography (OCT) printout of a circular scan around the optic nerve head of a healthy subject. The scan location and cross-sectional images appear in the right upper corner. Retinal nerve fiber layer (RNFL) thickness profiles along the scan line with a comparison to color-coded normative data appear in the left column. Quantitative data for the right (OD) and left (OS) eyes are located in the center column.

the reference arm is fixed rather than oscillating as in TD-OCT. In SD-OCT, all wavelengths reflected back along the axial scan are collected simultaneously, and their interference with the fixed reference arm reflection is Fourier-transformed from the frequency domain to the time domain. In this way it is possible to acquire all points along the depth of the axial scan simultaneously without reference arm movement. Use of broader-bandwidth light and a stationary reference arm has enabled improvement in the in vivo axial resolution to 3 to 6 μm and scanning speed of 24,000 to 55,000 axial scans per second with a scanning depth in the tissue of approximately 2 mm. The faster acquisition rate reduces motion artifacts and enables denser tomograms as well as the collection of three-dimensional data sets. Other novel scan patterns and averaging of repetitive scans to reduce the background noise level are possible with SD-OCT, due to the greatly increased scan speed. The improved axial resolution enhances the ability to visualize fine structures. SD-OCT raster scanning allows the construction of a three-dimensional data cube, providing a large array of post-processing opportunities (Figure 3.3). The optimal setting, analysis, and clinical performance of SD-OCT systems are currently being explored, but it is clear that SD-OCT improves reproducibility of measurements and may enhance disease discrimination and the detection of disease progression.

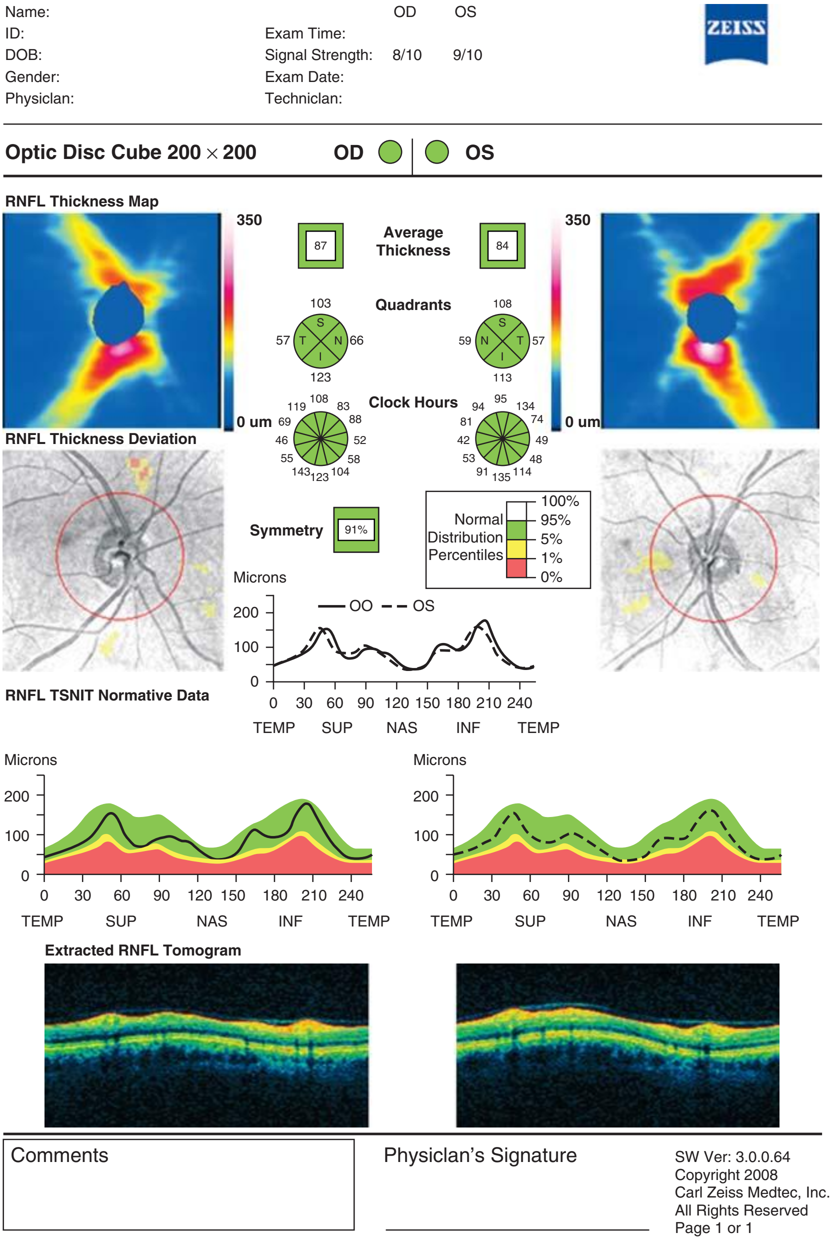

|  |  |  | OD | OS |
|---|---|---|---|---|
| Name: |  |  |  |  |
| ID: | Exam Time: |  |  |  |
| DOB: | Signal Strength: |  | 8/10 | 9/10 |
| Gender: | Exam Date: |  |  |  |
| Physiclan: | Techniclan: |  |  |  |

**Optic Disc Cube 200 × 200 OD ● | ● OS**

ZEISS
RNFL Thickness Map
350
0 um
Average Thickness
87
84
Quadrants
103
57
66
123
S
T
N
I
108
59
57
113
Clock Hours
119 108 83
69 88
46 52
55 58
143 123 104
94 95 134
81 74
42 49
53 48
91 135 114
RNFL Thickness Deviation
Symmetry
91%
Normal Distribution Percentiles
100%
95%
5%
1%
0%
Microns
200
100
0
OO
OS
0 30 60 90 120 150 180 210 240
TEMP SUP NAS INF TEMP
RNFL TSNIT Normative Data
Microns
200
100
0
0 30 60 90 120 150 180 210 240
TEMP SUP NAS INF TEMP
Microns
200
100
0
0 30 60 90 120 150 180 210 240
TEMP SUP NAS INF TEMP
Extracted RNFL Tomogram

Comments

Physician's Signature

SW Ver: 3.0.0.64
Copyright 2008
Carl Zeiss Medtec, Inc.
All Rights Reserved
Page 1 or 1

**FIGURE 3.3** Spectral-domain optical coherence tomography printout of a raster scan of the optic nerve head region of healthy subject. *En face* images of the scanned area appear in the center of the right and left columns (gray-scale images) with an overlay of red circle where the retinal cross section is sampled and a nerve fiber layer thickness profile is created (lower panel). The upper panel in both the right and left columns demonstrates the retinal nerve fiber layer color-coded thickness map in the entire scanned region. Quantitative data are located in the center column.

### 3.1.8 Confocal Scanning Laser Ophthalmoscopy

Confocal scanning laser ophthalmoscopy (CSLO) is a real-time, noninvasive, and reproducible imaging technology that was designed primarily for optic nerve head imaging [21]. A diode laser light source emits light directed at the eye. The light is projected through a pinhole and the backreflected light is detected after passing through a conjugated pinhole. This pair ensures that only light reflected from a defined focal plane will reach the light detector. Light beams reflected from above or below the plane are not focused on the pinhole and do not reach the detector. CSLO uses raster scanning to acquire a set of sequential two-dimensional planar scans to create a three-dimensional topographic representation of the area scanned. Based on the location of the center of gravity of the reflected light in each pixel within the stack of two-dimensional scans, the machine automatically determines a topographical map of the scanned region.

The commercially available CSLO device [Heidelberg retina tomograph (HRT); Heidelberg Engineering, Heidelberg, Germany] acquires a set of 16 to 32 two-dimensional scans for a field of view of $15^\circ \times 15^\circ$, with an axial resolution of 300 μm, a transverse resolution of 10 μm, and a typical scanning time of 1.6 s. In order to calculate the absolute $Z$-axis measurements, the device automatically places a ring in the periphery of the scanned area to serve as the zero reference plane. HRT requires human intervention in defining the disk margin in order to provide quantitative measurements of the optic nerve region (Figure 3.4). Once the disk margin has been recorded, the machine automatically exports and aligns the margin to all consecutive tests. Automated analysis of the optic nerve head and peripapillary retinal topography without user input is currently offered by the software and provides performance similar to the traditional parameters in preliminary assessments [22,23]. The HRT has been shown to provide a high degree of measurement reproducibility [24].

CSLO is used mainly clinically for glaucoma evaluation and has been shown to have good discriminatory ability between healthy and glaucomatous eyes [5,6]. HRT software provides a progression analysis that highlights areas of topographic change that exceed the subject's intervisit variability as defined in the baseline tests [8].

### 3.1.9 Scanning Laser Polarimetry

Scanning laser polarimetry (SLP) is another real-time, noncontact imaging device mainly in clinical use for glaucoma evaluation. SLP is designed to evaluate the retinal nerve fiber layer by measuring the birefringence properties of the retina [25]. The parallel orientation of the retinal ganglion cell axons and the microtubules within those axons causes a quantifiable change in the polarization of light that passes through them. The device quantifies the change in polarization that corresponds to the retinal nerve fiber layer thickness. Other ocular structures, including the cornea, lens, retinal pigment epithelium, and sclera, have also been demonstrated to affect the reflected light's polarization properties and should be taken into account when measuring the ocular birefringence [26].

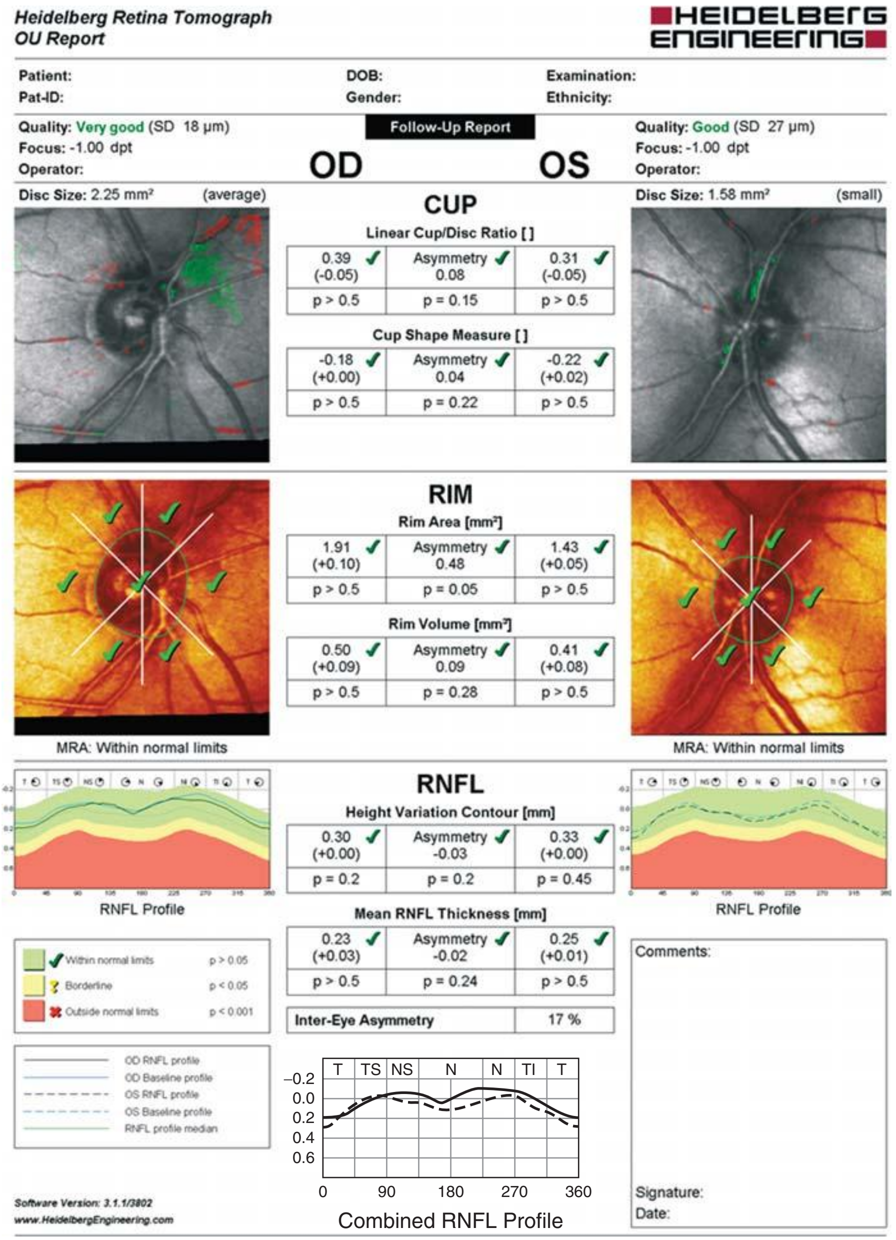

***Heidelberg Retina Tomograph***
***OU Report***

**HEIDELBERG ENGINEERING**

**Patient:**
**Pat-ID:**
**DOB:**
**Gender:**
**Examination:**
**Ethnicity:**

**Follow-Up Report**

| OD | | OS |
|---|---|---|
| **Quality:** Very good (SD 18 µm)<br>**Focus:** -1.00 dpt<br>**Operator:**<br>**Disc Size:** 2.25 mm² (average) | | **Quality:** Good (SD 27 µm)<br>**Focus:** -1.00 dpt<br>**Operator:**<br>**Disc Size:** 1.58 mm² (small) |

**CUP**

**Linear Cup/Disc Ratio [ ]**

| | | |
|---|---|---|
| 0.39 ✓<br>(-0.05) | Asymmetry ✓<br>0.08 | 0.31 ✓<br>(-0.05) |
| p > 0.5 | p = 0.15 | p > 0.5 |

**Cup Shape Measure [ ]**

| | | |
|---|---|---|
| -0.18 ✓<br>(+0.00) | Asymmetry ✓<br>0.04 | -0.22 ✓<br>(+0.02) |
| p > 0.5 | p = 0.22 | p > 0.5 |

**RIM**

**Rim Area [mm²]**

| | | |
|---|---|---|
| 1.91 ✓<br>(+0.10) | Asymmetry ✓<br>0.48 | 1.43 ✓<br>(+0.05) |
| p > 0.5 | p = 0.05 | p > 0.5 |

**Rim Volume [mm³]**

| | | |
|---|---|---|
| 0.50 ✓<br>(+0.09) | Asymmetry ✓<br>0.09 | 0.41 ✓<br>(+0.08) |
| p > 0.5 | p = 0.28 | p > 0.5 |

MRA: Within normal limits

MRA: Within normal limits

**RNFL**

**Height Variation Contour [mm]**

| | | |
|---|---|---|
| 0.30 ✓<br>(+0.00) | Asymmetry ✓<br>-0.03 | 0.33 ✓<br>(+0.00) |
| p = 0.2 | p = 0.2 | p = 0.45 |

**Mean RNFL Thickness [mm]**

| | | |
|---|---|---|
| 0.23 ✓<br>(+0.03) | Asymmetry ✓<br>-0.02 | 0.25 ✓<br>(+0.01) |
| p > 0.5 | p = 0.24 | p > 0.5 |

| | |
|---|---|
| Inter-Eye Asymmetry | 17 % |

RNFL Profile

RNFL Profile

| | | |
|---|---|---|
| 🟩 ✓ | Within normal limits | p > 0.05 |
| 🟨 ? | Borderline | p < 0.05 |
| 🟥 ✗ | Outside normal limits | p < 0.001 |

OD RNFL profile
OD Baseline profile
OS RNFL profile
OS Baseline profile
RNFL profile median

Combined RNFL Profile

Comments:

Signature:
Date:

***Software Version: 3.1.1/3802***
***www.HeidelbergEngineering.com***

**FIGURE 3.4** Confocal scanning laser ophthalmoscopy printout of the optic nerve head region of a healthy subject. The center images in the right and left columns demonstrate the reflectance images with the marking of the disk margin. The check marks signify that sectoral disk measurements are within the normal range. A retinal nerve fiber layer thickness profile along the disk margin appears in the lower panel with a comparison to normative data marked by the color-coded scale. Quantitative data are located in the center column.

The commercially available device (GDx-VCC, ECC or PRO; Carl Zeiss Meditec, Dublin, California) uses a diode laser light source that projects light toward the eye to cover an area of $40^\circ \times 20^\circ$ of the retina in less than 1 s. The scanning procedure starts by acquiring an image of the macula region. Since this region is less prone to anatomical variation than the optic nerve head region, the machine uses the image to determine the polarization properties of the cornea. Subsequently, the GDx scans the optic nerve head region to quantify the retinal nerve fiber layer thickness (Figure 3.5). SLP is mainly in use for glaucoma evaluation and has demonstrated a good ability to discriminate between healthy and glaucomatous eyes [7].

### 3.1.10 Summary

In this section we have introduced a broad range of clinically used imaging devices. These devices were created to answer the clinical need for accurate detection, follow-up, and documentation of ocular abnormalities. Although the devices have been proven to provide substantial clinically relevant information, there is an ongoing search for further improvement in our diagnostic ability. Although the technologies now available provide reproducible, accurate, objective, quantitative assessment of ocular structure, the devices still have an opportunity to improve the ease of operation, robustness, financial affordability, and insensitivity to media opacities. At the same time, eye-care professionals strive for higher resolution, faster acquisition, and quantitative and reliable imaging devices. The marked improvement in ocular imaging observed in recent years gives hope that we will be able to achieve these goals in the foreseeable future.

## 3.2 IMAGING OF THE GASTROINTESTINAL MUCOSA

Recent statistics indicate that cancer mortality has decreased for the first time in the past half century [27]. Advances in cancer diagnostic imaging are among the factors contributing to improved survival. Early cancer detection remains an important clinical strategy because treatment of a primary malignancy is often much more successful than treatment of advanced or metastatic disease. Histology, often derived by endoscopic biopsy, is the gold standard for the diagnosis of malignancy [28]. However, a histological diagnosis may be difficult to secure as a result of inadequate tissue acquisition or tumor inaccessibility.

Most gastrointestinal (GI) cancers develop over a period of several years and are accompanied by changes in tissue architecture and cellular structure before invasion and metastasis take place. Preceding the development of invasive adenocarcinoma is a stepwise progression of cellular atypia and tissue dysplasia. Clinical imaging techniques such as conventional radiography, computed tomography, magnetic resonance imaging, and ultrasound (US) play an important role in detecting solid-organ-based tumors and metastatic disease; however, identifying mucosal dysplasia with traditional cross-sectional and ultrasound radiology is very difficult [29].

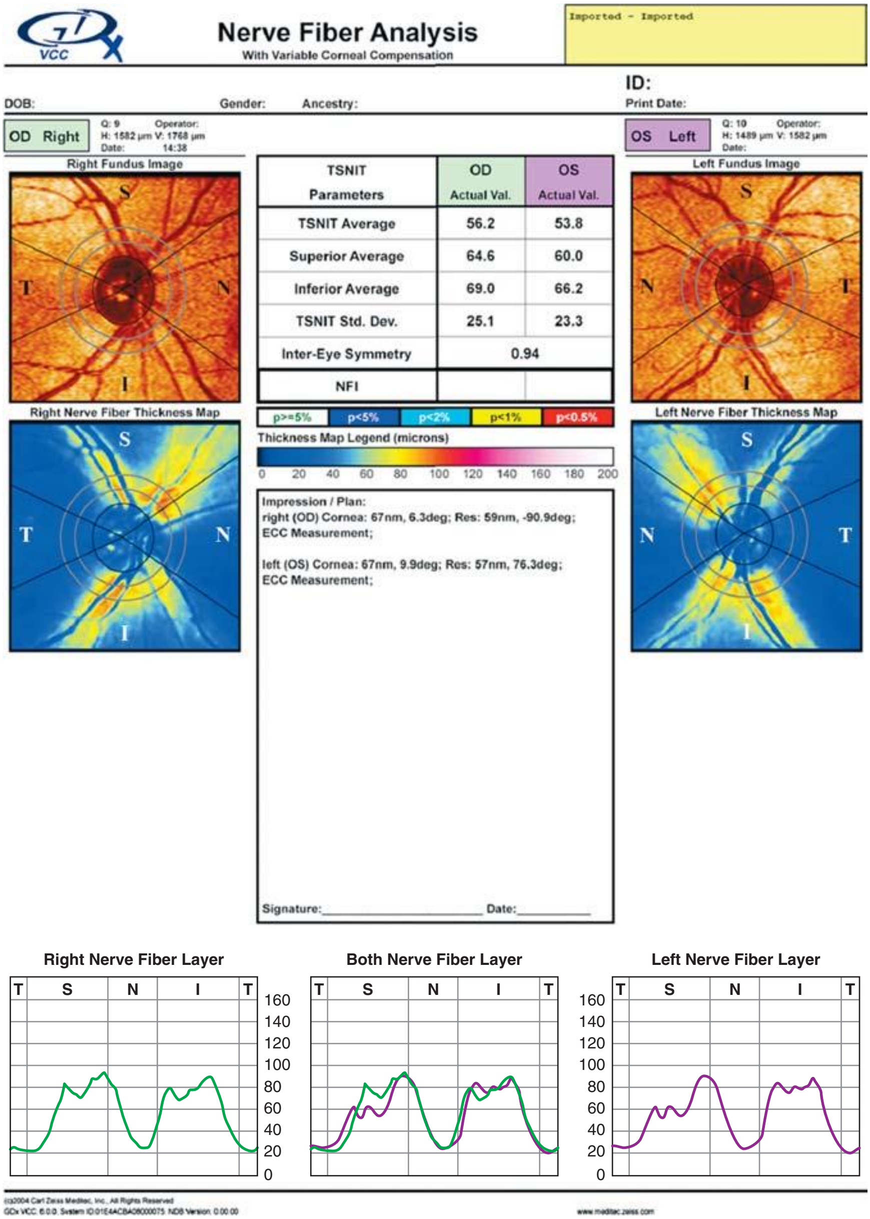

Nerve Fiber Analysis
With Variable Corneal Compensation

Imported - Imported

ID:

DOB: Gender: Ancestry: Print Date:

OD Right
Q: 9 Operator:
H: 1582 µm V: 1768 µm
Date: 14:38

OS Left
Q: 10 Operator:
H: 1489 µm V: 1582 µm
Date:

| TSNIT Parameters | OD Actual Val. | OS Actual Val. |
|---|---|---|
| TSNIT Average | 56.2 | 53.8 |
| Superior Average | 64.6 | 60.0 |
| Inferior Average | 69.0 | 66.2 |
| TSNIT Std. Dev. | 25.1 | 23.3 |
| Inter-Eye Symmetry | 0.94 | |
| NFI | | |

p>=5% p<5% p<2% p<1% p<0.5%

Thickness Map Legend (microns)

Impression / Plan:
right (OD) Cornea: 67nm, 6.3deg; Res: 59nm, -90.9deg;
ECC Measurement;

left (OS) Cornea: 67nm, 9.9deg; Res: 57nm, 76.3deg;
ECC Measurement;

Signature:____________________ Date:__________

(c)2004 Carl Zeiss Meditec, Inc., All Rights Reserved
GDx VCC 6.0.0; System ID:01E4ACBA08000075 NDB Version: 0.00.00
www.meditec.zeiss.com

VCC
Right Fundus Image
Left Fundus Image
S
T
N
I
Right Nerve Fiber Thickness Map
Left Nerve Fiber Thickness Map
0
20
40
60
80
100
120
140
160
180
200
Right Nerve Fiber Layer
Both Nerve Fiber Layer
Left Nerve Fiber Layer
T S N I T
160
140
120
100
80
60
40
20
0

**FIGURE 3.5** Scanning laser polarimetry printout of the optic nerve head region of a healthy subject. Reflectance images appear in the upper panel. A color-coded retinal nerve fiber layer thickness map appears underneath these images. Retinal nerve fiber layer thickness profiles along a band surrounding the optic nerve head appear in the lower panel. Quantitative data are located in the center column.

High-resolution imaging of the GI tract is critical for the detection and diagnosis of early GI mucosal malignancy. Traditional white-light endoscopy imaging has recently been improved through the introduction of high-resolution video endoscopy. The use of high-pixel-density charge-coupled devices (CCDs) on endoscopes provides high-resolution imaging as displayed on high-definition monitors. However, evidence of early malignancy on white-light imaging is dependent on secondary changes in the mucosa, such as ulceration or mass formation.

There are several new technologies available to the clinician for enhanced imaging of the GI mucosa. High-frequency US has been clinically available for several years and is widely used in endoscopy. Unfortunately, high-frequency endoscopic US lacks the necessary resolution and sensitivity to detect high-grade dysplasia or early cancer [29,30]. Optical coherence tomography (OCT), a high-resolution imaging modality, has undergone extensive investigation [31]. Confocal endoscopic microscopy has also received a great deal of attention because of the impressive imaging results in the gut [32]. It enables in vivo microscopy of the mucosal layer of the GI tract with subcellular resolution during ongoing endoscopy. The main goal of confocal endoscopic microscopy is to identify mucosal areas that appear suspicious for neoplasia and target the lesion for resection, biopsy, or continued monitoring. An example of imaging depth differences between these techniques is shown in Figure 3.6.

Among these optical imaging technologies, OCT seems to be the most appealing. OCT is the optical analog of ultrasound. It performs cross-sectional imaging by measuring the magnitude and echo-time delay of backscattered light. Image resolutions of 1 to 10 μm can be achieved, and imaging can be performed in situ and in real time. The incident light beam is directed at the object to be imaged, and the time delay and magnitude of backscattered or backreflected light is measured in the axial or longitudinal direction. The beam is scanned in the transverse direction, and rapid successive axial measurements are performed. The result is a two-dimensional data set image, which represents the optical reflection or backscattering in a cross-sectional plane through the material or tissue.

OCT was first demonstrated in 1991. Since that time, numerous applications of OCT for both biomedical and materials applications have emerged. Medical applications of OCT are currently evolving quickly. OCT has revolutionized the technology of superficial tissue imaging. Cross-sectional OCT imaging provides an axial resolution that is 10-fold better than that of available high-frequency US imagine devices. It is capable of visualizing subsurface microstructure in biological tissues such as villi, glands, crypts, lymphoid aggregates, and blood vessels [33–35]. Since OCT is based on single-mode optical fiber technology, narrow-diameter flexible probes can be developed for accessing internal organs. Therefore, OCT images can be obtained with a catheter device that is inserted through the accessory channel of a conventional endoscope. Endoscopic OCT is currently performed with probes capable of radial, linear, or transverse scanning [36]. Radial scanning provides a cross-sectional orientation, familiar to most

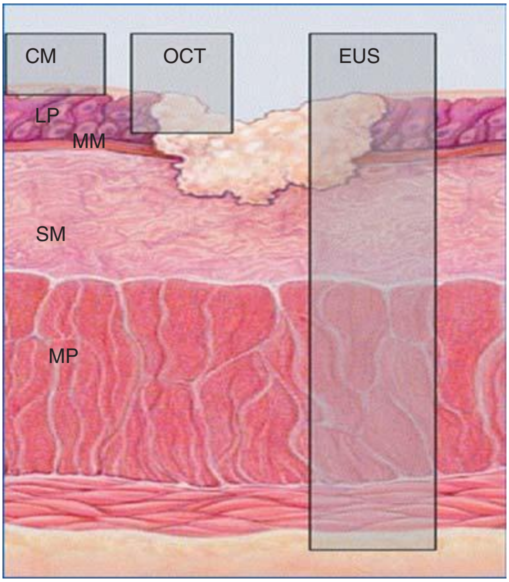

**FIGURE 3.6** Imaging depth for confocal microscopy (CM), optical coherence tomography (OCT), and endoscopic ultrasonography (EUS). The imaging depth is progressively greater, but with a penalty to resolution.

clinicians. Linear scanning has the advantage of demonstrating the relationship between the target lesion and the associated wall structure.

OCT could be useful in clinical situations in which conventional biopsy specimens are technically difficult to obtain, or are associated with risk, as in the biliary tree [37,38]. OCT imaging or OCT-guided biopsies might provide alternatives to repeated and random tissue biopsies of premalignant polypoid lesions such as those seen in long-standing ulcerative colitis. More recently, Doppler OCT has extended OCT capabilities by providing local blood flow velocities in vivo in addition to tissue architecture [35]. Doppler OCT provides noninvasive imaging of microcirculation in tissue blood vessels that are too small to be imaged by Doppler US. Potential clinical applications of Doppler OCT may include the surveillance and grading of esophageal varices and the evaluation of lesions such as gastric and duodenal ulcers. OCT catheters may eventually be placed within biopsy needles in order to provide high-resolution tissue imaging of targeted lesions. Furthermore, catheter-based OCT imaging may reveal vascular changes in early malignancy, such as small vessels in the lamina propria, medium vessels in submucosa, and surface vessels in superficial mucosa [33,34,36–40].

### 3.2.1 Gastrointestinal Conditions

***Barrett's Esophagus*** Barrett's esophagus (BE) is defined as the presence of specialized intestinal metaplasia within the tubular esophagus. Recent studies suggest that performing endoscopic surveillance in patients with BE is effective in preventing esophageal adenocarcinoma. The presence of specialized columnar epithelium in the esophagus is readily detected with white-light endoscopy. Although high-resolution endoscopy provides higher rates of diagnosis of BE, considerable diagnostic overlap between esophagitis and BE remains.

Methods of directing biopsies to regions of the esophagus containing dysplastic tissue might improve the effectiveness and efficiency of surveillance in patients with BE. Image-directed biopsies could increase surveillance intervals, enable minimally invasive surgical techniques at an earlier stage of disease progression, or prevent unnecessary interventional procedures. The use of various digital light filters, such as narrowband imaging, has improved the detection of Barrett's and early malignancy. Recently, OCT and endoscopic confocal microscopy have been introduced as high-resolution endoscopy imaging techniques for the diagnosis of BE [36,41–43].

Optical coherence tomography criteria for the diagnosis of BE can be used to differentiate specialized intestinal metaplasia (SIM) accurately from squamous and gastric epithelium in patients undergoing routine endoscopy. In a recent OCT study [44], specific features observed in the images, such as absence of the layered structure of normal squamous epithelium or absence of the vertical pit and crypt morphology of normal gastric mucosa, disorganized architecture with inhomogeneous tissue contrast and an irregular mucosal surface, and the presence of large submucosal glands, were used to stage the disease. The presence of at least two of these features was defined as a diagnostic criterion for SIM. When an experienced, blinded observer prospectively applied the criterion for specialized intestinal metaplasia to the test set ($n = 122$), the criterion was found to be 97% sensitive and 92% specific for specialized intestinal metaplasia. The positive predictive value of the OCT criteria for specialized intestinal metaplasia was 84%. False positive images for BE occurred as a result of inflamed gastric cardia tissue or gastric foveolar hyperplasia.

A similar study conducted by Zuccaro et al. [42] on 69 patients revealed that OCT can provide a highly detailed view of the GI mucosa, with clear delineation of a multilayered structure. OCT has revealed the specific features of normal squamous mucosa, gastric cardia, BE, and adenocarcinoma. The findings of dilated glands with poor light scattering was found to be characteristic of BE. The OCT image of adenocarcinoma was characterized by the total loss of an ordered, layered structure of the esophageal wall. The backscattering from malignant cells resulted in a loss of tissue penetration by OCT. A similar pattern of backscatter was observed in ulcerated tumors where connective tissue stroma interfered with infrared light of OCT. Li et al. [43] recently confirmed in a small descriptive study the ability of OCT to differentiate between normal squamous epithelium and BE. Several additional studies have evaluated the accuracy of OCT in the detection of dysplasia in BE [45–52].

Because the resolution of standard OCT is insufficient to assess the cellular features of dysplasia, an assessment of dysplasia and cancer is generally based on larger-scale features, such as glandular organization and epithelial scattering intensity. The OCT images of high-grade dysplasia reveal a more irregular glandular architecture (i.e., cribriform and irregular-shaped glands) and more inhomogeneous tissue contrast compared to nondysplastic Barrett's epithelium. The diagnosis of high-grade dysplasia is dependent on cytological and subcellular features which are beyond the resolution of current endoscopic OCT systems. However, some cytological features, such as an increased nuclear/cytoplasmic ratio, may alter the light reflection characteristics of Barrett's epithelium with high-grade dysplasia and may potentially make possible the identification of dysplasia (Figure 3.7).

OCT may also prove to be a useful tool for the early detection of esophageal adenocarcinoma. In a recent study conducted by Testoni and Mangiavillano [50], OCT images of six patients with adenocarcinoma of the distal esophagus arising from Barrett's epithelium were analyzed. They observed that OCT images of adenocarcinoma differed from those of normal esophageal mucosa. The main features of malignancy were a lack of regular esophageal layered morphology and a heterogeneous pattern (Figure 3.8). Morphological disorganization was also revealed in a similar study of patients with esophageal adenocarcinoma [51].

Optical coherence tomography may have other applications in BE management. There is increasing interest in staging of early cancer in BE, with application of endoscopic mucosal resection techniques or photodynamic ablation of these lesions as an alternative to esophagectomy.

***Early Gastric Cancer*** Early gastric cancer is usually an incidental finding in the United States, whereas in Asia, many patients are diagnosed with screening examinations. A high percentage of gastric malignancies are detected with

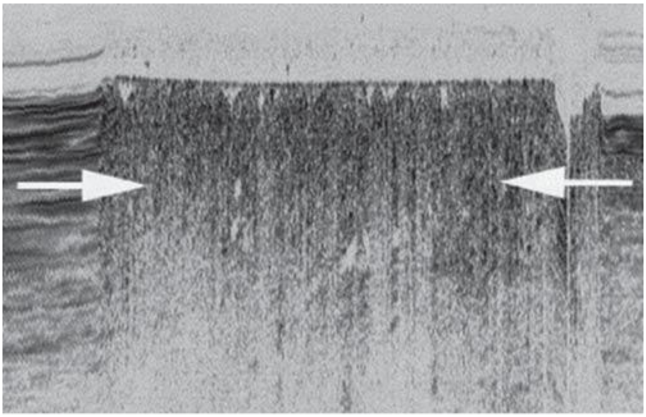

**FIGURE 3.7** Optical coherence tomography linear image of Barrett's epithelium with high-grade dysplasia. Note the absence of goblet cells. (Courtesy of Norman Nishioka, Massachusetts General Hospital.)

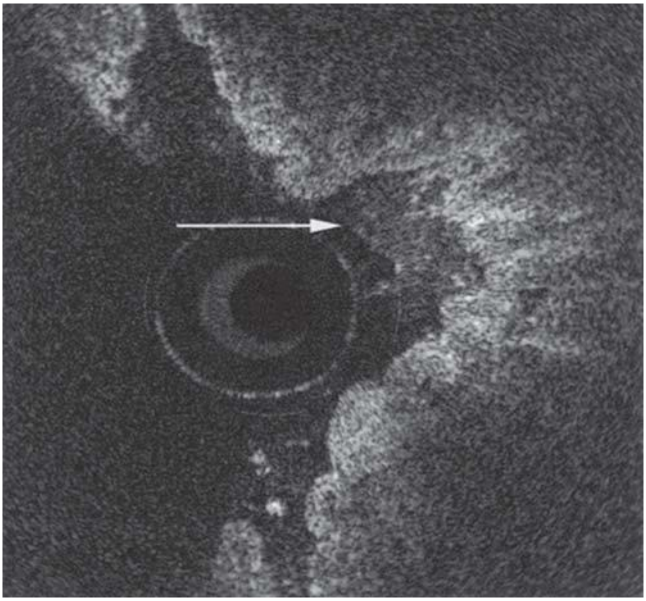

**FIGURE 3.8** Optical coherence tomography radial image of Barrett's epithelium with early esophageal cancer (arrow). (Courtesy of Pier Alberto Testoni, Milan, Italy.)

white-light endoscopy, using the presence of ulcerations, erosions, or masses. Chromoendoscopy has been used to map early gastric cancer and direct the endoscopic resection of the superficial lesions. The endoscopic application of contrast dyes, chromoendoscopy, makes use of the lack of uptake by malignant epithelium to enhance gastric cancer detection. These techniques for early gastric cancer detection have not been applied to large-scale screening programs for high-risk patients.

OCT has been used to detect early gastric cancer [50]. Typical OCT images of gastric mucosa demonstrate the characteristic *crypt-and-pit architecture*. The surface layer shows the gland structure, and three layers of high, low, and high reflective layers behind, which are thought to be the lamina propria (high reflective), mucosal muscle (low reflectivity), and interface layer of the submucosal layer (high reflectivity). There have been no large studies of OCT imaging in the stomach because of the relatively low tissue contrast in this organ [53]. The relatively thick superficial glandular epithelium also causes poor visualization of deeper layers, making it difficult to evaluate the muscularis propria [42].

***Dysplasia Associated with Inflammatory Bowel Disease*** Long-standing inflammation of the colon in ulcerative colitis (UC) and Crohn's disease (CD) has been associated with an increased risk of subsequent dysplasia and colorectal cancer. Therefore, early detection strategies have focused on the detection of dysplasia in flat mucosa. The use of OCT imaging may also provide new insights into the histology of UC and CD [54]. OCT has been evaluated in patients with inflammatory bowel disease (IBD) in order to distinguish CD from UC, with sensitivity and specificity rates of 90% and 83.3% using the presence of transmural inflammation as an indicator of CD. In UC, the majority of OCT images demonstrated an intact layered structure with the characteristic "fried bacon strip" pattern. In CD, OCT images demonstrated a loss of the layered structure of the colon wall. The images of superficial diseased areas appear bright and heterogeneous because of alterations in light scattering, propagation, and backreflection by inflammation, fibrosis, and disruption of tissue planes. OCT changes in light scattering and layering have been shown to correlate with pathological disease activity in UC [50]. Changes in tissue architecture and light scattering have also been shown to differentiate hyperplastic and adenomatous polyps. Hyperplastic polyps generally had an organized crypt pattern and an overall scattering intensity that were relatively similar to those of normal tissue, while adenomatous polyps feature the absence of an organized crypt pattern and a decrease in an overall scattering intensity [55].

Foci of dysplasia in inflammatory bowel disease cannot be readily identified with OCT. The resolution of current endoscopic OCT systems is not sufficient to identify tissue dysplasia in IBD. However, subsurface images of mucosal microvascular networks can be demonstrated with Doppler OCT. These vascular changes may be useful for detecting dysplasia and flat adenomas. With the development of better light sources and optics, improvements in both axial and lateral resolutions in the subcellular level are expected to provide distinct imaging of dysplasia. These advances may be useful for detecting malignant submucosal invasion and may aid in selecting appropriate patients for endoscopic resection.

***Dysplastic Polyps*** Detection of colonic polyps and adenocarcinoma of the colon have been demonstrated with OCT [40,56]. One study suggested that hyperplastic and adenomatous polyps have a distinct appearance on OCT. Adenomas had significantly less structure and scattered light on OCT imaging than did hyperplastic polyps. The appearance of hyperplastic polyps was similar in organization and light scattering to normal mucosa. By performing digital image analysis, the light-scattering property of hyperplastic polyps was demonstrated to be closer to normal mucosa than to adenomas. Adenomatous polyps demonstrated an absence of an organized crypt pattern and a decrease in overall scattering intensity. This study established the ability of OCT to distinguish precancerous polypoid tissue from benign lesions in the colon. Similar to the OCT data on esophageal adenocarcinoma, the OCT image of colon cancer revealed complete loss of the normal tissue morphology [57].

### 3.2.2 Imaging Modalities

***High-Frequency Endoscopic Ultrasonography*** High-frequency catheter US probes (12 to 30 MHz) are being used increasingly as a result of improvements in image quality and durability. Endosonography is an imaging method where a high-frequency ultrasound probe is inserted blindly or under endoscopic control into a lumen. Examination of the gastrointestinal tract is performed using dedicated echoendoscopes or transendoscopic miniprobes. The gastrointestinal wall, mediastinum, pancreas, bile ducts, retroperitoneum, and other structures surrounding the gastrointestinal tract are target organs for endosonography. A detailed image of pathological processes can thus be obtained. The method can be used both for primary diagnosis of lesions and in the follow-up of gastrointestinal diseases. It is accurate in local staging of cancer and in detecting small lesions that cannot be seen with other imaging modalities (Figure 3.9).

There are some limitations in optimal examination, such as stenoses or other factors prohibiting a precise position of the ultrasound transducer. The clinical importance of endosonographic examinations must be evaluated continuously on the basis of new technical modalities and changes in therapeutic procedures [58–62].

High-frequency probe endosonography is used primarily to evaluate small subepithelial lesions of the GI tract. The most common lesion examined is a focal mass in the gastric antrum and the colon. The imaging findings are used to provide a clear differentiation between lipomas, cysts, and solid malignancies (e.g., carcinoids, stromal cell tumors, granular cell tumors). The main weakness of this imaging modality is the need for water submersion. It also lacks Doppler information.

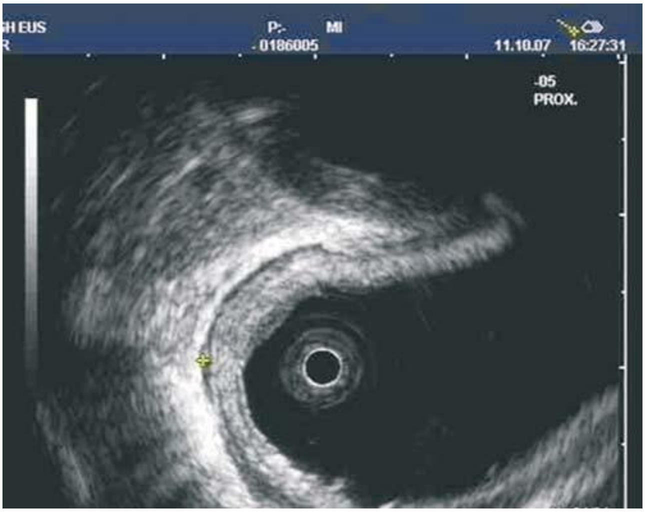

**FIGURE 3.9** High-frequency ultrasound imaging of early esophageal cancer associated with Barrett's esophagus. The subtle dark mucosa, in contrast to the other bright homogeneous lining reflects superficial adenocarcinoma.

***Endoscopic Microscopy*** Laser scanning confocal microscopy is an adaptation of white-light microscopy in which tissue structures are visualized by stimulating the emission of light from a low-powered laser beam. The intensity of emitted light is translated into a gray-scale image which represents microscopic tissue structures [32,63]. Currently, two contrast agents, fluorescein sodium and acriflavine hydrochloride, are used to provide fluorescence imaging. However, only the upper mucosal layer can be displayed endomicroscopically with these contrast agents. Recently, miniaturization efforts have provided integration of the confocal scanning devices into endoscopes, thus permitting in vivo imaging during endoscopy. Confocal imaging readily provides discrimination of normal and neoplastic tissue with high accuracy (Figure 3.10) [64–66].

The main goal of endomicroscopy is to identify mucosal areas suspicious for neoplasia or other changes, leading to real-time targeted biopsy or endoscopic therapy. Fluorescence-aided endomicroscopy makes it possible to identify columnar-lined lower esophagus macroscopically and goblet cell microscopically in the distal esophagus, providing a diagnosis of Barrett's esophagus. Gastric and Barrett's epithelium and Barrett's-associated neoplastic changes can be diagnosed with high accuracy. Goblet cells, which are pathognomonic for Barrett's epithelium, are easily identified in the columnar mucosa. High-grade intraepithelial neoplasias or early cancers can be recognized by a distinct cell type in endomicroscopy (Figure 3.11). Thus, endomicroscopy may be helpful in the management of patients with BE by providing more sensitive, real-time imaging of early malignancy [67].

*Helicobacter pylori* (Hp) organisms have been demonstrated by acriflavine-enhanced endomicroscopy. Acriflavine appears to be taken up actively by Hp bacteria. Following endoscopic laser stimulation, the bacteria are easily detected

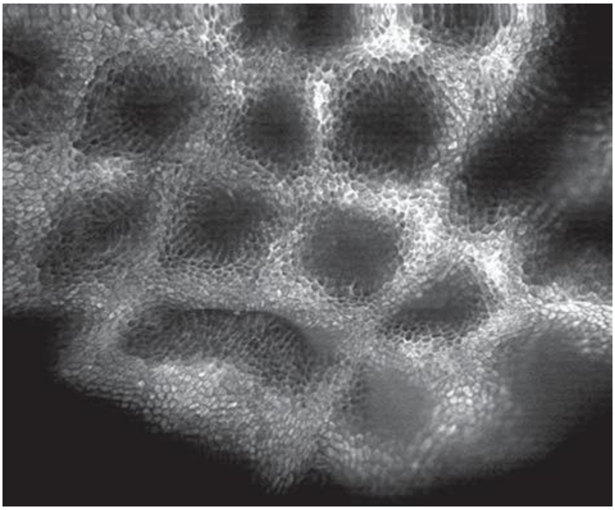

**FIGURE 3.10** Confocal microscopy image of a normal stomach.

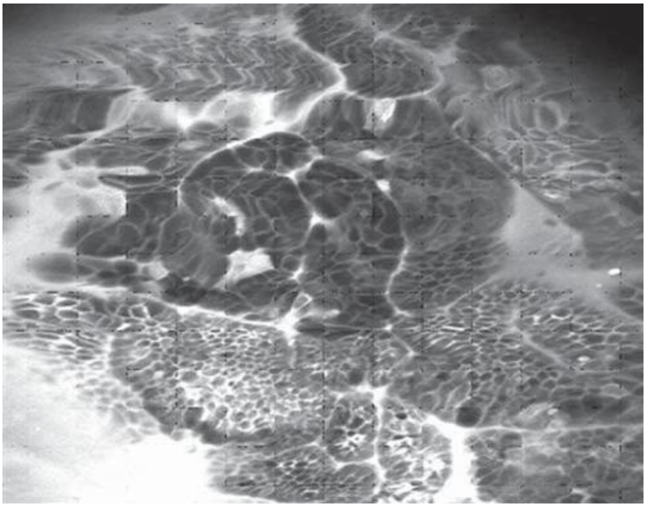

**FIGURE 3.11** Confocal microscopy image of Barrett's esophagus with high-grade dysplasia.

due to their characteristic morphology of spirochetes. The endomicroscopic detection was independent of the density or distribution of Hp bacteria, and even individual bacteria could be identified.

Gastric cancer traditionally carries a poor prognosis because of late presentation at an advanced stage of disease. If diagnosed at an early stage, it is a curable disease. The endoscopic detection of early gastric cancer is challenging. Characteristic alterations suspicious for gastric neoplasia are changes in mucosal color and surface structure using white-light endoscopy. Endomicroscopy can be used to guide biopsies to microscopically suspicious areas. Characteristic neoplastic features of the gastric mucosa observed by confocal laser endomicroscopy are changes in tissue and microvessel architecture as well as in cell morphology. The glands vary in size and shape, with corresponding differences in luminal crypt openings. The tissue pattern is disorganized or totally destroyed (Figure 3.12) [66,68].

Colorectal cancer is still one of the leading causes of cancer-related death in the Western world. The prognosis depends on early detection of preinvasive and neoplastic changes. Early detection makes it possible to cure a patient by means of immediate endoscopic resection. In a recent study, 42 patients with indications for screening or surveillance colonoscopy after previous polypectomy underwent in vivo imaging with the confocal laser endoscope. The aim of the study was to assess the potential for the use of confocal imaging during screening colonoscopy for colorectal cancer. Fluorescein-guided endomicroscopy of intraepithelial neoplasias and colon cancer demonstrated a tubular, villous, or irregular architecture, with a reduced number of goblet cells. In addition, neovascularization in neoplasms was identified by the presence of irregular vessel

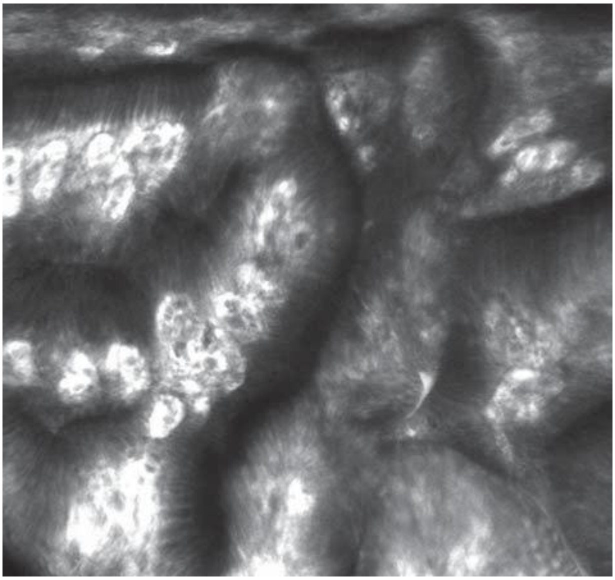

**FIGURE 3.12** Confocal microscopy image of early gastric cancer with focal high-grade dysplasia.

architecture with fluorescein leakage. The presence of neoplastic changes could be predicted with high accuracy (sensitivity, 97.4%; specificity, 99.4%; accuracy, 99.2%). Confocal laser endoscopy is a novel diagnostic tool to analyze living cells during colonoscopy—thereby the assessment of histology of neoplastic changes with high accuracy [68]. In the first prospective trial of endomicroscopy, patients with long-term ulcerative colitis were randomized to undergo either conventional colonoscopy or panchromoendoscopy in conjunction with endomicroscopy to detect intraepithelial neoplasia or colorectal cancer. Using chromoendoscopy in conjunction with endomicroscopy, significantly more intraepithelial neoplasia was detected than with standard colonoscopy. Confocal endomicroscopy can be used to confirm intraepithelial neoplasias with a high degree of accuracy [68].

### 3.2.3 Summary and Conclusions

Several clinical conditions and related diagnostic imaging approaches were discussed here. Although traditional imaging approaches such as endoscopy provide relevant clinical information, there is an ongoing search for further improvement in the diagnostic capacity of endoscopy. While the technologies now available provide reproducible, accurate, objective, quantitative assessment of gastrointestinal structure, there is still an increased need for higher resolution, faster acquisition, and quantitative and reliable imaging devices. Novel technologies such as OCT and confocal endomicroscopy show high promise for improved diagnosis of gastrointestinal diseases.

## 3.3 CARDIOIMAGING

Recent statistics show that over 1 million Americans have a new or recurrent heart attack every year. New cardiac research indicates that unstable plaques—arterial lesions that do not constrict the blood vessel but rather burst, releasing a bolus of lipids into the bloodstream—may be responsible for up to 70% of all heart attacks. These unstable plaques are presently impossible to identify with imaging technologies currently available. Recent research in optical spectroscopy and high-resolution optical imaging (e.g., fluorescence lifetime spectroscopy, optical coherence tomography) show that these new investigational methods have the potential to help change these statistics by enabling clinicians to detect early signs of the disease and to study its evolution in vivo. Even though these technologies are in their early stages and many technological challenges must be addressed prior to clinical use, their unique capabilities might have a prominent role in the future of interventional cardiology.

### 3.3.1 Current Imaging Modalities in Interventional Cardiology

Interventional cardiology is a medical subspecialty that relies heavily on imaging for diagnosis and treatment of coronary, vascular, and structural heart disease. For decades, coronary angiography has been considered the gold standard in the diagnosis of coronary artery disease. However, recent studies have shown that in the early phase of an atherosclerotic process, plaques are formed in the vessel wall without compromising lumen, called *expansive remodeling* [69]. Only when the total area of the plaque reaches approximately 40% on cross section does the lumen start to show narrowing on coronary angiogram. Moreover, since contrast fills the lumen, the angiogram does not provide any information on the characteristics of the plaque. Despite these limitations, coronary angiography is used in daily practice because it does not require high-level skill and provides adequate information to detect flow-limiting lesions which are responsible for angina. When these angiographically significant lesions are intervened upon, the symptom improves.

A recent advancement of knowledge on pathophysiology showed that the majority of acute myocardial infarctions are caused by non-flow-limiting lesions, which are not intervened upon at the time of catheterization [70]. These plaques, which are prone to rupture, leading to acute thrombotic occlusion, resulting in AMI or sudden cardiac death, are called *vulnerable* or *high-risk plaques* [71]. These plaques have certain features, such as a large lipid pool, thin fibrous cap, and increased macrophage density. Since an angiogram does not show the plaque itself but its adjacent lumen, it is not useful in detecting these dangerous plaques.

Intravascular ultrasound (IVUS) has been developed to provide cross-sectional images of vessels. IVUS has been used primarily to better assess lesion severity and lesion morphology in lesions located at ostia or bifurcations, calcified lesions, indeterminate lesions, or instent restenosis. More frequently, IVUS is utilized to evaluate the result of percutaneous coronary intervention (PCI), such as optimal stent deployment. However, in the United States, IVUS is used in only 10% of PCI cases. This low rate of IVUS utilization is due primarily to relatively weak data to support the fact that IVUS improves clinical outcomes, and furthermore, the interpretation of IVUS requires a learning period. Even after training it is often difficult to evaluate fine structural changes, due to the low resolution (100 μm) of IVUS.

### 3.3.2 Clinical Need for High-Resolution Imaging in Interventional Cardiology

Whether a high-resolution intravascular imaging technique such as optical coherence tomography (OCT) will become widely used is unknown. It is conceivable that better plaque characterization and accurate measurements of luminal diameter (delineation of lumen from the vessel wall is much easier with OCT than with IVUS) will lead to the rapid growth of intravascular imaging diagnostics. However, a clear clinical benefit with an improved outcome should be proven by well-designed, carefully conducted prospective studies to make widespread use of this high-resolution imaging modality. One promising field is the evaluation of surface coverage after insertion of a drug eluting stent (DES). Currently, stents are used in over 90% of PCI cases, and the majority of these are DESs. Although DESs reduced the restenosis rate significantly, they created a new problem of very late stent thrombosis. Even after several years, some cases with acute stent thrombosis and subsequent AMI or sudden death have been reported [72,73], a phenomenon that is very rare with bare metal stents. It is thought that these catastrophic events are due to delayed healing of DESs. Several groups, using OCT, demonstrated that even after a year, a significant number of DES struts are not covered and are exposed to circulation [74,75]. Potentially, these uncovered stent struts can be the nidus of acute stent thrombosis. With additional correlation studies between the OCT findings and clinical outcomes, OCT can be a valuable tool in determining the duration of dual antiplatelet therapy.

### 3.3.3 Conclusions and Future Directions

Even though many basic biological, clinical, and technological challenges must be addressed prior to widespread use of this technology, the unique capabilities of OCT ensure that it will have a prominent role in the future of interventional cardiology. Interference with blood and shallow tissue penetration remains a limitation of this optical technology. However, recently developed high-speed OCT has made it possible to scan a 40 to 50-mm arterial segment without interrupting blood flow or compromising image quality. This second-generation OCT, along with polarization-sensitive OCT, spectroscopy, Doppler imaging, and elastography, will improve coronary plaque characterization with additional information on biomechanical and chemical characteristics of the plaque.

## 3.4 NEUROIMAGING: CURRENT TECHNOLOGIES AND FURTHER NEEDS

Over the past 40 years, improvements in imaging have had the greatest impact on the field of clinical neuroscience. The ability to see neural anatomy in exacting detail has transformed the practice of neurology and neurosurgery, making it safer and more accurate. The latest techniques in neuroimaging and future developments in this fast-moving field are discussed in this section.

### 3.4.1 Neuroimaging History

Prior to the advent of cross-sectional imaging in the 1970s, clinicians were hampered in their ability to visualize the brain and spinal cord in vivo. Plain x-rays using ionizing radiation were developed in the late nineteenth century by William Roentgen and are still in use today, but in a more limited capacity. This imaging modality enables visualization of bone and soft tissue but lacks resolution, particularly within nonosseous tissue. X-ray images were improved through the use of contrasting agents such as air and iodinated contrast. Air contrast was used in a procedure called *pneumoencephalography*. In this painful procedure, air was injected into the spinal fluid in the lower back and allowed to float up into the brain. The patient was strapped into a rotating chair that distributed the air through the skull. The contrast between the air and the brain allowed for identification of masses within the skull; however, the mass itself was not visualized. Only its effect on the surrounding tissues could be discerned on the x-ray. This practice was discontinued because of the extreme discomfort it caused.

Contrast materials consisting of oil or iodinated agents were developed and injected into the spinal fluid to help increase brain and spinal cord visualization. These injection procedures, known as *myelograms*, were not without risk and discomfort for the patient, but represented an improvement over air contrast injection. Iodinated contrast was also injected into the central nervous system blood vessels. This cerebral angiogram procedure was exceptional at showing vascular anatomy and also allowed for identification of intracranial masses either through the distortion of the blood vessels caused by the mass or by the change in blood flow. These procedures were the state of the art until the late 1970s and early 1980s, when cross-sectional imaging was invented.

### 3.4.2 Computed Tomography

Computerized axial tomography, or computed tomography (CT), was developed in the 1970s and literally brought a new dimension to imaging of the central nervous system. For the first time, the soft tissue of the brain, spinal cord, and other neural structures could be visualized, adding to the improvement in quality and safety of treating patients who have strokes, tumors, and hemorrhages. Rather than relying on indirect evidence of a space-occupying mass, the mass itself could be visualized. Iodinated contrast agents, administered intravenously, could demonstrate vascular anatomy and, more importantly, alterations in the blood–brain barrier. This phenomenon, in which cerebral blood vessels lose the tight junctions normally found between epithelial blood vessels, is a reliable indicator of tumor growth and neovascularization. The integration of cross-sectional CT imaging with computerized intraoperative navigation allowed for the development of image-guided surgery. The technique of CT-guided stereotactic biopsy allowed for sampling of suspected neoplastic tissue in areas of the brain previously felt to be inaccessible. More recent developments in CT have resulted in multidetector machines in which images can be obtained much more rapidly and with greater detail. This rapid acquisition of imaging has improved the ability to visualize cerebral blood vessels without the need for more invasive arterial catheterization.

### 3.4.3 Magnetic Resonance Imaging

Magnetic resonance imaging (MRI) has further advanced the field of neuroimaging. Measuring the resonating frequency of spinning protons placed within a magnetic field has brought even closer the ability to see detail within the brain. Protons attached to water or fat molecules will resonate with a specific frequency that is determined by the type of molecule. Varying the radio frequencies affecting the proton alters the spin characteristics of that proton and generates a unique signal.

By exploiting the measurement techniques within an MRI sequence, certain aspects of the tissue can be demonstrated more clearly. Parameters known as $T_1$- and $T_2$-weighting are used to depict normal brain anatomy and tissue affected by increased water content (edema), respectively. Gradient-echo sequences take advantage of paramagnetic substances such as iron or hemosiderin, by-products of a previous hemorrhage, making these substances appear more prominent on an MRI scan.

Most commonly, MRI is used to reveal the intracranial and spinal anatomy in far greater detail than CT scan. Not only can MRI acquire images in multiple orientations (axial, coronal, and sagittal), but the resolution of an MRI scan far exceeds that of CT. In addition, MRI has the ability to distinguish tissue based not only on its structural differences, but also on the relative content of water and protein within the cells. Increased water content in the extracellular space, often a hallmark of brain injury or tumor invasion, is clearly seen on MRI. Cell injury through either cellular ischemia or cellular trauma will result in an increased amount of free water within the intracellular space. The water content of this injured tissue is elevated relative to normal tissue. The MRI sequences can be manipulated to exploit this fact, making the appearance of the edema quite striking on the image.

Intravenous contrast agents such as gadolinium can show deficiencies in the blood–brain barrier. Normal cerebral vessel endothelium is lined with cells that prohibit the movement of large molecules out of the intravascular space. Tumor cells, infection, and sometimes stroke can disrupt this barrier, leading to extravasation of these molecules into the extravascular space. Gadolinium is a large rare earth metal that, because of its size, is normally contained within blood vessels after intravenous injection. Enhancement of tissue occurs when the gadolinium leaks from the blood vessels; this appears quite prominently on images. This disruption of the blood–brain barrier is a marker for neoplastic growth or inflammatory conditions within the brain.

Movement of flowing blood through blood vessels can be measured and demonstrated on a magnetic resonance angiogram (MRA) and a magnetic resonance venogram (MRV). Due to the properties of the scan technique, flowing blood generates no radio-frequency signal and thus appears as a void of signal on the images. Blood flow can be measured and manipulated with computer graphics to display intracerebral anatomy as well as pathology such as aneurysms and arteriovenous malformations.

Diffusion-weighted MRI, which is capable of detecting the diffusion of intracellular water molecules, can provide information capable of distinguishing between various pathological processes. Both malignant tumors and infection can have similar MRI appearances in terms of edema formation and contrast enhancement. Diffusion-weighted scanning can differentiate between the two by analyzing the diffusion of water molecules through the tissue. Infections restrict the movement of water far more than tumors and therefore will have different MRI signatures.

Another use for diffusion scanning is to demonstrate the actual white matter fiber tracts connecting various regions of the brain. In the technique of diffusion tensor imaging, water molecules within the axons of neurons are restricted in their ability to flow and tend to move along in the direction of the axon. Measuring this motion of water allows for the three-dimensional reconstruction of the axons and thus shows the direction of white matter tracts within the brain (Figure 3.13). This information is critical to have when planning surgical resections of deeply seated lesions. Respecting the white matter tracts during surgery has a clear advantage in preserving neuroanatomy and function. Surgical trajectories that can parallel the white matter rather than traversing it will result in less damage and improved outcomes [76–78].

Functional MRI, which measures the amount of deoxyhemoglobin within a certain region, can be used to detect areas of increased neural activity. These neurons, generating action potentials at a higher rate relative to surrounding neurons, consume oxygen at a faster rate, thus increasing the amount of deoxyhemoglobin present. If this molecule is detected on a scan, it can show areas of increased activity. This has been used to map areas of motor cortex by having the patient move a certain muscle, or areas of language function by having the patient read or speak while undergoing MRI (Figure 3.14) [79].

Not only can MRI demonstrate anatomy, both normal and abnormal, but it can also show physiological processes associated with neural functions. The actual intracellular chemical composition can be derived by studying the

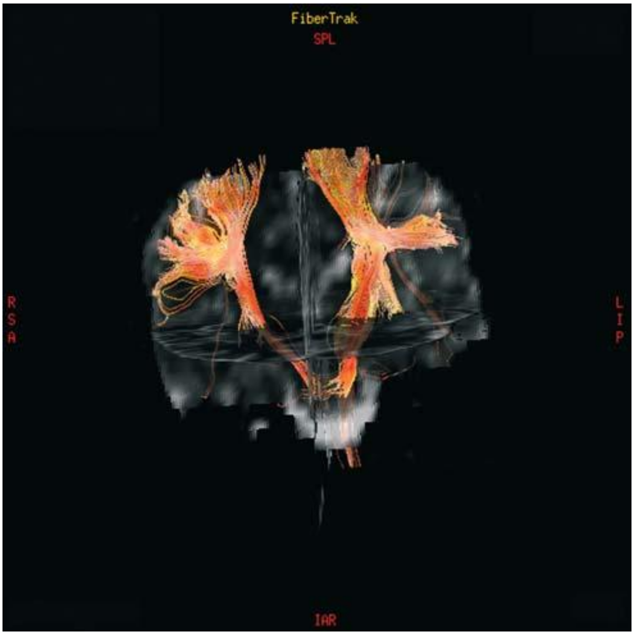

**FIGURE 3.13** Diffusion tensor image revealing white matter tracts comprising the corona radiata in the left and right cerebral hemispheres. The left side demonstrates distortion of the white matter due to the presence of a mass lesion in the cortex. (Courtesy of Grace Lee, Lahey Clinic Medical Center.)

spectrographic data within a certain volume. Alterations in certain compounds (choline and *N*-acetyl aspartate) provide information that may help distinguish between tumor and normal brain tissue. MRI spectroscopy measures the emission of spectrographic data from certain intracellular metabolites. If the content of these molecules is measured and compared to that of surrounding tissue, the presence or absence of tumor tissue as well as the possible degree of malignancy can be determined [80,81].

### 3.4.4 Positron Emission Tomography

Positron emission tomography (PET) scanning utilizes radiolabeled substances such as glucose to measure metabolic activity. A positron-emitting isotope is incorporated into metabolically active substances such as glucose. Tissue such as tumor cells will have a higher metabolic rate than surrounding tissue and thus utilizes more glucose. If the radioactive tracer is measured, these regions of hypermetabolism can indicate the presence of tumor tissue. When PET is coupled with CT or MRI, the resolution improves greatly, allowing both anatomical and

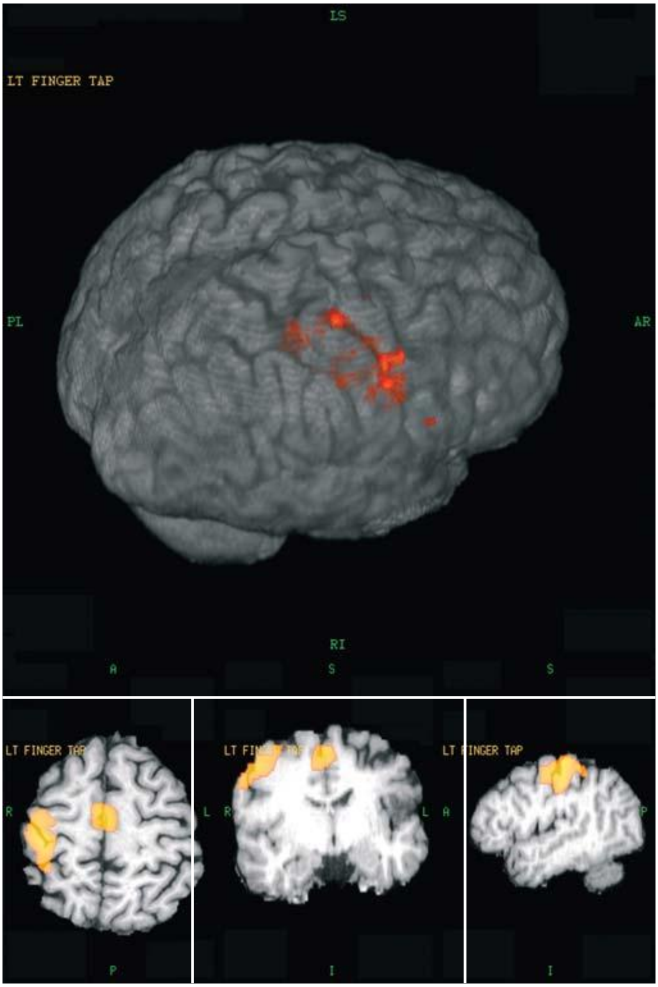

**FIGURE 3.14** Functional MRI showing increased metabolic activity associated with moving the left hand. The three-dimensional image at the top demonstrates the portion of the motor cortex responsible for this activity. The images at the bottom illustrate the same information in axial, coronal, and sagittal slice images. The yellow areas correspond to regions of increased metabolic activity. (Courtesy of Grace Lee, Lahey Clinic Medical Center.)

physiological data to be visualized simultaneously. Its greatest use to date has been in the diagnosis of disseminated cancer that has metastasized throughout the body. It has also been useful as a means to evaluate degenerative conditions of the brain such as Alzheimer's disease and other forms of dementia. Once again, glucose is labeled and injected. Areas of the brain with diminished neuronal activity, indicating the presence of decreased neural metabolism, will show a decrease in the uptake of labeled glucose compared to normal regions of brain function [82,83].

### 3.4.5 Optical Imaging

One area of great promise in neural imaging is optical imaging. Information regarding the chemical makeup within cells and the metabolic activity of these cells can be determined in a noninvasive fashion without the need to introduce specific substrates. Unlike traditional nuclear medicine studies, optical imaging relies on the native properties of proteins and other molecules found naturally in the body. Near-infrared lasers placed on the scalp can measure the absorption of light passed through the brain tissue. Changes in the absorption pattern are an indication of the metabolic activity taking place within the brain [84]. The molecules that are particularly suited for this are oxyhemoglobin and deoxyhemoglobin. The relative percentage of oxy- to deoxyhemoglobin is a direct correlation of metabolism and thus neural activity [85]. Techniques using optical imaging will allow investigators to study both the structure and function of the brain in a noninvasive fashion. Previously, anatomical studies looking at white matter connections required histological study of fiber tracts in in vitro specimens. Optical coherence tomography (OCT) allows not only for anatomical study but for functional research as well [86,87].

Another type of optical imaging, bioluminescence imaging, detects the emission of photons generated by enzymatic reactions. Many of these reactions are catalyzed by a type of enzyme known as a luciferase. Using genetic techniques, these enzymes can be inserted into cells. During cell metabolism, the reaction proceeds, and a photon is emitted and detected. This can provide information related to tumor activity [88]. Primary brain tumors remain a therapeutic challenge, due to limited, effective treatment options. Studying gene expression through molecular imaging may prove beneficial in curing this difficult tumor [89]. This technique has also been used to measure inflammation in the brain in order to study diseases such as encephalitis and multiple sclerosis [90].

The limitations of optical imaging lie in its difficulty in penetrating tissue to a significant depth and problems with spatial resolution. Some of these issues may be solved by implementing high-resolution optical imaging with ultrasound.

### 3.4.6 Conclusions

Improvements in imaging have revolutionized the practice of neurology and neurosurgery. The precision and anatomical detail now available to clinicians have resulted in dramatic improvements in patient care and markedly better outcomes following surgical procedures. With faster computer processing and higher-strength MRI magnets, the detail will only get better. Techniques that study metabolic and molecular function, rather than anatomical structure, will further enhance our understanding of the brain.

## REFERENCES

1. Wollstein, G., et al., Comparison of three optical coherence tomography scanning areas for detection of glaucomatous damage, *Am. J. Ophthalmol.*, Vol. 39, 2005, pp. 39–43.
2. Budenz, D.L., et al., Sensitivity and specificity of the Stratus OCT for perimetric glaucoma, *Ophthalmology*, Vol. 112, 2005, pp. 3–9.
3. Burgansky-Eliash, Z., et al., Optical coherence tomography machine learning classifiers for glaucoma detection: a preliminary study, *Invest. Ophthalmol. Vis. Sci.*, Vol. 46, 2005, pp. 4147–4152.
4. Greaney, M.J., Comparison of optic nerve imaging methods to distinguish normal eyes from those with glaucoma, *Invest. Ophthalmol. Vis. Sci.*, Vol. 43, 2002, pp. 140–145.
5. Deleon-Ortega, J.E., et al., Discrimination between glaucomatous and nonglaucomatous eyes using quantitative imaging devices and subjective optic nerve head assessment, *Invest. Ophthalmol. Vis. Sci.*, Vol. 47, 2006, pp. 3374–3380.
6. Wollstein, G., Garway-Heath, D.F., and Hitchings, R.A., Identification of early glaucoma cases with the scanning laser ophthalmoscope, *Ophthalmology*, Vol. 105, 1998, pp. 1557–1563.
7. Reus, N.J., and Lemij, H.G., Diagnostic accuracy of the GDx VCC for glaucoma, *Ophthalmology*, Vol. 111, 2004, pp. 1860–1865.
8. Chauhan, B.C., et al., Optic disc and visual field changes in a prospective longitudinal study of patients with glaucoma: comparison of scanning laser tomography with conventional perimetry and optic disc photography, *Arch. Ophthalmol.*, Vol. 119, 2001, pp. 1492–1499.
9. Wollstein, G., et al., Optical coherence tomography longitudinal evaluation of retinal nerve fiber layer thickness in glaucoma, *Arch. Ophthalmol.*, Vol. 123, 2005, pp. 464–470.
10. Azuara-Blanco, A., et al., Clinical agreement among glaucoma experts in the detection of glaucomatous changes of the optic disk using simultaneous stereoscopic photographs, *Am. J. Ophthalmol.*, Vol. 136, 2003, pp. 949–950.
11. Badala, F., et al., Optic disk and nerve fiber layer imaging to detect glaucoma, *Am. J. Ophthalmol.*, Vol. 144, 2007, pp. 724–732.
12. Townsend, K.A., Wollstein, G., and Schuman, J.S., Clinical application of MRI in ophthalmology, *NMR Biomed.*, Vol. 21, No. 9, 2008, pp. 997–1002.
13. Huang, D., et al., Optical coherence tomography, *Science*, Vol. 254, 1991, pp. 1178–1181.
14. Paunescu, L.A., et al., Reproducibility of nerve fiber thickness, macular thickness, and optic nerve head measurements using Stratus OCT, *Invest. Ophthalmol. Vis. Sci.*, Vol. 45, 2004, pp. 1716–1724.
15. Budenz, D.L., et al., Reproducibility of retinal nerve fiber thickness measurements using the Stratus OCT in normal and glaucomatous eyes, *Invest. Ophthalmol. Vis. Sci.*, Vol. 46, 2005, pp. 2440–2443.
16. Chan, A., et al., Stage 0 macular holes: observations by optical coherence tomography, *Ophthalmology*, Vol. 111, 2004, pp. 2027–2032.

17. Browning, D.J., et al., Optical coherence tomography measurements and analysis methods in optical coherence tomography studies of diabetic macular edema, *Ophthalmology*, Vol. 115, 2008, pp. 1366–1371.
18. Coscas, F., et al., Optical coherence tomography identification of occult choroidal neovascularization in age-related macular degeneration, *Am. J. Ophthalmol*., Vol. 144, 2007, pp. 592–599.
19. Montero, J.A., and Ruiz-Moreno, J.M., Optical coherence tomography characterisation of idiopathic central serous chorioretinopathy, *Br. J. Ophthalmol*., Vol. 89, 2005, pp. 562–564.
20. Drexler, W., and Fujimoto, J.G., State-of-the-art retinal optical coherence tomography, *Prog. Retin. Eye. Res*., Vol. 27, 2008, pp. 45–88.
21. Weinreb, R.N., Dreher, A.W., and Bille, J.F., Quantitative assessment of the optic nerve head with the laser tomographic scanner, *Int. Ophthalmol*., Vol. 13, 1989, pp. 25–29.
22. Burgansky-Eliash, Z., et al., Glaucoma detection with the Heidelberg retina tomograph 3, *Ophthalmology*, Vol. 114, 2007, pp. 466–471.
23. Gabriele, M.L., et al., Comparison of parameters from Heidelberg retina tomographs 2 and 3, *Ophthalmology*, Vol. 115, 2008, pp. 673–677.
24. Rohrschneider, K., et al., Reproducibility of the optic nerve head topography with a new laser tomographic scanning device, *Ophthalmology*, Vol. 101, 1994, pp. 1044–1049.
25. Weinreb, R.N., Shakiba, S., and Zangwill, L., Scanning laser polarimetry to measure the nerve fiber layer of normal and glaucomatous eyes, *Am. J. Ophthalmol*., Vol. 119, 1995, pp. 627–636.
26. Greenfield, D.S., Knighton, R.W., and Huang, X.R., Effect of corneal polarization axis on assessment of retinal nerve fiber layer thickness by scanning laser polarimetry, *Am. J. Ophthalmol*., Vol. 129, 2000, pp. 715–722.
27. Jemal, A., et al., Cancer statistics, *CA Cancer J. Clin*., Vol. 53, No. 1, 2003, pp. 5–26.
28. Smith, R.A., Cokkinides, V., and Eyre, H.J., American Cancer Society guidelines for the early detection of cancer, *CA Cancer J. Clin*., Vol. 53, No. 1, 2003, pp. 27–43.
29. Falk, G.W., et al., Endosonography in the evaluation of patients with Barrett's esophagus and high-grade dysplasia, *Gastrointest. Endosc*., Vol. 40, No. 2, 1994, pp. 207–212.
30. Adrain, A.L., et al., High-resolution endoluminal sonography is a sensitive modality for the identification of Barrett's metaplasia, *Gastrointest. Endosc*., Vol. 46, No. 2, 1997, pp. 147–151.
31. Bouma, B.E., and Tearney, G.J., Clinical imaging with optical coherence tomography, *Acad. Radiol*., Vol. 9, No. 8, 2002, pp. 942–953.
32. Goetz, M., et al., In vivo subsurface morphological and functional cellular and subcellular imaging of the gastrointestinal tract with confocal mini-microscopy, *World J. Gastroenterol*., Vol. 13, No. 15, 2007, pp. 2160–2165.
33. Tearney, G.J., et al., In vivo endoscopic optical biopsy with optical coherence tomography, *Science*, Vol. 276, No. 5321, 1997, pp. 2037–2039.
34. Tearney, G.J., et al., Porcine coronary imaging in vivo by optical coherence tomography, *Acta Cardiol*., Vol. 55, No. 4, 2000, pp. 233–237.

35. Huang, D., et al., Optical coherence tomography, *Science*, Vol. 254, No. 5035, 1991, pp. 1178–1181.

36. Suter, M.J., et al., Comprehensive microscopy of the esophagus in human patients with optical frequency domain imaging, *Gastrointest. Endosc*., Vol. 68, No. 4, 2008, pp. 745–753.

37. Poneros, J.M., et al., Optical coherence tomography of the biliary tree during ERCP, *Gastrointest. Endosc*., Vol. 55, No. 1, 2002, pp. 84–88.

38. Tearney, G.J., et al., Optical biopsy in human pancreatobiliary tissue using optical coherence tomography, *Dig. Dis. Sci*., Vol. 43, No. 6, 1998, pp. 1193–1199.

39. Yang, V.X., et al., Endoscopic Doppler optical coherence tomography in the human GI tract: initial experience, *Gastrointest. Endosc*., Vol. 61, No. 7, 2005, pp. 879–890.

40. DaCosta, R.S., Wilson, B.C., and Marcon, N.E., Optical techniques for the endoscopic detection of dysplastic colonic lesions, *Curr. Opin. Gastroenterol*., Vol. 21, No. 1, 2005, pp. 70–79.

41. Poneros, J.M., et al., Diagnosis of specialized intestinal metaplasia by optical coherence tomography, *Gastroenterology*, Vol. 120, No. 1, 2001, pp. 7–12.

42. Zuccaro, G., et al., Optical coherence tomography of the esophagus and proximal stomach in health and disease, *Am. J. Gastroenterol*., Vol. 96, No. 9, 2001, pp. 2633–2639.

43. Li, X.D., et al., Optical coherence tomography: advanced technology for the endoscopic imaging of Barrett's esophagus, *Endoscopy*, Vol. 32, No. 12, 2000, pp. 921–930.

44. Evans, J.A., et al., Identifying intestinal metaplasia at the squamocolumnar junction by using optical coherence tomography, *Gastrointest. Endosc*., Vol. 65, No. 1, 2007, pp. 50–56.

45. Evans, J.A., et al., Optical coherence tomography to identify intramucosal carcinoma and high-grade dysplasia in Barrett's esophagus, *Clin. Gastroenterol. Hepatol*., Vol. 4, No. 1, 2006, pp. 38–43.

46. Qi, X., et al., Computer-aided diagnosis of dysplasia in Barrett's esophagus using endoscopic optical coherence tomography, *J. Biomed. Opt*., Vol. 11, No. 4, 2006, p. 044010.

47. Evans, J.A., and Nishioka, N.S., The use of optical coherence tomography in screening and surveillance of Barrett's esophagus, *Clin. Gastroenterol. Hepatol*., Vol. 3, No. 7, Suppl. 1, 2005, pp. S8–S11.

48. Bouma, B.E., et al., High-resolution imaging of the human esophagus and stomach in vivo using optical coherence tomography, *Gastrointest. Endosc*., Vol. 51, No. 4, 2000, pp. 467–474.

49. Brand, S., et al., Optical coherence tomography in the gastrointestinal tract, *Endoscopy*, Vol. 32, No. 10, 2000, pp. 796–803.

50. Testoni, P. A., and Mangiavillano, B., Optical coherence tomography in detection of dysplasia and cancer of the gastrointestinal tract and bilio-pancreatic ductal system, *World J. Gastroenterol*., Vol. 14, No. 2, 2008, pp. 6444–6452.

51. Jackle, S., et al., In vivo endoscopic optical coherence tomography of esophagitis, Barrett's esophagus, and adenocarcinoma of the esophagus, *Endoscopy*, Vol. 32, No. 10, 2000, pp. 750–755.

52. Shen, B., et al., In vivo colonoscopic optical coherence tomography for transmural inflammation in inflammatory bowel disease, *Clin. Gastroenterol. Hepatol*., Vol. 2, No. 12, 2004, pp. 1080–1087.
53. Familiari, L., et al., Optical coherence tomography evaluation of ulcerative colitis: the patterns and the comparison with histology, *Am. J. Gastroenterol*., Vol. 101, No. 12, 2006, pp. 2833–2840.
54. Shen, B., et al., Ex vivo histology-correlated optical coherence tomography in the detection of transmural inflammation in Crohn's disease, *Clin. Gastroenterol. Hepatol*., Vol. 2, No. 9, 2004, pp. 754–760.
55. Pfau, P.R., et al., Criteria for the diagnosis of dysplasia by endoscopic optical coherence tomography, *Gastrointest. Endosc*., Vol. 58, No. 2, 2003, pp. 196–202.
56. Anandasabapathy, S., Endoscopic imaging: emerging optical techniques for the detection of colorectal neoplasia, *Curr. Opin. Gastroenterol*., Vol. 24, No. 1, 2008, pp. 64–69.
57. Jackle, S., et al., In vivo endoscopic optical coherence tomography of the human gastrointestinal tract: toward optical biopsy, *Endoscopy*, Vol. 32, No. 10, 2000, pp. 743–749.
58. Chak, A., et al., Clinical applications of a new through-the-scope ultrasound probe: prospective comparison with an ultrasound endoscope, *Gastrointest. Endosc*., Vol. 45, No. 3, 1997, pp. 291–295.
59. Schiano, T.D., et al., Use of high-resolution endoscopic ultrasonography to assess esophageal wall damage after pneumatic dilation and botulinum toxin injection to treat achalasia, *Gastrointest. Endosc*., Vol. 44, No. 2, 1996, pp. 151–157.
60. Menzel, J., et al., Preoperative diagnosis of bile duct strictures: comparison of intraductal ultrasonography with conventional endosonography, *Scand. J. Gastroenterol*., Vol. 35, No. 1, 2000, pp. 77–82.
61. Chemaly, M., et al., Miniprobe EUS in the pretherapeutic assessment of early esophageal neoplasia, *Endoscopy*, Vol. 40, No. 1, 2008, pp. 2–6.
62. Vazquez-Sequeiros, E., and Wiersema, M.J., High-frequency US catheter-based staging of early esophageal tumors, *Gastrointest. Endosc*., Vol. 55, No. 1, 2002, pp. 95–99.
63. Wright, S.J., and Wright, D.J., Introduction to confocal microscopy, *Methods Cell Biol*., Vol. 70, 2002, pp. 1–85.
64. Nathanson, M.H., Confocal colonoscopy: more than skin deep, *Gastroenterology*, Vol. 127, No. 3, 2004, pp. 987–989.
65. Polglase, A.L., et al., A fluorescence confocal endomicroscope for in vivo microscopy of the upper- and the lower-GI tract, *Gastrointest. Endosc*., Vol. 62, No. 5, 2005, pp. 686–695.
66. Gheorghe, C., et al., Confocal endomicroscopy for in vivo microscopic analysis of upper gastrointestinal tract premalignant and malignant lesions, *J. Gastrointest. Liver Dis*., Vol. 17, No. 1, 2008, pp. 95–100.
67. Kiesslich, R., et al., Diagnosing *Helicobacter pylori* in vivo by confocal laser endoscopy, *Gastroenterology*, Vol. 128, No. 7, 2005, pp. 2119–2123.
68. Kiesslich, R., et al., Confocal laser endoscopy for diagnosing intraepithelial neoplasias and colorectal cancer in vivo, *Gastroenterology*, Vol. 127, No. 3, 2004, pp. 706–713.

69. Glagov, S., et al., Compensatory enlargement of human atherosclerotic coronary arteries, *N. Engl. J. Med.*, Vol. 316, 1987, pp. 1371–1375.
70. Little, W.C., et al., Can coronary angiography predict the site of a subsequent myocardial infarction in patients with mild-to-moderate coronary artery disease? *Circulation*, Vol. 78, 1988, pp. 1157–1166.
71. Falk, E., Shah, P.K., and Fuster, V., Coronary plaque disruption, *Circulation*, Vol. 92, 1995, pp. 657–671.
72. Lagerqvist, B., et al., SCAAR Study Group, Long-term outcomes with drug-eluting stents versus bare-metal stents in Sweden, *N. Engl. J. Med.*, Vol. 356, No. 10, 2007, pp. 1009–1019.
73. Pfisterer, M., et al., BASKET-LATE Investigators, Late clinical events after clopidogrel discontinuation may limit the benefit of drug-eluting stents: an observational study of drug-eluting versus bare-metal stents, *J. Am. Coll. Cardiol.*, Vol. 48, No. 12, 2006, pp. 2584–2591.
74. Takano, M., et al., Long-term follow-up evaluation after sirolimus-eluting stent implantation by optical coherence tomography: Do uncovered struts persist? *J. Am. Coll. Cardiol.*, Vol. 51, No. 9, 2008, pp. 968–969.
75. Matsumoto, D., et al., Neointimal coverage of sirolimus-eluting stents at 6-month follow-up: evaluated by optical coherence tomography, *Eur. Heart J.*, Vol. 28, No. 8, 2007, pp. 961–967.
76. Wu, J., et al., Clinical evaluation and follow-up outcome of diffusion tensor imaging-based functional neuronavigation: a prospective, controlled study in patients with gliomas involving pyramidal tracts, *Neurosurgery*, Vol. 61, No. 5, 2007, pp. 935–949.
77. Bürgel, U., et al., White matter fiber tracts of the human brain: three-dimensional mapping at microscopic resolution, topography and intersubject variability, *Neuroimage*, Vol. 29, No. 4, 2006, pp. 1092–1105.
78. Concha, L., Gross, D.W., and Beaulieu, C., Diffusion tensor tractography of the limbic system, *Am. J. Neuroradiol.*, Vol. 26, No. 9, 2005, pp. 2267–2274.
79. Hennig, J., et al., Functional magnetic resonance imaging: a review of methodological aspects and clinical applications, *J. Magn. Reson. Imaging*, Vol. 18, No. 1, 2003, pp. 1–15.
80. Law, M., et al., Glioma grading: sensitivity, specificity, and predictive values of perfusion MR imaging and proton MR spectroscopic imaging compared with conventional MR imaging, *Am. J. Neuroradiol.*, Vol. 24, No. 10, 2003, pp. 1989–1998.
81. Zonari, P., Baraldi, P., and Crisi, G., Multimodal MRI in the characterization of glial neoplasms: the combined role of single-voxel MR spectroscopy, diffusion imaging and echo-planar perfusion imaging, *Neuroradiology*, Vol. 49, No. 10, 2007, pp. 795–803.
82. Jamieson, D., et al., Positron emission tomography in the investigation of central nervous system disorders, *Radiol. Clin. North Am.*, Vol. 26, No. 5, 1988, pp. 1075–1088.
83. Coleman, R.E., Positron emission tomography diagnosis of Alzheimer's disease, *Neuroimaging Clin. North Am.*, Vol. 15, No. 4, 2005, pp. 837–846.
84. Fujimoto, J.G., Optical coherence tomography for ultrahigh resolution in vivo imaging, *Nat. Biotechnol.*, Vol. 21, No. 11, 2003, pp. 1361–1367.
85. Gambhir, S.S., and Massoud, T.F., Molecular imaging in living subjects: seeing fundamental biological processes in a new light, *Genes Dev.*, Vol. 17, 2003, pp. 545–580.

86. Becerra, L., et al., Diffuse optical tomography of pain and tactile stimulation: activation in cortical sensory and emotional systems, *Neuroimage*, Vol. 41, No. 2, 2008, pp. 252–259.
87. Drexler, W., Ultrahigh-resolution optical coherence tomography, *J. Biomed. Opt*., Vol. 9, No. 1, 2004, pp. 47–74.
88. Weissleder, R., and Mahmood, U., Molecular imaging, *Radiology*, Vol. 219, 2001, pp. 316–333.
89. Jacobs, A.H., et al., Molecular imaging of gliomas, *Mol. Imaging*, Vol. 1, No. 4, 2002, pp. 309–335.
90. Luo, J., et al., Bioluminescence in vivo imaging of autoimmune encephalomyelitis predicts disease, *J. Neuroinflamm*., Vol. 1, 2008, pp. 5–6.

# 4

# ADVANCES IN RETINAL IMAGING

DANIEL X. HAMMER
*Physical Sciences, Inc., Andover, Massachusetts*

4.1 Introduction 86
  4.1.1 Basic anatomical features 87
4.2 Prevalent retinal diseases 91
  4.2.1 Optic nerve head disorders 92
  4.2.2 Macular diseases 95
  4.2.3 Vascular diseases 99
  4.2.4 Hereditary and congenital disorders 103
  4.2.5 Other retinal diseases 104
4.3 Traditional imaging technologies 104
  4.3.1 Direct and indirect ophthalmoscopy, and slit lamp biomicroscopy 106
  4.3.2 Fundus photography 107
  4.3.3 Angiography 107
  4.3.4 Autofluorescence imaging 110
  4.3.5 Scanning laser ophthalmoscopy 112
  4.3.6 Time-domain optical coherence tomography 113
4.4 Advanced imaging technologies 116
  4.4.1 Fourier-domain optical coherence tomography 119
  4.4.2 Adaptive optics 124
  4.4.3 Other modalities: doppler flowmetry and polarization-sensitive imaging 133
  4.4.4 Multimodal approaches 136
4.5 Imaging beyond disease detection 138
  4.5.1 Vision science 138
  4.5.2 Retinal architecture and physiology 138
  4.5.3 Functional imaging 139
  4.5.4 Precision beam delivery for stimulation and laser surgery 140

---

*Advances in Optical Imaging for Clinical Medicine*, Edited by Nicusor Iftimia, William R. Brugge, and Daniel X. Hammer
Copyright © 2011 John Wiley & Sons, Inc.

4.5.5 Visual psychophysics 141
4.5.6 Small-animal imaging and new drug therapies 141
4.6 Conclusions 143
References 143
Bibliography 161

> Now do you not see that the eye embraces the beauty of the whole world? It counsels and corrects all the arts of mankind . . . it is the prince of mathematics, and the sciences founded on it are absolutely certain. It has measured the distances and sizes of the stars; it has discovered the elements and their location . . . it has given birth to architecture and to perspective and to the divine art of painting.
>
> —Leonardo Da Vinci [1]

## 4.1 INTRODUCTION

Vision exists in some form in the majority of all eukaryotic organisms. Vision is arguably the most important sense in human beings because it provides the longest range of input from the external environment, and this in turn provides an extended boundary of our interconnectedness to the outside world. This capability allows us to function at the highest level of our intellects: from flying a plane to viewing and interpreting a piece of art. The visual system is also the most complex sensory system in the human body, with more optic nerve fibers (about 1 million) than in the afferent bundles that comprise the entire somatic sensory system [2].

The eye is also the organ with the most exposure to the external environment, and this has been exploited by researchers to study various aspects of physiology function. Indeed, during development, the retina is derived from the same neural tissue as the brain, and thus is defined as central nervous system tissue [3]. The retina is one of the most richly textured and organized tissue layers in the body. The primary classes of cells include photoreceptors (rods and cones), which are responsible for light transduction and whose cell bodies are in the outer nuclear layer; three major cell types (horizontal, amacrine, and bipolar cells) in the inner nuclear layer, which are responsible for interneural visual signal modification, mediation, and processing; and ganglion cells, the output neurons whose axons arc across the retina into the optic disc to form the optic nerve, the second cranial nerve. In Section 4.1.1 I describe further some of the major anatomical features of the retina.

From a scientific point of view, the eye is a window into the body. The pupillary light response has long been used by physicians to diagnose neurological problems and traumatic brain injury. Some researchers have recently found associations (which may have a genetic basis) between iris characteristics and personality [4]. It is through the eye that we can gain direct, relatively easy access to the cerebral spinal fluid in the subarachnoid space. Some researchers have used this access to measure intracranial pressure to detect brain trauma or other neurological pathologies [5]. It is also an access point to probe the blood–brain barrier. Other researchers have gained information on systemic cardiovascular properties through the eye [6]. As I discuss in Section 4.2, the eye often has manifestations associated with systemic conditions or diseases. Eye gaze, pupil response, and other characteristics of vision are also being exploited by cognitive scientists for a variety of uses, from image information extraction to enemy/terrorist tracking and profiling for military, border, and airport security applications [7]. The diversity of these scientific approaches and applications correlates with the rich spectrum of information that can be gained from the observation point of the eye as both an input and an output medium.

Ophthalmic imaging has gone through two periods of rapid change: one from the late 1980s to the early 1990s and another in the early 2000s. The former had to do with the invention of the scanning laser ophthalmoscope (SLO) [8] and optical coherence tomography (OCT) [9] and was also coincident with rapid technological advances in digital hardware (e.g., cameras, framegrabbers), computing, and signal and image processing algorithms. The latter had to do with the invention of Fourier-domain techniques. These changes provided new diagnostic tools that clinicians now use routinely. They have also begun to change the manner in which diagnoses and therapies are prescribed. Clinicians and researchers now have rapid access to three-dimensional, micrometer-level resolution, and structural (and in some cases, functional) information on the retina, cornea, and other major ocular tissues from their patients and subjects. In this chapter I describe these recent advances in optical imaging techniques and new ones that are currently making their way from the research laboratory to the clinic.

In Section 4.1.1 I describe briefly the major anatomical and physiological features of the eye and retina and in Section 4.2 provide a summary of the causes and characteristics of the major eye diseases. Section 4.3 covers some of the basic imaging technologies that have been in use for several decades, in particular SLO and OCT, and in Section 4.4 I describe some of the new technologies that have recently moved (e.g., Fourier-domain OCT) or soon will move (adaptive optics) from benchtop to bedside. Finally, in Section 4.5 I provide an overview of several imaging fields beyond disease detection. The latter part of the chapter is focused heavily on the advances in ophthalmic imaging techniques from an engineering and instrumentation standpoint. In this chapter I focus on posterior chamber imaging, because a thorough study of the anterior chamber would require an equally extensive description of diseases, physiology, and technology.

### 4.1.1 Basic Anatomical Features

Figure 4.1 shows the eye and the layers of the retina. The refractive index difference from air and the curvature of the tear film and cornea cause light rays to

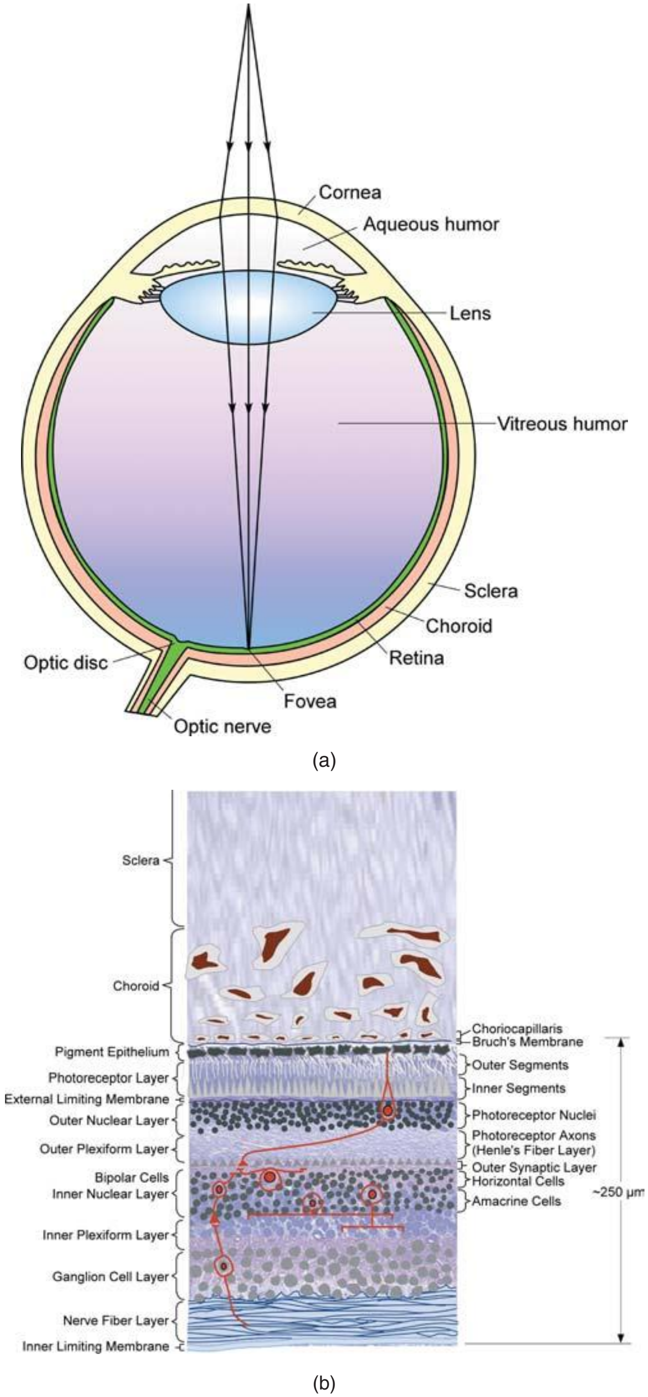
Cornea
Aqueous humor
Lens
Vitreous humor
Sclera
Choroid
Retina
Optic disc
Fovea
Optic nerve
(a)
Sclera
Choroid
Choriocapillaris
Bruch's Membrane
Pigment Epithelium
Photoreceptor Layer
External Limiting Membrane
Outer Nuclear Layer
Outer Plexiform Layer
Bipolar Cells
Inner Nuclear Layer
Inner Plexiform Layer
Ganglion Cell Layer
Nerve Fiber Layer
Inner Limiting Membrane
Outer Segments
Inner Segments
Photoreceptor Nuclei
Photoreceptor Axons (Henle's Fiber Layer)
Outer Synaptic Layer
Horizontal Cells
Amacrine Cells
~250 μm
(b)

**FIGURE 4.1** Diagrams of (a) the eye and (b) the retinal layers.

focus and form an image on the retina. The muscles around the lens compress and reshape the lens for accommodation (near-field focus), a function that in humans is lost ubiquitously around 40 to 45 years of age (presbyopia) from reduced lens elasticity. Light passes through the transparent inner retinal layers, is converted by the rod and cone photoreceptors into neural signals, which are modified by the cells in the inner retina, and is passed from the ganglion cell layer axons [in the nerve fiber layer (NFL)] through the optic nerve head (ONH) via the optic nerve, optic chiasm, and lateral geniculate nuclei to the visual cortex in the occipital lobe of the brain.

The macula is the central 5.5 mm (ca. 19°) of the retina on the temporal side of the optic disc. The macula is composed of the perifoveal area (diameter = 2.5 to 5.5 mm), parafoveal area (diameter = 1.5 to 2.5 mm), fovea (central 1.5 mm), foveola (central 0.35 mm), and umbo (diameter = 0.15 to 0.2 mm).

Light is absorbed by rods and cones, which both consist of stacks of membranous discs in the outer segment, the nucleus and other cellular structures (most notably mitochondria) in the inner segment, and the synaptic terminal. The inner and outer segments are combined at the connecting cilia, which has a bright reflection in a high-resolution OCT image (see Figure 4.2). The photopigment for rods (rhodopsin) and cones (iodopsin or photopsin) exists in the outer segments, which are constantly sloughed off and generated during the daily cycle. Rods are

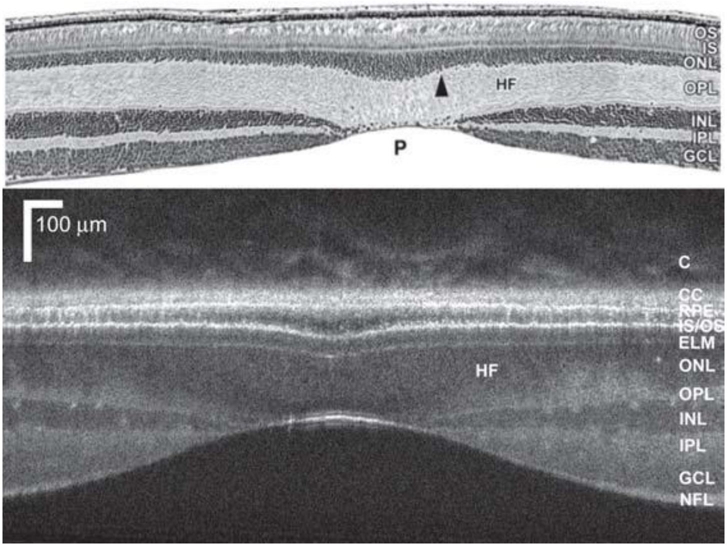

**FIGURE 4.2** Layers of the retina: histology (top) and OCT (bottom) cross sections. NFL, nerve fiber layer; GCL, ganglion cell layer; IPL, inner plexiform layer; INL, inner nuclear layer; OPL, outer plexiform layer; ONL, outer nuclear layer (Henle fiber indicated by arrow); ELM, external limiting membrane; IS/OS, junction between inner and outer segments; RPE, retinal pigment epithelium; CC, choriocapillaris; C, choroid; HF, Henle fibers. (From [15], with permission.)

specialized for night vision and are characterized by achromaticity, extremely high sensitivity (from greater amounts of photopigment), high amplification, more sensitivity to scattered light, lower spatial acuity, and lower temporal responsivity (flicker fusion frequency = 12 Hz). Cones are specialized for day vision and are characterized by trichromaticity, high acuity, lower sensitivity, lower amplification, and higher temporal response (flicker fusion frequency = 55 Hz) [3].

Phototransduction in the retina converts light photons into neural signals. The photoreceptors, horizontal, and bipolar cells communicate over relatively short distances via changes in membrane potential, while ganglion cells use traditional voltage-gated $Na^+$ channels to generate action potentials. Absorption of light by the photopigments in rods and cones triggers a cascade that results in photoreceptor hyperpolarization. The cascade includes stimulation of a G-protein (transducin in rods) by the activated pigment, which in turn activates the enzyme cGMP phosphodiesterase, which in turn lowers the amount of intracellular cGMP and closes cGMP-gated channels, causing membrane hyperpolarization. Glutamate is the major excitatory neurotransmitter in the retina [10]. Both bipolar and ganglion cells have two receptive fields (on-center and off-center) that have antagonistic surrounds. That is, an on-center field is excited when stimulated in the center and inhibited when stimulated in the surround, and an off-center responds in the opposite manner. This property allows weak contrast or rapidly changing images to be sensed in the visual cortex. In the center of the receptive field, a direct connection exists among the cone, bipolar, and ganglion cells. In the surround, lateral pathways are used via the horizontal and amacrine cells. Many types of ganglion cells exist which are specialized for scene features, including fine spatial detail, color, and movement [3].

The retina is supplied by two separate circulatory systems that both derive from the ophthalmic artery. The inner retinal layers are supplied by the retinal arteries that enter the eye through the ONH, while the photoreceptors are supplied by the choriocapillaris and choroid in the peripapillary and submacular region. The blood–retina barrier is thus formed by the tight junctions in both the retinal capillaries and the RPE. Retinal arteries are about 110 μm in diameter and the retinal capillaries are 5 to 6 μm in diameter. Retinal veins are about 150 μm in diameter. Vessels in the choriocapillaris are 20 to 25 μm in diameter. Flow in the retinal arteries can reach velocities of 70 mm/s, and total flow rates are 80 mL/min. Flow in the choroid is the highest in the body at 800 to 1000 mL/min. Regulation of flow in the choroid is controlled with the sympathetic nervous system, while the retinal vessels have no nerve fibers and are therefore autoregulated [11].

In humans, development of the human eye occurs throughout gestation. Similarly, retinal development progresses as a continuous process that does not end until several years after birth. In the sixth fetal week (time after conception), the RPE differentiates, followed by differentiation of the neuroblastic layer into the Muller, ganglion, and amacrine cells [12]. After the third month, all retinal layers (GCL, IPL, INL, OPL, ONL) are present and the precursors to cones and rods differentiate. The outer nuclear layer is a single cell layer at this point. By midgestation (fetal month 4 to 5), the retinal vasculature begins to form and the

GCL is very thick over the region that will become the fovea. After midgestation, the foveal pit forms, owing to differential elasticity in this avascular region compared to the adjacent macula and most likely driven by increased intraocular pressure (IOP) and retinal stretch (from eye growth) [13–15]. Cones differentiate from their precursors between fetal months 4 and 6 and rods in fetal month 7 [12]. Only cones are present in the central fovea (0.35 mm). Further foveal development is characterized by pit expansion, centrifugal displacement of the inner retinal layers, and centripetal displacement of the outer nuclear layer and photoreceptors. This leads to cone packing in the area of high visual acuity (i.e., fovea centralis), where the cones become narrow and elongated, a process that isn't completed until age 4 to 6 [16]. The number of human photoreceptors is fixed relatively early by midgestation [17]. The average number of rods and cones in the human retina is 92 million and 4.6 million, respectively, with an average peak cone density in the fovea centralis of 199,000 cones/mm$^2$ (range of 100,000 to 324,000 cones/mm$^2$) [18].

Figure 4.2 shows a comparison of histology and an AO-FDOCT image of the fovea. In an OCT image, the cellular layers have lower reflectivity than the plexiform layers, which presumably have increased light scatter arising from the cell axons. In the OCT image, all retinal layers can be identified, although in most layers individual cells cannot be resolved. The retinal capillaries in the inner cellular layers (GCL and INL) can also be resolved. The features of the normal human fovea (central $5^\circ$ or 1.5 mm) include a foveal pit or dimple, which can often be resolved in ophthalmoscopy (fundus photography or confocal SLO) from a reflex, or a bright spot, which is a virtual image caused by its concave retroreflector shape; the absence of inner retinal layers (NFL to OPL); the absence of vasculature [called the foveal avascular zone (FAZ)]; the absence of rod photoreceptors (called the rod-free zone); increased ONL thickness; and increased outer segment thickness from cone photoreceptor packing. The NFL thickness increases away from the fovea and has maximum thickness near the ONH. The Henle fiber layer can be resolved in the difference in reflectivity in the ONL. Furthermore, there is some indication that the difference in reflectivity in the IS/OS junction in the fovea compared to perifoveal regions is indicative of interference artifacts, which may be responsible for the inability of AOSLOs to resolve very small photoreceptors [19]. Recent algorithms have been developed to segment multiple layers precisely in an FDOCT image [20,21].

## 4.2 PREVALENT RETINAL DISEASES

It is beyond the scope of this chapter to describe all retinal diseases. However, three diseases—primary open angle glaucoma (POAG), age-related macular degeneration (AMD), and diabetic retinopathy (DR)—with the largest prevalence in the U.S. population are described in this section. These three diseases together affect nearly 7% (>8 million persons) of the U.S. population above the age of 40 years and represent a majority or significant fraction of the causes of blindness in

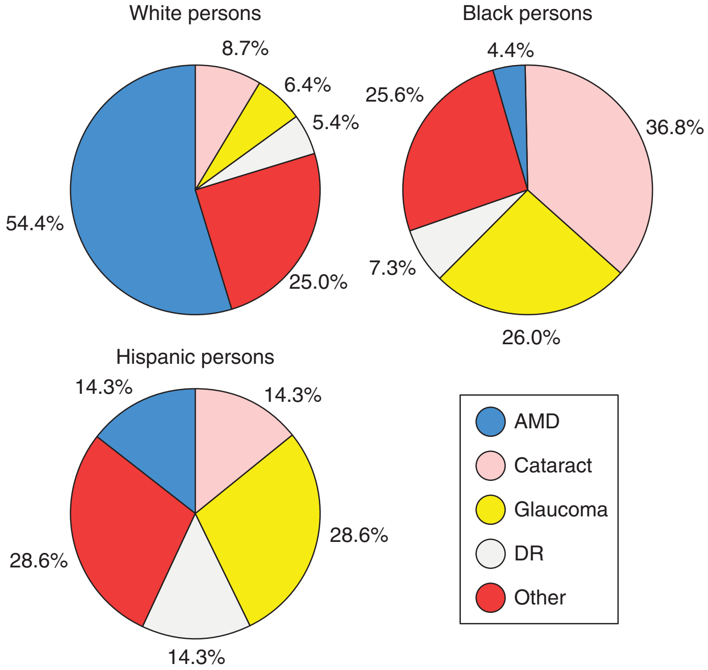

**FIGURE 4.3** Causes of blindness (best corrected visual acuity <20/200) by race. (From [33], with permission.)

all ethnic classes (see Figure 4.3). Moreover, AMD and DR rates are expected to increase significantly in the next 10 years (AMD: increase of 50% by 2020), as the population, age, and life expectancy of the United States (and other developed countries) increases and rates of type II diabetes mellitus (DM) increase. In addition to these three diseases, several more common retinal diseases are described. A sample of prevalence data for several common retinal diseases in the United States is listed in Table 4.1.

### 4.2.1 Optic Nerve Head Disorders

***Glaucoma*** Glaucoma is one of the leading causes of irreversible blindness in the world. Glaucoma is a family of pathologies with over 60 known types, that are subdivided into angle closure and the more common open-angle [primary open-angle glaucoma (POAG)] types. The prevalence of POAG is estimated to be 1.86% (2.2 million people) in the United States for persons over 40 years old. For Caucasians and blacks the prevalence is 1.69% (1.6 million people) and 3.37% (0.4 million), respectively. In 2020, the number of persons with glaucoma in the United States is expected to increase 50%, to 3.36 million [22]. The prevalence of angle closure glaucoma varies widely depending on the study; an average prevalence from several studies was calculated to be about 0.2% for persons over 40 years old [34].

**TABLE 4.1** **Prevalence of Retinal Disease in the United States**

| Disease | Prevalence (%) | Number | Modifiers | Ref. |
|---|---|---|---|---|
| POAG | 1.86 | 2.2 million | U.S., >40 years | [22] |
| AMD | 1.5 | 1.8 million | U.S., >40 years | [23] |
|  | 15 | — | White women, >80 years |  |
| Drusen (AMD risk) | — | 7 million | U.S., >40 years |  |
| DR | 3.4 | 4.1 million | U.S., >40 years | [24] |
|  | 0.75 | 0.9 million | U.S., >40 years, vision-threatening retinopathy |  |
|  | 40.3 | 4.1 million | Persons with DM, >40 years |  |
|  | 8.2 | 0.9 million | Persons with DM, >40 years, vision-threatening retinopathy |  |
| CSC | 0.000099 |  | Men, Olmsted County, Minnesota | [25] |
|  | 0.000017 |  | Women, Olmsted County, Minnesota |  |
| Retinitis pigmentosa | 0.02–0.04 | 100,000 | U.S. | [26] |
| Central artery obstruction | 0.01 | — | — | [27] |
| Central vein obstruction | 0.5 | — | — | [28] |
| ROP | 0.2 | — | New York State | [29] |
|  | 0.12 | — | U.S. | [30] |
| Stargardt's | 0.0001 | — | — | [31] |
| Retinoblastoma | 0.006 | — | — | [32] |

Glaucoma is characterized by elevated intraocular pressure (IOP), optic disc abnormalities, and a loss in the nerve fiber layer (ganglion cell axons). The disease mechanisms related to elevated IOP are fairly well known and involve blockage of the flow of aqueous humor in and around the ciliary body and trabecular meshwork. Aqueous humor is created in the ciliary body by active ion channels and interstitial fluid from the osmotic and pressure gradient between the ciliary vessels and the posterior chamber [35]. Aqueous humor flows over the lens, around the iris, back toward the anterior chamber angle, into the trabecular meshwork and Schlemm's canal, and into the aqueous veins via a multitude of collection channels. Glaucoma can occur if flow is blocked anywhere along this path, including ciliary blockage from inflammation or fibrin debris, pupil blockage from a swollen or improperly positioned lens (primary angle closure glaucoma), adhesion between the iris and the lens, and blockage of the trabecular meshwork from neovascular growth, cellular debris, or loss of function of the collector channels or aqueous vein [36].

The mechanisms of glaucoma related to optic disc abnormalities are less well understood, although the typical pattern of damage (from visual field tests) suggests that disruption occurs in the optic disc and not at the ganglion cell body. Two mechanisms that have been hypothesized are related to disruption of the axoplasmic transport of trophic factors in the optic nerve disc from elevated IOP, resulting in ganglion cell death by apoptosis [36]. The mechanical hypothesis proposes that bowing in the lamina cribrosa pinches the axons to block transport [37]. The vascular hypothesis proposes a disruption in the normal vascular supply in the disc capillaries in the presence of elevated IOP or secondary to IOP. The disruption in microcirculation at the disc can result in the release of vasoactive substances (e.g., angiotensin) that block axoplasmic transport by vasoconstriction [38].

Although a small percentage of those with glaucoma do not exhibit elevated IOP (normal tension glaucoma), IOP remains a central component (risk factor, cause) of glaucoma, and a clear therapeutic benefit results when it is lowered to acceptable levels. Thus, glaucoma screening and therapies have traditionally involved measurement of IOP via tonometry and management of IOP via topical medications (e.g., β-blockers, α-adrenergic agonists). Visual field testing is also a central component of glaucoma diagnosis, although significant nerve fiber loss can occur prior to any detectable changes in the peripheral visual field.

Imaging techniques for glaucoma diagnosis include stereoscopic optic disc photography, optic nerve head analyzers, SLO, scanning laser polarimetry, and OCT. Figure 4.4 illustrates high-resolution three-dimensional mapping for nerve fiber layer thickness using high-speed spectral domain OCT. Stereoscopic imaging enables subjective examination of optic nerve head size and volume. Quantitative information can be obtained from the nerve head analyzers. SLO allows depth discrimination via rejection of backscattered light from axial image planes outside the confocal range gate (ca. 300 μm). By taking multiple steps focused

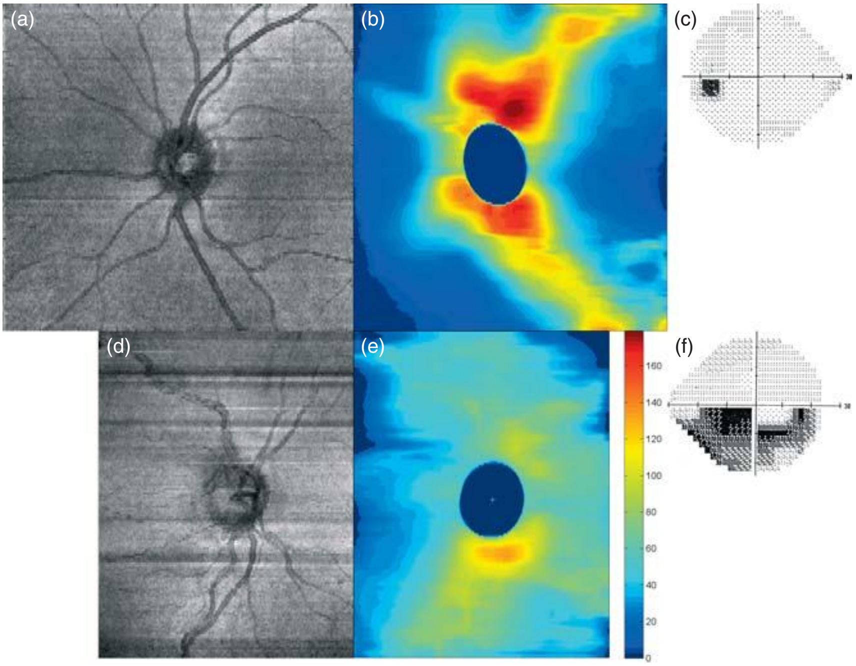

**FIGURE 4.4** NFL thickness maps with high-speed SDOCT in normal (top row) and glaucomatous (bottom row) eyes. Shown are integrated SDOCT reflectance images (a, d), NFL thickness maps (b, e), and corresponding visual field measurements. The scale bar is in units of micrometers. (Courtesy of J. de Boer.)

through the optic disc, the optic nerve head volume can be mapped very precisely. The clinical SLO most commonly used is the Heidelberg HRT (Heidelberg Engineering, Heidelberg, Germany).

***Other Optic Nerve Head Disorders*** Other ONH disorders include ONH drusen, melanocytoma of the disc, papilledema, and optic pits and other disc malformation, including optic nerve hypoplasia. Papilledema is swelling of the ONH caused by elevated intracranial pressure (see Figure 4.15). Melanocytoma is a congenital hyperpigmented tumor that is usually benign and stable but in a small number of cases can exhibit progressive growth [39]. ONH drusen is an idiopathic condition that consists of the presence of globular calcified cysts in the disc and which has symptoms similar to those of papilledema [40].

### 4.2.2 Macular Diseases

***Macular Degeneration*** Choroidal neovascularization (CNV) is associated with several lower-prevalence macular pathologies, including angioid streaks, intraocular inflammation, pathological myopia, choroidal rupture, chorioretinal scars, and chorioretinal dystrophy. Age-related macular degeneration (AMD) is the most common disease that causes CNV.

In the Western world, AMD is the leading cause of blindness in the elderly [23]. Metaanalysis of numerous population-based studies determined the prevalence of high-risk AMD (at least one macular drusen with a diameter $\geq 125\ \mu m$) to be 5.41% in the age range 60 to 64 years and to incline sharply to 23.56% by the age of 80 years and above [41]. The prevalence of advanced AMD was estimated to be 11.77% above the age of 80 years. With the aging of the population, the estimated number of subjects with AMD is expected to increase by 50% from 2000 to 2020.

AMD develops initially because of a disruption in the process of ingress of oxygen and nutrients to and egress of waste (e.g., phagocytosis of shed photoreceptor outer segments during the daily visual cycle) from the photoreceptors to the underlying choriocapillaris (CC). These two layers are separated by the pigmented monolayer, RPE, and by Bruch's membrane (BM), the extracellular matrix compartment composed of elastin and collagen. In early stages, AMD is associated with a buildup of either focal drusen or diffuse basal deposits and an elevation of the RPE (Figure 4.5). Molecular components of drusen have been characterized in numerous *ex vivum* studies, often with focal nonhomogeneous deposition of components, although these have not been imaged in vivo [42–45]. In its more advanced stages, AMD is characterized either by severe loss of photoreceptors and geographical atrophy (GA) of the RPE (nonneovascular or dry AMD) or by the development of choroidal neovascularization (CNV) extending through breaks in Bruch's membrane (neovascular or wet AMD). Figure 4.6 shows a subretinal neovascular lesion in a wet AMD subject. This neovascular sheet accompanied by glial tissue leads consecutively to disruption in the retinal anatomy and function. The cornerstone of current treatment methods is to prevent the conversion of nonneovascular disease into the neovascular form.

AMD is a complex disease with several genetic and environmental risk factors, including age, smoking, ocular pigmentation, high blood pressure, and family history [46–51]. Gene screening studies have implicated chromosomal region 1q25–q32 and other sites for several genes responsible for AMD [52–54]. Studies show that additional genes and environmental factors interrelate in the development of AMD [55]. Haplotype mapping and immunocytochemistry have further indicated that a variation in complement factor H (HF1/CFH) may play

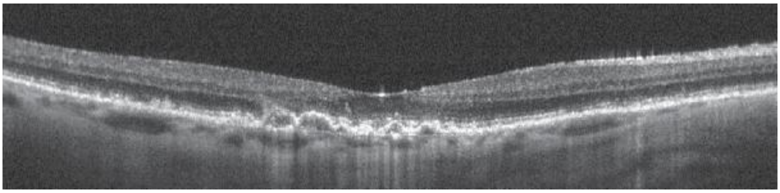

**FIGURE 4.5** FDOCT image of dry AMD. Note large regions of drusen in the RPE under the fovea. The scan length is 6 mm.

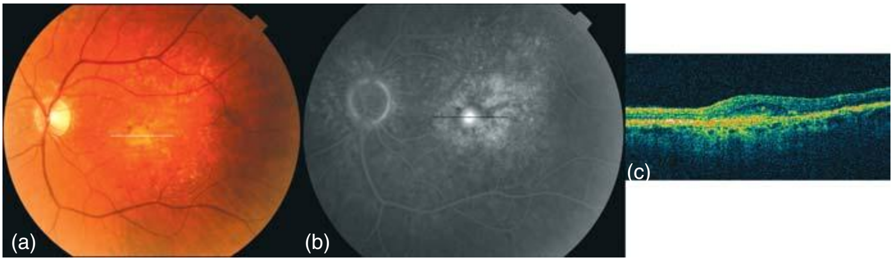

**FIGURE 4.6** (a) Fundus photograph, (b) late-phase fluorescein angiogram (FA), and (c) stratus OCT image of wet AMD lesion. The lines in the fundus and FA images show the approximate location of the OCT scan. (Courtesy of D. Husain.)

a significant role in the development of AMD [56]. CFH is an inhibitor of the complement cascade, which destroys microorganisms and antigens by disrupting their cell membranes. CFH regulates excessive inflammation caused by the complement system and has been linked to other diseases, such as Alzheimer's and atherosclerosis [42]. The evidence for an unchecked inflammatory process as a significant component in the development of this complex disease is strong and may lead to screening methods and the development of new pharmacological agents that inhibit or slow the development of AMD.

Evidence of a link between lipofuscin-mediated changes in RPE, drusen, and Bruch's membrane and the progression of AMD is growing [57,58]. Lipofuscin is an aggregate of lipid and proteins whose primary fluorophore, A2E containing vitamin A and ethanolamine, emits orange wavelengths [59]. It is known that fundus lipofuscin increases with age [60,61] and when photoexcited is toxic to in vitro RPE cells via the generation of free radicals [62]. Previous studies have reported a blue shift in fundus autofluorescence [63,64] and lipofuscin autofluorescence has been spatially correlated with the location of drusen [57].

The mechanism for retinal dysfunction producing the first stages of vision loss in AMD may be due to photoreceptor degeneration over drusen and over CNV [65,66]. In geographic atrophy, there are numerous mechanisms that may explain the timing and progression of new areas of photoreceptor degeneration and RPE atrophy. Lipofuscin accumulation in the RPE may precede progression of GA [55]; however, photoreceptor loss also extends beyond the site of GA, and outer segments may contribute to the basal deposits [67].

***Central Serous Chorioretinopathy*** Central serous chorioretinopathy (CSC), also called *central serous retinopathy*, is an idiopathic condition in which fluid accumulates between the RPE and the neural retina, causing a neural retinal detachment. The choroidal vessels are the source of the fluid. Evidence suggests that CSC is caused by the blockage of flow in the choroid and choriocapillaris, ischemia, and focal choroidal exudation, which causes RPE detachment and in turn causes the tight junctions between RPE cells to break, releasing fluid into the subneural space [68]. CSC is usually diagnosed with fluorescein angiography, which shows focal leakage in the early phase and pooling in the late phase. CSC often resolves spontaneously or with laser photocoagulation treatment.

***Macular Dystrophy*** The macular dystrophies are a family of relatively rare inherited retinal disorders, which include juvenile Stargardt's disease (the most prevalent), fundus flavimaculatus, Best's disease, adult vitelliform dystrophy, familial drusen, pattern dystrophy, dominant cystoid macular edema, Sorsby's macular dystrophy, North Carolina macular dystrophy, progressive bifocal chorioretinal atrophy, atrophia areata, cone degeneration, and central areolar choroidal dystrophy. The macular dystrophies are relatively easy to diagnose but more difficult to distinguish because the genetic abnormalities to which they give rise have overlapping phenotypes, and different phenotypes may result from the same genetic disorder [69]. The characteristic features of all macular dystrophies are loss of macular photoreceptors (and central vision) and RPE cells and yellow material within the RPE. There are no known treatment strategies to halt the progression of the disease except in the rare cases where choroidal neovascularization is present and can be controlled with laser therapy. However, because of their heritable nature, the macular dystrophies are prime targets for engineered gene therapies such as retroviral vectors.

***Other Macular Disorders: Macular Holes, Epiretinal Membranes, Cystoid Macular Edema, and Angioid Streaks*** There are several retinal pathologies that cause focal changes in the neural retina. Idiopathic macular holes are a spontaneous full-thickness loss in retinal layers, the cause of which may be tractional forces from the vitreous. Vitrectomy is a common successful treatment for macular holes, stage 2 (full-thickness defect of size 100 to 200 $\mu$m) or higher. Epiretinal membranes are avascular fibrocellular membranes that form on the inner surface of the retina. Epiretinal membranes are most often associated with posterior vitreous detachments and are believed to result from the migration, release, and accumulation of retinal glial cells through dehiscences in the inner limiting membrane. Epiretinal membranes can also develop from retinal detachments and are thought to result from the accumulation of RPE cells and other constituents that are released into the vitreous cavity [70].

Cystoid macular edema is a pathological response to cataract surgery and other conditions (vascular, inflammatory, or inherited diseases) that results in the formation of fluid-filled cysts in the outer plexiform layer, thickening of the macula, and loss of the foveal pit. The fluid accumulation is a result of damage to the retinal vascular endothelium from intraocular inflammation, diabetic retinopathy, and retinal vein obstructions. Cystoid macular edema is usually treated with topical corticosteroids, which inhibit phopholipase $A_2$, a membrane lipid responsible for the synthesis of prostaglandins [71].

Angioid streaks are breaks in a thickened and calcified Bruch's membrane, whose etiology is unknown. Angioid streaks are closely associated with several systemic diseases, including pseudoxanthoma elasticum and Paget's disease of bone.

### 4.2.3 Vascular Diseases

***Diabetic Retinopathy*** Diabetic retinopathy (DR) is a retinal vascular disorder that is a complication of diabetes mellitus (DM). It can develop in patients with both type I and type II diabetes. DR occurs in roughly half of all patients with DM (ca. 10.2 million persons). The incidence of retinopathy and vision-threatening retinopathy is 3.4% (4.1 million persons) and 0.75% (0.9 million persons), respectively, in the U.S. population 40 years of age and older. The incidence of DR increases with the duration of time after onset of the disease. The incidence of both DM and DR is expected to increase in the future with an aging population and increased incidence of DM. It is estimated that by the year 2020, the incidence of retinopathy and vision-threatening retinopathy in the U.S. population 40 years of age and older will rise to 4.6% (7.2 million persons) and 1.0% (1.6 million persons), respectively [24].

DR is thought to be induced by vasoproliferative factors such as vascular endothelial growth factor (VEGF) [72]. Increased concentration of aldose reductase, which converts sugar into alcohol, and abnormalities in platelet function and blood viscosity are also thought to contribute to the development of diabetic retinopathy [73]. Early DR is classified as nonproliferative diabetic retinopathy (NPDR) and is characterized by microaneurysms, intraretinal hemorrhages, macular edema, lipid exudates, and circinate retinopathy. Inner retinal hypoxia increases in advanced NPDR and is characterized by cotton wool spots (from ischemia), venous beading, and large areas of capillary nonperfusion. Late-stage DR, called *proliferative diabetic retinopathy* (PDR), has features that include severe vitreous hemorrhage, neovascularization with fibrous proliferation, and retinal detachments (caused either by traction alone or retinal breaks) [73]. Figure 4.7 show representative severe diabetic retinopathy with traction. The FA image (Figure 4.7b) shows capillary dropout.

The most commonly used and effective treatment for DR is panretinal photocoagulation [74]. The mechanism by which photocoagulation works is unknown but may be related to a decrease in vasoproliferative factors, an increase in antiangiogenic factors, or increased oxygenation via choroidal perfusion from retinal thinning [73]. Other DR treatments include administration of antiplatelet

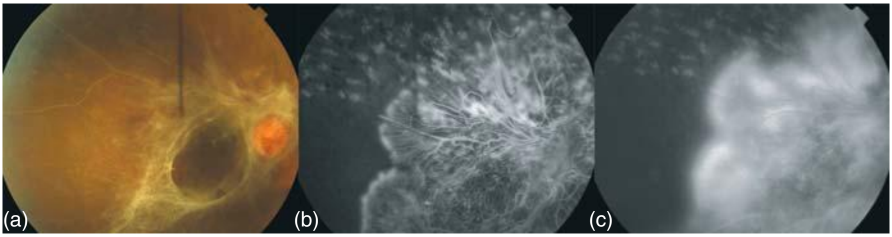

**FIGURE 4.7** Representative proliferative diabetic retinopathy: (a) color fundus photograph; (b) early-phase FA; (c) late-phase FA. (Courtesy of D. Husain.)

[75], antihypertensive [76], and antiangiogenesis agents [77], peripheral retinal cryotherapy (in cases where ocular media opacities prevents laser therapy) [78], and vitrectomy [79].

***Arterial and Venous Obstructive Disease*** Retinal arterial obstructions can occur in the central artery or branch arteries and lead to ischemia of the entire inner retina or be localized to the region supplied by the branch artery. Arterial obstructions are often associated with systemic conditions, including atherosclerosis, hypertension, and other cardiovascular disease. Most arterial obstructions are thrombolic or embolic, with branch obstructions more likely than central obstructions to be embolic [80]. Retinal emboli come in various types: cholesterol, usually originating from plaques in the carotid artery; platelet-fibrin, associated with cardiac thromboses; calcific, from heart valves and the aorta; and tumor cells [80]. Because central arterial obstructions occur proximal to the lamina cribrosa in the ONH, the obstruction site is not directly evident from fundus examination. The primary symptom of central retinal obstructions is painless, precipitous loss of vision [81]. Fundus imaging and angiography performed reveal constricted vessels, ischemic retinal whitening, and incomplete dye filling in the arteries. Central retinal artery obstruction has a low incidence rate of only 0.01% [27]. Branch arterial obstructions are even rarer than central arterial obstructions [80]. They can be detected by visual field deficits in the region supplied by the blocked artery. There is no proven treatment strategy for either central or branch arterial obstructions. The prognosis for central arterial obstruction is especially grim, since irreversible inner retina death occurs after about 100 minutes without normal arterial flow [82]. Only about a third of patients with central obstructions show any improvement in vision. For branch obstructions, a visual field defect usually remains, but good central acuity is retained in the vast majority of cases [80].

Unlike arterial obstructions, venous obstructions are the second most common retinal vascular disorder behind DR. Venous obstructive disease is also divided between central vein obstruction and branch vein obstruction. A central vein obstruction usually occurs near the lamina cribrosa and is the result of thrombosis from arteriosclerosis, endothelial cell proliferation, or as an ancillary condition from other inflammatory diseases [83]. Central vein obstruction is divided further between nonischemic and ischemic types. Both subtypes are characterized by dilated, tortuous veins and hemorrhages across the retina, as well as macula and ONH edema, capillary nonperfusion, cotton wool spots, and neovascularization of the retina and disc. Nonischemic central retinal vein obstruction is the milder of the two, with a very low incidence of neovascularization and a decreased number of cotton wool spots. Capillary nonperfusion may also be absent. Nonischemic vein obstruction often progresses to ischemic vein obstruction [84]. The ischemic subtype may be associated with severe arterial disease [85]. Although no treatment has been proven effective, panretinal photocoagulation is usually applied in cases with neovascularization, and the best course of action for physicians is to treat the systemic underlying causes of the obstructions. The prognosis for visual recovery depends on the subtype, with loss of visual acuity (20/200) in about 50% and 90% of nonischemic and ischemic cases, respectively [86].

Branch vein occlusion is more common than central vein obstruction and is characterized by macula edema, macula ischemia, and vitreous hemorrhages confined to the region supplied by the vein. Branch vein obstructions are treated with grid or panretinal photocoagulation for neovascularization and edema, but not for capillary nonperfusion. Laser treatment improves the chance for improvement of visual acuity significantly in branch vein obstructions [87]. About one-third of cases resolve spontaneously without laser treatment [88].

***Retinopathy of Prematurity*** Retinopathy of prematurity (ROP) is a proliferative disease that affects preterm infants of low gestational weight. In normal development, the retinal is vascularized with vessels that migrate from the optic disc starting at a gestational age of 16 weeks to the ora serrata by 36 (nasal) to 40 (temporal) weeks. In ROP, normal retinal vasculogenesis is interrupted. The retina is incompletely vascularized and a demarcation line between the vascular and avascular retina forms (stage I), elevates to a mesenchymal ridge (stage II), from which vessels protrude into the vitreous cavity, often causing hemorrhage (stage III) and retinal detachment (stages IV and V). When dilated veins and tortuous arteries are present in the posterior pole, the stage is termed *plus disease*. Macular dragging, traction, retinal folds, and retrolental fibroplasia are features commonly associated with ROP [89]. Figure 4.8 are fundus photographs of a former preterm with treated ROP that illustrate severe retinal traction.

ROP is estimated to cause visual loss in more than 1000 children born each year in the United States. [90]. The incidence of ROP is inversely proportional to the gestational age, occurring in over 80% of infants born at less than 28 weeks but in only 60% of infants born in weeks 28 to 31 [91,92]. ROP is also closely

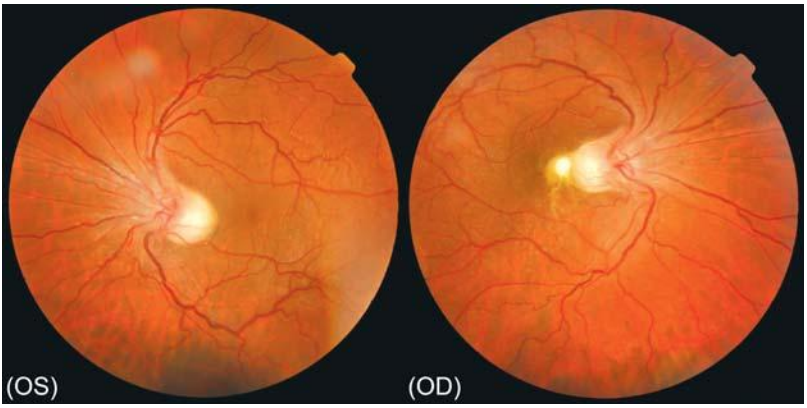

**FIGURE 4.8** Fundus images from a subject with severe ROP that was formerly treated with laser therapy. Note the significant retinal traction around the ONH. (Courtesy of A. Fulton.)

correlated to gestation weight, with over 80% incidence in infants that weigh less than 1 kg but under 50% in infants that weigh between 1 and 1.25 kg [91]. In mild ROP, the abnormal vessels regress spontaneously, and normal retinal vasculogenesis and migration proceed more or less normally. More severe ROP is usually treated with argon laser photocoagulation along the mesenchymal ridge, which causes the vessels to recede and prevents retinal detachment. Cryotherapy is used less frequently in cases of poor fundus visibility. The laser treatment threshold for an ROP eye, which is determined to be the 50% probability point for either spontaneous regression or disease progression (and retinal detachment), is defined by the stage and anatomical location and extent of the ridge [93]. After laser treatment, the vast majority of cases (85 to 95%) had favorable anatomical outcomes [94,95].

Even in cases of mild ROP that resolved spontaneously, there is evidence of subtle arrested migration of retinal layers and vessels. In a study of subjects with a history of mild ROP, Hammer et al. found a shallow foveal pit, contiguous inner retinal layers, and vessels overlying the fovea, but little disruption of cone packing (Figure 4.9) [96]. In the normal course of retinal development, the foveal pit forms due to the avascular zone causing centrifugal migration of inner retinal layers and centripetal migration of photoreceptor (cone packing) [14]. Thus, there is some evidence that this bidirectional migration of the inner and outer retinal is not coupled. ERG and multifocal ERG studies also showed differences in rod photoreceptor function [96–100]. The subjects in both of these studies had good corrected visual acuity, lending further evidence that the slight perturbation in development from ROP appears to affect rods more than cones.

***Other Vascular Diseases*** Other retinal vascular diseases include hemoglobinopathies, retinal telangiectasia, ocular ischemic syndrome, hypertensive retinopathy, radiation retinopathy, papillopathy, proliferative retinopathy, and retinal arterial macroaneurysm. Hemoglobinopathies are a group of diseases caused by inherited defects in hemoglobin (causing sickle red blood cells) that result in macula ischemia, peripheral neovascularization, and retinal hemorrhages. Retinal telangiectasia is a group of diseases, including the idiopathic

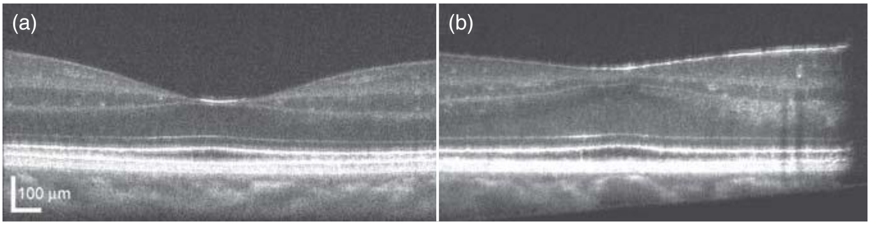

**FIGURE 4.9** Representative foveal cross-sectional composite images taken in (a) a normal subject (age 25) and (b) a subject with a history of ROP (age 16). Composite images were generated by co-adding four and six frames for (a) and (b), respectively. The scan length is 5°.

pathology Coat's disease, that result in aneurysmal dilation, telangiectasia, exudation, and leakage. Ocular ischemic syndrome is a condition of retinal hypoperfusion usually associated with severe carotid artery obstruction (from which the retinal artery branches). Hypertensive retinopathy is a condition that results from acute or chronic elevated systemic arterial hypertension. Radiation retinopathy and papillopathy are chronic progressive vascular diseases associated with the administration of radiation doses to the eye for the treatment of other conditions, such as tumors. Proliferative retinopathy are diseases associated with preretinal and optic disc neovascularization. Retinal arterial macroaneurysms are dilations of the retinal arterioles within the first three orders of bifurcation.

### 4.2.4 Hereditary and Congenital Disorders

***Retinitis Pigmentosa*** Retinitis pigmentosa (RP) is a broad category of inherited diseases, including X-linked recessive retinal dystrophies, congenital stationary night blindness, and juvenile retinoschisis, which affect primarily photoreceptors. RP leads to progressive photoreceptor death. Depending on whether the rods or cones are affected first, RP is generally classified as either rod–cone or cone–rod dystrophy, with quite different manifestations, symptoms, and prognoses.

Rod–cone dystrophy affects the peripheral rods first and has a conventional presentation that includes thinning and atrophy of the RPE in the periphery, waxy pallor of the ONH, intraneural retinal bone-spicule pigmentation, and severe constriction of the retinal arteries. Patients with rod–cone dystrophy have difficulty with night vision and experience tunnel vision in advanced stages. Visual function testing (ERG) exhibits degradation in scotopic (dark-adapted) responses with less diminished photopic (light-adapted) and 30-Hz flicker responses. Because the human retina has 92 million rods and 4.6 million cones [18], the prognosis for rod–cone dystrophy is worse than that for cone–rod dystrophy [101]. In the later stages of the disease, both rods and cones are affected, perhaps from a secondary mechanism that involves the RPE [102].

Cone–rod dystrophy affects cones in the central macula first. Patients present with reduced color vision, poor acuity, and sensitivity to bright lights. Their functional tests indicate a nearly normal scotopic response and significantly reduced photopic response. Unlike rod–cone dystrophy, cone–rod dystrophy often does not present until later in life, and the retainment of vision, albeit with significantly diminished central acuity, is possible.

RP is associated with more than 100 different gene mutations. These gene mutations involve components in the rod phototransduction cascade (e.g., rhodopsin [103]), rod structural proteins [104,105], and developmental genes [106]. The disease mechanisms may involve abnormal protein folding, disruption of cell metabolism, and other molecular reactions to the transduction disruption [101], which always leads eventually to apoptosis [107]. Treatment with vitamin A, docosahexaenoic acid (DHA), an important rod membrane lipid, and neurotrophic factors have shown delayed RP progression [108–110].

### 4.2.5 Other Retinal Diseases

***Inflammatory and Infectious Diseases*** Inflammatory eye diseases include posterior scleritis, pars planitis, sarcoidosis, uveal effusion syndrome, endophthalmitis, and white dot syndrome. White dot syndrome is a multifocal retinopathy that may have a viral origin and that affects primarily the RPE [111]. Inflammations of the vitreous (uveitis) and sclera (scleritis) are usually rare and can be caused by other systemic conditions or otherwise have unknown causes. These include posterior scleritis, a rare inflammation of the sclera that affects primarily the posterior eye [112]; uveal effusion syndrome, a condition that causes choroidal and retinal detachments [113]; pars planitis, a vitreous inflammation that causes pars plana exudates [114]; and sarcoidosis, a systemic pathology that causes retinal granulomas [115].

Systemic infectious diseases that affect vision include syphilis, tuberculosis, acute retinal necrosis, and fungal infections, including ocular histoplasmosis, acute retinal necrosis (caused by herpesvirus), taxoplasmosis, toxocariasis, cysticercosis, and cytomegalovirus retinitis. Excellent descriptions of these conditions can be found elsewhere [116].

***Tumors*** Retinal tumors can be classified as malignant or benign. Malignant tumors include retinoblastoma, uveal and choroidal melanoma, hematological malignancies (lymphoma and leukemia), tuberous sclerosis complex, and metastatic cancer. Benign tumors include choroidal nevus, hemangiomas (cavernous, capillary, choroidal), osteoma, astrocytoma, combined hamartoma, and RPE hypertrophy.

***Trauma and Retinal Detachments*** Retinal damage can occur from penetrating or nonpenetrating trauma directly to the globe or from systemic causes such as acute intracranial hemorrhage (Terson's syndrome), acute pancreatitis (Purtscher's retinopathy), and shaken baby syndrome [117,118]. Retinal lesions are also, of course, associated with focused laser beams, which have photochemical, photothermal, and photomechanical mechanisms. Toxic retinopathies are retinal injuries that occur from systemically administered drugs or exposure to certain chemicals. Besides those associated with the other diseases described in this chapter, retinal detachments can arise from peripheral retinal lesions, retinal breaks, proliferative vitreoretinopathy, and vitreous fluid inflow between the neural retina and RPE (rhegmatogenous retinal detachment).

## 4.3 TRADITIONAL IMAGING TECHNOLOGIES

For the first three quarters of the twentieth century, standard care in ophthalmology was performed using the direct and indirect ophthalmoscope and the slit lamp biomicroscope. Rapid progress in instrumentation occurred in the later part of the twentieth century with the invention of scanning laser ophthalmoscopy (SLO) by

Webb in the 1980s [8,119,120], optical coherence tomography (OCT) by Fujimoto and others in the 1990s [9,121], and the emergence of digital image acquisition, processing, and storage techniques that enabled digital fundus photography, SLO, and OCT technology to flourish [122]. The use of dye angiography [sodium fluoroscein angiography (FA) or indocyanine green angiography (ICGA)] coupled with either standard fundus imaging or confocal SLO emerged as a standard technique because of its excellent visualization of leakage and pooling from new vessels in AMD and DR. In addition to these exogenous probes, new techniques were developed to image the autofluorescence of specific endogenous macular pigments, fluorophores, and chemical constituents (e.g., lipofuscin, A2E, flavoprotein) [123–128].

Light–tissue interaction in the retina is governed by mechanisms common to other multilayer vascularized tissues with melanin (e.g., skin), albeit with considerations specific to its unique anatomy and physiology. The retina has two blood supplies: the choroid, which nourishes the RPE and photoreceptors, and the retinal vasculature, which nourishes the inner retinal layers. The RPE is a heavily pigmented monolayer that serves a variety of uses, including efficient thermal diffusion and regulation via absorption of visible light by melanin. The isosbestic point, where oxygenated and deoxygenated blood has the same absorbance, is 805 nm, and retinal oxygenation can be determined by quantifying the reflectivity at two wavelengths around this point (e.g., 660 and 905 nm), in a manner similar to pulse oximetry. Wavelengths shorter than 600 nm are absorbed by blood in the choroid and retinal vessels and reflected from the inner limiting membrane, RPE, and choriocapillaris [123]. Scattering decreases with wavelength, so longer near-infrared (NIR) wavelengths penetrate the choroid, where they scatter in blood and are reflected by the choroid and sclera. For this reason, NIR wavelengths within the water absorption window of 700 to 1100 nm are often used for retinal imaging. UV wavelengths (<400 nm) and NIR wavelengths greater than 1100 nm do not penetrate the eye efficiently past the anterior segment and vitreous.

The retina has many intrinsic fluorophores with different excitation and emission wavelengths that have various roles in visual pathways, retinal metabolism, retinal protection, and disease pathogenesis and progression. The autofluorescence concentration and spatial distribution of these fluorophores and their constituents has been investigated by many researchers. These include the visual pigments (rhodopsin in rods and the iodopsins, also called photopsins in cones), macular pigments (including carotenoids such as lutein and zeaxanthin), lipofuscin, melanin, flavoproteins, and other trace elements (e.g., sulfur, chloride, calcium, iron, zinc) [123–142].

As will be shown in the following sections, advances in ophthalmic imaging have come about most often through the invention of novel means to overcome fundamental limitations imposed by ocular geometry and optics and tissue optics. In any imaging device, the numerical aperture (NA) or $f/\#$ of the optics governs the lateral ($\propto 1/\text{NA}$) and axial ($\propto 1/\text{NA}^2$) resolution. Most ophthalmic devices use a Maxwellian illumination scheme, where the input beam fills only a small portion of the pupil (as opposed to a Newtonian illumination scheme, where the input beam overfills the pupil). Clearly, for in vivo applications in the posterior segment, the eye represents the final optic of the imaging system because the light has to pass though the eye's anterior optics. So the low NA of the eye (i.e., relatively long focal length and small pupil) limits the maximum achievable resolution. Furthermore, the performance of any ophthalmic imaging system is constrained by ocular aberrations. Finally, tissue scattering can limit the image contrast because light from adjacent tissue planes and volume elements (voxels) will corrupt and blur the signal of interest.

The eye can essentially produce a nearly diffraction-limited retinal spot for a small pupil diameter of less than approximately 2 mm. The eye has a NA of about 0.05 in this case and produces a spot of 5 to 15 μm and a depth of focus of 250 to 300 μm for near-infrared light. The NA for a dilated pupil (7 mm) increases to about 0.2. However, as the pupil diameter is increased, ocular aberrations negate any gains from increased numerical aperture, and the retinal spot size and depth of focus are essentially unchanged.

Retinal imaging systems that employ flood illumination and detection schemes have relatively poor resolution and contrast and no sectioning capabilities (Section 4.3.2). However, tricolor cameras can be used to provide an advantage in terms of the visualization of retinal pallor. Red-free detection schemes are used to filter out red light for enhanced viewing of blood vessels (Section 4.3.4). SLOs are confocal instruments that block light scattered from other retinal lateral positions and depths that are not conjugate to a detector pinhole (Section 4.3.5). They can achieve lateral and axial resolution of approximately 5 to 15 and 300 μm, respectively. The axial depth of focus for confocal instruments is often called the *confocal range gate*. Optical coherence tomography is a technique that uses low-coherence interferometry in a heterodyne configuration to detect light only from a short coherence range gate within the longer confocal range gate (Section 4.3.5). OCT systems achieve micrometer-level axial resolution with similar lateral resolution as SLOs. Adaptive optics is used to correct ocular aberrations to achieve the true NA potential of a dilated eye (Section 4.4.3). Nearly diffraction-limited spots (ca. 2.5 μm) and excellent optical sectioning (as low as 70 μm) have been reported for AOSLOs [143].

### 4.3.1 Direct and Indirect Ophthalmoscopy, and Slit Lamp Biomicroscopy

In 1851, Helmholtz invented the direct ophthalmoscope, which is still used by optometrists, ophthalmologists, and general practitioners [144]. By illuminating the eye with a halogen tungsten bulb along the same axis as is observed (the illumination and detection paths are made coaxial), an image of the retina is formed with the eyepiece (lens). A partially reflective mirror or mirror with a central aperture is used to direct the illumination beam into the eye. The handheld direct ophthalmoscope provides simple retinal views for quick diagnostic purposes. The indirect ophthalmoscope differs from the direct ophthalmoscope in that the illumination and observation beams are separated at the pupil plane and overlap at the retinal plane. This off-axis illumination scheme essentially removes corneal reflections from the image because those rays are directed out of the field subtended by the detection port or eyepiece. This concept was introduced by Gullstrand in 1910 [145] and is embodied in the slit lamp biomicroscope, fundus camera, and OCT systems used today (see Figure 4.17). The indirect ophthalmoscope is often configured as a binocular instrument for a stereoscopic retinal view and works best when the subject is dilated.

The modern slit lamp biomicroscope was introduced at the beginning of the twentieth century and remains one of the workhorses in an ophthalmology clinic. It provides direct visualization of the anterior segment and with various contact (e.g., Goldmann) and noncontact (e.g., 78D Volk) lenses, a view of the posterior segment as well. Slit lamps consist of a white-light illumination source that is focused to a slit and projected into the eye and stereo observation optics and eyepiece. The slit lamp illuminates a strip of a target (e.g., cornea, lens, retina) that can be observed directly, but it is not typically configured to capture and store images. The slit lamp biomicroscope is also often configured for therapeutic laser beam delivery in panretinal laser photocoagulation, PDT, and other laser treatment modes.

### 4.3.2 Fundus Photography

*Fundus photography* refers broadly to direct flood illumination and detection of light backscattered from the retina. The term is usually prefaced with *digital* or *flash* to refer to digital capture and storage techniques and xenon or krypton flash illumination, respectively. The illumination light is typically collected from a broadband white light source and the return light is captured by a two-dimensional CCD or CMOS detector. The return light can be filtered to produce red-free images. While color fundus images are a conventional diagnostic mode because they provide the clinician with information on retinal pallor, red-free images show increased contrast of vessels and certain structures or lesions important for disease diagnosis. Figure 4.10 shows images acquired from a clinical digital fundus imager (TopCon TRC.50IX) in standard color and red-free modes for a patient with nonproliferative diabetic retinopathy.

### 4.3.3 Angiography

The inner retina is nourished by the retinal vessels that branch from the central retinal artery. The outer retina, including the photoreceptor layer, is nourished by the underlying choriocapillaris and choroid via the retinal pigment epithelium (RPE) cellular monolayer and Bruch's membrane. Angiography uses the fluorescence of exogenous dyes injected into the bloodstream of a patient to visualize defects in retinal or choroidal flow and/or new vessel growth associated with retinal disease. All clinical (i.e., nonexperimental) angiography for diagnostic purposes (vs. those used for therapeutic purposes, such as PDT) is performed using either sodium fluorescein angiography (FA) or indocyanine green angiography (ICGA).

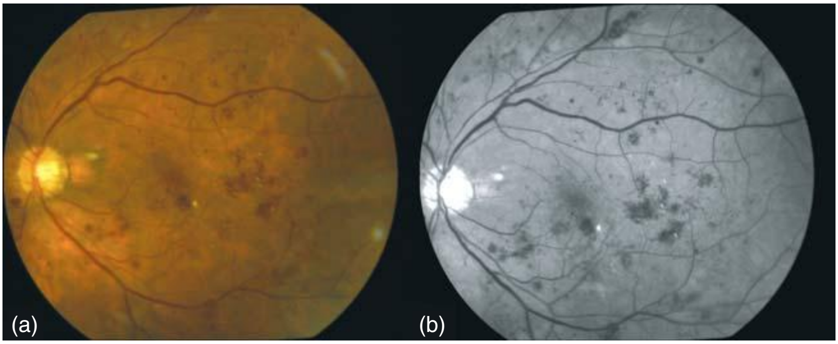

**FIGURE 4.10** Color and red-free images of moderate nonproliferative DR. (Courtesy of D. Husain.)

Angiography can be performed with either fundus photography or scanning laser ophthalmoscopy. To be configured for angiography, imaging systems require a narrowband excitation filter (for white light illumination sources such as xenon arc lamps) or a narrowband illumination source (i.e., laser), a narrowband barrier filter that passes the emitted light while blocking the excitation light, and a dichroic beamsplitter with a sharp cutoff (or cut-on) between excitation and emission wavelengths to separate the illumination and detection paths efficiently. Systems that perform both FA and ICGA often have multiple dichroic beamsplitters and use barrier filters in a computer-controlled filter wheel.

Angiography can be characterized and segmented into several phases across the dye transit time, which for both fluorescein and indocyanine green is 5 to 30 s [146]. Often, they are simply segmented into two phases: an early phase, where the dye is present and the fluorescence strong in the arteries and perfused across the entire retinal capillaries; and a late phase, where the veins (and any leakage) fluoresce and the arteries begin to clear dye. FA and ICGA are often performed simultaneously because of the difference in transit times, with early-phase FA performed first, followed by early- and late-phase ICGA, and finally, late-phase FA. Figure 4.11 shows FA images over the time course of dye diffusion for a patient with a wet AMD lesion. (The images were taken prior to PDT treatment.) Note that immediately after dye injection the arteries are strongly fluorescent (Figure 4.11a and b) while the region near the lesion is hypofluorescence. After, the dye begins to perfuse into the retinal capillaries (Figure 4.11c and d). Finally, as the dye drains with circulation, dye leakage can be seen in the subretinal membrane (Figure 4.11e and f).

Sodium fluorescein binds to plasma proteins (albumin) and in an eye without disease cannot pass through the tight endothelial cell junctions of the retinal vessels. However, fluorescein can extravasate through the fenestrated walls of the choriocapillaris into the extracellular space below the RPE, through which it is unable to pass (in a normal eye). Fluorescein is excited with a relatively broad band of blue light from 460 to 490 nm and emits green wavelengths from 520 to

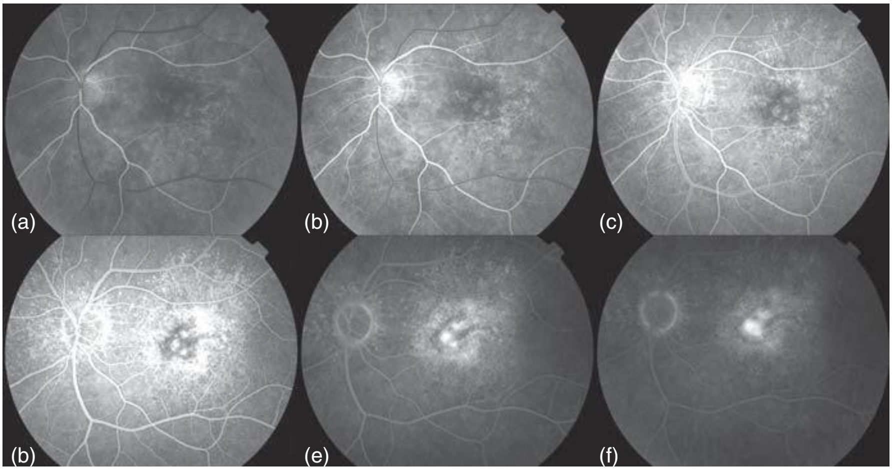

**FIGURE 4.11** FA phases of a wet AMD lesion. (a) Earliest (arterial) phase shows dye filling in the arteries. (b–d) In the middle (recirculation and venous) phases the dye continues to perfuse into the retinal capillaries. (e,f) In the late phases leakage from the subretinal neovascular membranes is most evident. (Courtesy of D. Husain.)

530 nm. Macular pigments (e.g., xanthophyll) cause macular hypofluorescence by blocking light from the choroidal vessels.

FA, introduced more than a decade before ICGA [147], is used to visualize hypoperfusion and hyperperfusion in lesions and structures associated with retinal disease. Hypoperfusion is a sign of either incomplete dye filling (from arterial or venous obstructions) or blocking of fluorescence signal (from vitreous or subretinal hemorrhages, melanin, lipid, lipofuscin, etc.). Hyperfluorescence can be a sign of a window defect, where RPE atrophy or loss of the choriocapillaris allows visualization of dye accumulation in the choroid (e.g., cone dystrophy). However, hyperfluorescence more often indicates a break in the blood–retina barrier, either dye leakage from increased vascular permeability or dye pooling. This can occur in existing vessels from inflammation or with malformed new vessels in both the retinal and choroidal vasculature. Hyperfluorescence is often used to diagnose choroidal neovascularization (CNV) associated with exudative AMD (Figures 4.10 and 4.11), neovascularization, edema, and microaneurysms in DR, macular edema, macroaneurysms, central serous chorioretinopathy, choroidal melanoma, and retinal and RPE detachments [148].

ICGA was first performed in 1972 by Flower and Hochheimer [149] and, like FA, became widespread in the 1990s with the development and proliferation of digital fundus imaging technologies, including those that provided capabilities for narrowband filtering and enhanced-sensitivity light detection. ICG is excited by a broad band of light with a peak near 800 nm and emits light with a peak near 835 nm. Deeper NIR light penetration provides better visualization of the choroidal vasculature with ICGA than with FA. Operation at infrared

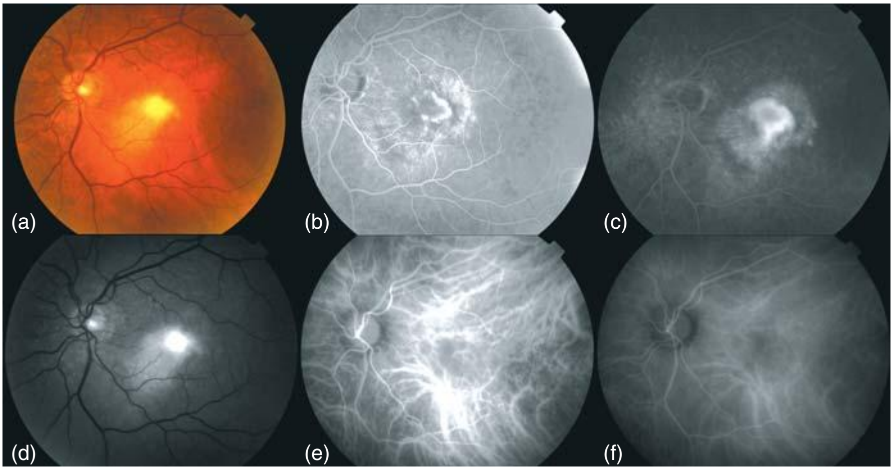

**FIGURE 4.12** Comparison of FA and ICGA. Images show a wet AMD CNV lesion: (a) color fundus image; (b) early-phase FA; (c) late-phase FA; (d) red-free fundus image; (e) early-phase ICGA; (f) late-phase ICGA. (Courtesy of D. Husain.)

wavelengths also allows enhanced contrast through intervening structures that absorb visible wavelengths, including macular pigments and other fluorophores, blood (hemorrhages), melanin, serous fluid, and lipids. ICG dye is highly protein bound, especially to blood globulins, so in contrast to FA cannot leak through the choriocapillaris. ICGA is often used to diagnose occult CNV in AMD, central serous chorioretinopathy, intraocular tumors, and some rare chorioretinal inflammatory diseases. In AMD, RPE detachment often causes hypofluorescence, while plaques, choroidal neovascularization, and retinal choroidal anastomosis will cause hyperfluorescence [150].

Figure 4.12 shows a comparison of FA and ICGA for a subject with a subretinal neovascular membrane associated with exudative AMD. Shown are the color fundus image (Figure 4.12a), the red-free image (Figure 4.12d), early-phase FA (Figure 4.12b), late-phase FA (Figure 4.12c), early-phase ICGA (Figure 4.12e), and late-phase ICGA (Figure 4.12f).

### 4.3.4 Autofluorescence Imaging

Clinical retinal imagers that measure the distribution of fluorophore autofluorescence (AF), such as the HRA or Spectralis (Heidelberg Engineering), typically use the differential absorption, excitation, and emission of macular pigments and lipofuscin. In the central retina, macular pigment resides primarily in the Henle fiber layer in the fovea and the inner nuclear layer in the parafovea [142], while lipofuscin granules reside in RPE cells. AF imaging instruments use two argon laser excitation lines (488 and 514 nm) or other visible sources (e.g., filtered white light from xenon arc lamps) and barrier filters to block the reflected excitation light and differentiate the light emitted from various fluorophores. Blue light (488 nm) is absorbed by the macular pigments (and blood), while both the blue and green (514 nm) laser lines excite lipofuscin, which emits a broad band of light from 500 to 750, with a peak centered near 600 nm. Since the amount of AF light emitted is small, averaging (with registration) is often used to generate a composite AF image with sufficient brightness and contrast to discriminate spatial features [151]. In wide-field SLO HRA, 16 to 32 images are typically obtained, while in small-field AO-SLO, hundreds or thousands of images are often required [152,153]. Also, because the excited fluorescence light makes a single pass through the eye, the reflections and scatter commonly observed in NIR SLO reflectance images are not seen. This reduces the background noise and enhances the contrast of the AF images [154].

Lipofuscin is an important fluorophore in the RPE. It is an aggregate of lipid and proteins whose primary fluorophore, A2E containing vitamin A and ethanolamine, emits orange wavelengths (ca. 600 nm). Unlike the macular pigments, which have a genetically determined distribution and therefore a predetermined role in disease initiation and progression, lipofuscin levels are determined by environmental factors associated with the normal daily visual cycle. Lipofuscin accumulates with age from phagocytosis of photoreceptor outer segments and when photoexcited, is toxic to in vitro RPE cells via the generation of free radicals [125].

Figure 4.13 shows AF images of normal and AMD subjects. Blue light is absorbed by macular pigment, preventing excitation of lipofuscin [155], so the macula is dark compared to the peripheral retina, where macular pigment is absent. The lipofuscin fluorescence signal is also blocked in the vessels from blood absorption, and in the ONH, which lacks an RPE layer. In the diseased eye (Figure 4.13b), regions with increased AF (horizontal arrows) are attributed

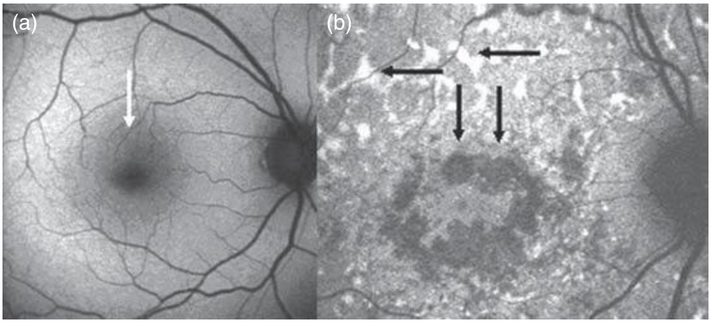

**FIGURE 4.13** Macular pigments and lipofuscin imaged with (a) the Heidelberg HRA II and (b) the Zeiss SLO. (a) AF image shown in a subject without retinal disease. Arrow indicates lipofuscin fluorescent signal attenuation in the macula. (b) Image from a subject with inherited retinal degeneration. Horizontal and vertical arrows indicate increased and decreased lipofuscin autofluorescence, respectively. (Courtesy of F. J. Vankuijk and A. Bird.)

either to increased RPE lipofuscin or possibly to folding of fluorophore-rich layers and cells. Regions with decreased AF (vertical arrows) indicate RPE atrophy and photoreceptor loss.

### 4.3.5 Scanning Laser Ophthalmoscopy

Scanning laser ophthalmoscopy (SLO) was invented by Webb [8,119,120]. SLO or confocal SLO (cSLO) is a technique used to reduce the amount of light detected that is scattered from lateral or axial voxels adjacent to the imaged voxel of interest. Flood illumination and detection techniques such as fundus photography suffer reduced contrast because light is scattered back and received from all planes and regions. SLO is essentially the application of confocal microscopy principles, invented in 1957 by Marvin Minsky [156] to ophthalmic imaging. Confocal detection reduces scattering with a pinhole placed in front of the detector at a conjugate focal plane (Figure 4.14). *Confocal range gate* refers to the individual axial component or length in which scattered light from the tissue layers of interest is imaged.

Although a conventional confocal microscope can achieve submicrometer lateral and axial resolution with the use of high-NA microscope objectives, in retinal imaging the eye is the final optic and its low NA constrains the lateral and axial resolution to about 10 and 300 μm, respectively. SLOs are typically arranged in a flying-spot configuration, where a high-speed optic (e.g., resonant scanner, spinning polygon) is used to achieve the kilohertz line scan rates necessary for video rate imaging. Line scanning techniques with a cylindrical lens and a linear detector have also been demonstrated for quasi-confocal operation with good imaging performance [157]. In the flying-spot arrangement, the spot is scanning in a raster pattern on the retina and the return light is simultaneously de-scanned back to the detector. The detector (e.g., avalanche photodiode, photomultiplier tube) records the temporal changes in the signal and encodes the signal for an analog framegrabber.

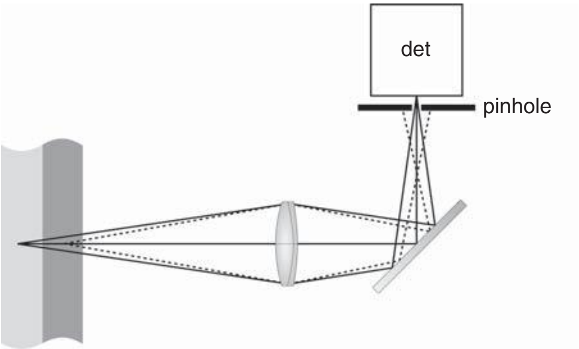

**FIGURE 4.14** Confocal setup. Solid lines indicate light focused to a pinhole placed at the conjugate focal plane. Dashed lines indicate light from other planes blocked by the pinhole.

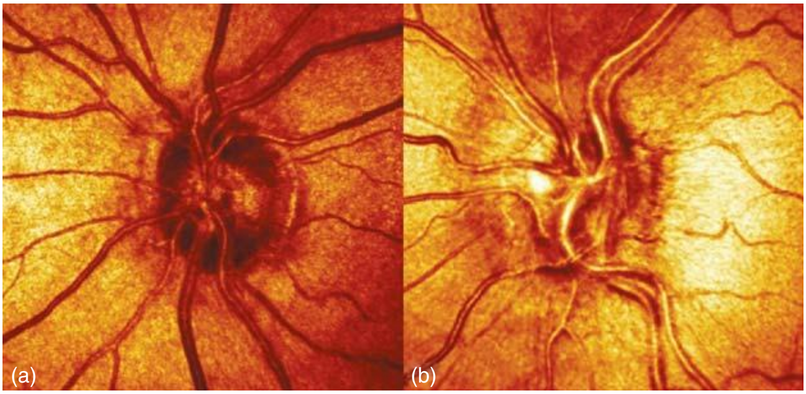

**FIGURE 4.15** Heidelberg HRT SLO images of (a) a normal ONH and (b) papillaedema. (Courtesy of Heidelberg Engineering, Inc.)

The SLO has been commercialized by Rodenstock (since discontinued), Heidelberg Engineering (HRT and HRA), and Laser Diagnostic Technologies (GDx) for various applications: from optic nerve head volumetric sizing in glaucoma to angiography and blood flow mapping in AMD and DR. The LDT GDx instrument adds polarization detection to an SLO to map form birefringence in the NFL that arises from the arrangement of microtubules in the ganglion cell axon nerve fiber bundles. The light retardance is proportional to the NFL thickness and can be used to map and quantify losses around the ONH associated with glaucoma. The Heidelberg HRT takes a series of SLO images of the ONH at different tissue depths (by adjusting the instrument focus). The image sequence is analyzed to produce various clinically useful volumetric parameters (e.g., cup/disc area ratio, rim/disc area ratio) of six sectors around the ONH. The HRT also provides topographical maps, RNFL profiles, glaucoma probability scores, and topographical change analysis for glaucoma progression detection. A clinical comparison of glaucoma analysis from the GDx, HRT, and OCT instruments is given in Section 3.1. Figure 4.15 shows HRT images from a normal eye and from an eye with papillaedema. The Heidelberg HRA builds up successive scans of a strip of the retina (usually near the ONH) to generate flow maps from the Doppler shifts detected between successive scans. A similar technique has been used with retinal tracking to produce wide-field global views of perfusion [158].

### 4.3.6 Time-Domain Optical Coherence Tomography

Optical coherence tomography (OCT) is a low-coherence interferometric technique that achieves micrometer-level axial resolution for in vivo tissue-sectioning capabilities [9,159–161]. Interference is an optical phenomenon that exploits the coherence property of light. When a beam of light is split into two separate paths, it remains coherent and when recombined will result in constructive or destructive interference, depending on the relative phase of the resultant lights waves in the two paths. When the two pathlengths are separated in phase by a distance of $2\pi m$ ($m = 0, 1, 2, \ldots$) constructive interference will result and when the pathlengths are separated by $\pi m$ ($m = 1, 2, \ldots$), destructive interference will result. The alternating pattern of constructive (light) and destructive (dark) interference is referred to as *fringes*. Several interferometer configurations can be used to separate and recombine light (e.g., Fabry–Perot, Mach–Zehnder), but the simplest and most commonly used is a Michelson interferometer [162]. The Michelson setup is comprised of a beamsplitter, which separates the input beam into two paths or arms (often called *sample* and *reference paths and arms*); partial or total reflectors in the paths to send the light back to the beamsplitter, where it interferes; and a detector to record the fringe pattern (Figure 4.16).

The properties of light determine how long the beams will remain coherent. In particular, the bandwidth is inversely proportional to the coherence length. Laser light has a very narrow linewidth and hence a very long coherence length. A conventional laboratory helium–neon laser ($\lambda = 632.8$ nm, $\Delta\lambda = 0.002$ nm) can produce fringes at the interferometer detector even if the pathlength difference is quite long (typically, 10 to 20 cm and >5 m for stabilized lasers). Conversely, a source with a very broad bandwidth has a very short coherence length and will produce fringes only when the pathlengths are matched to within the source coherence length. In a low-coherence interferometer used to image biological samples, light from a mirror in the reference path and light backscattered from the sample will interfere only when the pathlengths are matched. The window over which the pathlengths are matched is the coherence range gate. A depth profile of the intensity of the light backreflected from individual layers can be created by scanning the reference mirror in the axial direction, thereby effectively scanning the coherence range gate in depth. For a source spectrum with a Gaussian shape,

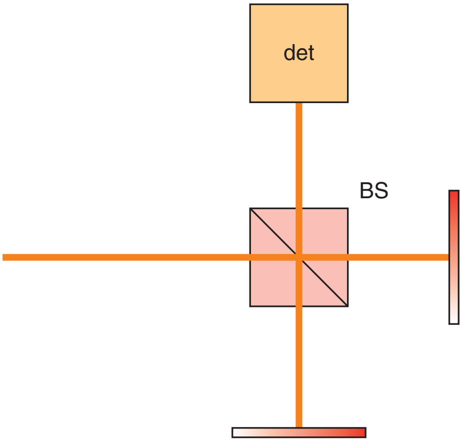

**FIGURE 4.16** Michelson interferometer.

the axial resolution, $\Delta z$, and bandwidth $\Delta\lambda$ are related by

$$\Delta z = \frac{2\ln 2}{n\pi}\frac{\lambda_0^2}{\Delta\lambda} \tag{4.1}$$

where $n$ is the refractive index and $\lambda_0$ is the source center wavelength. A source with a moderate bandwidth of 25 nm ($\lambda_0 = 830$ nm) will produce an axial resolution in tissue ($n = 1.38$) of approximately 9 μm. Thus, a low-coherence interferometer exploits the coherent property of light to effectively circumvent the normal restriction placed on axial resolution by conventional geometric optics. This is central among the reasons that OCT has had success first in ophthalmology, where the optics of the eye can limit imaging performance.

The source most often used in OCT systems is a superluminescent diode (SLD), which is not technically a laser source. SLDs have a center wavelength in ranges that for biomedical imaging applications include 650 to 680 nm, 780 to 980 nm, 1020 to 1200 nm, and 1270 to 1410 nm. A single SLD produces a bandwidth between 5 and 65 nm, and schemes have been employed by commercial manufacturers to combine multiple SLDs to produce extremely broadband sources exceeding 200 nm. Commercial clinical OCT instruments generally have bandwidths of about 25 nm, whereas some research systems have been reported with very broadband sources to achieve very high axial resolution, approaching 1 μm [163–165].

The Michelson interferometer uses a heterodyne detection scheme, where light from the interferometer reference and sample paths are interfered with or “beat” to produce the fringes (as opposed to homodyne detection schemes, where the light is beat against itself to produce fringes). These schemes are mathematically analogous to cross-correlation and autocorrelation, respectively. Several examples of OCT systems that use homodyne detection (e.g., light interference between reflective layers in a probe) have been reported [166].) Signal processing for a conventional time-domain OCT configuration is fairly straightforward: The ac detector signal is demodulated (with a low-pass filter and rectifier), and the resulting envelope is encoded to gray scale or false color with logarithmic mapping to represent the backscattered intensity. For OCT Doppler blood flow applications, the phase shift in the fringes is detected (with, e.g., a lock-in amplifier) [167–169].

OCT instruments generally use a fiber interferometer to remain less impervious to misalignment and vibration artifacts. Single axial or depth profiles (A-scan), produced by scanning the reference mirror along the optical axis, can be built up by using optomechanical components (galvanometers, etc.) to scan in one or two lateral dimensions for the generation of cross-sectional (B-scans) and three-dimensional volumetric maps (C-scans). Various techniques have been employed to increase the image speed to video rates, including the use of rapid scanning optical delay lines, in which the light is dispersed with a grating and scanned rapidly with a resonant scanner [170].

For low-coherence interferometry, sample dispersion must be managed to achieve optimal axial resolution. Group velocity dispersion is present in most real samples and results in a wavelength-dependent phase shift in the OCT interference signal. In other words, after passing through the sample, there is a delay in the individual color components that comprise the spectrum. This delay makes it impossible for all the individual color components to interfere simultaneously, and individual peaks in the axial profile will therefore become broadened. Dispersion is most often managed simply by matching the amount of material or glass in both arms of the interferometer. For ophthalmology, a cube or water cell can be placed in the reference path to match ocular dispersion. Although there is some variability in the eye length within the human population (ca. 20 to 28 mm), these small differences do not lead to large differences in OCT image quality. However, for ultrahigh-resolution systems with very broad spectra, dispersion must be managed extremely carefully to achieve the theoretical axial resolution.

Figure 4.17 illustrates a typical OCT setup and an image taken from a Zeiss Stratus OCT instrument. A 2 × 2 fiber coupler constitutes the interferometer. The source is a single SLD with a center wavelength of about 830 nm and a bandwidth of 25 nm to achieve an axial resolution of about 10 μm. The Stratus system uses a rapid scanning optical delay line (not shown) for axial scanning and an automated polarization controller (not shown) and fixed dispersion compensation optic for signal optimization in the reference path. In the sample path, the light from the interferometer is scanned laterally with a pair of galvanometer-driven mirrors and relayed to the eye with a scan lens and 78D ophthalmoscopic lens. An auxiliary fundus imager also provides the clinician with an *en face* view for global orientation. The visible fundus beam and NIR OCT beams are combined with a dichroic beamsplitter. The light from the sample and that from reference paths are mixed and detected on a photodiode. The resulting signal is amplified and demodulated and then displayed to the user. The Stratus OCT system provides an extensive set of scan types (e.g., circle, concentric circle, radial) for various pathologies as well as a normative database for glaucoma detection.

Despite the impressive advances in ophthalmic instrumentation in the 1990s, even greater strides were made at the beginning of the twentieth century. The new tools developed recently, which are described in the next section, have begun to fulfill the promise of optical imaging toward the visualization of cells and structures on a microscopic scale with nearly the fidelity of traditional histological methodology.

## 4.4 ADVANCED IMAGING TECHNOLOGIES

Recent progress in the last decade in optical imaging of the eye has come about by invention and improvement in techniques that achieve high performance in three general areas. First, improved resolution allows visualization of retinal cells, structures, and layers heretofore not resolved in the live eye and examined only via histology. Second, improved speed allows larger areas to be mapped with less corruption from eye motion. Third, alternate contrast modes designed to exploit

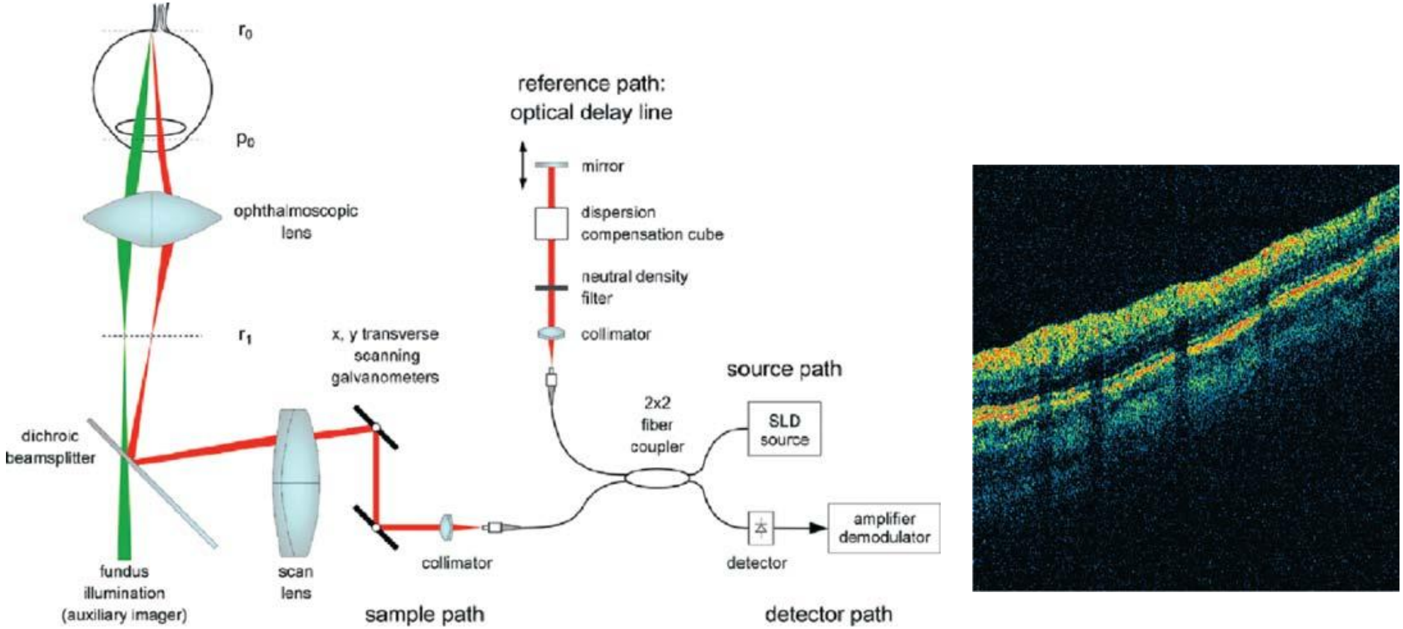
r0
p0
ophthalmoscopic lens
r1
x, y transverse scanning galvanometers
dichroic beamsplitter
fundus illumination (auxiliary imager)
scan lens
collimator
sample path
reference path: optical delay line
mirror
dispersion compensation cube
neutral density filter
collimator
2x2 fiber coupler
source path
SLD source
detector
amplifier demodulator
detector path

**FIGURE 4.17** Typical TD-OCT setup for ophthalmology and an image of the retina acquired with a clinical instrument (CZMI Stratus).

various fundamental properties of ocular light–tissue interaction allow enhanced visualization of specific retinal targets.

The recent improvements in image resolution have often come about through the use of adaptive optics (AO), which dynamically corrects ocular aberrations to allow imagers (fundus cameras, SLOs, OCT instruments) to achieve diffraction-limited focus using the eye as the final objective [171,172]. AO uses the full NA of a 7 to 8-mm dilated eye to achieve a lateral resolution of a few micrometers and a depth of focus of 50 to 100 μm [143]. As discussed in Section 4.3.6, low-coherence interferometry, as embodied in OCT systems, provided unprecedented axial resolution and depth-sectioning capabilities. Because the OCT axial resolution is inversely proportional to the source bandwidth, improvements in OCT axial resolution have come about through the use of very high bandwidth sources and careful management of system and ocular dispersion.

All in vivo retinal imaging instruments except those with very short exposure durations [on the order of a few milliseconds (e.g., flash fundus photography)] must contend with natural eye motion. Although eye motion is less perturbing to digital fundus cameras and SLOs that generally operate at video frame rates (ca. 30 ft/s), identification of the location of structures on the retinal can be difficult for some high-resolution systems with a narrow field of view (1 to 2°) in the presence of excessive eye motion [173]. Slow imaging speed especially plagues time-domain OCT instruments, and several high-speed techniques have been invented to scan the reference path mirror rapidly for video-rate imaging [170,174]. However, high scan speeds are generally achieved with a concomitant reduction in the signal-to-noise ratio (SNR) [174]. Clinical TDOCT instruments (e.g., CZMI Stratus) have a maximum scan rate of 400 A-lines per second and a 512 × 512 pixel frame rate of <1 ft/s. Eye motion is evident within a single Stratus B-scan (see Figur 4.13), and only very coarse three-dimensional mapping of layers (i.e., generation of C-scans) is possible. A disruptive technology widely adopted in the early 2000s is called Fourier-domain OCT (FDOCT) or spectral-domain OCT (SDOCT). FDOCT uses a multiplexed approach to achieve tens to hundreds of thousands of A-lines per second. The very high line and frame rates mean that the majority of eye motion is absent from individual B-scans and three-dimensional mapping of the retinal can be achieved with sufficient sampling to provide a meaningful *en face* display.

The eye in general and the retina in particular is extremely richly textured. This has provided significant opportunity for the development of tools that exploit various characteristics of light–tissue interaction to provide enhanced contrast and visualization of targeted structures and cells. Ocular fluorescence imaging of endogenous fluorophores (e.g., macular pigments, lipofuscin, flavoprotein) and exogenous biomarkers (e.g., fluoroscein, ICG) are examples where accumulation or dye leakage can provide information about the relative health of retinal tissue. Doppler flowmetry, defined roughly as the measurement and mapping of blood flow and perfusion by discrimination of relative phase shifts of light scattered from moving particles, is another technique that can be used to increase the contrast derived from targeted cells. Another example is polarization imaging, which exploits form birefringence in specific layers of the anterior (cornea, lens) and posterior (nerve fiber layer) segment. Other than the traditional fluorescence imaging techniques discussed in Sections 4.3.3 and 4.3.4, these techniques have found limited, niche areas where they are able to provide researchers and clinicians with enhanced capabilities. In this section I focus on FDOCT and AO. FDOCT and other high-resolution techniques are discussed in Section 4.4.1. Advances in retinal imaging from the use of AO are described in Section 4.4.2. In Section 4.4.3 I discuss briefly some emerging technologies, including multimodal approaches, which provide synergism from several complementary imaging modes.

### 4.4.1 Fourier-Domain Optical Coherence Tomography

Fourier-domain OCT (FD-OCT) was invented by Fercher et al. in the mid-1990s [175,176] but oddly—for such a competitive research field as OCT—did not gain wide acceptance until nearly 10 years later, in the early part of the 2000s [177–180]. FD-OCT works by simultaneous (or rapid) multiplexed detection of an entire interference spectrum and hence all coherence range gates within a sample. Rather than scanning the interferometer reference path mirror to match the reference pathlengths to individual sample layers as in TD-OCT, an FD-OCT instrument detects the interference of individual spectral (i.e., color) components that make up the source and that travel different distances in dispersive media such as tissue. This is done either by spatially spreading the spectral components in the detection path or by temporally spreading (or sweeping) the spectral components in the source path. The resulting interference spectrum can be Fourier-transformed to yield a depth reflectance profile (A-scan), and these can be combined in the usual manner with transverse scanning to produce two-dimensional B-scans or three-dimensional C-scans.

Both FD-OCT and TD-OCT require significant processing of signals for image optimization. For TD-OCT this involves demodulation, which can be done in hardware or software, and typically includes rectification followed by low-pass filtering. Because an FFT is applied to each spectrum to produce a depth profile, FD-OCT requires more processor-intensive postprocessing. Also, to convert the spectrum from $\lambda$ to $k$-space requires resampling. Both TD-OCT and FD-OCT signals require dispersion compensation and are scaled logarithmically prior to display. Dispersion leads to profile broadening and is compensated by matching the amount of dispersive material in the reference and sample paths. FD-OCT is amenable to software algorithms for dispersion compensation, where the phase is optimized [180–182]. Real-time FD-OCT signal processing hardware has been developed for rapid display of acquired images [182].

The two varieties of FD-OCT instruments shown in Figure 4.18 are referred to as *spectrometer-based FD-OCT*, also called *spectral-domain OCT* (SD-OCT) and *swept-source OCT* (SS-OCT), also called *optical frequency-domain imaging* (OFDI). SD-OCT systems use a spectrometer in the detection path to extract the frequency-encoded depth information by Fourier transformation of the spectrum detected. In a typical SD-OCT configuration, the spectrometer is comprised of

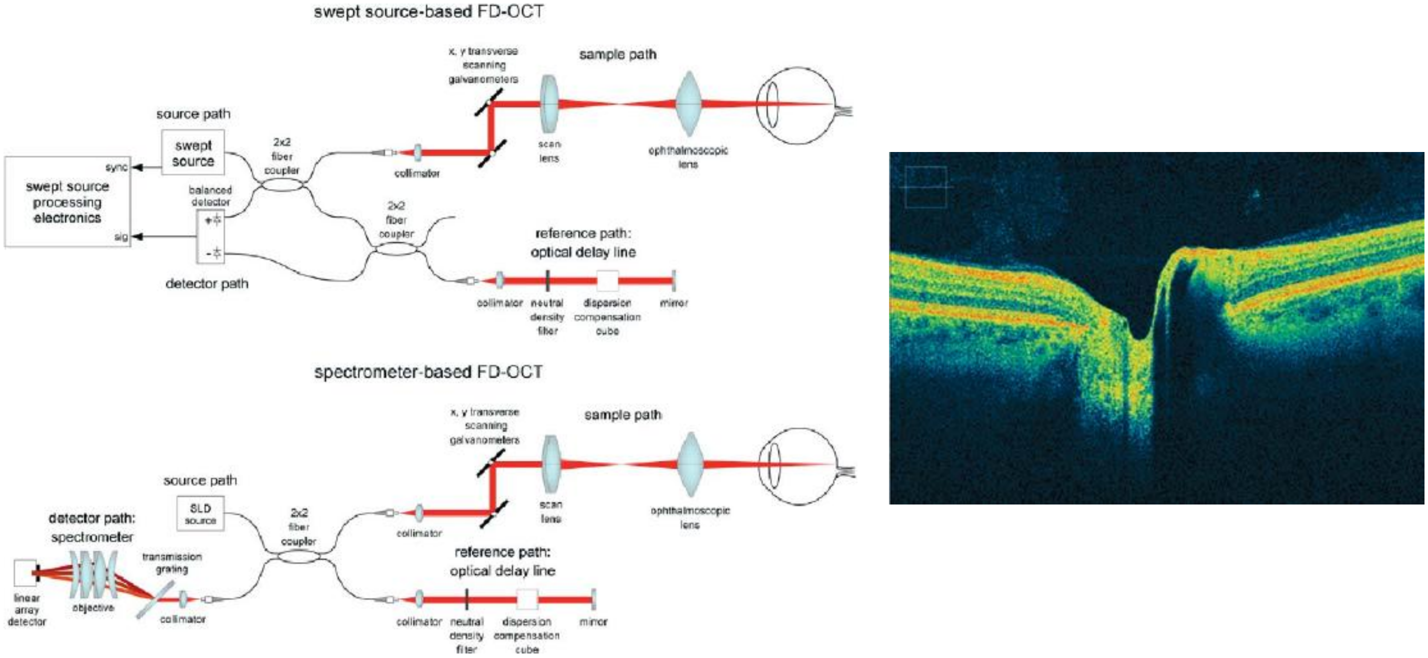
swept source-based FD-OCT
x, y transverse scanning galvanometers
sample path
source path
swept source
2x2 fiber coupler
collimator
scan lens
ophthalmoscopic lens
sync
swept source processing electronics
sig
balanced detector
2x2 fiber coupler
reference path: optical delay line
detector path
collimator
neutral density filter
dispersion compensation cube
mirror
spectrometer-based FD-OCT
x, y transverse scanning galvanometers
sample path
source path
SLD source
detector path: spectrometer
2x2 fiber coupler
collimator
scan lens
ophthalmoscopic lens
transmission grating
reference path: optical delay line
linear array detector
objective
collimator
collimator
neutral density filter
dispersion compensation cube
mirror

**FIGURE 4.18** Typical optical schematics for swept-source- and spectrometer-based FD-OCT systems and an image of the optic disc acquired with a clinical instrument (Zeiss Cirrus).

a transmission grating and CCD or CMOS linear array detector. Swept-source OCT instruments use a broadband source that is swept rapidly over a range of narrowband wavelengths and a single-point detector (similar to that used in TD-OCT) [183].

FD-OCT has several significant advantages and relatively few disadvantages compared to TD-OCT. Because the reference path mirror does not have to be scanned mechanically, much higher A-scan rates are possible. Also, FD-OCT achieves a higher SNR via simultaneous multiplexed acquisition of depth voxels. In contrast to TD-OCT, the higher scan speeds do not come at the price of reduced SNR. In practical terms, this means that retinal images can be produced at A-scan rates of tens to hundreds of kilohertz with comparable or lower power levels. FD-OCT instruments also typically have much lower phase noise because the reference mirror is not scanned mechanically. Furthermore, because the raw spectrum is acquired, phase-processing techniques (e.g., optical Doppler tomography, dispersion compensation) are readily available without modification to the hardware.

FD-OCT does suffer a few disadvantages when compared to TD-OCT. FD-OCT imagers usually have a much more limited range (2 mm, compared to 4 or 5 mm) than that of TD-OCT imagers. The FD-OCT range is determined by the spectrometer resolution and is ultimately limited by the spectrometer optics and detector pixel size. Because the FD-OCT range exceeds the penetration depth for most tissues, including the retina, this is of consequence only with respect to axial (i.e., head) motion for retinal imaging. Because after Fourier transformation, both the real and complex conjugates of the spectrum are acquired about the zero fringe (dc component), an improperly positioned target signal can wrap upon itself. FD-OCT also suffers an inherent depth attenuation of the spectrum, which results from a reduced modulation contrast ratio for the finite pixel size of the linear array detector. The depth attenuation is typically on the order of 5 to 15 dB, and losses can be minimized by careful adjustment of the axial position of the sample close to the zero fringe. Finally, because the A-scan is acquired simultaneously, images in the *en face* plane cannot be acquired rapidly as they are in transverse scanning OCT [184–186]. The significant advantages of FD-OOCT far outweigh the minor (controllable) disadvantages, and for that reason, FD-OCT has all but supplanted TD-OCT in both research labs and clinics.

The two different FD-OCT configurations also have advantages and disadvantages with respect to one another. SD-OCT instruments have the advantage that simple broadband sources can be used [e.g., ultrashort laser or superluminescent diodes (SLDs)] and typically achieve a much higher axial resolution (5 μm vs. 10 μm). SD-OCT has disadvantages, including a more complicated detection path with spectrometer optics that need to be controlled precisely for chromatic dispersion. SD-OCT is readily available at shorter wavelengths (ca. 850 nm) using standard silicon linear detectors and also at 1.06 and 1.3 μm using newly available indium gallium arsenide (InGaAs) detectors. Longer NIR wavelengths at water absorption windows are used for increased depth penetration from reduced light scatter.

***Swept-Source OCT*** Swept-source systems sacrifice complicated source optics for simple single-element detection. SS systems have several advantages over their SD counterparts. The interferometer throughput is inherently much higher because single fiber-coupled detectors are used rather than free-space spectrometers with gratings and lower-sensitivity linear detectors. For a well-designed source, the depth-dependent signal attenuation can be reduced significantly. Moreover, the depth range, which for SS systems is determined by the instantaneous source linewidth, is typically much longer for SS systems. SS systems often employ dual balanced detection schemes, which automatically subtract the dc component of the interferogram and enable higher dynamic range digitization of the ac component with source intensity noise reduction. Also, SS systems are more impervious to fringe washout, which can corrupt SD-OCT systems during a high-velocity scan or in the presence of axial and transverse motion [187]. Because of the single-point detection, frequency-shifting schemes can be used to double the range and eliminate folding about the zero-order fringe [188,189]. These advantages have rightly caused SS to gain popularity among OCT researchers. However, current swept sources generally have a lower axial resolution, as determined by the free spectral range of the intracavity filter. Future development of filter designs will likely increase axial resolution in SS systems to close to that achieved by spectrometer-based systems. Swept-source systems were introduced for biomedical imaging at 1300 nm [183] and have recently been configured for retinal imaging at 1 μm [190] and 800 nm [191].

SS-OCT typically use a laser source comprising an external cavity ring laser with a semiconductor optical amplifier (SOA) and a tunable narrowband filter [192], the free spectral range of which defines the sweep range and hence the axial resolution. The tunable filter used in SS-OCT is generally either a Fabry–Perot filter [193], which modulates the spacing between parallel mirrors or a spinning polygon configuration [194], which scans the incident beam angle on a grating for wavelength tuning. These configurations have sweep speeds comparable to spectrometer-based systems. Recently, Fourier-domain mode-locked (FDML) lasers, in which the spectral modulation is synchronized or locked to the round-trip pathlength of the cavity, were used to achieve line rates of 370 kilolines/s [195,196]. Mode locking obviates the buildup time necessary to achieve lasing from spontaneous emission, a limitation in other types of swept sources. Intracavity dispersion in these lasers must be managed carefully because of the long fibers used; 1300 nm is a zero point in the dispersion curve of glasses typically used in optical fibers. The FDML approach is more difficult at shorter wavelengths. Still, scan rates in excess of 100 kHz have recently been achieved [197]. Figure 4.19 shows three-dimensional mapping of the ONH and lamina cribrosa in which the data cubes were acquired at 249 kilolines/s using a FDML source at 1060 nm.

***Parallel and Line Field Optical Coherence Tomography*** Besides ultrahigh-speed swept-source OCT via the use of FDML sources, parallel OCT is also beginning to emerge as a technique to achieve very high frame rates. Parallel

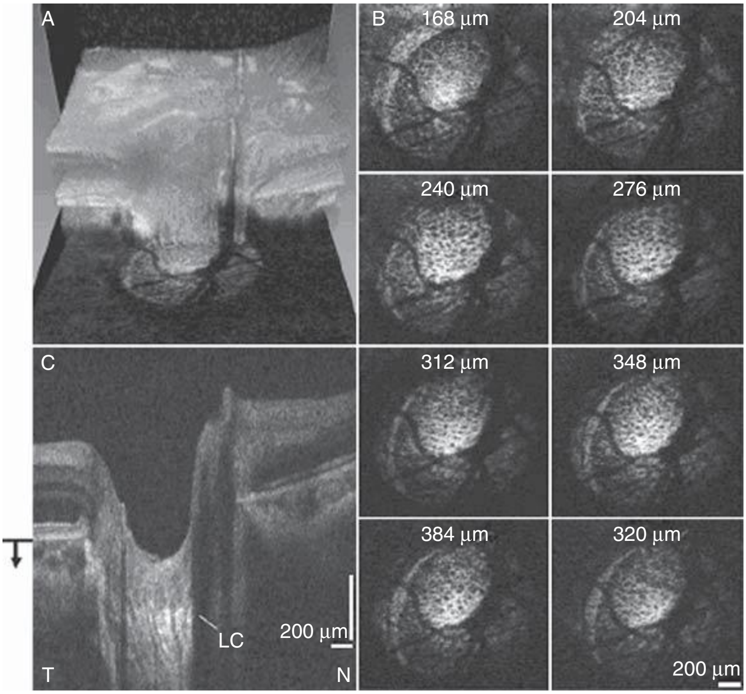

**FIGURE 4.19** Ultrahigh-speed three-dimensional mapping of the ONH and lamina cribrosa: (A) three-dimensional volumetric image; (B) individual *en face* images at different depths relative to Bruch's membrane; (C) composite image of six consecutive OCT cross-sectional frames. (From [198], with permission.)

OCT is a nascent technology that includes full-field and line-field modalities [199–206]. Full-field OCT is also known as optical coherence microscopy (OCM) when used in a high-resolution microscopic arrangement with a high-numerical-aperture objective. Full- and line-field OCT systems are similar in motivation and principle but distinguished by the use of a cylindrical lens for the latter. In contrast to traditional OCT, where a focused beam is scanned for image formation, full-field OCT instruments use various methodologies (e.g., piezotransducers for pathlength modulation) to apply low-coherence interferometry to a conventional imaging approach with full image and object fields. Both line- and full-field OCT provide parallel spatial detection and therefore potentially increased speed and stability and reduced complexity compared to a scanning spot system. Full-field OCT is currently being developed along a separate track for applications such as high-resolution microscopy and endoscopy [205–207].

Line-field OCT was invented simultaneously by several groups [208–214]. For line-field Fourier-domain OCT, a spectrometer comprised of a grating and a two-dimensional CCD (or CMOS) array is used in the interferometer detector path. The line-field spectrometer is configured in an arrangement familiar in spectroscopy as a spectrograph, with wavelength spread in one axis and the spatial line spread in the other axis. Nakamura et al. recently reported retinal images with an integration time of 311 μs [213]. Although this full-frame integration time potentially represents a huge increase in the effective line rate to nearly 1 MHz, the actual system used a much lower line rate of 51.5 kHz for continuous imaging, which represents only marginal improvement over current spinning polygon-based swept-source systems [183]. The line-field approach has also been applied recently to OCM [215], and in a time domain, a fiber-based system for endoscopy [216]. Lee and Kim were the first to report a line-field swept-source instrument, which is composed of line illumination and detection with a linear array coupled with a swept source, and has certain advantages over line-field OCT with a two-dimensional detector [214].

For OCM, Chen et al. have shown an increase in sensitivity of nearly 10 dB for the line-field approach compared to the full-field approach [215]. The sensitivity increase comes from the reduced illumination volume—and amount of incoherent scattered background light that ultimately limits OCM sensitivity—outside the coherence volume for the line-field approach. Nakamura et al. also show a potential increase in sensitivity for the spatially multiplexed line-field OCT technique compared to a traditional flying-spot FDOCT technique [213]. For ophthalmology, line-field illumination also allows the use of much higher input powers to the eye within the ANSI safety limits, because the power is spread across a larger retinal patch. Currently, line-field illumination and detection require a free-space interferometer, which is more susceptible to vibration-induced fringe washout and precludes the compactness and portability of a fiber optic–based interferometer. Full- and line-field OCT may eventually prove to be an attractive technique to achieve ultrahigh-speed imaging and video-rate three-dimensional mapping of tissues such as the retina.

### 4.4.2 Adaptive Optics

Adaptive optics (AO) refers to the use of components whose optical properties can be modified dynamically in response to some external change in a scene or sample. AO, first proposed by Babcock [217], was first used in astronomy in 1977 [218], where it is now used routinely in ground-based telescopes to correct for atmospheric turbulence and distortion. Dreher et al. were the first to apply AO to ophthalmology with the use a deformable mirror in an SLO imaging setup for the correction of astigmatism in the eye [171]. Liang et al. first used both wavefront sensing and compensation of higher-order aberrations to achieve unprecedented resolution in retinal images acquired with flash fundus photography [172]. This was followed by early work to quantify the cone mosaic across a range of eccentricities and to map the arrangements of the three cone classes in live human eyes [219].

Since then AO has begun to change optometry, ophthalmology, and the way we commonly perceive vision in general in a profound manner. First, ideas about our visual ability have changed. Supernormal vision (i.e., the attainment of visual acuity greater than "perfect" and limited only by the individual retinal cone spacing) is on the cusp of becoming a part of many vision-corrective procedures. Customized refractive surgical procedures are being developed in which the static wavefront of every person's eyes are measured precisely and mapped to the corneal. Many researchers are also working on custom spectacles, contact lenses, and intraocular lenses that have a shape tailored to one's eye [220–222].

Adaptive optics has also changed the way we look at and understand retinal function during pathogenesis and progression of such diseases as glaucoma, macular degeneration, and diabetic retinopathy. Although the SLO is able to achieve high contrast images and moderate depth discrimination of retina layers compared to imaging systems that use area detectors and flood illumination (e.g., fundus camera), the spatial resolution and contrast are still limited in part by ocular aberrations arising largely from the cornea and lens. In ophthalmology, AO is used to sense ocular aberrations that arise primarily from the tear film, cornea, and lens. Correction of optical distortions caused by imperfections in the eye can provide diffraction-limited performance in optical ocular imaging instruments. AO utilizes the full NA of a dilated eye to improve both lateral resolution and depth of focus. This can improve the performance of purely diagnostic instruments and also enable precision stimulation or therapeutic beams to be delivered to the eye.

AO instrumentation typically involves a sensing component, which detects and measures optical aberrations, and a compensating element, which is able arbitrarily to distort the wavefront of a beam. Between the sensor and compensator is a feedback control algorithm, which transforms a representation of aberrations into control voltages for the compensator. Figure 4.20 shows a typical arrangement. Light from a beacon (or the imaging beam itself) is directed toward the sample (e.g., galaxy, star, eye, tissue) and the wavefront distortions are quantified by the sensor. After calculation of the appropriate control voltages, the compensator takes on a predistorted wavefront shape, producing plane waves and diffraction-limited focus after passing through the sample. In general, the closed-loop bandwidth requirements for AO systems in astronomy are very high (kilohertz) because of the rapidly varying nature of perturbations in the atmosphere. For the eye, most dynamic changes arise from changes in the tear film thickness between blinks, so a bandwidth of a few hertz is usually sufficient. Although some researchers have reported ocular aberrations changes at much higher frequencies [223–225], other have found good performance from static customizable phase plates [226].

The wavefront sensor most commonly used in astronomy and ophthalmology was constructed by Platt and Shack [227] based on the concept by Hartmann [228]. A Hartmann–Shack wavefront sensor (HS-WS) is composed of a lenslet array and a CCD camera. The lenslet array subdivides the pupil into many subapertures. A distorted wavefront passing through the lenslet array will have a local tilt or slope, and by measuring the distance the focused spot moves for each lenslet, the magnitude of the local slope can be quantified. The global wavefront

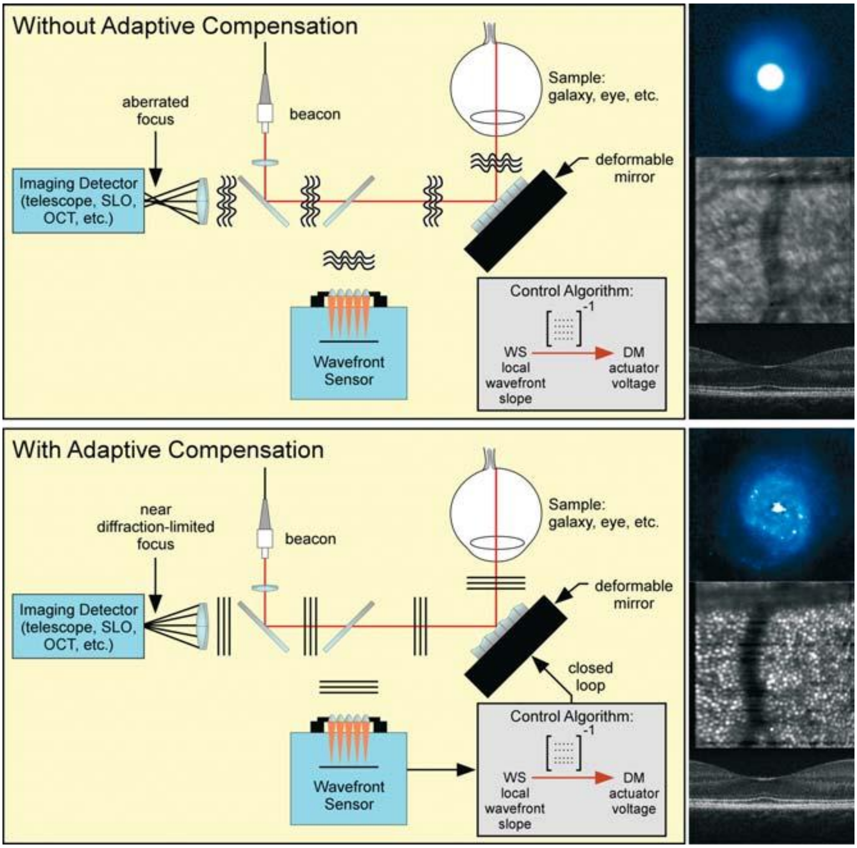
Without Adaptive Compensation
aberrated focus
beacon
Sample: galaxy, eye, etc.
deformable mirror
Imaging Detector (telescope, SLO, OCT, etc.)
Wavefront Sensor
Control Algorithm:
-1
WS local wavefront slope
DM actuator voltage
With Adaptive Compensation
near diffraction-limited focus
beacon
Sample: galaxy, eye, etc.
deformable mirror
Imaging Detector (telescope, SLO, OCT, etc.)
closed loop
Wavefront Sensor
Control Algorithm:
-1
WS local wavefront slope
DM actuator voltage

**FIGURE 4.20** Principle of adaptive optics. An AO system senses and corrects beam distortions with a wavefront sensor, deformable mirror, and feedback loop between them. Nearly diffraction-limited beam focus allows increased axial resolution of a galaxy, photoreceptor mosaic, or retinal layers.

is then reconstructed from the local slopes. For AO, the number of spots across the pupil must be critically matched or oversampled with respect to the number of compensator actuators; otherwise, "null space" errors (e.g., waffle mode error) can cause the DM to drift toward an unstable state. HS-WSs are used because they can sense optical aberrations very rapidly (up to thousands of times per second for some cameras). However, other wavefront sensing techniques have been used successfully, including spatially resolved refractometry, radial shearing interferometry, point-diffraction interferometry, Foucalt knife-edge tests, and double-pass retinal imaging using phase retrieval [229–231].

There are also many techniques for wavefront correction, including those with segmented and continuous mirror surfaces, and different actuator types and mechanisms. Examples of wavefront compensators that have been used successfully include piezo-driven segmented mirrors [172,232], liquid-crystal spatial light modulators [233–235], static phase-correcting plates [226], an electrostatic membrane deformable mirror (DM) [224,236,237], a MEMS-based DM [238], and magnetic actuator-driven, flexible surface DMs [239].

The wavefront compensator must also have good temporal response (for high closed-loop bandwidths), surface quality (to prevent losses), and for ophthalmology, a small size (to reduce pathlengths and overall instrument footprint). Wavefront spatial frequencies are often represented by Zernike coefficients (or some other appropriate orthogonal representation), and the higher the spatial frequency, the higher the order. Therefore, the actuator count determines the maximum aberration order that can be corrected. One of the most important specifications for the wavefront compensator is the stroke, in order to correct a large range of ocular aberration magnitudes. This is important in clinical ophthalmic AO systems to achieve improved imaging across the wide range of aberrations (e.g., keratoconic eyes) present in the general population [240].

Segmented mirrors were used widely early in AO development because they generally have a moderate stroke and the highest response time, since each element is addressable independently. (For this reason they are also widely used in astronomy.) However, they are extremely expensive, have poorer surface quality (from gaps between segments), lower actuator counts, and are quite large. SLMs are also relatively expensive, require monochromatic and polarized light, and have a slow response time. Micromachined membrane DMs are lower in cost than segmented mirrors, SLMs, or MEMS-based and magnetic DMs but generally have inferior performance because of limited stroke and nonindependent control of a portion of the mirror. Use of phase-correcting plates manufactured with a photolithographic process is an attractive extremely low-cost option for static correction of ocular aberrations. MEMS-based DMs are extremely small in size (ca. 4 to 5 mm) and typically have high actuator counts [238], while magnetic actuator DMs have an extremely large stroke (ca. 50 $\mu$m). MEMS-based and magnetic actuator DMs are relatively expensive but are most often used in AO systems fabricated for ophthalmology.

AO has recently achieved success in a range of applications in ophthalmology. It has been integrated into flood illumination full-field retinal cameras, confocal SLOs, and OCT instruments for high-resolution reflectance imaging [171,172,232,241–246]. AO is being used as a tool to understand the structural and functional aspects of vision, the elegant but complex retinal circuitry, and the dissolution of that structure, together with the wiring and processes, during the execrable progression of disease. It has been used in direct measurements of the foveal avascular zone, retinal capillary erythrocyte and leukocyte velocity, pulsatility, and other functional dynamics [247,248]. AO stimulation is also being used to measure and begin to understand the characteristics and causes of intrinsic retinal signals [249–251]. It has been used to study the organization of the human trichromatic cone mosaic and defects in color vision and compared to standard psychophysical tests [219,252–254]. The waveguiding properties and aspects of cone directionality (i.e., the Stiles–Crawford effect) have also been confirmed with measurements using adaptive optics instruments [255]. AO-corrected microperimetry to probe fixation loci and retinal microscotomas have also been reported recently [256,257]. The RPE cell mosaic is being mapped in monkeys and humans and correlated to the cone mosaic [152,258]. Ganglion cell function has been explored with exogenous dyes [152,259]. In many of the aforementioned studies, genetic defects are confirmed and explored directly in the live eye [260]. Diseases such as rod–cone dystrophy are also being examined [261–263]. Systems are slowly migrating from the research lab into the clinic for use on patients with a variety of diseases and conditions [96,264,265]. It is also being applied to advanced molecular and gene therapies, both in their development and as the primary method to determine treatment efficacy at the cellular level.

***AO Fundus Imagers*** AO was first applied to ophthalmology using standard fundus imaging techniques [171,172]. AO in flood illumination and detection cameras provided significant improvement in resolution and depth of focus for visualization of photoreceptors (cones), and this provided an opportunity to characterize deficiencies directly in color vision and other aspects of vision [219,252,253,257,266–268]. Like traditional fundus cameras, these AO imagers tended to produce images with increased light scatter from adjacent voxels. However, their strong waveguiding properties allowed the resolution of cone photoreceptors, even in the presence of light scatter. AO fundus cameras can operate at very high speeds and are also significantly less complex than AOSLOs [269]. They have been used recently in functional studies of cone scintillation [250] and in the investigation of visual defects such as microscotomas [256].

***AOSLO*** AO was first integrated into a scanning laser ophthalmoscope by Roorda et al. in 2002 [232]. Like conventional SLOs, AOSLOs provide significant reduction in light scatter for extremely high-contrast retinal images and improved lateral resolution and depth-sectioning capabilities [143]. AOSLOs have been developed with novel instrumentation, including with an auxiliary SLO imager [173,270], an integrated retinal tracker [173,270], a dual-DM [271], a stroke amplifier [272], a fluorescence channel [152], polarization optics [273], and a multiple visible light stimulation source [249]. Besides significant investigation of the photoreceptor cone mosaic [274,275], AOSLOs have also been used to examine the RPE mosaic [152,258,263], leukocyte and erythrocyte flow [247,248], the features of the lamina cribrosa [276], and other characteristics of the retina.

***AO-FDOCT*** Hermann et al. were the first to integrate AO into a (TD-) OCT system [241]. Others constructed AO instruments for spectrometer-based FDOCT [242–244] and parallel FD-OCT approaches [211]. Like AO for scanning laser ophthalmoscopy, AO provides improvement in lateral resolution and increased SNR [243,244]. Because of its micrometer-level axial sectioning capabilities, OCT is more sensitive than SLO to changes in depth of focus. A reduced depth of focus from AO leads to OCT signal and lateral resolution loss for regions outside the isotropic voxel where the focus is set. So AO-OCT instruments (with 7 to 8-mm beam diameters) often produce images with decreased quality for layers away from focus compared to their clinical counterparts (with 2 to 3-mm beam diameters), even with adaptive compensation [277]. Focus adjustment is therefore important for AO-FDOCT systems [244,277]. Because OCT instruments use broadband illumination (the bandwidth for sources used in ultrahigh-resolution OCT system can exceed 200 nm), care must also be paid to correct chromatic aberrations [21]. An achromatizing lens has been developed by several groups to minimize chromatic aberration over the wavelength range of the source [21,245,246]. The achromatizing lens minimizes lateral chromatic aberration by adding the opposite average ocular chromatic aberration to the sample path.

Figure 4.21 shows AO-FDOCT *en face* slices through the retina in a region near two stable CSR lesions. The AO-FDOCT show excellent resolution of the capillaries at the top and base of the inner nuclear layer (Figure 4.21c and 4.21d) and the photoreceptor mosaic (distorted by eye motion) can be seen in Figure 4.21g.

***High-Resolution Capabilities*** AO has provided extraordinary visualization of cells, layers, and structures never before seen in the live eye. Because they are so central to the mechanism of vision but also because they have features (size, shape, location) and properties (waveguides) that are ideally amenable for AO imaging, photoreceptors have been a natural target. The cone photoreceptor mosaic is now mapped routinely, and characteristics of cone spacing with eccentricity are often quantified in investigations of disease and vision [274,275,279]. Figure 4.22 shows a strip of the photoreceptor cone mosaic from the fovea to an eccentricity of about 0.83 μm (2.8°). Whereas cones have been imaged and mapped routinely with AO, rods—which are nearly equally important for vision and the study thereof—are not routinely resolved in normal eyes. This is because of their much smaller size (1 to 3 μm), their dearth in the central macula (they are absent altogether from the fovea and become closely spaced only in the periphery), and their lack of waveguiding properties.

AOSLOs equipped with fluorescence channels are able to resolve the RPE mosaic from the lipofuscin autofluorescence within the cells [152,258]. Figure 4.23 shows images of the RPE cell mosaic at the fovea and 10° eccentricity. The RPE has also been resolved in humans [258]. Both images in Figure 4.23 were created by summing 1000 frames and using a dual-beam registration technique [152,249]. Dual-beam registration is necessary because of the low lipofuscin signal intensity. The AOSLO is essentially configured with two paraxial and parfocal beams: one NIR beam that collects a standard AOSLO reflectance image and one visible beam that collects the fluorescence image. After acquisition, the reflectance image is registered and the same corrections (translation, rotation, de-warping, etc.) are then applied to the fluorescence image. The composite images, averaged from several hundred or thousand

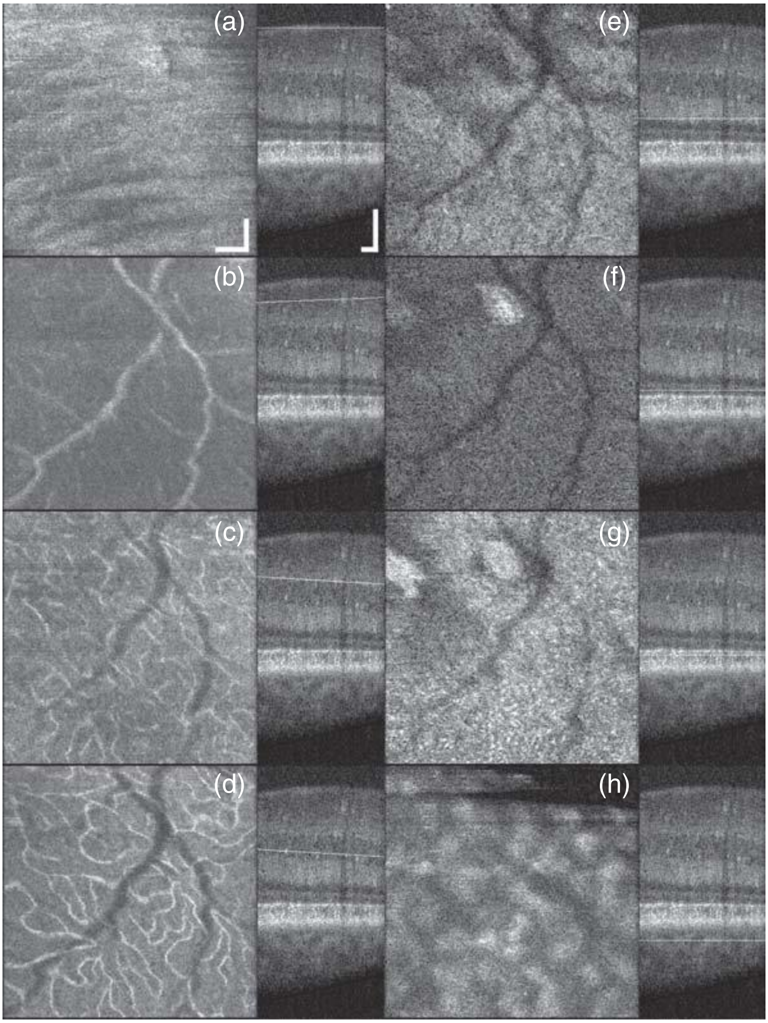

**FIGURE 4.21** AO-FDOCT montage of retinal layers. *En face* images were constructed from an OCT raster scan. A corresponding layer in a cross-sectional scan is shown to the right of each *en face* image. (a) A nerve fiber layer (fibers bundles just visible running slightly off horizontal); (b) large retinal vessels in the ganglion cell layer; (c) small capillaries between inner plexiform and inner nuclear layers; (d) small capillaries at the base of an inner nuclear layer; (e) posterior outer plexiform layer (top of lesions); (f) photoreceptor outer segments; (g) photoreceptor inner segments; (h) choroid. Scale bar, 100 μm. (From [278], with permission.)

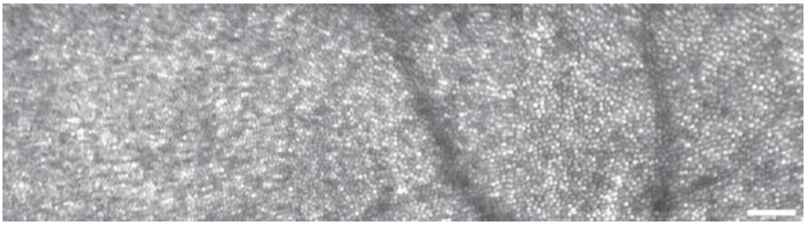

**FIGURE 4.22** In vivo AOSLO image of the human photoreceptor cone mosaic for eccentricity up to 0.83 μm (2.8°). The fovea is in the upper left corner. Scale bar, 50 μm.

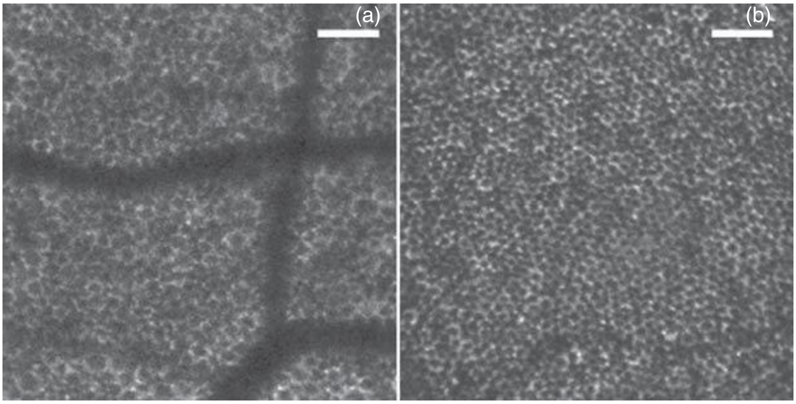

**FIGURE 4.23** In vivo AOSLO images of RPE mosaic in a healthy adult macaque nemestrina monkey: (a) eccentricity = 10°; (b) centered on the fovea. Scale bar, 75 μm. (From [152].)

frames, are thus corrected for eye motion. Because eye motion has been for the most part fixed in the monkey, it is less of an issue for the long-duration scans (ca. 10 to 60 s) that need to be acquired. In humans, eye motion is much more problematic, and this may delay or limit the availability of RPE cell mapping for clinical investigations.

Retinal targets in the inner retina have also been examined. Ganglion cells bodies, axons, and dendritic arborization have been resolved with AOSLO in primates using retrograde transport and subsequent photofilling of rhodamine dextrane from the lateral geniculate nucleus [259] (see Section 4.5.2). Leukocyte and erythrocyte velocity and pulsatility have also been quantified in the capillaries surrounding the fovea [247,248,280]. The fovea is normally avascular, and some conditions (e.g., ROP, albinism) disrupt the neurovascular mechanism in the retina and lead to a malformed or absent foveal avascular zone (FAZ). AO is able to resolve the finest capillaries in the retina, and one technique that has shown promise for mapping the capillaries involves calculation of the standard error map from a sequence of AOSLO images collected from the same retinal

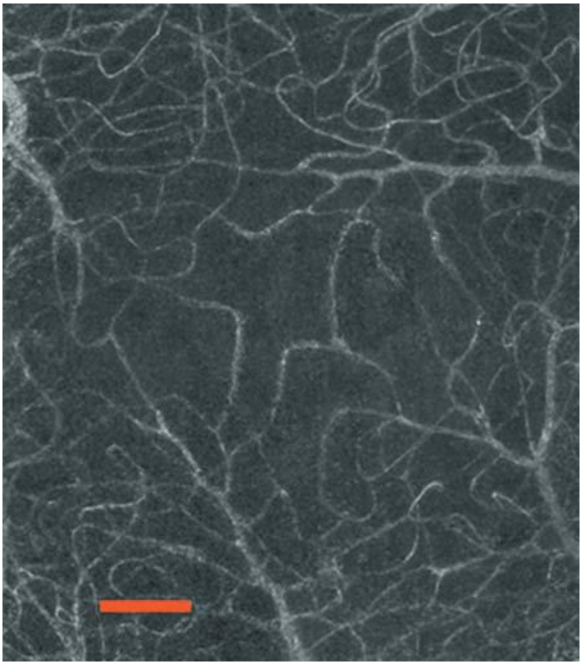

**FIGURE 4.24** In vivo AOSLO montage of the foveal avascular zone using the standard error-mapping technique. Scale bar = 100 μm. (Courtesy of S. Burns.)

location, after registration [281]. Figure 4.24 shows the capillaries around the AVZ resolved in humans using this standard error-mapping approach. The cells and structures surrounding the capillaries and vessels are also of importance to researchers. Figure 4.25 shows images of nerve fiber bundles, glial cell endfeet, and the interstitial and connective tissue near a pair of vessels in the inner retina.

***Clinical Applications*** AO is now beginning to transition from a tool used by vision researchers, psychophysicists, and biomedical optics researchers to a tool used by clinicians to understand, diagnose, and treat retinal diseases. Choi et al. used an AO fundus imager to correlate cone densities to functional findings (visual field and multifocal ERG) in rod–cone, cone–rod, and juvenile macular dystrophies [261]. Others have used AOSLO to examine patients with inherited retinal disease, including cone–rod dystrophy, retinitis pigmentosa, and bilateral progressive maculopathy [260,263,264]. These studies were done in conjunction with genetic screening to determine any correlation between structural malformation and genetic mutations. Both groups found regions of intact cone photoreceptors but with increased spacing and abnormal reflectivity in cone–rod dystrophy. These findings were also correlated to measures of foveal threshold, visual acuity, and mfERG. Hammer et al. used AO-FDOCT to examine the structural differences in eyes with retinopathy of prematurity [96]. Choi et al.

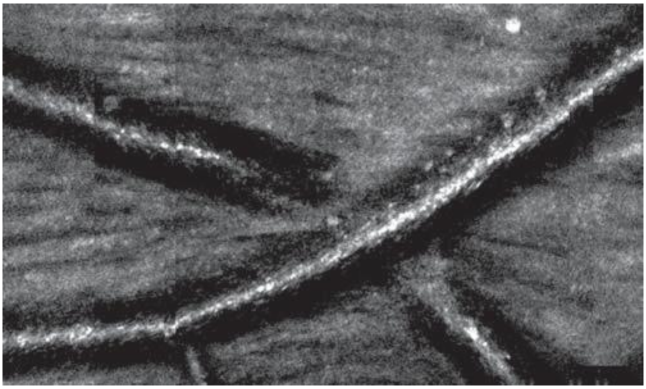

**FIGURE 4.25** In vivo AOSLO montage of a crossing vessels and nerve bundles in the inner retina of a human subject. (Courtesy of S. Burns.)

used AO fundus imaging and AO-FDOCT to examine changes in cone density and retinal layers in subjects with five types of optic neuropathy [265]. These important diagnostic findings will proliferate exponentially as high-resolution techniques such as AO move toward more widespread clinical implementation. Furthermore, they will guide the development and characterize the efficacy of new therapies, including those that are gene-based, for a wide variety of retinal diseases.

### 4.4.3 Other Modalities: Doppler Flowmetry and Polarization-Sensitive Imaging

Various other technologies have been developed over the last decade to increase and improve the information extracted from retinal images. In general, the most innovative techniques exploit some characteristic of either the tissue itself or the interaction of light with the tissue. For example, single-point and imaging techniques that measure Doppler shifts that arise from flowing blood in the retinal vessels is a fertile field of research with a long history [282]. Furthermore, the birefringent properties of the eye, including the cornea, lens, and nerve fiber layer, have long been known [283–285]. The properties are now being exploited in new variants of traditional imaging techniques.

Optical Doppler tomography has been developed and refined for time- and frequency-domain OCT imaging to measure blood flow in retinal circulation [286–289]. This technique involves measurement of the phase shift in the OCT spectrum that arises from moving particles. FDOCT allows a wider dynamic range (i.e., minimum phase sensitivity to maximum phase before wrapping) and improved phase stability [288]. The OCT phase shift gives the Doppler frequency shift, which in turn can be used to calculate the flow velocity with knowledge of the angle between the beam and the vessel. Typically, the angle is hard to

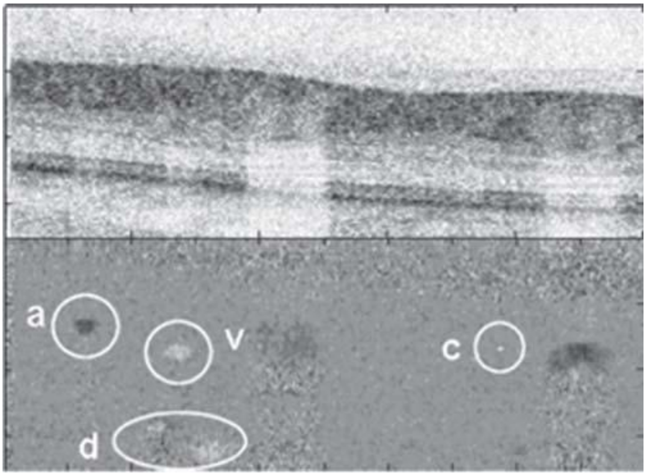

**FIGURE 4.26** FDOCT reflectance image of retinal tissue (top) and corresponding Doppler phase map (bottom). The map shows flow in a large artery–vein pair as well as in a small capillary and choroidal vessels. (From [288], with permission.)

determine, so the absolute velocity is usually not reported, but relative flow magnitudes and directions can easily be determined from the phase shifts, and these provide a wealth of information about flow. Figure 4.26 shows a FDOCT reflectance image and a corresponding phase image of flow in retinal vessels.

Recently, new sources near 1 μm have been used in TD-OCT [290,291] and swept-source FDOCT (i.e., OFDI) systems [190] to enable enhanced visualization of choroidal vessels. Figure 4.27 shows high-speed OFDI 1-μm OCT cross-sectional and *en face* images of choroidal vessels. The *en face* planes were integrated selectively over specific layers in the outer retina.

One of the drawbacks of Doppler techniques for retinal blood flow measurement is the cos θ angular dependence of the flow velocity. Since this angle is usually nearly normal for beams entering the eye, the measured Doppler velocity magnitudes can be very small or zero. For a single-scattering technique such as OCT, this situation is particularly confounding, and measurement of flow in even moderately sized vessels is difficult or impossible. Doppler techniques applied to other multiple-scatter imaging techniques are usually able to resolve flow in smaller vessels. For example, Doppler techniques have been applied in unique ways to SLO and other *en face* fundus imaging techniques. Figure 4.28 shows a line scanning laser ophthalmoscope (LSLO) image created from a Doppler data cube where the frequency content has been binned to separate flow in different vessels [158]. The high-speed Doppler shifts from the large arcades and arterioles are shown in the blue plane; the middle-speed Doppler shifts from medium-sized retinal vessels are displayed in the green plane; the low-speed Doppler shifts from the capillaries (i.e., a perfusion map) are shown in the red plane. The Doppler data cube took 35 s to acquire and was possible only with retinal tracking.

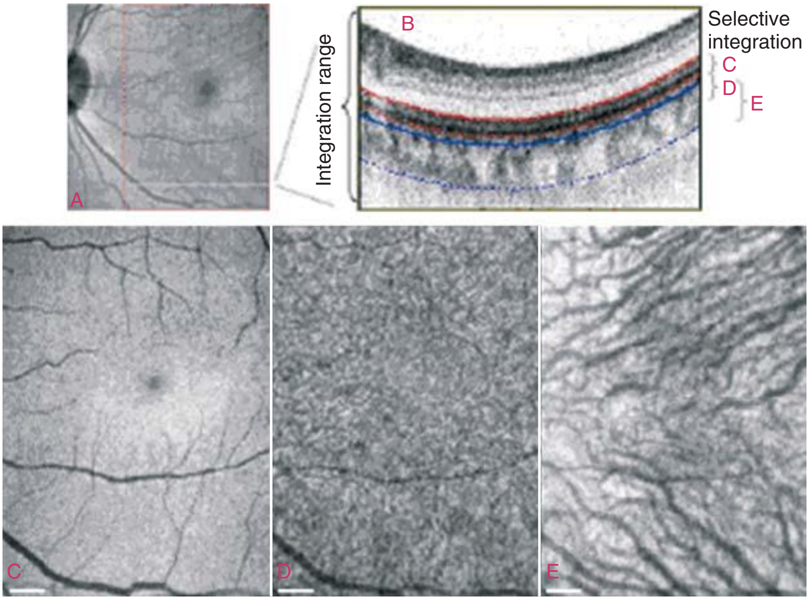
A
B
Integration range
Selective integration
C
D
E
C
D
E

**FIGURE 4.27** OFDI images of the choroid: (A) full-range integration of the OCT 3-D data cube; (B) cross section indicating regions integrated in (C–E); (C) photoreceptor/RPE layers; (D) inner choroid near the choriocapillaris; (E) outer choroid. (From [190], with permission.)

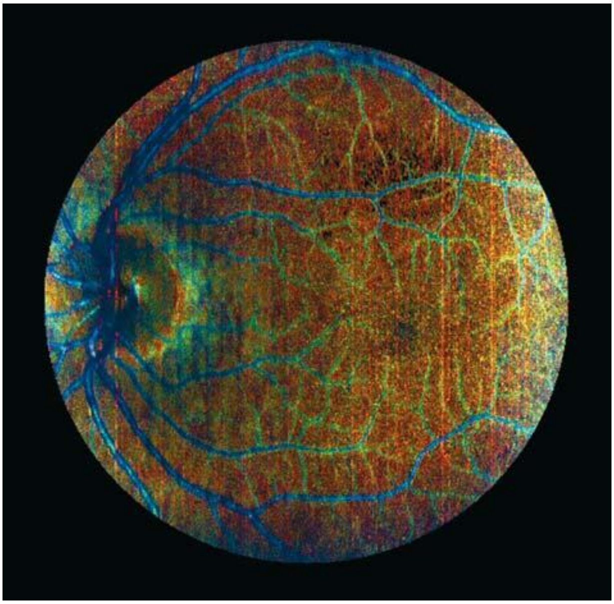

**FIGURE 4.28** Pseudocolor LSLO map where the Doppler frequency shifts have been binned for low speed (red, $f < 400$ Hz), middle speed (green, $f = 400$ to $1000$ Hz), and high speed (blue, $f > 1000$ Hz).

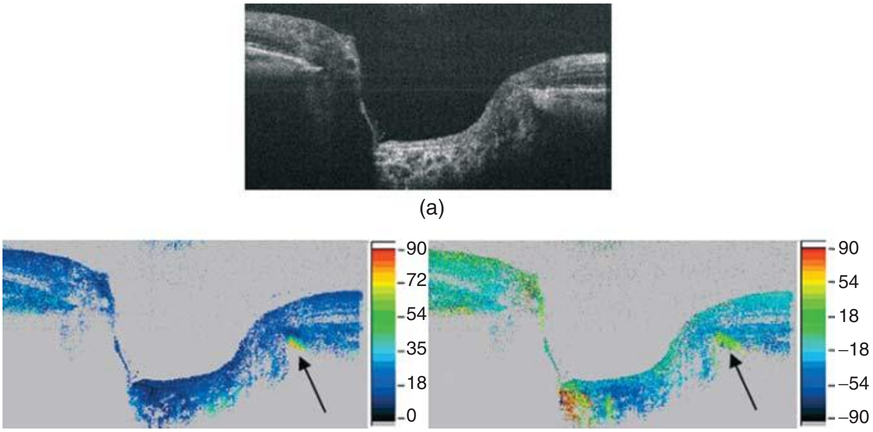

(a)

(b)

(c)

**FIGURE 4.29** Polarization images of the ONH: (a) OCT reflectance image; (b) retardation image; (c) fast axis orientation. Image size, 3 mm (horizontal) ×1.75 mm (vertical); values on color bars, degrees; arrow, temporal rim of scleral canal. (From [299], with permission.)

OCT has long been used to map the retinal nerve fiber layer (RNFL) in subjects with glaucoma—in fact, this was the primary clinical application in ophthalmology that drove development of OCT. The idea behind polarization imaging is to obtain increased image contrast of certain layers or structures by measuring its birefringent properties. Polarization imaging is often applied to the anterior segment because of the birefringence of the cornea and lens [292]. It has also been applied to map the thickness of the RNFL around the ONH, which has form birefringence from the ordered structure of the fibers and fiber bundles. Scanning laser polarimetry is now a standard clinical diagnosis [293–295]. In addition, time- and Fourier-domain polarization-sensitive OCT (PS-OCT) has been developed to provide micrometer-level axial sectioning capabilities to polarization imaging [292,296–299]. Polarization imaging instruments, including PS-OCT, typically operate by separation of the orthogonal polarization vectors into two detection channels, which can be manipulated in various ways to measure and map the Stokes vector, retardation, birefringence, diattenuation, and other polarization properties of the tissue. Polarization imaging was used recently to segment the RPE layer [292] Polarization imaging channels have also been applied recently to an AO system [273,300]. Figure 4.29 shows in vivo PS images (retardance and fast axis orientation) of the ONH in a human.

### 4.4.4 Multimodal Approaches

SLO and OCT are complementary tools for imaging the retina. OCT is an interferometric technique, with micrometer or submicrometer-level axial resolution that yields excellent sectioning capability. OCT is therefore better suited for visualization of retinal layers. The axial resolution of SLO is determined by the confocal range gate (or, equivalently, the imaging depth of focus), which is limited by the low numerical aperture of the eye (ca. 0.2 for a dilated pupil) to about 50 to 100 μm. However, because the confocal range gate is larger than the coherence range gate, SLO is sensitive to multiply-scattered light, whereas OCT can detect ballistic photons only from singly-scattered events. Because of this, OCT images integrated in depth are not equivalent to SLO images. Detection of multiply-scattered light has advantages for imaging certain retinal structures. For example, the waveguiding properties of cones and the interference of light from junctions in the inner and outer segments result in higher-contrast SLO images of the cone mosaic. For similar reasons (i.e., multiple scattering of light from moving erythrocytes and the vessel wall), SLO is generally better able than OCT to resolve blood flow and capillaries with high contrast. Also, SLO systems can be configured to collect fluorescence signals. The necessity of a reference arm signal makes configuration of OCT systems for fluorescence imaging impossible. To date, with very few exceptions [184,301–303], retinal imaging systems have been built that operate in either SLO or OCT modes. However, the hardware differences between instruments are minimal: OCT has an additional 2 × 2 coupler and reference arm optical delay line between the source and the detector.

Therefore, it is not surprising that new developmental efforts have focused on the combination of the two techniques [304], often also with AO [305–307]. Heidelberg Engineering now sells a clinical retinal imager (Spectralis) that combines up to six modes, including autofluorescence, FA, ICGA, NIR SLO, red-free imaging, and FDOCT. Sample images from the Spectralis system are shown in Figure 4.30. Other multimodal systems have been developed that combine polarization, AO, and either SLO or OCT [273,300]. These systems are powerful but quite complex, and engineering for simplification and automation will continue to be a challenge, as they are transitioned toward routine clinical use.

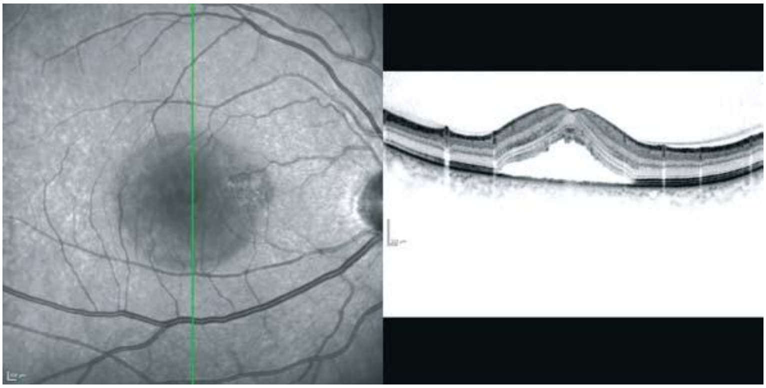

**FIGURE 4.30** Heidelberg Spectralis SLO and OCT images of central serous retinopathy. (Courtesy of Heidelberg Engineering, Inc.)

## 4.5 IMAGING BEYOND DISEASE DETECTION

For the most part, in the preceding section I described new technologies and methodology with respect to the detection of disease. Advances in retinal imaging have, of course, progressed for a wide range of scientific investigation beyond clinical diagnostic applications. These include the fields of vision science, physiology, pyschophysics, and drug discovery. These areas of investigation are large, and this section is designed to provide just a sampling of the amazing advances that have recently been reported.

### 4.5.1 Vision Science

AO was first applied to investigate features of color vision in vivo, and research in this area continues [219]. In tests of color vision, AO imaging is combined with fully bleached, selectively bleached (470- and 650-nm illumination), or dark-adapted visual stimulation to discriminate short (S), medium (M), and long (L) wavelength-sensitive cones. In the first paper directly mapping cone distribution with AO, Roorda and Williams found significant variability in M-cone distribution in subjects with normal color vision [219]. In eight subjects using the same technique, Hofer et al. also found significant variability in the L/M ratio and nearly identical S-cone densities [253]. Figure 4.31 shows false color images of the cone mosaics in these subjects. Their findings were also well correlated with flicker photometric electroretinography (ERG). Carroll et al. studied two dichromats (one protanope and one deuteranope) and in the deuteranope discovered patches or the retinal mosaic without cones, indicating functional loss of an entire cone class when the first two genes in the X-chromosome array are substituted by a gene that encodes a nonfunctional pigment [252]. Other than color vision defects, this subject displayed excellent visual acuity and no other vision deficit, despite having large patches of the retinal mosaic without cone photoreceptors. Other recent color vision studies have quantified S-cone dystrophy in Tritan color vision deficiency [268]. These investigations indicate the powerful capability of AO when combined with other psychophysical techniques to directly quantify the number and arrangement of cone classes in various color vision deficiencies.

### 4.5.2 Retinal Architecture and Physiology

Although an immense amount of knowledge can be gained about retinal anatomy from primate and human histology [18,308–312], it is more difficult to tease information about physiology and the interconnections and functional architecture of the retina from fixed, mounted tissue sections using this methodology. For example, the function of the majority of the 15 to 20 classes of ganglion cell is unknown [152]. Ganglion cells, which play an essential role in image information transfer to the brain, are generally classified by dendritic field diameter, branching, and axial stratification [259]. The techniques of exogenous dye injection and

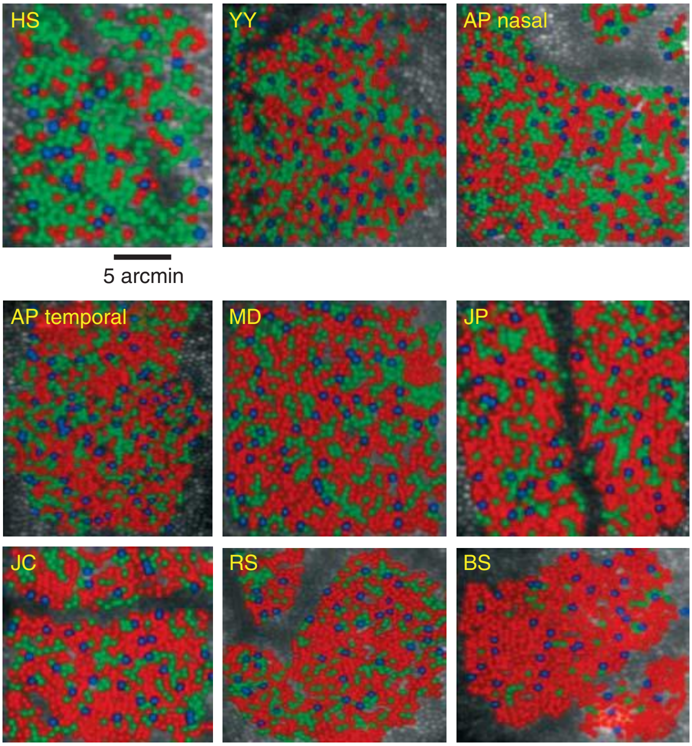

**FIGURE 4.31** Pseudocolor images of the trichromatic cone mosaic showing the arrangement of L (red), M (green), and S (blue) cones in several subjects. (From [253], with permission.)

adaptive optics can provide extrinsic signal enhancement and increased resolution to assist in cell classification. Figure 4.32 shows AO improvement in ganglion cells imaged in vivo in a macque monkey using retrograde transport of rhodamin dextran dye injected into the lateral geniculate nuclei.

### 4.5.3 Functional Imaging

Functional retinal testing is conventionally conducted using electroretinography (ERG), in which electrodes placed on the cornea record visually evoked neural responses to full-field stimulation patterns; or multifocal electroretinography (mfERG), in which electrodes record frequency-encoded patterns from distinct visual fields across the retina. Recently, several investigators have used optical imaging techniques to record intrinsic signals from the retina. This technique, often called *optophysiology* when applied to OCT [313,314], is still in its infancy. AO and OCT techniques are often used to provide precise lateral stimulation and depth-resolved measurement of the signals detected. Intrinsic retinal signals can be divided into slow signals (duration = seconds to minutes) and fast

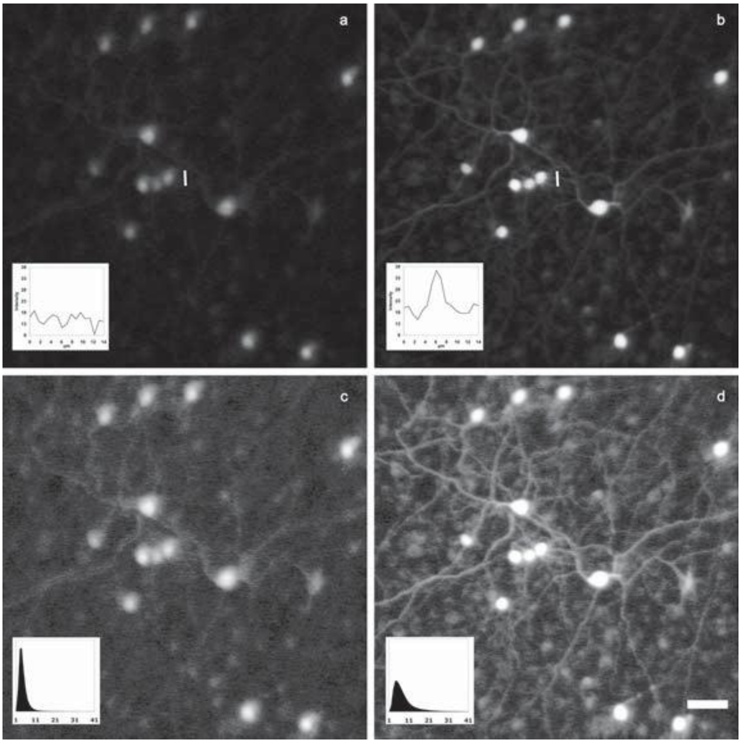

**FIGURE 4.32** In vivo ganglion cells imaged without (a,c) and with (b,d) adaptive optics. The lower row is a composite image averaged from 400 frames. The upper insets show a line profile across a dendrite, and the lower insets show the gray-scale image histograms. (From [259], with permission.)

signals (duration = hundreds of milliseconds) [251]. Slow signals usually have negative polarity (from a decrease in scattering) and arise from swelling, blood flow changes, and photopigment bleaching [315,316]. Fast signals usually have positive polarity (from an increase in scattering) and arise from neural signals (changes in membrane potentials) in the photoreceptors [317]. Jonnal et al. have called the fast changes in reflectivity in individual cones that are associated with phototransduction *scintillation* [250]. The measurement of visual evoked potentials using optical imaging techniques often produces erratic results (e.g., hyperpolarization and depolarization from similar stimuli, no response in some subjects). These difficulties result from weak signals from multiple confounding sources, eye motion, and low speed and resolution.

### 4.5.4 Precision Beam Delivery for Stimulation and Laser Surgery

Another potential clinical benefit of AO is in the development of instruments and techniques for precise retinal stimulation or laser microsurgery. For stimulation, the capability to stimulate individual cones, rods, and ganglion cells precisely will lead to methods to better understand light transduction and the primary and secondary neural processing that occurs in the retina. Significant strides have been made in the development of instrumentation for this purpose [318]. For laser microsurgery, AO could potentially allow precise targeting of RPE cells that have accumulated drusen or other proteins associated with AMD and feeder vessels associated with choroidal neovascularization in DR [319,320]. Laser safety considerations using AO instruments also need to be revisited [258].

### 4.5.5 Visual Psychophysics

The study of vision plays an important role in the field of neuroscience. Visual psychophysicists study the relationship between performance in visual tasks and light stimuli in order to gain an understanding of the neural processing involved in the human visual system [218]. As introduced in the preceding section, diffraction-limited presentation of visual stimuli using AO offers a tool to describe features of the spatial properties of the neural preprocessing that occurs in the retina. As an example, researchers have recently used AO to determine the degree to which the brain applies neural compensation for ocular aberrations [266,267]. These studies also have implications for customized vision-correction procedures (refractive surgery, custom contact lenses, etc.).

### 4.5.6 Small-Animal Imaging and New Drug Therapies

The mouse is the animal model used most often for human disease because the mouse genome has been mapped entirely, and transgenic and knockout mice have been developed for a multitude of diseases [321]. However, to study disease etiology and progression is often difficult because histology on an individual animal provides no temporal information content, so large numbers of animals must be used to gain a complete picture of disease [322]. In vivo studies are therefore preferred for efficiency.

In ophthalmology, there is increasing interest in the use of rodents to model diseases such as glaucoma, diabetic retinopathy, and macular degeneration [323]. Noninvasive imaging can be used in longitudinal studies to detect and track retinal changes associated both with the development of the disease and the administration of pharmacological agents designed to halt or reverse disease progression. However, rodents have particularly poor vision, and imaging rodents is difficult for various reasons, including increased aberrations, differences in retinal thickness, and the difficulty in designing focusing optics for the rodent eye's low $f/\#$ [324]. Moreover, because the rodent has evolved as a nocturnal animal, its retina consists predominantly of rod photoreceptors. So the rodent model may have limited utility for the study of macular degeneration, which affects primarily cone photoreceptors [325]. However, if AO can be used to correct the rodent's ocular aberrations and other technical problems are solved, the high NA of the rodent eye

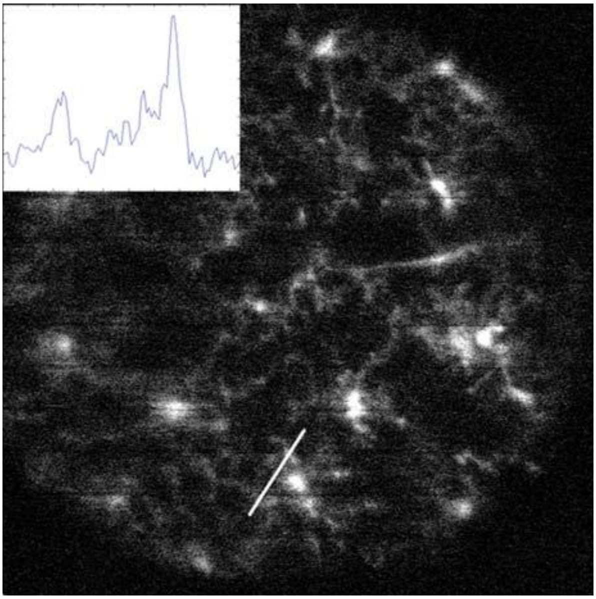

**FIGURE 4.33** In vivo AO images of GFP-labeled microglia in the mouse retina. (From [322], with permission.)

may provide better resolution of structures and capabilities for the use of technologies not possible in the human eye, such as multiphoton microscopy [326]. These new investigations have implications for the study of vision, retinal diseases, and the development of therapies to cure them or abate their detrimental spread.

Thus, AO may significantly enhance small-animal imaging for the development of new pharmaceutical agents and therapies. Initial investigation on AO applied to small-animal imaging has yielded positive results. Figure 4.33 shows in vivo images of GFP-labeled microglia in the mouse retina.

One of the most exciting new areas of research in ophthalmology is in the application of gene therapies to treat inherited retinal diseases. Viral vectors are often employed to transduce cells with specific known genetic mutations. Viral vectors are generally safe because their replication genes are removed. They are often created by transfecting cell lines (e.g., HEK 293) with various packaging and vector plasmids. Once in the cell, the vector delivers its genetic package by reverse transcription or other gene expression modality. In ophthalmology, viral vectors are usually introduced intraocularly into the subretinal space via sclerotomy, a microsurgical procedure that can often introduce complications. Several groups have recently reported initial clinical (toxicity) trials using the recombinant adeno-associated viral (rAAV) vector, AAV2-CBSB-hRPE65 [327] for treatment of Leber congenital amaurosis, an autosomal recessive disorder of the retina [328–330]. No vector-related or systemic complications were associated with the rAAV2 therapy, although no improvement was observed in measured visual acuity. It is not known if this lack of effectiveness is related to the advanced stage of retinal disease for the subjects in the trial or the low doses applied [330]. Clearly, many more studies are needed to verify safety and to determine effective doses and other treatment-related parameters.

## 4.6 CONCLUSIONS

The last 10 years have seen immense progress in the development of optical tools and instrumentation to guide and assist ophthalmologist and vision researchers alike in the discovery of key aspects of vision and its disruption from disease. At the beginning of the twentieth century, physicians could, with immense effort, view the coarse features—the large vessels and optic nerve head—in the living eye. At the end of the twentieth century, physicians could easily visualize with immense precision all the layers and cells responsible for the transduction of light into neural signals. The ability to image a single photoreceptor in a live eye that has a diameter 10 to 100 times less than the diameter of a human hair is truly remarkable.

So what does the future hold? The rapid pace of discovery in vision science may only just be beginning. Although new automation, control, optical engineering, and processing techniques will continue to be invented, the key discoveries will come in the fine structural, molecular, and functional features of vision and retinal disease. The trends of research have already begun to shift from engineering novel optical instruments to the application of optical tools to scientific discovery. This trend will certainly be hastened by the proliferation and exploitation of all the capabilities of FDOCT and AO systems. Furthermore, vision scientists will continue to use the tools of genetics to aid in the exploration of the molecular mechanisms of diseases and the discovery of new therapies to cure those diseases. The hereditary retinal diseases, such as retinitis pigmentosa, are certainly prime targets for cures, as are those for which many of the genetic mutations are already known (e.g., age-related macular degeneration). Personalized medicine will also come to ophthalmology. One day ophthalmologists will have a genetic therapeutic toolkit at their disposal that will make the prevalent laser therapies of the twentieth century look like the ophthalmoscopes used in Helmholtz's time. It is truly an exciting time.

## REFERENCES

1. Richter, J.R., *The Notebooks of Leonardo Da Vinci*, Dover Publications, Mineola, NY, 1970.
2. Mason, C., and Kandel, E.R., Central visual pathways, in *Principles of Neural Science*, pp. 420–439, E.R. Kandel, J.H. Schwartz, and T.M. Jessell (eds.), Appleton & Lange, Norwalk, CT, 1991.
3. Tessier-Lavigne, M., Phototransduction and information processing in the retina, in *Principles of Neural Science*, pp. 400–418, E.R. Kandel, J.H. Schwartz, and T.M. Jessell (eds.), Appleton & Lange, Norwalk, CT, 1991.

4. Larsson, M., Pedersen, N.L., and Stattin, H., Associations between iris characteristics and personality in adulthood, *Biol. Psychol.*, Vol. 75, 2007, pp. 165–175.
5. Firsching, R., et al., Venous ophthalmodynamometry: a noninvasive method for assessment of intracranial pressure, *J. Neurosurg.*, Vol. 93, 2000, pp. 33–36.
6. Iftimia, N.V., et al., Toward noninvasive measurement of blood hematocrit using spectral domain low coherence interferometry and retinal tracking, *Opt. Express*, Vol. 14, 2006, pp. 3377–3388.
7. Das, S.R., et al., Sensitivity to motion features in point light displays of biological motion, *Spat. Vis.*, Vol. 22, 2009, pp. 105–125.
8. Webb, R.H., and Hughes, G.W., Scanning laser ophthalmoscope, *IEEE Trans. Biomed. Eng.*, Vol. 28, 1981, pp. 488–492.
9. Huang, D., et al., Optical coherence tomography, *Science*, Vol. 254, 1991, pp. 1178–1181.
10. Schubert, H.D., Structure and function of the neural retina, in *Ophthalmology*, pp. 771–774, M. Yanoff and J.S. Duker (eds.), Mosby, St. Louis, MO, 2004.
11. Roh, S., and Weiter, J.J., Retinal and choroidal circulation, in *Ophthalmology*, pp. 780–782, M. Yanoff and J.S. Duker (eds.), Mosby, St. Louis, MO, 2004.
12. Azar, N.F., and Davis, E.A., Embryology of the eye, in *Ophthalmology*, pp. 22–27, M. Yanoff and J.S. Duker (eds.), Mosby, St. Louis, MO, 2004.
13. Springer, A.D., New role for the primate fovea: a retinal excavation determines photoreceptor deployment and shape, *Vis. Neurosci.*, Vol. 16, 1999, pp. 629–636.
14. Springer, A.D., and Hendrickson, A.E., Development of the primate area of high acuity: 1. Use of finite-element analysis models to identify mechanical variables affecting pit formation, *Vis. Neurosci.*, Vol. 21, 2004, pp. 53–62.
15. Springer, A.D., and Hendrickson, A.E., Development of the primate area of high acuity: 2. Quantitative morphological changes associated with retinal and pars plana growth, *Vis. Neurosci.*, Vol. 21, 2004, pp. 775–790.
16. Springer, A.D., and Hendrickson, A.E., Development of the primate area of high acuity: 3. Temporal relationships between pit formation, retinal elongation and cone packing, *Vis. Neurosci.*, Vol. 22, 2005, pp. 171–185.
17. Yuodelis, C., and Hendrickson, A., A qualitative and quantitative analysis of the human fovea during development, *Vis. Res.*, Vol. 26, 1986, pp. 847–855.
18. Curcio, C.A., et al., Human photoreceptor topography, *J. Comp. Neurol.*, Vol. 292, 1990, pp. 497–523.
19. Putnum, N.M., Hammer, D.X., and Roorda, A., *Optical Properties of Foveal Cones: Consequences for Imaging*, ARVO Abstract 4202, Association for Research in Vision and Ophthalmology, Rockville, MD, 2008.
20. Ishikawa, H., et al., Macular segmentation with optical coherence tomography, *Invest. Ophthalmol. Vis. Sci.*, Vol. 46, 2005, pp. 2012–2017.
21. Fernández, E., and Drexler, W., Influence of ocular chromatic aberration and pupil size on transverse resolution in ophthalmic adaptive optics optical coherence tomography, *Opt. Express*, Vol. 13, 2005, pp. 8184–8197.
22. Eye Diseases Prevalence Research Group, Prevalence of open-angle glaucoma among adults in the United States, *Arch. Ophthalmol.*, Vol. 122, 2004, pp. 532–538.
23. Eye Diseases Prevalence Research Group, Prevalence of age-related macular degeneration in the United States, *Arch. Ophthalmol.*, Vol. 122, 2004, 2004, pp. 564–572.

24. Eye Diseases Prevalence Research Group, The prevalence of diabetic retinopathy among adults in the United States, *Arch. Ophthalmol.*, Vol. 122, 2004, pp. 552–563.
25. Kitzmann, A.S., et al., The incidence of central serous chorioretinopathy in Olmsted County, Minnesota, 1980–2002, *Ophthalmology*, Vol. 115, No. 1, 2008, pp. 169–173.
26. Boughman, J.A., Conneally, P.M., and Nance, W.E., Population genetic studies of retinitis pigmentosa, *Am. J. Hum. Genet.*, Vol. 32, 1980, pp. 223–235.
27. Brown, G.C., Retinal arterial obstructive disease, in *Medical Retina*, pp. 1361–1377, A.P. Schachat, R.B. Murphy, and A. Patz (eds.), Vol. 2 of *Retina*, S.J. Ryan (ed.), Mosby, St. Louis, MO, 1989.
28. Klein, R., et al., The 15-year cumulative incidence of retinal vein occlusion: The Beaver Dam Eye Study, *Arch. Ophthalmol.*, Vol. 126, No. 4, 2008, pp. 513–518.
29. Chiang, M.F., et al., Incidence of retinopathy of prematurity from 1996 to 2000: analysis of a comprehensive New York State patient database, *Ophthalmology*, Vol. 111, 2004, pp. 1317–1325.
30. Lad, E.M., Retinopathy of prematurity in the United States, *Br. J. Ophthalmol.*, Vol. 92, 2008, pp. 320–325.
31. Onofrey, B.E., Skorin, L., and Holdeman, N.R., *Stargardts: Ocular Therapeutics Handbook: A Clinical Manual*, Lippincott Williams & Wilkins, Philadelphia, 2005.
32. Berrocal, A.M., Mavrofrides, E.C., and Murray, T.G., Retinoblastoma, in *Retinal Imaging*, pp. 471–479, D. Huang, P.K. Kaiser, C.Y. Lowder, and E.I. Traboulsi (eds.), Elsevier, St. Louis, MO., 2006.
33. Eye Diseases Prevalence Research Group, Causes and prevalence of visual impairment among adults in the United States, *Arch. Ophthalmol.*, Vol. 122, 2004, pp. 477–485.
34. Quigley, H.A., Number of people with glaucoma worldwide, *Br. J. Ophthalmol.*, Vol. 80, 1996, pp. 389–393.
35. Krupin, T., and Civan, M.M., Physiologic basis of aqueous human formation, in *The Glaucomas*, Vol. 1, *Basic Sciences*, pp. 251–280, R. Ritch, M.B. Shields, and T. Krupin (eds.), Mosby, St. Louis, MO, 1996.
36. Palmberg, P.F., and Wiggs, J.L., Mechanisms of glaucoma, in *Ophthalmology*, pp. 1423–1430, M. Yanoff and J.S. Duker (eds.), Mosby, St. Louis, MO, 2004.
37. Quigley, A.F., and Addicks, E.M., Regional difference in the structure of the lamina cribrosa and their reaction to glaucomatous damage, *Arch. Ophthalmol.*, Vol. 99, 1981, pp. 137–143.
38. Anderson, D.R., Glaucoma, capillaries, and pericytes: 1. Blood flow regulation, *Ophthalmologica*, Vol. 210, 1996, pp. 257–262.
39. Singh, A.D., Melanocytoma of the optic disc, in *Retinal Imaging*, pp. 556–558, D. Huang, P.K. Kaiser, C.Y. Lowder, and E.I. Traboulsi (eds.), Elsevier, St. Louis, MO, 2006.
40. Im, L., and Schuman, J.S., Optic nerve head drusen, in *Retinal Imaging*, pp. 548–555, D. Huang, P.K. Kaiser, C.Y. Lowder, and E.I. Traboulsi (eds.), Elsevier, St. Louis, MO, 2006.
41. Friedman, D.S., et al., Prevalence of age-related macular degeneration in the United States, *Arch. Ophthalmol.*, Vol. 122, 2004, pp. 564–572.

42. Mullins, R.F., et al., Drusen associated with aging and age-related macular degeneration contain proteins common to extracellular deposits associated with atherosclerosis, elastosis, amyloidosis, and dense deposit disease, *FASEB J*., Vol. 14, 2000, pp. 835–846.
43. Russell, S.R., et al., Location, substructure, and composition of basal laminar drusen compared with drusen associated with aging and age-related macular degeneration, *Am. J. Ophthalmol*., Vol. 129, 2000, pp. 205–214.
44. Anderson, D.H., et al., A role for local inflammation in the formation of drusen in the aging eye, *Am. J. Ophthalmol*., Vol. 134, 2002, pp. 411–431.
45. Anderson, D.H., et al., Characterization of beta amyloid assemblies in drusen: the deposits associated with aging and age-related macular degeneration, *Exp. Eye Res*., Vol. 78, 2004, pp. 243–256.
46. Wang, J.J., Foran, S., and Mitchell, P., Age-specific prevalence and causes of bilateral and unilateral visual impairment in older Australians: the Blue Mountains Eye Study, *Clin. Exp. Ophthalmol*., Vol. 28, 2000, pp. 268–273.
47. Allikmets, R., Further evidence for an association of ABCR alleles with age-related macular degeneration, *Am. J. Hum. Genet*., Vol. 67, 2000, pp. 487–491.
48. van Leeuwen, R., et al., Epidemiology of age-related maculopathy: a review, *Eur. J. Epidemiol*., Vol. 18, 2003, pp. 845–854.
49. Stone, E.M., et al., Missense variations in the Fibulin 5 gene and age-related macular degeneration, *N. Engl. J. Med*., Vol. 351, 2004, pp. 346–353.
50. Klein, R.J., et al., Complement Factor H polymorphism in age-related macular degeneration, *Science*, Vol. 308, 2005, pp. 385–389.
51. Schmidt, S., et al., Joint effects of smoking history and APOE genotypes in age-related macular degeneration, *Mol. Vis*., Vol. 11, 2005, pp. 941–949.
52. Haines, J.L., et al., Complement Factor H variant increases the risk of age-related macular degeneration, *Science*, Vol. 308, 2005, pp. 419–421.
53. Edwards, A.O., et al., Complement Factor H polymorphism and age-related macular degeneration, *Science*, Vol. 308, 2005, pp. 421–424.
54. Haines, J.L., et al., Functional candidate genes in age-related macular degeneration: significant association with VEGF, VLDLR, and LRP6, *Invest. Ophthalmol. Vis. Sci*., Vol. 47, 2006, pp. 329–335.
55. Schmitz-Valckenberg, S., et al., Correlation between the area of increased autofluorescence surrounding geographic atrophy and disease progression in patients with AMD, *Invest. Ophthalmol. Vis. Sci*., Vol. 47, 2006, pp. 2648–2654.
56. Hageman, G.S., et al., A common haplotype in the complement regulatory gene Factor H (HF1/CFH) predisposes individuals to age-related macular degeneration, *Proc. Natl. Acad. Sci. USA*, Vol, 102, 2005, pp. 7227–7232.
57. Delori, F.C., et al., Autofluorescence distribution associated with drusen in age-related macular degeneration, *Invest. Ophthalmol. Vis. Sci*., Vol. 41, 2000, pp. 496–504.
58. Holz, F.G., et al., Fundus autofluorescence and development of geographic atrophy in age-related macular degeneration, *Invest. Ophthalmol. Vis. Sci*., Vol. 42, 2001, pp. 1051–1056.
59. Eldred, G.E., and Katz, M.L., Fluorophores of the human retinal pigment epithelium: separation and spectral characterization, *Exp. Eye. Res*., Vol. 47, 1988, pp. 71–86.

60. Wing, G.L., Blanchard, G.C., and Weiter, J.J., The topography and age relationship of lipofuscin concentration in the retinal pigment epithelium, *Invest. Ophthalmol. Vis. Sci*., Vol. 27, 1978, pp. 145–152.
61. Feeney-Burns, L., Hilderbrand, E.S., and Eldridge, S., Aging human RPE: morphometric analysis of macular, equatorial, and peripheral cells, *Invest. Ophthalmol. Vis. Sci*., Vol. 25, 1984, pp. 195–200.
62. Rozanowska, M., et al., Age-related changes in the photoreactivity of retinal lipofuscin granules: role of chloroform-insoluble components, *Invest. Ophthalmol. Vis. Sci*., Vol. 45, 2004, pp. 1052–1060.
63. Arend, O.A., et al., In-vivo Fundus-Fluoreszenz-Messungen bei Patienten mit alterabhangiger Makulardegeneration, *Ophthalmologie*, Vol. 92, 1995, pp. 647–653.
64. Marmorstein, A.D., et al., Spectral profiling of autofluorescence associated with lipofuscin, Bruch's membrane, and sub-RPE deposits in normal and AMD eyes, *Invest. Ophthalmol. Vis. Sci*., Vol. 43, 2002, pp. 2435–2441.
65. Johnson, P.T., et al., Synaptic pathology, altered gene expression, and degeneration in photoreceptors impacted by drusen, *Invest. Ophthalmol. Vis. Sci*., Vol. 46, 2005, pp. 4788–4795.
66. Caicedo, A., et al., Photoreceptor synapses degenerate early in experimental choroidal neovascularization, *J. Comp. Neurol*., Vol. 483, 2005, pp. 263–277.
67. Curcio, C.A., et al., Esterified and unesterified cholesterol in Drusen and basal deposits of eyes with age-related maculopathy, *Exp. Eye. Res*., Vol. 81, 2005, pp. 731–741.
68. Wirostko, W.J., and Pulido, J.S., Central serous chorioretinopathy, in *Ophthalmology*, pp. 938–941, M. Yanoff and J.S. Duker (eds.), Mosby, St. Louis, MO, 2004.
69. Drenser, K., and Small, K.W., Macular dystrophies, in *Ophthalmology*, pp. 824–832, M. Yanoff and J.S. Duker (eds.), Mosby, St. Louis, MO, 2004.
70. Johnson, M.W., Epiretinal membrane, in *Ophthalmology*, pp. 947–950, M. Yanoff and J.S. Duker (eds.), Mosby, St. Louis, MO, 2004.
71. Fu, A., Ahmed, I., and Ai, E., Cystoid macular edema, in *Ophthalmology*, pp. 956–962, M. Yanoff and J.S. Duker (eds.), Mosby, St. Louis, MO, 2004.
72. Aiello, L., et al., Vascular endothelial growth factor in ocular fluid of patients with diabetic retinopathy and other retinal disorders, *N. Engl. J. Med*., Vol. 331, 1994, pp. 1480–1487.
73. Rosenblatt, B.J., and Benson, W.E., Diabetic retinopathy, in *Ophthalmology*, pp. 877–886, M. Yanoff and J.S. Duker (eds.), Mosby, St. Louis, MO, 2004.
74. Diabetes Retinopathy Study Research Group, Four risk factors for severe visual loss in diabetic retinopathy: the Third Report from the Diabetic Retinopathy Study, *Arch. Ophthalmol*., Vol. 97, 1979, pp. 654–665.
75. Chew, E., et al., Effects of aspirin on vitreous/preretinal hemorrhage in patients with diabetes mellitus, ETDRS Report No. 20, *Arch. Ophthalmol*., Vol. 113, 1995, pp. 52–55.
76. United Kingdom Prospective Diabetes Study Group, Tight blood pressure control and risk of macrovascular and microvascular complications in Type 2 diabetes, UKPDS 38, *BMJ*, Vol. 317, 1998, pp. 703–713.
77. Danis, R., et al., Inhibition of intraocular neovascularization caused by retinal ischemia in pigs by PKC with LY333531, *Invest. Ophthalmol. Vis. Sci*., Vol. 39, 1998, pp. 171–179.

78. Daily, M., and Gieser, R., Treatment of proliferative diabetic retinopathy with panretinal cryotherapy, *Ophthalmic Surg*., Vol. 15, 1984, pp. 741–745.
79. Lewis, H., et al., Vitrectomy for diabetic macular traction and edema associated with posterior hyaloidal traction, *Opthalmology*, Vol. 99, 1992, pp. 753–759.
80. Duker, J.S., Retinal arterial obstruction, in *Ophthalmology*, pp. 856–863, M. Yanoff and J.S. Duker (eds.), Mosby, St. Louis, MO, 2004.
81. Sanborn, G.E., and Magargal, L.E., Arterial obstructive disease of the eye, in *Clinical Ophthalmology*, Vol. 3, pp. 1–29, W.S. Tasman and E.A. Jaegar (eds.), Lippincott, Philadelphia, 1993.
82. Hayreh, S.S., and Weingeist, T.A., Experimental occlusion of the central artery of the retina, *Br. J. Ophthalmol*., Vol. 64, 1989, pp. 896–912,
83. Morley, M.G., and Heier, J.S., Venous obstructive disease of the retina, in *Ophthalmology*, pp. 864–871, M. Yanoff and J.S. Duker (eds.), Mosby, St. Louis, MO, 2004.
84. Central Vein Occlusion Study Group, Natural history and clinical management of central retinal vein occlusion, *Arch. Ophthalmol*., Vol. 115, 1997, pp. 486–491.
85. Hayreh, S.S., Zimmerman, M.B., and Podhajsky, P., Incidence of various types of retinal vein occlusion and their recurrence and demographic characteristics, *Am. J. Ophthalmol*., Vol. 117, 1994, pp. 429–441.
86. Quinlan, P.M. et al., The natural course of central retinal vein occlusion, *Am. J. Ophthalmol*., Vol. 110, 1990, pp. 118–123.
87. Branch Vein Occlusion Study Group, Argon laser scatter photocoagulation for prevention of neovascularization and vitreous hemorrhage in branch vein occlusion, *Arch. Ophthalmol*., Vol. 104, 1986, pp. 34–41.
88. Glacet-Bernard, A., et al., Prognostic factors for retinal vein occlusion: a prospective study of 175 cases, *Ophthalmology*, Vol. 103, 1996, pp. 551–560.
89. Recchia, F.M., and Capone, A., Retinopathy of prematurity, in *Ophthalmology*, pp. 872–878, M. Yanoff and J.S. Duker (eds.), Mosby, St. Louis, MO, 2004.
90. Phelps, D.L., Retinopathy of prematurity: an estimate of vision loss in the United States, 1979, *Pediatrics*, Vol. 67, 1981, pp. 924–926.
91. Palmer, E.A., et al., Incidence and early course of retinopathy of prematurity, *Ophthalmology*, Vol. 98, 1991, pp. 1628–1640.
92. Hussain, N., Clive, J., and Bhandari, V., Current incidence of retinopathy of prematurity, 1989–97, *Pediatrics*, Vol. 104. No. 3, 1999, p. e26.
93. Cryotherapy for Retinopathy of Prematurity Cooperative Group, Multicenter trial of cryotherapy for retinopathy of prematurity: preliminary results, *Arch. Ophthalmol*., Vol. 106, 1988, pp. 471– 479.
94. Foroozan, R. Connolly, B.P., and Tasman, W.S., Outcomes after laser therapy for threshold retinopathy of prematurity, *Ophthalmology*, Vol. 108, 2001, pp. 1644–1646.
95. Dejonge, M.H., Ferrone, P.J., and Trese, M.T., Diode laser ablation for threshold retinopathy of prematurity, *Arch. Ophthalmol*., Vol. 118, 2000, pp. 365–367.
96. Hammer, D.X., et al., Foveal fine structure in retinopathy of prematurity: an adaptive optics Fourier domain optical coherence tomography study, *Invest. Ophthalmol. Vis. Sci*., Vol. 49, 2008, pp. 2061–2070.

97. Fulton, A.B., et al., Multifocal ERG in subjects with a history of retinopathy of prematurity, *Doc. Ophthalmol.*, Vol. 111, 2005, pp. 7–13.
98. Barnaby, A.M., et al., Development of scotopic thresholds in retinopathy of prematurity, *Invest. Ophthalmol. Vis. Sci.*, Vol. 48, 2007, pp. 4854–4860.
99. Akula, J.D., et al., Rod photoreceptor function predicts blood vessel abnormalities in retinopathy of prematurity, *Invest. Ophthalmol. Vis. Sci.*, Vol. 48, 2007, pp. 4351–4359.
100. Hansen, R.M., Moskowitz, A., and Fulton, A.B., Multifocal ERG responses in infants, *Invest. Ophthalmol. Vis. Sci.*, Vol. 50, 2009, pp. 470–475.
101. Fulton, A.B., Hansen, R.M., and Moskowitz, A., The cone electroretinogram in retinopathy of prematurity, *Invest. Ophthalmol. Vis. Sci.*, Vol. 49, 2008 pp. 814–819.
102. Ripps, H., Cell death in retinitis pigmentosa: gap junctions and the “bystander” effect, *Exp. Eye Res.*, Vol. 74, 2002, pp. 327–336.
103. Dryja, T.P., et al., A point mutation of the rhodopsin gene in one form of retinitis pigmentosa, *Nature*, Vol. 343, 1990, pp. 364–366.
104. Farrar, G.J., et al., A three-base-pair deletion in the peripherin-RDS gene in one form of retinitis pigmentosa, *Nature*, Vol. 354, 1991, pp. 478–480.
105. Maw, M.A., et al., Mutation of the gene encoding cellular retinaldehyde-binding protein in autosomal recessive retinitis pigmentosa, *Nat. Genet.*, Vol. 17, 1997, pp. 198–200.
106. Swain, P.K., et al., Mutations in the cone-rod homeobox gene are associated with the cone-rod dystrophy photoreceptor degeneration, *Neuron*, Vol. 19, 1997, pp. 1329–1336.
107. Chang, G.-Q., Hao, Y., and Wong, F., Apoptosis: final common pathway of photoreceptor death in rd, rds, and rhodopsin mutant mice, *Neuron*, Vol. 11, 1993, pp. 595–605.
108. Berson, E.L., et al., A randomized trial of vitamin A and vitamin E supplementation for retinitis pigmentosa, *Arch. Ophthalmol.*, Vol. 111, 1993, pp. 761–772.
109. Hoffman, D.R., and Birch, D.G., Docosahexaenoic acid in red blood cells of patients with X-linked retinitis pigmentosa, *Retina*, Vol. 36, 1995, pp. 1009–1018.
110. Faktorovich, E.G., et al., Photoreceptor degeneration in inherited retina dystrophy delayed by basic fibroblast growth factor, *Nature*, Vol. 347, 1990, pp. 83–86.
111. Dodds, E.M., White dot syndromes, in *Retinal Imaging*, pp. 317–339, D. Huang, P.K. Kaiser, C.Y. Lowder, and E.I. Traboulsi (eds.), Elsevier, St. Louis, MO, 2006.
112. Lai, W.W., Goldstein, D.A., and Tessler, H.H., Posterior scleritis, in *Retinal Imaging*, pp. 303–306, D. Huang, P.K. Kaiser, C.Y. Lowder, and E.I. Traboulsi (eds.), Elsevier, St. Louis, MO, 2006.
113. Stewart, J.M., Uveal effusion syndrome, in *Retinal Imaging*, pp. 314–316, D. Huang, P.K. Kaiser, C.Y. Lowder, and E.I. Traboulsi (eds.), Elsevier, St. Louis, MO, 2006.
114. Arellanes-García, L., and Ruiz-Cruz, M., Pars planitis, in *Retinal Imaging*, pp. 307–309, D. Huang, P.K. Kaiser, C.Y. Lowder, and E.I. Traboulsi (eds.), Elsevier, St. Louis, MO, 2006.
115. Lowder, C.Y., Sarcoidosis, in *Retinal Imaging*, pp. 310–313, D. Huang, P.K. Kaiser, C.Y. Lowder, and E.I. Traboulsi (eds.), Elsevier, St. Louis, MO, 2006.
116. Huang, D., et al., eds., *Retinal Imaging*, Elsevier, St. Louis, MO, 2006.

117. Rubsamen, P.E., Posterior segment ocular trauma, in *Ophthalmology*, pp. 1007–1012, M. Yanoff and J.S. Duker (eds.), Mosby, St. Louis, MO, 2004.
118. Regillo, C.D., Distant trauma with posterior segment effects, in *Ophthalmology*, pp. 1013–1017, M. Yanoff and J.S. Duker (eds.), Mosby, St. Louis, MO, 2004.
119. Webb, R.H., Hughes, G.W., and Pomerantzeff, O., Flying spot TV ophthalmoscope, *Appl. Opt*., Vol. 19, 1980, pp. 2991–2997.
120. Webb, R.H., Hughes, G.W., and Delori, F.C., Confocal scanning laser ophthalmoscope, *Appl. Opt*., Vol. 26, 1987, pp. 1492–1499.
121. Puliafito, C.A., et al., *Optical Coherence Tomography of Ocular Diseases*, Slack, Inc., Thorofare, NJ, 1996.
122. Gonzalez, R.C., and Woods R.E., *Digital Image Processing*, Addison-Wesley, Reading, MA, 1992, pp. 1–19.
123. Delori, F.C., et al., In vivo fluorescence of the ocular fundus exhibits retinal pigment epithelium lipofuscin characteristics, *Invest. Ophthalmol. Vis. Sci*., Vol. 36, 1995, pp. 718–729.
124. Delori, F.C., et al., Autofluorescence distribution associated with Drusen in age-related macular degeneration, *Invest. Ophthalmol. Vis. Sci*., Vol. 41, 2000, pp. 496–504.
125. Delori, F.C., Goger, D.G., and Dorey, C.K., Age-related accumulation and spatial distribution of Lipofuscin in RPE of normal subjects, *Invest. Ophthalmol. Vis. Sci*., Vol. 42, 2001, pp. 1855–1866.
126. Schweitzer, D., Toward metabolic mapping of the human retina, *Microsc. Res. Tech*., Vol. 70, 2007, pp. 410–419.
127. Elner, V.M., et al., Flavoprotein autofluorescence detection of early ocular dysfunction, *Arch. Ophthalmol*. Vol. 126, No. 2, 2008, pp. 259–260.
128. Field, M.G., et al., Rapid, noninvasive detection of diabetes-induced retinal metabolic stress, *Arch. Ophthalmol*., Vol. 126, No. 7, 2008, pp. 934–938.
129. Brindley, G.S., and Willmer, E.N., The reflection of light from the macular and peripheral fundus oculi in man, *J. Physiol*., Vol. 116, 1952, pp. 350–356.
130. Vos, J.J., Munnik, A.A., and Boogaard, J., Absolute spectral reflectance of the fundus oculi, *J. Opt. Soc. Am*., Vol. 55, 1965, pp. 573–574.
131. Hunold, W., and Malessa, P., Spectrophotometric determination of melanin pigmentation in the human ocular fundus in vivo, *Ophthalm. Res*., Vol. 6, 1974, pp. 355–362.
132. van Norren, D., and Tiemeijer, L.F., Spectral reflectance of the human eye, *Vis. Res*., Vol. 26, 1986, pp. 313–320.
133. Weiter, J.J., et al., Retinal pigment epithelial lipofuscin and melanin and choroidal melanin in human eyes, *Invest. Ophthalmol. Vis. Sci*., Vol. 27, 1986, pp. 145–152.
134. Delori, F.C., and Pflibsen, K.P., Spectral reflectance of the human ocular fundus, *Appl. Opt*., Vol. 28, 1989, pp. 1061–1077.
135. van Kuijk, F.J., et al., Spectrophotometric quantitation of rhodopsin in the human retina, *Invest. Ophthalmol. Vis. Sci*., Vol. 32, 1991, pp. 1962–1967.
136. Elsner, A.E., Burns, S.A., and Webb, R.H., Mapping cone photopigment optical density, *J. Opt. Soc. Am*., Vol. A10, 1993, pp. 52–58.

137. Keilhauer, C.N., and Delori, F.C., Near-infrared autofluorescence imaging of the fundus: visualization of ocular melanin, *Invest. Ophthalmol. Vis. Sci*., Vol. 47, 2006, pp. 3556–3564.

138. Lengyel, I., et al., High concentration of zinc in sub-retinal pigment epithelial deposits, *Exp. Eye Res*., Vol. 84, 2007, pp. 772–780.

139. Holz, F.G., et al., Progression of geographic atrophy and impact of fundus autofluorescence patterns in age-related macular degeneration, *Am. J. Ophthalmol*., Vol. 143, 2007, pp. 463–472.

140. Schmitz-Valckenberg, S., et al., Fundus autofluorescence imaging: review and perspectives, *Retina*, Vol. 28, 2008, 385–409.

141. Schmitz-Valckenberg, S., et al., Evaluation of autofluorescence imaging with the scanning laser ophthalmoscope and the fundus camera in age-related geographic atrophy, *Am. J. Ophthalmol*., Vol. 146, 2008, pp. 183–192.

142. Trieschmann, M., Macular pigment in the human retina: histological evaluation of localization and distribution, *Eye*, Vol. 22, 2008, pp. 132–137.

143. Romero-Borja, F., et al., Optical slicing of human retinal tissue in vivo with the adaptive optics scanning laser ophthalmoscope, *Appl. Opt*., Vol. 44, 2005, pp. 4032–4040.

144. von Helmholtz, H., Über eine neue einfachste Form des Augenspiegel, *Arch. Physiol. Heilbron*, Vol. 2, 1852, pp. 827–840.

145. Gullstrand, A., Neue Methoden der reflexlosen Ophthalmopskiepie, *Ber. Disch. Ophthalmol*., Vol. 30, 1910, pp. 36–75.

146. Stein, M.R., and Parker, C.W., Reactions following intravenous fluorescein, *Am. J. Ophthalmol*., Vol. 72, 1971, pp. 861–868.

147. Novotny, H.R., and Alvis, D.L., A method of photographing fluorescence in circulation blood in the human retina, *Circulation*, Vol. 24, 1961, pp. 82–86.

148. Olson, J.L., and Mandava, N., Fluorescein angiography, in *Retinal Imaging*, pp. 3–21, D. Huang, P.K. Kaiser, C.Y. Lowder, and E.I. Traboulsi (eds.), Elsevier, St. Louis, MO, 2006.

149. Flower, R.W., and Hochheimer, B.F., Clinical infrared absorption angiography of the choroid, *Am. J. Ophthalmol*., Vol. 73, 1972, pp. 458–459.

150. Ciardella, A.P., et al., Indocyanine green angiography, in *Retinal Imaging*, pp. 22–46, D. Huang, P.K. Kaiser, C.Y. Lowder, and E.I. Traboulsi (eds.), Elsevier, St. Louis, MO, 2006.

151. von Rückmann, A., Fitzke, F.W., and Bird, A.C., The retinal pigment epithelium, in *The Retinal Pigment Epithelium*, pp. 224–234, M.F. Marmor and T.J. Wolfensberger (eds.), Oxford University Press, New York, 1998.

152. Gray, D.C., et al., In vivo fluorescence imaging of primate retinal ganglion cells and retinal pigment epithelial cells, *Opt. Express*, Vol. 14, 2006, pp. 7144–7158.

153. Morgan, J.I. W., et al., In vivo autofluorescence imaging of the human and Macaque retinal pigment epithelial cell mosaic, *Invest. Ophthalmol. Vis. Sci*., Vol. 50, 2009, pp. 1350–1359.

154. Lois, N., et al., Quantitative evaluation of fundus autofluorescence imaged in vivo in eyes with retinal disease, *Br. J. Ophthalmol*., Vol. 84, 2000, pp. 741–745.

155. Robson, A.G., et al., Macular pigment density and distribution: comparison of fundus autofluorescence with minimum motion photometry, *Vis. Res.*, Vol. 43, 2003, pp. 1765–1775.
156. Minsky, M., Microscopy apparatus, U.S. patent 3,013,467, 1961.
157. Hammer, D.X., et al., Line-scanning laser ophthalmoscope, *J. Biomed. Opt.*, Vol. 11, 2006, p. 041126.
158. Ferguson, R.D., et al., Wide-field retinal hemodynamic imaging with the tracking scanning laser ophthalmoscope, *Opt. Express*, Vol. 12, 2004, pp. 5198–5208.
159. Swanson, E.A., et al., High-speed optical coherence domain reflectometry, *Opt. Lett.*, Vol. 17, 1992, pp. 151–153.
160. Swanson, E.A., et al., In vivo retinal imaging by optical coherence tomography, *Opt. Lett.*, Vol. 18, 1993, pp. 1864–1866.
161. Izatt, J.A., et al., Micrometer-scale resolution imaging of the anterior eye in vivo with optical coherence tomography, *Arch. Ophthalmol.*, Vol. 112, 1994, pp. 1584–1589.
162. Michelson, A.A., and Morley, E.W., On the relative motion of the Earth and the luminiferous ether, *Am. J. Sci.*, Vol. 34, No. 203, 1887, pp. 333–345.
163. Drexler, W., et al., In vivo ultrahigh-resolution optical coherence tomography, *Opt. Lett.*, Vol. 24, 1999, pp. 1221–1223.
164. Drexler, W., et al., Ultrahigh-resolution ophthalmic optical coherence tomography, *Nat. Med.*, Vol. 7, 2001, pp. 502–507.
165. Povazay, B., et al., Submicrometer axial resolution optical coherence tomography, *Opt. Lett.*, Vol. 27, 2002, pp. 1800–1802.
166. Rovati, L., and Docchio, F., Low-coherence interfometry using a self-mixing super-luminescent diode, *IEEE Photon. Technol. Lett.*, Vol. 10, No. 1, 1998, pp. 123–125.
167. Izatt, J.A., et al., In vivo bidirectional color Doppler flow imaging of picoliter blood volumes using optical coherence tomography, *Opt. Lett.*, Vol. 22, 1997, pp. 1439–1441.
168. Yazdanfar, S., Kulkarni, M.D., and Izatt, J.A., High resolution imaging of in vivo cardiac dynamics using color Doppler optical coherence tomography, *Opt. Express*, Vol. 1, 1997, pp. 424–431.
169. Barton, J.K., Izatt, J.A., and Welch, A.J., Investigating pulsed dye laser–blood vessel interaction with color Doppler optical coherence tomography, *Opt. Express*, Vol. 2, 1998, pp. 251–256.
170. Tearney, G.J., Bouma, B.E., and Fujimoto, J.G., High speed phase- and group-delay scanning with a grating-based phase control delay line, *Opt. Lett.*, Vol. 22, 1997, pp. 1811–1813.
171. Dreher, A.W., Bille, J.F., and Weinreb, R.N., Active optical depth resolution improvement of the laser tomographic scanner, *Appl. Opt.*, Vol. 28, 1989, pp. 804–808.
172. Liang, J., Williams, D., and Miller, D., Supernormal vision and high-resolution retinal imaging through adaptive optics, *J. Opt. Soc. Am. A*, Vol. 14, 1997, pp. 2884–2892.
173. Hammer, D.X., et al., Adaptive optics scanning laser ophthalmoscope for stabilized retinal imaging, *Opt. Express*, Vol. 14, 2006, pp. 3354–3367.
174. Rollins, A.M., et al., In vivo video rate optical coherence tomography, *Opt. Express*, Vol. 3, 1998, pp. 219–229.

175. Fercher, A.F., et al., Measurement of intraocular distances by backscattering spectral interferometry, *Opt. Commun.*, Vol. 117, 1995, pp. 43–48.
176. Wojtkowski, M., et al., In vivo human retinal imaging by Fourier domain optical coherence tomography, *J. Biomed. Opt.*, Vol. 7, 2002, pp. 457–463.
177. Wojtkowski, M., et al., Sensitivity advantage of swept source and Fourier domain optical coherence tomography, *Opt. Express*, Vol. 12, 2004, pp. 2404–2422.
178. Leitgeb, R.A., Hitzenberger, C.K., and Fercher, A.F., Performance of Fourier domain vs. time domain optical coherence tomography, *Opt. Express*, Vol. 11, 2003, pp. 889–894.
179. Nassif, N., et al., In vivo human retinal imaging by ultrahigh-speed spectral domain optical coherence tomography, *Opt. Lett.*, Vol. 29, 2004, pp. 480–482.
180. Cense, B., et al., Ultrahigh-resolution high-speed retinal imaging using spectral-domain optical coherence tomography, *Opt. Express*, Vol. 12, 2004, pp. 2435–2447.
181. Leitgeb, R., et al., Ultrahigh resolution Fourier domain optical coherence tomography, *Opt. Express*, Vol. 12, 2004, pp. 2156–2165.
182. Ustun, T.E., et al., Real-time processing for Fourier domain optical coherence tomography using a field programmable gate array, *Rev. Sci. Instrum.*, Vol. 79, 2008, p. 114301.
183. Yun, S., et al., High-speed optical frequency-domain imaging, *Opt. Express*, Vol. 11, 2003, pp. 2953–2963.
184. Podoleanu, A.G., and Jackson, D.A., Combined optical coherence tomograph and scanning laser ophthalmoscope, *Electron Lett.*, Vol. 34, 1998, pp. 1088–1090.
185. Hitzenberger, C., et al., Three-dimensional imaging of the human retina by high-speed optical coherence tomography, *Opt. Express*, Vol. 11, 2003, pp. 2753–2761.
186. Pircher, M., et al., Retinal cone mosaic imaged with transverse scanning optical coherence tomography, *Opt. Lett.*, Vol. 31, 2006, pp. 1821–1823.
187. Yun, S.H., et al., Motion artifacts in optical coherence tomography with frequency-domain ranging, *Opt. Express*, Vol. 12, 2004, pp. 2977–2998.
188. Yun, S., et al., Removing the depth-degeneracy in optical frequency domain imaging with frequency shifting, *Opt. Express*, Vol. 12, 2004, pp. 4822–4828.
189. Kerbage, C., et al., Large depth-high resolution full 3D imaging of the anterior segments of the eye using high speed optical frequency domain imaging, *Opt. Express*, Vol. 15, 2007, pp. 7117–7125.
190. Lee, E.C. W., et al., In vivo optical frequency domain imaging of human retina and choroid, *Opt. Express*, Vol. 14, 2006, pp. 4403–4411.
191. Lim, H., et al., Optical frequency domain imaging with a rapidly swept laser in the 815–870 nm range, *Opt. Express*, Vol. 14, 2006, pp. 5937–5944.
192. Huber, R., et al., Three-dimensional and C-mode OCT imaging with a compact, frequency swept laser source at 1300 nm, *Opt. Express*, Vol. 13, 2005, pp. 10523–10538.
193. Huber, R., et al., Amplified, frequency swept lasers for frequency domain reflectometry and OCT imaging: design and scaling principles, *Opt. Express*, Vol. 13, 2005, pp. 3513–3528.
194. Yun, S. H, et al., High speed wavelength-swept semiconductor laser with a polygon-scanner-based wavelength filter, *Opt. Lett.*, Vol. 28, 2003, pp. 1981–1983.

195. Huber, R., Adler, D.C., and Fujimoto, J.G., Buffered Fourier domain mode locking: unidirectional swept laser sources for optical coherence tomograph imaging at 370,000 lines/s, *Opt. Lett.*, Vol. 31, 2006, pp. 2975–2977.

196. Adler, D.C., Huber, R., and Fujimoto, J.G., Phase-sensitive optical coherence tomography at up to 370,000 lines per second using buffered Fourier domain mode-locked lasers, *Opt. Lett.*, Vol. 32, 2007, pp. 626–628.

197. Huber, R., Wojtkowski, M., and Fujimoto, J.G., Fourier domain mode locking (FDML): a new laser operating regime and applications for optical coherence tomography, *Opt. Express*, Vol. 14, 2006, pp. 3225–3237.

198. Srinivasan, V.J., et al., Ultrahigh-speed optical coherence tomography for three-dimensional and *en face* imaging of the retina and optic nerve head, *Invest. Ophthalmol. Vis. Sci.*, Vol. 49, 2008, pp. 5103–5110.

199. Zuluaga, A.F., and Richards-Kortum, R., Spatially resolved spectral interferometry for determination of subsurface structure, *Opt. Lett.*, Vol. 24, 1999, pp. 519–521.

200. Bourquin, S., et al., Video-rate optical low-coherence reflectometry based on a linear smart detector array, *Opt. Lett.*, Vol. 25, 2000, pp. 102–104.

201. Dubois, A., et al., High-resolution full-field optical coherence tomography with a Linnik microscope, *Appl. Opt.*, Vol. 41, 2002, pp. 805–812.

202. Vabre, L., Dubois, A., and Boccara, A.C., Thermal-light full-field optical coherence tomography, *Opt. Lett.*, Vol. 27, 2002, pp. 530–532.

203. Dubois, A., et al., Ultrahigh-resolution full-field optical coherence tomography, *Appl. Opt.*, Vol. 43, 2004, pp. 2874–2883.

204. Grieve, K., et al., In vivo anterior segment imaging in the rat eye with high speed white light full-field optical coherence tomography, *Opt. Express*, Vol. 13, 2005, pp. 6286–6295.

205. Oh, W.Y., et al., Ultrahigh-resolution full-field optical coherence microscopy using ingaas camera, *Opt. Express*, Vol. 14, 2006, pp. 726–735.

206. Oh, W.Y., et al., Spectrally-modulated full-field optical coherence microscopy for ultrahigh-resolution endoscopic imaging, *Opt. Express*, Vol. 14, 2006, pp. 8675–8684.

207. Huang, S.W., et al., Swept source optical coherence microscopy using a Fourier domain mode-locked laser, *Opt. Express*, Vol. 15, 2007, pp. 6210–6217.

208. Endo, T., et al., Profilometry with line-field Fourier-domain interferometry, *Opt. Express*, Vol. 13, 2005, pp. 695–701.

209. Grajciar, B., et al., Parallel Fourier domain optical coherence tomography for in vivo measurement of the human eye, *Opt. Express*, Vol. 13, 2005, pp. 1131–1137.

210. Zhang, Y., et al., Adaptive optics parallel spectral domain optical coherence tomography for imaging the living retina, *Opt. Express*, Vol. 13, 2005, pp. 4792–4811.

211. Watanabe, Y., et al., Axial-lateral parallel time domain OCT with optical zoom lens and high order diffracted lights for variable imaging range, *Opt. Express*, Vol. 15, 2007, pp. 5208–5217.

212. Watanabe, Y., Yamada, K., and Sato, M., Three-dimensional imaging by ultrahigh-speed axial-lateral parallel time domain optical coherence tomography, *Opt. Express*, Vol. 14, 2006, pp. 5201–5209.

213. Nakamura, Y., et al., High-speed three-dimensional human retinal imaging by line-field spectral domain optical coherence tomography, *Opt. Express*, Vol. 15, 2007, pp. 7103–7116.
214. Lee, S., and Kim, B., Line-field optical coherence tomography using frequency-sweeping source, *IEEE J. Sel. Top. Quantum Electron.*, Vol. 14, 2008, pp. 50–55.
215. Chen, Y., et al., High-resolution line scanning optical coherence microscopy, *Opt. Lett.*, Vol. 32, 2007, pp. 1971–1973.
216. Luo, Y., et al., Parallel optical coherence tomography system, *Appl. Opt.*, Vol. 46, 2007, pp. 8291–8297.
217. Babcock, H.W., The possibility of compensating astronomical sensing, *Publ. Astron. Soc. Pac.*, Vol. 65, 1953, pp. 229–236.
218. Hardy, J.L., Delahunt, P.B., and Werner, J.S., Visual psychophysics with adaptive optics, in *Adaptive Optics for Visual Science*, pp. 363–394, Porter, J., Queener, H., Lin, J., Thorn, K., and Awwal, A.A.W. (eds.), Wiley, Hoboken, NJ, 2006.
219. Roorda, A., and Williams, D.R., The arrangement of the three cone classes in the living human eye, *Nature*, Vol. 397, 1999, pp. 520–522.
220. Vdovin, G., Loktev, M., and Naumov, A., On the possibility of intraocular adaptive optics, *Opt. Express*, Vol. 11, 2003, p. 810.
221. Marsack, J.D., Parker, K.E., and Applegate, R.A., Performance of wavefront-guided soft lenses in three keratoconus subjects, *Optom. Vis. Sci.*, Vol. 85, 2008, pp. E1172–E1178.
222. Marsack, J.D., et al., On-eye performance of custom wavefront guided soft contact lenses in one habitual soft contact lens wearing keratoconic, *J. Refract. Surg.*, Vol. 23, 2007, pp. 960–964.
223. Hofer, H., et al., Dynamics of the eye's wave aberration, *J. Opt. Soc. Am. A*, Vol. 18, 2001, p. 497.
224. Diaz-Santana, L., et al., Benefit of higher closed-loop bandwidths in ocular adaptive optics, *Opt. Express*, Vol. 11, 2004, p. 2597.
225. Nirmaier, T., Pudasaini, G., and Bille, J., Very fast wave-front measurement at the human eye with a custom CMOS-based Hartmann–Shack sensor, *Opt. Express*, Vol. 11, 2003, p. 2704.
226. Burns, S.A., et al., Contrast improvement of confocal retinal imaging by use of phase-correcting plates, *Opt. Lett.*, Vol. 27, 2002, pp. 400–402.
227. Platt, B.C., and Shack, R., History and principles of Shack–Hartmann wavefront sensing, *J. Refract. Surg.*, Vol. 17, 2001, pp. S573–S577.
228. Hartmann, J., Bemerkungen über den Bau und die Justirung von Spektrographen, *Z. Instrum.*, Vol. 20, 1900, p. 47.
229. Rimmer, M.P., Method for evaluating lateral shearing interferograms, *Appl. Opt.*, Vol. 13, 1974, pp. 623–629.
230. Prieto, P.M., et al., Analysis of the performance of the Hartmann–Shack sensor in the human eye, *J. Opt. Soc. Am. A*, Vol. 17, 2000, p. 1388.
231. Webb, R.H., et al., The SRR: a null-seeking aberrometer, *Appl. Opt.*, Vol. 42, 2003, pp. 736–744.
232. Roorda, A., et al., Adaptive optics scanning laser ophthalmoscopy, *Opt. Express*, Vol. 10, 2002, pp. 405–412.

233. Dale, S.R., et al., Wave-front correction using a self-referencing phase conjugation system based on a Zernike cell, *Opt. Commun.*, Vol. 191, 2001, pp. 31–38.

234. Vargas-Martin, F., Prieto, P.M., and Artal, P., Correction of the aberrations in the human eye with a liquid-crystal spatial light modulator: limits to performance, *J. Opt. Soc. Am. A*, Vol. 15, 1998, pp. 2552–2562.

235. Shirai, T., Liquid-crystal adaptive optics based on feedback interferometry for high-resolution retinal imaging, *Appl. Opt.*, Vol. 41, 2002, p. 4013.

236. Paterson, C., Munro, I., and Dainty, J.C., A low cost adaptive optics system using a membrane mirror, *Opt. Express*, Vol. 6, 2000, pp. 175–185.

237. Bartsch, D., et al., Retinal imaging with a low-cost micromachined membrane deformable mirror, *J. Biomed. Opt.*, Vol. 7, 2002, pp. 451–456.

238. Doble, N., et al., Use of a microelectromechanical mirror for adaptive optics in the human eye, *Opt. Lett.*, Vol. 27, 2002, p. 1537.

239. Fernandez, E.J., et al., Adaptive optics with a magnetic deformable mirror: applications in the human eye, *Opt. Express*, Vol. 14, 2006, pp. 8900–8917.

240. Porter, J., et al., Monochromatic aberrations of the human eye in a large population, *J. Opt. Soc. Am. A*, Vol. 18, 2001, pp. 1793–1803.

241. Hermann, B., et al., Adaptive-optics ultrahigh resolution optical coherence tomography, *Opt. Lett.*, Vol. 29, 2004, pp. 2142–2144.

242. Zawadzki, R., et al., Adaptive-optics optical coherence tomography for high-resolution and high-speed 3D retinal in vivo imaging, *Opt. Express*, Vol. 13, 2005, pp. 8532–8546.

243. Zhang, Y., et al., High-speed volumetric imaging of cone photoreceptors with adaptive optics spectral-domain optical coherence tomography, *Opt. Express*, Vol. 14, 2006, pp. 4380–4394.

244. Bigelow, C.E., et al., Compact multimodal adaptive optics spectral domain optical coherence tomography instrument for retinal imaging, *J. Opt. Soc. Am. A*, Vol. 24, 2007, pp. 1327–1336.

245. Zawadzki, R.J., et al., Ultrahigh-resolution optical coherence tomography with monochromatic and chromatic aberration correction, *Opt. Express*, Vol. 16, 2008, pp. 8126–8143.

246. Fernández, E.J., et al., Ultrahigh resolution optical coherence tomography and pan-correction for cellular imaging of the living human retina, *Opt. Express*, Vol. 16, 2008, pp. 11083–11094.

247. Martin, J.A., and Roorda, A., Direct and noninvasive assessment of parafoveal capillary leukocyte velocity, *Ophthalmology*, Vol. 112, 2005, pp. 2219–2224.

248. Zhong, Z., et al., In vivo measurement of erythrocyte velocity and retinal blood flow using adaptive optics scanning laser ophthalmoscopy, *Opt. Express*, Vol. 16, 2008, pp. 12746–12756.

249. Grieve, K., et al., Multi-wavelength imaging with the adaptive optics scanning laser ophthalmoscope, *Opt Express*, Vol. 14, 2006, pp. 12230–12242.

250. Jonnal, R.S., et al., In vivo functional imaging of human cone photoreceptors, *Opt. Express*, Vol. 15, No. 24, 2007, pp. 16141–16160.

251. Grieve, K., and Roorda, A., Intrinsic signals from human cone photoreceptors, *Invest. Ophthalmol. Vis. Sci.*, Vol. 49, 2008, pp. 713–719.

252. Carroll, J., et al., Functional photoreceptor loss revealed with adaptive optics: an alternate cause of color blindness, *Proc. Natl. Acad. Sci. USA*, Vol. 101, 2004, pp. 8461–8466.

253. Hofer, H., et al., Organization of the human trichromatic cone mosaic, *J. Neurosci*., Vol. 25, 2005, pp. 9669–9679.

254. Hofer, H., Singer, B., and Williams, D.R., Different sensations from cones with the same pigment, *J. Vis*., Vol. 5, 2005, pp. 444–454.

255. Roorda, A., and Williams, D.R., Optical fiber properties of individual human cones, *J. Vis*., Vol. 2, 2002, pp. 404–412.

256. Makous, W., et al., Retinal microscotomas revealed with adaptive-optics microflashes, *Invest. Ophthalmol. Vis. Sci*., Vol. 47, 2006, pp. 4160–4167.

257. Putnum, N.M., et al., The locus of fixation and the foveal cone mosaic, *J. Vis*., Vol. 5, 2005, pp. 632–639.

258. Morgan, J.I., et al., Light-induced retinal changes observed using high-resolution autofluorescence imaging of the retinal pigment epithelium, *Invest. Ophthalmol. Vis. Sci*., Vol. 49, 2008, pp. 3715–3729.

259. Gray, D.C., et al., In vivo imaging of the fine structure of rhodamine-labeled macaque retinal ganglion cells, *Invest. Ophthalmol. Vis. Sci*., Vol. 49, 2008, pp. 467–473.

260. Yoon, M.K., et al., Adaptive optics scanning laser ophthalmoscopy images in a family with the mitochondrial DNA T8993C mutation, *Invest. Ophthalmol. Vis. Sci*., Vol. 50, 2009, pp. 1838–1847.

261. Choi, S.S., et al., In vivo imaging of the photoreceptor mosaic in retinal dystrophies and correlations with visual function, *Invest. Ophthalmol. Vis. Sci*., Vol. 47, No. 5, 2006, pp. 2080–2092.

262. Wolfing, J.I., et al., High-resolution retinal imaging of cone–rod dystrophy, *Ophthalmology*, Vol. 113, 2006, p. 1019.

263. Roorda, A., Zhang, Y., and Duncan, J.L., High-resolution in vivo imaging of the RPE mosaic in eyes with retinal disease, *Invest. Ophthalmol. Vis. Sci*., Vol. 48, 2007, pp. 2297–2303.

264. Duncan, J.L., et al., High-resolution imaging with adaptive optics in patients with inherited retinal degeneration, *Invest. Ophthalmol. Vis. Sci*., Vol. 48, 2007, pp. 3283–3291.

265. Choi, S.S., et al., Changes in cellular structures revealed by ultra-high resolution retinal imaging in optic neuropathies, *Invest. Ophthalmol. Vis. Sci*., Vol. 49, 2008, pp. 2103–2119.

266. Artal, P., et al., Neural compensation for the eye's optical aberrations, *J. Vis*., Vol. 4, 2004, pp. 281–287.

267. Chen, L., Artal, P., Gutierrez, D., and Williams, D.R., Neural compensation for the best aberration correction, *J. Vis*., Vol. 7, No. 10, 2007, pp. 1–9.

268. Baraas, R.C., et al., Adaptive optics retinal imaging reveals S-cone dystrophy in tritan color-vision deficiency, *J. Opt. Soc. Am. A*, Vol. 24, No. 5, 2007, pp. 1438–1447.

269. Rha, J., et al., Adaptive optics flood-illumination camera for high speed retinal imaging, *Opt. Express*, Vol. 14, 2006, pp. 4552–4569.

270. Burns, S.A., et al., Large field of view, modular, stabilized, adaptive-optics-based scanning laser ophthalmoscope, *J. Opt. Soc. Am. A*, Vol. 24, 2007, pp. 1313–1326.

271. Chen, D.C., et al., High-resolution adaptive optics scanning laser ophthalmoscope with dual deformable mirrors, *J. Opt. Soc. Am. A*, Vol. 24, 2007, pp. 1305–1312.
272. Webb, R.H., et al., Stroke amplifier for deformable mirrors, *Appl. Opt*., Vol. 43, 2004, pp. 5330–5333.
273. Song, H., et al., Stokes vector analysis of adaptive optics images of the retina, *Opt. Lett*., Vol. 33, 2008, pp. 137–139.
274. Chui, Y., Song, H., and Burns, S.A., Individual variations in human cone photoreceptor packing density: variations with refractive error, *Invest. Ophthalmol. Vis. Sci*., Vol. 49, 2008, pp. 4679–4687.
275. Chui, T.Y. P., Song, H., and Burns, S.A., Adaptive-optics imaging of human cone photoreceptor distribution, *J. Opt. Soc. Am. A*, Vol. 25, No. 12, 2008, pp. 3021–3029.
276. Vilupuru, A.S., Adaptive optics scanning laser ophthalmoscopy for in vivo imaging of lamina cribrosa, *J. Opt. Soc. Am. A*, Vol. 24, No. 5, 2007, pp. 1417–1425.
277. Zawadzki, R.J., et al., Adaptive optics–optical coherence tomography: optimizing visualization of microscopic retinal structures in three dimensions, *J. Opt. Soc. Am. A*, Vol. 24, 2007, pp. 1373–1383.
278. Hammer, D.X., et al., High resolution retinal imaging with a compact adaptive optics spectral domain optical coherence tomography system, in *Ophthalmic Technologies XVII*, F. Manns, P.G. Söderberg, and A. Ho (eds.), *Proc. SPIE*, Vol. 6426A, 2007.
279. Xue, B., et al., Photoreceptor counting and montaging of en-face retinal images from an adaptive optics fundus camera, *J. Opt. Soc. Am. A*, Vol. 24, 2007, pp. 1364–1372.
280. Martin, J., and Roorda, A., *Direct and Non-invasive Parafoveal Microvascular Density and Foveal Avascular Zone Measurement*, ARVO Abstract 3505, Association for Research in Vision and Ophthalmology, Rockville, MD, 2006.
281. Burns, S.A., et al., *Imaging the Inner Retina Using Adaptive Optics*, ARVO Abstract 4512, Association for Research in Vision and Ophthalmology, Rockville, MD, 2008.
282. Riva, C., Ross, B., and Benedek, G., Laser Doppler measurements of blood flow in capillary tubes and retinal arteries, *Invest. Ophthalmol*., Vol. 11, 1972, pp. 936–944.
283. Weale, R.A., On the birefringence of rods and cones, *Pfluegers Arch*., Vol. 329, 1971, pp. 244–257.
284. Hochheimer, B.F., and Kues, H.E., Retinal polarization effects, *Appl. Opt*., Vol. 21, 1982, pp. 3811–3818.
285. klein Brink, H.B., and van Blokland, G.J., Birefringence of the human foveal area assessed in vivo with Mueller-matrix ellipsometry, *J. Opt. Soc. Am*., Vol. A5, 1988, pp. 49–57.
286. Yazdanfar, S., Rollins, A.M., and Izatt, J.A., Imaging and velocimetry of the human retinal circulation with color Doppler optical coherence tomography, *Opt. Lett*., Vol. 25, 2000, pp. 1448–1450.
287. Yazdanfar, S., and Izatt, J.A., Self-referenced Doppler optical coherence tomography, *Opt. Lett*., Vol. 27, 2002, pp. 2085–2087.
288. White, B.R., et al., In vivo dynamic human retinal blood flow imaging using ultra-high-speed spectral domain optical Doppler tomography, *Opt. Express*, Vol. 11, 2003, pp. 3490–3497.
289. Leitgeb, R.A., Hitzenberger, C.A., and Fercher, A.F., Performance of Fourier domain vs. time domain optical coherence tomography, *Opt. Express*, Vol. 11, 2003, pp. 889–894.

290. Považay, B., et al., Enhanced visualization of choroidal vessels using ultrahigh resolution ophthalmic OCT at 1050 nm, *Opt. Express*, Vol. 11, 2003, pp. 1980–1986.
291. Unterhuber, A., et al., In vivo retinal optical coherence tomography at 1040 nm: enhanced penetration into the choroid, *Opt. Express*, Vol. 13, 2005, pp. 3252–3258.
292. Goetzinger, E., et al., Measurement and imaging of birefringent properties of the human cornea with phase-resolved polarization-sensitive optical coherence tomography, *J. Biomed. Opt*., Vol. 9, 2004, pp. 94–102.
293. Weinreb, R.N., Bowd, C., and Zangwill, L.M., Glaucoma detection using scanning laser polarimetry with variable corneal polarization compensation, *Arch. Ophthalmol*., Vol. 121, 2003, pp. 218–224.
294. Weber, A., et al., Polarimetric imaging and blood vessel quantification, *Opt. Express*, Vol. 12, 2004, p. 5178.
295. Miura, M. et al., Imaging polarimetry and retinal blood vessel quantification at the epiretinal membrane, *J. Opt. Soc. Am. A*, Vol. 24, 2007, p. 1431.
296. Cense, B., et al., In vivo depth-resolved birefringence measurements of the human retinal nerve fiber layer by polarization-sensitive optical coherence tomography, *Opt. Lett*., Vol. 27, 2002, pp. 1610–1612.
297. Cense, B., et al., In vivo birefringence and thickness measurements of the human retinal nerve fiber layer using polarization-sensitive optical coherence tomography, *J. Biomed. Opt*., Vol. 9, 2004, p. 121.
298. Pircher, M., et al., Imaging of polarization properties of human retina in vivo with phase resolved transversal PS-OCT, *Opt. Express*, Vol. 12, 2004, pp. 5940–5951.
299. Götzinger, E., et al., High speed spectral domain polarization sensitive optical coherence tomography of the human retina, *Opt. Express*, Vol. 13, 2004, pp. 10217–10229.
300. Cense, B., et al., Quantifying polarization properties of the in vivo retina with adaptive optics and polarization-sensitive optical coherence tomography, in *Opthalmic Technologies XVIII*, F. Manns, P.G., Söderberg, and A. Ho (eds.), 6844A–41, *Proc. SPIE*, Vol. 6844A, 2008.
301. Podoleanu, A.G., and Jackson, D.A., Noise analysis of a combined optical coherence tomograph and a confocal scanning ophthalmoscope, *Appl. Opt*., Vol. 38, 1999, pp. 2116–2127.
302. Podoleanu, A.G., et al., Combined multiplanar optical coherence tomography and confocal scanning ophthalmoscopy, *J. Biomed. Opt*., Vol. 9, 2004, pp. 86–93.
303. Pircher, M., et al., Simultaneous SLO/OCT imaging of the human retina with axial eye motion correction, *Opt. Express*, Vol. 15, 2007, pp. 16922–16932.
304. Iftimia, N.V., et al., Hybrid retinal imager using line scanning laser ophthalmoscopy and spectral domain optical coherence tomography, *Opt. Express*, Vol. 14, 2006, pp. 12909–12914.
305. Merino, D., et al., Adaptive optics enhanced simultaneous *en-face* optical coherence tomography and scanning laser ophthalmoscopy, *Opt. Express*, Vol. 14, 2006, pp. 3345–3353.
306. Burns, S.A., et al., *High Resolution Imaging Modalities Provide Complementary Information*, Association for Research in Vision and Ophthalmology, Ft. Lauderdale, FL, May 2007.

307. Zawadzki, R., et al., Retinal imaging with combined adaptive optics optical coherence tomography and adaptive optics scanning laser ophthalmoscopy, in *Opthalmic Technologies XIX*, F. Manns, P.G. Söderberg, and A. Ho (eds.), 7163–14, *Proc. SPIE*, Vol. 7163, 2009.
308. Curcio, C.A., and Sloan, K.R., Packing geometry of human cone photoreceptors: variation with eccentricity and evidence for local anisotropy, *Vis. Neurosci*., Vol. 9, 1992, pp. 169–180.
309. Hendrickson, A.E., and Kupfer, C., The histogenesis of the fovea in the macaque monkey, *Invest. Ophthalmol*., Vol. 15, 1976, pp. 746–756.
310. Hendrickson, A.E., and Yuodelis, C., The morphological development of the human fovea, *Ophthalmology*, Vol. 91, 1984, pp. 603–612.
311. Hendrickson, A.E., A morphological comparison of foveal development in man and monkey, *Eye*, Vol. 6, 1992, pp. 136–144.
312. Hendrickson, A.E., et al., Development of the neural retina and its vasculature in the Marmoset *Callithrix jacchus*, *J. Comp. Neurol*., Vol. 497, 2006, pp. 270–286.
313. Bizheva, K., et al., Optophysiology: depth-resolved probing of retinal physiology with functional ultrahigh-resolution optical coherence tomography, *Proc. Natl. Acad. Sci. USA*, Vol. 103, 2006, pp. 5066–5071.
314. Srinivasan, V.J., et al., In vivo measurement of retinal physiology with high-speed ultrahigh-resolution optical coherence tomography, *Opt. Lett*., Vol. 31, 2006, pp. 2308–2310.
315. DeLint, P.J., et al., Slow optical changes in human photoreceptors induced by light, *Invest. Ophthalmol. Vis. Sci*., Vol. 41, 2000, pp. 282–289.
316. Hanazono, G., et al., Intrinsic signal imaging in macaque retina reveals different types of flash-induced light reflectance changes of different origins, *Invest. Ophthalmol. Vis. Sci*., Vol. 48, 2007, pp. 2903–2912.
317. Yao, X., and George, J., Near-infrared imaging of fast intrinsic optical responses in visible light-activated amphibian retina, *J. Biomed. Opt*., Vol. 11, 2006, p. 064030.
318. Arathorn, D.W., et al., Retinally stabilized cone-targeted stimulus delivery, *Opt. Express*, Vol, 15, 2007, pp. 13731–13744.
319. Song, Q., et al., Selective targeting of pigmented retinal pigment epithelial (RPE) cells by a single pulsed laser irradiation: an in vitro study, *Opt. Express*, Vol. 16, 2008, pp. 10518–10528.
320. Hammer, D.X., et al., Precision targeting with a tracking adaptive optics scanning laser ophthalmoscope, in *Ophthalmic Technologies XVI*, F. Manns, P.G. Söderberg, and A. Ho (eds.), *Proc. SPIE*, Vol. 6138, 2006, p. 613811.
321. García de la Cera, E., et al., Optical aberrations in the mouse eye, *Vis. Res*., Vol. 46, 2006, pp. 2546–2553.
322. Biss, D.P., et al., In vivo fluorescent imaging of the mouse retina using adaptive optics, *Opt. Lett*., Vol. 32, 2007, pp. 659–661.
323. Chang, B., et al., Retinal degeneration mutants in the mouse, *Vis. Res*., Vol. 42, 2002, pp. 517–525.
324. Artal, P., et al., Retinal image quality in the rodent eye, *Vis. Neurosci*., Vol. 15, 1998, pp. 597–605.
325. Adler, R., et al., Cell death in age-related macular degeneration, *Mol. Vis*., Vol. 5, 1999, p. 31.301.

326. Rueckel, M., Mack-Bucher, J.A., and Denk, W., Adaptive wavefront correction in two-photon microscopy using coherence-gated wavefront sensing, *Proc. Natl. Acad. Sci. USA*, Vol. 103, No. 46, 2006, pp. 17137–17142.

327. Jacobson, S.G., et al., Safety of recombinant adeno-associated virus type 2-RPE65 vector delivered by ocular subretinal injection, *Mol. Ther.*, Vol. 13, 2006, pp. 1074–1084.

328. Bainbridge, J.W., et al., Effect of gene therapy on visual function in Leber's congenital amaurosis, *N. Engl. J. Med.*, Vol. 358, 2008, pp. 2231–2239.

329. Maguire, A.M., et al., Safety and efficacy of gene transfer for Leber's congenital amaurosis, *N. Engl. J. Med.*, Vol. 358, 2008, pp. 2240–2248.

330. Hauswirth, W.W., et al., Treatment of Leber congenital amaurosis due to RPE65 mutations by ocular subretinal injection of adeno-associated virus gene vector: short-term results of a phase I trial, *Hum. Gene Ther.*, Vol. 19, 2008, pp. 979–990.

## BIBLIOGRAPHY

Ciulla, T.A., Regillo, C.D., and Harris, A. (eds.), *Retina and Optic Nerve Imaging*, Lippincott Williams & Wilkins, Philadelphia, 2003.

Hecht, E., *Optics*, 3rd ed., Addison Wesley Longman, Reading, MA, 1998.

Huang, D., Kaiser, P.K., Lowder, C.Y., and Traboulsi, E.I. (eds.), *Retinal Imaging*, Elsevier, St. Louis, MO, 2006.

Kandel, E.R., Schwartz, J.H., and Jessell, T.M. (eds.), *Principles of Neural Science*, 3rd ed., Appleton & Lange, Norwalk, CT, 1991.

Porter, J., Queener, H., Lin, J., Thorn, K., and Awwal, A. (eds.), *Adaptive Optics for Vision Science*, Wiley, Hoboken, NJ, 2006.

Puliafito, C.A., Hee, M.R., Schuman, J.S. and Fujimoto, J.G. (eds.), *Optical Coherence Tomography of Ocular Diseases*, Slack, Inc., Thorofare, NJ, 1996.

Tyson, R.K., *Principles of Adaptive Optics*, 2nd ed., Academic Press, Boston, 1998.

Yanoff M., and Duker, J.S. (eds.), *Ophthalmology*, 2nd ed., Mosby, St. Louis, MO, 2004.

# 5

# CONFOCAL MICROSCOPY OF SKIN CANCERS

JULIANA CASAGRANDE TAVOLONI BRAGA
*Hospital A. C. Camargo, São Paulo, Brazil*

ITAY KLAZ AND ALON SCOPE
*Memorial Sloan–Kettering Cancer Center, New York, New York*

DANIEL GAREAU
*Oregon Health and Science University, Portland, Oregon*

MILIND RAJADHYAKSHA AND ASHFAQ A. MARGHOOB
*Memorial Sloan–Kettering Cancer Center, New York, New York*

5.1 Introduction 164
5.2 Imaging of normal skin in vivo 166
    5.2.1 Epidermis 166
    5.2.2 Dermal–epidermal junction 166
    5.2.3 Dermis 167
5.3 Imaging of cutaneous neoplasms in vivo: correlation with dermoscopy and histopathology 168
    5.3.1 Basal cell carcinoma 168
    5.3.2 Actinic keratosis and squamous cell carcinoma 170
    5.3.3 Melanoma 171
5.4 Mosaicing of excised skin ex vivo 174
5.5 Intraoperative mapping of surgical margins 177
5.6 Challenging cases 177
5.7 Future perspectives 182
References 183

---

*Advances in Optical Imaging for Clinical Medicine*, Edited by Nicusor Iftimia, William R. Brugge, and Daniel X. Hammer
Copyright © 2011 John Wiley & Sons, Inc.

## 5.1 INTRODUCTION

Although Marvin Minsky invented the confocal microscope in 1957, the instrumentation and applications for the in vivo evaluation, diagnosis, and management of cutaneous tumors has only evolved during the past decade. Reflectance confocal microscopy (RCM) consists of a point source of light, produced by a laser beam, which passes through an objective lens and illuminates a probe volume in skin. The light backscattered from the probe volume passes through an optically conjugate point aperture, consisting of a pinhole, and is then captured by a detector to produce a pixel. Scanning the probe volume in two dimensions permits the operator to capture a corresponding two-dimensional array of pixels, which produces an image of a thin optical section within thick tissue. Imaging of thin optical sections is noninvasive, in contrast to conventional histology, which requires physical sectioning of tissue.

RCM enables real-time visualization of nuclear and cellular morphology in vivo. The ability to observe nuclear and cellular details clearly sets this imaging modality apart from other noninvasive imaging instruments, such as magnetic resonance imaging [1], optical coherence tomography [2], and high-frequency ultrasound [3]. The lateral resolution of RCM is typically 0.2 to 1.0 μm, and the thickness of optical sectioning is 1 to 3 μm [4,5], which is analogous to viewing histology at high magnification power and high resolution. As a result, RCM is being developed as a portable bedside tool for diagnosis of melanoma [6] and nonmelanoma [7] skin cancers.

At present, there is a commercially available reflectance confocal microscope (VivaScope 1500, Lucid Inc., Rochester, New York), consisting of a scanning unit that is mounted on an articulating arm for positioning on the patient. A metal ring fixture with an adhesive window is applied to the skin. The microscope is then coupled to the metal ring, thereby creating a stable contact between the skin and the objective lens. A gel with a refractive index close to that of water (i.e., 1.33) is placed between the objective lens and the tissue. With a 30× lens, the field of view in the tissue is 0.5 × 0.5 mm. However, larger fields of view are achievable by "stitching" together, via computer software, sequentially acquired adjacent images to create and display a mosaic. The current version of this software allows up to 16 × 16 images to be "stitched" together, thereby creating and displaying up to an 8 × 8 mm field of view. This is analogous to a low magnifying power of 2×. Imaging more than 16 × 16 images is currently impractical, due to the long acquisition times required for imaging such a large field. Use of a near-infrared wavelength of 830 nm permits imaging to depths of 100 to 200 μm in normal skin. This allows for visualization of the epidermis and superficial dermis. Although 830 nm is the wavelength of choice for most clinical applications, longer wavelengths such as 1064 nm, as well as shorter visible wavelengths of 488 to 700 nm, have been used. While shorter wavelengths provide higher resolution and thinner optical sectioning, longer near-infrared wavelengths allow deeper imaging, due to reduced scattering.

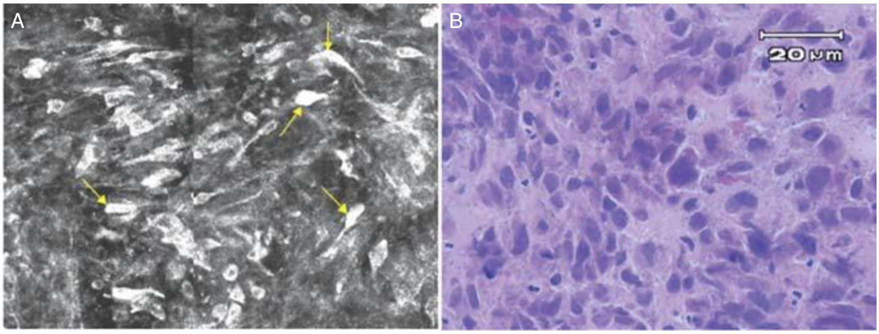

**FIGURE 5.1** (A) RCM image of skin and (B) corresponding histology. Melanocytes appear in the black-and-white RCM images as bright cells against a dark background. The roundish dark structures within the outline of some of the cells correspond to the nucleus. In contrast, melanocytes in the corresponding H& E-stained histopathology section show purple nuclei and pink cytoplasm on a light pink background. The melanocytes shown are those of a melanoma; they are abnormal because they display variability in the size, shape, and refractivity of cells on RCM and variability in the size and shape of nuclei on H& E histopathology. The scale pertains to both images.

Although RCM is able to image at a resolution comparable to histology, there are some important differences between RCM and conventional histopathology. First, RCM images appear in black and white as opposed to the purple and pink colors seen in hematoxylin and eosin (H&E)–stained histology. Second, there is a contrast inversion with RCM. In routine histological staining with H&E, structures that absorb the stain appear dark in contrast to the nonstained bright background (Figure 5.1). In other words, H& E histology represents bright-field imaging. However, in RCM, the background tissue appears dark, while cells with higher reflectance appear brighter (Figure 5.1). This is equivalent to dark-field imaging. Third, although the nominal resolution and optical sectioning of RCM is similar to that of histopathology, the RCM image quality degrades with increasing depth in the tissue. At deeper dermis levels, strong scattering and aberrations at the dermal–epidermal junction (DEJ) and superficial dermis cause loss of optical sectioning, loss of resolution, and loss of contrast. Since structure-specific stains are not being applied in vivo to living human skin, we must rely solely on endogenous reflectance contrast for imaging. Unfortunately, image quality does degrade with loss of endogenous contrast. By comparison, observation of physically prepared thin histopathologic sections is superior to RCM images obtained in vivo because there is no overlying tissue to degrade the image and because of the benefit of stains to enhance contrasts. This fact, in turn, explains the reason for why ex vivo RCM imaging of tissue can produce an image quality that closely approaches that of histopathology.

Melanin provides the best source of endogenous contrast by strongly backscattering light. Cells that contain melanin, including melanocytes (Figure 5.1), keratinocytes, and dermal melanophages, appear bright on RCM. In general, the greater the melanin content and concentration within cells, the brighter the

RCM images will appear. Some organelles and cytoplasmic granules, such as keratohyaline granules in keratinocytes and Birbeck granules in Langerhans cells, also provide contrast, thus allowing them to be visualized as well [5].

## 5.2 IMAGING OF NORMAL SKIN IN VIVO

An essential component of recognizing cutaneous pathology via RCM is the ability to first recognize the features of normal skin. RCM images thin optical sections of tissue in the *en face* (horizontal) plane, allowing for evaluation of each of the different layers of epidermis, as well as the DEJ and superficial dermis. The normal skin appearance with RCM varies according to skin color, anatomical site, sun exposure, age, and physiological condition [8].

### 5.2.1 Epidermis

The epidermis is composed primarily of keratinocytes, which are arranged in four layers: stratum corneum, granular layer, spinous layer, and basal layer. In addition to keratinocytes, few melanocytes and Langerhans cells can also be seen occasionally. Each epidermal layer has specific features on RCM. The most superficial layer, the stratum corneum (Figure 5.2A), is located 0 to 15 μm from the skin surface and composed of flat anucleated keratinocytes (25 to 50 μm in size). The keratinocytes appear as groups of bright cells separated by dark, nonreflective skin folds or dermotoglyphics [5,8,9]. The second layer from the surface is the stratum granulosum (Figure 5.2B), located 10 to 20 μm from the skin surface; it is two to four cells in thickness and composed of polygonal cells (25 to 35 μm in size). Next is the stratum spinosum (Figure 5.2C), located 20 to 100 μm under the stratum corneum and also containing polygonal keratinocytes (15 to 25 μm in size). Individual keratinocytes of the granular and spinous layers are recognized by their outline of roundish dark center and surrounding bright ring, corresponding to nucleus and cytoplasm, respectively. This outline is probably due to the fact that native chromatin in the nucleus scatters much less light than keratin in the surrounding cytoplasm. Aside from the size difference, the refractive cytoplasm of keratinocytes of the stratum granulosum appears on RCM brighter and more granular than that of the stratum spinosum keratinocytes. The back-to-back arrangement of the polygonal keratinocytes in these two layers forms a pattern on RCM that resembles a honeycomb (Figure 5.2B and C). The basal layer of the epidermis is located 40 to 130 μm below the skin surface. It consists of a single layer of keratinocytes (7 to 12 μm in size), with episodic intervening melanocytes. The keratinocytes are usually uniform in shape and size and appear brighter than those in the spinous layer [5,8,9], forming a pattern that resembles a cobblestone (Figure 5.2D). The brightness of the basal keratinocytes is due to melanin that accumulates over the nucleus like a cap.

### 5.2.2 Dermal–Epidermal Junction

At this level the dermis forms upward fingerlike projections into the epidermis called *dermal papillae*. They appear on RCM images as round dark areas, often

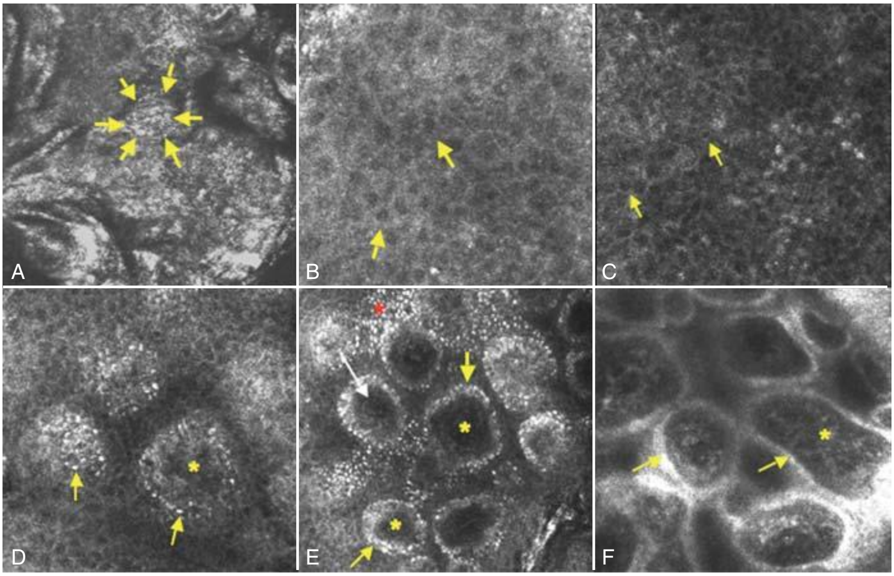

**FIGURE 5.2** RCM images (0.5 × 0.5 mm) of normal skin. (A) The stratum corneum appears as highly refractile surface with dark skin folds. The cells appear to blend together because of poorly demarcated cell borders (arrows). (B) Stratum granulosum shows a honeycomb pattern made of polygonal keratinocytes with grainy cytoplasms and dark central nuclei (arrows). (C) Stratum spinosum also shows a honeycomb pattern; spinous keratinocytes are smaller, but otherwise also show a dark central nucleus surrounded by a rim of bright cytoplasm (arrows). (D) The basal layer consists of a pattern resembling cobblestone, formed by clusters of small bright basal keratinocytes (arrows). The dark area in the center of one of these clusters is a dermal papillae (asterisk). (E) The DEJ consists of rings of bright basal keratinocytes (yellow arrows) surrounding dark dermal papillae (yellow asterisks). A cobblestone pattern is seen (red asterisk), indicating that these cells are probabaly basal keratinocytes. Curved dark canalicular structures, corresponding to capillary loops, are also seen in the dermal papillae (white arrow). (F) In the dermal papillae, a network of reticulated gray fibers (asterisk) is seen around the central capillary. The dermal papillae are surrounded by bright rings of basal keratinocytes (arrows).

containing a central vascular lumen (papillary dermal vascular loops) that displays blood flow in real-time imaging. The dark dermal papillae are surrounded by a ring of bright keratinocytes of the epidermal basal layer (Figure 5.2E). In dark-skinned persons the rings formed by pigmented basal keratinocytes are brighter and more discernible than in light-skinned people, because basal keratinocytes in dark-skinned people contain more melanin [9].

### 5.2.3 Dermis

The dermis is located below the DEJ and varies, in thickness from 0.3 to 3.0 mm, depending on the anatomical site (e.g., relatively thin on the face and thick on the back). The dermis consists of blood vessels, nerves, inflammatory cells, and fibroblasts enveloped in a network of collagen and elastic fibers. The dermis is divided into two regions, papillary and reticular dermis. The papillary dermis is located 50 to 150 μm beneath the skin surface and appears, on RCM, as thin intersecting collagen fibers. Where the DEJ is undulating (due to a pattern of alternating epidermal rete ridges and dermal papillae), the papillary dermis appears, as noted above, as round dark spaces surrounded by bright rings of basal keratinocytes (Figure 5.2F). In a flat DEJ, as seen in sun-damaged skin of the face, this pattern of bright rings around dermal papillae is usually absent. The reticular dermis is located more than 150 μm below the skin surface and only its upper portion can sometimes be visualized. Thicker collagen arranged in bundles is the main RCM feature of the reticular dermis.

Skin appendages such as eccrine ducts and follicular-sebaceous units can also be seen on RCM. Eccrine ducts appear as bright round structures that spiral through the epidermis. The hair follicles appears as a hollow structure whose wall is composed of elliptical keratinocyltes and whose center lumen displays a highly reflective hair shaft [5,8,9].

## 5.3 IMAGING OF CUTANEOUS NEOPLASMS IN VIVO: CORRELATION WITH DERMOSCOPY AND HISTOPATHOLOGY

In the past two decades, new imaging tools have become available to clinicians who screen patients for skin cancer. Dermoscopy (also known as dermatoscopy and epiluminescence microscopy) is a very important skin screening tool that has been used increasingly over the past 15 years. A dermoscope is a handheld tool that appears similar to an otoscope; dermoscopy allows the clinician to see structures of skin beneath the stratum corneum (which is normally not translucent), down to the depth of the superficial dermis, at a magnification of up to 10×. Many structures of skin seen on dermoscopy can be correlated with findings on histopathology, allowing the clinician using dermoscopy to make inferences about tissue pathology in vivo, prior to the actual biopsy. To this end, RCM has further enhanced our ability to assess skin cancer at the bedside, since RCM correlates well with both dermoscopy and histopathology. The fact that like dermoscopy, RCM images tissue in the horizontal plane (different from conventional histopathology, which views skin sections at the vertical plane) while having high magnification with cell-level resolution akin to histopathology makes RCM a bridge to correlation between dermoscopy and histopathology.

The use of RCM in the evaluation of skin cancers represents an important area of clinical research. Key RCM features of different cutaneous neoplasms have been described in the literature [9].

### 5.3.1 Basal Cell Carcinoma

Basal cell carcinoma (BCC) is the most common skin cancer in humans (Figure 5.3A and 5.3B) [10,11]. Histopathologically, BCCs are composed of

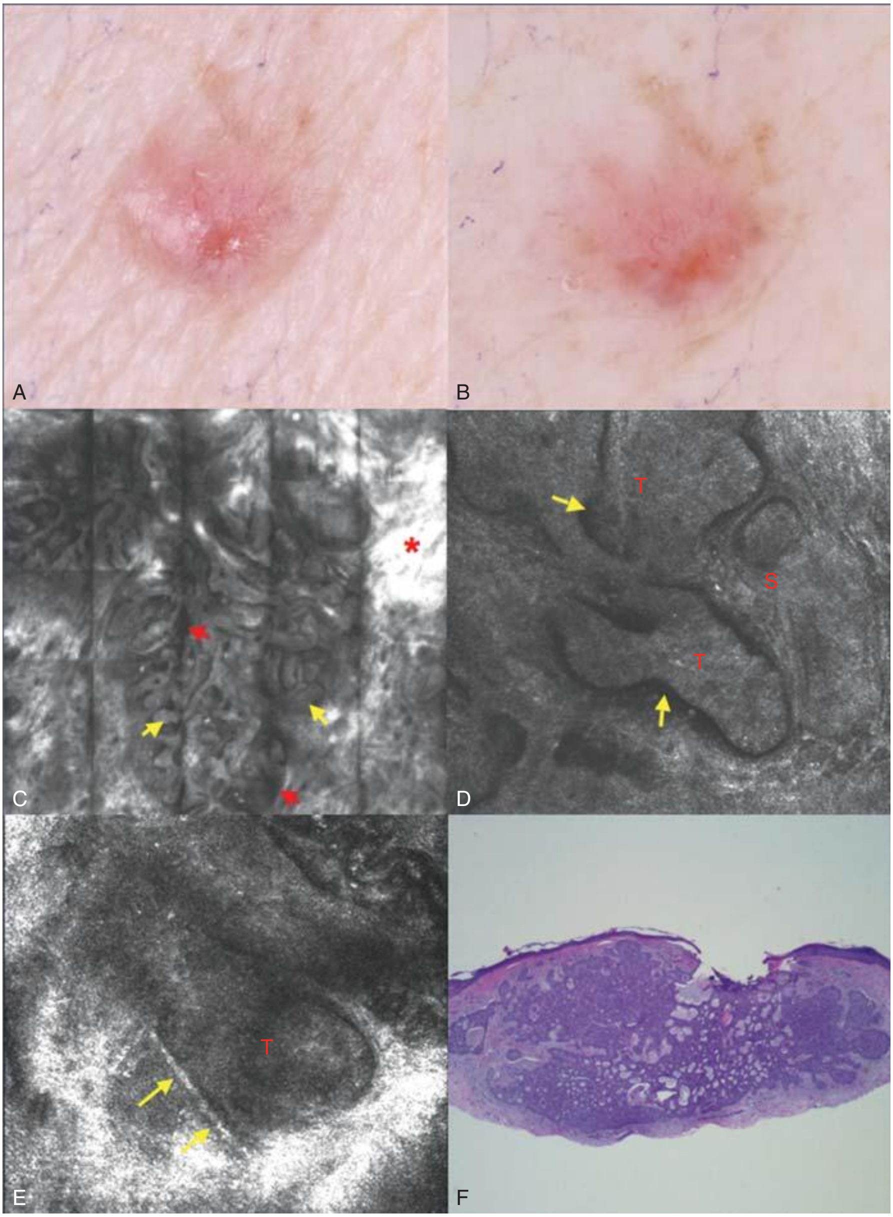

**FIGURE 5.3** (A) Clinical photograph of an erythematous shiny papule on the upper arm. (B) On dermoscopy the lesion shows bluish-gray ovoid nest and arborizing telangiectasias. (C) RCM mosaic image (2.5 × 2.5 mm) at the level of DEJ shows tumor cell islands (yellow arrows) surrounded by dark cleft-like spaces (red arrows) and refractile linear fibrous bundles (asterisk). (D) Individual RCM image (0.5 × 0.5 mm) at the level of the superficial dermis shows lobulated tumor islands (T) composed of weakly refractile cells with peripheral palisading of nuclei surrounded by moderately refractile stroma (S). (E) Peritumoral dark cleftlike spaces (arrows) are also seen. The RCM image (0.5 × 0.5 mm) at the level of the superficial dermis shows a dilated blood vessel (arrows) coursing through the tumor (T). (F) On histopathology, the lesion proved to be a nodular BCC.

nodules, islands, cords, or elongated strands of crowded, atypical basaloid cells (Figure 5.3F). The cells have a dark oval nucleus and scant cytoplasm. The tumor aggregates frequently show peripheral palisading of nuclei [11,12].

On RCM, BCCs display tumor islands composed of ill-demarcated cells (Figure 5.3C and 5.3D). In pigmented BCCs, the tumor islands appear bright and are sometimes admixed with dendritic melanocytes. Reactive stromal fibrosis is manifested as thick, bright collagen bundles around the tumor islands (Figure 5.3C). Interestingly, a dark cleft separating the tumor island from the surrounding stroma can sometimes be seen in vivo, similar to the cleft seen in BCC around the neoplastic aggregates on histopathology. This dark cleft is probably due to mucin that envelopes tumor islands. Particularly in nonpigmented BCCs, the tumor islands themselves are often not discernible, but their presence can nevertheless be deduced by their appearance as “dark silhouettes” within the bright collagenous stroma. Additional features are the prominent inflammatory infiltrate in the dermis and the increased blood flow in dilated vessels that course *en face* (i.e., parallel to the skin surface) (Figure 5.3E) [13–15]. These blood vessels correlate with the telangiectatic vessels seen on clinical examination of BCC and with the arborizing vessels seen with dermoscopy. The RCM features of BCCs of various histopathologic subtypes of BCC, such as morpheaform BCC, need to be delineated further in the future.

### 5.3.2 Actinic Keratosis and Squamous Cell Carcinoma

Actinic keratoses (AKs) and squamous cell carcinomas (SCCs) present clinically (i.e., to the naked eye) as erythematous, hyperkeratotic macules, papules, and plaques occurring on sun-damaged skin. Although the clinical diagnosis is usually straightforward, histopathologic evaluation remains the gold standard for diagnosis.

***Actinic Keratosis*** AKs are keratinocytic neoplasms that can develop into invasive SCCs [16]. Dermoscopic findings are often nonspecific [9,17]. Histopathologically, AKs are usually characterized by abnormal keratinocytes that display crowding of nuclei and nuclear atypia, including nuclear enlargement, pleomorphism, and hyperchromasia. There is abnormal maturation of keratinocytes with overlying parakeratosis. The portion of the epidermis traversed by sweat ducts and hair follicles is usually spared and displays orthokeratosis [9].

RCM findings correlate well with routine histopathology [16] and the main features of AKs are nuclear pleomorphism and disorganized spinous and granular layers, resulting in an abnormal or absent honeycomb pattern; hyperkeratosis or parakeratosis; and inflammatory cells, blood vessel dilatation, and solar elastosis in the dermis. Ulrich et al. studied RCM characteristics in 46 AKs compared to normal skin and concluded that architectural disarray at the level of spinous layer (i.e., loss of the honeycomb pattern) and keratinocytic pleomorphism are the best discriminatory features of AKs compared to normal skin, with sensitivity values ranging from 91.2 to 100% and specificity ranging from 95.2 to 100% [18].

***Squamous Cell Carcinoma*** Squamous cell carcinoma (SCC) is the second most common skin malignancy in humans [19]. Clinically, SCC appears as scaly, erythematous papules or plaques, sometimes with a history of bleeding, or as ulcers with an irregular fleshy surface (Figure 5.4A). Dermoscopy may reveal findings such as focal glomerular blood vessels, scale, and hemorrhagic or serous crusting (Figure 5.4B) [20]. Histopathologically, there is a proliferation of abnormal keratinocytes, displaying crowding and pleomorphism of nuclei; dyskeratotic keratinocytes showing abundant eosinophilic cytoplasm as evidence of abnormal, premature cornification; confluent parakeratosis without sparing over hair follicles and sweat ducts. The abnormal keratinocytes may be confined to the full thickness of the epidermis (SCC in situ), sometimes with extension down follicular epithelium, or the proliferation of neoplastic cells may extend into the reticular dermis (invasive SCC) [9,21].

The typical features of SCC may be identified by RCM if hyperkeratosis, which obstructs the penetration depth of imaging (because keratin is highly refractive), is minimal. The use of keratolytic agents to remove the surface scale may facilitate RCM evaluation of hyperkeratotic lesions. The main RCM findings in SCCs are full-thickness architectural disarray (Figure 5.4C) and enlargement and pleomorphism of nuclei of keratinocytes (Figure 5.4D and E). Aggregates of keratinocytes in the dermis may also be seen on occasion and attest to an invasive SCC.

RCM may be limited in the ability to differentiate, with conviction, AKs from SCC, as there is overlap in the RCM features of these entities that span the spectrum of keratinocytic neoplasms; RCM is also limited in evaluation of the dermis for invasive SCC, due to insufficient penetration depth of imaging, particularly in hyperkeratotic lesions. Nevertheless, the epidermal changes in SCC generally involve broader areas and are more pronounced; a complete loss of the honeycomb pattern of the spinous layer (termed *disarranged pattern*) is characteristic for SCC [9]. In AKs, the superficial layers of the epidermis may be uninvolved or display an abnormal, yet discernible honeycomb pattern; areas showing epidermal abnormality are less broad than in SCC.

### 5.3.3 Melanoma

Malignant melanoma is one of the most aggressive skin cancers in humans, and its diagnosis can be challenging even for the best of clinicians (Figure 5.5A, E, and F). Visual inspection and dermoscopic evaluation (Figure 5.5A) allows for a diagnostic accuracy of up to 85% for experienced physicians. The ability to recognize individual melanocytes and to analyze their morphology and distribution provides the basis for using RCM for the in vivo diagnosis of melanoma [6,22–26].

RCM imaging of melanoma reveals enlarged atypical cells with pleomorphic morphology (oval, stellate, or fusiform), coarse branching dendritic processes, and eccentrically placed large dark nuclei. These cells may be found in superficial layers of the epidermis (pagetoid dissemination) and in the dermis (Figure 5.5C

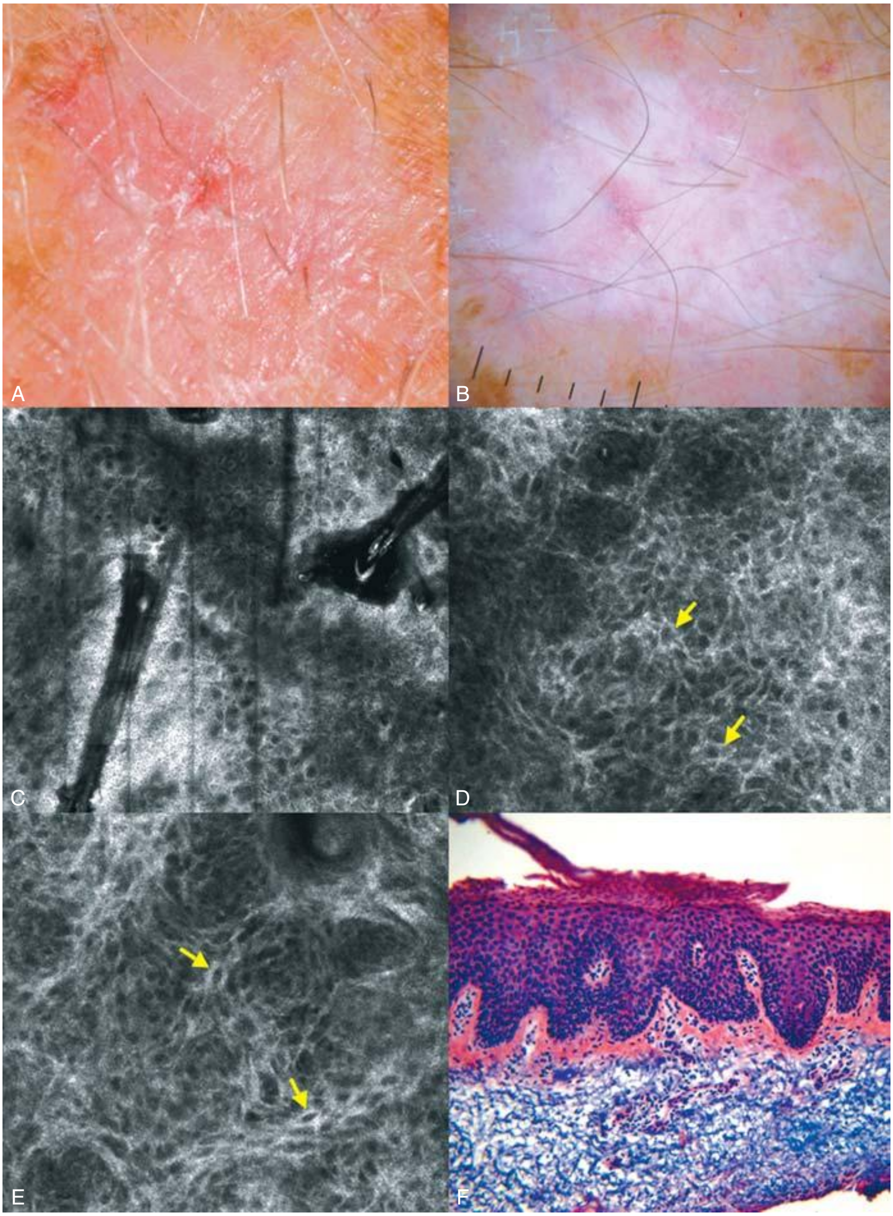

**FIGURE 5.4** (A) Clinical photograph of an erythematous scaly plaque on the forearm. (B) On dermoscopy, this lesion reveals a central scale and diffuse dotted vessels. (C) RCM mosaic image (3.5 × 3.5 mm) at the level of spinous-granular layers shows areas of an atypical honeycomb pattern. (D,E) Individual RCM images (0.5 × 0.5 mm) at the level of the spinous-granular layer show an atypical honeycomb pattern composed of large nucleated cells with variability in nuclear size and cellular brightness (arrows), indicating keratinocytic atypia. (F) On histopathology, this proved to be a squamous cell carcinoma in situ. The epidermis shows abnormal crowding of nuclei of keratinocytes (inset).

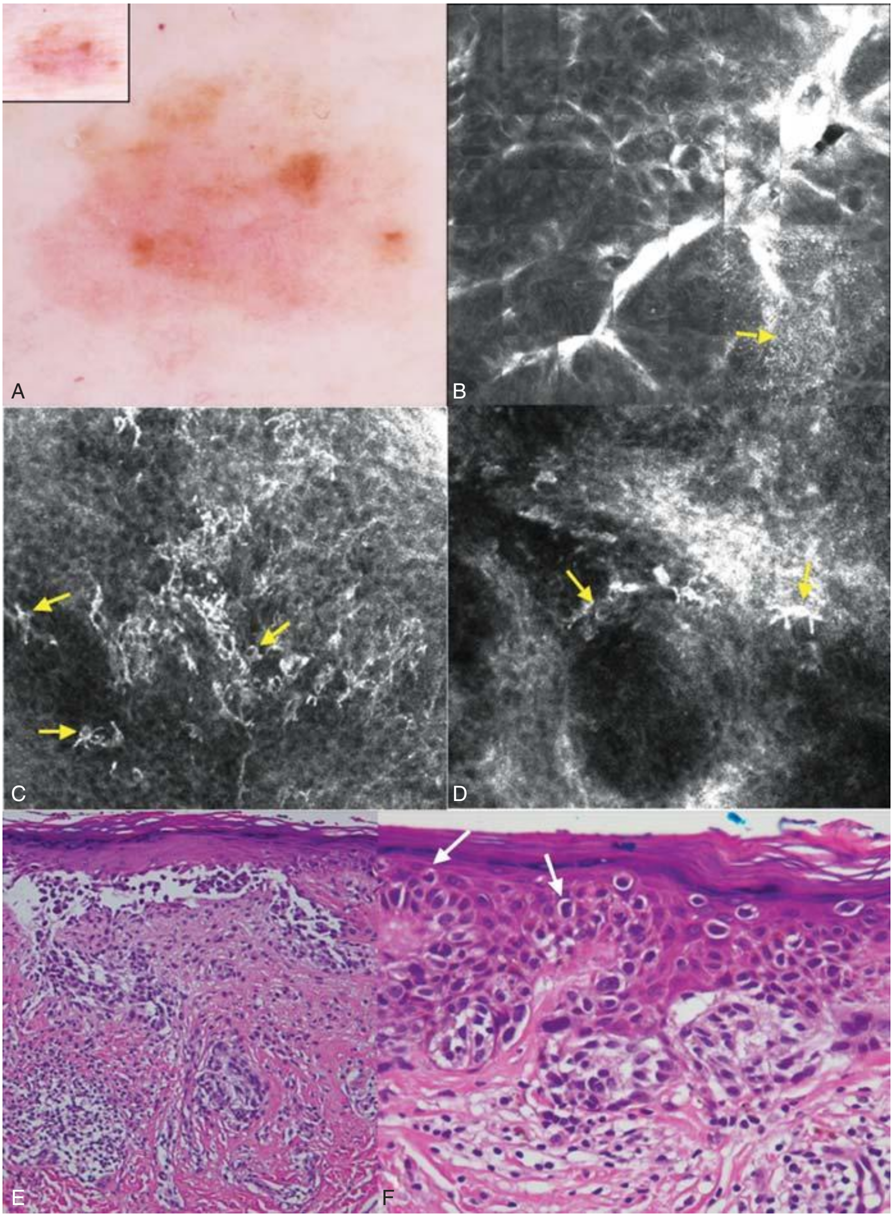

**FIGURE 5.5** (A) This lesion, on the lower back, shows clinically (inset) and dermoscopically a structureless pattern, mostly pink in color with few foci of tan pigmentation and an indistinct border. (B) RCM mosaic image (4 × 4 mm) at the level of the DEJ shows nonuniform brightness, with a focus that reveals a sheet of cells (arrow). (C,D) Individual RCM images (0.5 × 0.5 mm) show numerous stellate (dendritic) nucleated cells in the spinous layer (arrows), with partial (C) and complete (D) loss of the normal honeycomb pattern. (E,F) On histopathology, this proved to be an invasive malignant melanoma with an in situ component. Pagetoid cells can be seen in the spinous layer (F, arrows).

and D). It is also common to observe a disruption of the regular honeycomb architectural pattern of the stratum spinosum, indistinct cell borders and bright grainy particles, which probably represent melanin ("melanin dust"), distributed within the epidermis (Figure 5.5B) [26]. The dendrites seen in melanoma appear thickened and bright (Figure 5.5D). Dermal papillae in melanoma may be irregular in size and shape, with ill-defined borders that lack the surrounding ring of bright basal cells ("nonedged papillae"), or may be completely unapparent, due to flattening of the dermal–epidermal junction. Cerebriform clusters or sparse cell nests can also be seen in the dermis on occasion. These structures consist of irregularly bright cell aggregates, with nondemarcated cell borders and pleomorphism, surrounded by melanin dust.

Criteria to distinguish between benign and malignant pigmented lesions are currently in flux. Despite this, RCM images from the DEJ allow for the discrimination between nevi and melanomas with a high degree of certainty [27,28]. The ability of RCM to discriminate nevi from melanoma is based on the evaluation of the lesion's overall architecture and melanocytic cytomorphology.

A diagnostic algorithm for RCM evaluation of clinically (i.e., to the naked eye) and dermoscopically equivocal melanocytic lesions has recently been proposed by Pellacani et al. [29]. This algorithm has two major and four minor confocal criteria associated with malignancy, with a total score that ranges from zero to eight. Major criteria (scored 2 points each in the diagnostic algorithm) are the presence of nonedged papillae (lack of a ring of bright basal cells around dermal papilla) and the presence of atypical melanocytes (larger than normal melanocytes, abnormal in shape and refractivity) at the basal layer. Minor criteria (scored 1 point each) are the presence of pagetoid cells—round, bright, and nucleated cells (corresponding to melanocytes) within the epidermis above the basal layer; widespread infiltration of pagetoid cells throughout the lesion; cerebriform clusters—confluent aggregates, brainlike in appearance, of low-reflecting cells in the dermis (corresponding to dermal aggregates of abnormal melanocytes in melanoma); and bright nucleated cells within the dermal papilla (corresponding to single melanocytes in the dermis). A score $\geq 3$ suggests the diagnosis of melanoma with 97.3% sensitivity and 72.3% specificity [29]. In addition, Gerger et al. found that another important criterion for melanoma diagnosis was border disruption between keratinocytes [30].

The presence of melanocytes in the dermis of a lesion that shows features of melanoma raises suspicion for an invasive melanoma. It is important to mention that detection of melanocytes in the superficial dermis with RCM is limited by effective imaging depth of up to 200 $\mu$m, due to a decrease in resolution [31].

## 5.4 MOSAICING OF EXCISED SKIN EX VIVO

Precise surgical excision of epithelial cancers with minimal damage to the surrounding normal tissue requires accurate determination of the borders of the lesion, which is usually guided by the examination of either frozen or permanent histology sectioning. A well-established technique is Mohs micrographic surgery, which is commonly used to excise BCCs and SCCs on the face. The excision is performed in stages. After each stage the histopathologic sections of the excised tissue are prepared and examined to determine the extent and borders of the tumor. This, in turn, provides guidance on how to proceed with the subsequent excision, if necessary. The preparation of histology is slow and labor intensive, especially in surgical settings, in which speed and efficiency are important. Frozen histology usually requires minutes to hours and permanent histology may require hours to days. Real-time confocal mosaicing microscopy, combined with clinically useful contrast agents, may help detect the cancers directly in the fresh surgical excisions, at the bedside, while minimizing the need for frozen histology. Since the cancer-to-normal tissue margins are to be detected on the surface or in the superficial layers of the excision, confocal microscopy is very well suited for this application. Rapid examination for cancers at low (2×) magnification, followed by inspection of nuclear morphology at high (10 to 30×) magnification may be possible, in a manner that directly mimics the standard for examining Mohs histology sections. Both the patient and surgeon may benefit by saving time, labor, and costs.

Confocal microscopy, at high resolution, is limited to small fields of view of 0.2 to 1 mm. However, stitching together of a two-dimensional matrix of adjacent images, with computer software, allows for the creation and display of mosaics with substantially larger fields of view. These larger fields of view display Mohs surgical excision specimens of size 10 to 20 mm, which is equivalent to viewing with a magnification of 2× [32]. Confocal mosaicing microscopy shows promise in providing pathology-like images of large areas of excised tissue, with low magnification and high resolution, to potentially guide Mohs surgery [7,33]. Confocal mosaicing techniques can map large samples with high resolution. Furthermore, mapping the entire margin enables the rapid detection of residual tumors in surgical excisions. A typical first-stage Mohs excision takes approximately 5 min to image with mosaicing, which is faster than the time required to prepare conventional frozen histology.

Similar to the use of stains in histology, the use of contrast agents increases the detectability of tumors. In reflectance mode, immersion in 1 to 10% acetic acid causes the compaction of chromatin and rapidly enhances nuclear-to-dermis contrast within 0.5 to 5 min, enabling detection of superficial and nodular-type BCC tumors with an accuracy that is comparable to that of routine histology [32,33]. However, infiltrative BCC with small tumor foci remain obscured by the surrounding dermis in reflectance mode imaging.

In fluorescence mode, stains such as acridine orange [7] and toluidine blue [34] yield enhancement of nuclear contrast compared to the background dermal tissue, enabling detection of the smallest micronodular and infiltrative types of BCC tumors. Future work to integrate multiple modes may increase the diagnostic accuracy of confocal mosaicing microscopy to eventually meet or potentially exceed that of frozen histology.

To be able to acquire a two-dimensional matrix of images (to create mosaics) of fresh excised tissue requires that the tissue be flat and properly oriented. For frozen histology, this is usually not a problem, since the tissue is made to conform by freezing the position and orientation in the cryostat so as subsequently to enable proper sectioning. Fresh excision specimens, however, are living, hydrated, supple, and have complex shapes. Thus, to enable mosaicing over large areas, a tissue fixture was engineered for mounting Mohs surgical excisions [7,32,33]. The fixture allows repeatable and accurate control of the flattening, tilt, sag, and stability of the tissue surface to be imaged. The functionality of the tissue fixture mimics the operation of cryostats.

At present, up to 36 × 36 images may be mosaiced to create a field of view of up to 15 × 15 mm (Figure 5.6). The large field of view displays the entire excision with resolution and magnification equivalent to 2×, which corresponds to that used routinely by Mohs surgeons for examining histology. Submosaics

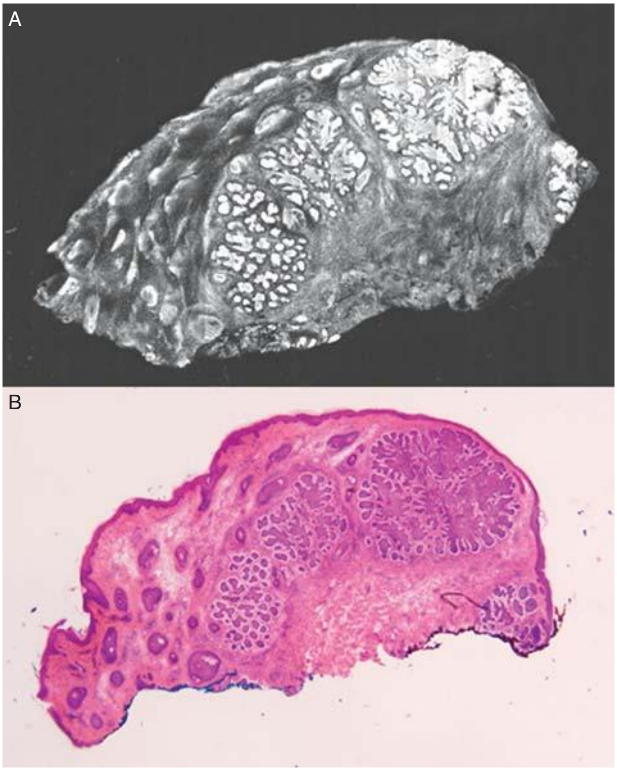

**FIGURE 5.6** (A) Fluorescence confocal mosaic (9 mm wide) of a tissue specimen from Mohs surgery showing nodular and micronodular BCC in the dermis. Fluorescent staining was achieved with immersion of the specimen in 1 mM acridine orange (pH 6.0) in saline solution for 20 s. (B) The corresponding H&E histopathologic micrograph shows excellent correlation with the confocal mosaic.

display smaller fields of view at 4× to 10× magnifications with corresponding higher resolution. This corresponds to the Mohs surgeons' use of 4× and 10× magnifications, when necessary, for closer examination of histology.

In a recently completed study, 160 fluorescence submosaics were examined at 4× magnfication by two Mohs surgeons who were blinded to the correspondingly frozen histology. Their overall sensitivity was 96.6% and specificity was 89.2% for detecting the presence and absence, respectively, of all four subtypes (i.e., superficial, nodular, micronodular, and infiltrative) BCC tumors [35].

## 5.5 INTRAOPERATIVE MAPPING OF SURGICAL MARGINS

Another application of RCM is intraoperative mapping of surgical margins. Malignant neoplasms are often asymmetric, and their margins may not be obvious to the clinical eye. Therefore, these tumors may involve the surgical margins. As mentioned earlier, in Mohs surgery the margins involved are identified by frozen histopathologic sections, and further surgery is undertaken to remove residual tumor, a time-consuming process. However, identifying residual tumor in vivo, directly in the skin surrounding the surgical defect by RCM could allow the surgeon to adjust the surgical margins in real time and would greatly expedite Mohs surgery.

We have begun the research that lays the foundations for intraoperative margin mapping. Challenges for imaging using current technology include adapting the concavity of the surgical defect to the flat plane of RCM imaging, maintaining a sterile wound environment during imaging, and enhancing the visibility of the tumor from the surrounding skin in RCM images. We have found that filling the cavity with a sterile surgical gel and covering with a sterile transparent adhesive address the issues of contour and sterility. The hemostatic agent currently used in skin surgery, aluminum chloride, was found to enhance contrast between nuclei and surrounding dermis, similar to the use of acetic acid ex vivo. Using mosaicing technology of RCM, the clinician can visualize the epidermal, superficial, and deep dermal margins of the surgical defect, and identify residual tumor. Undoubtedly, further miniaturization of the RCM device into a small handheld probe that will fit the surgical defect and discovery of new contrast agent could make intraoperative RCM margin mapping into a practical technique.

## 5.6 CHALLENGING CASES

In this section we describe two patients who presented at our clinic with skin lesions suspicious for skin cancer, for which RCM enabled the clinician to make the correct diagnosis at the bedside. The first case describes an early diagnosis of melanoma with RCM, enabling timely treatment of this potentially lethal skin cancer. In the second case, the clinician was able to diagnose a much more indolent skin neoplasm, actinic keratosis, and at the same time, to exclude melanoma based on RCM findings.

### *Case 1*

*Clinical Presentation* A 41-year-old man with a family history of melanoma presented with an enlarging pigmented lesion on the back. He denied pruritus, bleeding, or other complaints. On general skin examination, the patient had multiple pigmented lesions on his torso and limbs. A brown, asymmetrical, slightly raised lesion, 6 × 4 mm in size, was observed on the midback (Figure 5.7A). Regional lymph nodes were not enlarged on palpation.

*Dermoscopic Features* The lesion was dark brown and showed a diffuse network that was focally thickened (Figure 5.7B). A peripheral structureless area imparted asymmetry to the lesion. The overall impression was that the lesion is probably a dysplastic nevus, however, the history of change and asymmetric morphology prompted further investigation by RCM.

*RCM Features* The lesion was scanned using the Vivascope 1500. Three RCM mosaic images (5 × 5 mm field of view) were obtained at the epidermal, DEJ, and dermal levels. Stacks of consecutive individual images (0.5 × 0.5 mm field of view) from the skin surface to the superficial dermis were also obtained at the lesion's center and border. The RCM mosaic at the level of the spinous layer of the epidermis demonstrated heterogeneous reflectivity and the presence of multiple bright cells (Figure 5.7C). The individual RCM images (analogous to higher-magnification examination on histopathology) at the level of the spinous layer showed absence of the normal honeycomb pattern, replaced by sheets of bright round and dendritic nucleated cells (Figure 5.7D). Imaging at the DEJ level revealed widening of the spaces between dermal papillae (corresponding to epidermal rete ridges) and abnormal density of dendritic cells (Figure 5.7E). The RCM examination was suggestive of a melanoma and the lesion was fully excised.

*Histopathologic Examination* The biopsy revealed junctional proliferation melanocytes as nests and solitary units with few melanocytes scattered in the spinous layer of the epidermis. The papillary dermis showed fibrosis and inflammation. After deliberation and consistent with the RCM findings, the dermatopathologist diagnosed the lesion as an early in situ melanoma (Figure 5.7F).

### *Case 2*

*Clinical Presentation* A 74-year-old man presented to our clinic with a pigmented lesion on the nose. He did not recall any changes in the lesion over the past five years. On general skin examination, several solar lentigines were seen on the face, suggestive of sun-damaged skin. A brown variegated elliptical 8 × 4 mm lesion was seen on the right side of the nose, below the right eye (Figure 5.8A). No regional lymph nodes were palpable. The differential diagnosis included AK, early SCC, and melanoma.

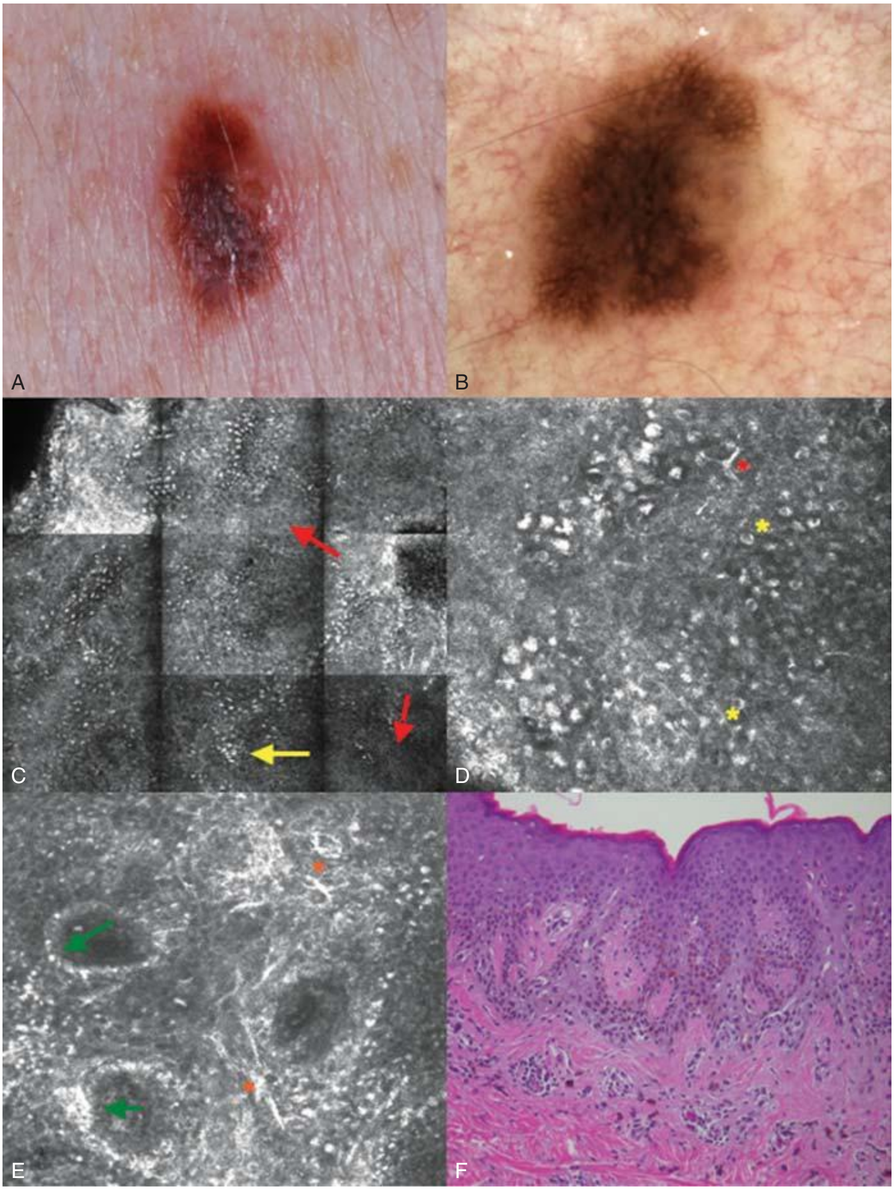

**FIGURE 5.7** (A) Clinical image. (B) Dermoscopic image. (C) At the level of the epidermal spinous layer, the RCM mosaic (1.5 × 1.5 mm) shows heterogeneous reflectivity with sheets of bright cells (yellow arrow) standing out from the background epidermis (red arrows). (D) The RCM individual image (0.5 × 0.5 mm) at the spinous layer level shows bright nucleated round (yellow asterisks) and dendritic cells (red asterisk). (E) An individual RCM image at the DEJ level shows that the dermal papillae (green arrows) are abnormally separated by widened rete ridges that contain an abnormal density of dendritic nucleated cells (orange asterisks). (F) On histopathology, the lesion proved to be an early in situ melanoma.

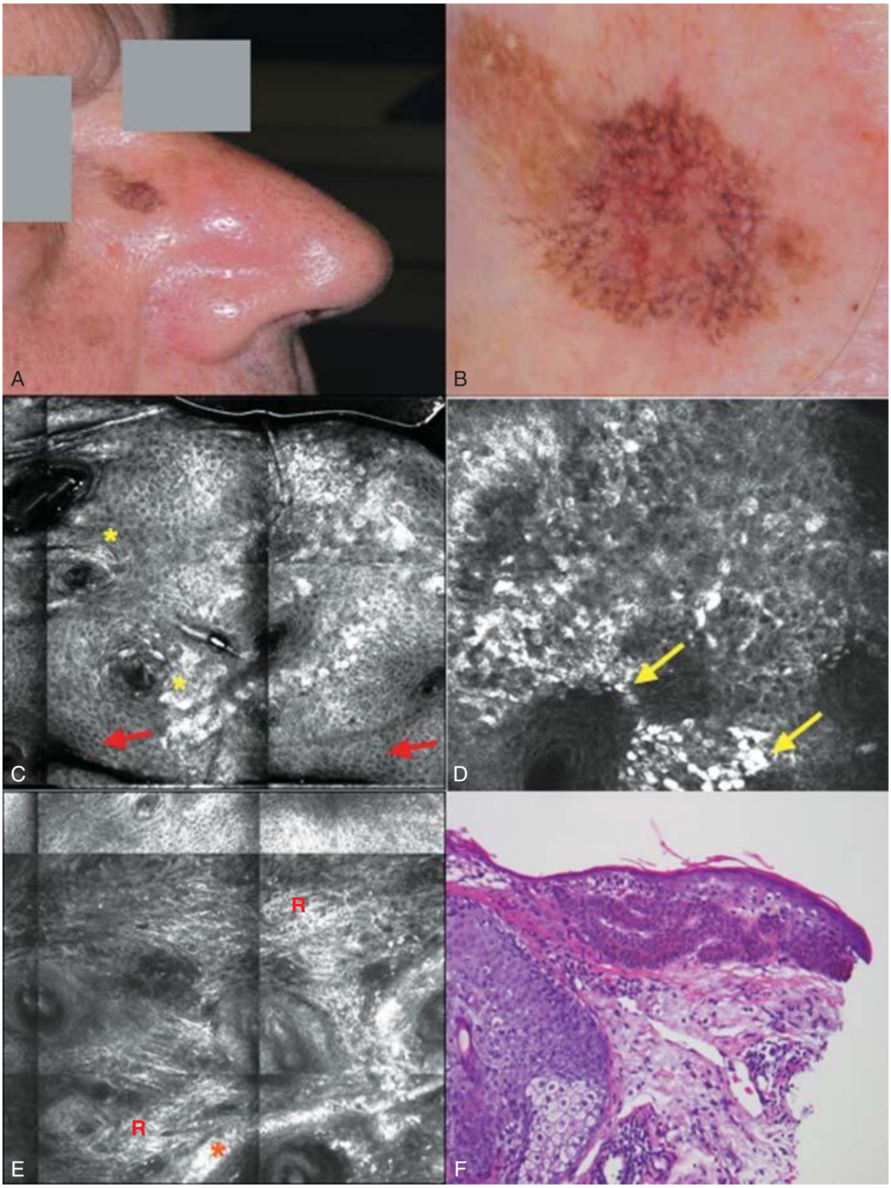

**FIGURE 5.8** (A) Clinical image. (B) Dermoscopic image. (C) The RCM mosaic (2 × 2 mm), at the level of the epidermal spinous layer, showing heterogeneous reflectivity with mostly typical honeycombed pattern (red arrows) and some atypical areas. The honeycomb pattern at foci is disrupted, showing abnormal bright granularity (yellow asterisks). (D) The RCM individual image (0.5 × 0.5 mm) at the level of the basal and spinous layers of the epidermis shows bright cells with some variability of size, shape, and refractility (yellow arrows), compatible with atypical pigmented keratinocytes. (E) The RCM individual image (0.5 × 0.5 mm) at the DEJ and superficial dermis level shows elongated pigmented rete ridges (orange asterisk) and abundant reticular collagen (red R), with many small, bright cells. (F) On histopathology, the lesion proved to be a pigmented proliferative actinic keratosis.

*Dermoscopic Features* The lesion was asymmetric with a gray-brown network-like pattern (Figure 5.8B). The clinician was still unable to make a specific diagnosis, based on the dermoscopic findings, and therefore decided to proceed to RCM examination.

*RCM Features* Three RCM mosaic images (5 × 5 mm field of view) were obtained at the epidermal, DEJ, and dermal levels. Stacks of consecutive individual images (0.5 × 0.5 mm field of view) from the skin surface to the superficial dermis were also obtained. A mosaic imager at the level of the epidermal spinous layer showed areas of a typical honeycomb pattern alternating with areas showing disrupted pattern with heterogeneous reflectivity and scattered bright cells (Figure 5.8C). An atypical honeycomb pattern was seen focally (Figure 5.8D). RCM imaging at the level of the superficial dermis showed abundant reticular collagen and many bright small cells, corresponding to inflammatory cells (Figure 5.8E). No nucleated cells or nests were seen; there were also no dermal tumor islands or "dark silhouettes" to suggest BCC. The focal pleomorphism of keratinocytes, seen as atypical honeycomb, along with lack of pagetoid cellular spread or atypical melanocytes, suggested the diagnosis of AK/early SCC, not melanoma or BCC. A biopsy was performed to rule out an SCC.

*Histopathologic Examination* The lesion was diagnosed as a pigmented, proliferative actinic keratosis (Figure 5.8F).

These two cases demonstrate the immense potential that RCM presents to the trained clinician as a sensitive and specific bedside diagnostic tool for the early detection of melanoma and nonmelanoma skin cancer. By adhering to a methodical imaging protocol followed by algorithm-driven diagnostic criteria, RCM allows for both an overall architectural evaluation of the epidermis, DEJ, and upper dermis and cytomorphologic evaluation. Cellular atypia and polymorphism, including certain nuclear morphologies, can also be visualized in vivo and assist in diagnosis.

At present, diagnosis with RCM also presents certain challenges. First, the depth of imaging is limited, which hampers evaluation of lesion morphology in the deeper dermis and in hyperkeratotic lesions. Second, cellular resolution is suboptimal, and in particular, nuclear details which are indispensable to histopathologic evaluation are difficult to visualize with RCM. Third, in vivo imaging precludes the use of chemical dyes, which at times are useful in histopathology to identify cell types with specificity.

Despite these limitations, RCM shows great potential to serve as an adjunct that significantly improves the bedside accuracy of diagnosis of melanocytic lesions. Pellacani et al. [28] and Guitera et al. [27] have shown recently that in the diagnosis of melanoma, RCM imaging and interpretation by experts resulted in comparable sensitivity to dermoscopy (about 90%) while doubling the diagnostic specificity (RCM 70% vs. dermoscopy 32%). The difference in specificity was even more pronounced in favor of RCM in the evaluation of lightly pigmented or pink melanocytic lesions, which often lack specific dermoscopic features. The authors conclude that RCM has added value in the management of melanocytic lesions.

## 5.7 FUTURE PERSPECTIVES

Reflectance confocal microscopy is an exciting technology with significant promise for clinical utility in dermatology. However, for confocal microscopy to succeed in diverse clinical settings worldwide, the instrumentation must be made smaller, simpler, more robust with repeatable performance, and less expensive. Toward these goals, a handheld confocal microscope (VivaScope 3000) has been developed by Lucid Inc. Alternative simpler designs based on line scanning (instead of the standard point scanning), along with the use of linear array detectors, are being investigated. Such designs, if successful, may eventually reduce the cost of an RCM to less than 20% of its current cost.

Other developments include synergistic multimodal combinations of imaging and spectroscopy. For example, confocal microscopy to visualize nuclear morphology in the epidermis may be combined with optical coherence tomography that shows overall tissue architecture at increased depths in the dermis. Similarly, confocal imaging to observe morphology is being combined with Raman spectroscopy, which provides biochemical information. While the imaging may provide high sensitivity for the detection of cancer, the spectroscopy may provide higher specificity values.

As the translation of RCM from the laboratory into the clinic (i.e., bench to bedside) continues to progress, there are both opportunities and challenges for clinicians and engineers. The key opportunity for the clinician is the ability to observe large volumes of tissue at near-histological resolution in vivo and in real time, and the corresponding challenge is to determine clinical utility and new paradigms. In the short term, the imaging may guide biopsy and lead to intelligent pathology: pathology that is better directed by the subsurface nuclear-level features shown by confocal microscopy. In the longer term, entirely noninvasive screening and diagnosis may be possible. Screening for detection (and prognosis) of early precancers in the epidermis may be a particularly exciting opportunity. The key challenge is image understanding: developing the ability to interpret black-and-white images without the benefit of stains. Image understanding will be crucial for improving sensitivity and specificity (especially, specificity) and may in the long term lead to new paradigms in pathology.

The opportunities and challenges for engineers include the development of very low-cost confocal microscopes, along with telemedicine networks that will enable images to be evaluated rapidly, improved endogenous and exogenous modes of contrast (stains), and multimodal instrumentation aimed at providing clinically relevant sensitivity and specificity values.

## Acknowledgments

The development of RCM technology and translational/clinical research was supported primarily by grants from the National Institutes of Health (NCI and NIBIB). Additional funding support was provided by the Whitaker Foundation, Byrne Fund, Geoffrey Beene Cancer Research Center, and Lucid Inc. We thank Jay Eastman and William Fox for Lucid's support and partnership.

## REFERENCES

1. el Gammal, S., et al., Improved resolution of magnetic resonance microscopy in examination of skin tumors, *J. Invest. Dermatol.*, Vol. 106, 1996, pp. 1287–1292.
2. Wezel, J., Optical coherence tomography in dermatology: a review, *Skin Res. Technol.*, Vol. 7, 2001, pp. 1–9.
3. Jemec, G.B., Gniadecka, M., and Ulrich, J., Ultrasound in dermatology: I. High frequency ultrasound, *Eur. J. Dermatol.*, Vol. 6, 2000, pp. 492–497.
4. Corcuff, P., Bertrand, C., and Leveque, J.L., Morphometry of human epidermis in vivo by real-time confocal microscopy, *Arch. Dermatol. Res.*, Vol. 285, No. 8, 2003, pp. 475–481.
5. Rajadhyaksha, M., et al., In Vivo confocal scanning laser microscopy of human skin: melanin provides strong contrast, *J. Invest. Dermatol.*, Vol. 113, No. 3, 1995, pp. 329–303.
6. Pellacani, G., et al., The impact of in vivo reflectance confocal microscopy for the diagnostic accuracy of melanoma and equivocal melanotic lesions, *J. Invest. Dermatol.*, Vol. 127, No. 12, 2007, pp. 2759–2765.
7. Gareau, D.S., et al., Confocal mosaicing microscopy in Mohs skin excisions: feasibility of rapid surgical pathology, *J. Biomed. Opt.*, Vol. 13, 2008, p. 054001.
8. Huzaira, M., et al., Topographic variations in normal skin, as viewed by in vivo reflectance confocal microscopy, *J. Invest. Dermatol.*, Vol. 116, 2001, pp. 846–852.
9. Gonzalez, S., Gill, M., and Halpern, A.C., *Reflectance Confocal Microscopy of Cutaneous Tumors: An Atlas with Clinical, Dermoscopic and Histological Correlations*, Informa Healthcare, London, 2008.
10. Rubin, A.I., Chen, E.H., and Ratner, D., Basal-cell carcinoma, *N. Engl. J. Med.*, Vol. 353, 2005, pp. 2262–2269.
11. Carucci, J.L. D., Basal cell carcinoma, in *Fitzpatrick's Dermatology in General Medicine*, I.M. Freedberg, A.Z. Eisen, K. Wolff, K.F. Austen, L.A. Goldsmith, and S.I. Katz (eds.), McGraw-Hill, New York, 2003.
12. Brenn, T.M. P., Tumors of the surface epithelium: basal cell carcinoma, in *Pathology of the Skin with Clinical Correlations*, P.H. McKee, E. Calonje, and S.R. Granter (eds.), Elsevier Mosby, St. Louis, MO, 2005.
13. Gonzalez, S., and Tannous, Z., Real-time, in vivo confocal reflectance microscopy of basal cell carcinoma, *J. Am. Acad. Dermatol.*, Vol. 47, 2002, pp. 869–874.
14. Nori, S., Sensitivity and specificity of reflectance-mode confocal microscopy for in vivo diagnosis of basal cell carcinoma: a multicenter study, *J. Am. Acad. Dermatol.*, Vol. 51, 2004, pp. 923–930.

15. Sauermann, K., Investigation of basal cell carcinoma [correction of *carcionoma*] by confocal laser scanning microscopy in vivo, *Skin Res. Technol.*, Vol. 8, 2002, pp. 141–147.
16. Aghassi, D., Anderson, R.R., and Gonzalez, S., Confocal laser microscopic imaging of actinic keratoses in vivo: a preliminary report, *J. Am. Acad. Dermatol.*, Vol. 43, 2000, pp. 42–48.
17. Zalaudek, I., et al., Dermoscopy of facial nonpigmented actinic keratosis, *Br. J. Dermatol.*, Vol. 155, 2006, pp. 951–956.
18. Ulrich, M., et al., Clinical applicability of in vivo reflectance confocal microscopy for the diagnosis of actinic keratoses, *Dermatol. Surg.*, Vol. 34, No. 5, 2008, pp. 610–619.
19. Marks, R., Rennie, G., and Selwood, T.S., Malignant transformation of solar keratoses to squamous cell carcinoma, *Lancet*, Vol. 1, 1988, pp. 795–797.
20. Zalaudek, I., Dermoscopy features of pigmented squamous cell carcinoma: a case report, *Dermatol. Surg.*, Vol. 30, 2004, pp. 539–540.
21. Rinker, M.H., et al., Histologic variants of squamous cell carcinoma of the skin, *Cancer Control*, Vol. 8, 2001, pp. 354–363.
22. Busam, K.J., et al., Detection of intraepidermal malignant melanoma in vivo by confocal scanning laser microscopy, *Melanoma Res.*, Vol. 12, 2002, pp. 349–355.
23. Busam, K.J., Detection of clinically amelanotic malignant melanoma and assessment of its margins by in vivo confocal scanning laser microscopy, *Arch. Dermatol.*, Vol. 137, 2001, pp. 923–929.
24. Langley, R.G., et al., Confocal scanning laser microscopy of benign and malignant melanocytic skin lesions in vivo, *J. Am. Acad. Dermatol.*, Vol. 45, 2001, pp. 365–376.
25. Gerger, A., et al., Diagnostic applicability of in vivo confocal laser scanning microscopy in melanocytic skin tumors, *J. Invest. Dermatol.*, Vol. 124, 2005, pp. 493–498.
26. Pellacani, G., et al., Microscopic in vivo description of cellular architecture of dermoscopic pigment network in nevi and melanomas, *Arch. Dermatol.*, Vol. 141, 2005, pp. 147–154.
27. Guitera, P., et al., In Vivo reflectance confocal microscopy enhances secondary evaluation of melanocytic lesions, *J. Invest. Dermatol.*, Vol. 129, No. 1, 2009, pp. 131–138.
28. Pellacani, G., et al., The impact of in vivo reflectance confocal microscopy for the diagnostic accuracy of melanoma and equivocal melanocytic lesions, *J. Invest. Dermatol.*, Vol. 127, No. 12, 2007, pp. 2759–2765.
29. Pellacani, G., Cesinaro, A.M., and Seidenari, S., Reflectance-mode confocal microscopy of pigmented skin lesions-improvement in melanoma diagnostic specificity, *J. Am. Acad. Dermatol.*, Vol. 53, No. 6, 2005, pp. 979–985.
30. Gerger, A., et al., Sensitivity and specificity of confocal laser-scanning microscopy for in vivo diagnosis of malignant skin tumors, *Cancer*, Vol. 107, 2006, pp. 193–200.
31. Curiel-Lewandrowski, C., et al., Use of in vivo confocal microscopy in malignant melanoma: an aid in diagnosis and assessment of surgical and nonsurgical therapeutic approaches, *Arch. Dermatol.*, Vol. 140, 2004, pp. 1127–1132.
32. Patel, Y.G., et al., Confocal reflectance mosaicing of basal cell carcinomas in Mohs surgical skin excisions, *J. Biomed. Opt.*, Vol. 12, No. 3, 2007, p. 034027.

33. Gareau, D.S., Confocal mosaicing microscopy in skin excisions: a demonstration of rapid surgical pathology, *J. Microsc.*, Vol. 233, 2009, pp. 149–159.
34. Al-Arashi, M.Y., Salomatina, E., and Yaroslavsky, A.N., Multimodal confocal microscopy for diagnosing nonmelanoma skin cancers, *Lasers Surg. Med.*, Vol. 39, 2007, pp. 696–705.
35. Karen, J.K., et al., Detection of basal cell carcinomas in Mohs excisions with fluorescence confocal mosaicing microscopy, *Br. J. Dermatol.*, Vol. 160, No. 6, 2009, pp. 1242–1250.

# 6

# HIGH-RESOLUTION OPTICAL COHERENCE TOMOGRAPHY IMAGING IN GASTROENTEROLOGY

MELISSA J. SUTER, BRETT E. BOUMA, AND GUILLERMO J. TEARNEY

*Harvard Medical School and Wellman Center for Photomedicine at the Massachusetts General Hospital, Boston, Massachusetts*

6.1 Introduction 187
6.2 Optical coherence tomography 188
  6.2.1 Principle of OCT imaging 188
  6.2.2 OCT catheters 189
6.3 Clinical gastrointestinal imaging 192
  6.3.1 Esophagus 192
  6.3.2 Colon 198
  6.3.3 Duodenum 199
  6.3.4 Pancreatobiliary ductal system 199
6.4 Future directions 201
6.5 Conclusions 202
References 203

## 6.1 INTRODUCTION

Optical coherence tomography (OCT) is a high-resolution optical imaging modality that provides cross-sectional images of tissue microstructure. Routinely used clinically in ophthalmic applications, OCT to date has not been widely adopted

---

*Advances in Optical Imaging for Clinical Medicine*, Edited by Nicusor Iftimia, William R. Brugge, and Daniel X. Hammer
Copyright © 2011 John Wiley & Sons, Inc.

as a clinical tool in other disciplines, including gastroenterology, due in part to limited fields of view. OCT is, however, an attractive tool for the interrogation of gastrointestinal tissues, as it rapidly acquires images at resolutions comparable with those of architectural histology, is a noncontact imaging modality, does not require a transducing medium, relies on endogenous contrast, and unlike the collection of forceps biopsy, is a nonexcisional imaging modality. Traditional assessment of gastrointestinal tissues is typically performed by endoscopy with accompanying forceps biopsy in larger-diameter lumens such as the esophagus or the colon, or with brush cytology in the pancreatic or biliary ducts. OCT has shown promise for targeting premalignant mucosal lesions, grading and staging cancer progression, and reducing the risks and sampling error associated with biopsy acquisition. While biopsy is traditionally considered the gold standard for diagnosis of gastrointestinal pathology, in many cases this assessment suffers greatly from sampling errors, with only a small percentage of the involved tissue being imaged. This is especially evident in cases where the disease may be focally distributed. Recent studies of OCT in the gastrointestinal tract have made significant strides toward comprehensive imaging, which may help to reduce the sampling error associated with the current assessment.

The chapter begins with a brief overview of some of the catheters used for in vivo OCT imaging of gastrointestinal tissues. The remainder of the chapter is devoted to the clinical applications of OCT in gastroenterology, including the esophagus, stomach, colon, duodenum, and the pancreatic and biliary ducts.

## 6.2 OPTICAL COHERENCE TOMOGRAPHY

### 6.2.1 Principle of OCT Imaging

Optical coherence tomography is a high-resolution imaging modality that has been demonstrated to provide cross-sectional images of gastrointestinal tissues with a resolution ($<10$ μm) comparable with that of low-power bright-field microscopy [1–3]. OCT images are generated by directing broadband light into tissue and collecting the reflected light using low-coherence interferometry. The broadband source is split into two arms, a reference arm and a sample arm. When the optical pathlength of the light traveled by each arm is identical, the combined light from each channel forms an interference pattern. To construct a single-depth reflectivity profile, in the time-domain implementation of OCT, the reference arm reflector is translated, effectively changing the optical length of the reference arm and hence the depth of the signal measured in the tissue. Three-dimensional images are subsequently comprised of two-dimensional arrays of individual depth profiles generated by scanning the imaging beam with respect to the sample. The image penetration of OCT in tissue is limited to $<2$ mm [2]; however, this is comparable to the depth of tissue specimens obtained by forceps biopsy, the standard of care, and is typically sufficient for diagnosis of epithelial diseases of the gastrointestinal tract.

OCT has many advantages over other imaging techniques used in gastroenterology, including the fact that it is based on fiber optic technology and therefore is amenable to miniaturization into very small-diameter probes that can be delivered through a standard endoscope. OCT does not require removal of the tissue as is the case with assessment by biopsy, and therefore permits monitoring of tissue regions of interest overtime, is a noncontact imaging modality that unlike ultrasound does not require a transducing medium, and relies on endogenous contrast.

Optical frequency-domain imaging (OFDI), also termed swept-source OCT or frequency-domain OCT, is a high-speed second-generation OCT imaging technology [4]. OCT imaging of in vivo tissue had traditionally been limited to relatively small fields of view, due in part to limited acquisition speeds. OFDI is capable of acquiring images at significantly higher rates than those of standard OCT while preserving image contrast and resolution. This capability to image at significantly faster imaging speeds opens up the possibility of imaging very large areas of gastrointestinal mucosa in times that are compatible with incorporation into standard endoscopy procedures. In addition to increasing the field of view that can be imaged with OCT, the decreased image acquisition times of OFDI also act to reduce the motion artifacts that may occur when imaging in vivo. Possible causes of motion artifacts include peristalsis, respiratory, cardiac, or other physiological processes, or gross patient movement with respect to the endoscope or catheter delivery device. Uncontrolled movement of the organ of interest with respect to the imaging catheter may result in nonlinear scanning of the tissue and therefore spatial distortion of the images acquired.

### 6.2.2 OCT Catheters

In vivo OCT imaging requires the use of catheters to deliver and focus the optical imaging beam onto, and to collect the reflected signal from, tissue subsurface structures. In addition, scanning mechanisms must be employed to generate two- or three-dimensional images. Unlike ultrasound, OCT does not require a transducing medium, therefore in many cases allowing for simpler catheter delivery designs. Because OCT is based on fiber optic technology it is possible to develop very small flexible catheters to facilitate in vivo imaging of luminal organs.

In addition to the optical specifications there are several key elements that need to be considered when designing catheters for in vivo use in the gastrointestinal tract, including how the catheter will be delivered to the tissue of interest: in conjunction with an endoscope or in a stand-alone fashion. The mechanical properties of the catheter, including the flexibility, pushability, friction, and torque, are all important characteristics, as is the catheter's overall geometric dimensions. An additional consideration is the possible effect of pressure that the catheter applies on the tissue and how the pressure may alter the images acquired. In 2005, Westphal et al. [5] studied the effect of pressure applied from an imaging catheter on a number of lower gastrointestinal tissues ex vivo. It was found that the OCT image penetration increased with increasing pressures;

however, in many cases the architectural features of the tissues were distorted, specifically the thickness of the mucosa and submucosa of the colon [5]. It is therefore important when interpreting OCT images of gastrointestinal tissues to keep in mind how the images were acquired.

A number of different catheter designs have been used to perform in vivo imaging in gastroenterology, including linear scanning [6], circumferential or radial scanning [7], galvanometric scanners [8], and MEMS scanning catheters [9,10]. Galvanometric scanners and MEMS scanning catheters are both examples of catheters that employ distal actuation, requiring power to be supplied to the distal tip of the catheters. As a result, in clinical gastrointestinal studies, linear and circumferential scanning catheters with proximal actuation have been used predominantly and are an attractive choice, as the design allows the imaging console to be isolated electrically from the OCT catheter, thereby reducing the risk of electric shock to the patient. Design of linear and circumferential scanning catheters is described in greater detail below.

***Linear Scanning Catheters*** In vivo OCT imaging of the gastrointestinal tract has been demonstrated using linear scanning catheters in a number of clinical studies [2,11–13]. Catheters of this design are still frequently utilized in clinical studies for many reasons, including ease of use and the ability to obtain a relatively simple direct registration of histological results obtained from forceps biopsy. The linear scanning imaging catheters typically consist of an optical inner core encased inside an optically transparent sheath. The primary purpose of the sheath, which is typically single-use, is to protect the patient from contact with the reusable inner optical core and to prevent contamination of the optical core with bodily fluids. A common design of the inner optical core consists of a fiber to transmit the OCT signal, coupled to a gradient index lens or other focusing element, and a prism to redirect the signal to the tissue surface. More recent designs often include an additional cylindrical lens to compensate for the astigmatism caused by the sheath. The entire optical assembly is encased inside a metal drive shaft to provide added protection to the optical components against breakage and to convey the necessary translational actuation from the proximal end during tissue scanning. Imaging catheters of this type are typically passed through the auxiliary channel of standard endoscopes, where they are then held adjacent to the tissue regions of interest.

***Circumferential Scanning Catheters*** The optical design of circumferential scanning catheters is in many ways identical to linear scanning catheters; however, the proximal end of the catheter is coupled to an optical rotary junction. Rather than translating the imaging core mechanically, the core is rotated within the outer sheath by a rotary junction. The first demonstration of an optical rotary junction for endoscopic catheter–based imaging was published in 1996 and consisted of a stationary fiber coupled to a rotating fiber through an air gap [7]. Improvements to this design have been made over the years to increase the optical coupling and rotational speeds achievable [14].

Linear and circumferential scanning catheters have been used predominantly for clinical gastrointestinal OCT studies. The advent of OFDI, however, brought forth a need for faster scanning catheters to keep pace with the unprecedented imaging speeds intrinsic to the second-generation OCT technology. Imaging at a faster rate suggested that with appropriate catheter designs, imaging very large volumes, not previously possible with traditional OCT, might be achievable. This led to the development and use of new volumetric imaging paradigms achieved through the combination of circumferential scanning coupled with secondary longitudinal pullbacks to facilitate spiral cross-sectional imaging [14].

Due to the limited ranging depth of OCT, helical scanning catheters were not used routinely in gastroenterology as the large luminal diameters of the esophagus and colon did not accommodate full 360° OCT imaging. One solution to this dilemma was to use a balloon-based centering device (Figure 6.1A). Balloon-based helical scanning catheters act to dilate the esophagus and to center and stabilize the imaging optics within the lumen [15–17]. This is advantageous when the lumen size is large and exceeds the ranging depth of the OCT imaging system. The first reported use of a balloon-based helical scanning catheter in swine in vivo studies was published in 2007 [17], and the first clinical experience with a modified version of this catheter was subsequently published in 2008 [16].

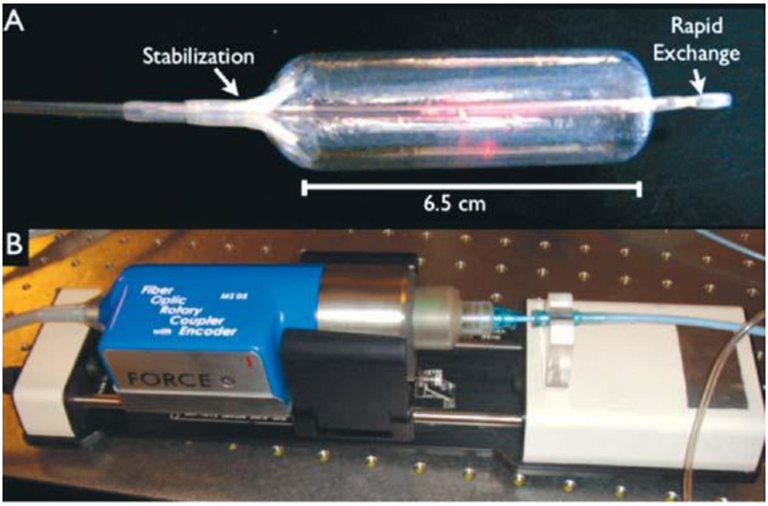

**FIGURE 6.1** (A) Balloon catheter with proximal stabilization device and distal rapid guidewire exchange provision. The balloon acts to dilate the esophageal lumen and center the inner optical core. The inflation diameter of the balloon is 25 mm, and the imaging window is 6.5 cm. The inner optical core (1 mm in diameter) is contained inside a sheath that allows the core to move (rotate and translate) independent of the balloon catheter. (B) Optical rotary junction mounted on the pullback tray and connected to the proximal portion of the imaging catheter. (From [16], with permission.)

## 6.3 CLINICAL GASTROINTESTINAL IMAGING

While OCT imaging has the potential of being applied to essentially any luminal organ within the considerable extents of the gastrointestinal tract, clinical trials have been focused predominantly on imaging the esophagus, and to a smaller extent, the colon, duodenum, pancreas, and biliary ducts. These clinical studies are discussed in detail below.

### 6.3.1 Esophagus

The vast majority of OCT imaging in the gastrointestinal tract has occurred in the esophagus primarily for the purpose of screening for, and the management of, patients with Barrett's esophagus (BE). BE is a condition in which healthy squamous epithelium is replaced by specialized intestinal metaplasia (SIM), placing patients at a higher risk for developing esophageal adenocarcinoma. The development of esophageal adenocarcinoma is thought to involve a stepwise progression from gastroesophageal reflux disease, through SIM, low-grade dysplasia (LGD), high-grade dysplasia (HGD), and finally, adenocarcinoma [18]. Current guidelines for screening of patients with reflux disease for SIM, and surveillance of patients with SIM for dysplasia, recommend regular endoscopy procedures accompanied by the collection of tissue specimens, through forceps biopsy, for histological evaluation [19]. There is much debate about the efficacy of this approach for screening and surveillance due to the large sampling error associated with the systematic but unguided biopsy acquisition, the low diagnostic yield, the high cost associated with the endoscopy procedure, and the knowledge that only a relatively small percentage of individuals will ultimately develop neoplastic changes.

In vivo OCT images of the human esophagus were first published in 1997 by Sergeev et al. using a transverse galvanometric scanning catheter [8]. This initial proof-of-principle pilot study was soon followed by larger in vivo studies by other groups [2,3,8,20,21]. Early in vivo OCT studies of the upper gastrointestinal tract implied that OCT may be a powerful diagnostic tool for the discrimination of different forms of esophageal pathology; however, it wasn't until 2001 that the first study was conducted to develop and prospectively test possible diagnostic criteria to support this supposition [13]. For OCT to be a clinically viable diagnostic device, identification of SIM at the squamocolumnar junction (SCJ) for screening, and identification and grading of dysplasia in patients with SIM for surveillance, is necessary.

***Normal Esophageal Squamous Mucosa and Gastric Cardia*** A number of investigators have reported on the OCT appearance of normal esophageal squamous mucosa and gastric cardia [2,3,22,23]. OCT characteristics of the healthy esophagus reveal a horizontal layered morphology of the squamous epithelium. Figure 6.2A shows an example of normal squamous mucosa with clear delineation of five layers of the mucosa, including the epithelium, lamina

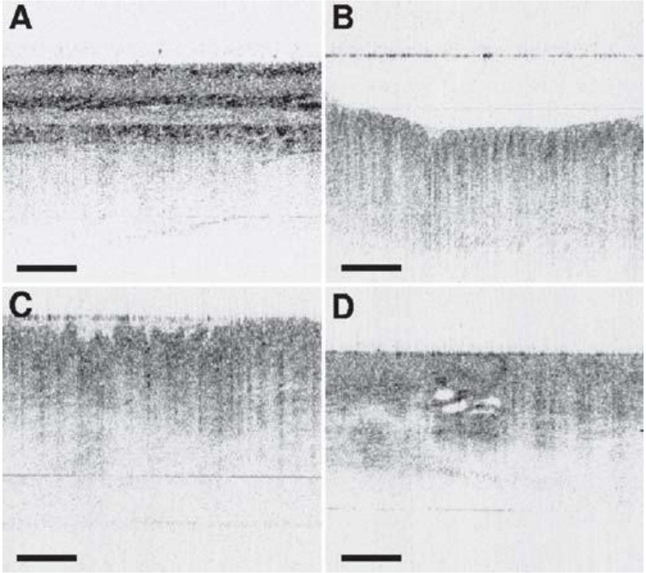

**FIGURE 6.2** (A) OCT image of normal squamous epithelium (bar = 0.5 mm) shows a five-layered appearance (epithelium, lamina propria, muscularis mucosa, submucosa, and muscularis propria). (B) OCT image of gastric mucosa with "pit and crypt" architecture. (C) OCT image of specialized intestinal metaplasia without dysplasia with irregular mucosal surface and absence of a layered or pit and crypt architecture. (D) OCT image of specialized intestinal metaplasia without dysplasia with submucosal glands (circled). (From [11], with permission.)

propria, muscularis mucosa, submucosa, and the muscularis propria. The presence of vessels and glands in the mucosa may also be observed. The OCT image penetration is greater in the squamous mucosa than in other GI tissues, and without significant compression, is approximately 2 mm.

The gastroesophageal junction (GEJ) is the transition region of the GI tract, where the esophagus meets the stomach. OCT images of the gastric cardia, the mucosa at the GEJ, show a regular vertical banding architecture with a pit and crypt appearance, a high superficial surface reflectivity, decreased image penetration (<1 mm), and broad regular glandular architecture. The morphology of the squamous mucosa (Figure 6.2A) and gastric cardia (Figure 6.2B) observed in the OCT images are easily identifiable and clearly distinct.

***Identification of Specialized Intestinal Metaplasia*** OCT images of SIM in the human esophagus have been characterized in a number of OCT studies. A lack of the horizontal layered structure of the squamous mucosa, the lack of the vertical pit and crypt architecture of cardia, heterogeneous scattering, irregular surface topology, and glands in the epithelium with layered architecture are all OCT indicators of SIM (Figure 6.2C and D) [12,13]. Poneros et al., developed diagnostic criteria for the detection of SIM by collecting OCT–biopsy correlated pairs [13]. The investigators performed in vivo OCT imaging using a linear scanning catheter in 121 patients. In addition to the OCT imaging beam, a visible guiding beam was directed through the imaging catheter to highlight the OCT image location within the esophagus. Following OCT imaging the catheter was withdrawn from the endoscope and a forceps biopsy specimen was obtained of the target location. A total of 288 biopsy-correlated OCT images were obtained, and 75 image pairs were used to develop the diagnostic criteria. The criteria were subsequently applied retrospectively to the entire training set of 166 image pairs, resulting in a sensitivity of 100% and a specificity of 93%. When the same diagnostic criteria were applied to an independent validation set comprised of 122 OCT–biopsy correlated pairs, the criteria were found to be 97% sensitive and 92% specific for SIM with or without dysplasia [13]. Although this study made significant advancements toward confirmation that OCT may be a powerful diagnostic tool for the detection of SIM compared to other upper GI tissues, a number of false positives, secondary to inflamed cardia, were noted. For this reason the same group conducted a second study in 2007 focused specifically on the identification of SIM at the SCJ [12]. A similar study design was defined with the acquisition of 196 OCT–biopsy pairs, this time limited to the SCJ region. With refined diagnostic criteria, the investigators reported a sensitivity of 85% and a specificity of 95% when applied retrospectively to a training set of 40 images, and a sensitivity of 81% and a specificity ranging from 57 to 66% when applied prospectively to a validation set of 156 images [12]. A summary of the diagnostic criteria used in the two foregoing studies is given in Table 6.1.

***Identification of Dysplasia*** Identification and diagnosis of dysplasia in SIM is essential for effective surveillance of Barrett's patients. Two groups have investigated the diagnostic potential of OCT to detect dysplasia in the esophagus [11,24]. In 2005, Isenberg et al. obtained OCT–biopsy pairs with a circumferential scanning catheter held at a fixed 30° angle with respect to the esophageal wall [24]. A total of 314 usable OCT–biopsy pairs were obtained from 33 patients. The endoscopist performing the procedure rendered a diagnosis of each of the OCT images immediately following the procedure, and therefore with a priori knowledge of the patient history and prior diagnoses. The pathologist interpreting the biopsies was, however, blinded to the OCT findings. If the endoscopist determined that the OCT image contained dysplasia, the image was further categorized as LGD, HGD, or intramucosal carcinoma (IMC). The authors state that two criteria were used to determine a diagnosis of dysplasia: (1) reduced light scattering and (2) loss of tissue architecture, which they deduced from an earlier pilot study [25]. The reported sensitivity and specificity for the detection of dysplasia were 68% and 82%, respectively, and if the analysis was limited to the detection of HGD, the sensitivity dropped to 50% with a corresponding specificity of 72% [24].

Evans et al. performed a similar study using the same linear scanning probe and approach published in their studies aimed at the detection of SIM [11–13]. The study was designed to develop OCT diagnostic criteria for the identification

**TABLE 6.1 OCT Diagnostic Criteria Developed and Tested Prospectively to Diagnose SIM and to Grade Dysplasia**

| Diagnosis | OCT Finding |
|---|---|
| Normal squamous mucosa | 1. Layered architecture |
| Normal cardia[a] | 1. Vertical pit and crypt architecture<br>2. Highly reflective surface<br>3. Broad, regular glandular architecture<br>4. Poor image penetration |
| SIM[b] | 1. Lack of layered or vertical pit and crypt architecture<br>2. Heterogeneous scattering<br>3. Irregular surface<br>4. Glands in epithelium with layered architecture |
| HGD/IMC[c] | 1. Increased surface/subsurface reflectivity (score 0–2)<br>2. Irregular gland/duct architecture (score 0–2) |

*Source:* Data from [11–13].

[a] See the algorithm in [12].

[b] Two of the first three criteria or the fourth criterion indicate SIM.

[c] A total score of $\geq 2$ indicates HGD/IMC.

of HGD and IMC in SIM. The investigators assessed a total of 177 OCT–biopsy correlated images from 55 patients undergoing surveillance endoscopy for BE. OCT diagnostic criteria were based on histopathologic characteristics, specifically a scoring of surface maturation and gland architecture (Table 6.1). A blinded investigator prospectively analyzed all of the OCT images and assigned a score and corresponding diagnosis. A score of greater than or equal to 2 was considered positive for IMC/HGD. The sensitivity of distinguishing IMC/HGD from all other tissue types was determined to be 83.3%, with a corresponding specificity of 75% [11]. Figure 6.3 shows OCT images of different forms of dysplasia, highlighting features used as diagnostic criteria. A summary of the three studies conducted by this group is presented in Table 6.2.

***Second-Generation OCT Imaging of the Esophagus*** Studies have suggested that OCT imaging of the esophagus can detect and diagnose esophageal pathology relevant to screening and surveillance for BE. Until recently, however, OCT imaging of the esophagus had been restricted to imaging small areas, in a point-sampling fashion similar to that of random biopsy. With <1% of the involved tissue generally being assessed, traditional OCT imaging of BE suffers from the

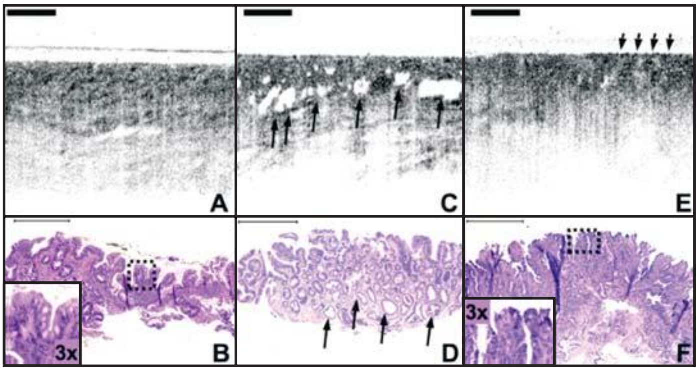

**FIGURE 6.3** OCT images of SIM with and without IMC/HGD. (A) OCT image of SIM without dysplasia demonstrates glandular architecture with a relatively low reflectivity. (B) Histology corresponding to (A) with inset demonstrates a low nuclear/cytoplasm ratio in the superficial epithelium. (C) OCT image of IMC/HGD enables visualization of large and irregular glands (arrows). (D) Irregular, dilated glands are also seen in the histology corresponding to (C) (arrows). (E) OCT image of IMC/HGD shows a disorganized architecture and increased surface reflectivity (arrows). (F) Histology corresponding to (E) demonstrates abnormal glandular architecture and an increased superficial nuclear/cytoplasm ratio (inset). Histology hematoxylin and eosin; original magnification, 40×. Scale bars, 0.5 mm. (From [11], with permission.)

**TABLE 6.2** **Summary of OCT Clinical Studies in Barrett's Esophagus**

| Test | Number of Patients | Number of Biopsies | Sensitivity (%) | Specificity (%) |
|---|---|---|---|---|
| SIM vs. other GI tract tissues | 121 | 288 | 97 | 92 |
| SIM vs. cardia at SCJ | 113 | 196 | 81 | 57–66 |
| IMC/HGD vs. indeterminate-grade dysplasia/LGD/ SIM without dysplasia | 55 | 242 | 83 | 75 |

*Source:* Data from [11–13].

same sampling error as does the standard surveillance biopsy approach, limiting the clinical utility of the technology. Recently, a pilot clinical study was published where large-area comprehensive OFDI of the entire distal esophagus was performed [16]. A balloon-based imaging catheter was used to dilate the esophagus and center the optical imaging core within the lumen. Combined circumferential and longitudinal scanning techniques were implemented to produce spiral cross-sectional images of the entire distal esophagus in longitudinal segments up to 6 cm in length. Figures 6.4 and 6.5 show sample OFDI images of

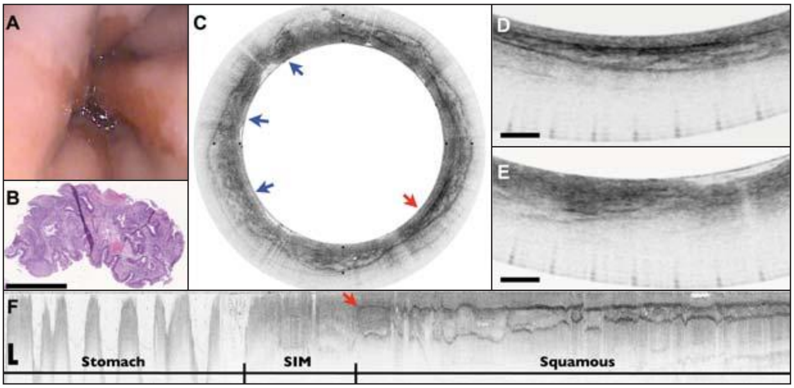

**FIGURE 6.4** Barrett's esophagus. (A) Videoendoscopic image demonstrates an irregular SCJ. (B) Histopathological image of a biopsy specimen obtained from the SCJ demonstrates SIM without dysplasia (H&E, original magnification 2x). (C) Cross-sectional OFDI image reveals both the normal layered appearance of squamous mucosa (red arrow, expanded in D) and tissue that satisfies the OCT criteria for SIM (blue arrows, expanded in E). (F) Longitudinal section across the gastroesophageal junction shows the transition from squamous mucosa to SIM to cardia. The length of the BE segment is 7 mm in this OFDI reconstruction. Scale bars (B, D, E, and F) and tick marks (C) represent 1 mm. (From [16], with permission.)

BE, and BE with dysplasia, acquired with the balloon-based imaging catheter. The endoscopy images in Figures 6.4A and 6.5A depict an irregular transition zone (z-line) between the squamous mucosa (pale pink in color) and the glandular tissue of the gastric cardia (dark pink in appearance), which is consistent with the presence of SIM. Endoscopy alone is, however, generally insufficient to detect further changes, such as the presence of dysplasia, which was detected successfully with OFDI in Figure 6.5E. Although this study has demonstrated that large-area high-resolution OFDI imaging of the entire distal esophagus is possible, to date the investigators could not perform direct correspondence of the OFDI data with histopathological analysis of biopsy specimens, the gold standard. Two solutions are suggested to address this limitation. The first involves reimaging the esophagus following biopsy and co-registering the pre- and post-biopsy OFDI data sets to determine the biopsy locations. The second approach involves esophageal marking immediately following OFDI imaging with the balloon catheter still in place, which would provide the foundation for a guided biopsy platform. Direct registration of the OFDI data sets and histopathology would enable a study to compare the accuracy of the OCT diagnostic criteria developed previously when applied to the balloon-based OFDI images, a critical step in translating this technology to clinical practice. If successful, the capability to obtain microscopic image data noninvasively over large epithelial surface areas may aid in early detection, diagnosis, and intervention, resulting in a consequent reduction in morbidity and mortality associated with BE.

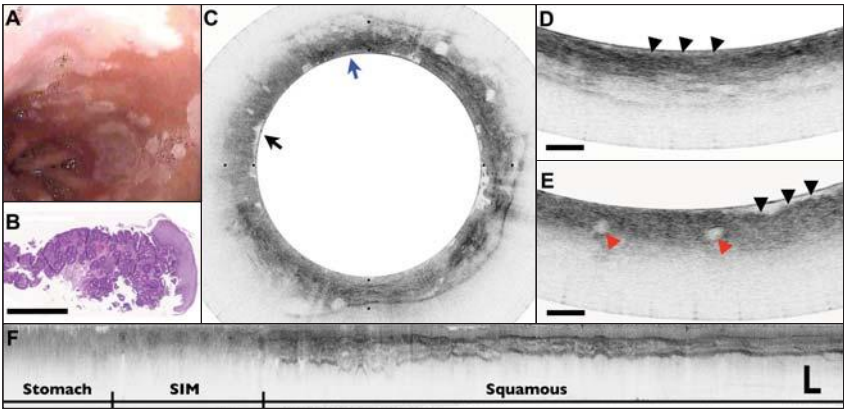

**FIGURE 6.5** Barrett's esophagus with dysplasia. (A) Videoendoscope image reveals a patchy mucosa consistent with SIM. (B) Histopathologic image of the biopsy taken from the SCJ demonstrates intestinal metaplasia and low-grade dysplasia. (C) Cross-sectional OFDI image, demonstrating regions consistent with SIM without dysplasia (blue arrow) and SIM with HGD (black arrow). (D) Expanded view of C, taken from the region denoted by the blue arrow in C, demonstrating good surface maturation (arrowheads), which is consistent with SIM without dysplasia. (E) Expanded view of C, taken from the region denoted by the black arrow in C, demonstrating features consistent with HGD, including poor surface maturation (black arrowheads) and the presence of dilated glands (red arrowheads) in the mucosa. (F) A longitudinal slice highlights the transition from gastric cardia, through a 9-mm segment of SIM, and finally, into squamous mucosa. Scale bars (B, D, E, and F) and tick marks (C) represent 1 mm. (From [16], with permission.)

### 6.3.2 Colon

OCT imaging of the colon has been suggested to have potential clinical utility for the differentiation of colonic polyps, the detection and staging of early carcinoma of the colon [3,21], and the evaluation of inflammation in Crohn's disease and ulcerative colitis [26,27]. The first in vivo OCT imaging of the colon demonstrated that OCT provides sufficient resolution and contrast to identify the mucosa, including colonic crypts, the muscularis mucosa, and the submucosa of the colon [3,21]. As is the case in the esophagus, OCT images of carcinoma of the colon reveal a loss of the layered architecture found in healthy mucosa [3]. Future studies are required to further investigate the diagnostic potential of OCT for the detection of carcinoma of the colon.

Differentiation of Crohn's disease from ulcerative colitis, both inflammatory bowel diseases, is important, as treatment options may vary greatly. The correct diagnosis is often difficult, even by histopathology, as the depth of endoscopic biopsy is insufficient to determine transmural inflammation, which is an indicator of Crohn's disease. In 2004, Shen et al. demonstrated the diagnostic potential of OCT to differentiate Crohn's disease from ulcerative colitis in an ex vivo imaging study of 585 histology-correlated OCT images obtained from 48 patients [26].

The sensitivity for the detection of transmural disease by OCT was found to be 86% sensitive and 91% specific. The same investigators have also performed an in vivo OCT study using the diagnostic criteria developed previously in the ex vivo study [27]. 601 OCT images were obtained from 70 patients with prior clinical diagnosis of either Crohn's disease or ulcerative colitis. The in vivo sensitivity and specificity for the diagnosis of transmural inflammation in Crohn's disease was found to be 90.0% and 83.3%, respectively [27]. These studies demonstrate that OCT can accurately detect a disruption in the normal layered structure of the colon wall indicative of transmural inflammation, a hallmark feature of Crohn's disease.

### 6.3.3 Duodenum

Investigating the duodenal mucosa with OCT may have clinical utility in the early detection of celiac disease in the pediatric population, and to a lesser extent in adults. OCT imaging of the human duodenum has been demonstrated in vivo previously in a number of pilot studies [21,28]. In 2000, Sivak et al. used a circumferential scanning catheter to obtain images from healthy gastrointestinal tissues, including 12 duodenum sites [21] The acquired OCT images allow differentiation of individual villi; however, when the imaging probe was in contact with the duodenum, differentiation of individual villi was more ambiguous. In 2007, Masci et al. published the first OCT images of the duodenum of patients with celiac disease [28]. The duodenum of 18 patients with, and 22 without, suspicion of celiac disease were imaged with OCT, and the locations imaged were subsequently biopsied for histopathologic analysis. Blinded interpretation of the villi morphology in the OCT images and in the histology slides gave identical results in all samples [28]. The promising results from this pilot study indicate that OCT imaging of the duodenum may aid in the detection and diagnosis of celiac disease. In addition, comprehensive large-area OCT imaging of the duodenum may reduce the large sampling error associated with the detection of celiac disease where the distribution of mucosal lesions is often sporadic.

### 6.3.4 Pancreatobiliary Ductal System

Diagnosis of cholangiocarcinoma, an adenocarcinoma of the bile ducts, and adenocarcinomas associated with the pancreatic ducts, typically occur in the advanced stages, leaving patients with a poor prognosis. When suspected, an endoscopic retrograde cholangiopancreatography (ERCP) imaging procedure may be performed to investigate the biliary and pancreatic ducts and to provide access for diagnostic tests, such as forceps biopsy or brush cytology. Unfortunately, the diagnostic yields of forceps biopsy and brush cytology are low, are difficult to obtain, and may be associated with a high risk of complications. For this reason, high-resolution imaging of the pancreatic and hepatobiliary ductal system may prove beneficial.

The first clinical OCT demonstration in the common bile duct was performed in 2001 [29]. Seitz et al. utilized both a 2.8-mm-diameter forward-viewing catheter in three patients and a longitudinal scanning catheter in one patient [29]. The OCT imaging probe was delivered through the working channel of a standard duodenoscope during an ERCP procedure. OCT images of the biliary duct wall revealed a layered architecture as seen in histology. In addition, the presence of glands and vessels in the stroma were identified [29]. This pilot study demonstrated the feasibility of OCT for investigating the human bile ducts and in addition provided preliminary results suggesting that OCT may afford images with sufficient detail to detect biliary pathology.

In 2002, Poneros et al. performed in vivo OCT imaging of the extra- and intrahepatic bile duct using a 2.6-mm circumferential scanning catheter [30]. The goal of this pilot study was to demonstrate the feasibility of intraductal OCT of the biliary tract as a diagnostic tool. In vivo images were obtained of the bile ducts in five patients. The architectural features identified in the OCT images acquired in vivo were compared to OCT–histology image pairs obtained from five cadaver specimens. Figure 6.6 shows an OCT image obtained in vivo of the extrahepatic biliary epithelium. Based on the layered architecture, including the epithelium, a highly scattering submucoa, and the serosa, the OCT image was classified as normal. Figure 6.7 shows an example of an OCT image of a presumed cholangiocarcinoma obtained in vivo. Histologically, diagnosis of cholangiocarcinoma may be made by the presence of villiform papillary morphology. These features were observed in the OCT images of Figure 6.7 (arrow). Although images obtained during this study indicate that OCT imaging of the biliary tree does provide images with sufficient resolution and contrast for the

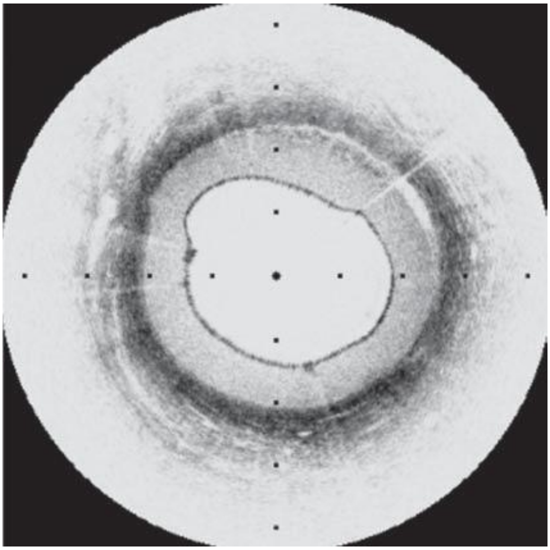

**FIGURE 6.6** Circularized OCT image of the extrahepatic biliary epithelium obtained in vivo demonstrating different layers (scale bar, 0.5 mm). (From [30], with permission.)

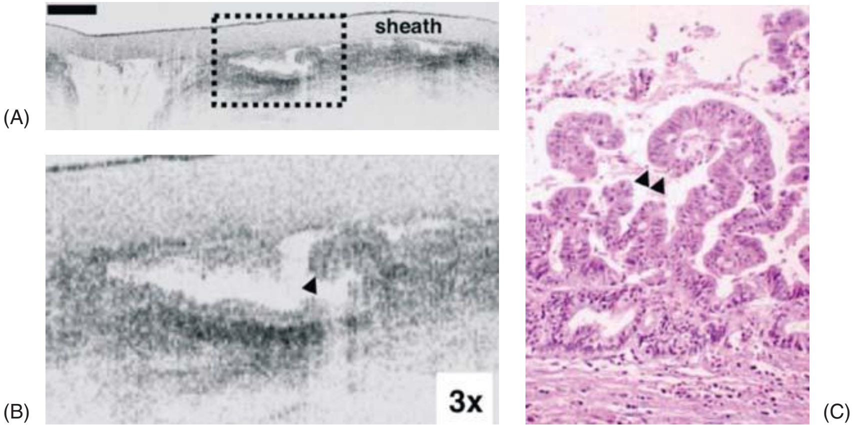

**FIGURE 6.7** (A) OCT image of cholangiocarcinoma obtained in vivo (scale bar, 0.5 mm). (B) Expanded view of (A) taken from the region denoted by the box, showing papillary fronds. (C) Photomicrography of a reference histological section of papiliary cholangiocarcinoma showing papillary fronds similar to those seen by OCT (H&E, original magnification 40×). (From [30], with permission.)

evaluation of biliary strictures, to date no further more rigorous clinical studies have been performed.

Testoni et al. published the first demonstration of in vivo OCT of the pancreatic duct in 2007 [31]. The investigators imaged the main pancreatic ducts of 12 patients with main pancreatic duct strictures using a 1.2-mm-diameter circumferential scanning catheter during an ERCP procedure [31]. A layered architecture was observed in all cases of normal pancreatic ductal epithelium, and a loss of the layered architecture was observed in neoplastic lesions [31]. This pilot study demonstrates that OCT is a feasible tool for the investigation of pancreatic strictures during an ERCP procedure and may aid in the diagnosis of neoplasia. Further clinical studies are needed to determine the diagnostic utility of OCT imaging of the pancreatic duct; however, given that the vast majority of pancreatic cancers arise in the ductal epithelium, screening of patients at an increased risk of developing pancreatic malignancies with an optical imaging technology such as OCT may be warranted.

## 6.4 FUTURE DIRECTIONS

Many clinical studies, primarily in the esophagus, have demonstrated conclusively that OCT has the potential to become a valuable tool in the routine care of patients with gastrointestinal disorders. In addition to larger clinical OCT studies required in all gastrointestinal organs, there are technical barriers that need to be overcome before this becomes a reality. First, traditional small-area imaging with OCT suffers from the same sampling errors as does standard endoscopic biopsy and therefore does not improve on the current standard of care. The newly demonstrated volumetric imaging through helical scanning is making steps toward addressing this issue; however, there is currently no reliable way of directly registering the OCT images with histology for diagnostic confirmation, a step that is essential in the validation of the imaging paradigm as a future diagnostic tool. With further modifications, such as the capability to mark or tattoo the tissue to act as registration points for confirmation by biopsy or to guide biopsy, volumetric OCT imaging may overcome many of the limitations inherent in the current random biopsy approach. Additional technical advancement, including Doppler OCT imaging, which has been demonstrated successfully in the swine esophagus [32] and in a pilot clinical study [33], and ultrahigh-resolution OCT [34,35] may additionally increase the diagnostic sensitivity of OCT.

Data storage, manipulation, and display are key elements that will need to be tackled before OCT is adopted into the clinical diagnostic realm. Comprehensive OCT imaging of large areas generates staggering amounts of data at very fast acquisition rates. Navigating these data sets compatible with procedural times poses a technical challenge and suggests a need for the development of automated or semiautomated image analysis programs to highlight suspicious tissue regions of interest in real time, or close to real time, and to guide the treating physician to these regions.

To date, clinical gastrointestinal OCT imaging has been restricted to regions accessible by endoscopes; however, the development of new needle-based OCT imaging probes may open up the possibility of imaging solid tissues such as liver nodules, lymph nodes, pancreatic cysts, or tissue regions that are inaccessible by endoscopy or extend beyond the 1- to 2-mm imaging depth of OCT. In one such preclinical feasibility study, published in 2000 by Li et al. [36], the authors utilized a 27-gauge needle–based OCT catheter to image the swine pancreatic parenchyma. Although needle-based OCT catheters have not yet been incorporated into clinical studies, this early preclinical study suggests that it may have a role in gastroenterology in the interrogation of solid tissues and organs.

## 6.5 CONCLUSIONS

For OCT to become a widely adopted clinical tool in gastrointestinal imaging, it needs to surpass current assessment techniques. OCT has been demonstrated in both the biliary and pancreatic ducts, where biopsy acquisition is difficult and in some instances unsafe, and it has also been demonstrated in larger luminal organs, including the esophagus and colon, where the diagnostic yield of current biopsy assessment suffers greatly from sampling errors. With further clinical studies in all gastrointestinal organ systems coupled with the technological advancements constantly occurring in the optical imaging field, the diagnostic power, clinical utility, and hence use of OCT in gastroenterology will no doubt increase.

## REFERENCES

1. Tearney, G.J., et al., In vivo endoscopic optical biopsy with optical coherence tomography, *Science*, Vol. 276, 1997, pp. 2037–2039.
2. Bouma, B.E., et al., High-resolution imaging of the human esophagus and stomach in vivo using optical coherence tomography, *Gastrointest. Endosc.*, Vol. 51, 2000, pp. 467–474.
3. Jackle, S., et al., In vivo endoscopic optical coherence tomography of the human gastrointestinal tract: toward optical biopsy, *Endoscopy*, Vol. 32, No. 10, 2000, pp. 743–749.
4. Yun, S.H., et al., High-speed optical frequency-domain imaging, *Opt. Express*, Vol. 11, 2003, pp. 2953–2963.
5. Westphal, V., et al., Correlation of endoscopic optical coherence tomography with histology in the lower-GI tract, *Gastrointest. Endosc.*, Vol. 61, No. 4, 2005, pp. 537–546.
6. Bouma, B.E., and Tearney, G.J., Power-efficient nonreciprocal interferometer and linear-scanning fiber-optic catheter for optical coherence tomography, *Opt. Lett.*, Vol. 24, No. 8, 1999, pp. 531–533.
7. Tearney, G.J., et al., Scanning single-mode fiber optic catheter-endoscope for optical coherence tomography, *Opt. Lett.*, Vol. 21, No. 7, 1996, pp. 543–545.
8. Sergeev, A.M., et al., In vivo endoscopic OCT imaging of precancer and cancer states of human mucosa, *Opt. Express*, Vol. 1, 1997, pp. 432–440.
9. Liu, X., et al., Rapid-scanning forward-imaging miniature endoscope for real-time optical coherence tomography, *Opt. Lett.*, Vol. 29, No. 15, 2004, pp. 1763–1765.
10. Kim, K.H., et al., Two-axis magnetically-driven MEMS scanning catheter for endoscopic high-speed optical coherence tomography, *Opt. Express*, Vol. 15, No. 26, 2007, pp. 18130–18140.
11. Evans, J.A., et al., Optical coherence tomography to identify intramucosal carcinoma and high-grade dysplasia in Barrett's esophagus, *Clin. Gastroenterol. Hepatol.*, Vol. 4, No. 1, 2006, pp. 38–43.
12. Evans, J.A., et al., Identifying intestinal metaplasia at the squamocolumnar junction using optical coherence tomography, *Gastrointest. Endosc.*, Vol. 65, 2007, pp. 50–56.
13. Poneros, J.M., et al., Diagnosis of specialized intestinal metaplasia by optical coherence tomography, *Gastroenterology*, Vol. 120, No. 1, 2001, pp. 7–12.
14. Yun, S.H., et al., Comprehensive volumetric optical microscopy in vivo, *Nat. Med.*, Vol. 12, No. 12, 2006, pp. 1429–1433.
15. Fu, H.L., et al., Flexible miniature compound lens design for high-resolution optical coherence tomography balloon imaging catheter, *J. Biomed. Opt.*, Vol. 13, No. 6, 2008, p. 060502.
16. Suter, M.J., et al., Comprehensive microscopy of the esophagus in human patients with optical frequency domain imaging, *Gastrointest. Endosc.*, Vol. 68, No. 4, 2008, pp. 745–753.
17. Vakoc, B.J., et al., Comprehensive esophageal microscopy by using optical frequency-domain imaging, *Gastrointest. Endosc.*, Vol. 65, No. 6, 2007, pp. 898–905.
18. Lagergren, J., et al., Symptomatic gastroesophageal reflux and a risk factor for esophageal adenocarcinoma, *N. Engl. J. Med.*, Vol. 340, No. 11, 1999, pp. 825–831.

19. Incarbone, R., et al., Outcome of esophageal adenocarcinoma detected during endoscopic biopsy surveillance for Barrett's esophagus, *Surg. Endosc.*, Vol. 16, 2002, pp. 263–266.
20. Jackle, S., et al., In vivo endoscopic optical coherence tomography of esophagitis, Barrett's esophagus, and adenocarcinoma of the esophagus, *Endoscopy*, Vol. 32, No. 10, 2000, pp. 750–755.
21. Sivak, M.V., Jr., et al., High-resolution endoscopic imaging of the GI tract using optical coherence tomography, *Gastrointest. Endosc.*, Vol. 51, 2000, pp. 474–479.
22. Brand, S., et al., Optical coherence tomography in the gastrointestinal tract, *Endoscopy*, Vol. 32, No. 10, 2000, pp. 796–803.
23. Li, X.D., et al., Optical coherence tomography: advanced technology for the endoscopic imaging of Barrett's esophagus, *Endoscopy*, Vol. 32, 2000, pp. 921–930.
24. Isenberg, G., et al., Accuracy of endoscopic optical coherence tomography in the detection of dysplasia in Barrett's esophagus: a prospective, double-blinded study, *Gastrointest. Endosc.*, Vol. 62, No. 6, 2005, pp. 825–831.
25. Das, A., et al., High-resolution endoscopic imaging of the GI tract: a comparative study of optical coherence tomography versus high-frequency catheter probe EUS, *Gastrointest. Endosc.*, Vol. 54, No. 2, 2001, pp. 219–224.
26. Shen, B., et al., Ex vivo histology-correlated optical coherence tomography in the detection of transmural inflammation in Crohn's disease, *Clin. Gastroenterol. Hepatol.*, Vol. 2, No. 9, 2004, pp. 754–760.
27. Shen, B., et al., In vivo colonoscopic optical coherence tomography for transmural inflammation in inflammatory bowel disease, *Clin. Gastroenterol. Hepatol.*, Vol. 2, No. 12, 2004, pp. 1080–1087.
28. Masci, E., et al., Pilot study on the correlation of optical coherence tomography with histology in celiac disease and normal subjects, *J. Gastroenterol. Hepatol.*, Vol. 22, No. 12, 2007, pp. 2256–2260.
29. Seitz, U., et al., First in vivo optical coherence tomography in the human bile duct, *Endoscopy*, Vol. 33, No. 12, 2001, pp. 1018–1021.
30. Poneros, J.M., et al., Optical coherence tomography of the biliary tree during ERCP, *Gastrointest. Endosc.*, Vol. 55, No. 1, 2002, pp. 84–88.
31. Testoni, P.A., et al., Intraductal optical coherence tomography for investigating main pancreatic duct strictures, *Am. J. Gastroenterol.*, Vol. 102, No. 2, 2007, pp. 269–274.
32. Vakoc, B.J., et al., Comprehensive esophageal microscopy by using optical frequency-domain imaging (with video), *Gastrointest. Endosc.*, Vol. 65, No. 6, 2007, pp. 898–905.
33. Yang, V.X. D., et al., Endoscopic Doppler optical coherence tomography in the human GI tract: initial experience, *Gastrointest. Endosc.*, Vol. 61, No. 7, 2005, pp. 879–890.
34. Chen, Y., et al., Ultrahigh resolution optical coherence tomography of Barrett's esophagus: preliminary descriptive clinical study correlating images with histology, *Endoscopy*, Vol. 39, No. 7, 2007, pp. 599–605.
35. Hsiung, P.-L., et al., Ultrahigh-resolution and 3-dimensional optical coherence tomography ex vivo imaging of the large and small intestines, *Gastrointest. Endosc.*, Vol. 62, No. 4, 2005, pp. 561–574.
36. Li, X., et al., Imaging needle for optical coherence tomography, *Opt. Lett.*, Vol. 25, No. 20, 2000, pp. 1520–1522.

# 7

# HIGH-RESOLUTION CONFOCAL ENDOMICROSCOPY FOR GASTROINTESTINAL CANCER DETECTION

JONATHAN T. C. LIU
*State University of New York at Stony Brook, Stony Brook, New York*
JONATHAN W. HARDY AND CHRISTOPHER H. CONTAG
*Stanford University School of Medicine, Stanford, California*

7.1 Introduction and motivation 206
  7.1.1 The emerging field of in vivo pathology 206
  7.1.2 Clinical needs addressed by GI confocal endomicroscopy 207
  7.1.3 Needs for instrument development 209
  7.1.4 Needs for reagent development 211
7.2 Conventional confocal endomicroscopy 212
  7.2.1 Miniature optics 215
  7.2.2 Fiber-bundle vs. single-fiber approaches 216
  7.2.3 Laser scanning approaches 218
7.3 Dual-axis confocal endomicroscopy 220
  7.3.1 Background 220
  7.3.2 Theory 222
  7.3.3 Deep tissue imaging 223
7.4 Toward larger fields of view: mosaicing 223
7.5 Summary and future directions 225
  7.5.1 Advances and accomplishments 225
  7.5.2 Telepathology 226
  7.5.3 Future of instrumentation development 226
References 227

---

*Advances in Optical Imaging for Clinical Medicine*, Edited by Nicusor Iftimia, William R. Brugge, and Daniel X. Hammer
Copyright © 2011 John Wiley & Sons, Inc.

## 7.1 INTRODUCTION AND MOTIVATION

Advances in confocal microscopy have contributed greatly to our understanding of cell biology [1–4]. Following upon these advances has been the development of miniaturized microscopes, in the emerging field of confocal endomicroscopy, for visualizing live tissues inside the body. Some of the greatest advances in this burgeoning field have been in the area of gastrointestinal imaging for disease detection. Thus, in this chapter we focus on the design and implementation of confocal microscopes for use during upper and lower gastrointestinal (GI) endoscopy. The past decade has witnessed significant developments in this field, as driven by clinical needs. Initially, we focus on these clinical motivations as well as design parameters for GI endomicroscopy. The principles and theory of confocal microscopy have been covered thoroughly by many others [5–7]. Therefore, we provide only the essentials for understanding GI endomicroscopy and focus on the latest efforts to develop miniature confocal microscopes that are compatible with GI endoscopy. In particular, the application of confocal microscopy for the interrogation of epithelial surfaces of the GI tract presents unique design challenges. We review the various instrument designs and discuss both the issues that they address and those that remain problematic. We also describe some of the new directions being pursued for the advancement of these technologies. Miniature two-photon microscopes are also being developed to enable optical sectioning of GI tissues. However, these technologies are not covered in this chapter.

### 7.1.1 The Emerging Field of In Vivo Pathology

The advent of confocal endomicroscopes has helped to usher in the emerging field of in vivo pathology. Since histopathology has long been considered the gold standard for diagnosing disease, bringing the microscope to the patient rather than the tissue biopsy to the pathology lab is one way that accurate real-time diagnoses of disease states may be made at the bedside. This has been the goal of many optical technologies and it is becoming a reality as these technologies advance. Microscopic visualization of tissue microarchitecture, including visualization of cellular and glandular morphology, nuclear atypia, cellular polarity, and other morphological features, has proven to be one of the most reliable methods for identifying and staging disease states. For excised tissues, visualization of these microstructures has been aided by the use of histological stains, where functional changes can be revealed using labeled ligands and antibodies. These reagents allow pathologists to identify and often quantify molecular markers of disease. This has enabled improved diagnoses and advances in molecular medicine, where an understanding of the molecular basis of disease reveals new targets for therapy. For endomicroscopy to shift the clinical paradigm toward in vivo pathology, similar molecular probes will need to be developed for in vivo microscopy.

There are significant distinguishing features between endomicroscopy and conventional histopathology. Conventional histology slides are constructed from three-dimensional tissues that have been excised, dehydrated, fixed, stained, sliced, and exposed to any number of other blocking, rinsing, and contrast-enhancing reagents. These exacting protocols are required to visualize tissue microarchitecture using conventional bright-field and fluorescence microscopes. Unfortunately, such tissue-processing procedures can lead to image artifacts. These have become, in some cases, integrated into a pathologist's image interpretation and used as diagnostic cues. For example, certain shrinkage artifacts are used as features that contribute to the diagnosis. Furthermore, the orientation of these tissue sections is often arbitrary, leaving the pathologist with the task of inferring tissue orientation through morphological clues under the microscope. Although this may not be difficult to accomplish for well-ordered normal tissues, tissue orientation may be impossible to determine in a malignant tissue sample such as a tumor biopsy. Obviously, for the purposes of staging cancer, knowledge of tissue orientation and depth could be of great value. Finally, there are a number of studies indicating that there are significant interobserver discrepancies, even between well-trained pathologists who view the same tissue sections [8–10]. What in vivo pathology offers is the potential to visualize tissues in their native, undisturbed, and fully functioning physiological state. It is anticipated that observing pathological changes in the context of the intact organ may offer the pathologist additional insights that may aid in a diagnosis, in addition to having the added advantage of being more rapid. Efforts are being made to develop miniature confocal microscopes for in vivo use. In particular, a number of academic and industrial groups are developing confocal microscopes that are compatible with gastrointestinal endoscopy (see Sections 7.1 to 7.3). The ability to visualize three-dimensional cellular physiology and pathophysiology in real time is now within the realm of possibility in clinical settings.

In summary, confocal endomicroscopy seeks to move away from the paradigm in which tissues are excised, processed, and brought to a large microscope for imaging; and toward the paradigm in which the microscope is miniaturized and brought to the living tissue in its native environment. This will enable real-time imaging of three-dimensional cellular, morphological, molecular, and physiological features for improved understanding and diagnosis of gastrointestinal diseases.

### 7.1.2 Clinical Needs Addressed by GI Confocal Endomicroscopy

Confocal endomicroscopes continue to be developed for unique clinical applications. Perhaps the most basic application of such a device would be to provide a real-time "optical biopsy." Physical biopsies are currently the most common procedures performed during endoscopy. In the lower GI tract, polyps and other suspicious lesions are routinely biopsied and submitted for histopathological examination. Such biopsies are used to determine if polyps are benign (hyperplastic) lesions or adenomatous (dysplastic) lesions with precancerous potential. In the upper GI tract, biopsies are taken similarly from patients exhibiting various esophageal or gastric malignancies. For example, in the case of Barrett's esophagus, which often arises in patients afflicted with gastroesophageal reflux disease (GERD), up to dozens of biopsies are obtained in order to monitor for precancerous dysplasia. More specifically, the Seattle protocol, which is considered the optimal method for detecting early cancers in patients with Barrett's esophagus, calls for random four-quadrant biopsies to be taken at 1-cm intervals along suspicious lengths of the esophagus [11]. Even though multiple biopsies are obtained in these cases, the tissue samples are often pooled, resulting in a loss of spatial information. In in vivo microscopy, the tissue coordinates are intrinsically linked to the data sets, offering a significant advantage for the endoscopist during interrogation of a suspicious area of the tissue.

Although endoscopic biopsies are generally simple procedures, complications may still arise, including uncontrollable bleeding and perforation of the tissue. This is especially true for patients on blood thinners or with existing blood-related conditions such as anemia. Another disadvantage of biopsies is the lack of real-time information. Therefore, following a diagnosis, endoscopic procedures will often be repeated to treat the pathologically determined condition. This obviously leads to higher clinical costs as well as lost time for the patient. It is a well-known fact that there are not enough endoscopists, even within a developed country such as the United States, to cover every person for whom routine endoscopy is recommended. An optical biopsy device, which could provide instant pathological feedback to an endoscopist and allow for immediate therapeutic intervention, could greatly reduce the time, cost, and inconvenience of endoscopic procedures.

Although the eventual goal of optical biopsy would be to replace physical biopsy, the performance of early technologies may not trump the gold standard of traditional histopathology. Nevertheless, there is much interest in confocal endomicroscopes that could inform the endoscopist and provide a guide for physical biopsy. Early optical biopsy devices may not be powerful enough to enable the staging of disease, due to limitations in imaging depth, resolution, and/or contrast. However, they should be able to distinguish between normal and abnormal tissues [12–14]. Such a tool could reduce the number of unnecessary biopsies that are taken and sent for histological processing, thus providing a great reduction in clinical and laboratory effort, as well as cost. Examples of in vivo images currently obtainable with confocal endomicroscopy are shown in Figure 7.1. The images shown were all acquired with a commercially available confocal endomicroscope that has been integrated into a custom endoscope co-developed by Pentax/Optiscan [12].

In addition to optical biopsy, confocal endomicroscopy has the potential to see beyond what's possible with traditional biopsy. Near-video-rate microscopes are being developed, not only to reduce motion artifacts during imaging, but also to observe physiological processes in real time. Future explorations are bound to uncover new diagnostic methods using video-rate in vivo microscopy. Potential applications include monitoring real-time transport of fluorescent molecules through colonic crypts (glands), or the trafficking of cells through blood and lymphatic vasculature. An example of a commercially available fibered confocal endomicroscope, with rapid imaging capabilities, is the Cellvizio GI. With an

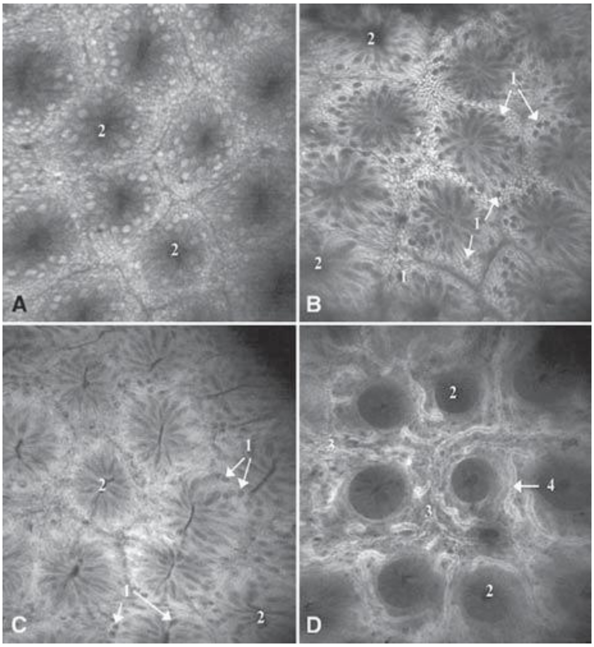

**FIGURE 7.1** Single-frame images (500 × 500 μm) of in vivo normal human colon and terminal ileum, obtained with a confocal endomicroscope manufactured by Pentax/Optiscan: (A) rectal mucosa with topical application of acriflavine contrast agent; (B) descending colon mucosa with topical application of acriflavine contrast agent; (C) surface epithelium of the cecum with intravenous injection of fluorescein; (D) deeper layers of the cecum with intravenous injection of fluorescein, where the microvasculature is visualized. 1, Goblet cells; 2, crypt lumen; 3, lamina propria; 4, capillary with erythrocytes. (From [12], with permission.)

imaging rate of 12 frames per second, this device, produced by Mauna Kea Technologies, Inc., has the ability to observe dynamic processes such as cell trafficking and dye uptake into glands [13,14]. For example, in Figure 7.2, a rapid image sequence is shown in which the uptake of topically applied sodium fluorescein contrast agent can be seen into one crypt (gland) in a human colon [13].

### 7.1.3 Needs for Instrument Development

Perhaps the most obvious challenge in developing endomicroscopic tools is the size constraint that endoscopy imposes. While one commercial device, co-developed by Optiscan and Pentax Corporations, integrates a confocal microscope into a custom full-function endoscope [12], the goal of most engineers thus far has been to design a tool that may be deployed as an accessory through the instrument channel of a conventional endoscope. Standard endoscopes are equipped with instrument channels that range from 2.4 to 6.0 mm in diameter. These multipurpose channels allow for the deployment of various tools, such as biopsy

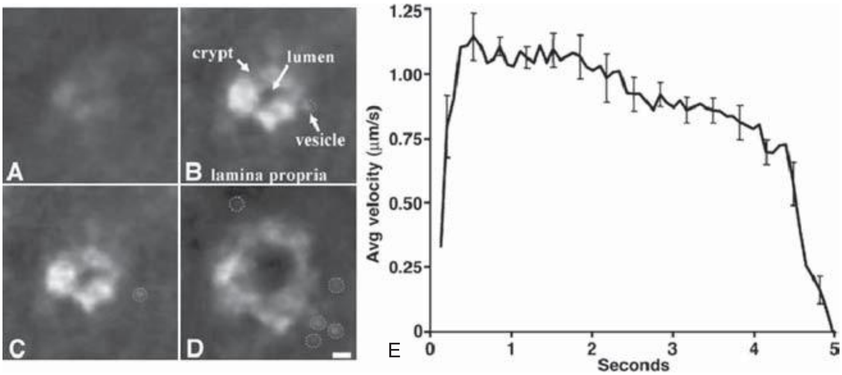

**FIGURE 7.2** Fluorescein transport in colonic mucosa: (A) initial uptake by crypt ($t = 0.08$ s); (B) expansion from lumen toward basolateral aspect of epithelium and accumulation into focused points of fluorescence (dotted red circle labeled vesicle) ($t = 0.67$ s); (C) point of fluorescence enters the lamina propria ($t = 0.75$ s); (D) concurrent appearance of multiple points in the lamina propria ($t = 4.5$ s; scale bar, 20 μm); (E) instantaneous radial speed of *en face* fluorescein movement through epithelium in the direction of the lumen to the lamina propria (peak occurring at $t = 0.5$ s). (From [13], with permission.)

forceps, ablation devices, clips, and snares (with and without cautery). The diameter of an endoscope's instrument channel is unfortunately not the only dimension that dictates the maximum size of an accessory such as an endomicroscope. The instrument channel of standard endoscopes bends at the proximal (back) end of the endoscope near the user controls. This bend radius, along with the diameter of the channel, therefore constrains the maximum length and diameter of a rigid device that may be deployed through the instrument channel. Although preloading a device through the distal (front) end of an instrument channel may be an option for research purposes, it is not a feasible clinical option, and thus the dimensions of these devices must conform to the constraints of the endoscopes.

Up to 90% of cancers originate in epithelial tissues, in part due to the fact that such tissues are exposed to external carcinogens such as ionizing radiation and harsh chemicals. In the gastrointestinal tract, the epithelium is the mucosa that extends on average to a depth of about 500 μm beneath the luminal surface of the gut. The ability to observe microscopic transformations within the entire mucosal layer would be of great value. In particular, there would be significant prognostic value in the ability to determine if disease has extended beyond the mucosal layer and through the basement membrane into underlying layers. Such a diagnosis has important implications for staging disease progression. In terms of imaging depth, conventional confocal microscopes generally do not permit reasonable imaging performance through more than about 100 μm in tissues. One relatively new confocal architecture, the dual-axis confocal microscope, has demonstrated the ability to image cells up to 500 μm deep in gastrointestinal mucosal tissues, albeit at the cost of decreased light-collection efficiency (see below).

In addition to minimizing size and maximizing imaging depth, another important design specification for endomicroscopes is imaging speed. Faster is better, in terms of visualizing dynamic processes as well as avoiding motion artifacts such as image blur. However, trade-offs may be warranted to improve the field of view or to improve sensitivity (signal/noise ratio). Obtaining a large field of view (FOV), in particular, is a major challenge for microscopic imaging. While geometrical constraints largely limit the attainable FOV during endomicroscopy, several efforts have been made to develop image-processing software for stitching together overlapping image frames to generate larger image mosaics. These efforts are discussed briefly in a later section of the chapter.

The advantages of multispectral imaging in the study and diagnosis of disease have been made apparent in numerous studies that employ endomicroscopy and intravital microscopy. Here, we define *multispectral* as simultaneous imaging of more than one channel, including detection at just two different wavelengths. More than multiplying the information content by the number of additional channels, multispectral microscopy allows one to observe a functional change in the context of the tissue microanatomy, and to visualize interactions between different labeled components in a tissue, or to monitor the correlation between various tissue components in diseased versus normal tissues. This is especially valuable since microscopy is exceedingly difficult to perform in a quantitative manner. A microscope image is the result of a convolution of factors related to the optics, source/detector gain settings, distribution of contrast agents, and many other variables. Multispectral approaches often provide a frame of reference and point of normalization that allows for more reliable image interpretation. Examples of multispectral fluorescence imaging include ratiometric imaging approaches that provide increased sensitivity and/or image quantitation, as well as numerous studies of cellular interactions. For reflectance imaging, multispectral imaging enables reflectance spectroscopy. Reports indicate that elastic light-scattering spectroscopy has the ability to detect the onset of disease in tissues due to changes in the size and distribution of submicrometer-sized particles that are responsible for determining the shape of the scattering spectra [15,16]. Recently, this technique has been implemented with a confocal microscope as well [17]. Eventually, as multispectral versions of endomicroscopes are developed, strategies such as confocal light-scattering spectroscopy may find new clinical applications during endoscopy.

### 7.1.4 Needs for Reagent Development

Within endomicroscopy, both reflectance and fluorescence imaging modalities have been developed. Reflectance microscopy utilizes the contrast due to light scattering from endogenous tissue components such as cell nuclei, cell membranes, and other tissue structures, and as such can provide the microanatomic features that are useful for both aiding in diagnosis and putting functional data in context. Exogenous reagents have been used to enhance this contrast. For example, 5% acetic acid (vinegar) has been applied to tissues during in vivo reflectance endomicroscopy to enhance contrast [18], as have chromogenic dyes [19]. Alternative reagents include gold nanoparticles and microspheres. A major challenge for reflectance techniques has been poor image quality due to the limited contrast that is possible as well as other complications, such as coherent speckle noise.

Fluorescence endomicroscopy may be used to image endogenous contrast from tissue autofluorescence, as well as exogenous contrast agents that exhibit varying degrees of molecular specificity in binding to tissues (for more information, see Chapter 17). Autofluorescence has not been utilized extensively for monitoring and detecting disease since changes in tissue autofluorescence are often subtle and contaminated by non-disease-specific factors such as diet. In addition, autofluorescence signals tend to be weak except at short wavelengths where tissue scattering is most significant and limits the depth of penetration of light. Therefore, it is not very compatible with confocal microscopy, in which subsurface imaging is a primary goal.

Early efforts to use exogenous contrast agents during fluorescence endomicroscopy have understandably utilized the few clinically approved fluorophores that exist. These contrast agents, such as sodium fluorescein, provide general morphological contrast but are not targeted toward specific molecular markers of disease progression. In recent years, there has been a great push to understand the molecular mechanisms of disease and to utilize this knowledge for targeted therapy and imaging. In particular, small-molecule reagents seem promising as in vivo imaging contrast agents for a number of reasons. Compared to traditional large antibodies (molecular weight ca. 150 kDa), small molecules tend to be less immunogenic, exhibit improved clearance properties if systemic delivery is utilized, have less nonspecific binding effects in tissue, and may be discovered and synthesized relatively easily. Well-designed small molecules may also display large binding affinities and may be discovered using high-throughput methods such as screening phage-display libraries for high-affinity peptide binders. Figure 7.3 shows an image taken during in vivo confocal endomicroscopy with the Cellvizio GI (Mauna Kea Technologies, Inc.). A targeted fluorescent peptide, developed using phage-display screening methods on fresh human colonic biopsies, was applied topically within the lumen of the colon for this study, and exhibited enhanced binding at the site of dysplastic tissues [20].

A survey of some of the more popular small-molecule reagents currently being considered for GI imaging is provided in Chapter 17. The ultimate objective of molecular probe development is the creation of probes that provide binary data (i.e., the cell is malignant or normal).

## 7.2 CONVENTIONAL CONFOCAL ENDOMICROSCOPY

Over the past decade, numerous conventional confocal endomicroscopes have been designed. A “conventional” confocal microscope, or *single-axis confocal*, is defined as one in which the illumination and collection beam paths are identical

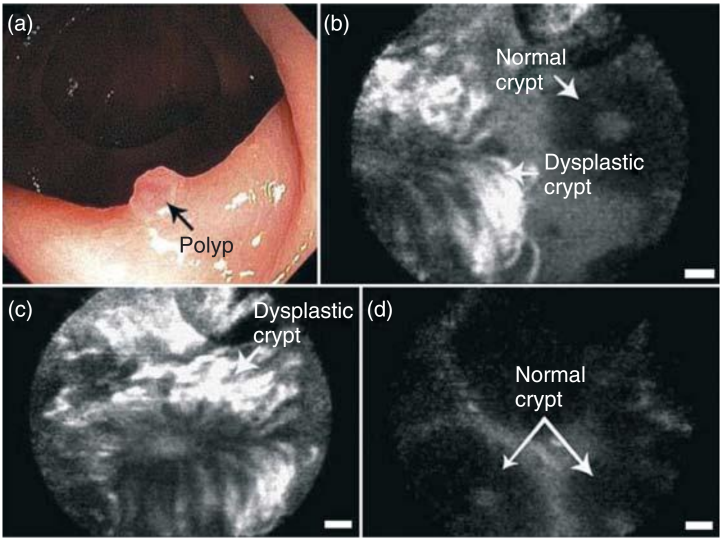

**FIGURE 7.3** In vivo confocal microscopy of a peptide reagent binding to dysplastic colonic mucosa: (a) conventional wide-field white-light endoscopy image; (b) microscopic image at the border between dysplastic and normal colon; (c) dysplastic crypt; (d) adjacent normal mucosa. The images show increased fluorescence intensity in an adenomatous (dysplastic) colon compared to the normal, suggesting preferential binding of the peptide probe to dysplasia. Scale bars, 20 μm. (From [20], with permission.)

through the imaged tissue. Generally speaking, for a miniature device, this implies that the illumination pinhole is the same as the collection pinhole. Various design implementations are surveyed in the following sections.

Confocal microscopy was developed in early 1980s for improved visualization of relatively thin (<100 μm) biological samples. A confocal microscope is essentially a standard microscope that contains a spatial filter that rejects light originating from above and below the focal plane of the microscope. A high-numerical aperture (large focusing cone angle) lens is used to image a small pinhole into a scattering medium. The reflected or fluorescent light originating from the small diffraction-limited focus of the microscope is also collected through a pinhole. Both the illumination and collection pinholes are therefore *confocal* because they are focused to exactly the same point in the tissue. In fact, for a conventional single-axis confocal microscope, the illumination beam path and the collection beam path through the tissue sample are identical.

As a result of the spatial filtering properties of the confocal pinhole, the confocal microscope is able to reject light that originates from outside the focus. Regular light microscopes are able to distinguish between points in the lateral, or horizontal, direction due to the imaging properties of lenses. However, confocal microscopes offer the additional ability to perform *optical sectioning*, in which the axial, or vertical, direction may be distinguished as well (see Figure 7.4).

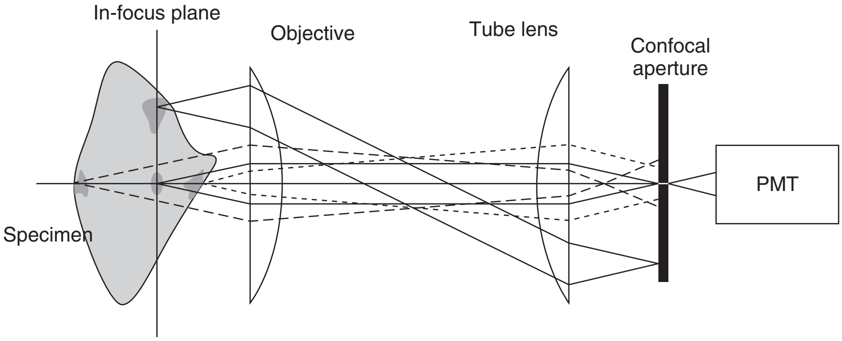

**FIGURE 7.4** Confocal microscope. A small pinhole aperture is imaged to a specific point within the sample. Light originating from this point in the sample is focused through the pinhole aperture and is collected effectively. Light originating from other points in the sample are poorly transmitted through the pinhole and are spatially filtered out. An optical section may be imaged either by physically translating the sample or by scanning the optical path over a two-dimensional plane. (From [7], with permission.)

One major trade-off is imaging speed. While standard microscopes are able to image an entire two-dimensional horizontal image plane at once, confocal microscopes utilize a pinhole to image one focal spot at a time. Therefore, elaborate two- or three-dimensional scanning mechanisms must be introduced into a confocal microscope system in order to reconstruct an image one voxel at a time. An exception to this is with confocal line-scan microscopes, in which a slit is imaged into the sample rather than a pinhole. By scanning the focal line in one orthogonal dimension, a two-dimensional image is generated relatively quickly. However, the sectioning performance of a line-scan confocal microscope is degraded compared to a conventional pinhole approach, due to less efficient spatial filtering.

Although the exact details are beyond the scope of this chapter, diffraction theory may be used to calculate the optical-sectioning behavior of a conventional confocal microscope [6,21]. Diffraction theory provides a mathematical description of the intensity distribution (and complex amplitude) of light that is focused into a microscope sample, taking into account interactions between this light and any surfaces along the way, such as apertures. This mathematical description is termed the *point-spread function* (PSF) because the image of an infinitely small point source at the focus, through the same microscope optics, would have this shape. As the numerical aperture (NA), or cone angle, of the focused beam increases, diffraction theory reveals that the resulting PSF is reduced in size. For example, the lateral width of the PSF scales as $\lambda/\text{NA}$, where $\lambda$ is the wavelength of the light.

The response of a confocal microscope to an isotropic point source (reflective or fluorescent), as a function of distance, is calculated as the square of the product of the overlapping illumination and collection PSFs. Since these PSFs are identical for a conventional confocal microscope, the confocal microscope has a signal response that is the square of a typical wide-field microscope response function. Therefore, the spatial resolution of a confocal microscope is slightly improved compared to that of a regular microscope (about 1.4 times better if uniform illumination is assumed). If we define spatial resolution as the full width between half maximum (FWHM) intensity points, a confocal microscope with uniform illumination has an axial resolution $\Delta z$ given by [6]

$$\Delta z(\mathrm{FWHM}) \approx 0.89\lambda/\mathrm{NA}^2 \tag{7.1}$$

where $z$ is the axial or vertical direction.

In addition to resolution, the contrast of a confocal microscope, or its ability to suppress out-of-focus light, is of utmost importance for high-quality imaging in tissues. This is determined by two major factors: (1) the axial sectioning response of the microscope and (2) the ability to effectively filter out scattered light that is originating from outside the focal volume. The first factor may be calculated with diffraction theory. For a conventional confocal microscope, the axial response scales as $1/z^2$, meaning that the amount of out-of-focus light that is detected in a diffraction-limited confocal microscope, in the absence of scattering effects, decays according to an inverse square law with respect to axial distance, $z$, from the focal point. The second factor listed above is more difficult to predict analytically. Monte Carlo scattering simulations have been the method of choice for calculating the ability of various microscope configurations to filter out multiply-scattering light. A number of studies have indicated that for a conventional confocal microscope, a larger focusing NA leads to improved rejection of out-of-focus scattered light, thereby improving image contrast in thick tissues [22,23]. More recently, finite-difference time domain (FDTD) simulations have also been employed to study the interaction of light with scattering media in a confocal microscope [24].

### 7.2.1 Miniature Optics

In terms of engineering, the major challenge in designing confocal endomicroscopes is miniaturization. As described in the preceding section, achieving high resolution and high contrast in confocal microscopy is dependent on large-NA optics. Large-NA optics introduce a number of challenges, which have been addressed with various degrees of success by numerous researchers. For example, aberrations increase with increasing NA, necessitating the use of compound optics for aberration correction, as shown, for example, in Figure 7.5. Complex miniature optics has been developed using conventional glass lenses as well as injection-molded aspheric lenses, to enable uniform telecentric imaging [25–27]. Unfortunately, one unavoidable fact is that field of view is sacrificed as NA is increased, requiring larger scan angles, which may, in turn, introduce greater aberrations.

Gradient-index (GRIN) optics have also been utilized for confocal endomicroscopy [28]. While the maximum NA of commercial GRIN optics is limited

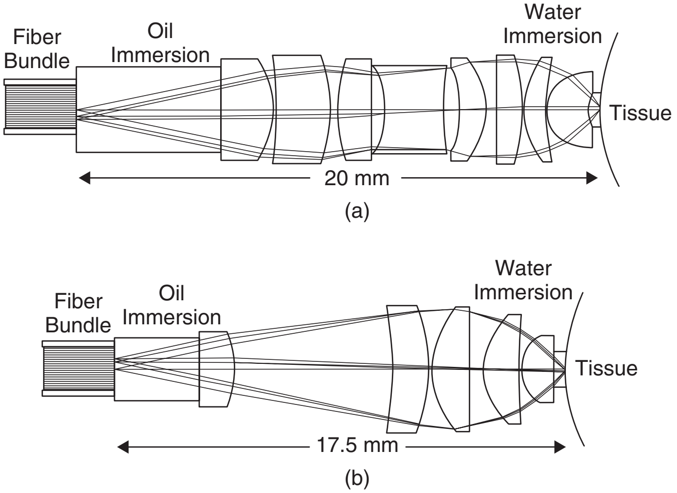

**FIGURE 7.5** Optical design of miniature objective lenses used in fiber optic confocal reflectance microscopy. Here the fiber bundle is located to the left of the lenses, with oil immersion. The sample is placed to the right, with water immersion. (a) Previous glass lens design with eight lens elements; (b) new plastic lens design with five lens elements utilizing aspheric surfaces. (From [25], with permission.)

to about 0.6, they display near-diffraction limited performance and are available as small-diameter (ca. 1 mm) cylinders.

### 7.2.2 Fiber-Bundle vs. Single-Fiber Approaches

Two major categories of endomicroscope designs have emerged: those that utilize a fiber-bundle approach and those that utilize a single optical fiber. Fiber bundles are advantageous in that proximal laser scanning may be performed outside the patient. Each individual fiber in the bundle is imaged to a unique point within the sample. By illuminating and collecting light from one fiber at a time, a two-dimensional image may be reconstructed. A schematic of an example optical circuit is shown in Figure 7.6.

The fiber-bundle approach has the advantage of little or no moving parts within the miniaturized distal scan head, which allows for impressive miniaturization of the endomicroscope to submillimeter dimensions in some cases [28,30]. However, such devices generally have a fixed imaging depth. Axial scanning would require a linear actuator within the distal scan head to adjust the position of the focusing optics, which would limit the extent of miniaturization [26,31]. In the majority of fiber-bundle designs thus far, miniaturization has been a design priority, and axial scanning has not been implemented.

An additional limitation in using a fiber-bundle approach is that the lateral resolution is determined by the fiber-to-fiber spacing within the bundle, and is limited

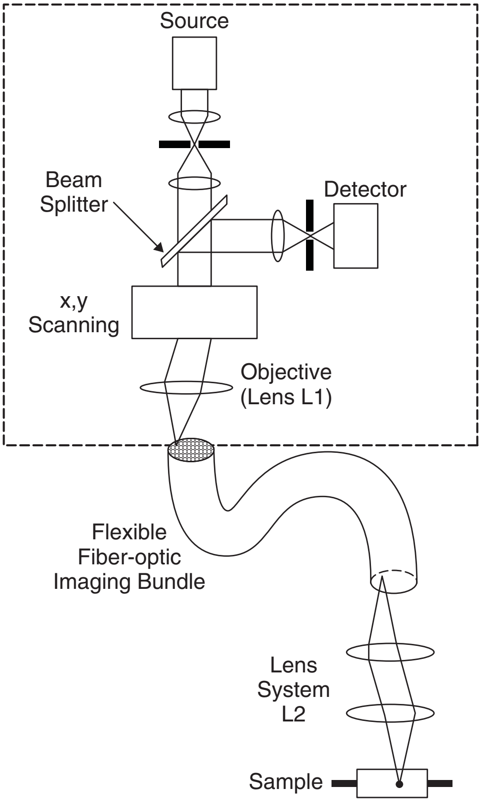

**FIGURE 7.6** Confocal endomicroscope using a fiber optic imaging bundle. The components of a regular confocal microscope are shown within the dashed lines. (From [29], with permission.)

by the Nyquist sampling criterion to about twice the spacing between adjacent fibers, divided by the magnification factor [32]. This spacing also leads to pixilation artifacts, which have been dealt with effectively through image-processing algorithms such as a Gaussian low-pass filter [32]. Despite the limitations introduced by the fiber spacing, however, lateral resolutions as fine as a 1 μm have been achieved in practice [33].

With fiber bundles, another concern is that some crosstalk between adjacent fibers in a bundle is possible, thus reducing image contrast. One strategy for mitigating this effect has been to use bundles in which fibers at one end are mapped into a different configuration at the other end [34]. Some light is invariably coupled into the interfiber spaces and cladding modes of a bundle, resulting in degraded resolution and contrast [35,36].

Single-fiber approaches rely on microoptics and scanning mechanisms integrated into the distal scan head of the endomicroscope to enable two- or even three-dimensional imaging. Two major strategies have been used to enable this:

microelectromechanical system (MEMS) scanning mirrors, and mechanical fiber-optical component deflectors. The challenge of designing such miniature scanning mechanisms is the subject of the following section.

### 7.2.3 Laser Scanning Approaches

Since confocal microscopy, in general, requires the scanning of a focal spot in order to reconstruct an image, one of the major challenges of miniaturization is designing the scanning mechanism. A recent review article summarizes some of the most common scanning approaches [37]. These implementations are shown in Figure 7.7. Parts a to c of Figure 7.7 depict proximal scanning mechanisms used with fiber-bundle approaches to confocal endomicroscopy. In Figure 7.7a, a pair of galvanometric scanning mirrors is used to steer a laser beam into individual fibers within the bundle [25,27–30,34]. In Figure 7.7b, a line-scan approach

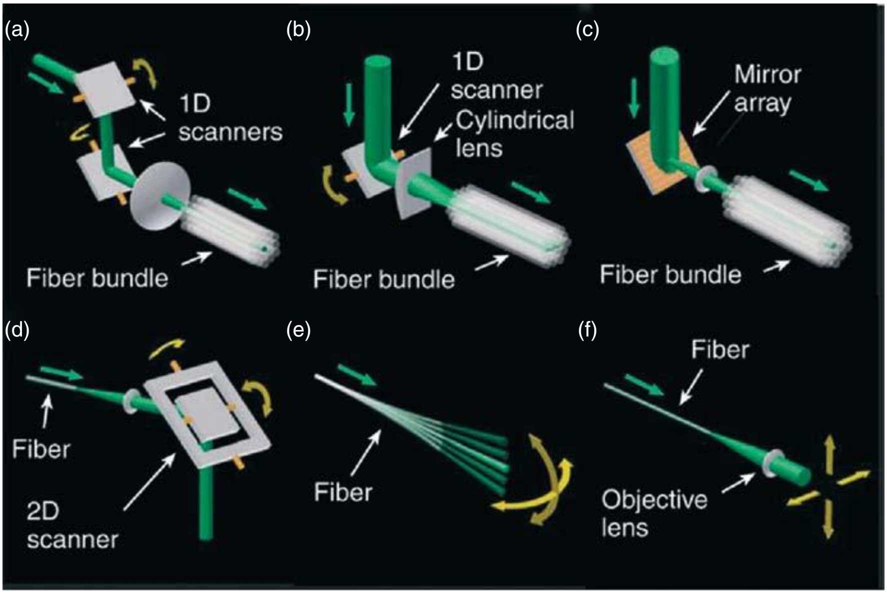

**FIGURE 7.7** (a) Proximal scanning. Cascaded galvanometer-mounted mirrors scan the excitation beam across the proximal end of a fiber bundle. (b) Proximal line scanning. A cylindrical lens focuses the illumination to a line that is scanned across the face of a fiber bundle in one dimension. (c) Proximal scanning with a spatial light modulator, which can illuminate pixels sequentially without sweeping the beam. (d) Distal two-dimensional mirror scanning. A piezoelectric-driven tip-tilt mirror or a miniaturized MEMS mirror pivots in two angular dimensions. (e) Distal fiber tip scanning. The tip of the excitation delivery fiber is vibrated at resonance by an actuator (not shown). (f) Distal fiber-objective scanning. Both the fiber and the objective lens are mounted together on a cantilever (not shown) that is vibrated at resonance by an actuator. (From [37], with permission.)

is depicted, in which a line of illumination is used to illuminate an entire row of fibers at once, thus requiring only one scanning mirror to image in two dimensions [26,31,35]. Line-scan approaches provide increased speed and simplicity of design. However, this is at the cost of reduced confocal sectioning ability, as compared to point scanning, since one dimension of confocal spatial filtering has been removed. Finally, Figure 7.7c illustrates the use of a spatial light modulator (digital micro-mirror device) to address individual fibers in a bundle. Spatial light modulators have been shown to enable effective coupling of light into individual fiber cores. However, a majority of the light is wasted on the “off” pixels [38].

Parts d to f of Figure 7.7 portray distal scanning approaches. Figure 7.7d shows a gimbaled two-dimensional scanning mirror. While miniature piezoelectric mirrors of this type exist, they are not small enough for incorporation into endoscopic devices. Over the past decade, many researchers have tried to incorporate MEMS mirrors, which are fabricated using silicon wafer–processing techniques, into endomicroscope designs [39–45]. Although the cost to develop prototype mirrors is prohibitive, large-volume MEMS fabrication would be cost-effective for a successful commercial device. Figure 7.7e and 7.7f illustrate designs in which piezoelectric [46,47] or electromagnetically excited [48] actuators drive mechanical resonances in a fiber tip, or in a combined fiber-plus-focusing-optic package [49–51]. The advantage of scanning the fiber tip alone is that high speeds and large deflection angles are easily achieved. The disadvantage is that the focusing optic needs to compensate for off-axis aberrations. By scanning the fiber and the focusing lens as one unit, the light always travels down the optical axis, resulting in simpler optics. However, the combined package is more bulky and more difficult to scan at high speeds and over large angles.

In terms of scanning patterns, raster scanning is the most common approach to reconstructing an image. This is a highly efficient method of scanning in which a two-dimensional plane is scanned one point at a time, much like the words are being read from this page: from left to right and then from top to bottom. Raster scanning implies that there is one fast axis (left to right) as well as a much slower axis (top to bottom). The fast axis is often a sinusoidal scan driven at a mechanical resonance frequency. Therefore, the imaging speed may be doubled by collecting data on both the forward (left to right) and reverse (right to left) portions of the sinusoid. Unfortunately, because the fast and slow axes of a raster scan operate at such disparate frequencies, large-amplitude resonant scanning is limited to the fast axis only. In cases where resonant scanning is desired for both axes, such as when mechanical fiber scanners are employed, Lissajous scan patterns have been used [39,46]. In a Lissajous scan, two comparable frequencies (generally near resonance) are chosen for the two orthogonal scan axes. A periodic pattern is scanned that tends to oversample the edges of the image. Finally, a spiral scan has also been utilized for a miniature multiphoton microscope. In this device, both axes were operated at the same resonant frequency, with a phase shift between the axes, to create a circular scan pattern. Adjusting the amplitude of the scan changed the radius of the circle such that a spiral pattern was traced [52]. The spiral scan has the advantage that exactly the same resonant frequency is used to drive both axes, whereas with a Lissajous scan, a stiffening mechanism often must be introduced to separate the resonant frequencies along the orthogonal axes.

## 7.3 DUAL-AXIS CONFOCAL ENDOMICROSCOPY

Although confocal microscopy is a powerful tool for biomedical discovery, scattered photons are not efficiently rejected in the conventional single-axis confocal architecture, leading to rapid deterioration in resolution and contrast with imaging depth [5–7]. Recently, a form of confocal microscopy known as confocal *theta* or *dual-axis confocal microscopy*, has been shown to image relatively deeply within biological tissues. Dual-axis confocal microscopy also possesses certain advantages for miniaturization as well.

### 7.3.1 Background

The inspiration for the dual-axis confocal microscope design was provided by a method to achieve improved resolution through off-axis illumination and collection of light with high-NA objectives, known as *theta microscopy* [53–55]. Later, low-NA optics was proposed as a method to achieve a long working distance and a large field of view [56]. More recently, it has been shown that the dual-axis architecture may be fiber coupled and combined with postobjective scanning to provide scalability of the design to millimeter dimensions [57–59]. Furthermore, it was shown that compared to a single-axis confocal microscope, this configuration has the additional benefit of superior rejection of scattered light and improved optical sectioning deep within tissues. [58,60,61]. The combination of a long working distance and excellent rejection of out-of-focus scattered light allows the dual-axis confocal microscope to image deeply in gastrointestinal mucosal tissues [58,61]. Thus, dual-axis confocal technology has the ability to perform deep three-dimensional optical sectioning using simple and inexpensive optical components and light sources.

As discussed previously, high-NA optics, necessary for high-resolution and high-contrast optical sectioning in a conventional confocal microscope, leads to a short working distance. As a result, the scan mirror must be placed prior to the objective. Preobjective beam scanning leads to off-axis aberrations that must be mitigated by the use of multiple corrective lenses, further increasing the objective size. Furthermore, light scattered by the illumination beam outside the focal volume, indicated by the blue region in Figure 7.8a, has a high probability of being collected by the high-NA objective as background noise, thus decreasing dynamic range and contrast. This is a consequence of the fact that the illumination and collection cone of light (blue region in Figure 7.8a) travels a common path in a conventional single-axis confocal microscope.

In the dual-axis architecture, as shown in Figure 7.8b, two simple low-NA lenses are oriented with the illumination and collection axes crossing the midline at an angle $\theta$. The point spread function of the illumination objective can be

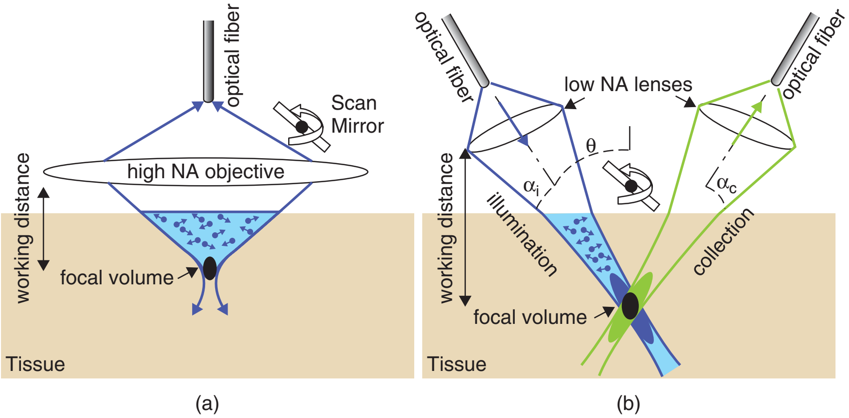

**FIGURE 7.8** (a) Single-axis architecture uses a high-NA objective to excite and collect light from tissue. (b) The dual-axis configuration uses separate low-NA lenses to excite and collect light off-axis.

represented by the dark blue oval, which has a narrow transverse but long axial dimension. The point spread function of the collection objective is similar in shape, as represented by the green oval. The overall detection focal volume can be represented by the intersecting region, shown as a black oval.

The dual-axis design demonstrates several advantages over the single-axis design for deep tissue imaging. First, subcellular resolution can be achieved in the axial as well as the transverse dimensions with low-NA beams. This is due to the fact that the focal volume is roughly spherical, so that the spatial resolution is relatively balanced in all three dimensions. Second, simple low-NA lenses are less sensitive to aberrations and are easy to fabricate. Third, a long working distance is created, which allows a miniature mirror to be placed on the focused-beam side of the objective (postobjective side) to provide a large field of view. Fourth, light scattered along the illumination path outside the focal volume (blue region) is less likely to be collected, thus enhancing detection sensitivity (dynamic range) and contrast. Diffraction-theory calculations have been performed, as well as Monte Carlo tissue scattering simulations, to show that compared to a conventional single-axis confocal architecture, the dual-axis configuration provides superior optical sectioning and rejection of scattered light. As a result, the dual-axis confocal fluorescence microscope is able to perform three-dimensional optical sectioning of thick tissue specimens with enhanced penetration depth.

The dual-axis architecture can be reduced in size to millimeter dimensions using postobjective scanning. In contrast to the single-axis scanning configuration shown in Figure 7.9a, the long working distance of the dual-axis system provides space for the scanning mechanism to be located at the distal side of objective, as shown in Figure 7.9b. The beam is incident on-axis to the lens at all times. Thus, a diffraction-limited point spread function can be scanned over a large field of

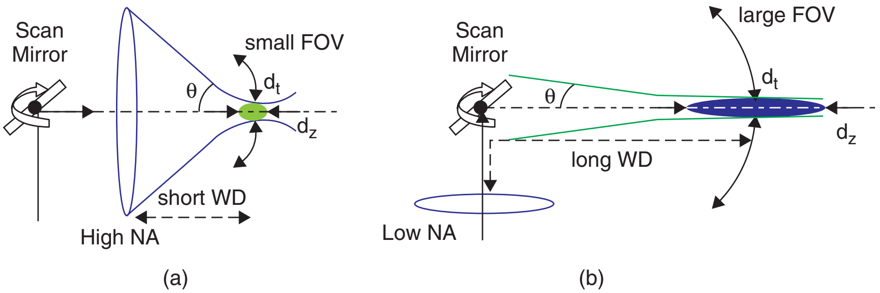

**FIGURE 7.9** Location of the scan mirror in the (a) pre- and (b) postobjective orientations. FOV, field of view; WD, working distance.

view. The long working distance also provides a long lever arm for scanning, such that a conservative scan angle will still result in a significant field of view.

### 7.3.2 Theory

The point-spread function for the dual-axis confocal architecture has been derived from diffraction theory, using the paraxial approximation, to calculate the response and resolution of the system [58]. The simulated axial response is plotted in Figure 7.10 for a dual-axis system, along with the theoretical axial

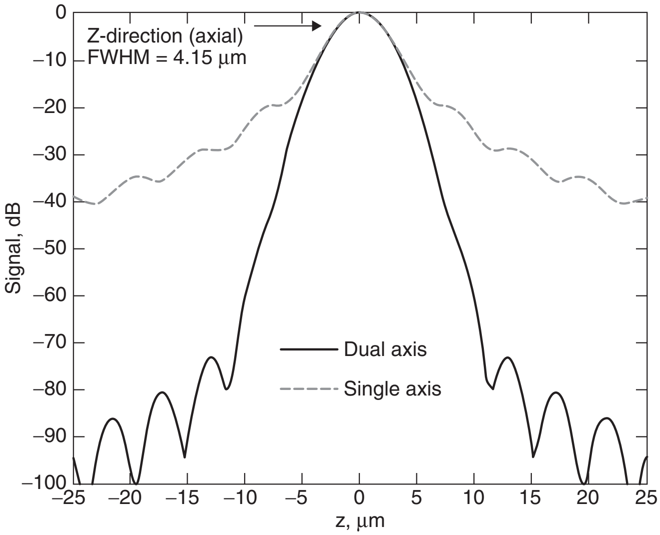

**FIGURE 7.10** Theoretical axial response ($z_d$) to a point reflector for a dual- and a single-axis confocal with equivalent −3 dB (FWHM) axial resolutions of 4.15 μm. The main lobe of the single-axis response falls off as $1/z^2$, whereas the dual-axis response falls off as $\exp(-kz^2)$, offering improved optical sectioning contrast. (From [58], with permission.)

response of a single-axis confocal with an identical $-3$ dB (FWHM) axial resolution. The main lobe of the single-axis response falls off as $1/z^2$, whereas the dual-axis response falls off as a Gaussian as $\exp(-kz^2)$, offering superior optical sectioning response and rejection of out-of-focus scattered light.

While diffraction theory demonstrates the optical-sectioning superiority of the dual-axis architecture over the single-axis architecture in the absence of scattering, Monte Carlo simulations are used to demonstrate the advantages of dual-axis architecture for rejecting multiply-scattered photons in real tissues. Published results show improved contrast and scatter rejection, resulting in increased tissue penetration over that of a conventional single-axis confocal with an identical axial resolution [60,61].

### 7.3.3 Deep Tissue Imaging

Figure 7.11 shows vertical and horizontal image sections of ex vivo tissue samples of normal squamous esophagus and Barrett's esophagus (precancerous) acquired with a tabletop dual-axis confocal fluorescence microscope. Cellular resolution is maintained to a depth of 500 μm, which is several times deeper than that achievable with conventional single-axis confocals. This imaging performance is comparable to two-photon microscopy but is obtained with simple low-NA optics that are easily miniaturized and an inexpensive low-power diode laser source.

Several miniature and MEMS-scanned dual-axis confocal microscopes have been developed by various groups [59,62,63]. The first prototype had an outer diameter of 10 mm for subsurface imaging of biological tissues with 5- to 7-μm resolution [59]. Depth-resolved *en face* images were obtained at a video rate (30 frames per second), and a maximum field of view of 800 × 450 μm was attained by employing a two-dimensional MEMS mirror. Design drawings of the miniature device are shown in Figure 7.12. A parabolic reflector ensures that the two collimated beams are focused on the same spot, with $\theta = 24^\circ$ and $\alpha = 0.13$. The dogbone-shaped MEMS mirror has two square reflector surfaces to scan the illumination and collection beams in tandem over a large two-dimensional field of view.

## 7.4 TOWARD LARGER FIELDS OF VIEW: MOSAICING

One major practical concern for confocal endomicroscopy is the limited field of view (FOV) of the images generated by such devices. This is especially true for a miniature endoscope-compatible device, since the FOV generally must scale with the size of the optics. Therefore, efforts have been made to develop image-processing algorithms to form large image mosaics. At their simplest, these algorithms stitch together successive images based on overlapping features. However, confocal endomicroscopy presents two major challenges for image mosaicing. First, biological tissues are deformable, leading to slight changes in their imaged appearance over time. Second, motion artifacts are common,

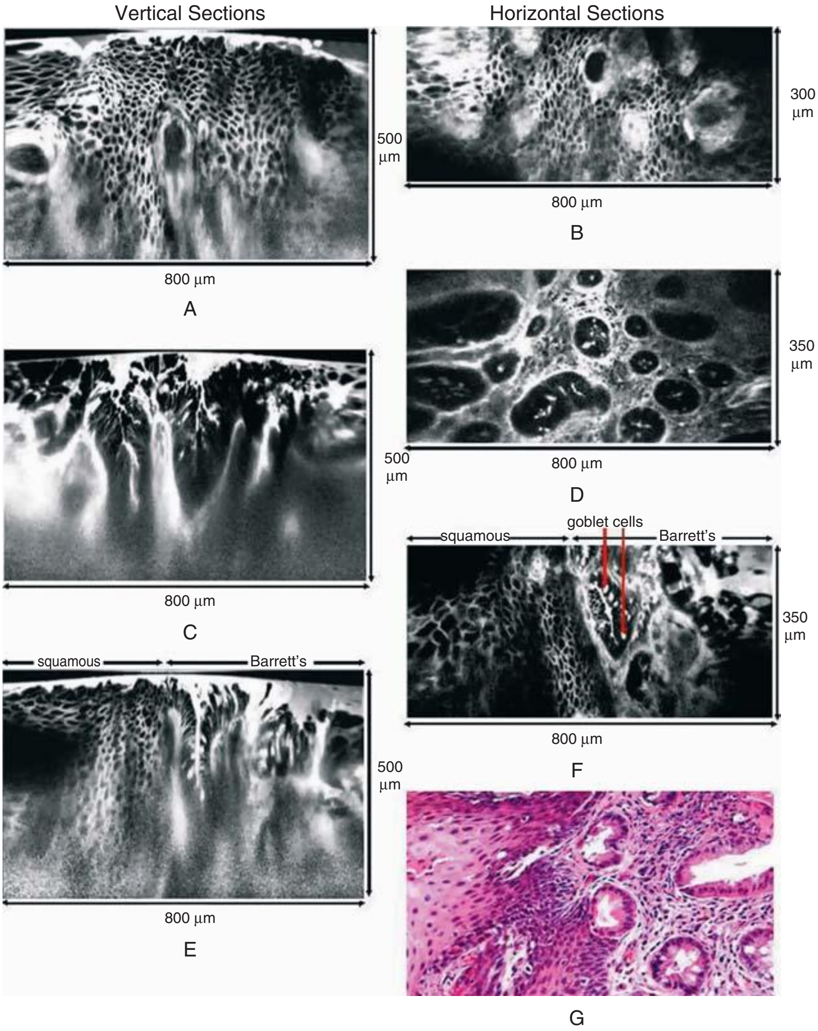
Vertical Sections
Horizontal Sections
500 µm
800 µm
A
300 µm
800 µm
B
500 µm
800 µm
C
350 µm
800 µm
D
squamous
Barrett's
500 µm
800 µm
E
squamous
goblet cells
Barrett's
350 µm
800 µm
F
G

**FIGURE 7.11** Structural images of normal squamous esophagus tissue and Barrett's esophagus: (A) vertical section of a normal squamous esophagus biopsy; (B) horizontal section of a normal squamous esophagus biopsy (the image shown is at a depth of 275 µm); (C) vertical section of a Barrett's esophagus biopsy; (D) horizontal section of Barrett's esophagus (the image shown is at a depth of 200 µm); (E) vertical section of a biopsy showing the transition junction between squamous and Barrett's esophagus; (F) horizontal section of a biopsy showing the transition junction between squamous and Barrett's esophagus. The image shown is at a depth of 200 µm. The presence of mucin-secreting goblet cells, brightly stained vacuoles in these images, confirms the existence of specialized intestinal metaplasia (Barrett's esophagus). (G) A histological section (H&E staining) of a biopsy at the transition junction between squamous and Barrett's esophagus is shown for comparison with the images of thick tissues using the dual-axis confocal microscope. (From [61], with permission.)

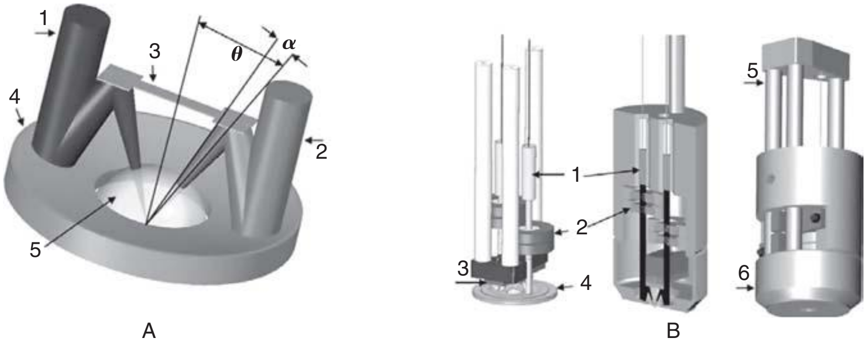

**FIGURE 7.12** (A) Miniature dual-axis confocal scan head optics. 1, Collimated illumination beam; 2, collimated collection beam; 3, MEMS two-dimensional scanner; 4, parabolic reflecting surface; 5, index-matching hemisphere. (B) Miniature dual-axis microscope package design drawings. The outer diameter for this device is 10 mm, with all essential optics and optical paths contained within the central 5-mm diameter. 1, Fibered collimators; 2, Risley alignment prisms; 3, MEMS printed circuit board; 4, parabolic reflector; 5, axial sliding mechanism to control imaging depth; 6, removable end cap holding the parabolic reflector. (From [59], with permission.)

leading to images that appear stretched or distorted. Mosaicing algorithms have been designed specifically to compensate for such tissue deformations and motion artifacts, and algorithms have been described elsewhere [33,64–67].

In addition to providing a wider FOV for improved image interpretation and visualization of tissue morphology, mosaicing can also improve image quality, due to the averaging effect over multiple overlapping image frames. For example, in Figure 7.13, an example is shown of an image mosaic generated with the fibered confocal endomicroscope manufactured by Mauna Kea Technologies in Paris, France.

## 7.5 SUMMARY AND FUTURE DIRECTIONS

### 7.5.1 Advances and Accomplishments

Confocal endomicroscopy is a rapidly developing optical imaging modality that is seeking translation into routine clinical use. Advances in miniaturization have led to the development of numerous fibered confocal microscopes that may be deployed through the instrument channel of a conventional endoscope, or packaged permanently within the tip of a custom endoscope. Confocal endomicroscopes can enable real-time high-resolution three-dimensional visualization of epithelial tissues for improved early detection of disease, or even for image-guided interventions such as physical biopsies and endoscopic mucosal resection. Reflectance imaging may be used to visualize cellular and glandular morphology, and fluorescence imaging may be used to image molecular biomarkers of disease

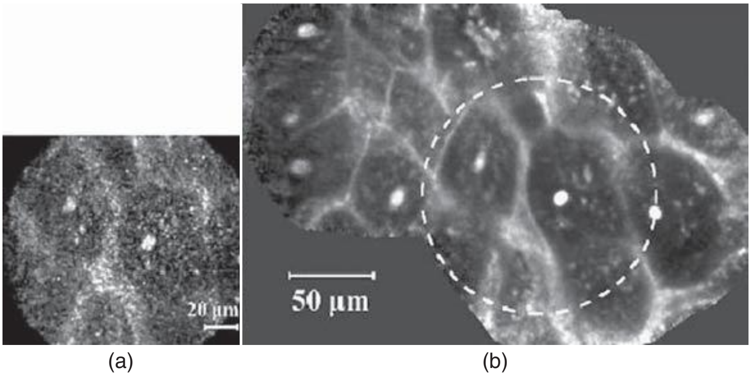

**FIGURE 7.13** Reflectance image of human mouth mucosa, acquired with a device from Mauna Kea Technologies, Inc.: (a) one image frame, taken at the location shown by the dashed circle in the mosaic; (b) an image mosaic from 101 image frames. Image quality is improved by mosaicing. (From [65], with permission.)

progression. Most important, this may all be done in real time and on intact living tissues. The development of near-video-rate devices has already enabled the observation of dynamic tissue processes that have not been possible with conventional histopahology. Efforts are being made through real-time image mosaicing to address some of the limitations of confocal microscopy: for example, their limited field of view.

### 7.5.2 Telepathology

Confocal endomicroscopy has the potential to play a central role in the emerging area of telepathology. In its simplest form, telepathology is the visualization of histology via a monitor rather than the eyepiece of a microscope. Confocal microscopy is fundamentally a digital technology in which cross-sectional images are reconstructed and visualized on a computer. The transmission of such data to outside observers is straightforward. As medicine becomes increasingly specialized, patients at rural clinics suffer the disadvantage of not having access to cutting-edge technologies or the personnel trained to utilize those technologies. Telepathology allows distant experts to observe and help diagnose patients in such rural settings. In addition, it allows for increased opportunity for peer review in pathology, in which multiple trained viewers may help with a diagnosis, whether in an urban or a rural setting. Finally, telepathology may play an important role in consensus building among pathologists, who often may disagree in their interpretations due to differences in training and experience.

### 7.5.3 Future of Instrumentation Development

Traditional histopathology is a poor gold standard for disease diagnosis because of the subjective nature behind many aspects of interpreting histology slides under a microscope. As confocal endomicroscopy continues to advance, it will enable better and more quantitative methods for disease diagnosis. For example, molecularly targeted imaging probes are being developed to diagnose disease at earlier stages and with increased accuracy. Methods such as ratiometric imaging [68] may be developed to further quantify such molecular biomarker expression levels in tissue. Much future work remains to be done to develop molecular probes with high specificity and sensitivity for disease detection, as well as probes that possess the necessary chemical transport and clearance properties for effective use in an in vivo setting. Along with the new imaging capabilities that confocal endomicroscopy brings, such as video-rate imaging and three-dimensional optical sectioning, new probes will be developed to specifically capitalize on those imaging features. A more detailed summary of some of the current directions in probe development for GI cancer detection is provided in Chapter 17.

As for instrumentation development, some of the most immediate barriers to translation include high cost, large size, insufficient imaging speed, insufficient depth of imaging (or lack of axial-scanning ability), poor image quality/contrast, difficulty of use, field-of-view limitations, and a lack of specific detection protocols or consensus guidelines for image interpretation. These are all areas of current and future work for researchers and developers. As with many emerging clinical tools, the path to clinical acceptance will take time and much effort in a field that is often resistant to changes in established practices. In addition, current efforts are being made to develop multispectral confocal endomicroscopes [31,69,70]. As mentioned in Section 7.1.3, multispectral imaging is a powerful feature that would enable many novel strategies for improving disease detection.

Finally, many of the developments being made to develop confocal endomicroscopes for gastrointestinal use have direct applicability for use in imaging many other organs and for diagnosing a host of other clinical problems. Examples include imaging the interior of the bladder and lungs [71], as well as guiding precision surgical resection of skin cancer [72,73] or brain tumors [74]. Confocal and multiphoton endomicroscopes and microendoscopes have also been used extensively for preclinical and exploratory small-animal imaging studies, in which the small size of an imaging device is of great value. The next decade will certainly witness many exciting new developments and applications of such technologies that provide an unprecedented view of living tissues and cells and, especially, of the molecular processes associated with them.

## REFERENCES

1. Amos, W.B., and White, J.G., How the confocal laser scanning microscope entered biological research, *Biol. Cell*, Vol. 95, 2003, pp. 335–342.
2. Cox, G., Biological confocal microscopy, *Mater. Today*, Vol. 5, 2002, pp. 34–41.
3. Wright, S.J., and Wright, D.J., Introduction to confocal microscopy, *Methods Cell Biol.*, Vol. 70, 2002, pp. 1–85.

4. Halbhuber, K.J., and König, K., Modern laser scanning microscopy in biology, biotechnology and medicine, *Ann. Anat*., Vol. 185, 2003, pp. 1–20.
5. Pawley, J. (ed.), *Handbook of Biological Confocal Microscopy*, 3rd ed., Plenum Press, New York, 1996.
6. Corle, T.R., and Kino, G.S., *Confocal Scanning Optical Microscopy and Related Imaging Systems*, Academic Press, San Diego, CA, 1996.
7. Conchello, J.-A., and Lichtman, J.W., Optical sectioning microscopy, *Nat. Methods*, Vol. 2, 2005, pp. 920–931.
8. Choi, Y.J., et al., Interobserver variability and aberrant E-cadherin immunostaining of lobular neoplasia and infiltrating lobular carcinoma, *Mod. Pathol*., Vol. 21, 2008, pp. 1224–1237.
9. Pech, O., et al., Inter-observer variability in the diagnosis of low-grade dysplasia in pathologists: a comparison between experienced and in-experienced pathologists, *Gastrointest. Endosc*., Vol. 63, 2006, pp. AB130–AB130.
10. Komuta, K., et al., Interobserver variability in the pathological assessment of malignant colorectal polyps, *Br. J. Surg*., Vol. 91, 2004, pp. 1479–1484.
11. Levine, D.S., et al., An endoscopic biopsy protocol can differentiate high-grade dysplasia from early adenocarcinoma in Barrett's esophagus, *Gastroenterology*, Vol. 105, 1993, pp. 40–50.
12. Polgase, A.L., et al., A fluorescence confocal endomicroscope for in vivo microscopy of the upper- and lower-GI tract, *Gastrointest. Endosc*., Vol. 62, 2005, pp. 686–695.
13. Wang, T.D., et al., Functional imaging of colonic mucosa with a fibered confocal microscope for real time in vivo pathology, *Clin. Gastroenterol. Hepatol*., Vol. 5, 2007, pp. 1300–1305.
14. Martina, M.-S., et al., Magentic targeting of rhodamine-labeled superparamagnetic liposomes to solid tumors: in vivo tracking by fibered confocal fluorescence microscopy, *Mol. Imaging*, Vol. 6, 2007, pp. 140–146.
15. Wallace, M., et al., Endoscopic detection of dysplasia in patients with Barrett's esophagus using light scattering spectroscopy, *Gastroenterology*, Vol. 119, 2000, pp. 677–682.
16. Backman, V., et al., Detection of preinvasive cancer cells in situ, *Nature*, Vol. 406, 2000, pp. 35–36.
17. Itzkan, I., et al., Confocal light absorption and scattering spectroscopic microscopy monitors organelles in live cells with no exogenous labels, *Proc. Nat'l. Acad. Sci. USA*, Vol. 104, 2007, pp. 17255–17260.
18. Gillenwater, A.L., et al., Confocal microscopy for real-time detection of oral cavity neoplasia, *Clin. Cancer Res*., Vol. 9, 2003, pp. 4714–4721.
19. Hurlstone, D.P., and Sanders, D.S., Recent advances in chromoscopic colonoscopy and endomicroscopy, *Curr. Gastroenterol. Rep*., Vol. 8, 2007, pp. 409–415.
20. Hsiung, P.L., et al., Detection of colonic dysplasia in vivo using a targeted heptapeptide and confocal microendoscopy, *Nat. Med*., Vol. 14, 2008, pp. 454–458.
21. Born, M., and Wolf, E., *Principles of Optics*, 7th ed., Cambridge University Press, Cambridge, UK, 1999.
22. Kempe, M., Rudolph, W., and Welsch, E., Comparative study of confocal and heterodyne microscopy for imaging through scattering media, *J. Opt. Soc. Am. A*, Vol. 13, 1996, pp. 46–52.

23. Schmitt, J.M., Knüttel, A., and Yadlowsky, M., Confocal microscopy in turbid media, *J. Opt. Soc. Am. A*, Vol. 11, 1994, pp. 2226–2235.
24. Simon, B., and DiMarzio, C.A., Simulation of a theta line-scanning confocal microscope, *J. Biomed. Opt*., Vol. 12, 2007, p. 064020.
25. Carlson, K., et al., In vivo fiber-optic confocal reflectance microscope with an injection-molded miniature objective lens, *Appl. Opt*., Vol. 44, 2005, pp. 1792–1796.
26. Rouse, A.R., et al., Design and demonstration of a miniature catheter for a confocal microendoscope, *Appl. Opt*., Vol. 43, 2004, pp. 5763–5771.
27. Liang, C., et al., Design of a high-numerical aperture miniature microscope objective for an endoscopic fiber confocal reflectance microscope, *Appl. Opt*., Vol. 41, 2002, pp. 4603–4610.
28. Knittel, J., et al., Endoscope-compatible confocal microscope using a gradient index-lens system, *Opt. Commun*., Vol. 188, 2001, pp. 267–273.
29. Gmitro, A.F., and Aziz, D., Confocal microscopy through a fiber-optic imaging bundle, *Opt. Lett*., Vol. 18, 1993, pp. 565–567.
30. Laemmel, E., et al., Fibered confocal fluorescence microscopy (Cell-viZio™) facilitates extended imaging in the field of microcirculation, *J. Vasc. Res*., Vol. 41, 2004, pp. 400–411.
31. Rouse, A.R., and Gmitro, A.F., Multispectral imaging with a confocal microendoscope, *Opt. Lett*., Vol. 25, 2000, pp. 1708–1710.
32. Bozinovic, N., et al., Fluorescence endomicroscopy with structured illumination, *Opt. Express*, Vol. 16, 2008, pp. 8016–8025.
33. Becker, V., et al., High-resolution miniprobe-based confocal microscopy in combination with video mosaicing, *Gastrointest. Endosc*., Vol. 66, 2007, pp. 1001–1007.
34. Lin, C.H., and Webb, R.H., Fiber-coupled multiplexed confocal microscope, *Opt. Lett*., Vol. 25, 2000, pp. 954–957.
35. Sabharwal, Y.S., et al., Slit-scanning confocal microendoscope for high-resolution in vivo imaging, *Appl. Opt*., Vol. 38, 1999, pp. 7133–7144.
36. Juskaitis, R., Wilson, T., and Watson, T.F., Real time white light reflection confocal microscopy using a fiber-optic bundle, *Scanning*, Vol. 19, 1997, pp. 15–19.
37. Flusberg, B.A., et al., Fiber-optic fluorescence imaging, *Nat. Methods*, Vol. 2, 2005, pp. 941–950.
38. Lane, P.M., et al., Fiber-optic confocal microscopy using a spatial light modulator, *Opt. Lett*., Vol. 25, 2000, pp. 1780–1782.
39. Dickensheets, D.L., and Kino, G.S., Micromachined scanning confocal optical microscope, *Opt. Lett*., Vol. 21, 1996, pp. 764–766.
40. Dickensheets, D.L., and Kino, G.S., Silicon-micromachined scanning confocal optical microscope, *IEEE J. Microelectromech. Syst*., Vol. 7, 1998, pp. 38–47.
41. Hofmann, U., et al., Electrostatically driven micromirrors for a miniaturized confocal laser scanning microscope, *Proc. SPIE*, Vol. 3878, 1999, pp. 29–38.
42. Piyawattanametha, W., et al., Surface micromachined confocal scanning optical microscope, *Technical Digest Series of Conference on Lasers and Electro-Optics* (*CLEO*), San Francisco, 2000, pp. 447–448.
43. Piyawattanametha, W., et al., A 2D scanner by surface and bulk micromachined angular vertical comb actuators, *IEEE/LEOS International Conference on Optical MEMS*, Waikaloa, HI, 2003, pp. 93–94.

44. Schenk, H., et al., Large deflection micromechanical scanning mirrors for linear scans and pattern generation, *J. Select. Top. Quantum Electron.*, Vol. 6, 2000, pp. 715–722.
45. Lee, D., and Solgaard, O., Two-axis gimbaled microscanner in double SOI layers actuated by self-aligned vertical electrostatic combdrive, *Proceedings of the Solid-State Sensor and Actuator Workshop*, Hilton Head, SC, 2004, pp. 352–355.
46. Flusberg, B.A., et al., In vivo brain imaging using a portable 3.9 gram two-photon fluorescence microendoscope, *Opt. Lett.*, Vol. 30, 2005, pp. 2272–2274.
47. Seibel, E.J., and Smithwick, Q.Y., Unique features of optical scanning, single fiber endoscopy, *Lasers Surg. Med.*, Vol. 30, 2002, pp. 177–183.
48. Delaney, P.M., and Harris, M.R., in *Handbook of Biological Confocal Microscopy*, pp. 515–523, J. Pawley (ed.), Plenum Press, New York, 1995.
49. Dickensheets, D.L., and Kino, G.S., A scanned optical fiber confocal microscope, *Proc. SPIE*, Vol. 2184, 1994, pp. 39–47.
50. Giniunas, L., Juskaitis, R., and Shatalin, S.V., Scanning fibre-optic microscope, *Electron. Lett.*, Vol. 27, 1991, pp. 724–726.
51. Ota, T., et al., In situ fluorescence imaging of organs through compact scanning head for confocal laser microscopy, *J. Biomed. Opt.*, Vol. 10, 2005, pp. 1–4.
52. Myaing, M.T., MacDonald, D.J., and Li, X., Fiber-optic scanning two-photon fluorescence endoscope, *Opt. Lett.*, Vol. 31, 2006, pp. 1076–1078.
53. Stelzer, E.H.K., and Lindek, S., Fundamental reduction of the observation volume in far-field light microscopy by detection orthogonal to the illumination axis: confocal theta microscopy, *Opt. Commun.*, Vol. 111, 1994, pp. 536–547.
54. Stelzer, E.H.K., et al., A new tool for the observation of embryos and other large specimens: confocal theta fluorescence microscopy, *J. Microsc.*, Vol. 179, 1995, pp. 1–10.
55. Lindek, S., and Stelzer, E.H.K., Optical transfer functions for confocal theta fluorescence microscopy, *J. Opt. Soc. Am. A*, Vol. 13, 1996, pp. 479–482.
56. Webb, R.H., and Rogomentich, F., Confocal microscope with large field and working distance, *Appl. Opt.*, Vol. 38, 1999, pp. 4870–4875.
57. Wang, T.D., et al., Dual axes confocal microscope with post-objective scanning and low coherence heterodyne detection, *Opt. Lett.*, Vol. 28, 2003, pp. 1915–1917.
58. Liu, J.T.C., et al., Dual-axes confocal reflectance microscope for distinguishing colonic neoplasia, *J. Biomed. Opt.*, Vol. 11, 2006, p. 054019.
59. Liu, J.T.C., et al., Miniature near-infrared dual-axes confocal microscope utilizing a two-dimensional microelectromechanical systems scanner, *Opt. Lett.*, Vol. 32, 2007, pp. 256–258.
60. Wong, L.K., et al., Improved rejection of multiply-scattered photons in confocal microscopy using dual-axes architecture, *Opt. Lett.*, Vol. 32, 2007, pp. 1674–1676.
61. Liu, J.T.C., et al., Efficient rejection of scattered light enables deep optical sectioning in turbid media with low-NA optics in a dual-axis confocal architecture, *J. Biomed. Opt.*, Vol. 13, 2008, p. 034020.
62. Ra, H., et al., Two-dimensional MEMS scanner for dual-axes confocal microscopy, *J. Microelectromech. Syst.*, Vol. 16, 2007, pp. 969–976.
63. Ra, H., et al., Three-dimensional in vivo imaging by a handheld dual-axes confocal microscope, *Opt. Express*, Vol. 16, 2008, pp. 7224–7232.

64. Vercauteren, T., et al., Real time autonomous video image registration for endomicroscopy: fighting the compromises, *Proceedings of SPIE BIOS*, San Jose, CA, Jan. 19–24, 2008, p. 68610C.

65. Vercauteren, T., et al., Robust mosaicing with correction of motion distortions and tissue deformation for in vivo fibered microscopy, *Med. Image Anal.*, Vol. 10, 2006, pp. 673–692.

66. Loewke, K., et al., Deformable image mosaicing for optical biopsy, *Proceedings of the 11th IEEE International Conference on Computer Vision*, Rio de Janeiro, Brazil, Oct. 14–20, 2007.

67. Loewke, K., et al., Real-time image mosaicing with a hand-held dual-axes confocal microscope, *Proceedings of SPIE BIOS*, San Jose, CA, Jan. 19–24, 2008, p. 68510F.

68. Liu, J.T.C., et al., Quantifying cell-surface biomarker expression in thick tissues with ratiometric three-dimensional microscopy, *Biophys. J.*, Vol. 96, 2009, pp. 2405–2414.

69. Makhlouf, H., et al., Multispectral confocal microendoscope for in vivo and in situ imaging, *J. Biomed. Opt.*, Vol. 13, 2008, p. 044016.

70. Kim, P., et al., In vivo confocal and multiphoton microendoscopy, *J. Biomed. Opt.*, Vol. 13, 2008, p. 010501.

71. Thiberville, L., et al., In vivo imaging of the bronchial wall microstructure using fibered confocal fluorescence microscopy, *Am. J. Respir. Crit. Care Med.*, Vol. 175, 2007, pp. 22–31.

72. Meyer, L.E., et al., In vivo confocal scanning laser microscopy: comparison of the reflectance and fluorescence mode by imaging human skin, *J. Biomed. Opt.*, Vol. 11, 2006, p. 044012.

73. Gerger, A., et al., In vivo confocal laser scanning microscopy in the diagnosis of melanocytic skin tumours, *Br. J. Dermatol.*, Vol. 160, 2009, pp. 475–481.

74. Lin, J.T.C., et al., Micromirror-scanned dual-axis confocal microscope utilizing a gradient-index relay lens for image guidance during brain surgery, *J. Biomed. Opt.*, Vol. 15, 2010, p. 026029.

# 8

# HIGH-RESOLUTION OPTICAL IMAGING IN INTERVENTIONAL CARDIOLOGY

THOMAS J. KIERNAN, BRYAN P. YAN, AND KYOICHI MIZUNO

*Massachusetts General Hospital, Harvard Medical School, Boston, Massachusetts; Nippon Medical School, Tokyo, Japan*

IK-KYUNG JANG

*Massachusetts General Hospital, Harvard Medical School, Boston, Massachusetts*

8.1 Introduction 234
8.2 Current invasive imaging modalities in interventional cardiology 234
  8.2.1 Coronary angiography 234
  8.2.2 Intravascular ultrasound 235
  8.2.3 Angioscopy 236
  8.2.4 Intracoronary MRI 237
  8.2.5 Thermography 237
  8.2.6 Near-infrared spectroscopy 237
  8.2.7 Palpography 238
8.3 High-resolution optical coherence tomography imaging in cardiology 238
  8.3.1 Plaque characterization 238
  8.3.2 Detection of vulnerable plaque 241
  8.3.3 OCT and percutaneous coronary intervention 241
  8.3.4 Current OCT imaging systems for percutaneous coronary intervention 243
  8.3.5 OCT imaging of post-intracoronary stents 245
  8.3.6 OCT and drug-eluting stents 246
  8.3.7 OCT for fibrous cap disruption and erosion characterization 247
  8.3.8 OCT for intracoronary thrombus characterization 248
8.4 Current limitation of OCT 248

---

*Advances in Optical Imaging for Clinical Medicine*, Edited by Nicusor Iftimia, William R. Brugge, and Daniel X. Hammer
Copyright © 2011 John Wiley & Sons, Inc.

8.5 Future developments 249
8.6 Conclusions 250
References 251

## 8.1 INTRODUCTION

Rupture of vulnerable plaques is responsible for most coronary events. Plaques prone to rupture are frequently at nonobstructive lesions characterized by the presence of (1) a large lipid core, (2) a thin fibrous cap $\leq$65 μm thick, and (3) activated macrophages. Postmortem studies have shown that most fatal acute coronary events occur at the site of a ruptured, macrophage-rich, thin-capped fibroatheroma (TCFA) with a minority due to endothelial erosion. Although not all TCFA will rupture, what instigates plaque rupture in one site as opposed to another is unknown.

Identification and visualization of high-risk plaques are the keys to realizing improved understanding of vulnerable plaques. The ultimate goal is to accurately risk-stratify patients, target therapy to appropriate areas of vulnerable plaque, and thus prevent adverse events. Contrast angiography is limited by its low resolution, which does not allow one to visualize the components of atherosclerotic plaque. A number of invasive imaging modalities are currently in use [intravascular ultrasound (IVUS) and angioscopy] or under investigation [optical coherence tomography (OCT), intracoronary thermography, near-infrared spectroscopy, and intracoronary MRI] for the evaluation of vulnerable plaque. Among them, IVUS is currently the most commonly employed adjunctive intravascular method to better define lesions, but it is also limited by low resolution. OCT is a developing technique that uses near-infrared light for the cross-sectional visualization of the vessel wall at the microscopic level. It enables excellent resolution of coronary architecture and precise characterization of plaque morphology. Quantification of macrophage within the plaque is also possible. These capabilities enable identification of TCFA, which is the most common type of vulnerable plaque.

## 8.2 CURRENT INVASIVE IMAGING MODALITIES IN INTERVENTIONAL CARDIOLOGY

### 8.2.1 Coronary Angiography

Coronary contrast angiogram reflects the luminal diameter and provides a measure of stenosis that displays an irregular luminal surface, implying the presence of atherosclerotic disease. Although coronary angiography represents the standard clinical modality for visualization of the coronary arteries, there may be a discrepancy between the appearance of the opacified lumen and the actual degree of atherosclerosis. The presence of diffuse disease and positive remodeling may lead to underestimation of the extent of atherosclerotic disease. The percentage diameter stenosis of a lesion is not a reliable predictor of myocardial infarction or death, as the majority of ruptured plaque occurs at nonobstructive lesions. Contrast angiography is limited by its low resolution, which does not allow one to visualize the components of atherosclerotic plaque and therefore makes it difficult to distinguish between stable and high-risk, vulnerable plaques.

The addition of physiological assessment of coronary artery lesions—fractional flow reserve and coronary flow reserve—complements angiographic information and is essential for determining the functional severity of coronary stenosis and for an accurate decision to either perform or defer revascularization, especially in angiographically intermediate lesions. These physiological measurements are made possible by using a guidewire-mounted pressure sensor and intracoronary or intravenous adenosine to induce maximal hyperemia. The fractional flow reserve can then be calculated as the ratio between maximal myocardial flow in the stenotic vessel and maximal myocardial flow in the same vessel without stenosis.

### 8.2.2 Intravascular Ultrasound

Intravascular ultrasound is currently the gold standard for clinical intracoronary imaging in the cardiac catheterization laboratory. Positive vessel remodeling can readily be evaluated by IVUS. In addition to the lumen and vessel border, IVUS can provide real-time images of the plaque. Ruptured plaques and a tear in the fibrous cap can be identified by IVUS. Assessment of plaque echogenicity may provide semiquantitative tissue characterization by using a computer-aided gray-scale value analysis. Calcification can be identified with a sensitivity and specificity of 90 to 100% as bright echo signals with acoustic shadowing. Lipid deposits visualized as echolucent zones can be detected with high sensitivity (67 to 95%) but low specificity (30 to 95%). However, the axial resolution of IVUS is in the range 150 to 200 μm, whereas TCFA is thinner than 65 μm, and therefore measurement of the thickness of the fibrous cap by IVUS is not possible.

The limitation of conventional gray-scale IVUS for tissue characterization can be improved by analyzing the backscatter ultrasound signal with more sophisticated techniques. Three different mathematical methods have been applied to radio-frequency data analysis: autoregressive modeling with IVUS virtual histology (IVUS-VH), fast Fourier transformation (FFT) [integrated backscatter (IB-IVUS)], and wavelet analysis.

IVUS-VH evaluates different spectral parameters to construct color-coded tissue maps that classify plaques into four major components: fibrous, fibrolipidic, necrotic core, and calcium. Ex vivo correlation studies have shown good sensitivity and specificity for fibrous tissue (86% and 90.5%), fibrofatty (79.3% and 100%), necrotic core (67.3% and 92.9%), and dense calcium (50% and 98.9%, respectively).

IB-IVUS determines the average power of the backscattered ultrasound signal from a small volume of tissue by calculating the fast Fourier transform power spectrum. The IB signals are used to create a two-dimensional color-coded map of plaque tissue composition, with a separation between calcification, fibrous tissue, lipid core, thrombus, or intimal hyperplasia. Compared to histology, the sensitivity of IB-IVUS for calcification, fibrosis, and lipid pool was 100, 94, and 84%, respectively, and the specificity was 99, 84, and 97%, respectively [1]. However, the in vivo validation of IB-IVUS has been limited to comparisons with angioscopy, which is a relatively insensitive tool to assess plaque composition.

### 8.2.3 Angioscopy

Intracoronary angioscopy is a well-established technique that allows direct visualization of the plaque surface and intraluminal structures. Use of the angioscopy in an epicardial coronary artery provides direct visual examination of the surface morphology of a vessel, such as plaque visualization. It enables assessment of the plaque color (i.e., white, red, yellow) and can detect plaque complications such as rupture, intimal tear, and thrombosis, with high sensitivity compared to angiography. Plaques seen as yellow on angioscopy may have many characteristics of vulnerable plaques. When analyzed histologically, they are lipid rich and often have an irregular intimal surface. Such plaques are commonly found in patients with acute coronary syndrome (ACS) [2]. Yellow plaques have also been described as having increased distensibility and that they are associated with outward remodeling that can confer mechanical and structural weakness to the plaque [3]. Angioscopy can also be used to assess the effect of preventive treatment. Therapy with atorvastatin has shown changes within the lesion color from yellow to white, suggesting plaque stabilization [4].

The major limitation of angioscopy is that only a large-caliber vessel can be studied, and it requires a blood-free field during image acquisition (displacing the column of blood during the procedure), which may induce a significant ischemia. Angioscopy of the vessel surface alone may not be sufficiently sensitive to detect subtle alteration in plaque composition or plaque burden in the presence of positive remodeling.

Due to the fact that several factors can affect color perception during angioscopy, such as the intensity of light, imaging angle, and distance [5,6], a quantitative colorimetric method of measuring coronary plaque color after proper adjustment for brightness has been developed [7]. This method overcomes the effects of these variables and eliminates the subjective element of visual color assessment. Using this method, it has been reported that high yellow color intensity (HYCI) in ex vivo arterial tissue samples can be associated with lipid cores underneath thin ($<100$ μm) fibrous caps [7], which are indeed commonly found in culprit sites of ACS [8]. On a practical level, angioscopy still represents a research tool only and is not yet used clinically in the cardiac catheterization laboratory.

### 8.2.4 Intracoronary MRI

Intravascular MRI (IVMRI) has been developed for local high-resolution MR imaging of the coronary arteries. It uses tissue contrast differences to determine the extent and location of increased vascular lipid infiltration. This method is currently used in the research arena only. The IVMRI catheter system is transportable and eliminates the need for external magnets and a bulky and expensive MRI scanner.

The first-in-man IVMRI study has enrolled 29 patients in four European centers and was designed to demonstrate the safety and feasibility of the self-contained IVMRI system during a diagnostic or therapeutic cardiac catheterization [9]. A single nonobstructive plaque with a minimal arterial luminal diameter between 2 and 4 mm in diameter was interrogated. The study demonstrated that the IVMRI catheter was safe, as no catheter-related complications at 30-day follow-up were observed [absent a composite of cardiac death, MI (Q wave and non-Q wave)]. The IVMRI data suggested that the plaque lipid fraction in the study population showed a frequency distribution similar to that found in the ex vivo study of aortic plaques [10].

### 8.2.5 Thermography

Studies have shown that heat released by activated inflammatory cells of atherosclerotic plaques may predict plaque disruption and thrombosis. Using a catheter-based technique, the thermal heterogeneity was found to be larger in patients with unstable angina or acute myocardial infarction compared with those with stable angina [11] and at the culprit segment compared with the nonculprit segment [12]. It has also been shown that statins, which have a proven anti-inflammatory vascular effect, decrease the temperature difference in patients with stable angina, unstable angina, and ACS [13]. In another study, Stefanadis et al. [14] showed that the temperature difference was a strong predictor of adverse cardiac events. Currently, several thermography catheters are being studied in clinical trials, which will determine the safety, reproducibility, and benefits of this imaging method.

### 8.2.6 Near-Infrared Spectroscopy

Near-infrared (NIR) spectroscopy is based on the proven theory that different substances absorb and scatter NIR light to different degrees at various wavelengths. An NIR spectrometer emits light into a sample and measures the proportion of light that is returned over a wide range of optical wavelengths. NIR spectroscopy has the advantage of deep penetration. This imaging modality yields information on the chemical composition of plaques, which may be helpful in identifying vulnerability. NIR has been shown to identify lipid-rich plaque in coronary autopsies [15]. A catheter-based NIR spectroscopy device, similar in size and use to an IVUS catheter, was tested successfully in humans. High-quality spectra were obtained that were similar to those obtained in autopsy studies [16]. Additional studies have shown the excellent ability of NIR spectroscopy to image coronary artery plaques [17–19].

### 8.2.7 Palpography

Plaque rupture related to weakening of the atheromatous cap is prone to occur in regions with increased mechanical stress caused by the pulsatile intravascular blood pressure, which strains the vessel wall. Intravascular palpography can measure strain using cross-correlation analysis of radio-frequency ultrasound signals recorded at different intravascular pressures. A plaque is considered vulnerable when a high-strain region was present at the lumen–plaque boundary that is surrounded by low strain values. As such, lipid-rich plaques will deform more and thus show a higher strain value than those associated with calcified or fibrous plaques [20]. It has been shown that in postmortem coronary arteries the presence of high strain indicates plaque vulnerability with a sensitivity of 88% and a specificity of 89% [21]. Three-dimensional palpography allowed the identification of highly deformable plaques in human coronary arteries, and the results were confirmed by both clinical presentation and markers of inflammation [22]. However, much larger studies are needed to determine the clinical utility of this modality.

The last three modalities discussed, thermography, NIR spectroscopy, and palpography, are all research imaging tools and are not yet used in a clinical context.

## 8.3 HIGH-RESOLUTION OPTICAL COHERENCE TOMOGRAPHY IMAGING IN CARDIOLOGY

OCT is an optical analog of ultrasound; it measures the intensity of the reflected light and translates these multiple optical echoes into high-resolution two-dimensional tomographic images of tissue at the microscopic level. OCT has the highest resolution of any vascular imaging modality, ranging from 4 to 20 μm, which is an order of magnitude higher than the spatial resolution of a 40-MHz IVUS.

Compared to other invasive intracoronary imaging modalities described above, OCT has the highest axial resolution and has superior ability in detecting fibrous cap, lipid core, and calcium (Table 8.1). However, OCT is inferior to thermography in the detection of inflammation and to angioscopy in the detection of thrombus.

### 8.3.1 Plaque Characterization

The characterization of human atherosclerotic plaques with OCT was first detailed in 2002 in an ex vivo study on 357 postmortem atherosclerotic segments from 90

**TABLE 8.1** **Comparison of Current Invasive Imaging Modalities**

| Technology | Axial Resolution | Detection | | | | | Application |
|---|---|---|---|---|---|---|---|
| | | Fibrous Cap | Lipid Core | Inflammation | Calcium | Thrombus | |
| IVUS | 100 μm | + | + | − | +++ | + | Plaque morphology and structure |
| Angioscopy | 100 μm | + | ++ | − | − | +++ | Plaque surface visualization |
| OCT | 10 μm | +++ | +++ | ++ | +++ | + | Detailed morphology, including macrophages |
| Thermography | 500 μm | − | − | +++ | − | − | Surface temperature |
| NIR spectroscopy | — | + | ++ | ++ | ++ | − | Chemical and tissue characteristics |
| IVMRI | 160 μm | + | ++ | + | ++ | + | Plaque morphology and structure |
| Angiography | 1 mm | − | − | − | + | + | Luminogram to detect stenosis |

cadavers [23]. This study established OCT criteria for the various plaque components and enabled identification of the three types of histological plaques: fibrous, fibrocalcific, and lipid-rich (Figure 8.1). Fibrous plaques were characterized as homogeneous, signal-rich regions with low attenuation; fibrocalcific plaques as well-delineated signal-poor regions with sharp borders; and lipid-rich plaques as signal-poor regions with diffuse borders. Using histology as a gold standard, high sensitivity and specificity values have been obtained: 96% and 97%, respectively, for calcific plaques; 90% and 92%, respectively, for lipid-rich plaques; and 71 to 79% and 97%, respectively, for fibrotic plaques.

In addition to characterization of the basic anatomy of arterial wall, OCT has also been shown to be able to detect and quantify macrophages in atherosclerotic plaques [25]. Good correlation ($r = 0.84$, $p < 0.0001$) was shown between OCT and histological measurements of fibrous cap macrophage density. This ability of OCT to detect macrophages is due to the direct correlation of strong back deflections to macrophage density within atherosclerotic caps.

The first study of OCT in human coronaries involved 10 patients undergoing percutaneous coronary intervention and established the feasibility and the safety of OCT compared to IVUS [26]. A mean axial resolution of 13 μm [standard deviation (SD) 3 μm] was achieved with OCT compared to the IVUS axial resolution of 98 μm (SD 19 μm). Tissue penetration averaged 1.25 mm with OCT

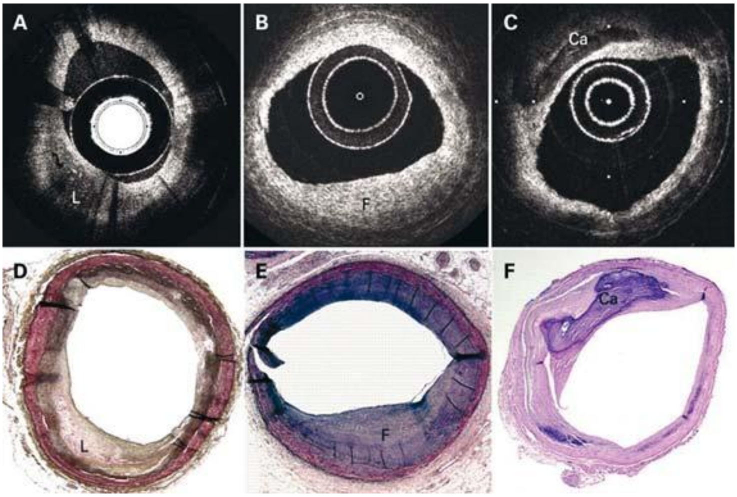

**FIGURE 8.1** OCT images and corresponding histology for fibrous (A,B), calcific (C,D) and lipid-rich (E,F) plaque types (obtained ex vivo). In fibrous plaques, the OCT signal (Fib) is observed to be strong and homogeneous. In comparison, both calcific (arrows) and lipid-rich regions (L) appear as signal-poor regions within the vessel wall. Lipid-rich plaques have diffuse or poorly demarcated borders, while the borders of calcific nodules are sharply delineated. (B,D) Hematoxylin and eosin; (F) Masson's trichome. Original magnification 40×. Scale bars, tick marks, 500 μm. (From [24], with permission.)

and 5 mm with IVUS. Both methods were able to detect the same vessel wall structures, although OCT allowed for better visualization of calcified areas without the problem of acoustic shadowing inherent in IVUS. Acoustic shadowing in this regard is defined as an artifact created by the vessel calcification seen by IVUS imaging in which an intensely echogenic line appears at the surface and blocks the passage of sound waves. OCT was also able to characterize intimal hyperplasia and lipid pools, which were not evident with IVUS. The present capabilities of OCT are well suited for the identification and study of plaques in which the relevant morphologic features are localized primarily within 500 μm of the luminal surface.

### 8.3.2 Detection of Vulnerable Plaque

Acute coronary syndromes frequently arise consequent to rupture of an angiographically moderate plaque with occlusive thrombus formation [27]. Plaques prone to rupture have certain characteristics and are often referred to as vulnerable or high-risk plaques. Such plaques contain a large lipid pool, often covered by a thin fibrous cap, typically less than 65 μm [28]. Increased macrophage density is also seen, especially in the shoulder regions. Since these important characteristics are microstructural changes, high-resolution OCT imaging method will assist in the identification of vulnerable plaques.

OCT has been shown to provide detailed in vivo characterization of coronary plaque morphology among patients presenting with stable angina, acute coronary syndrome, and ST segment elevation myocardial infarction (STEMI) [29] (see Figure 8.2). Patients with an acute coronary syndrome had discernible plaque characteristics compared to the patients with stable angina. A higher frequency of thin-capped fibroatheroma (defined as plaque with a lipid content in two or more quadrants on cross-sectional analysis and a fibrous cap thickness of 65 μm or more) was observed in patients with STEMI and acute coronary syndrome than in patients with stable angina (72, 50, and 20%, respectively; $p = 0.012$). In another study, OCT imaging of 225 plaques from 49 patients revealed an increase in both multifocal and local macrophage densities in patients presenting with an acute coronary event. This work also showed that macrophage concentrations were higher focally at rupture sites and at the surface of plaques in culprit lesions of acute patients (Figure 8.3).

### 8.3.3 OCT and Percutaneous Coronary Intervention

OCT has the ability to delineate mural and luminal structures with high sensitivity and allows the precise assessment of lumen dimensions, plaques, thrombi, and dissections, while also being able to assess both immediate and late results of stent implantation. As a result, the scope of OCT as both a research and a clinical tool remains vast.

Intravascular ultrasound has been the standard modality to assess the outcome of coronary intervention. Although IVUS is able to accurately determine cross-sectional dimensions of postpercutaneous coronary interventions (PCI) and assess

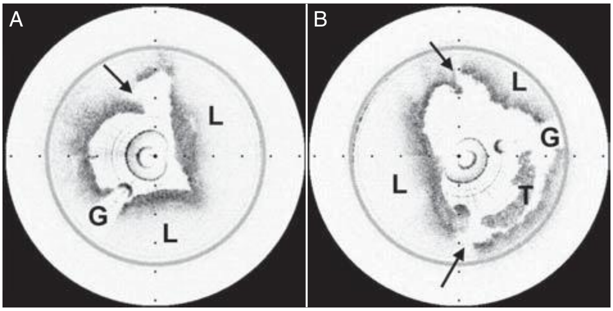

**FIGURE 8.2** Examples of plaque disruption in patients with recent myocardial infarction: (A) Large lipid-rich plaque (L) with localized rupture of a fibrous cap, with a flap protruding into the lumen (arrow); (B) severe disruption of plaque (arrows), with a large mural thrombus (T). Lipid is present in the entire circumference (L). G, guidewire artifact (From [29], with permission.)

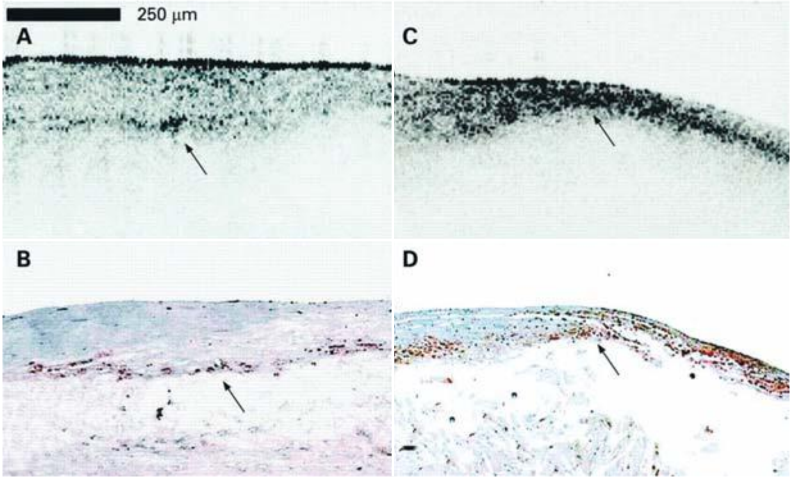

**FIGURE 8.3** Images of atherosclerotic plaques (obtained Ex vivo): (A) OCT image of a fibroatheroma with a low density of macrophages within the fibrous cap (arrow); (C) OCT image of a fibroatheroma with a high density of macrophages within the fibrous cap (arrow); (B,D) histology corresponding to (A) and (C), respectively. Masson's trichome. Original magnification 40×. Scale bars for both OCT and histology, 500 μm. (From [24], with permission.)

stent symmetry and expansion, detailed information related to the stented area is restricted, due to limited IVUS resolution and image quality impairment caused by the metal stent struts. Therefore, the true incidence and clinical relevance of such features as edge dissections, tissue prolapse, and residual thrombus are not known. A study by Cheneau et al. showed that the postintervention IVUS identified at least one of the abnormal findings, such as inadequate stent apposition, dissection, or thrombus, in 78% of patients with subacute stent thrombosis, and multiple findings in 48% of the patients [30].

High resolution of OCT imaging has helped us to observe increased details in the detection of small stent features. Bouma et al. demonstrated that compared with IVUS, OCT detected inadequate stent apposition (17% vs. 7%), tissue protrusion (69% vs. 29%), and dissection (19% vs. 5%) more frequently after stent implantation [31].

One of the important challenges in the field of interventional cardiology is to identify minor or silent plaques that carry the risk of thrombosis, which can result in severe cardiac events. Angiography is limited in its ability to detect these plaques. Although IVUS has been used routinely in interventional cardiology, its limited resolution limits its potential for plaque characterization. Intravascular OCT provides high-resolution cross-sectional images of tissue with a resolution of 10 μm. OCT is also capable of detecting several different features of intravascular pathology, such as the disruption of the fibrous cap of lipid-rich plaques, the presence of intracoronary thrombus, the depth of dissections caused by balloon inflations (which cannot be fully appreciated by IVUS), the cuts in the atherosclerotic plaques made by the blades of the cutting balloons, tissue protruding through stent struts, underdeployed struts otherwise missed by IVUS, and intimal hyperplasia in cases of in-stent restenosis. All these allow for a new assessment and understanding of these particular target areas, which could influence and guide an appropriate patient-specific therapeutic approach (e.g., pharmacologically, balloon angioplasty, stenting, local drug delivery therapy, brachytherapy). In the development of new treatment approaches (e.g., drug-eluting stents, genetic therapies), OCT could play an important role by monitoring and precisely detecting structural changes occurring after application of these new concepts.

### 8.3.4 Current OCT Imaging Systems for Percutaneous Coronary Intervention

OCT systems for intravascular use became commercially available within the last two to three years. Such systems consist of (1) an optical fiber probe, (2) a proximal low-pressure occlusion balloon catheter (Helios Goodman, Advantec Vascular Corp., Sunnyvale, California), and (3) an OCT system mobile cart containing the optical imaging engine and computer for signal acquisition, analysis, and image reconstruction. One commercially available system (M2CV OCT Imaging System, LightLab, Westford, Massachusetts) is shown in Figure 8.4. This system uses as a light source a broadband superluminescent diode (1310 nm) with an output power in the range 8.0 to 10 mW. The imaging depth is around 1.5 mm, and the axial and lateral resolutions are on the order of 15 and 25 μm, respectively. Unlike the IVUS, the OCT catheter contains no transducer, simply an optical fiber that terminates with a microlens.

OCT guidewire-based catheters with profiles as small as 0.014 inch are commercially available (e.g., Imagewire, LightLab Imaging). During imaging, the rotating fiber, encased in a stationary transparent protective sheath, scans the

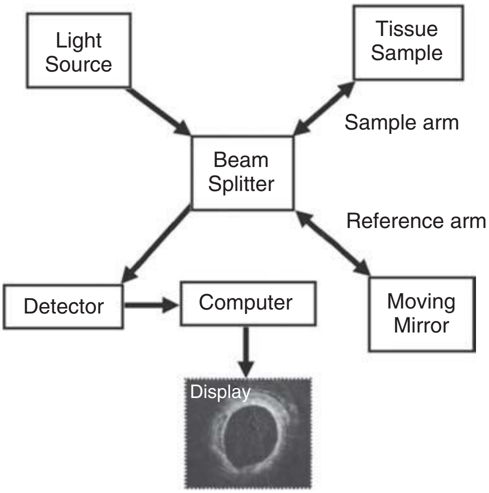

**FIGURE 8.4** OCT system. A low-coherence light source is divided by a beamsplitter; part is sent to the tissue sample down the sample arm, and the other is sent down the reference arm to a moving mirror. The reflected signals are overlaid on a photodetector. Constructive interference occurs when the light in both arms has traveled the same optical distance. The intensity of interference is detected and used to create images.

OCT beam radially. The OCT ImageWire is not torquable and therefore needs to be advanced beyond the region of interest using an over-the-wire Helios occlusion balloon catheter. The occlusion balloon is then pulled back and positioned in a healthy (normal) segment proximal to the region of interest and inflated gently up to 0.4 to 0.7 atm.

To reduce blood influence on image quality, either saline flushes or balloon occlusion is used. While hand saline flushes allow scanning of the stent only up to a few seconds at a time before new blood interference occurs, the use of a balloon occlusion catheter with constant flush of warm lactated Ringer's solution at 0.5 to 1.0 $cm^3/s$ through the distal tip results in better image quality. Infusion should start a few seconds before balloon inflation to get images clean from blood contamination when recording starts. The region of interest is imaged using an automated pullback (1.0 mm/s) from distal to proximal. Images are acquired at 15.4 frames/s and displayed in a real-time two-dimensional array at different transverse positions (tomographic views).

Vessels suitable for OCT scan are normally between 2.5 and 3.75 mm in diameter, without excessive tortuosity ($<90^\circ$ bend) and without visible collaterals. Penetration depth is dependent on the optical scattering properties of the tissue being imaged. Penetration into a native, healthy arterial wall is estimated to be around 2 to 2.5 mm. Human stented coronary vessels with advance atherosclerotic pathological components attenuate the current penetration and create a heterogeneous penetration depth ranging from only few hundred micrometers to a millimeter. Currently, assessment of large stented vessels (>4 mm in diameter) is difficult. Because the catheter may rest against one side of the vessel wall, a large portion of the stent may be outside the imaging range, preventing full cross-sectional visualization. Adaptive ranging is a new, efficient method that enables screening of large arteries, extending the scan range from 3 mm to 7 mm.

### 8.3.5 OCT Imaging of Post-Intracoronary Stents

Since OCT infrared light cannot penetrate metal, stent struts appear in the OCT image as bright local reflections with shadowing sectors radially behind them. However, additional information about the metal struts is desirable. Therefore, OCT signal analysis techniques have been considered for indirect estimations of metal strut thickness. Parameters considered into this analysis are:

1. *Lateral width*. The surface reflections from thinner struts appear narrower in angular dimension; however, this difference is less apparent at distances far from the probe, because the angular sampling frequency (200 lines/frame) limits the angular resolution.
2. *Surface brightness*. The surface reflection of thinner struts tends to appear dimmer because a greater fraction of the focused beam reflects back in the direction of the probe; however, the brightness depends heavily on the orientation of the strut.
3. *Distance from the stent surface reflection to the wall*. Measured from the center of the reflection, the distance to the wall should equal the strut thickness. The edges of the stent act like mirrors and spread the light equally in both directions around the edge on either side of the strut shadow.

Using this approach to assess the *stent strut level* (interpolated linear measurement of stent strut malapposition and coverage), Raffel et al. [32] have developed an automated contour detection algorithm for coronary OCT imaging. This algorithm enables precise measurements of the lumen, stent, malapposition (lumen−stent), and intimal hyperplasia (stent−lumen) areas (Figure 8.5). The ability of OCT to evaluate neointimal hyperplasia is far greater than that of IVUS imaging (Figure 8.6). An important aspect of the stent strut level analysis by OCT is the ability to evaluate intimal hyperplasia per stent strut in an automated fashion and assure that measurements of intimal hyperplasia are always perpendicular to the lumen. In this manner, the relationship between the stent strut and the vessel wall can be defined, which may be important in differentiating the arterial healing response of different endovascular devices. Determination of the percentage of potentially malapposed struts per stent may provide an estimate of the healing process as well. Whether this level of assessment will correlate with clinical outcomes has yet to be determined, but the utilization of automated quantitative systems to evaluate OCT images at high resolution certainly represents a major advance in the way we evaluate coronary atherosclerosis and vascular response to endovascular devices in humans.

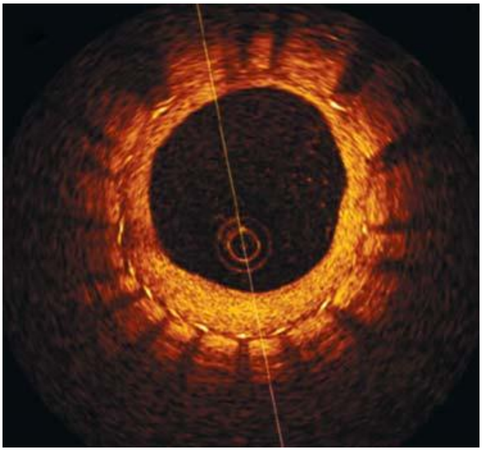

**FIGURE 8.5** OCT image demonstrating the spectrum of neointimal growth in a bare metal stent with generous neointimal growth three months after bare metal stent implantation. (After [32], with permission.)

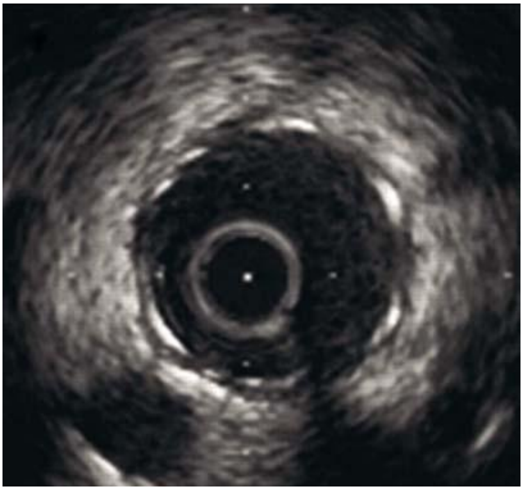

**FIGURE 8.6** The corresponding IVUS image of Figure 8.5 is unable to resolve the thin neointimal layer and clearly demonstrates the advantage of the superior spatial resolution of OCT. (After [32], with permission.)

### 8.3.6 OCT and Drug-Eluting Stents

The risk of late stent thrombosis, albeit small, represents a concern for patients treated with drug-eluting stents (DESs). Delayed healing and poor endothelialization are common findings in pathologic specimens of vessels treated with DESs.

Currently, the only method available to evaluate vascular healing following stent implantation is histopathology, which has limitations, including a small number of cases, selection bias, and tissue preparation. In vivo assessment of the stent coverage has been limited by the low spatial resolution of current image modalities. Methods to assess the response of the stented vessel in vivo and over several time points may lead to better understanding of the types and temporal course of vessel healing.

OCT enables real-time, full tomographic, in vivo visualization of the coronary vessel microstructure. Struts coverage and vessel response of a DES compared to a BMS are the most immediate clinical applications of OCT. Thickness of coverage and strut apposition can be quantified at the micrometer-scale level with a resolution 10 to 30 times higher than that of conventional IVUS. Current clinical experience demonstrates the high level of accuracy of OCT in evaluating the heterogeneity of vascular healing following DES implantation. Neointimal coverage at the strut level assessed by OCT seems a reasonable intermediate endpoint to use in preclinical studies to quickly scrutinize the safety profile of the next generation of DESs.

Considering that stent coverage is not uniform and that the details of this heterogeneity cannot be derived angiographically or by IVUS, the use of OCT represents a great opportunity to evaluate such variability in vascular healing following stenting. Thickness of coverage on each sirolimus DES strut and the strut apposition to the vessel wall were recently evaluated by OCT and IVUS at six months follow-up [33]. OCT identified 91% of the struts to be well apposed and covered, 7% well apposed without coverage, and 1% malapposed, lacking coverage. A high percentage (64%) of struts covered by a thin tissue layer detected by OCT was undetected by IVUS, due to limited resolution [34]. In a recent study, OCT was used to analyze strut apposition and neointimal coverage of DES compared with that of bare metal stents (BMS) at follow-up in 24 patients [35]. In BMS, OCT images showed that all stent struts were completely apposed, with almost all strut surfaces covered by neointima, as well as some struts covered by hyperproliferative neointima, which resulted in re-stenosis. Strut apposition and neointimal thickness were stable in BMS group five months after stenting. Compared with BMS, DES visualized by OCT had more incomplete apposition, with more struts uncovered and thinner neointimal thickness. These results verify the results of numerous earlier studies in which the short-term follow-up showed that DES can significantly reduce neointimal growth and re-stenosis. However, more SES stent struts were uncovered or malapposed than were BMS stent struts. Both of these conditions may lead to late or very late thrombosis. Overall, OCT outperforms IVUS in the identification of incomplete stent apposition, a common finding at the time of DES implant in complex lesions.

### 8.3.7 OCT for Fibrous Cap Disruption and Erosion Characterization

OCT allowed us to evaluate clearly fibrous cap disruption in patients with acute myocardial infarction (AMI). Retrospective pathological studies in patients with coronary artery disease who died suddenly showed fibrous cap disruption in 70% of patients [36]. One angioscopic evaluation revealed that the prevalence of fibrous cap disruption was 55.5% in patients with AMI [37]. Intravascular ultrasound studies have reported varying frequencies of infarct-related fibrous cap disruption (15.8% to 66%) in AMI patients [38], and the durations from symptom onset to IVUS imaging were from 10 h to 4 weeks. In a recent study using OCT, the time from symptom onset to OCT imaging was 3.8 ± 1.0 h, and the prevalence of fibrous cap disruption was 73%, which was similar to that in postmortem pathohistological examinations and more frequent than those in vivo studies using coronary angioscopy and IVUS [39]. In addition, OCT was able to evaluate the fibrous cap erosion clearly, and the prevalence of fibrous cap erosion was 23% in patients with AMI, which is thought to be similar in frequency to that in postmortem histopathology.

### 8.3.8 OCT for Intracoronary Thrombus Characterization

Intracoronary thrombosis might play a critical role in the pathogenesis and the clinical manifestations of AMI. But coronary angiography and IVUS could not reliably identify thrombus. The ability of OCT to detect thrombus deposition has also been reported. Differentiation of various histological types of thrombi might be possible using OCT with high sensitivity and specificity. The capability to detect and delineate different factors that might have a role in stent thrombosis (e.g., incomplete coverage and/or strut apposition, thrombus deposition, aggressive neointimal formation) could indicate a use for OCT if applied during acute stent thrombosis. Jang et al. reported that the frequency of thrombus using OCT imaging was only 20% in patients with recent myocardial infarction who had thrombolytic therapy, and that the average interval between the onset of symptoms and OCT imaging was 4.6 ± 5.3 days [29]. These OCT investigations revealed that the intraluminal thrombus was an important characteristic of vulnerable plaque, and pharmacological thrombolytic intervention could have dissolved some thrombi in the AMI patients.

## 8.4 CURRENT LIMITATION OF OCT

Although OCT has proven its utility in interventional cardiology, it still has some limitations that might be possible to overcome in the future. OCT requires a blood-free imaging field because red blood cells scatter or absorb light and reduce imaging contrast and penetration depth. Saline flushes are used to overcome this issue, but they still limit scan times to approximately 2 s per flush and restrict the length of vessel segments that can be imaged. Techniques such as balloon occlusion for a static saline column or continuous saline flush may allow scanning of longer vessel segments. However, this approach results in transient ischemia and may be cumbersome.

Limited scan depth is another limitation of OCT. Reliable delineation of morphologic structures is currently restricted to a radius of 3 to 4 mm. Therefore, visualization of the complete plaque and evaluation of pathologies beyond the elastin lamina are difficult. However, most features of coronary arteries relevant to plaque vulnerability (except remodeling) are superficial and therefore readily evaluated by OCT. With second-generation high-speed OCT using the frequency domain, scanning of 40 to 50 mm without an occluding balloon has become possible.

## 8.5 FUTURE DEVELOPMENTS

Second-generation Fourier-domain OCT systems have now been developed that have the potential to overcome many of the limitations of conventional time-domain OCT systems. The new technology utilizes a detection method termed Fourier or frequency-domain detection, which allows high-speed acquisition and real-time imaging, which in turn reduces motion artifacts and allows for screening of larger tissue volumes [40]. Such systems have been developed by various groups, including those from the Wellman Laboratories at the Massachusetts General Hospital and LightLab Imaging (Westford, Massachusetts), and their use in human studies has begun. Using guide catheter flush without balloon occlusion, imaging at $\geq$100 frames/s with a pull-back of up to 25 mm/s has been achieved. This is a vast improvement over conventional OCT systems, which had a sampling rate of 4 to 16 frames/s and a pull-back rate of 1 mm/s. This translates into an ability to image an entire coronary artery in a matter of a few seconds. In addition, the superior A-line density of the newer systems results in improved image quality and provides the ability to perform three-dimensional reconstruction.

In addition, the introduction of fluorescence probes that emit in the near-infrared region have opened up a vista for in vivo molecular imaging in cardiology [41]. The use of near-infrared dyes with absorption characteristics within the OCT source spectrum may enhance contrast and further improve the information attainable at depth [42,43]. Such dyes can be attached to nanoparticles with improved optical properties and reduced susceptibility to chemical and thermal denaturation. The combined molecular probe will further enhance OCT imaging capabilities and potentially, could also serve for thermal therapy [44]. This combination of biophotonics and nanotechnology offers the feasibility of new strategies in the detection and therapy of atherosclerotic disease.

One exciting development is the possibility of physiologic evaluation in addition to anatomical information. Currently, the commercial Doppler-based JoMetrics FloWire system (Volcano Corporation, Rancho Cordova, CA, California), allows flow measurements at the distal wire tip and is an established tool in determining the significance of an intermediate lesion and in the assessment of intervention results [45]. Light from a moving particle is Doppler shifted when compared with that from a stationary particle, and thus the direction and velocity of blood flow can be determined. Distinct and complementary information on the physiology of blood flow at the plaque site can therefore be gathered. The detection of blood flow with OCT in human skin has already been demonstrated, and a prototype catheter has been tested [46,47]. The use of this capability could further extend OCT utility in interventional cardiology. The ability to obtain both anatomical and physiological measurements will be very beneficial to the interventionist's armamentarium.

Recent work shows that information on the biomechanical properties of plaque (elastography) may also be obtained with OCT [48–50] These data are especially relevant given that plaque rupture behavior is asymptomatic. A better understanding of plaque vulnerability is critical for determining the optimum treatment of this disease. Elastography is the estimation of biomechanical properties of a tissue using imaging techniques. Because abnormal tissues typically have different biomechanical properties than those of normal tissues, elastography can be used to monitor pathological states such as the abnormal weakening of vessel walls. The principal advantage of OCT elastography over US elastography is its high spatial resolution, which allows for more precise characterization of the biomechanical properties of tissue. Studies have confirmed the feasibility of this approach, albeit in an ex vivo setting with phantom models [51,52].

Although OCT imaging remains largely a research tool, we expect greater use in routine coronary angiography with the publication of data substantiating its use in the broader population. The introduction of 0.014-inch (0.36-mm) wire-based systems without the necessity of utilizing an occlusion balloon will facilitate its use in intervention. The future incorporation of physiological measurements is expected to improve the preference of OCT over IVUS or pressure or Doppler wire methods because additional information can be obtained without incurring the cost of using separate equipment. We envision that OCT will complement emerging noninvasive methods such as multidetector CT or MRI, which might in the future serve as primary prevention measures in high-risk persons. OCT might also prove its usefulness in follow-up population screenings with risk-scoring systems or measurement of biomarkers in asymptomatic people at risk of a cardiac event. The patient can then be evaluated further by the use of a variety of noninvasive imaging techniques, and ultimately proceed to OCT to better define vulnerable lesions with a view to primary prevention.

## 8.6 CONCLUSIONS

OCT is a rapidly evolving technique with a promising outcome in interventional cardiology. It allows for detailed structural analysis of the coronary vessel, including coronary plaque characterization at preselected locations. In the future, however, it will be desirable to provide not only detailed structural information of the vessel wall, but also additional complementary data on flow dynamics and vessel biomechanical properties. Novel methods combining OCT-fluorescence and nanoparticle markers could further expand OCT potential in cardioimaging. The combination of all these technologies could allow for better identification of vulnerable plaques and provide therapy guidance. All these will reduce health care costs and improve patient health status.

## REFERENCES

1. Kawasaki, M., et al., Diagnostic accuracy of optical coherence tomography and integrated backscatter intravascular ultrasound images for tissue characterization of human coronary plaques, *J. Am. Coll. Cardiol.*, Vol. 48, No. 1, 2006, pp. 81–88.
2. Thieme, T., et al., Angioscopic evaluation of atherosclerotic plaques: validation by histomorphologic analysis and association with stable and unstable coronary syndromes, *J. Am. Coll. Cardiol.*, Vol. 28, 1996, pp. 1–6.
3. Takano, M., et al., Mechanical and structural characteristics of vulnerable plaques: analysis by coronary angioscopy and intravascular ultrasound, *J. Am. Coll. Cardiol.*, Vol. 39, 2001, pp. 99–104.
4. Takano, M., et al., Changes in coronary plaque color and morphology by lipid-lowering therapy with atorvastatin: serial evaluation by coronary angioscopy, *J. Am. Coll. Cardiol.*, Vol. 42, 2003, pp. 680–686.
5. Lehmann, K.G., et al., Chromatic distortion during angioscopy: assessment and correction by quantitative colorimetric angioscopic analysis, *Catheter Cardiovasc. Diagn.*, Vol. 45, 1998, pp. 191–201A.
6. Miyamoto, A.R., et al., Atheromatous plaque cap thickness can be determined by quantitative color analysis during angioscopy: implications for identifying the vulnerable plaque, *Clin. Cardiol.*, Vol. 27, 2004, pp. 9–15.
7. Ishibashi, F., et al., Quantitative colorimetry of atherosclerotic plaque using the $L^*a^*b^*$ color space during angioscopy for the detection of lipid cores underneath thin fibrous caps, *Int. J. Cardiovasc. Imaging*, Vol. 23, No. 6, 2007, pp. 679–691.
8. Libby, P., and Ridker, P.M., Inflammation and atherothrombosis from population biology and bench research to clinical practice, *J. Am. Coll. Cardiol.*, Vol. 48, 2006, pp. A33–A46.
9. Regar, E., et al., First in men application of a miniature self-contained intracoronary magnetic resonance imaging probe: a multi-center safety and feasibility trial, *Eur. Intervent.*, Vol. 2, 2006, pp. 77–83.
10. Schneiderman, J., et al., Diagnosis of thin cap fibroatheromas by a self-contained intravascular magnetic resonance imaging probe in ex vivo human aorta and in-situ coronary arteries, *J. Am. Coll. Cardiol.*, Vol. 45, 2005, pp. 1961–1969.
11. Stefanadis, C., et al., Thermal heterogeneity within human atherosclerotic coronary arteries detected in vivo: a new method of detection by application of a special thermography catheter, *Circulation*, Vol. 99, No. 51, 1999, pp. 1965–1971.
12. Dudek, D., et al., Culprit plaque temperature assessment in patients with acute coronary syndromes: intracoronary thermography study in Poland, *Eur. Heart J.*, Vol. 25, 2004, pp. 232–239.
13. Stefanadis, C., et al., Statin treatment is associated with reduced thermal heterogeneity in human atherosclerotic plaques, *Eur. Heart J.*, Vol. 23, 2002, pp. 1664–1669.

14. Stefanadis, C., Toutouzas, K., and Tsiamis, E., Increased local temperature in human coronary atherosclerotic plaques: an independent predictor of clinical outcome in patients undergoing a percutaneous coronary intervention, *J. Am. Coll. Cardiol*., Vol. 37, 2001, pp. 1277–1283.
15. Moreno, P.R., et al., Characterization of composition and vulnerability of atherosclerotic plaques by near-infrared spectroscopy, *Circulation*, Vol. 98, Suppl. 1, 1998, pp. 1–146.
16. Caplan, J.D., et al., Near-infrared spectroscopy for the detection of vulnerable coronary artery plaque, *J. Am. Coll. Cardiol*., Vol. 47, 2006, pp. C92–C96.
17. Moreno, P.R., et al., Detection of lipid pool, thin fibrous cap, and inflammatory cells in human aortic atherosclerotic plaques by near-infrared spectroscopy, *Circulation*, Vol. 105, No. 8, 2002, pp. 923–927.
18. Wang, J., et al., Near-infrared spectroscopic characterization of human advanced atherosclerotic plaques, *J. Am. Coll. Cardiol*., Vol. 39, No. 8, 2002, pp. 1305–1313.
19. Waxman, S., Near-infrared spectroscopy for plaque characterization, *J. Intervent. Cardiol*., Vol. 21, No. 6, 2008, pp. 452–458.
20. de Korte, C.L., et al., Identification of atherosclerotic plaque components with intravascular ultrasound elastography in vivo: a Yucatan pig study, *Circulation*, Vol. 105, 2002, pp. 1627–1630.
21. Schaar, J.A., et al., Characterizing vulnerable plaque features with intravascular elastography, *Circulation*, Vol. 108, 2003, pp. 2636–2641.
22. Schaar, J.A., et al., Incidence of high-strain patterns in human coronary arteries: assessment with three-dimensional intravascular palpography and correlation with clinical presentation, *Circulation*, Vol. 109, 2004, pp. 2716–2719.
23. Yabushita, H., et al., Characterization of human atherosclerosis by optical coherence tomography, *Circulation*, Vol. 106, No. 13, 2002, pp. 1640–1645.
24. Tearney, G.J., et al., Optical coherence tomography for imaging the vulnerable plaque, *J. Biomed. Opt*., Vol. 11, No. 2, 2006, p. 021002.
25. Tearney, G.J., et al., Quantification of macrophage content in atherosclerotic plaques by optical coherence tomography, *Circulation*, Vol. 107, No.1, 2003, pp. 113–119.
26. Jang, I.K., et al., Visualization of coronary atherosclerotic plaques in patients using optical coherence tomography: comparison with intravascular ultrasound, *J. Am. Coll. Cardiol*., Vol. 39, No. 4, 2002, pp. 604–609.
27. Libby, P., Current concepts of the pathogenesis of the acute coronary syndromes, *Circulation*, Vol. 104, 2001, pp. 365–372.
28. Burke, A.P., et al., Coronary risk factors and plaque morphology in men with coronary disease who died suddenly, *N. Engl. J. Med*., Vol. 336, 1997, pp. 1276–1282.
29. Jang, I.K., et al., In vivo characterization of coronary atherosclerotic plaque by use of optical coherence tomography, *Circulation*, Vol. 111, No. 12, 2005, pp. 1551–1555.
30. Cheneau, E., et al., Predictors of subacute stent thrombosis: results of a systematic intravascular ultrasound study, *Circulation*, Vol. 108, No. 1, 2003, pp. 43–47.
31. Bouma, B.E., et al., Evaluation of intracoronary stenting by intravascular optical coherence tomography, *Heart*, Vol. 89, 2003, pp. 317–320.
32. Raffel, A., et al., Cardiac optical coherence tomography, *Heart*, Vol. 94, 2008, pp. 1200–1210.

33. Matsumoto, D., et al., Neointimal coverage of sirolimus-eluting stents at 6-month follow-up: evaluated by optical coherence tomography, *Eur. Heart J*., Vol. 28, No. 8, 2007, pp. 961–967.

34. Takano, M., et al., Evaluation by optical coherence tomography of neointimal coverage of sirolimus eluting stent three months after implantation, *Am. J. Cardiol*., Vol. 99, No. 8, 2007, pp. 1033–1038.

35. Chen, B.X., et al., Neointimal coverage of bare-metal and sirolimus-eluting stents evaluated with optical coherence tomography, *Heart*, Vol. 94, No. 5, 2008, pp. 566–570.

36. Davies, M.J., and Thomas, A., Thrombosis and acute coronary-artery lesions in sudden cardiac ischemic death, *N. Engl. J. Med*., Vol. 310, No. 18, 1984, pp. 1137–1140.

37. Mizote, I., et al., Distal protection improved reperfusion and reduced left ventricular dysfunction in patients with acute myocardial infarction who had angioscopically defined ruptured plaque, *Circulation*, Vol. 112, No. 7, 2005, pp. 1001–1007.

38. Hong, M.K., et al., Comparison of coronary plaque rupture between stable angina and acute myocardial infarction: a three-vessel intravascular ultrasound study in 235 patients, *Circulation*, Vol. 110, No. 8, 2004, pp. 928–933.

39. Kubo, T., et al., Assessment of culprit lesion morphology in acute myocardial infarction: ability of optical coherence tomography compared with intravascular ultrasound and coronary angioscopy, *J. Am. Coll. Cardiol*., Vol. 50, No. 10, 2007, pp. 933–939.

40. Yun, S.H., et al., High-speed optical frequency-domain imaging, *Opt. Express*, Vol. 11, 2003, pp. 2953–2963.

41. Jaffer, F.A., and Weissleder, R., Seeing within: molecular imaging of the cardiovascular system, *Circ. Res*., Vol. 94, 2004, pp. 433–445.

42. Xu, C., et al., Near-infrared dyes as contrast-enhancing agents for spectroscopic optical coherence tomography, *Opt. Lett*., Vol. 29, 2004, pp. 1647–1649.

43. Tumlinson, A.R., et al., Miniature endoscope for simultaneous optical coherence tomography and laser-induced fluorescence measurement, *Appl. Opt*., Vol. 43, 2004, pp. 113–121.

44. Loo, C., et al., Nanoshell-enabled photonics-based imaging and therapy of cancer, *Technol. Cancer Res. Treat*., Vol. 3, 2004, pp. 33–40.

45. Bishop, A.H., and Samady, H., Fractional flow reserve: critical review of an important physiologic adjunct to angiography, *Am. Heart J*., Vol. 147, 2004, pp. 792–802.

46. Pierce, M.C., et al., Advances in optical coherence tomography imaging for dermatology, *J. Invest. Dermatol*., Vol. 123, 2004, pp. 458–463.

47. Li, X., et al., Intraluminal fiber-optic Doppler imaging catheter for structural and functional optical coherence tomography, *Opt. Lett*., Vol. 26, 2001, pp. 1906–1908.

48. de Korte, C.L., et al., Characterization of plaque components with intravascular ultrasound elastography in human femoral and coronary arteries in vitro, *Circulation*, Vol. 102, 2000, pp. 617–623.

49. Muthupillai, R., et al., Magnetic resonance elastography by direct visualization of propagating acoustic strain waves, *Science*, Vol. 269, 1995, pp. 1854–1857.

50. Schaar, J.A., et al., Characterizing vulnerable plaque features with intravascular elastography, *Circulation*, Vol. 108, 2003, pp. 2636–2641.

51. Rogowska, J., et al., Optical coherence tomographic elastography technique for measuring deformation and strain of atherosclerotic tissues, *Heart*, Vol. 90, 2004, pp. 556–562.
52. Chan, R.C., et al., OCT-based arterial elastography: robust estimation exploiting tissue biomechanics, *Opt. Express*, Vol. 12, 2004, pp. 4558–4572.

# 9

# FLUORESCENCE LIFETIME SPECTROSCOPY IN CARDIO- AND NEUROIMAGING

LAURA MARCU
*University of California–Davis, Davis, California*

JAVIER A. JO
*Texas A&M University, College Station, Texas*

PRAMOD BUTTE
*Cedars–Sinai Medical Center, Los Angeles, California*

9.1 Introduction 256
9.2 Fluorescence lifetime spectroscopy in tissue characterization 256
9.3 Time-resolved fluorescence spectroscopy: instrumentation 257
9.4 Time-resolved fluorescence spectroscopy: data analysis methods 261
  9.4.1 Laguerre expansion technique for deconvolution of TRFS data 262
  9.4.2 Biomedical application of the laguerre expansion technique for deconvolution of TRFS data 263
9.5 Atherosclerotic plaque 264
  9.5.1 Clinical diagnosis and challenges 264
  9.5.2 Fluorescence spectroscopy and atherosclerotic plaque characterization 265
  9.5.3 Detection of compositional features related to plaque vulnerability using fluorescence lifetime spectroscopy 266
9.6 Primary brain tumors 271
  9.6.1 Clinical diagnosis of primary brain tumors 272
  9.6.2 Fluorescence spectroscopy of brain tumors 273
  9.6.3 Diagnosis of brain tumors using fluorescence lifetime spectroscopy 274
9.7 Concluding remarks 278
References 280

---

*Advances in Optical Imaging for Clinical Medicine*, Edited by Nicusor Iftimia, William R. Brugge, and Daniel X. Hammer
Copyright © 2011 John Wiley & Sons, Inc.

## 9.1 INTRODUCTION

This chapter is intended to present an overview of time-resolved (lifetime) fluorescence spectroscopy techniques and the potential of tissue autofluorescence measured using such techniques to provide useful label-free contrast for biomedical research and clinical applications. In particular, we review the development of time-resolved laser-induced fluorescence spectroscopy (TR-LIFS) instrumentation and associated methodologies which allow for in vivo characterization and diagnosis of biological systems. Emphasis is placed on the translational research potential of TR-LIFS and on determining whether intrinsic fluorescence signals can be used to provide useful contrast for the diagnosis of high-risk atherosclerotic plaque and brain tumors intraoperatively.

## 9.2 FLUORESCENCE LIFETIME SPECTROSCOPY IN TISSUE CHARACTERIZATION

Fluorescence is a ubiquitous approach to achieving optical molecular contrast using a wide range of instruments, including spectrophotometers, microarrays, microscopes, and endoscopes. Fluorescence measurements can provide information not only on the specific molecular makeup of a sample but also on the local environment surrounding the fluorophore (fluorescence molecule). Distinct species of fluorophores may be characterized based on their excitation and emission spectra, their quantum efficiency, their polarization, and their fluorescence lifetime [1]. Most common fluorophores in biological tissue include aromatic amino acids (tyrosine, tryptophane, and phenylalanine), structural proteins (elastin and collagen and its cross-links), enzyme metabolic cofactors [nicotinamide adenine dinucleotide (NADH) and flavins], lipid components and porphyrins. The absorption and emission characteristics of these fluorophores have been reviewed in numerous publications [1–4].

The fluorescence measurements have the potential to provide information about biochemical, functional, and structural changes in fluorescent biomolecular complexes in tissues and cells that occur as a result of either pathological transformation or therapeutic intervention [1–12]. As light delivery and collection can be achieved using fiber optics, fluorescence-based techniques can facilitate non- or minimally invasive, remote investigations of tissues; thus, they are suitable for clinical intraoperative applications [13]. A wide range of applications of fluorescence techniques to tissue diagnostics, ranging from a variety of tumors to cardiovascular and bioengineered tissues, were reported and presented in several review papers and other pertinent publications [1–12,14–21].

Fluorescence measurements can be conducted as either steady-state (spectrally resolved) or time resolved. The steady-state techniques for measurement of tissue autofluorescence are relatively well established [3,9,12]. However, time-resolved techniques are still evolving and currently are being actively investigated as a tool for enhanced free-label contrast in biological tissues. Such techniques are thought to improve the specificity of fluorescence measurements by resolving the fluorescence intensity decay in terms of lifetimes and thus provide additional information about the underlying fluorescence dynamics [1,7,8]. Conceptually, the fluorescence lifetime is the average time a fluorophore spends in the excited states following excitation from its ground energy level. As many of the fluorophores in biological tissues have an overlapping spectrum [3,4], fluorescence lifetime properties can provide a contrast parameter. Also, the fluorescence lifetime varies with the molecular environment and is independent of fluorophore concentration and its quantum yield [1,4,7]. Overall, the use of time-resolved fluorescence for studying biological systems offers several distinct advantages. First, biomolecules with overlapping fluorescence emission spectra but different fluorescence decay times can be discriminated. In addition, the measurements are sensitive to various parameters of the biological microenvironment (including pH, ion concentration and binding, enzymatic activity, and temperature), thus allowing these variables to be analyzed, and are more robust to changes in fluorescence excitation-collection geometry, presence of endogenous absorbers (e.g., hemoglobin), photobleaching, and changes in fluorophore concentration, light scattering, and excitation intensity. Despite these recognized inherent advantages, the potential value of fluorescence lifetime information has not been implemented broadly in clinical settings, due to such barriers as complexity of instrumentation, lengthy data acquisition and analysis, and high instrumentation cost. However, there is currently an increased interest in identifying solutions that enable the development of appropriate fluorescence lifetime-based instrumentation for clinical applications.

## 9.3 TIME-RESOLVED FLUORESCENCE SPECTROSCOPY: INSTRUMENTATION

Fluorescence lifetime or time-resolved measurements can be conducted in either the time or the frequency domain. The first approach relies on instrumentation that measures the fluorescence signal as a function of time delay following pulsed excitation. The second derives the lifetime information from measurements of phase difference between a sinusoidally modulated excitation and the resulting sinusoidally modulated fluorescence signal [1,22]. Both approaches provide equivalent information on the fluorescence intensity decay. However, there are significant differences and balancing factors in the implementation and application of these two approaches. Frequency-domain detection was preferred initially, due to the simpler electronic instrumentation and excitation source requirements. However, measurements of complex intensity decay require repeated experiments at different excitation modulation frequency in order to encompass the entire fluorescence decay dynamics. This results in increased data acquisition and analysis time, which limits the suitability of this approach for clinical applications. In contrast, the time-domain techniques require complex optoelectronic equipment, including fast-gated cameras, streak cameras, and fast (gigahertz bandwidth) sampling oscilloscopes, working in conjunction with ultrashort (subnanosecond) pulsed lasers. Yet there are limited options for such pulsed lasers in the ultraviolet range (330 to 400 nm), where most of endogenous fluorophores are excited efficiently. Time-domain systems present some unique advantages, however [7]. These include the fact that the Fourier spectrum of a short laser pulse is broad enough to provide a wideband stimulus that allows complex fluorescence decay dynamics (multiple lifetimes) to be measured at once. In addition, pulsed laser systems working at a low (10 kHz) repetition rate do not require complete darkness and can be operated at room light, which make them compatible with the clinical environment [7].

Overall, fluorescence lifetime information from biological system can be determined through either spectroscopy systems for point measurements or imaging systems known as fluorescence lifetime imaging microscopy (FLIM). This chapter concerns primarily point spectroscopy techniques. A comprehensive overview of FLIM systems, both scanning and wide field, and their potential applications has been given by Elson et al. [22].

The most commonly used technique for point measurement spectroscopy systems is time-correlated single-photon counting (TCSPC) [1]. This technique is generally preferred and became the method of choice due to its high sensitivity and low degree of systematic errors. In TCSPC the standard deviation of each channel can be estimated from Poisson statistics. This is important when the goal of the experiment is the resolution of complex intensity decay. TCSPS is described widely in the literature and has been already implemented in commercial systems such as those developed by PicoQuant GmbH [23] and Becker and Hickl GmbH [24]. In recent years, however, we have witnessed the reintroduction [25–27] of an alternative method—pulse sampling (transient pulse recording) with gated detection. This approach was used prior to the introduction of TCSPC and consists of measuring the intensity decay using stroboscopic or pulse sampling (repetitively sample the intensity decay during pulse excitation). Nowadays, by taking advantage of fast digitizers and gated photomultipliers, this approach permits detection of many photons per laser pulse, and thus the entire intensity decay profile can be rapidly recorded and digitized. Also, gated detection can be used with low-repetition-rate lasers; thus, as noted above, it allows for measurements at room light. These two features are particularly important for studies in clinical settings. In this chapter we focus primarily on the development of the time-resolved time-domain pulse sampling/gated detection technique and its applications to the diagnosis of diseased tissues.

An example of a pulse sampling and time-gated technique for recording of spectrally resolved fluorescence intensity decays (lifetimes) is depicted in Figure 9.1a. This time-resolved laser-induced fluorescence spectroscopy system (TR-LIFS) apparatus [25] was used in a variety of tissue autofluorescence studies [28–30]. Although distinct in the way that this apparatus was implemented, principally it is similar to other systems reported earlier by our group [31–36] and others [26,27]. It follows a modular design consisting of:

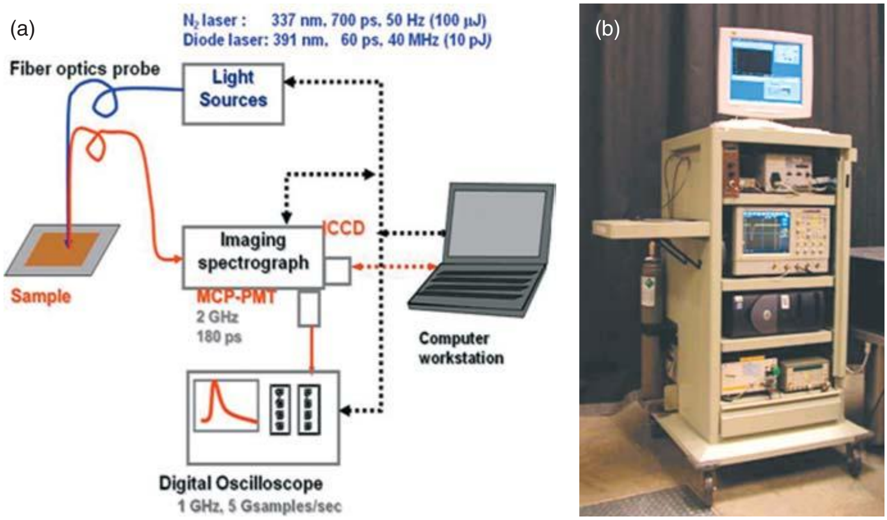
(a)
$N_2$ laser: 337 nm, 700 ps, 50 Hz (100 μJ)
Diode laser: 391 nm, 60 ps, 40 MHz (10 pJ)
Fiber optics probe
Light Sources
Sample
Imaging spectrograph
ICCD
MCP-PMT
2 GHz
180 ps
Computer workstation
Digital Oscilloscope
1 GHz, 5 Gsamples/sec
(b)

**FIGURE 9.1** (a) Spectroscopy setup used to measure the spectrally resolved (through a scanning system) time-resolved fluorescence emission of a biological sample; (b) TR-LIFS apparatus, which allows for clinical investigations. (After [25], with permission.)

1. A nitrogen laser as an excitation source (337.1 nm, 700 ns pulse width, 100 mJ and 50 Hz maximum output and repetition rate, respectively) equipped with a dye module (400 to 900 nm).
2. A fiber optic probe for light delivery and collection which can be implemented using various designs, including a bifurcated configuration or a single fiber coupled to a dichroic module. The fiber probe is sterilizable, includes standard fiber optic connectors, and thus requires no alignment when changing probes or light sources.
3. A $f/4$ dual-mode imaging spectrograph with two associated detectors.
4. A digital oscilloscope (1 GHz, sampling rate: 5 GS/s), a computer workstation, and peripheral electronics.

The fluorescence emitted is captured and directed, via the collection channel of the probe, into the entrance slit of the spectrometer and detected by a multichannel plate photomultiplier tube (MCP-PMT: rise time 180 ps, spectral response 160 to 850 nm, bandwidth: continuous wave to 2.0 GHz). The temporal resolution of this system is about 200 ps. The scanning monochromator allows for TR-LIFS measurements at discrete steps across the emission spectrum, an important feature when the TR-LIFS is used to characterize a new biological system (e.g., tissue type) and to determine which spectral range(s) can be used to provide useful contrast. In the configuration reported, the scanning of a 200-nm (5-nm step) spectral range, including the acquisition and display of fluorescence decay, can be completed within approximate 30 s (ca. 0.8 s/wavelength).

The apparatus was fully contained in a modified endoscopic cart (70 × 70 × 150 $cm^3$), as shown in Figure 9.1b, and allows for clinical research investigations. The laser triggering, wavelength scanning, and data acquisition, storage, and processing were controlled using a computer and custom software written in LabVIEW and MATLAB. Typically, the TR-LIFS measurements are conducted with the fiber optic probe placed perpendicularly to the sample. After each measurement sequence, the laser pulse temporal profile is measured at a wavelength slightly below the excitation laser line. This profile is used as input to the deconvolution algorithm for the estimation of fluorescence lifetimes.

In the configuration described above, however, practical clinical application of TR-LIFS still faces challenges. These include time-expensive data acquisition due to scanning of the monochromator. Recently, Sun et al. [37] reported a novel concept which allows for near real-time acquisition of spectrally resolved fluorescence intensity transients through the combination of optical fibers and bandpass filters (Figure 9.2).

A single detector is used to record multiple fluorescence intensity decay profiles (fluorescence response pulses) simultaneously in response to a single pulse excitation event. Simultaneous time- and wavelength-resolved fluorescence spectroscopy (STWRFS) allows the recording of both fluorescence lifetime and

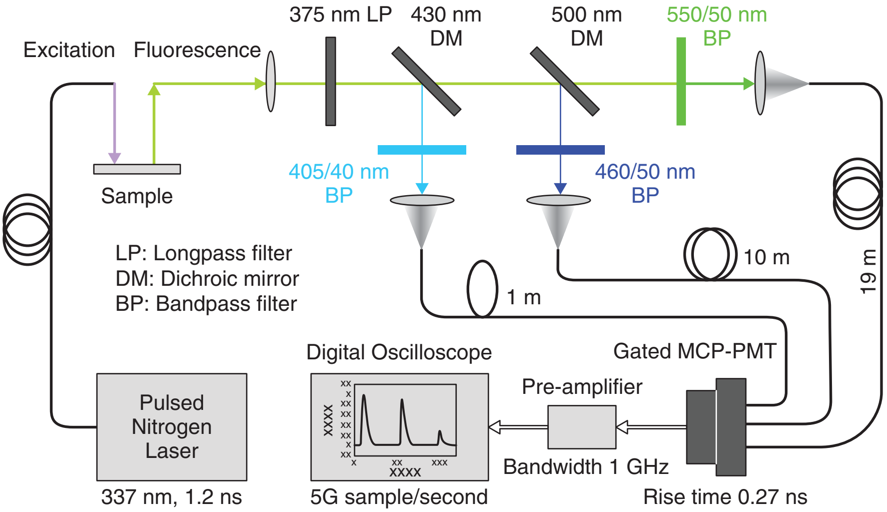
375 nm LP
430 nm DM
500 nm DM
550/50 nm BP
Excitation
Fluorescence
Sample
405/40 nm BP
460/50 nm BP
LP: Longpass filter
DM: Dichroic mirror
BP: Bandpass filter
10 m
1 m
19 m
Digital Oscilloscope
Gated MCP-PMT
Pre-amplifier
Pulsed Nitrogen Laser
Bandwidth 1 GHz
337 nm, 1.2 ns
5G sample/second
Rise time 0.27 ns

**FIGURE 9.2** Simultaneous time- and wavelength-resolved fluorescence spectroscopy (STWRFS) system. By combining multiple bandpass and dichroic filters (405/40, 460/50, and 550/50) with different lengths of optical fiber (1, 10, and 19 m) acting as an optical delay, this system enables the near real-time acquisition and characterization of time-resolved fluorescence spectra using a single detector and excitation input. The recording of multiple fluorescence response pulses at selected wavelengths can be completed in hundreds of nanoseconds, which provides the capability of a real-time characterization of biological systems. (After [37], with permission.)

spectral intensity information within hundreds of nanoseconds within multiple spectral bands. In addition, this system can be optimized for the characterization of a particular disease/tissue with suitable spectral bands, thus simplifying the data analysis and tissue classification algorithms. Since the objective of medical diagnosis is to identify conditions in tissue by rapid recognition of signatures corresponding to specific states, this approach has an inherent potential for a direct recording of representative tissue fluorescence features. Once this apparatus is interfaced with classification models that enable online diagnosis, the STWRFS device can evolve into a clinical diagnosis tool.

## 9.4 TIME-RESOLVED FLUORESCENCE SPECTROSCOPY: DATA ANALYSIS METHODS

In the context of time-domain time-resolved fluorescence measurements, the fluorescence impulse response function (IRF) contains all the temporal information of a single fluorescence decay measurement. Mathematically, the fluorescence intensity decay measured is the convolution of the IRF with the instrument response. Thus, to estimate the fluorescence IRF of a sample, the instrument response must be deconvolved from the measured fluorescence intensity pulse [38]. Traditionally, the most commonly applied deconvolution method is least-squares iterative reconvolution (LSIR) [38,39]. LSIR applies nonlinear least-squares optimization methods (i.e., Gauss–Newton, Lavenberg–Marquardt) to estimate the parameters of a multiexponential IRF that would best fit its convolution with the instrument response to the fluorescence decay data. Since the optimization process involves iterative convolutions, LSIR is computationally expensive. Moreover, since exponential functions do not form an orthonormal basis, different multiexponential combinations can be fitted equally well to fluorescence decay data, due to the correlation of the fitting parameters in the multiexponential model. As noted above, fluorescence emission in tissues originates from several endogenous fluorophores and is affected by light absorption and scattering. From such a complex medium, it is not entirely adequate to analyze time-resolved fluorescence decay in terms of multiexponential components, since they cannot be interpreted in terms of fluorophore content or number of lifetime components [1]. Thus, for tissue TR-LIFS data analysis, there is an advantage in avoiding any a priori photophysical assumption about the functional form of the IRF decay. An alternative model-free deconvolution method for TR-LIFS data analysis, based on the Laguerre expansion of the kernel technique (LET), has been reported more recently [40–41]. This method was found to provide important advantages over the more traditional methods when used in the context of tissue characterization.

LET was adapted and popularized in the early 1990s by Marmarelis for the linear and nonlinear modeling of physiological systems [42]. LET is based on the expansion of the kernels (IRF, for linear systems) on a set of orthonormal discrete Laguerre functions (DLFs), allowing fast-converging kernel estimation from short input–output data records, using least-squares calculation of the expansion coefficients. This method has been applied extensively since then to the modeling of different physiological systems, including renal autoregulation and cardiac autonomic control [101]. Taking advantage of the asymptotic exponential decline characteristics of the DLFs, the LET was recently adapted for the deconvolution of TR-LIFS decay data and estimation of fluorescence IRFs [34–36,40]. The resulting Laguerre deconvolution method has been proven to be a fast, robust, and model-free alternative for the analysis of TR-LIFS, properties highly desirable for tissue diagnostic applications. Also interesting, the potential of the Laguerre expansion coefficients derived from this method has recently been explored for direct quantification of the fluorescence characteristics of complex biological systems [41]. In the following we review the Laguerre deconvolution technique in the context of TR-LIFS data analysis.

### 9.4.1 Laguerre Expansion Technique for Deconvolution of TRFS Data

In the context of TR-LIFS, the measured fluorescence intensity decay data $y(n)$ is given by the convolution of the fluorescence IRF $h(n)$ with the instrument response $x(n)$:

$$y(n) = T\sum_{m=0}^{K-1} h(m)x(n-m), \qquad n = 0, \ldots, N-1 \tag{9.1}$$

The parameter $K$ determines the length of the fluorescence decay (IRF), $N$ is the number of time samples recorded for both $y(n)$ and $x(n)$, and $T$ is the sampling interval (time resolution of the intrument). The Laguerre deconvolution technique expands the fluorescence IRF on an orthonormal set of discrete-time Laguerre functions (DLFs) $b_j^{\alpha}(n)$:

$$h(n) = T\sum_{j=0}^{L-1} c_j^{\alpha} b_j^{\alpha}(n) \tag{9.2}$$

In equation (9.2), $c_j^{\alpha}$ are the unknown Laguerre expansion coefficients (LECs), which are to be estimated from the input–output data; $b_j^{\alpha}(n)$ denotes the $j$th-order orthonormal DLF; and $L$ is the number of DLFs used to model the IRF, thus defining the order of the expansion. Functions of higher order converge more slowly to zero.

The Laguerre parameter $\alpha$ $(0 < \alpha < 1)$ determines the rate of exponential (asymptotic) decline of the DLFs. Thus, higher-order and larger $\alpha$ values imply longer convergence time to zero. By inserting equation (9.2) into (9.1), the convolution equation (9.1) becomes

$$\begin{aligned} y(n) &= \sum_{j=0}^{L-1} c_j^{\alpha} v_j^{\alpha}(n) \\ v_j^{\alpha}(n) &= \sum_{i=0}^{K-1} b_j^{\alpha}(m)x(n-m) \end{aligned} \tag{9.3}$$

The functions $v_j^{\alpha}(n)$, representing the digital convolution of the input $x(n)$ with each of the Laguerre functions $b_j^{\alpha}(n)$, are denoted as the *key variables*.

The system of linear equations (9.3) can be expressed in matrix notation as follows:

$$\underbrace{\begin{bmatrix} y(0) \\ y(1) \\ \vdots \\ y(N-1) \end{bmatrix}}_{\overline{y}_{[N\times 1]}} = \underbrace{\begin{bmatrix} v_0^{\alpha}(0) & v_1^{\alpha}(0) & \cdots & v_{L-1}^{\alpha}(0) \\ v_0^{\alpha}(1) & v_1^{\alpha}(1) & \cdots & v_{L-1}^{\alpha}(1) \\ \vdots & \vdots & \ddots & \vdots \\ v_0^{\alpha}(N-1) & v_1^{\alpha}(N-1) & \cdots & v_{L-1}^{\alpha}(N-1) \end{bmatrix}}_{V_{\alpha,[N\times L]}} \underbrace{\begin{bmatrix} c_0^{\alpha} \\ c_1^{\alpha} \\ \vdots \\ c_{L-1}^{\alpha} \end{bmatrix}}_{\overline{c}_{\alpha,[L\times 1]}} \tag{9.4}$$

The least-squares analytical solution for (9.4) is given as

$$\overline{c}_{\alpha} = (V_{\alpha}^{\mathrm{T}} V_{\alpha})^{-1} V_{\alpha}^{\mathrm{T}} \overline{y} \tag{9.5}$$

Once the expansion coefficient $\overline{c}_{\alpha}$ has been calculated, the fluorescence IRF $h(n)$ can be computed from equation (9.2). The choice of the parameter $\alpha$ is critical in achieving accurate IRF estimations. In general, fluorescence IRF with a longer lifetime would require larger values of $\alpha$ for efficient representation, and vice versa. In practice, the parameter $\alpha$ can be selected based on the length of $h(n)$ and the number of DLFs used for the expansion, so that all the functions converge to zero by the end of the impulse response. Alternatively, these parameters could also be optimized iteratively.

### 9.4.2 Biomedical Application of the Laguerre Expansion Technique for Deconvolution of TRFS Data

The LET was first applied to the analysis of TR-LIFS data by Stavridi et al. [43] and Snyder et al. [44]. In the latter, time-resolved fluorescence decays of anthracene and type II collagen powder were deconvolved using the Laguerre method, and it was observed that LET was computationally more efficient and robust to experimental noise than was the LSIR method. Subsequent studies further validated the accuracy of the Laguerre deconvolution in TR-LIFS data measured upon ultraviolet (UV) laser excitation from various endogenous fluorophores commonly found in normal and atherosclerotic arteries (e.g., elastin, collagen, cholesterol), and from aortic and coronary arteries [35,36,40]. In all these initial studies, optimal values of the parameters $\alpha$ and $L$ and the LECs were determined iteratively by least-squares minimization of the weighted sum of residuals, similar to the LSIR method. The estimated IRF were then fitted to a multiexponential function to compare the decay constant values to those reported previously.

Although accurate estimation of fluorescence IRF was achieved using iterative implementation of the Laguerre deconvolution method, the full potential of the LET was not fully utilized in these earlier studies. One of the most important features of the LET is its capability to express the convolution equation (9.1) in terms of a linear expansions on the key variables $v(n)$. In the context of the Laguerre deconvolution method, this implies that the LEC (and thus the fluorescence IRF) can be estimated directly by solving the overdetermined system of linear equations defined in (9.4) using linear least-squares fitting, yielding an analytical solution given in (9.5). This noniterative implementation of the Laguerre deconvolution was thoroughly evaluated by Jo et al. using simulated and experimental TR-LIFS data [41]. In this study, $L$ was estimated by minimizing the weighted sum of residuals. The optimal parameter $\alpha$ was selected so that all DLFs declined sufficiently close to zero by the end of the IRF. Finally, once both $L$ and $\alpha$ were fixed, the LECs were estimated by linear least-squares fitting. It was demonstrated that (1) a unique Laguerre expansion can always be found for any fluorescence IRF of arbitrary form, and (2) the Laguerre deconvolution performs at least three times faster than the conventional multiexponential LSIR.

Taking advantage of the linear formulation of the fluorescence IRF as an expansion in the DLFs, a method for the prediction of relative concentrations in a mixture of fluorophores was also developed and validated [41]. This method assumes that fluorescence IRFs from the mixture and individual fluorophores can be expanded using the same DLFs. By mathematical manipulation of the resulting LECs from these expansions, relative fluorophore concentrations can be estimated by linear least-square estimation. These findings suggested that the use of the LECs could represent a faster approach to characterize and discriminate complex biological systems such as tissues, in terms of their fluorescence emission temporal characteristics [45]. Consequently, use of the LEC for direct characterization and diagnosis of tissue was explored further and applied more recently in TR-LIFS studies of pathologies in tissues in both the cardiovascular and oncological areas [28–30,45]. Representative results from these studies are presented in Sections 9.5.3 and 9.6.3.

## 9.5 ATHEROSCLEROTIC PLAQUE

### 9.5.1 Clinical Diagnosis and Challenges

Despite significant progress in treatment of atherosclerotic cardiovascular disease, it results in more than 19 millions deaths annually. A large number of victims of the disease die suddenly, without prior symptoms, due to plaque rupture [46]. This critical event has to a large extent been associated with “vulnerable” plaque. A recent consensus document [46] had emphasized that existing screening and diagnostic methods are insufficient to identify the victims before the event occurs. Most techniques identify luminal diameter (stenosis), wall thickness, and plaque volume, but are inefficient in identifying the rupture-prone plaque [46–48]. Consequently, new diagnostic techniques (including catheter-based) to localize and characterize vulnerable plaques are needed. It is envisioned that recently developed assays (C-reactive protein), imaging techniques (CT, MRI), noninvasive electrophysiological tests, and emerging catheters, in combination with genomic and proteomic techniques, will guide the search for “vulnerable patients.” This will potentially lead to development of new therapies and reduce the incidence of acute cardiovascular syndromes and sudden death.

Potential intravascular diagnostic techniques investigated as tools for assessment of plaque vulnerability include nuclear magnetic resonance (NMR) spectroscopy, intravascular ultrasound (IVUS), optical coherence tomography (OCT), thermography, and spectroscopic methods [48–67]. It was also emphasized [46] that sensitivity, specificity, and overall predictive value of each potential diagnostic technique need to be assessed before entering clinical practice. Several optical spectroscopy techniques have already been used in atherosclerosis research, such as Raman, near-infrared (NIR), diffuse reflectance NIR, and fluorescence spectroscopy. Recent reviews of these techniques include those by Moreno and Muller [64], Fayad and Fuster [65], MacNeil et al. [48], Pasterkamp et al. [66], and Honda and Fitzgerald [67]. These studies concluded that (1) spectroscopic techniques are highly likely to be used in the essential clinical task of identifying vulnerable plaques; and (2) some combination of these techniques, or a combination of these technique with other catheter-based imaging techniques such as IVUS, will be most useful. Although noninvasive high-resolution imaging techniques such as MRI would be preferable in the search for vulnerable plaques, improvement in signal/noise ratio and resolution can be only achieved with the application of intravascular catheter-based techniques that allow enhanced sensitivity for detecting changes within atherosclerotic plaques.

### 9.5.2 Fluorescence Spectroscopy and Atherosclerotic Plaque Characterization

Fluorescence spectroscopy–based techniques have been shown to detect elastin, collagen, lipids, and other sources of autofluorescence in normal and diseased arterial walls as well as to characterize the biochemical composition of atherosclerotic plaques both ex vivo and in vivo [2,64,67–74]. More recently, a few studies have reported the application of fluorescence techniques to the identification of plaque disruption [72], detection of plaques with thin fibrous cap [73], and discrimination of lipid-rich lesions [35]: all features associated with plaque vulnerability.

Atherosclerotic plaques with active inflammation, including extensive macrophage accumulation [46,64], are also considered to be at high risk. Thus, techniques able to detect macrophages in vivo were researched as tools for assessing the risk of plaque vulnerability. A set of imaging technologies has been identified as potential tools for the diagnostic of macrophage infiltration. These include intravascular techniques such as thermography [61–63], contrast-enhanced MRI [51], fluorodeoxyglucose positron emission tomography [75,76], immunoscintigraphy [76], optical coherence tomography [49,50,67], and fluorescence spectroscopy combined with reflectance spectroscopy [76]. In addition, Marcu et al. [29,30] demonstrated that TR-LIFS represents an alternative approach for the detection of inflammatory cells. Results from these TR-LIFS studies are reviewed below.

### 9.5.3 Detection of Compositional Features Related to Plaque Vulnerability Using Fluorescence Lifetime Spectroscopy

Summarized below are results and main findings from TR-LIFS studies conducted in human arterial atherosclerotic samples from three major arterial beds: aorta, coronary, and carotid.

***Aorta*** The first systematic study characterizing the time-resolved fluorescence emission of normal artery and various stages of atherosclerosis was conducted in human aortic specimens (94 samples, postmortem) [21,36]. The Laguerre deconvolution method for TR-LIFS data analysis was applied to estimate the intrinsic fluorescence decays, from which the time-integrated fluorescence emission spectrum and fluorescence lifetime were computed. Representative trends of emission spectra and average fluorescence lifetime from this study are depicted in Figure 9.3. This study established that the time-resolved fluorescence emission spectra of aortic samples vary with the progression of atherosclerosis. Characteristic changes in parameters derived from the time-resolved spectra were related to the type of lesion assigned to the sample based on histological examination. Spectral and temporal features of the emission were interpreted for normal aortic wall and lesions ranging from early type I to advanced type V in terms of intimal content in fluorescent compounds and intimal thickness. Trends in the average lifetime and decay-associated spectra at selected wavelengths were identified,

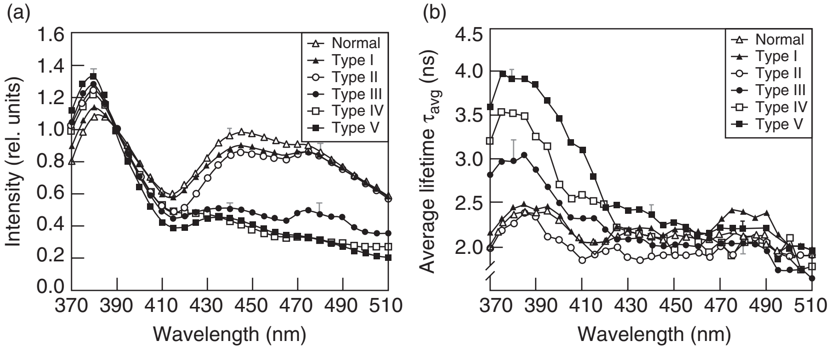

**FIGURE 9.3** (a) Normalized time-integrated emission spectra for normal aorta and atherosclerotic lesions. Each data point represents the mean value of normalized emission intensities for all samples of a given type. As the lesion type progresses toward more advanced atherosclerosis, the emission spectra are increasingly more pointed in the blue range and depressed in the red range of the spectrum. (b) Average lifetime $\tau_{avg}$ as a function of emission wavelength for normal aorta and for atherosclerotic lesions. Each data point represents the mean value of the average lifetimes for all samples of a given type. To illustrate the variability of the results, the standard error of the mean is shown for the lifetime values of normal, type III, and type V lesions at 380, 440, and 480 nm. The atherosclerotic lesions were characterized according with AHA classification. (From [26], with permission.)

which could serve as diagnostic markers for in situ optical analysis of the aortic wall. Also, it was determined [21] that a set of five predictor variables (fluorescence time-decay parameters at 390 and 460 nm, and fluorescence intensity values at 490 nm) allows for discrimination of the lipid-rich lesions (rupture-prone) from collagenous/fibrous lesions (stable) with a sensitivity and specificity higher than 95%.

***Coronary Artery*** In a subsequent study, time-resolved fluorescence emission of normal and atherosclerotic human coronary arteries (58 coronary segments, postmortem) were analyzed using the Laguerre deconvolution method. Representative results are depicted in Figure 9.4. Similar to the previous study in aorta, these results showed that analysis of the time-resolved fluorescence spectra can be used to enhance the discrimination between different grades of atherosclerotic lesions as defined by the American Heart Association (AHA). Also, it demonstrated that the lipid-rich lesions can be differentiated from the other lesion types (in particular, fibrous lesions) and normal arterial wall. It was determined that spectroscopic features derived for lipid components are reflected in the emission of lipid-rich lesions, whereas characteristics of type I collagen are identified in the emission of fibrous lesions. In addition, the results suggested that a few parameters that combine spectral features at longer wavelengths and time-resolved characteristics from the peak emission region are the best selections for coronary artery lesion discrimination. For example, parameters derived from time-resolved spectra, such as the lifetime and the fast-time decay constants determined using a biexponential approximation of the intensity decay, are most likely to differentiate between lipid-rich and fibrous lesions and be used for diagnosis. These findings further validated the potential of TR-LIFS for discriminating lipid-rich plaques from fibrotic lesions. In addition, the relationship between the autofluorescence

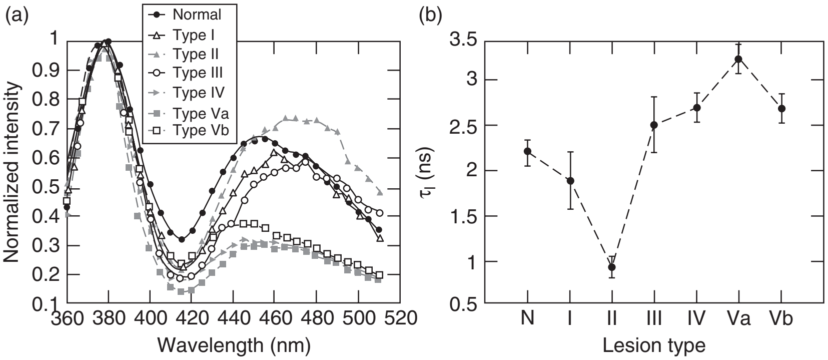

**FIGURE 9.4** (a) Spectral emission: normalized average for each type of coronary sample; variation of fluorescence emission intensity. (b) Lifetime, $\tau_f$ (mean ± SE): variation for 390-nm emission as a function of lesion type. The atherosclerotic lesions were characterized according to AHA classification. SE, standard error. (From [35], with permission.)

features of the coronary artery samples and the intrinsic fluorophores in coronary wall was presented.

***Carotid Artery*** More recently, a TR-LIFS study [30] was conducted in fresh excised carotid plaques from 65 endarterectomy patients. It resulted in an extensive database of more than 800 fluorescence data points and their underlying plaque histopathology. This study was designed to (1) demonstrate whether TR-LIFS signatures can distinguish fibrotic caps rich in macrophages and inflammatory cells and plaques with a necrotic/lipid core under a thin cap (rupture-prone) from plaques with caps rich in collagen (stable); and (2) identify TR-LIFS-derived spectroscopic parameters that can be correlated to features of plaque vulnerability. Results of this study indicated that spectral features derived from the normalized time-integrated fluorescence emission spectra provide means of discriminating early lesions (intima thickening) from more advanced stable (fibrotic, fibrocalcified) and unstable (inflamed, necrotic) plaques (Figure 9.5). Also, it

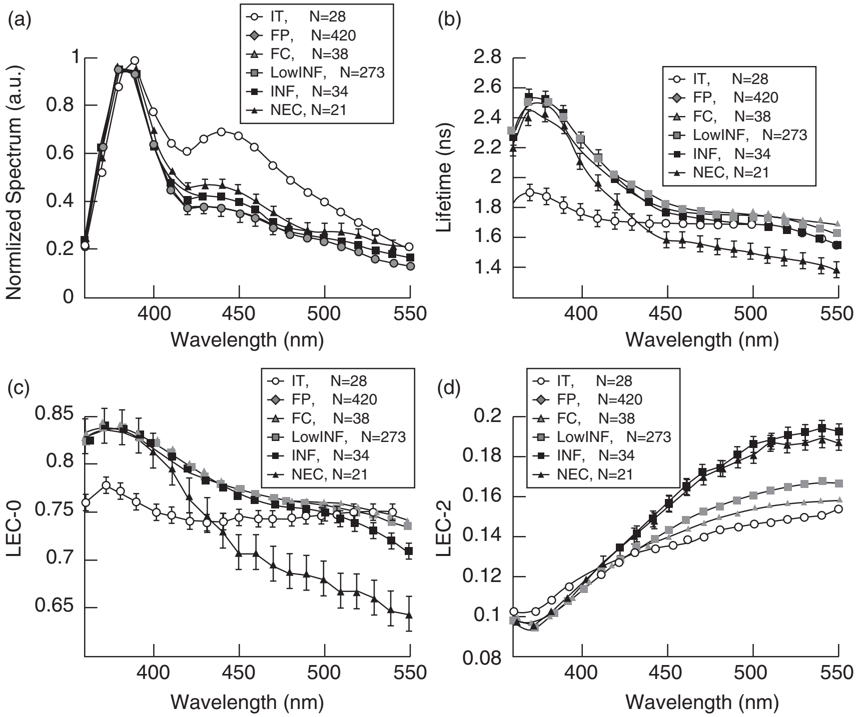

**FIGURE 9.5** Group spectroscopic parameters (mean ± SE) as a function of emission wavelength from atherosclerotic plaques, derived from time-resolved spectra estimated using the Laguerre deconvolution method: (a) normalized intensity; (b) lifetime; (c) LEC-0; (d) LEC-2. IT, intima thickening; FP, fibrous plaque; FC, fibrocalcified plaque; LowINF, minimal inflammation; INF, inflamed cap; NEC, necortic core with thin cap. SE, standard error. (After [30], with permission.)

indicated that time-resolved properties of the autofluorescence emission enable detection of superficial necrotic core and inflammation, additional features of plaque vulnerability.

This study also demonstrated the important role the Laguerre expansion coefficients (LECs) play in atherosclerotic plaque discrimination. As in previous studies, the Laguerre deconvolution method was also used to estimate the intrinsic fluorescence decay emission from carotid plaques. In this study, however, the resulting LEC were adopted for the first time as additional parameters for quantifying the time-resolved fluorescence emission (Figure 9.5c and 9.5d). Interestingly, it was one of these expansion coefficients (LEC-2) that was able to discriminate both inflamed and necrotic lesions from the stable plaques. Moreover, a combination of spectral and time-resolved fluorescence parameters, including LECs, were used as features in a linear discriminant analysis (LDA)–based classifier, which was able to discern inflamed and necrotic lesions from early and advanced fibrotic lesions with high sensitivity (>80%) and specificity (>90%). These results provide a strong indication that the LECs offer a new domain for representing time-resolved information from tissue fluorescence emission in a very compact, accurate, complete, and computationally efficient way.

To further validate the potential of the LECs time-resolved fluorescence features for tissue characterization, a biexponential deconvolution was also applied to the TR-LIFS carotid data, and the correlation between the multiexponential parameters and the underlying plaque histopathology was assessed. The results of the biexponential deconvolution showed that the multiexponential parameters do not provide the same level of discriminatory information as the LECs (Figure 9.6). Exponential functions do not constitute an orthonormal basis; thus, a multiexponential model of the fluorescence decay can yield a number of solutions to the same decay data. It is most likely that this challenges the model's ability to capture the decay dynamics that permit discriminatation of different plaque types. On the other hand, the Laguerre functions form a complete and orthogonal basis, allowing unambiguous expansion of the fluorescence decay; therefore, a unique set of LEC can be used directly to characterize the fluorescence decay dynamics. This study clearly demonstrated that the LECs derived from the TR-LIFS data analysis can characterize arterial tissue composition, and most important, detect features of vulnerable plaques, such as superficial necrosis and inflammation.

In summary, these three studies taken together provide ample evidence to infer that TR-LIFS can potentially become a powerful clinical tool for detecting high-risk vulnerable atherosclerotic lesions during intravascular catheterization. All three studies confirmed that elastin is the major source of endogenous fluorescence in all normal arteries and early lesions, while collagen is the main source of fluorescence in more advanced lesions. Since these two endogenous fluorophores have very distinct spectral and time-resolved characteristics, discrimination between normal arterial wall and early lesions from more advanced lesions is possible using TR-LIFS. These studies also indicate that lipid-rich lesions, including those with thin cap fibroatheromas and a large lipid pool, and

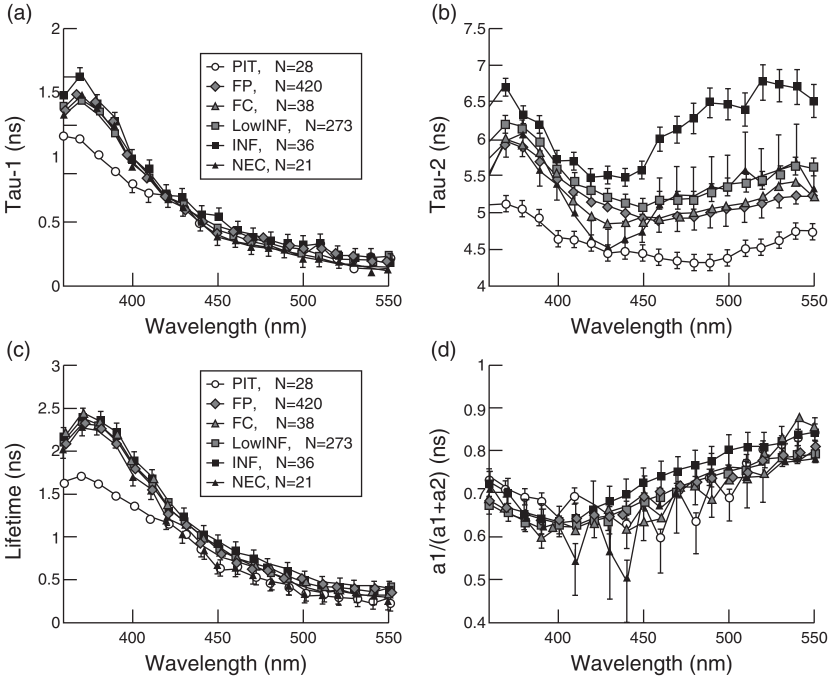

**FIGURE 9.6** Group spectroscopic parameters (mean ± SE) as a function of emission wavelength from atherosclerotic plaques derived from time-resolved spectra estimated using the biexponential LSIR deconvolution method: (a) shortest time constant, Tau-1; (b) longest time constant, Tau-2; (c) average lifetime; (d) normalized preexponential factor of the shortest time constant. SE, standard error.

inflamed lesions with superficial foam cells, can be discriminated from more stable collagen-rich lesions, based on time-resolved fluorescence characteristics. In addition, these studies have demonstrated that a small subset of spectral and time-resolved parameters (fewer than 10 parameters) retrieved from a limited number of emission wavelengths (about four wavelengths) can provide a means of delineating early from advanced lesions, and more important, the presence of lipid-rich lesions as well as of an inflamed fibrotic cap. This finding is particularly important, as it allows for the design of TR-LIFS systems that collect fluorescence decay at a limited number of wavelength bandwidths as recently reported by Sun et al. [37]. Such an approach will provide a means of rapid data acquisition and analysis—a critical feature for clinical applications.

A main limitation of fluorescence-based techniques in the evaluation of biological systems, including arterial plaques, is the relatively shallow UV light penetration of excitation light (ca. 250 μm). Although UV excitation of the fluorophores in the arterial wall makes TR-LIFS a suitable method for detection of markers of plaque vulnerability in thin fibrotic caps, it also limits the ability of this technique to assess plaque morphology associated with other markers of plaque vulnerability, such as the size of the lipid pool or expansive (positive) remodeling, or to distinguish other important features involved in plaque pathology, including pathologic intimal thickening [77] versus fibrous thick-cap atheroma. Such limitations, however, can be addressed further using complementary imaging techniques. As suggested earlier [46] for other spectroscopic methods currently evaluated for clinical diagnostic of vulnerable plaques (e.g., NIR and Raman spectroscopy), an optimum approach to vulnerable plaque detection would need to incorporate the structural definition of a high-resolution modality (e.g., OCT, intravascular MRI, high-frequency IVUS) with biochemical processes detected by TR-LIFS. Concurrent studies in our lab are investigating the potential of combining TR-LIFS and IVUS modalities for simultaneous discrimination of the morphological and compositional features of atherosclerotic plaques.

## 9.6 PRIMARY BRAIN TUMORS

Primary brain tumors are tumors that originate in the cranial cavity from various tissues, such as glial cells, meninges, and neural tissue. It is estimated that 51,410 new cases of primary brain tumors are diagnosed every year [78]. Distribution of tumors according to the histology represents the commonest tumor to be benign meningioma, which accounts for 32.1% of all tumors, followed by glioblastoma (18.5%) and astrocytoma [78], making glioma and meningioma the two most important tumors from a clinical standpoint. Gliomas are tumors that arise from glial cells and include astrocytoma, glioblastoma, mixed gliomas, malignant gliomas NOS (not otherwise specified), and neuroepithelial tumors. The five- and 10-year survival rates for malignant brain tumors by histology are 30% and 26%, respectively [78]. However, there is a large variation in survival rates between different tumor histologies. Five-year survival rates exceed 95% for pilocytic astrocytoma but are less than 4% for glioblastomas [78]. Astrocytoma and glioblastomas are the most common type of malignant brain tumor in adults, accounting for more than 75% of gliomas. Histologically, gliomas are categorized as low-grade (grade I), intermediate-grade (grades II and III) and high-grade (grade IV) gliomas or glioblastoma multiforme based on Kernohan and Sayred [79]. Meningiomas arise from the arachnoidal cells in the meninges. Histologically, meningiomas are characterized in many groups, such as meningothelial meningioma, which shows the presence of meningothelial cells; fibroblastic meningioma, which shows the presence of fibrous tissue with spindle-shaped cells; psammomatous meningioma, which has psammoma bodies, which are islands of calcified tissue with aggregates of meningothelial cells into whorls and lobules around the island; angiomatous or angioblastic meningioma, which resembles a vascular malformation. It was reported that even after a perceived "total resection," the disease recurrence was 9%. A review from Massachusetts General Hospital showed that a total resection is followed by a 7%, 20%, and 32% recurrence rate at 5, 10, and 15 years, respectively [80]. The extent of tumor resection correlates directly with prevention of recurrence.

### 9.6.1 Clinical Diagnosis of Primary Brain Tumors

Current neuroimaging techniques include CT, MRI and PET for preoperative diagnosis. MRI has been shown to be more effective than CT in diagnosing brain tumors [81]. Typically, multiple MRI images obtained prior to surgery provide valuable information regarding the localization of tumor and are used for stereotactic neuronavigation, aiding the surgeon during tumor resection. PET is the most reliable noninvasive scanning method for differentiating radiation-induced necrosis from tumor recurrence. Sometimes, however, biopsy is required to confirm the diagnosis.

Despite the advent of techniques such as radiotherapy and chemotherapy, surgery remains the fastest way to reduce the tumor mass, with the ultimate goal of nearly complete resection. It has been shown that for primary brain tumors the extent of resection is the most important variable in improving the prognosis [82,83]. The degree to which a complete resection can be achieved in the brain is limited primarily by the difficulty of visually detecting differences between normal brain and malignant tissue during surgery. This necessitates rapid intraoperative preliminary neuropathological diagnosis. The standard intraoperative approach to intraoperative diagnosis is the frozen section. This is a 15- to 25-minute process whereby a tissue specimen removed via biopsy is frozen, sliced with a microtome, and then stained and analyzed. Multiple intraoperative frozen-section specimen requests can lead to an increase in the operation time as well as of the neuropathologist workload.

Other methods used for intraoperative diagnosis include intraoperative ultrasound, intraoperative MRI (i-MRI), and 5-aminolevulinic acid (5-ALA) fluorescence-guided resection and are briefly reviewed in the following. Intraoperative ultrasound shows the contrast between tumor and normal brain; however, tumor also appears frequently as normal brain on ultrasound, and normal brain that contains edema or bleeding can frequently appear as tumor [84]. More recently, neurosurgeons at several major centers have employed i-MRI to correct for brain shift during surgery [85,86]; however, this technique still has limitations. MRI does not necessarily identify tumor, the image quality of the i-MRI may not be as good as the preoperative MRI, which is typically acquired at higher resolution in a higher field magnet; its use requires major modifications of the operating room and special surgical instruments; and it prolongs the surgery (>30 min). Notably, this is a very expensive procedure that only a few medical centers can afford. 5-Aminolevulinic acid (5-ALA) fluorescence-guided resection is currently under investigation as a possible new method for intraoperative diagnosis of brain tumors [82,83,87]. It relies on specific synthesis and accumulation by 5-ALA of fluorescent porphyrins in malignant glioma tissues. Current studies demonstrate that this approach resulted in almost a doubling of the number of patients without residual contrast-enhancing tumor on early MRI. Nevertheless, high-grade gliomas are heterogeneous in nature with areas of low-grade differentiation, highly proliferative regions, and necrosis [87]. Typically, areas of necrosis and regions consisting of low-grade glioma do not show porphyrin fluorescence. Another shortcoming is the inconsistent ability of different high-grade glioma cells to produce porphyrins (e.g., PpIX) after administration of ALA [82,83,87].

### 9.6.2 Fluorescence Spectroscopy of Brain Tumors

As surgery remains the first line of offense against tumors, and complete resection has been shown to be a key factor in treating brain tumors, additional aid can be provided to the surgeon by using newer techniques such as time-resolved laser-induced fluorescence spectroscopy (TR-LIFS) to distinguish the tumor tissue from normal brain matter. It was shown previously that fluorescence spectroscopy is effective in characterization of different tissues in the body. Autofluorescence is broadly classified into two types of measurement: static (steady-state) and dynamic (time-resolved). Several types of brain tumors have been investigated, both in vivo and ex vivo, using these techniques. These include studies of glioblastoma [88–93], astrocytoma, oligodendroglioma, and metastatic carcinoma [90]. For example, combining fluorescence (excitation 337 nm) with diffuse reflectance spectroscopy at multiple excitation wavelengths [90] or using microspectrofluorometric measurements at a few excitation wavelengths [89], it has been shown that brain tumors can be distinguished from normal brain tissue with good sensitivity and specificity. Previously, the Marcu et al. research group reported results on the time-resolved fluorescence of glioblastoma [92,93] and meningioma [94].

***Steady-State Fluorescence Spectroscopy*** Several groups have reported on the potential of steady-state fluorescence spectroscopy for the delineation of brain tumors from normal brain tissue. Chung et al. [88] used an excitation-emission matrix on in vivo samples of glioma in the rat brain and in vitro samples of human brain tissue. On excitation using 360 nm of wavelength, a fluorescence emission peak was observed at 470 nm, on excitation with 440 nm of wavelength, a peak was observed at 520 nm of wavelength, and on excitation using 490 nm of wavelength, a fluorescence emission peak was observed at 630 nm of wavelength. These results were hypothesized to be from NADH, flavins, and porphyrins, respectively. There was less fluorescence emission from tumor tissue than from normal brain tissue.

Butte et al. [94] and Bottiroli et al. [95] characterized frozen tissue sections from excised specimens of normal brain and glioblastoma using microspectrofluorometry. Bottiroli et al. also reported that the fluorescence from both normal tissue and glioblastoma was characterized by blue–green fluorescence. The normal tissue demonstrated significantly higher fluorescence emission intensity than did tumor tissue. On excitation at 366 nm of wavelength, peaks were reported at 440, 460, and 520 nm. Normal tissue showed a narrowband emission at 440 nm and a shoulder at 460 nm of wavelength. A slight tumor borderline shoulder became detectable at wavelengths longer that 500 nm. When the tissue was excited using 405 nm of excitation, the difference in the fluorescence intensities between normal and neoplastic tissue increased.

Subsequently, Croce et al. [89] used a similar method to analyze the autofluorescence properties of nonneoplastic and neoplastic tissues, those of homogenates by means of a microspectrofluorometer, and directly on patients affected by glioblastoma multiforme, during surgery, with a fiber optic probe. Fluorescence spectra of supernatants of both tumor and nonneoplastic tissue homogenates were excited using 366 and 405 nm. Under excitation at 366 nm, normal tissue has a main emission band that peaks at about 440 nm, with a minor shoulder at wavelengths longer than 490 nm. In the tumor tissue the main emission band is red-shifted and the long-wavelength shoulder becomes more marked. Three distinct bands of fluorescence were measured: at 470, 520, and 580 nm of wavelength. The fluorescence intensity ratios $FI_{520}/FI_{470}$ and $FI_{580}/FI_{470}$ were found to be higher in tumor tissue. Upon estimating the total NADH amount, it was observed that tumor tissue had 21% less emission than that in normal tissue. Under excitation at 405 nm, the fluorescence emission amplitude was higher in normal than in tumor tissue. The main emission band of normal tissue extracted demonstrated an emission peak at 475 nm. A red shift was found in tumor tissue. A shoulder at about 570 nm was also observed, which is more evident in tumor than in normal tissue.

Mahadevan's research group at Vanderbilt University is at the forefront of combining steady-state fluorescence spectroscopy with diffuse reflectance spectroscopy and reported [90,91,96,97] extensive results from fluorescence and diffuse reflectance spectra from normal and tumor human brain tissues in vitro. The brain tissue was excited using 330 nm of wavelength. The intensity of the fluorescence peak 460-nm emissions was found to be consistently lower in tumorous than in normal brain tissues. In addition, a small shift in the peak location of this fluorescence emission was observed in brain tumors compared to normal brain tissues. Diffuse reflectance of most brain tissues reached the maximum around 625 nm and then decreased gradually as the wavelength increased. Later, the same group reported results from in vivo experiments on normal brain tissue and the infiltrating tumor margins. Peak fluorescence in the majority of in vivo brain tissues occurred between 455 and 480 nm. The difference in fluorescence emission intensity between normal brain tissues and brain tumors was found to be statistically significant. The comparison showed no evidence of a red shift in the fluorescence spectra of glioblastoma multiforme (GBM) sites compared with normal tissues, as reported previously by Bottiroli et al. Diffuse reflectance of brain tissues decreased gradually from 650 nm to 800 nm, similar to that observed in vitro. Normal white matter and tumor margins involving white matter demonstrate strong diffuse reflectance between 600 and 800 nm.

### 9.6.3 Diagnosis of Brain Tumors Using Fluorescence Lifetime Spectroscopy

Compared to steady-state fluorescence spectroscopy, time-resolved spectroscopy offers additional information about the biochemical nature of tissue. Marcu's research group at the University of California, Davis (previously at Cedars–Sinai Medical Center) reported results on both ex vivo and in vivo specimens of normal brain and tumors, mainly glioma and meningioma [92–94].

***Gliomas*** Yong et al. [93] employed time-resolved fluorescence spectroscopy apparatus to achieve a fluorescence temporal response across the emission spectra of tissue specimens; thus, both steady-state spectra and time-resolved intensity decay can be recovered from a single measurement sequence, as shown in Figure 9.7. They observed that the normal cortex was characterized by a broad fluorescence emission spectrum with a well-defined peak between 440- and 460-nm wavelengths, which is consistent with emission of enzyme cofactor NADH. Compared with low- and high-grade glioma, a small emission shoulder is observed at 390 nm of wavelength. The attenuation of fluorescence intensity at about 415 nm corresponds to a hemoglobin absorption band. Across the entire spectrum, the fluorescence emission was short lasting, with an average lifetime mainly below 1.5 ns. The normal white matter was characterized by a broad fluorescence emission spectrum (Figure 9.8) with two well-defined peaks at 390- and 440-nm wavelength, each corresponding to emission of connective tissue protein and enzyme cofactor NADH, respectively [98,99]. The fluorescence intensity decay (lifetime) was found to be wavelength dependent, with higher time-decay values in the region of peak fluorescence at 390 nm of wavelength compared with red-shifted wavelengths at 460 nm. The time-resolved fluorescence emission of low- and high-grade glioma samples showed a relatively narrow broadband emission, characterized by a well-defined peak at 460-nm wavelength, lasting for more than 1.1 ns. Based on various parameters derived from these data it was shown that it is possible to identify high- and low-grade glioma from normal cortex and normal white matter with more than 90% sensitivity and specificity.

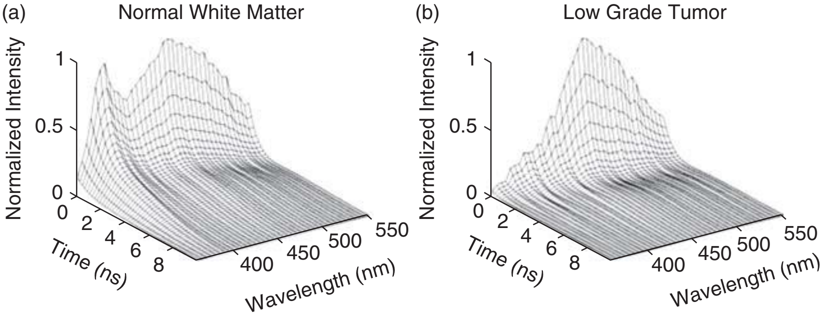

**FIGURE 9.7** Representative examples of time-resolved fluorescence emission kernels of (a) normal white matter and (b) low-grade glioma after deconvolution of the fluorescence emission transient by the laser signal. Normal white matter shows a distinct peak at 390 nm of wavelength, which is absent in low-grade glioma. It is possible to discern that low-grade glioma demonstrated a faster lifetime at 390 nm than did normal white matter.

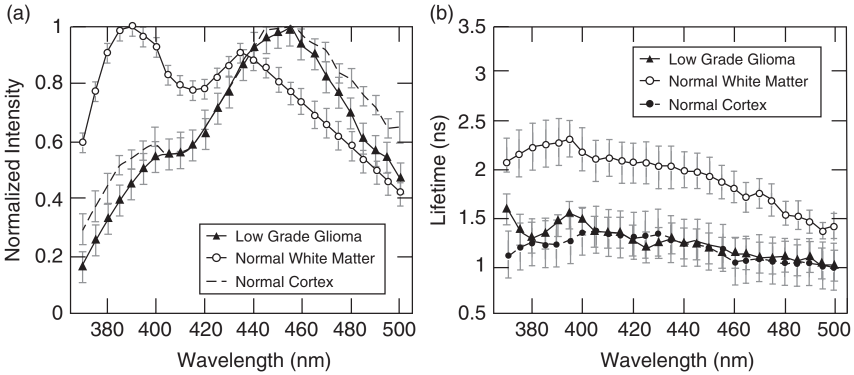

**FIGURE 9.8** (a) Spectral emission (mean ± SE) and (b) lifetime (mean ± SE) plots from normal cortex, normal white matter, and low-grade glioma ex vivo. The fluorescence emission from normal white matter is distinct compared with that of low-grade glioma, as seen in the emission intensity and fluorescence lifetime at 390 nm of wavelength.

A portable time-resolved fluorescence spectroscopy instrument was developed by us to measure the fluorescence emission of normal cortex and gliomas in vivo. We observed that normal cortex was characterized by a broad fluorescence emission spectrum with a well-defined peak between 440 and 460 nm of wavelength, which is consistent with emission of enzyme cofactor NADH. A small emission shoulder is observed at 390 nm of wavelength, while normal white matter was characterized by a broad fluorescence emission spectrum with two well-defined peaks at 390 and 440 nm. The fluorescence intensity decay from both normal cortex and normal white matter was found to be wavelength dependent, with higher time-decay values in the region of peak fluorescence of 390 nm of wavelength (2 ns) compared with the red-shifted wavelengths of 460 nm (0.8 ns). The time-resolved fluorescence emission of low-grade glioma (Figure 9.9) samples showed a relatively narrow broadband emission characterized by a well-defined peak at 460 nm of wavelength, lasting for less than 1 ns across the entire spectrum. It was observed that the low-grade glioma fluorescence decay lifetime was distinctly low compared with normal cortex at both 390 and 460 nm of wavelength. Unlike low-grade glioma, high-grade glioma does not show any significant difference in fluorescence lifetime compared with normal cortex. Time-resolved emission spectra of high-grade glioma when necrosis or fibrosis is present due to radiation or treatment are very different from high-grade glioma spectra with no necrosis. The emission spectra in these tissues were characterized by a broad wavelength band with two emission peaks. The main peak is centered at about 385 to 390 nm, the second at about 440 nm. The fluorescence lifetime was found to be longer in the region of main peak emission (2.7 ns) than in the red-shifted wavelengths (0.8 ns).

***Meningiomas*** Butte et al. [94] reported on the use of time-resolved laser-induced fluorescence spectroscopy of meningioma compared with normal dura

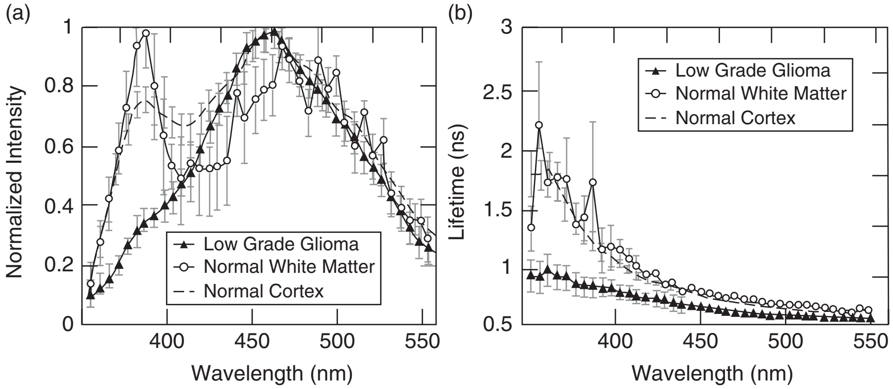

**FIGURE 9.9** (a) Fluorescence emission spectra and (b) average lifetime of various tissues in vivo. Note the distinctly lower lifetime in low-grade glioma samples than in normal tissue and high-grade glioma.

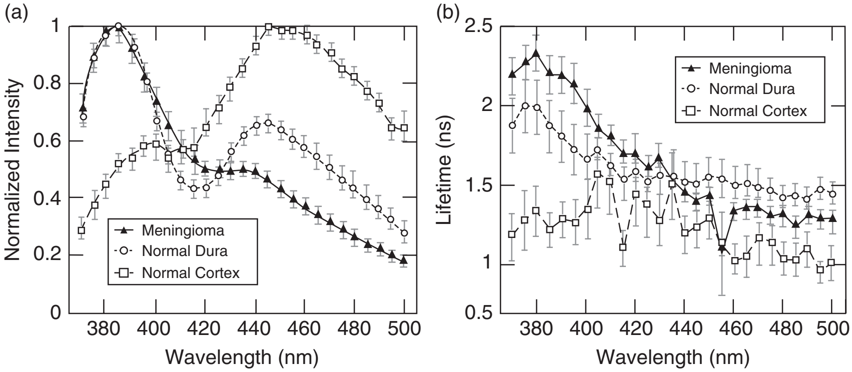

**FIGURE 9.10** (a) Normalized integrated fluorescence emission spectra and (b) lifetime of meningioma, dura mater, and normal cortex. The emission at 460 nm in tumor samples was lower than that in both normal dura and normal cortex samples.

and normal brain tissue. The time-resolved fluorescence emission of meningioma samples showed a relatively narrow broadband emission characterized by a well-defined peak at 385 to 390 nm of wavelengths lasting for more than 2 ns (Figure 9.10). Compared to a typical time-resolved emission spectrum of dura mater, the emission spectrum was characterized by a broad wavelength band with two emission peaks. The main peak was centered at about 385 to 390 nm, the second at about 440 nm. The fluorescence lifetime was found to be slightly longer in the region of main peak emission at 390 nm of wavelength (1.8 ± 0.15 ns) than with the red-shifted wavelengths at 460 nm (1.4 ± 0.1 ns). When various features from these data, such as lifetime at 390 and 460 nm of wavelength as well as emission intensity values were used to determine classification using discriminant function analysis, more than 90% of specificity and sensitivity for diagnosing meningioma from normal tissue such as normal cortex and normal dura mater was observed.

In summary, all the studies cited in Table 9.1 assist in establishing the potential of fluorescence spectroscopy as a effective tool for delineating brain tumors in order to facilitate complete excision during surgery. TR-LIFS has shown that it can be deployed as a rapid identification of neoplastic versus normal tissue and that using fluorescence-based diagnostics would be a highly beneficial tool for both the surgical pathologist and the neurosurgeon. In all the studies described above, the autofluorescence properties of tissue were used as a diagnostic tool. For clinical or intraoperative diagnosis of diseased tissue, such an approach has inherent advantages over the use of exogenous fluorophores (molecular probes). Measurements of endogenous fluorescence do not require any systemic or local administration of an external imaging agent; thus, problems associated with toxicity and pharmacodynamics/kinetics of the external agent are not to be encountered. Additionally, the studies noted in the table have shown that parameters derived from a small band of wavelengths (e.g., 390 nm, 460 nm) can help in delineating various tissues and reducing the acquisition time. A fast real-time classification algorithm can be developed by assigning a discriminant score for different tissues. This discriminant score can then be compared with the acquired fluorescence from the unknown tissue so as to classify the tissue in real time. Accuracy of classification by linear discriminant analysis can be improved by continuously acquiring samples for training. Such a combination of analytical methods with fast acquisition can aid the neurosurgeon with a real-time optical biopsy of tissue in the near future.

## 9.7 CONCLUDING REMARKS

In recent years, advances in time-resolved fluorescence spectroscopy techniques demonstrate that fluorescence lifetime provides a powerful means of achieving optical molecular contrast in biological tissues. Consequently, the possibility arises of utilizing autofluorescence-based fluorescence lifetime contrast for clinical and biomedical research. The studies summarized in this chapter demonstrate the translational research potential of TR-LIFS and show that the intrinsic fluorescence signals can be used to provide useful contrast for the diagnosis of high-risk atherosclerotic plaque and primary brain tumors. A combination of new technological advances for fast recording of spectrally resolved fluorescence lifetime information and new analytical methods and algorithms for fast processing of the fluorescence intensity decay data enable further development of

**TABLE 9.1** **Summary of Fluorescence Spectroscopy Studies Conducted in Brain Tumors**

| Study | Tissue Types | Techniques | Excitation λ (nm) | Emission λ (nm) | Comments |
|---|---|---|---|---|---|
| Chung et al. [88] | In vitro human brain samples | Steady-state fluorescence | 360/440/490 | 470/520/630 | NADH/flavins/ porphyrins |
| | Glioma in rat brain | — | — | — | ↓ emission intensity |
| Bottiroli et al. [100] | Normal brain | Microspectro-flurometry | 366 | 440, 460, 520 | |
| Croce et al. [89] | Normal neoplastic homogenate | Microspectro-flurometry | 366 | 440, 490 | Red-shifted in tumor |
| | | | 405 | 475, 570 | 570 nm ↑ in tumor |
| Mahadevan et al. [90,91] | Brain tissue + tumor ex vivo | Steady-state fluorescence + diffuse reflectance spectroscopy | 330 | 460 | ↓ Intensity in brain tumors |
| Yong et al. [93] | Normal + glioma (ex vivo) | Time-resolved fluorescence spectroscopy | 337 | 390, 460 | Average lifetime 1.5 (390 nm) ns, 1.1 (460 nm) ns |
| Butte et al. [94] | Normal + glioma (in vivo) | Time-resolved fluorescence spectroscopy | 337 | 390, 460 | Average lifetime 1.2 ns (390 nm), 0.8 ns (460 nm) in normal tissue; 0.8 ns (390 and 460 nm) in low grade glioma |

compact TR-LIFS diagnostic systems for near-real-time diagnosis of biological system.

### Acknowledgments

We thank all our colleagues, collaborators, and research mentors who contributed to the fluorescence lifetime studies presented in this chapter. Colleagues: Thanassis Papaioannou, Qiyin Fang, Yang Sun, and Daniel Elson; clinical collaborators: Michael C. Fishbein, Julie A. Freischlag, J. Dennis Baker, J.-H. Qiao, Keith L. Black, Brian Pikul, and William H. Yong; and mentors: Warren S. Grundfest, Jean-Michel Maarek, and Vasilis Marmarelis. This work was supported in part by National Institutes of Health grant R01 HL 67 377 and the Whitaker Foundation.

## REFERENCES

1. Lakowicz, J.R., *Principles of Fluorescence Spectroscopy*, 2nd ed., Kluwer Academic/Plenum Press, New York, 1999.
2. Richards-Kortum, R., and Sevick-Muraca, E.M., Quantitative optical spectroscopy for tissue diagnosis, *Annu. Rev. Phys. Chem.*, Vol. 47, 1996, pp. 555–606.
3. Wagnieres, G.A., Star, W.M., and Wilson, B.C., In vivo fluorescence spectroscopy and imaging for oncological applications, *Photochem. Photobiol.*, Vol. 68, No. 5, 1998, pp. 603–632.
4. Mycek, M.-A., and Pogue, B.W. (eds.), *Handbook of Biomedical Fluorescence*, Marcel Dekker, New York, 2003.
5. Andersson-Engels, S., et al., In vivo fluorescence imaging for tissue diagnostics, *Phys. Med. Biol.*, Vol. 42, 1997, pp. 815–824.
6. Bigio, I.J., and Mourant, J.R., Ultraviolet and visible spectroscopies for tissue diagnostics: fluorescence spectroscopy and elastic-scattering spectroscopy, *Phys. Med. Biol.*, Vol. 42, 1997, pp. 803–814.
7. Cubeddu, R., et al., Time-resolved fluorescence imaging in biology and medicine, *J. Phys. D*, Vol. 35, 2002, pp. R61–R76.
8. Das, B.B., Liu, F., and Alfano, R.R., Time-resolved fluorescence and photon migration studies in biomedical and model random media, *Rep. Prog. Phys.*, Vol. 60, 1997, pp. 227–292.
9. Drezek, R.A., et al., Optical imaging of the cervix, *Cancer*, Vol. 98, 2003, pp. 2015–2027.
10. Glanzmann, T., et al., Time-resolved spectrofluorometer for clinical tissue characterization during endoscopy, *Rev. Sci. Instrum.*, Vol. 70, 1999, pp. 4067–4077.
11. Mycek, M.A., Schomacker, K.T., and Nishioka, N.S., Colonic polyp differentiation using time-resolved autofluorescence spectroscopy, *Gastrointest. Endosc.*, Vol. 48, 1998, pp. 390–394.
12. Ramanujam, N., Fluorescence spectroscopy of neoplastic and non-neoplastic tissues, *Neoplasia*, Vol. 2, 2000, pp. 89–117.
13. Utzinger, U., and Richards-Kortum, R.R., Fiber optic probes for biomedical optical spectroscopy, *J. Biomed. Opt.*, Vol. 8, 2003, pp. 121–147.

14. Papazoglou, T.G., et al., Laser-induced fluorescence detection of cardiovascular atherosclerotic deposits via their natural emission and hypocrellin (Ha) probing, *J. Photochem. Photobiol. B*, Vol. 22, 1994, pp. 139–144.
15. Morguet, A.J., et al., Autofluorescence spectroscopy using a XeCl excimer laser system for simultaneous plaque ablation and fluorescence excitation, *Lasers Surg. Med.*, Vol. 14, 1994, pp. 238–248.
16. Morguet, A.J., et al., Development and evaluation of a spectroscopy system for classification of laser-induced arterial fluorescence spectra, *Biomed. Technol.* (*Berl.*), Vol. 42, 1997, pp. 176–182.
17. Baraga, J.J., et al., Laser induced fluorescence spectroscopy of normal and atherosclerotic human aorta using 306–310nm excitation, *Lasers Surg. Med.*, Vol. 10, 1990, pp. 245–261.
18. Bartorelli, A.L., et al., In vivo human atherosclerotic plaque recognition by laser-excited fluorescence spectroscopy, *J. Am. Coll. Cardiol.*, Vol. 17, 1991, pp. 160B–168B.
19. Christov, A., et al., "Optical detection of triggered atherosclerotic plaque disruption by fluorescence emission analysis," *Photochem. Photobiol.*, Vol. 72, 2000, pp. 242–252.
20. Arakawa, K., et al., "Fluorescence analysis of biochemical constituents identifies atherosclerotic plaque with a thin fibrous cap," *Arterioscler., Thromb. Vasc. Biol.*, Vol. 22, 2002, pp. 1002–1007.
21. Marcu, L., Grundfest, W.S., and Fishbein, M., Time-resolved laser-induced fluorescence spectroscopy for staging atherosclerotic lesions, in *Fluorescence in Biomedicine*, M.-A. Mycek and B. Pogue (eds.), Marcel Dekker, New York, 2002.
22. Elson, D.S., et al., "Multidimensional Fluorescence Imaging applied to biological tissues," in *Annual Reviews in Fluorescence 2006*, C.D. Geddes and J.R. Lakowicz (eds.), Springer, 2006.
23. http://www.picoquant.com/.
24. http://www.becker-hickl.de/.
25. Fang, Q.Y., et al., Time-domain laser-induced fluorescence spectroscopy apparatus for clinical diagnostics, *Rev. Sci. Instrum.*, Vol. 75, 2004, pp. 151–162.
26. Pitts, J.D., and Mycek, M.-A., Design and development of a rapid acquisition laser-based fluorometer with simultaneous spectral and temporal resolution, *Rev. Sci. Instrum.*, Vol. 72, 2001, p. 3061.
27. Pfefer, T.J., et al., Temporally and spectrally resolved fluorescence spectroscopy for the detection of high grade dysplasia in Barrett's esophagus, *Lasers Surg. Med.*, Vol. 32, No. 1, 2003, pp. 10–16.
28. Marcu, L., et al., Applications of time-resolved fluorescence spectroscopy to atherosclerotic cardiovascular disease and brain tumors diagnosis, *CLEO/QELS*, Baltimore, May 22–27, 2005, Vol. 1, pp. CFJ3–J5.
29. Marcu, L., et al., In-vivo detection of macrophages in a rabbit atherosclerotic model by time-resolved laser-induced fluorescence spectroscopy, *Atherosclerosis*, Vol. 181, No. 2, 2005, pp. 295–303.
30. Marcu, L., et al., Detection of rupture-prone atherosclerotic plaques by time-resolved laser induced fluorescence spectroscopy, *Atherosclerosis*, Vol. 204, No. 1, 2008, pp. 156–164.

31. Yong, W.H., et al., Distinction of brain tissue, low grade and high grade glioma with time-resolved fluorescence spectroscopy, *Front. Biosci*., Vol. 11, 2006, pp. 1255–1263.
32. Butte, P.V., et al., Diagnosis of meningiomas by time-resolved fluorescence spectroscopy, *J. Biomed. Opt*., Vol. 10, No. 6, 2005, p. 064026.
33. Marcu, L., et al., Fluorescence lifetime spectroscopy of glioblastoma multiforme, *Photochem. Photobiol*., Vol. 80, No. 1, 2004, pp. 95–103.
34. Ashjian, P., et al., Non-invasive in-situ evaluation of osteogenic differentiation by time-resolved laser-induced fluorescence spectroscopy, *Tissue Eng*., Vol. 10, No. 3–4, 2004, pp. 411–420.
35. Marcu, L., et al., Discrimination of lipid-rich atherosclerotic lesions of human coronary artery by time-resolved laser-induced fluorescence spectroscopy, *Arterioscler. Thromb. Vasc. Biol*., Vol. 21, 2001, pp. 1244–1250.
36. Maarek, J.M., et al., Time-resolved fluorescence of aortic wall: use for improved identification of atherosclerotic lesions, *Lasers Surg. Med*., Vol. 27, 2000, pp. 241–254.
37. Sun, Y.H., et al., Simultaneous time- and wavelength-resolved fluorescence spectroscopy for near real-time tissue diagnosis, *Opt. Lett*., Vol. 33, No. 6, 2008, pp. 630–632.
38. Ware, W.R., Doemeny, L.J., and Nemzek, T.L., Deconvolution of fluorescence and phosphorescence decay curves: least-squares method, *J. Phys. Chem*., Vol. 77, No. 17, 1973, pp. 2038–2048.
39. O'Connor, D.V., Ware, W.R., and Andre, J.C., Deconvolution of fluorescence decay curves: critical comparison of techniques, *J. Phys. Chem*., Vol. 83, No. 10, 1979, pp. 1333–1343.
40. Maarek, J.M.I., et al., Time-resolved fluorescence spectra of arterial fluorescent compounds: reconstruction with the Laguerre expansion technique, *Photochem. Photobiol*., Vol. 71, No. 2, 2000, pp. 178–187.
41. Jo, J.A., et al., Fast model-free deconvolution of fluorescence decay for analysis of biological systems, *J. Biomed. Opt*., Vol. 9, No. 4, 2004, pp. 743–752.
42. Marmarelis, V.Z., Identification of nonlinear biological-systems using Laguerre expansions of kernels, *Ann. Biomed. Eng*., Vol. 21, No. 6, 1993, pp. 573–589.
43. Stavridi, M., Marmarelis, V.Z., and Grundfest, W.S., Spectro-temporal studies of Xe–Cl excimer laser-induced arterial-wall fluorescence, *Med. Eng. Phys*., Vol. 17, No. 8, 1995, pp. 595–601.
44. Snyder, W.J., et al., Biologic fluorescence decay characteristics: determination by Laguerre expansion technique, *Proc. SPIE*, Vol. 2679, 1996, p. 150.
45. Jo, J.A., et al., Laguerre-based method for analysis of time-resolved fluorescence data: application to in-vivo characterization and diagnosis of atherosclerotic lesions, *J. Biomed. Opt*., Vol. 11, No. 2, 2006, p. 021004.
46. Naghavi, M., et al., From vulnerable plaque to vulnerable patient: a call for new definitions and risk assessment strategies: I, *Circulation*, Vol. 108, 2003, pp. 1664–1672.
47. Libby, P., and Aikawa, M., Stabilization of atherosclerotic plaques: new mechanisms and clinical targets, *Nat. Med*., Vol. 8, 2002, pp. 1257–1262.

48. MacNeill, B.D., et al., Intravascular modalities for detection of vulnerable plaque: current status, *Arterioscler. Thromb. Vasc. Biol*., Vol. 23, 2003, pp. 1333–1342.
49. Tearney, G.J., et al., Quantification of macrophage content in atherosclerotic plaques by optical coherence tomography, *Circulation*, Vol. 107, 2003, pp. 113–119.
50. Jang, I.K., Tearney, G., and Bouma, B., Visualization of tissue prolapse between coronary stent struts by optical coherence tomography: comparison with intravascular ultrasound, *Circulation*, Vol. 104, 2001, p. 2754.
51. Hatsukami, T.S., et al., Visualization of fibrous cap thickness and rupture in human atherosclerotic carotid plaque in vivo with high-resolution magnetic resonance imaging, *Circulation*, Vol. 102, 2000, pp. 959–964.
52. Zimmermann, G.G., et al., Intravascular MR imaging of atherosclerotic plaque: ex vivo analysis of human femoral arteries with histologic correlation, *Radiology*, Vol. 204, 1997, pp. 769–774.
53. de Korte, C.L., et al., Morphological and mechanical information of coronary arteries obtained with intravascular elastography: feasibility study in vivo, *Eur. Heart J*., Vol. 23, 2002, pp. 405–413.
54. Foster, F.S., et al., Advances in ultrasound biomicroscopy, *Ultrasound Med. Biol*., Vol. 26, 2000, pp. 1–27.
55. Jang, I.K., et al., Comparison of optical coherence tomography and intravascular ultrasound for detection of coronary plaques with large lipid-core in living patients, *Circulation*, Vol. 102, 2000, p. 509.
56. Maruvada, S., Shung, K.K., and Wang, S.H., High-frequency backscatter and attenuation measurements of porcine erythrocyte suspensions between 30–90MHz, *Ultrasound Med. Biol*., Vol. 28, 2002, pp. 1081–1088.
57. Saijo, Y., and Steen, A.F.W., *Vascular Ultrasound*, Springer, Tokyo, 2003.
58. Yock, P.G., and Fitzgerald, P.J., Intravascular ultrasound: state of the art and future directions, *Am. J. Cardiol*., Vol. 81, 1998, pp. 27E–32E.
59. Bouma, B.E., et al., Evaluation of intracoronary stenting by intravascular optical coherence tomography, *Heart*, Vol. 89, 2003, pp. 317–320.
60. Fujimoto, J.G., et al., High resolution in vivo intra-arterial imaging with optical coherence tomography, *Heart*, Vol. 82, 1999, pp. 128–133.
61. Verheye, S., et al., In vivo temperature heterogeneity of atherosclerotic plaques is determined by plaque composition, *Circulation*, Vol. 105, 2002, pp. 1596–1601.
62. Casscells, W., et al., Thermal detection of cellular infiltrates in living atherosclerotic plaques: possible implications for plaque rupture and thrombosis, *Lancet*, Vol. 347, 1996, pp. 1447–1451.
63. Stefanadis, C., et al., Statin treatment is associated with reduced thermal heterogeneity in human atherosclerotic plaques, *Eur. Heart J*., Vol. 23, 2002, pp. 1664–1669.
64. Moreno, P.R., and Muller, J.E., Identification of high-risk atherosclerotic plaques: a survey of spectroscopic methods, *Curr. Opin. Cardiol*., Vol. 17, 2002, pp. 638–647.
65. Fayad, Z.A., and Fuster, V., Clinical imaging of the high-risk or vulnerable atherosclerotic plaque, *Circ. Res*., Vol. 89, 2001, pp. 305–316.
66. Pasterkamp, G., et al., Techniques characterizing the coronary atherosclerotic plaque: influence on clinical decision making, *J. Am. Coll. Cardiol*., Vol. 36, 2000, pp. 13–21.

67. Honda, Y., and Fitzgerald, P.J., Frontiers in intravascular imaging technologies, *Circulation*, Vol. 117, 2008, pp. 2024–2037.
68. Papazoglou, T.G., et al., Laser-induced fluorescence detection of cardiovascular atherosclerotic deposits via their natural emission and hypocrellin (Ha) probing, *J. Photochem. Photobiol. B*, Vol. 22, 1994, pp. 139–144.
69. Morguet, A.J., et al., Autofluorescence spectroscopy using a XeCl excimer laser system for simultaneous plaque ablation and fluorescence excitation, *Lasers Surg. Med.*, Vol. 14, 1994, pp. 238–248.
70. Baraga, J.J., et al., Laser induced fluorescence spectroscopy of normal and atherosclerotic human aorta using 306–310nm excitation, *Lasers Surg. Med.*, Vol. 10, 1990, pp. 245–261.
71. Bartorelli, A.L., et al., In vivo human atherosclerotic plaque recognition by laser-excited fluorescence spectroscopy, *J. Am. Coll. Cardiol.*, Vol. 17, 1991, pp. 160B–168B.
72. Christov, A., et al., Optical detection of triggered atherosclerotic plaque disruption by fluorescence emission analysis, *Photochem. Photobiol.*, Vol. 72, 2000, pp. 242–252.
73. Arakawa, K., et al., Fluorescence analysis of biochemical constituents identifies atherosclerotic plaque with a thin fibrous cap, *Arterioscler. Thromb. Vasc. Biol.*, Vol. 22, 2002, pp. 1002–1007.
74. Angheloiu, G.O., et al., Intrinsic fluorescence and diffuse reflectance spectroscopy identify superficial foam cells in coronary plaques prone to erosion, *Arterioscler. Thromb. Vasc. Biol.*, Vol. 26, 2006, pp. 1594–1600.
75. Gropler, R.J., and Soto, P., Recent advances in cardiac positron emission tomography in the clinical management of the cardiac patient, *Curr. Cardiol. Rep.*, Vol. 6, 2004, pp. 20–26.
76. Tsimikas, S., Noninvasive imaging of oxidized low-density lipoprotein in atherosclerotic plaques with tagged oxidation-specific antibodies, *Am. J. Cardiol.*, Vol. 90, 2002, pp. 22L–27L.
77. Virmani, R., et al., Pathology of the vulnerable plaque, *J. Am. Coll. Cardiol.*, Vol. 47, 2006, pp. 13–18.
78. CBTRUS, *2002–2004 Statistical Report: Primary Brain Tumors in the United States, 1995–1999*, Central Brain Tumor Registry of the United States, Hinsdale, IL, 2008.
79. Louis, D.N., Ohgaki, H., Wiestler, O.D., Cavanee, W.K., *WHO Classification of Tumors of Central Nervous System*, Lyon, France, International Agency for Research on Cancer, 2007.
80. Mirimanoff, R.O., et al., Meningioma: analysis of recurrence and progression following neurosurgical resection, *J. Neurosurg.*, Vol. 62, No. 1, 1985, pp. 18–24.
81. Bruner, J.M., Neuropathology of malignant gliomas, *Semin. Oncol.*, Vol. 21, No. 2, 1994, pp. 126–138.
82. Stummer, W., et al., Extent of resection and survival in glioblastoma multiforme: identification of and adjustment for bias, *Neurosurgery*, Vol. 62, No. 3, 2008, pp. 564–576.
83. Krammer, B., et al., ALA and its clinical impact, from bench to bedside, *Photochem. Photobiol. Sci.*, Vol. 7, No. 3, 2008, pp. 283–289.
84. Unsgaard, G., et al., Brain operations guided by real-time two-dimensional ultrasound: new possibilities as a result of improved image quality, *Neurosurgery*, Vol. 51, No. 2, 2002, pp. 402–412.

85. Sutherland, G.R., and Louw, D.F., Intraoperative MRI: a moving magnet, *Can. Med. Assoc. J*., Vol. 161, 1999, p. 1293.
86. Kollias, S.S., et al., Target definition and trajectory optimization for interactive MR-guided biopsies of brain tumors in an open configuration MRI system, *J. Magn. Reson. Imaging*, Vol. 8, 1998, pp. 143–159.
87. Stummer, W., et al., Long-sustaining response in a patient with non-resectable, distant recurrence of glioblastoma multiforme treated by interstitial photodynamic therapy using 5-ALA: case report, *J. Neurooncol*., Vol. 87, No. 1, 2008, pp. 103–109.
88. Chung, Y.G., et al., Diagnostic potential of laser-induced autofluorescence emission in brain tissue, *J. Korean Med. Sci*., Vol. 12, No. 2, 1997, pp. 135–142.
89. Croce, A.C., et al., Diagnostic potential of autofluorescence for an assisted intraoperative delineation of glioblastoma resection margins, *Photochem. Photobiol*., Vol. 77, No. 3, 2003, pp. 309–318.
90. Lin, W.C., et al., In vivo brain tumor demarcation using optical spectroscopy, *Photochem. Photobiol*., Vol. 73, No. 4, 2001, pp. 396–402.
91. Lin, W.C., et al., Brain tumor demarcation using optical spectroscopy: an in vitro study, *J. Biomed. Opt*., Vol. 5, No. 2, 2000, pp. 214–220.
92. Marcu, L., et al., Fluorescence lifetime spectroscopy of glioblastoma multiforme, *Photochem. Photobiol*., Vol. 80, 2004, pp. 98–103.
93. Yong, W.H., et al., Distinction of brain tissue, low grade and high grade glioma with time-resolved fluorescence spectroscopy, *Front. Biosci*., Vol. 11, 2006, pp. 1255–1263.
94. Butte, P.V., et al., Diagnosis of meningioma by time-resolved fluorescence spectroscopy, *J. Biomed. Opt*., Vol. 10, No. 6, 2005, p. 064026.
95. Bottiroli, G., et al., Natural fluorescence of normal and neoplastic human colon: a comprehensive “ex vivo” study, *Lasers Surg. Med*., Vol. 16, No. 1, 1995, pp. 48–60.
96. Lin, W.C., et al., In vivo optical spectroscopy detects radiation damage in brain tissue, *Neurosurgery*, Vol. 57, No. 3, 2005, pp. 518–525.
97. Toms, S.A., et al., Intraoperative optical spectroscopy identifies infiltrating glioma margins with high sensitivity, *Neurosurgery*, Vol. 57, No. 4, Suppl., 2005, pp. 382–391.
98. Pradhan, A., et al., Steady state and time-resolved fluorescence properties of metastatic and non-metastatic malignant cells from different species, *J. Photochem. Photobiol. B*, Vol. 31, No. 3, 1995, pp. 101–112.
99. Reinert, K.C., et al., Flavoprotein autofluorescence imaging of neuronal activation in the cerebellar cortex in vivo, *J. Neurophysiol*., Vol. 92, No. 1, 2004, 199–211.
100. Bottiroli, G., et al., Brain tissue autofluorescence: an aid for intraoperative delineation of tumor resection margins, *Cancer Detect. Prev*., Vol. 22, No. 4, 1998, pp. 330–339.
101. Jo, J.A., et al., A nonlinear model of cardiac autonomic control in obstructive sleep apnea syndrome, *Ann. Biomed. Eng*., Vol. 35, No. 8, 2007, pp. 1425–1443.

# 10

# ADVANCED OPTICAL METHODS FOR FUNCTIONAL BRAIN IMAGING: TIME-DOMAIN FUNCTIONAL NEAR-INFRARED SPECTROSCOPY

ALESSANDRO TORRICELLI AND DAVIDE CONTINI
*Politècnico di Milano, Milan, Italy*

LORENZO SPINELLI
*Istituto di Fotonica e Nanotecnologie–Seziόne di Milano, Milan, Italy*

MATTEO CAFFINI, ANTONIO PIFFERI, AND RINALDO CUBEDDU
*Politècnico di Milano, Milan, Italy*

10.1 Introduction 288
10.2 Optical technologies for noninvasive neural activity mapping 289
  10.2.1 Photon migration in biological tissue 289
  10.2.2 Functional near-infrared spectroscopy 291
  10.2.3 Advantages of the TD approach 292
  10.2.4 Instrumentation for TD fNIRS 293
10.3 Optical imaging of depth-resolved functional activity in the cortex 294
  10.3.1 Motor tasks 294
  10.3.2 Verbal fluence tasks 295
  10.3.3 Survey of TD fNIRS 296
10.4 Novel approaches to TD fNIRS 297
  10.4.1 Fluorescence as contrast agent 297
  10.4.2 Multimodality imaging 298
  10.4.3 Null distance approach 298
10.5 Conclusions 299
References 300

---

*Advances in Optical Imaging for Clinical Medicine*, Edited by Nicusor Iftimia, William R. Brugge, and Daniel X. Hammer
Copyright © 2011 John Wiley & Sons, Inc.

## 10.1 INTRODUCTION

The possibility to noninvasively monitor hemodynamics (i.e., evolution of blood distribution within a biological tissue) and oxidative metabolism (i.e., oxygenation status) in the brain is a challenging and important task. It can lead to the monitoring of cerebral activity in response to stimuli (motor, visual, and cognitive), and thus it can help in the study of functional processes, and also for diagnosis of mental diseases, and localization of brain injuries. The capabilities offered by functional magnetic resonance imaging (fMRI) and positron emission tomography (PET) fostered this emerging field [1,2]. In this framework light is a powerful diagnostic tool, especially in the region between 600 and 1100 nm [red and near infrared (NIR)], where biological tissues are weakly absorbing and penetration depth is relatively high, allowing for the noninvasive investigation of deep tissues. Moreover, main tissue constituents (water, lipid, oxygenated hemoglobin, and deoxygenated hemoglobin) exhibit distinct spectral features (see Figure 10.1), which may be helpful to distinguish them and to derive information on the physiopathology of tissue [3].

A detailed description of the sources of contrast for light signals in the brain can be found elsewhere [4]. Both light absorption and light scattering may yield valuable information related to brain function. Similar to fMRI, neurovascular coupling is the major source of contrast for NIR light [5]. However, optical methods take advantage of the different absorption spectra of the two hemoglobin

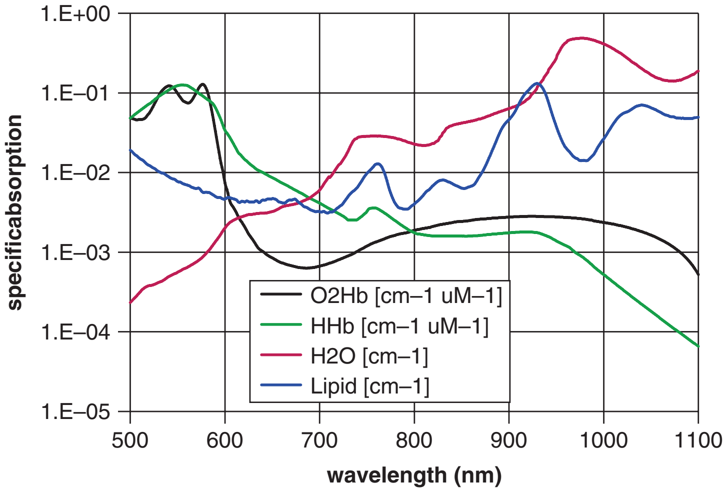

**FIGURE 10.1** Absorption spectra of main tissue constituents in the 600 to 1100-nm spectral region.

species, whereas fMRI exploits the paramagnetic properties of deoxygenated hemoglobin. The widespread use of light for noninvasive investigation has been partially hampered by the high scattering coefficient typical of biological tissues, which hinders collection of spatial and spectral information contained in endogenous chromophores. This is particularly true for the brain, since brain cortex is covered by 1 to 2 cm of highly scattering biological tissue (i.e., scalp and skull). Therefore, the use of optical tools has initially been restricted to invasive methods such as exposed-cortex imaging and microscopy. Invasive approaches using visible and NIR light, also in combination with endogenous and exogenous dyes, may be found in the reviews by Hillman [6] and Obrig and Villringer [7].

Recently, advances in the understanding of light propagation in diffusive media (also known as photon migration) and technical developments in optoelectronics components have made it possible to extract valuable optical information from thick turbid media, opening the way to noninvasive functional brain monitoring. The term *functional near-infrared spectroscopy* (fNIRS or, simply, NIRS) is typically used for noninvasive brain spectroscopy and imaging applications. Different fNIRS instruments—either commercial systems or laboratory prototypes—have been developed and used effectively in preclinical and clinical studies. In the following sections of this chapter we briefly introduce the basics of light propagation in biological tissue and emphasize the differences between the various noninvasive approaches (e.g., continuous wave vs. time-domain methods, topography vs. tomography). We then present a gallery of results, and finally, we introduce very recent advances based on the combined use of contrast agents and multimodality imaging.

## 10.2 OPTICAL TECHNOLOGIES FOR NONINVASIVE NEURAL ACTIVITY MAPPING

### 10.2.1 Photon Migration in Biological Tissue

Like many other natural substances (e.g., paints, powders, clouds, foams), biological tissues are opaque to visible and NIR light (600 to 1000 nm). Light absorption and light scattering are the physical phenomena responsible for opacity. Absorption depends on the presence of endogenous or exogenous chromophores within the medium, whereas (elastic) scattering depends on microscopic discontinuities in the dielectric properties (i.e., refractive index) of the medium.

A simplified model of light–tissue interaction includes biological tissue, made up of scattering and absorbing centers irradiated by a stream of discrete photons. Whenever a photon strikes a scattering center it changes its trajectory and continues to propagate in the tissue until it is eventually remitted across a boundary or is captured by an absorbing center. According to this description, the characteristic parameters of light propagation within the tissue are the scattering length $L_s$ and the absorption length $L_a$ (typically, expressed in units of mm or cm), representing the photon mean path between consecutive scattering and absorption events, respectively. Equivalently, and more frequently, the scattering coefficient $\mu_s = 1/L_s$ and the absorption coefficient $\mu_a = 1/L_a$ (typically expressed in units of $\text{mm}^{-1}$ or $\text{cm}^{-1}$) are used to indicate the scattering and the absorption probability per unit length, respectively. To account for the change in angular direction due to the scattering events, the anisotropy factor $g = <\cos\theta>$ (where the brackets are an operator used in an averaging sense) is also introduced [8], where $\theta$ is the angle between the photon directions before and after the scattering event. The reduced scattering coefficient $\mu_s' = \mu_s(1 - g)$ is used as a comprehensive parameter for scattering interactions. For biological tissue in the NIR spectral range, $g$ is close to 0.9, indicating predominantly forward scattering [9].

In biological tissue in the NIR spectral region, light scattering is typically stronger than light absorption, even when the latter is significant. Typical values for $\mu_s'$ are in the range 5 to 25 $\text{cm}^{-1}$, while $\mu_a$ is typically lower than 0.5 $\text{cm}^{-1}$ [10]. This implies that light can be scattered many times before being absorbed or remitted from the tissue. Because of this multiple scattering phenomenon, with rare exceptions biological tissues are considered turbid or diffusive. Multiple scattering of light in a diffusive medium introduces an uncertainty in the pathlength traveled by photons; therefore, light propagation in diffusive medium is termed photon migration. The striking difference between light propagation in a clear (i.e., nondiffusive) medium and in a diffusive medium is illustrated in Figure 10.2. When a a glass cuvette filled with clear water is illuminated by a collimated laser beam, light travels in a ballistic way, following a rectilinear trajectory. Conversely, if a few drops of milk are added to the water, the light

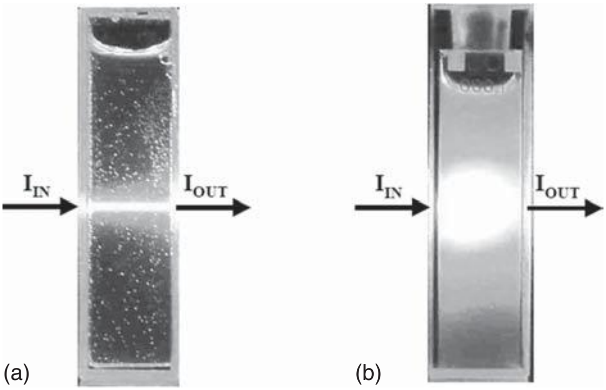

**FIGURE 10.2** Collimated laser light traveling in (a) clear and (b) a diffusive medium.

distribution in the turbid medium is altered significantly and light tends to diffuse into the whole medium.

### 10.2.2 Functional Near-Infrared Spectroscopy

Starting almost 30 years ago with the pioneering work of Jobsis [3], noninvasive functional near-infrared spectroscopy (fNIRS) has been used first to investigate experimentally and clinically brain oxygenation in neonates and adults, and later to assess muscle oxidative metabolism in pathophysiology [11,12]. fNIRS employs optical radiation in the range 600 to 1000 nm, where light attenuation by tissue constituents (water, lipid, oxyhemoglobin, and deoxyhemoglobin) is relatively low and accounts for an optical penetration through several centimeters of tissue. The difference in the absorption spectra of oxyhemoglobin ($O_2Hb$) and deoxyhemoglobin (HHb) allows the separate measurements of the concentration of these two species, and the derivation of physiologically relevant parameters such as the total hemoglobin content ($tHb = HHb + O_2Hb$) and blood oxygen saturation ($SO_2 = O_2Hb/tHb$). An interesting feature in the absorption spectra of HHb and $O_2Hb$ is that total hemoglobin can in principle be measured by using only one wavelength at an isosbestic points of spectra where the absorption is equal for the two species. In the range 600 to 1000 nm there is one isosbestic point around 800 nm.

The most common approach of fNIRS is in the continuous-wave (CW) regime: Light attenuation at two wavelengths between a couple of optical fibers set normal to the tissue surface at a known relative distance (typically, 2 to 4 cm) is measured. A fixed value of the scattering coefficient is assumed, and the relative changes in HHb and $O_2Hb$ are obtained by applying the Lambert–Beer law [13,14]. This rather straightforward technique has grown in time and led to instruments working at more wavelengths or with multiple sources and using a multiple-detector geometry. In particular, the latter feature offers the possibility to probe different regions in the tissue simultaneously to produce functional maps. Wolf et al. recently provided a detailed review of CW fNIRS instruments [15].

The key limitations of CW fNIRS technique are the coupling between the absorption and the scattering coefficients, causing a lack of quantitative assessment (e.g., results for HHb and $O_2Hb$ are reported in relative normalized units), sensitivity to artifacts (e.g., corruption of absorption images from scattering contrast in structural features), and experimental conditions (e.g., irregularities in the head surface due to the presence of hairs).

One way to uncouple absorption from scattering using a CW source is to use the space-resolved spectroscopy (SRS) approach. Measurements at a multiple source–detector distance are acquired simultaneously and the spatial decay of remitted light is analyzed [16]. Some commercial instruments are available that exploit this principle, yet the method relies on a strong correlation between different interfiber distances and thus is based on the assumption of a homogeneous medium. Deleterious effects caused by the inherent layered structure of the

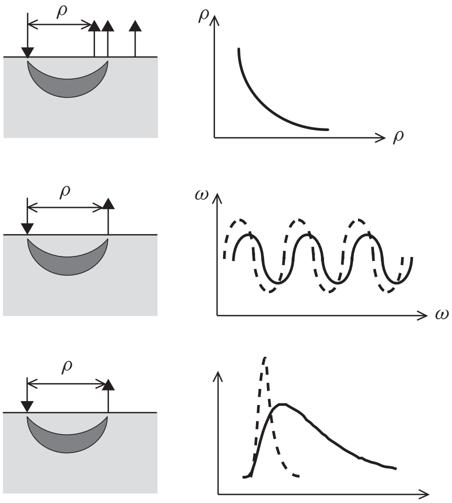

**FIGURE 10.3** Diffuse optical imaging techniques: (a) CW-SRS; (b) FD; (c) TD.

human head (i.e., scalp, skull, cerebrospinal fluid, gray matter, and white matter) have yet to be overcome [17].

The frequency-domain (FD) technique is another method to uncouple absorption from scattering. FD uses modulated laser sources to measure changes in signal phase and absolute amplitude caused by light propagation. Because the FD technique is based on absolute measurement of light intensity, it requires a nontrivial calibration of collection efficiencies. Nonetheless, this approach was used successfully to measure tissue oxygenation and led to the first identification of a rapid change of scattering coefficient following a cerebral stimulus [18].

Yet another approach is to study photon migration in the time domain (TD), sometimes referred to as the dual approach to FD, since TD in principle contains both CW and FD information at all frequencies. The TD approach is based on the detection of attenuation, broadening, and delay experienced by short (few tens to hundreds of picoseconds) laser pulses injected in a diffusive medium [19,20]. In the past, the cost, size, and complexity of TD instrumentation prevented this technique from being used effectively in tissue oxygenation studies. Recently, several groups have developed compact systems for TD fNIRS, taking advantage of technological advances in optoelectronics instrumentation. A review of the performance of various TD systems can be found elsewhere [21,22]. Figure 10.3 illustrates the different diffuse optical imaging techniques (CW-SRS, FD, and TD) showing input light waveform and typical measurement output.

### 10.2.3 Advantages of the TD Approach

It is not clear which method among CW, FD, and TD performs the best. In principle, TD data should have the highest information content. In the TD approach, the pathlength is determined for each detected photon, as opposed to the FD approach, which detects ensemble averages. Moreover, an FD signal at one frequency is one Fourier mode in the Fourier transform of a TD signal. A comparison of the TD and FD methods has been reported by Nissilä et al. for a specific tomographic setup [23]. A more general comparison is difficult, however, and eventually depends on many factors in a particular experimental arrangement (both hardware and software) [24].

In TD fNIRS, the time of flight of the photon in part determines the tissue penetration depth. Therefore, depth resolution of absorption changes can be accomplished [25]. In this way, cerebral and extracerebral absorption changes can be discriminated. This is particularly important since brain activation can be accompanied by systemic physiological changes that influence the absorption within extracerebral tissue, thus contaminating cerebral NIRS signals.

Moreover, single-distance CW and FD measurements are not able to determine blood oxygen saturation in brain tissue (also known as the *tissue oxygenation index*). This index is defined as the ratio of the absolute concentration of $HbO_2$ to the total hemoglobin. Accordingly, some tissue oximeters (e.g., NIRO-300, Hamamatsu, Japan and OxiplexTS, ISS Inc., United States) rely on a multidistance measurement [26,27] and make use of the fact that increasing source–detector separation increases the CW signal contribution from the brain. Unfortunately, this approach cannot be extended to topographical imaging. However, TD fNIRS can solve the problem by emphasizing the contribution of late-arriving photons, so that the relative sensitivity is enhanced considerably. Compared to a multidistance approach, the single-distance TD measurement has the additional advantage that it does not depend on skin homogeneity or equal coupling conditions for several detectors.

### 10.2.4 Instrumentation for TD fNIRS

The two key parameters in the design of a TD fNIRS system are temporal resolution and sensitivity. TD-fNIRS relies on recording the temporal distribution of the remitted light following the injection of a picosecond laser pulse in a diffusive medium. Typical values of the optical parameters in the near-infrared spectral region set the time scale of TD fNIRS events in the range 1 to 10 ns and fix the ratio of detected to injected power at about −80 dB. Pulsed lasers, which produce short (10 to 100 ps) and ultrashort (10 to 100 fs) light pulses with a repetition frequency of up to 100 MHz, and detection systems with temporal resolution in the range 50 to 250 ps are readily available. Some of these laser sources are able to provide high average power in the range 0.1 to 1 W. It is important to limit laser power to avoid possible damage or injury to the sample. Federal regulations limit the maximum permissible exposure value for biological tissue to 2 $mW/mm^2$ [28].

The time-correlated single-photon counting (TCSPC) technique has been used extensively for time-resolved measurements in diffusive media [29] and for TD fNIRS [30]. Recently also, a time-gated intensified charge-coupled-device camera

(ICCD) has been used [31–33]. In a TCSPC experiment, the temporal profile of the remittance curve is not measured directly but is retrieved by repeated measurement of the delay between an excitation event and a remittance event for a statistically significant number of photons. A key parameter is the count rate, the number of photons per second [counts per second (cps)], which can be processed without exceeding the single-photon statistics. Standard TCSPC systems have a maximum count rate of about $5 \times 10^6$ cps. A complete and updated description of TCSPC systems and applications (including TD fNIRS) can be found elsewhere [30].

Like TCSPC, an ICCD camera is characterized by ultimate sensitivity down to single-photon detection. It consists basically of a photocathode, a microchannel plate photomultiplier (MCP-PMT), and a phosphor screen. In addition, high temporal resolution can be achieved with an ICCD by fast gating the intensifier cathode. Recently, smaller image tubes achieved ultrashort gates ($<$100 ps), surpassing the 1-ns time-resolution limitation imposed by conventional ICCDs [34]. The time-gated ICCD system is thus potentially able to measure the spatial and temporal profile of the remitted light from a diffusive medium by acquiring different images synchronized to different time delays with respect to the excitation. Every image contains instantaneous spatial information, while successive images reveal the temporal distribution of the signal detected.

The TCSPC technique is currently more prevalent in prototypes and instruments for TD fNIRS (see also Section 10.3.3). Since there is no striking advantage of TCSPC over time-gated ICCD, the choice of the technique is determined by a trade-off among cost, complexity, and performance in relation to a specific clinical application.

## 10.3 OPTICAL IMAGING OF DEPTH-RESOLVED FUNCTIONAL ACTIVITY IN THE CORTEX

Several papers have recently presented a review of fNIRS clinical and research applications, focusing primarily on CW and FD [6,15,35,36]. In this section we present some applications of TD fNIRS and a survey of TD fNIRS instrument and research groups.

### 10.3.1 Motor Tasks

Several research groups have typically used simple motor tasks (e.g., finger tapping) as a paradigm to assess performances of fNIRS instruments (CW, FD, and TD) and to validate the technique itself during in vivo tests [37]. Here we use such a protocol to show the depth sensitivity of TD fNIRS.

Measurements were performed on one adult volunteer (male, 38 years, right-handed). The experimental design consisted of eight trials formed by a baseline 20 s long during which the subject was asked to relax, keeping his arms still (rest condition), then 20 s of a motor task (sequential finger-to-thumb opposition

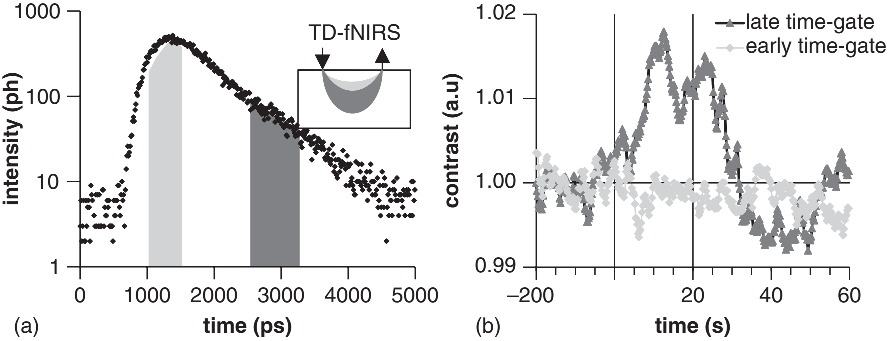

**FIGURE 10.4** (a) TD-fNIRS curve. The inset shows a scheme of the measurement geometry and of the paths traveled by early (light gray, time-gate delay 250 ps, time-gate width 250 ps) and late (dark gray, time-gate delay 2000 ps, time-gate width 500 ps) photons. (b) Contrast time courses at 690 nm for early (light gray) and late (dark gray) time gates during motor activity (baseline −20 to 0 s, finger tapping 0 to 20 s, recovery 20 to 40 s). Data are an average of eight trials and are normalized to the average baseline value.

movements of the right hand at a frequency of 3 Hz), followed by 40 s of rest to allow recovery of the response.

Figure 10.4a shows a scheme of the measurement geometry and the paths traveled by early and late photons. Contrast time courses at 690 nm are shown in Figure 10.4b for early and late time gates during motor activity. The results indicate that with a single source–detector distance (2 cm), it is possible to discriminate signals from upper and deeper layers in the adult head by exploiting the information encoded in the time of flight of diffusing photons. This is a unique capability of TD fNIRS, not possible with CW or FD systems. An approximate depth limit in relation to acceptable signal/noise ratio can be estimated as 2 to 3 cm, depending on the system performances [25,33].

### 10.3.2 Verbal Fluence Tasks

The prefrontal cortex (the anterior portion of the frontal lobe) and the frontal lobe (the front part of the brain involved in planning, organizing, problem solving, selective attention, etc.), are both involved in higher cognitive functions and in the determination of personality and have been studied using various neuropsychological tests (e.g., mental calculation tasks, continuous performance tasks, Wisconsin Card Sorting task) [38]. The verbal fluency task (VFT) is a cognitive paradigm known to activate the prefrontal cortex. VFT enables assessment of a subject's ability to retrieve nouns based on a common criterion.

CW fNIRS has been used to measure relative changes of $O_2$Hb and HHb during a VFT study in healthy volunteers and psychiatric patients [39]. We have shown that by TD fNIRS it is possible to estimate absolute values for the hemodynamic quantities and $SO_2$ [40]. Figure 10.5 shows the time courses

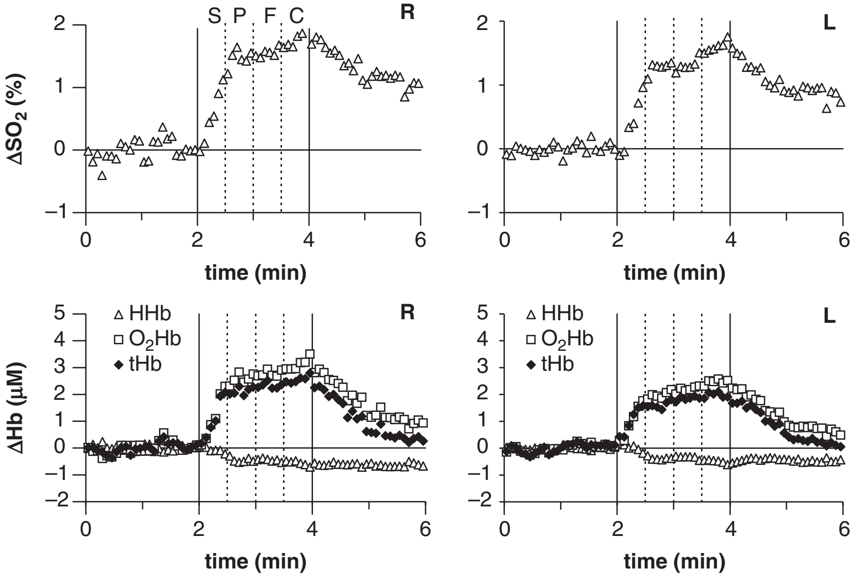

**FIGURE 10.5** Time courses of $\Delta SO_2$, $\Delta HbO_2$, $\Delta HHb$, and $\Delta tHb$ during VFT in the right (R) and left (L) prefrontal cortex of a volunteer. Measurements are average of four channels located in the right and left prefrontal cortex. Solid vertical lines indicate total duration of the VFT, which is in turn subdivided by the three dashed vertical lines in four intervals. Each interval represents the allocated time for each subject to produce as many nouns as possible, beginning with the corresponding letter reported.

of hemodynamic absolute quantities ($\Delta SO_2$, $\Delta HbO_2$, $\Delta HHb$, and $\Delta tHb$) with respect to their baseline value during VFT in the right (R) and left (L) prefrontal cortex of a volunteer.

Cerebral cortex $SO_2$ predominantly reflects saturation of the intracranial venous compartment of circulation [41]. $SO_2$ measurements are extremely important in clinics, suggesting potential use of TD fNIRS instruments for cortical $SO_2$ mapping (i.e., to evaluate the cerebrovascular reactivity in the neurovascular diseases and/or to evaluate the efficacy of stroke therapy/rehabilitation). For medical applications, the normal range of $SO_2$ in the brain should be studied in a large population to determine normal and abnormal value ranges. The cross-subject ($n = 6$) mean $SO_2$ values in our study were $69 \pm 3\%$ and $71 \pm 4\%$ in the right and left prefrontal cortex, respectively. Mean values for tHb were $70 \pm 10$ μM and $69 \pm 10$ μM.

### 10.3.3 Survey of TD fNIRS

Only one commercial TD fNIRS system has been developed in Japan (TRS-10, Hamamatsu), while there are several prototypes, the majority of which employ the TCSPC technique [29,30]. The key issue in the choice of TCSPC is the availability of relatively low-cost laser sources, detectors, and acquisition electronics. Moreover, portable and compact systems can be built. Recently, intensified CCD camera–based systems have been developed and used for measurements on tissue phantoms and volunteers [33,42].

The first demonstrations of TD fNIRS were developed in the United States [43] and Japan [44]. Currently, leading research in TD fNIRS is also performed by several European groups. The research group at Physikalisch-Technische Bundesanstalt in Berlin, Germany has developed a three-wavelength, four-detection-channel TCSPC instrument [45] that has been used effectively for bedside assessment of cerebral perfusion in stroke patients [46,47].

At the Institute of Biocybernetics and Biomedical Engineering in Warsaw, Poland, a 32-channel configuration has been assembled by doubling the switching and detection elements [48]. Current and foreseen clinical applications are brain oxygenation measurements during carotid endartectomy and the detection of brain traumatic lesions. The research group at the Department of Medical Physics and Bioengineering, University College, London has developed a tomographic TD fNIRS system that is used for functional and pathological studies in newborn babies [49–51].

The research group in Strasbourg used an eight-channel system based on picosecond laser sources and a multianode microchannel plate (MCP) PMT together with two-dimensional finite-element model (FEM) simulations to perform a single point measurement during a finger tapping experiment [52,53]. Researchers from Hamamatsu Photonics K. K. in Japan reported the use of a 16-channel time-domain system for human brain mapping by means of diffuse optical tomography [54], while single-channel devices have been used for research studies on piglets [55], newborn babies [56], and adults [57]. However, commercial devices for functional studies by time-domain measurement are not currently available outside Japan.

Interestingly, TD systems and devices have found a clinical application in the field of optical mammography [58] (see Chapter 11). Since the components are similar, it is expected that fNIRS will also migrate to applications beyond neuroimaging.

## 10.4 NOVEL APPROACHES TO TD fNIRS

### 10.4.1 Fluorescence as Contrast Agent

A new major application for optical brain monitoring concerns recording the bolus transit of an optical contrast agent [e.g., indocyanine green (ICG)] for the assessment of cerebral perfusion. Such studies have been performed on neonates and adults [59,60] using CW fNIRS devices. However, as we demonstrated in a pilot study on stroke patients [46], a TD approach is essential to obtain meaningful bolus signals from the brain. A particularly promising extension of this technique is fluorescence detection of ICG boli, the feasibility of which has already been shown in healthy volunteers [61,62]. Background-free fluorescence signals are less subject to biological noise than changes in diffuse reflectance, and molecular imaging of the brain becomes an exciting prospect. Although the detection of bolus fluorescence has been shown in principle, its practical implementation necessitates instrumental improvements as well as advances in the analysis of time-resolved fluorescence signals.

### 10.4.2 Multimodality Imaging

Neuronal processing and metabolic and vascular responses are highly correlated in space and time, but the details of the neurovascular coupling (i.e., the change between a collection of firing neurons and the resulting increase in focal cerebral blood flow) remain controversial. Multimodality imaging may offer a better manner to understand the underlying physiological processes following brain stimulation. There are no fundamental limitations to prevent the coregistration of fNIRS with other neuroimaging modalities, such as EEG, fMRI, and PET. Recent studies have combined fMRI with fNIRS, as reviewed by Steinbrink [63]. These studies aimed not only at validating fNIRS per se as a brain mapping technique, but also to elucidate the blood oxygen level–dependent (BOLD) effect in fMRI [37]. Until recently, only CW [64] or FD [65] fNIRS/fMRI studies have been reported. The use of TD fNIRS allows better depth discrimination and possibly more robust assessment of absolute changes in the hemodynamic parameters. However, since the fNIRS instrument must necessarily be operated at a safe distance from the MR scanner, long (e.g., 10 m) optical fibers are required for light delivery and collection from the head of the subject. As a consequence, temporal dispersion in the optical fibers significantly reduces the time resolution and overall performance of a TD apparatus. This problem has already been tackled in concurrent MRI and optical mammography by the use of small numerical aperture (NA) fiber bundles and photomultipliers with fast response time and low jitter [66]. Still, the reduced sensitivity necessitated a 20-s acquisition time [67], which is unfortunately not suited for functional studies of the hemodynamic responses in the adult brain. We have recently shown an experimental setup for simultaneous acquisition of fMRI and TD fNIRS [68,69]. The system has been tested during motor task experiments with a 200-ms acquisition time. Coregistration of TD fNIRS with MEG and PET have been reported by other groups [70,71].

### 10.4.3 Null Distance Approach

A major criticism regarding the present status of the TD fNIRS technique is that for topographical and tomographical imaging the number of source and detection optodes is rather low. In particular, an increase in the number of detection channels beyond four or eight makes an instrument bulky and expensive. To address this issue, developments in photonic technologies are directed toward increased parallelization of detection channels. A major step in optical brain imaging will

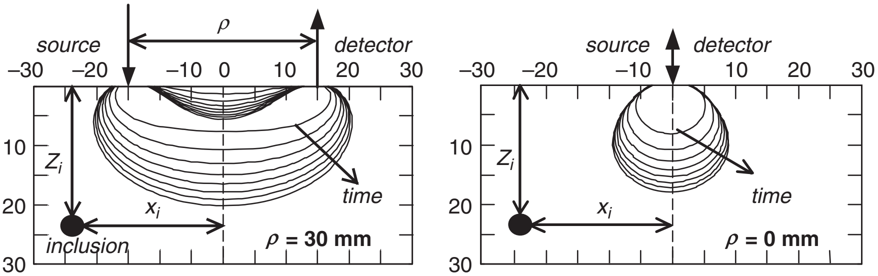

**FIGURE 10.6** Sensitivity profiles for the classical approach ($\rho = 30$ mm) and for the novel approach ($\rho = 0$ mm) in a homogeneous medium ($\mu_a = 0.005$ mm$^{-1}$ and $\mu_s' = 1$ mm$^{-1}$, $n = 1.4$) with an inclusion (depth $z_i$, volume 1 mm$^3$, $\mu_{si}' = 1$ mm$^{-1}$, $\mu_{ai} = 0.020$ mm$^{-1}$). Each line represents the contour edge of the contrast at 4% of maximum at a given time (only data from time $t = 0.5$ to 4 ns, in 0.5-ns steps, are shown for clarity).

be implementation of the null source–detector separation method [72,73]. With this approach, the volume sampled by the light is much more concentrated than with the usual source–detector separation of 2 to 4 cm (see Figure 10.6).

By tightly packing sources and detectors on the head, in combination with an increased number of detector channels, lateral spatial resolution can be increased substantially. In addition, the number of late photons that visited the brain is larger. Such null source–detector separation is not possible with the CW and FD approaches. However, with the null source–detector separation approach, early, very intense parts of the TD fNIRS signal will saturate the detection electronics. A possible remedy would be to use a detector operated with a time gate that is delayed with respect to the arrival time of initial photons and which exhibits a fast (subnanosecond) rise time. However, even if the gain of a photomultiplier tube could be switched in such a way, initial photons would still impinge onto the photocathode and extract electrons, causing damage to the active surface and significantly increasing the background noise. Single-photon avalanche diode (SPAD) detectors are one solution. A key feature of SPAD detectors is the possibility to gate the device. When the SPAD is disabled, the avalanche process cannot start, and most of the electron–hole pairs generated by the incoming photons recombine within the active area in a few tens of picoseconds. Thus, this device is not damaged by the burst of initial photons, and a strong rejection of early photons can be achieved. A preliminary demonstration of the null distance approach on a tissue phantom and in vivo was presented by Pifferi et al. [74].

## 10.5 CONCLUSIONS

The clinical use of photonics technology is expected to increase in the future, due in part to advances in the development of laser sources and optoelectronic devices. In particular, we foresee a major breakthrough for cutting-edge techniques such as TD fNIRS. Powerful (>1 W) picosecond broadband fiber lasers [75] can replace low-power-pulsed diode lasers currently employed in the majority of prototypes. Moreover, miniaturized, sensitive, and fast photonic crystal devices [76], combined with high-throughput photodetection electronics [77], are expected to increase the detection signal/noise ratio.

The four-year project nEUROPt [78], financed by the European Union under the Seventh Framework Programme for research and technological development (FP7) for the period 2008–2011 and coordinated by the authors, aims at the development and clinical validation of advanced noninvasive optical methodologies for in vivo diagnosis, monitoring, and prognosis of major neurological diseases (stroke, epilepsy, ischemia), based on diffuse optical imaging of pulsed near-infrared light. The consortium plans major developments in technology and data analysis that will enhance TD fNIRS with respect to spatial resolution, sensitivity, robustness of quantification, and the performance of related instruments in clinical diagnosis and monitoring. The diagnostic value of TD fNIRS will be assessed by clinical pilot studies addressing specific neurological disorders, compared with established neurophysiological and neuroimaging techniques. Perspectives regarding clinical application of TD fNIRS will be estimated and a reliable basis for a potential commercialization of this novel technique by European system manufacturers will be created.

### Acknowledgment

We wish to acknowledge partial support from the EC's Seventh Framework Programme (FP7/2007-2013) under grant 201076.

## REFERENCES

1. Matthews, P.M., Honey, G.D., and Bullmore, E.T., Applications of fMRI in translational medicine and clinical practice, *Nat. Rev. Neurosci*., Vol. 7, No. 9, 2006, pp. 732–744.
2. Hoh, C.K., Clinical use of FDG PET, *Nucl. Med. Biol*., Vol. 34, No. 7, 2007, pp. 737–742.
3. Jobsis, F.F., Non invasive, infrared monitoring of cerebral and myocardial oxygen sufficiency and circulatory parameters, *Science*, Vol. 198, No. 4323, 1977, pp. 1264–1267.
4. Villringer, A., and Chance, B., Non invasive optical spectroscopy and imaging of human brain function, *Trends Neurosci*., Vol. 20, No. 10, 1997, pp. 435–442.
5. Villringer, A., and Dirnagl, U., Coupling of brain activity and cerebral blood flow: basis of functional neuroimaging, *Cerebrovasc. Brain Metab. Rev*., Vol. 7, No. 3, 1995, pp. 240–276.
6. Hillman, E.M.C., Optical brain imaging in vivo: techniques and applications from animal to man, *J. Biomed. Opt*., Vol. 12, No. 5, 2007, p. 051402.
7. Obrig H., and Villringer, A., Beyond the visible: imaging the human brain with light, *J. Cereb. Blood Flow Metab*., Vol. 23, No. 1, 2003, pp. 1–18.

8. Henyey, L.G., and Greenstein, J.L., Diffuse radiation in the galaxy, *Astrophys. J.*, Vol. 93, No. 1, 1941, pp. 70–83.
9. Cheong, W.F., Prahl, S.A., and Welch, A.J., A review of the optical properties of biological tissues, *IEEE J. Quantum Electron.*, Vol. 26, No. 12, 1990, pp. 2166–2185.
10. Torricelli, A., et al. In vivo optical characterization of human tissues from 610 to 1010 nm by time-resolved reflectance spectroscopy, *Phys. Med. Biol.*, Vol. 46, No. 8, 2001, pp. 2227–2237.
11. Delpy, D.T., and Cope, M., Quantitation in tissue near-infrared spectroscopy, *Philos. Trans. R. Soc. Lond. B*, Vol. 352, No. 1354, 1997, pp. 649–659.
12. Madsen, P.L., et al., Near-infrared oximetry of the brain, *Prog. Neurobiol.*, Vol. 58, No. 6, 1999, pp. 541–560.
13. Reynolds, E.O., et al., New noninvasive methods for assessing brain oxygenation and hemodynamics, *Br. Med. Bull.*, Vol. 44, No. 4, 1988, pp. 1052–1075.
14. Cope, M., et al., A CCD spectrophotometer to quantitate the concentration of chromophores in living tissue utilising the absorption peak of water at 975 nm, *Adv. Exp. Med. Biol.*, Vol. 248, No. 1, 1989, pp. 33–40.
15. Wolf, M., Ferrari, M., and Quaresima V., Progress of near infrared spectroscopy and topography for brain and muscle clinical application, *J. Biomed. Opt.*, Vol. 12, No. 6, 2007, p. 062104.
16. Kienle, A., et al., Spatially resolved absolute diffuse reflectance measurements for noninvasive determination of the optical scattering and absorption coefficients of biological tissue, *Appl. Opt.*, Vol. 35, No. 13, 1996, pp. 2304–2314.
17. Farrell, T.J., Patterson, M.S., and Essenpreis, M., Influence of layered tissue architecture on estimates of tissue optical properties obtained from spatially resolved diffuse reflectometry, *Appl. Opt.*, Vol. 37, No. 10, 1998, pp. 1958–1972.
18. Gratton, E., et al., Measurements of scattering and absorption changes in muscle and brain, *Philos. Trans. R. Soc. Lond. B*, Vol. 352, No. 1354, 1997, pp. 727–735.
19. Jacques, S.L., Time resolved propagation of ultrashort laser pulses within turbid tissues, *Appl. Opt.*, Vol. 28, No. 12, 1989, pp. 2223–2229.
20. Delpy, D.T., et al., Estimation of optical pathlength through tissue from direct time of flight measurement, *Phys. Med. Biol.*, Vol. 33, No. 12, 1988, pp. 1433–1442.
21. Torricelli, A., et al., Mapping of calf muscle oxygenation and haemoglobin content during dynamic plantar flexion exercise by multi-channel time-resolved near infrared spectroscopy, *Phys. Med. Biol.*, Vol. 49, No. 5, 2004, pp. 685–699.
22. Contini, D., et al., A multi-channel time-resolved system for functional near infrared spectroscopy, *Opt. Express*, Vol. 14, No. 12, 2006, pp. 5418–5432.
23. Nissilä, I., et al. Comparison between a time-domain and a frequency-domain system for optical tomography, *J. Biomed. Opt.*, Vol. 11, No. 6, 2006, p. 064015.
24. Pifferi, A., et al., Performance assessment of photon migration instruments: the MEDPHOT protocol, *Appl. Opt.*, Vol. 44, No. 11, 2005, pp. 2104–2114.
25. Steinbrink, J., et al., Determining changes in NIR absorption using a layered model of the human head, *Phys. Med. Biol.*, Vol. 46, No. 3, 2001, pp. 879–896.
26. Matcher, J., et al., Absolute quantification methods in tissue near-infrared spectroscopy, in *Optical Tomography, Photon Migration, and Spectroscopy of Tissue and Model Media: Theory, Human Studies, and Instrumentation*, B. Chance and R.R. Alfano (eds.), *Proc. SPIE*, Vol. 2389, 1995, pp. 486–495.

27. Fantini, S., Franceschini, M.A., and Gratton, E., Semi-infinite-geometry boundary problem for light migration in highly scattering media: a frequency-domain study in the diffusion approximation, *J. Opt. Soc. Am. B*, Vol. 11, No. 10, 1994, pp. 2128–2138.
28. U.S. Department of Health and Human Services, *Compliance Guide for Laser Products*, HHS Publication FDA86-8260, FDA, Lanham, MD, 1985.
29. O'Connor, D.V., and Philip, D., *Time Correlated Single Photon Counting*, Academic Press, London, 1984.
30. Becker, W., *Advanced Time-Correlated Single-Photon Counting*, Springer-Verlag, Berlin, 2005.
31. D'Andrea, C., et al., Time-resolved optical imaging through turbid media using a fast data acquisition system based on a gated CCD camera, *J. Phys. D*, Vol. 36, No. 14, 2003, pp. 1675–1681.
32. Niedre, M.J., et al., Time-resolved imaging of optical coefficients through murine chest cavities, *J. Biomed. Opt*., Vol. 11, No.1, 2006, p. 064017.
33. Selb, J., et al., Improved sensitivity to cerebral hemodynamics during brain activation with a time-gated optical system: analytical model and experimental validation, *J. Biomed. Opt*., Vol. 10, No. 1, 2005, p. 11013.
34. http://www.lavision.de/products/cameras/ultrafast_gated_cameras.php.
35. Hoshi, Y., Functional near-infrared spectroscopy: current status and future prospects, *J. Biomed. Opt*., Vol. 12, No. 6, 2007, p. 062106.
36. Shibasaki, H., Human brain mapping: hemodynamic response and electrophysiology, *Clin. Neurophysiol*., Vol. 119, No. 4, 2008, pp. 731–743.
37. Huppert, T.J., et al., A temporal comparison of BOLD, ASL and NIRS hemodynamic responses to motor stimuli in adult humans, *Neuroimage*, Vol. 29, No. 2, 2006, pp. 368–382.
38. Spreen, O., and Strauss, E.A., *Compendium of Neuropsychological Tests*, Oxford University Press, New York, 1997.
39. Herrmann, M.J., Ehlis, A., and Fallgatter, A.J., Frontal activation during a verbal-fluency task as measured by near infrared spectroscopy, *Brain Res. Bull*., Vol. 61, No. 1, 2003, pp. 51–56.
40. Quaresima, V., et al., Bilateral prefrontal cortex oxygenation responses to a verbal fluency task: a multichannel time-resolved near-infrared topography study, *J. Biomed. Opt*., Vol. 10, No. 1, 2005, p. 011012.
41. Quaresima, V., et al., Non invasive measurement of cerebral hemoglobin oxygen saturation using two near infrared spectroscopy approaches, *J. Biomed. Opt*., Vol. 5, No. 2, 2000, pp. 201–205.
42. Sase, I., et al., Noncontact backscatter-mode near infrared time-resolved imaging system: preliminary study for functional brain mapping, *J. Biomed. Opt*., Vol. 11, No. 5, 2006, p. 054006.
43. Chance, B., et al., Comparison of time-resolved and -unresolved measurements of deoxyhaemoglobin in brain, *Proc. Natl. Acad. Sci. USA*, Vol. 85, No. 14, 1988, pp. 4971–4975.
44. Hoshi, Y., and Tamura, M., Detection of dynamic changes in cerebral oxygenation coupled to neuronal function during mental work in man, *Neurosci. Lett*., Vol. 150, No. 1, 1993, pp. 5–8.

45. Liebert, A., et al., Time-resolved multidistance near-infrared spectroscopy of the adult head: intracerebral and extracerebral absorption changes from moments of distribution of times of flight of photons, *Appl. Opt*., Vol. 43, No. 15, 2004, pp. 3037–3047.
46. Liebert, A., et al., Bed-side assessment of cerebral perfusion in stroke patients based on optical monitoring of a dye bolus by time-resolved diffuse reflectance, *Neuroimage*, Vol. 24, No. 2, 2005, pp. 426–435.
47. Wabnitz, H., et al., A time-domain NIR brain imager applied in functional simulation experiments, in *Photon Migration and Diffuse-Light Imaging II*, K. Licha and R. Cubeddu (eds.), *Proc. SPIE*, Vol. 5859, 2005, p. 58590H.
48. Kacprzak, M., Liebert, A., and Maniewski, R., A time-resolved NIR topography system for two hemispheres of the brain, JBO Non è che intendevi questo: Kacprzak, M., et al., Time-resolved optical imager for assessment of cerebral oxygenation, *J. Biomed. Opt*., Vol. 12, No. 3, 2007, p. 034019.
49. Hebden, J.C., et al., Imaging changes in blood volume and oxygenation in the newborn infant brain using three-dimensional optical tomography, *Phys. Med. Biol*., Vol. 49, No. 7, 2004, pp. 1117–1130.
50. Austin, T., et al., Three-dimensional optical imaging of blood volume and oxygenation in the preterm brain, *Neuroimage*, Vol. 31, No. 4, 2006, pp. 1426–1433.
51. Gibson, A.P., et al., Three-dimensional whole-head optical tomography of passive motor evoked responses in the neonate, *Neuroimage*, Vol. 30, No. 2, 2006, pp. 521–528.
52. Montcel, B., Chabrier, R., and Poulet, P., Detection of cortical activation with time-resolved diffuse optical methods, *Appl. Opt*., Vol. 44, No. 10, 2005, pp. 1942–1947.
53. Montcel, B., Chabrier, R., and Poulet, P., Time-resolved absorption and hemoglobin concentration difference maps: a method to retrieve depth-related information on cerebral hemodynamics, *Opt. Express*, Vol. 14, No. 25, 2006, pp. 12271–12287.
54. Ueda, Y., et al., Reflectance diffuse optical tomography: its application to human brain mapping, *Jpn. J. Appl. Phys*., Vol. 44, No. 38, 2005, pp. L1203–L1206.
55. Ijichi, S., et al., Quantification of cerebral hemoglobin as a function of oxygenation using near-infrared time-resolved spectroscopy in a piglet model of hypoxia, *J. Biomed. Opt*., Vol. 10, No. 2, 2005, p. 024026.
56. Ijichi, S., et al., Developmental changes of optical properties in neonates determined by near-infrared time-resolved spectroscopy, *Pediatr. Res*., Vol. 58, No. 3, 2005, pp. 568–573.
57. Sato, C., et al., Intraoperative monitoring of depth dependent hemoglobin concentration changes during carotid endartectomy by time-resolved spectroscopy, *Appl. Opt*., Vol. 46, No. 14, 2007, pp. 2785–2792.
58. Intes, X., Time-domain optical mammography softscan initial results, *Acad. Radiol*., Vol. 12, No. 8, 2005, pp. 934–947.
59. Leung, T.S., et al., A new method for the measurement of cerebral blood volume and total circulating blood volume using near infrared spatially resolved spectroscopy and indocyanine green: application and validation in neonates, *Pediatr. Res*., Vol. 55, No. 1, 2004, pp. 134–141.
60. Terborg, C., et al., Bedside assessment of cerebral perfusion reductions in patients with acute ischaemic stroke by near-infrared spectroscopy and indocyanine green, *J. Neurol. Neurosurg. Psychiatry*, Vol. 75, No. 1, 2004, pp. 38–42.

61. Liebert, A., et al., Non-invasive detection of fluorescence from exogenous chromophores in the adult human brain, *Neuroimage*, Vol. 31, No. 2, 2006, pp. 600–608.

62. Steinbrink, J., et al., Relevance of depth resolution for cerebral blood flow monitoring by near-infrared spectroscopic bolus tracking during cardiopulmonary bypass, *J. Thorac. Cardiovasc. Surg*., Vol. 132, No. 5, 2006, pp. 1172–1178.

63. Steinbrink, J., et al., Illuminating the BOLD signal: combined fMRI–fNIRS studies, *Magn. Reson. Imaging*, Vol. 24, No. 4, 2006, pp. 495–505.

64. Boas, D.A., et al., Can the cerebral metabolic rate of oxygen be estimated with near-infrared spectroscopy? *Phys. Med. Biol*., Vol. 48, No. 15, 2003, pp. 2405–2418.

65. Toronov, V., et al., The roles of changes in deoxyhemoglobin concentration and regional cerebral blood volume in the fMRI BOLD signal, *Neuroimage*, Vol. 19, No. 4, 2003, pp. 1521–1531.

66. Ntziachristos, V., Ma, X.H., and Chance, B., Time-correlated single photon counting imager for simultaneous magnetic resonance and near-infrared mammography, *Rev. Sci. Instrum*., Vol. 69, No. 12, 1998, pp. 4221–4233.

67. Ntziachristos, V., et al., Concurrent MRI and diffuse optical tomography of breast after indocyanine green enhancement, *Proc. Natl. Acad. Sci. USA*, Vol. 97, No. 6, 2000, pp. 2767–2772.

68. Torricelli, A., et al., Simultaneous acquisition of time-domain fNIRS and fMRI during motor activity, in *Novel Optical Instrumentation for Biomedical Applications III*, C.D. Depeursinge (ed.), *Proc. SPIE*, Vol. 6631, 2007, p. 66310A.

69. Brühl, R., et al., Concurrent time-resolved near-infrared spectroscopy and fMRI measurements of visually stimulated humans, *Proceedings of the 13th Scientific Meeting and Exhibition of the International Society for Magnetic Resonance in Medicine* (*ISMRM*), 2005, p. 499.

70. Mackert, B.M., et al., Dynamics of cortical neurovascular coupling analyzed by simultaneous dc-magnetoencephalography and time-resolved near-infrared spectroscopy, *Neuroimage*, Vol. 39, No. 3, 2008, pp. 979–986.

71. Omahe, E., et al., Cerebral hemodynamics evaluation by near infrared time-resolved spectroscopy: correlation with simultaneous positron emission tomography measurements, *Neuroimage*, Vol. 29, No. 3, 2006, pp. 697–705.

72. Torricelli, A., et al., Time-resolved reflectance at null source-detector separation: improving contrast and resolution in diffuse optical imaging, *Phys. Rev. Lett*., Vol. 95, No. 7, 2005, p. 078101.

73. Spinelli, L., et al., Absorption and scattering perturbations in homogeneous and layered diffusive media probed by time-resolved reflectance at null source–detector separation, *Phys. Rev. E*, Vol. 74, No. 2, 2006, p. 021919.

74. Pifferi, A., et al., Time-resolved diffuse reflectance using small source–detector separation and fast single-photon gating, *Phys. Rev. Lett*., Vol. 100, No. 13, 2008, p. 138101.

75. Rusu, M., et al., Slicing the supercontinuum radiation generated in photonic crystal fiber using an all-fiber chirped-pulse amplification system, *Opt. Express*, Vol. 13, No. 17, 2005, pp. 6390–6400.

76. Leon-Saval, S.G., et al., Multimode fiber devices with single-mode performance, *Opt. Lett*., Vol. 30, No. 10, 2005, pp. 2545–2547.
77. Zappa, F., et al., Complete single-photon counting and timing module in a microchip, *Opt. Lett*., Vol. 30, No. 11, 2005, pp. 1327–1329.
78. http://www.neuropt.eu.

# 11

# ADVANCES IN OPTICAL MAMMOGRAPHY

XAVIER INTES

*Rensselaer Polytechnic Institute, Troy, New York*

FRED S. AZAR

*Siemens Corporate Research, Inc., Princeton, New Jersey*

11.1 Introduction 308
11.2 Structure and physiology of the human female breast: an optical perspective 308
  11.2.1 Tissue composition of a healthy breast 308
  11.2.2 Light absorption in the human breast 309
  11.2.3 Light scattering in the human breast 310
11.3 Optical imaging breast technology 311
  11.3.1 Brief historical perspective 311
  11.3.2 Experimental techniques 312
  11.3.3 Modeling and reconstruction 316
11.4 In vivo optical properties of a healthy breast 318
  11.4.1 Optical and functional properties 318
  11.4.2 Correlations with demographics 320
  11.4.3 Menstrual cycle or menopausal status 320
11.5 Optical imaging in breast oncology 321
  11.5.1 Detection and characterization of suspicious lesions 322
  11.5.2 Monitoring of neoadjuvant chemotherapy response 324
11.6 Multimodality approaches 325
11.7 Summary 328
References 328

---

*Advances in Optical Imaging for Clinical Medicine*, Edited by Nicusor Iftimia, William R. Brugge, and Daniel X. Hammer
Copyright © 2011 John Wiley & Sons, Inc.

## 11.1 INTRODUCTION

Medical optical diagnostic techniques for oncology rely on capturing and quantifying perturbations in the reflected, transmitted, and/or emitted light created by a pathological state. In the case of optical mammography, diagnosis is based on the detection of local variations in the concentrations of endogenous absorbers and/or scatterers between normal and diseased breast tissue [1]. Thus, a refined understanding of the structural and functional properties of the human female breast that can influence optical diagnosis is required.

In the last several decades, significant effort has been put forth toward better understanding of the optical properties of the breast [2–4]. In this chapter we provide an overview of the relevant structural, physiological, and metabolic properties of the human female breast that affect the absorption and scattering tissue signatures that are the basis of optical mammography.

## 11.2 STRUCTURE AND PHYSIOLOGY OF THE HUMAN FEMALE BREAST: AN OPTICAL PERSPECTIVE

### 11.2.1 Tissue Composition of a Healthy Breast

An optical examination of the excised adult breast tissue with the naked eye demonstrates the structural and chemical complexity of this organ. For example, adipose tissue will appear as bright yellow, glandular tissue appears light pinkish tan, and fibrous stroma will appear white. Such well-defined color contrasts in the visible emphasize the variations in distribution of optically active chromophores within the breast. Such variations, which are often intermixed, are associated with the structure of the breast [2].

Beginning at the surface, the breast is covered with skin consisting of the superficial epidermis (containing keratins and melanin) and the underlying dense collagenous dermis with dermal blood and lymphatic vessels close to the surface [5]. Then a layer of adipose tissue encases the glandular tissue and its supporting fibrous stroma. In general, the breast is richly supplied with blood, but more vessels are found in the glandular breast than in the fibrous and adipose stroma.

The glandular breast is the most complex structure of the breast, and its physiological properties are dependent on numerous factors that are patient specific (age, hormonal status, weight, and other demographic factors). Such intra- and interpatient variations adversely affect the effectiveness of imaging modalities, restricting wide clinical use to specific demographics or a specific time window. In the case of optical mammography, a few physiological naturally occurring modulations may affect the diagnostic potential.

A human breast has many lobes (15 to 20), which are highly variable in size and shape, each with one central duct (for milk discharge), its peripheral branches, and their associated glandular tissues [6]. Lobes comprise lobular clusters and associated ducts, with breast lobules sized from 0.5 to 3–5 mm, depending on

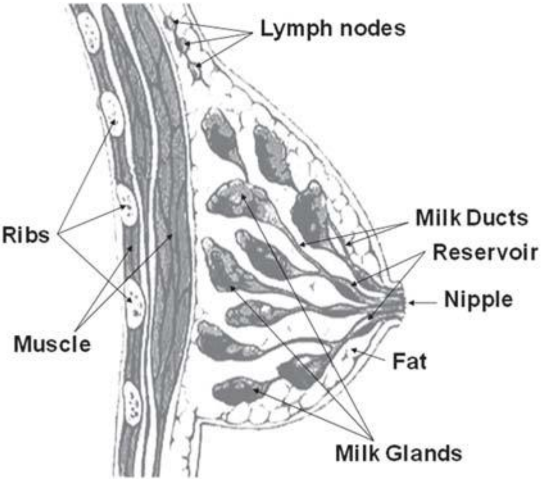

**FIGURE 11.1** Breast architecture.

their hormonal status (Figure 11.1). They are supported by the stroma, a dense fibrous collagenous scaffold that intermixes with adipose tissue. The ratio of stroma and adipose tissues intermixed is dependent on a patient's weight, age, heritage, and general habitus [7].

Such a ratio can be affected further by the menstrual cycle. Also, blood flow and the overall size of the breast change during the menstrual cycle, affecting optical readings. The blood flow can increase by 50% and breast parenchymal water by 25% at the time of ovulation [8,9], remaining high until menstruation, and some women can experience as much as a 20% breast enlargement by the end of their monthly cycle [10]. Conversely, at menopause, the lobular components atrophy from the average total volume of 25 to 35% at age 35 to less than 5% after age 60 [11]. In turn, relative adipose and stroma volumes increase, with a predominance of fat after age 60 years.

### 11.2.2 Light Absorption in the Human Breast

Functional parameters such as total blood volume (HbT) or relative blood saturation ($StO_2$) are derived from spectroscopic measurement of strong biological absorbers. In the intact living human breast, the most important naturally occurring chromophores are hemoglobin, lipids, melanin, water, carotene, other proteins, and DNA [12]. However, within the preferred therapeutic spectral window [the near infrared (NIR), $\lambda \in 600$ to 1000 nm], the main contributors to absorption are reduced to water, hemoglobin, lipids, and melanin [13,14] (see Figure 11.2).

Apart from hemoglobin, which contributes significantly to the optical absorption of vascularized tissues up to approximately $\lambda = 1000$ nm, water and other

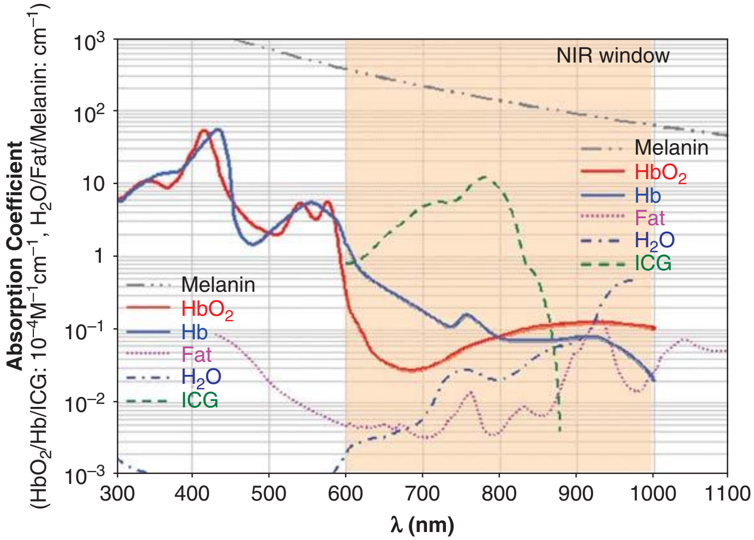

**FIGURE 11.2** Absorption coefficient spectra for the main tissue absorbers.

proteins are the principal tissue chromophores in the infrared (IR) spectral region. Water is the most important tissue chromophore in the infrared and begins to contribute significantly to tissue absorption at $\lambda > 1000$ nm. The optical absorption of water in the near infrared is initially quite weak, but rises quite rapidly with wavelength. From the visible spectral region, the absorption of water increases by nearly six orders of magnitude, restricting noninvasive imaging of the full breast to wavelengths below $\lambda < 1000$ nm. Similarly, lipids (fat) exhibit an initial weak absorption, rising to a maximum peak at $\lambda \sim 930$ nm, contributing significantly to the overall absorption to be monitored spectroscopically [15].

In addition to hemoglobin, many proteins contribute strongly to absorption in the ultraviolet (UV) range but, only melanin exhibits strong absorption in the NIR spectral window. Melanin is confined in epidermal cells located at the junction of the epidermis and dermis. In optical mammography, due to the limited contribution of the skin layer on the overall optical pathlength experienced by the photons detected (generally, >10 cm), melanin is considered only for safety reasons and is not taken into account in spectroscopic data analysis. Melanin will affect the maximum permissible exposure, such as that defined by laser safety standards [16], without hampering the diagnostic potential of optical mammography.

### 11.2.3 Light Scattering in the Human Breast

As in all biological tissues, light scattering in tissue at a macroscopic level is a complex association of light redirection at the microscopic level, due to variations in the cellular and extracellular index of refraction, but also to the architectural assembly at the tissue level [1]. Membrane-bound subcellular organelles [17] such as nuclei (6 to 8 $\mu$m in noncancerous breast epithelial cells), mitochondria (less than 1 $\mu$m), secretory vacuaoles (1 to 10 $\mu$m), and other, similar-sized intracytoplasmic granules are the major contributors to scattering in breast tissue, as demonstrated by experimental evidence [18–20]. It is expected that the extracellular stromal matrix also contributes to light scattering, due to the presence of organized fibrous collagenous tissue [3].

Due to the nature of light transport in deep tissue (multiple scattering), it is difficult to elucidate precisely the nature of scattering signal in vivo. Thus, an empirical approach to Mie theory is generally preferred to relate light scattering and breast tissue architecture. Scattering data for tissue experimentally acquired over significant wavelength ranges indicate that the reduced scattering coefficient (see Section 11.3.2) is well characterized by the scaling law $\mu_s' \sim A\lambda^{-b}$, where $A$ and $b$ are model parameters for scattering amplitude and scattering power ($b \approx 0.5$ to 2 [21,22]) and $\lambda$ is the light wavelength.

## 11.3 OPTICAL IMAGING BREAST TECHNOLOGY

### 11.3.1 Brief Historical Perspective

The use of light for detection and characterization of breast masses can be tracked to the early nineteenth century [23], following a surge of interest in the use of light as a clinical diagnostic tool [24,25]. The technique, known as *diaphanography*, used white light produced by an electrical lamp shining through the breast to detect breast pathology. The clinical examination was performed in a darkened room, and lesions appeared as dark spots in the breast. Even if the concept fell rapidly into disuse due to patient discomfort associated with skin overheating and low sensitivity specificity, due to scattering blurring, this concept presaged much of current work. A contemporary example of diaphanographic readings is provided in Figure 11.3.

Along parallel lines, the field of near-infrared spectroscopy emerged as an robust functional monitoring tool. Millikan applied photoelectric methods to the kinetics of the reaction of oxygen and myoglobin [26], superseding the hemoglobin studies of Hartridge and Roughton [27]. The 1935 ear oxymeter of Karl Matthes, the father of oximetry, was the first clinical quantitative application of optics to tissues [28]. Applications such as Millikan's aviation ear oxymeter during World War II with lightweight and practical instrumentation followed shortly, establishing optical spectrophotometry as an invaluable functional monitoring tool [29].

NIR spectroscopy application to mammography was revived in the 1970s thanks to the introduction of new sources and detectors developed for optical communication. Following the work of Gros et al. [30], many technical improvements were achieved in the 1970s with the realization that optical contrast was spectrally dependent [31]. It led to the development of multispectral systems [32]

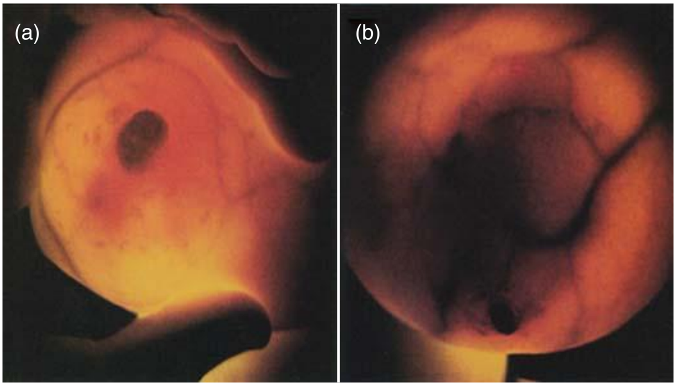

**FIGURE 11.3** Diaphanographic images. (a) 40-year-old woman with a palpable mass immediately caudal to the nipple. Mammography was normal. The image shows the palpable mass consisting of a clearly delimited fibroadenoma appearing just under the nipple. (b) 56-year-old woman with a palpable 5 × 5 cm mass. The image shows a brownish black mass typical of carcinoma. There is considerable hypervascularity, which is a common early sign of malignancy. (From [143], with permission.)

that are strikingly akin to current systems. Also, the multiplication of preliminary clinical trials with relatively appealing results sparked the interest of the industry. Spectrascan Inc. (South Windsor, Connecticut) developed a commercial dual-wavelength diaphanography system based on Carlsen's design [32]. However, due to an undesirable number of false positive and marginal contributions over mammography [33,34], digital spectroscopy clinical use was not pursued. As a consequence of the emergence of commercial products, the U.S. Food and Drug administration classified breast illuminators as class III devices in 1994, following the Obstretics and Gynecological Devices Panel recommendation [35]. Thus, premarket approval is required prior to commercial distribution of optical mammography devices. Since 1994, many concurrent advances in instrumentation and light transport modeling have rejuvenated the field of optical mammography [36].

### 11.3.2 Experimental Techniques

Three major experimental techniques exist in the NIR diffuse optical imaging field. These three techniques are categorized by the time dependence of the source intensity impinging on the tissues and are referred to as continuous-wave (CW), frequency-domain (FD), and time-domain (TD) photon migration. In this section we review these alternative technological approaches applied to optical mammography and discuss their relative merits and disadvantages. We restrict the discussion to systems that have been employed in published clinical trials.

***Continuous-Wave Systems*** Continuous-wave techniques were historically the first techniques used for optical mammography [23,30]. CW systems encompass systems based on a source that emits at a constant intensity, but also systems whose sources are modulated at low frequency (ca. kilohertz) to benefit from phase-locked detection techniques. CW techniques are attractive techniques, due to the availability of high-powered, spectrally narrow sources over a broad range of NIR wavelengths at low cost. Very sensitive affordable detectors with high quantum yield (the number of electron pairs generated per photon absorbed) are also available in this spectral range. The two main detectors commonly employed are avalanche photodiodes (APDs) and photomultipliers (PMTs) [37]. PMTs are the most sensitive detectors, with the drawback of reduced dynamic range and higher cost than those of APDs.

To probe the various tissues of the breast, two strategies are employed. Either the optodes (referring to either source or detector) are integrated in a handheld probe that will be scanned manually over the breast (or contralateral breast) [38,39], or numerous static source detectors are positioned in transmittance planar [40] or circular configuration [41,42]. Generally, the detectors collect data in parallel with the current systems, taking advantage of new developments in CCD (charge-coupled device) technology when dense data sets are required, whereas the sources are shining sequentially on different breast locations either by optical fiber coupling and switching or by galvomirror raster scanning.

Optical mammography requires probing deep tissues; thus, source–detector separation spans from several centimeters to a dozen centimeters, depending on the configuration selected. This contrasts with brain or muscle optical imaging [36], in which shallower tissues are sampled. Due to the strong attenuation of the signal over such propagation distances, the spectral information is acquired sequentially by time-multiplexing the wavelengths, as a hyperspectral source power is limited by ANSI standards and offers a limited signal/noise ratio. Thus, acquisition time can be rather lengthy, and fast hemodynamic monitoring is not feasible.

A few CW mammographers have been developed in the past several decades. In the late 1990s, Philips Research Laboratories in the Netherlands described a three-wavelength (679, 779, and 867 nm) clinical prototype for optical computed tomography based on 255 source–detector pairs [43]. The patient lies prone on a scanning table with one breast at a time immersed in a 13-cm-diameter conical chamber filled with a tissuelike scattering liquid. The data acquisition time is 9 minutes. Similarly, the Grable group developed a computed tomography laser breast imager using a stationary collimated circular array of 600 avalanche photodiodes and a laser fan beam produced by a rotating polygon mirror and an argon-pumped mode-locked Ti:sapphire laser (Coherent Laser, Mountain View, California). This design led to the development of a commercial system by Imaging Diagnostic Systems, Inc. [44], a design that did not require the use of a matching liquid. Recently, a more sophisticated system was developed by Schmitz et al. that made possible fast acquisition data for intrinsic dynamic optical imaging of the breast [45]. A commercial system with 32 sources and up to 64 detectors based on this design and able to image both breasts simultaneously has been proposed by NIRx Medical Technologies in the United States.

However, CW techniques suffer from intrinsic disadvantages that limit their use for optical mammography. First, monochromatic CW techniques are unable to distinguish between the effects of absorption and scattering [46]. Only recently has it been demonstrated that by using multiple wavelengths, absorption and scattering contributions could be unmixed [47], although in practical cases, such an approach requires accurate estimation of background optical properties, which is not attainable with a CW data set alone but is circumvented by implementing a few time-dependent channels [40].

Second, intensity data are extremely sensitive to the surface tissues compared to tissues in deeper regions. As a consequence, CW techniques are highly dependent on tissue–probe coupling. If such a drawback can be attenuated in the case of static systems with numerous optodes measurements [48,49], it renders optical examination based on a handheld probe highly operator dependent and sensitive to hemodynamic changes in the dermal capillaries.

***Frequency-Domain Systems*** To alleviate some of the drawbacks associated with CW techniques, the development of systems using a time-dependent source amplitude has been a key effort in optical mammography. Technically, two distinct approaches using time-dependent sources are feasible: frequency domain (FD) and time domain (TD). Frequency-domain techniques are based on a source whose amplitude is modulated in the megahertz range (up to 1 GHz), with detection performed at the same frequency. Such a technique provides a set of two measurements: modulation amplitude attenuation and phase shift due to light propagation [50]. In turn, these data make it possible to effectively separate the contributions of absorption and scattering [51,52].

Typically, sources and detectors will be required that allow us to work in the radio-frequency range. Thanks to technical developments associated with optical telecommunication, many sources and detectors are available in the NIR range, although with less spectral density than in CW techniques. Detection is performed in either heterodyne or homodyne mode, although heterodyning is generally preferred [53].

Development of FD optical mammographers is strongly influenced by the efforts of Carl Zeiss [54,55] and Siemens Medical Engineering [56] in the mid-1990s. The prototypes assembled by these two companies employed the same examination configuration. The breast was gently compressed between two clear windows and a multiwavelength source–detector pair, in transmittance configuration, was raster scanned over the compressed breast area. However, due to the lack of tomographic approach, both systems were deemed inadequate for breast screening. Subsequent work implementing reconstruction methods provided significant improvements [57,58], but no follow-up studies have been reported.

In academia, FD systems based on two different strategies have been developed. A handheld system developed at the University of California Irvine's Beckman Laser Institute combines seven diode lasers (672, 800, 806, 852, 896, 913, and 978 nm) amplitude-modulated at 251 modulation frequencies from 100 to 700 MHz, combined with a steady-state hyperspectral channel working in the spectral range 650 to 1000 nm with a resolution of 5 nm [59]. The probe is being moved in 1-cm increments over the area of interest on the breast to capture diseased and normal tissue signatures, with similar acquisition on the contralateral breast for comparison. The technique is sensitive to tissue–optode coupling, and light pressure should be applied to ensure contact. Also, due to limited source–detector separation in the reflectance mode, the system is maximally sensitive to the outer few centimeters of tissue under the probe, with poor sensitivity to deep tissues [60].

A tomographic system based on six laser diodes operating at wavelengths from 660 to 836 nm modulated at 100 MHz has been developed at Dartmouth College [61]. Light delivery and collection take place via fiber bundles that are rigidly coupled to a two-dimensional circular ring which rotates such that one of the 16 fiber bundles in the measured plane is aligned with the light source coupler, while the other 15 fiber bundles are each connected to a photomultiplier tube (PMT) detector. The fibers are in direct contact with the pendulant breast, and light pressure is applied to ensure proper contact. The system does not require a matching liquid. Acquisition is performed in the same plane, but multiple planes can be investigated for three-dimensional imaging.

FD instrumentation is also used to supplement CW techniques. A hybrid CW/frequency domain device for optical tomography has been developed at the University of Pennsylvania [62]. The system combines four amplitude-modulated laser diodes (690, 750, 786, and 830 nm) which are switched rapidly between 45 optical fibers on a 9 × 5 array and detected in reflectance, whereas transmitted light is detected by a CW CCD camera. The information obtained by the FD channels supplements the spatially dense CW information, for enhanced functional tomography [63].

***Time-Domain Systems*** The first implementations of time-resolved techniques for optical mammography were motivated by the notion that minimally scattered photons (ballistic photons) enabled the rendering of images similarly to x-ray computed tomography (CT) with relatively good resolution [1,64]. However, such photons can be detected reliably only for samples a few millimeter thick, and the idea was abandoned for noninvasive breast imaging applications.

Time-domain techniques are based on a source that produces a short pulse of light (typically, less than 200 ps) and detectors that record the time of flight of photons exiting the sampled volume with a temporal resolution in tenths of picoseconds or less. The temporal distribution of photons detected after propagation is known as the *temporal point-spread function* (TPSF). Such a data set is the richest in terms of information content and provides an unmatched set of data on amplitude, mean time of flight, variance, skew, and Laplace transform [65]. Such data types provide enhanced separation between absorption and scattering contributions over the frequency domain. However, such benefits come at the cost of more expensive instrumentation and greater difficulty in implementing clinical prototypes. Also, TD optical mammography is a photon-starved technique that requires a relatively long integration time (a few seconds, compared to subseconds for CW and FD systems) to obtain TPSF with good statistical distributions.

Current time-domain optical mammography systems are based on time-correlated single-photon counting (TCSPC) hardware, single-photon counting PMTs, and pulsed laser diodes. Significant technological advances have been made in these three areas in the past decade, leading to widespread acceptance of time-resolved techniques in various biophotonics fields. Incidentally, with the increased demand, subcomponents are becoming more affordable, making multispectral, multidetector systems the norm.

Due to the slow nature and extreme sensitivity of time-domain optical detectors, time-resolved optical mammography has been implemented in transillumination or tomographic geometry. The transillumination configuration was first investigated by Hebden et al. [66] to produce two-dimensional optical maps. Subsequently, European groups have championed this configuration. Prototypes similar to the Carl Zeiss and Siemens medical engineering systems, based on soft compression of the breast between two planar plates and raster scanning of multiwavelength source–detector pairs in transmittance geometry, have been developed by the Physikalisch-Technische Bundesanstalt group in Berlin [67] and the Politécnico di Milano groups [68]. Both systems have implemented off-axis detection channels to provide the depth information necessary for tomographic imaging. Advanced Research Technologies (ART), Inc. of Montreal, Canada, developed Softscan, a commercial system based on the same technology and principles. The main differences between this commercial system and the academic system is that in the ART system, the examination is performed in the prone position with the breast gently compressed in a chamber filled with a matching liquid, and in the academic system, the patient is in a supine position similar to that employed in mammographic systems. ART's system employs four pulsed laser diodes, a coaxial detection channel, and four off-axis channels.

Tomographic systems that do not employ mechanical scans of optodes but, rather, sequential point excitation of tissue based on source fiber multiplexing and parallel detection with fiber bundles have been developed at the University College of London (UCL) and the University of Pennsylvania. The UCL system is a two-wavelength (780 and 815 nm), 32-detection/excitation channel system [69], whereas the UPenn system is a six-wavelength (690, 750, 780, 800, 830 and 840 nm) system spatially multiplexed to 64 fiber positions and 16 detection channels acquiring the signal in parallel [70], designed for concurrent MRI examination. These systems acquire data from multiple projections, allowing accurate tomographic reconstructions.

### 11.3.3 Modeling and Reconstruction

The main factor adversely affecting optical mammography in early evaluation was contrast blurring due to the scattering-dominant light propagation regime [31,71]. It was recognized that optical signals are depth and sample-type dependent, necessitating rigorous models to achieve absolute quantification. Current successes of the technique are largely tied to the development of more realistic and efficient models of light transport in tissue and on solving the ill-posed inverse problem in a rigorous way. In this section we provide a brief overview of the two approaches employed in optical mammography: near-infrared spectroscopy (NIRS) and diffuse optical tomography (DOT). However, it is beyond our scope here to provide an extensive review of these different theoretical approaches. Especially, DOT is based on sophisticated mathematical inverse problem formulations. We refer readers interested in a more in-depth review of the various approaches employed in diffuse optical tomography to the literature [72–74].

The complexity of light–tissue interaction at a microscopic scale prevents the use of a classical light propagation model such as the Maxwell equation [75] or the spectroscopic Beer–Lambert law [76]. A breakthrough was achieved when models developed for other physics fields, such as neutron transport or heat transport, could be adapted to light propagation in diffuse media [77–79]. With such models it is possible to relate the NIR measurements to the macrooptical properties of the tissue: absorption, scattering, and mean cosine of the scattering phase function (angular distribution of the scattered photon) describing the anisotropic character of the light diffusion [80]. Moreover, in the case of predominant scattering, the diffusion equation, which is an approximation of the radiative transport equation, is preferred, due to its simpler mathematical expression. The problem is then rescaled as an isotropic scattering problem depending on two parameters: the absorption and reduced scattering coefficients. The reduced scattering coefficient is a lumped property incorporating the scattering coefficient and the scattering anisotropy property of the tissue to rescale scattering as an isotropic phenomenon.

NIRS was the first approach used to establish the potential of diffuse optical techniques [81]. NIRS estimates the optical properties of tissue probed by one source–detector pair. NIRS is based on the assumption that homogeneous tissue is being investigated. It retrieves the average optical properties of the volume probed by the light. Due to the scattering events, the photons probe a large volume. Thus, NIRS suffers from the partial volume effect (low sensitivity to focal changes in the optical parameters) when no spatial a priori information is available [82]. Moreover, due to the limited redundant information collected, NIRS is extremely sensitive to the quality of the optode–tissue coupling [83]. However, this approach is well suited for fast estimation of the functional state of biological tissue in the case of differential measurements and is mathematically straightforward.

DOT is a more ambitious approach that relies on a data set collected with an increased number of source–detector pairs [84]. DOT employs measurements recorded from tissue using multiple optical source–detector pairs and retrieves (reconstructs) the targeted chromophore distribution by synthesizing the measurements through solution of an inverse problem [85]. DOT first constructs the forward problem, which predicts the photon propagation for a known medium, and then inverts it. DOT falls in the class of nonlinear ill-posed inverse scattering problems, which present many challenges. However, DOT has enjoyed steady growth in the past decade, as it provides a quantified estimate of the local concentration of absorption, scattering, blood volume, oxygenation, and/or contrast agent uptake noninvasively. It is still a very active research area, with constant progress toward more accurate, more robust, and faster algorithms.

## 11.4 IN VIVO OPTICAL PROPERTIES OF A HEALTHY BREAST

The first reports on optical properties of human breast tissue were based on the in vitro examination of breast tissue using integrating spheres [86–88]. However, the surgical and pathological dissections of the breast resulted in blood drainage and blood denaturation from the cut surfaces, thus greatly diminishing the contributions of hemoglobin to the optical signal [89]. A summary of the early estimation of optical properties of the human female breast is provided in Table 11.1. Since then, thanks to recent advances in our understanding of light transport and optical diagnostic techniques and devices, estimation of in vivo optical properties of the intact healthy breast has been feasible.

### 11.4.1 Optical and Functional Properties

Numerous studies have reported on the bulk absorption and scattering optical properties of the human breast. These studies were conducted with either frequency- [90–92], or time-domain [93–100] instruments (or hyperspectral continuous-wave data assisted by a time-dependent data set) to separate the absorption and scattering contributions. Overall, the average optical properties reported demonstrate surprising consistency given the heterogeneity in the instrumentation (even within the same study due to the prototype nature of the instrumentation), the various collection configurations, the data-processing techniques employed, and the lack of instrumentation calibration standards. A summary of the average background optical properties extracted from the literature is presented in Table 11.2.

However, the appeal of diffuse optical techniques resides in their sensitivity to the functional state of tissue. Thus, the main focus of current studies is not

**TABLE 11.1 In Vitro Optical Properties of Human Female Breast**

| Optical Property | λ (nm) | Glandular Breast | Adipose Stroma | Fibroadenoma | Fibrocystic Disease | Ductal Carcinoma |
|---|---|---|---|---|---|---|
| Absorption coefficient ($\text{cm}^{-1}$) | 540 | 3.6 ± 2 | 2.3 ± 0.6 | 4.4 ± 3 | 1.6 ± 0.7 | 3.1 ± 1 |
| | 700 | 0.5 ± 0.1 | 0.7 ± 0.1 | 0.7 ± 0.5 | 0.2 ± 0.1 | 0.5 ± 0.1 |
| | 900 | 0.6 ± 0.1 | 0.8 ± 0.1 | 0.7 ± 0.5 | 0.3 ± 0.1 | 0.5 ± 0.2 |
| Scattering coefficient ($\text{cm}^{-1}$) | 540 | 24 ± 6 | 10 ± 2 | 11 ± 3 | 22 ± 3 | 19 ± 5 |
| | 700 | 14 ± 3 | 9 ± 1 | 7 ± 2 | 13 ± 2 | 12 ± 3 |
| | 900 | 10 ± 2 | 8 ± 1 | 5 ± 1 | 10 ± 2 | 9 ± 3 |

*Source:* Data from [2].

**TABLE 11.2 Average Background Optical Properties**

| | 600–700 nm | 700–800 nm | 800–900 nm |
|---|---|---|---|
| Absorption coefficient ($cm^{-1}$) | $0.04 \pm 0.02$ | $0.04 \pm 0.02$ | $0.05 \pm 0.03$ |
| Scattering coefficient ($cm^{-1}$) | $10 \pm 5$ | $8 \pm 4$ | $8 \pm 4$ |

*Source:* Data from [101].

accurate estimation of the optical properties but, rather, accurate estimation of their functional and structural correlates: Hb, $HbO_2$, $H_2O$, and Li (lipids). These parameters also provide a comprehensive avenue to assess the sensitivity of optical techniques to the functional and structural state of the human female breast, as its physiology and structure are relatively well known. A summary of the two main functional parameters, hemoglobin concentration and relative oxygen saturation, is provided in Table 11.3 (restricted to healthy volunteer data). Similar to the optical properties results, the optically derived functional parameters of the human female breast demonstrate excellent consistency and fall within the physiological range expected.

Even though their spectroscopic signatures can be elusive or their estimation based on empirical relationship established from the scattering power law

**TABLE 11.3 Summary of Hemoglobin Concentration and Oxygen Saturation**

| | Healthy | | Healthy Premenopausal | | Healthy Postmenopausal | |
|---|---|---|---|---|---|---|
| Study | HbT (μM/L) | $StO_2$ (%) | HbT (μM/L) | $StO_2$ (%) | HbT (μM/L) | $StO_2$ (%) |
| Pogue et al. [103] | $32 \pm 5$ | | | | | |
| Srinivasan et al. [104] | 20 | 65 | | | | |
| Grosenick et al. [105] | $17 \pm 8$ | $74 \pm 3$ | | | | |
| Spinelli et al. [106] | $16 \pm 4$ | $74 \pm 9$ | | | | |
| Taroni et al. [107] | $20 \pm 7$ | $71 \pm 8$ | | | | |
| Chance et al. [108] | — | 70 | | | | |
| Grosenick et al. [109] | $17 \pm 6$ | $74 \pm 7$ | | | | |
| Durduran et al. [110] | $34 \pm 9$ | $68 \pm 8$ | | | | |
| Spinelli et al. [111] | $16 \pm 5$ | $66 \pm 9$ | | | | |
| Pogue et al. [112] | $22 \pm 7$ | $61 \pm 1$ | | | | |
| Pifferi et al. [113] | 16 | | | | | |
| Srinivasan et al. [114] | $22 \pm 8$ | $58 \pm 9$ | | | | |
| Cerussi et al. [115] | — | — | $40 \pm 3$ | $73 \pm 6$ | $14 \pm 1$ | $83 \pm 1$ |
| Shah et al. [116] | — | — | — | $74 \pm 6$ | — | $75 \pm 8$ |
| Cerussi et al. [117] | — | — | 27 | 77 | 14 | 82 |
| Poplack et al. [118] | $24 \pm 12$ | $69 \pm 9$ | | | | |
| Global average | $21 \pm 6$ | $68 \pm 5$ | $34 \pm 9$ | $75 \pm 2$ | $14 \pm 0$ | $80 \pm 4$ |

*Source:* Adapted from [101].

[102], $H_2O$ and Li concentrations reported fall within expected values. For example, Intes [95] reported an average breast composition, defined as the sum of the estimated lipid and water concentrations, of $\overline{[H_2O] + [Li]} = 89.60 \pm 15.9\%$ ($n = 49$). This value is close to 100%, as expected, because water and lipids are the main constituents of the breast [12].

The average optically derived functional parameters may be consistent across studies and with the known physiology of the breast, but it must be noted that important intra- and interpatient variations have been observed. First, even though optical techniques probe rather large volumes, due to the diffusing nature of light propagation, different optodes positioning on the same patient during the same imaging session could lead to different functional values due to different partial volume sampling. This effect is more prominent in reflectance geometry, due to the particular nature of the breast structure (adipose encasing glandular tissues).

Second, as stated in Section 11.2, the demographic and hormonal status of the patient can greatly influence the physiological and structural state of the breast. If these variations can create unique challenges in term of engineering design and affect adversely optical mammography sensitivity and specificity, they also provide a unique means of establishing a level of confidence in the sensitivity of optical techniques. Thus, many studies have reported the correlation of optical readings with demographic factors, hormonal status, and radiographic breast density.

### 11.4.2 Correlations with Demographics

The two main demographic factors investigated are age and body mass index (BMI; $kg/m^2$). Both factors are expected to correlate with the optical readings, as they are indirect indicators of the glandular/adipose breast composition ratio and thus reflect the overall hormonal status of the patient. An example of a graphical representation of the correlations between functional/structural parameters and demographic factors is provided in Figure 11.4.

In current studies, BMI is the demographic factor exhibiting the most consistent correlation with optical parameters. The optical parameters that correlate with BMI are the lipid density and total hemoglobin concentration [92,93,95,114,117,118]. As expected, the higher the BMI value, the greater the lipid density, and conversely, the lower the total hemoglobin concentration. On the other hand, age does not provide such a strong consensus. From all the studies referenced above, only four described a correlation between age and blood volume [90,93,102,113]. The most significant correlation was noted by Spinelli et al. [93], Cerussi et al. [102] and Shah et al. [90], who reported an increase in blood volume with advancing age in premenopausal women and a decreasing blood volume in postmenopausal patients (>50 years of age).

### 11.4.3 Menstrual Cycle or Menopausal Status

Studies that directly investigate the effect of the menstrual cycle or menopausal status are less numerous. Shah et al. [90] and Pogue et al. [91] investigated the

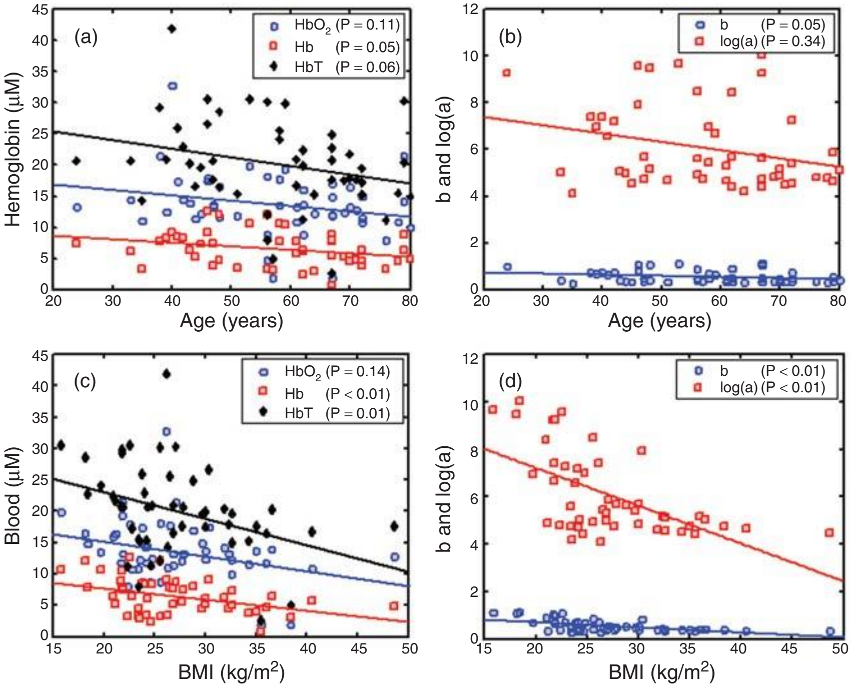

**FIGURE 11.4** Example of correlation between optical parameters quantified in vivo correlation and demographic factors: (a) age vs. $HbO_2$, Hb, and HbT; (b) age vs. *b* and log(*a*); (c) BMI vs. $HbO_2$, Hb, and HbT; (d) BMI vs. *b* and log(*a*). (From [95].)

effect of the menstrual cycle on optical readings and reported an increase in blood volume during the luteal phase, as expected. Concerning the menopausal status, Shah et al. [116] and Cerussi et al. [115,117] reported that the breasts of premenopausal patients exhibited higher blood volumes than those from postmenopausal women. Global average blood volume and relative saturation values from these studies are provided in Table 11.3.

## 11.5 OPTICAL IMAGING IN BREAST ONCOLOGY

The success of optical mammography rests on the specific functional, molecular, and structural signatures associated with alterations due to the diseased cells but also to alterations in the function and structure of the host tissue [2]. These local perturbations in the biodistribution of endogeneous absorbers and/or scatterers are expected to differ in nature and/or magnitude between pathologies, positioning optical mammography as a potential imaging tool for detection, diagnosis and clinical management of breast cancer [119]. These contrasts are generated by the progression of the disease, which induces an increase in tumor cell density, nuclear volume fraction, tumor vasculature, and increased metabolic activity [120].

### 11.5.1 Detection and Characterization of Suspicious Lesions

Even though numerous studies assessing the potential of optical mammography as a clinical tool have been reported, very few report a quantified evaluation of optical mammography potential to detect suspicious lesions [121–125]. These studies, all part of the OPTIMAMM program, are based on time-domain systems. They used a six-number grading scale called Visibility Grading Criteria (VGS) that classifies the detectability of a lesion based on its contrast versus the "normal" part of the examined breast. This subjective criterion is described in Table 11.4.

In a review of the Berlin time-domain optical mammography group results, Rinnerberg et al. [126] report the VSG scores from examinations carried out from 1999 to 2004 at the Robert-Rossle-Hospital, which provided 154 successful optical examinations. Among the 102 tumors validated by ulterior biopsy, 92 tumors (90.2%) were detected retrospectively in optical mammograms, based on a visibility score $\geq 2$, 72 tumors (70.6%) were identified in both craniocaudal and mediolateral optical projections, 20 tumors were identified in only one projection (19.6%), and 10 tumors were not detected. Moreover, 44 benign lesions were confirmed by histopatholgy (7 fibroadenomas, 34 mastopathy, and 3 cysts), leading to 90% of the detection rate for mastopathies, 70% for fibroadenomas, and 100% for cysts.

Similarly, Yates et al. [98], using a tomographic approach to image the breasts of three healthy subjects and 19 patients bearing breast lesions, reported excellent

**TABLE 11.4 Visibility Scores and Number of Associated Optical Mammograms of Tumor-Bearing Breasts**

| Score | Description | Projection Mammograms |
|---|---|---|
| 0 | Not visible | 25 |
| 1 | Hardly perceivable change in transmittance, indicating presence of an inhomogeneity | 14 |
| 2 | Weak contrast, tumor detectable only if the exact location of inhomogeneity is known | 27 |
| 3 | Contrast of tumor clearly distinguishable, yet inferior to that of other inhomogeneities | 21 |
| 4 | Contrast of tumor similar to that of other inhomogeneities | 33 |
| 5 | Contrast of tumor dominates mammogram | 83 |
| | | 203 |

*Source:* Data from [126].

**TABLE 11.5 Average Functional Parameters of Lesions**

| | Healthy | Fibroadenoma | Malignant |
|---|---|---|---|
| HbT ($\mu$M/L) | $21 \pm 6$ | $54 \pm 13$ | $65 \pm 34$ |
| $StO_2$ (%) | $68 \pm 5$ | $69 \pm 3$ | $66 \pm 5$ |

*Source:* Compiled from [101].

visibility scores for cysts (average of 5), in contrast to cases of suspected malignancy (average of 2.5), leading to a lesion detectability score of nearly 90%. Taroni et al. [125] reported simila r results from a study comprising 169 benign lesions and 56 malignant lesions (194 patients), with a detection rate of 83% for cancers, 37% for fibroadenomas, and 79% for cysts.

These studies identified parameters that adversely influence the detectability of lesions, especially cancers, with lesion size being the most important parameter and proximity to axilla and chest wall being the second parameter. Also, VSG scores are dependent on the probing wavelength. Rinnerberg et al. [126] based their visibility score on the highest contrast seen between 670, 785, or 834 nm. As the detection rate is based primarily on local blood volume contrasts (angiogenesis), Taroni et al. [127] investigated the benefits of employing shorter wavelengths and found that the optical contrast proved to increase upon decreasing wavelengths for the detection of cancers (637, 656, 683, and 785 nm).

In contrast to addressing the issue of detectability, numerous studies have focused on quantifying the differences between functional and structural parameters of lesions versus the background properties. Compiling findings from contemporary research, Leff et al. [101] reported that breast lesions contain at least twice the blood volume concentration of healthy background tissue, whereas no consensus was emerging from relative oxygen saturation contrasts (see Table 11.5).

Only a few studies reported a contrast in $StO_2$ (which is associated with hypermetabolism) between background tissue and breast lesions. Srinivasan et al. [114] and Grosenick et al. [96] demonstrated reduced $StO_2$ in tumors compared to background tissues. However, in subsequent studies, Grosenick et al. [97] did not report significant contrast in $StO_2$ between lesions and healthy background. Conversely, blood volume emerges as a reliable functional contrast parameter [95,96,103–105].

Recently, several articles have demonstrated the potential of optical mammography to distinguish between benign and malignant pathologies [19,27]. Srinivisan et al. [104] reported increased contrast in blood volume between background and lesion for malignant cases compared to benign cases, with good correlation between blood volume and estimated microvessel density. Malignant cases also exhibited a reduction in $StO_2$, in contrast to benign cases. Similarly, Intes et al. [95] reported significant contrast increase in blood volume ($p = 0.0184$), water content, and lower $StO_2$ in malignant cases compared to benign cases.

**TABLE 11.6 Statistical Comparison of the Softscan Platform in Discriminating Between Malignant and Benign Lesions**[a]

| Optical Index | AUC (Az) | Standard Error | $p$-Value | Asymptotic 95% Confidence Interval Lower Bound | Asymptotic 95% Confidence Interval Upper Bound | Sensitivity (%) | Specificity (%) |
|---|---|---|---|---|---|---|---|
| $HbO_2$ | 0.881 | 0.063 | $6 \times 10^{-6}$ | 0.758 | 1.004 | 88.20 | 88 |
| $StO_2$ | 0.786 | 0.074 | $1.6 \times 10^{-3}$ | 0.64 | 0.932 | 64.70 | 88 |
| $H_2O$ | 0.818 | 0.066 | $6 \times 10^{-6}$ | 0.759 | 0.998 | 88.20 | 88 |
| $\mu_s'$(830 nm) | 0.672 | 0.085 | $6.1 \times 10^{-2}$ | 0.505 | 0.838 | 88.20 | 48 |

*Source:* Data from [128].

[a] PET, 82.2%, 78.3%; scintimammography, 68.8%, 84.8%; MRI, 92.5%, 72.4%; US, 86.1%, 66.4% [129].

These results are encouraging but suffer from small sample size, modification of prototype within the same studies, lack of standardized algorithms, lack of cross-validation with public data sets, overspecialized operators and readers, retrospective readings, and other problems. Only recently, with the maturation of industrial prototypes and impetus from funding agencies, have multicenter trials with common instruments, analysis platforms, and clinical operators been ongoing. For example, Advanced Research Technologies (ART) of Montreal has reported sensitivity- and specificity-based multicenter trials utilizing their Softscan platform [95]. They reported a preliminary sensitivity of 88.2% and a specificity of 88% (see Table 11.6) based on an ongoing multicenter clinical trial that recruited 71 patients (benign 25, malignant 17, and healthy 29). These results suggest that optical mammography can potentially provide greater diagnostic value than exiting modalities as an adjunct to x-ray mammography based on certain optical indexes. A typical example of a Softscan reading display is provided in Figure 11.5.

### 11.5.2 Monitoring of Neoadjuvant Chemotherapy Response

In recent years, numerous efforts have been made to identify clinical scenarios in which optical techniques could play an increased role [129]. Besides addressing established clinical issues associated with mammography, such as imaging dense breast, imaging a high-risk population, or imaging younger women, monitoring neoadjuvant chemotherapy response emerged as the most compelling application [130]. This specific clinical problem (generally a large tumor located close to the surface) requires an imaging modality that can provide structural and functional measurements with frequent imaging sessions [131]. Early evaluations of the potential of optical mammography to monitor neoadjuvant therapy efficacy have been reported [132,133].

Cerussi et al. [134] described a diffuse optical spectroscopy study monitoring the therapeutic response in the first week of a three-month adriamycin/cytoxan

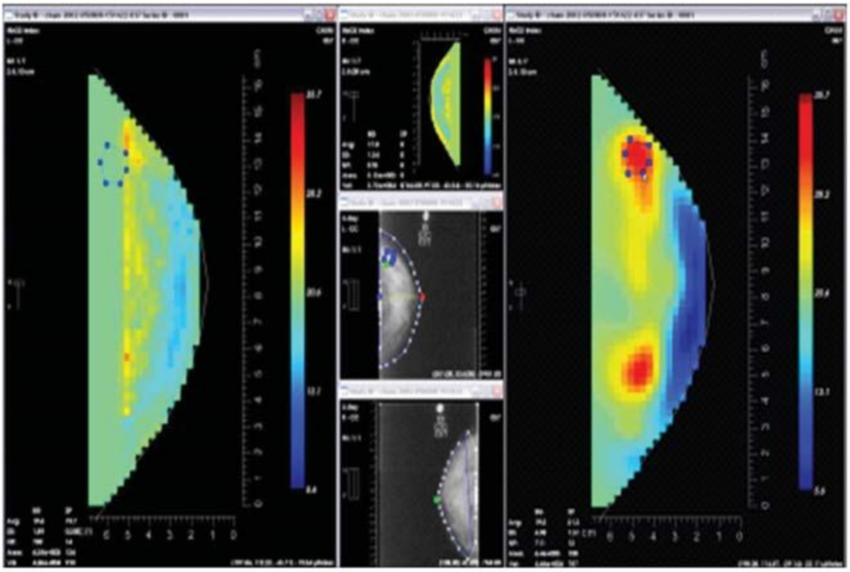

**FIGURE 11.5** DICOM mammogram with a CC view of a left breast (left), a CC view of the first slice of the left breast's three-dimensional oxyhemoglobin image (middle), and a third slice of a CC view of the oxyhemoglobin image (right) displayed on the review workstation of Softscan. The lesion is defined by the clinician on the two-dimensional mammogram (blue dotted circle). Through the colocalization software, the ROI is automatically remapped into an optical image and positioned automatically on every slice. (After [128], with permission.)

neoadjuvant chemotherapy regimen for 11 stage II/III patients. Based on postsurgical pathological evaluation, they established that the best single predictor of therapeutic response one week posttreatment was the deoxygenated hemoglobin concentration (83% sensitivity, 100% specificity), while discrimination analysis based on combined deoxygenated hemoglobin and water volume fraction changes classified responders versus nonresponders with 100% sensitivity and specificity. The technique is now evaluated through a multicenter trial and could prove invaluable in managing early or nonresponding patients.

## 11.6 MULTIMODALITY APPROACHES

Historically, medical imaging devices were developed independently to image either the structure or the functional state of tissues. Different imaging techniques were devised, based on different spectral regions of the electromagnetic spectrum [magnetic resonance imaging, (MRI), visible and near-infrared light, x-rays, gamma rays, single-photon emission computed tomography (SPECT), annihilation photons, positron emission tomography (PET)] or on high-frequency

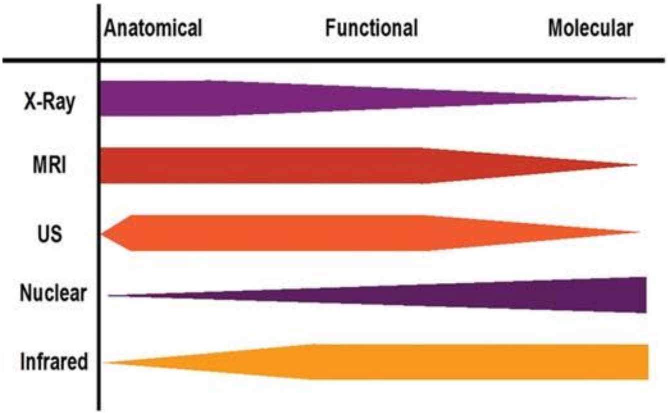

**FIGURE 11.6** Spectrum of anatomical and functional imaging modalities. A larger bar corresponds to an area of strength; a slim bar corresponds to a weakness. (From [136], with permission.)

sound waves (ultrasound) [135]. However, it was recognized that none of these stand-alone modalities provided a complete picture of the structure and function of tissue. A spectrum of established anatomical and functional imaging modalities in oncology is shown in Figure 11.6. Only recently, cross-fertilization between imaging modalities has become a major research area [137].

CT and MRI dominate the structural imaging modalities. Both imaging techniques are employed routinely for imaging the human anatomy with exquisite details; however, in diagnosing and staging disease or monitoring response to therapy, they provide a partial picture. They lack the ability to track functional or metabolic changes that can occur in the absence of corresponding anatomical correlates. Clinicians rely on nuclear medicine techniques to reveal such functional or metabolic information. These techniques, initiated in the late 1940s, are based on radioactive tracers. Until the development in the late 1980s of image fusion algorithms to register images from stand-alone clinical systems [138], acquisition and interpretation of anatomical and functional data were carried out in different departments. Since then, physicians have recognized the usefulness of combining anatomical and functional images, and image fusion using software techniques has evolved considerably [139,140] since its inception.

Optical techniques offer a potential to contribute greatly to the expansion of clinical multimodality techniques. Their ability to image structural, functional, and molecular information on different spatial and temporal scales makes them very attractive. In this case, the multimodality approach can be understood as the combination of multiple optical techniques in one instrument and/or as the fusion of an optical technique with another well-established clinical modality, such as CT, MRI, or PET.

All-optical multimodality (or multidimensional) techniques benefit from the unique contrast mechanisms of stand-alone optical techniques. Complementary information about the biochemical, architectural, and morphological state of tissue is obtained through a combination of different optical techniques and provides unprecedented diagnostic potential. Another active area of research is the combination of optical techniques with other clinical modalities. Similar to other fusion approaches, software and hardware fusion are being actively pursued. Software fusion is generally preferred for handheld optical devices when the patient would ideally be examined by the primary care physician or when an optimal optical imaging platform design is to be retained. Such software fusion faces the same challenges as do other nonconcurrent fusion techniques, such as CT–PET. Software fusion provides greater flexibility than physically integrated multimodality systems, thereby removing the requirements of the "other" imaging modality: for example, restrictions on metallic instrumentation for MRI, hard breast compression for x-ray mammography, limited optode combinations for ultrasound (and MRI, x-ray), and time constraints. It is therefore desirable to develop quantitative and systematic methods for data fusion that utilize the high-quality data and versatility of stand-alone imaging systems.

Hardware fusion follows the same development path of MR–PET fusion [141]. Light can be delivered to tissue efficiently and detected from tissue using light guides. Such flexibility allows efficient integration of optical techniques with clinical platforms such as CT and MRI. The concurrent acquisition of data is then feasible, leading to minimized errors in registration and reduced bias in anatomically assisted optical imaging. In this case, accurate anatomical templates allow alleviation of some of the intrinsic weaknesses of optical imaging of thick tissue [142].

Multimodal approaches are expected to yield improved sensitivity and specificity in breast cancer imaging, combining structural and functional information. For example, a high-resolution structure images can be used as a prior for functional imaging modality and could result in improved image quality and fewer artifacts [143–146]. Coregistration of the two modalities also facilitates interpretation of images and extrapolation of findings from one modality to another. Zhu et al. incorporated an ultrasound transducer into an optical imaging system for imaging both healthy and cancer breasts [147]. Brooksby et al. [148] used DOT–MRI to image healthy subjects and patients with tumors in their breasts, following earlier work by Ntziachristos et al. [149]. Similar work was reported by Choe et al. [150] and Klifa et al. [151]. A combined DOT–MRI system has also been used to monitor response to chemotherapy [150,152–155]. Konecky et al. [157] coregistered PET and DOT and described the potential to measure a large number of functional parameters, including glucose metabolism, hypoxia, tissue hemoglobin concentration and saturation, tissue scattering, and vascular permeability. Finally, combined x-ray tomosynthesis and DOT has been used to provide functional–structural information fusion in breast cancer screening and diagnosis [156].

## 11.7 SUMMARY

In optical mammography, diagnosis is based on the detection of local differential concentrations of endogenous absorbers and/or scatterers between normal and diseased breast tissue. Therefore, we require a refined understanding of the structural and functional properties of the human female breast that can influence optical diagnosis. In the last several decades, a significant effort toward better understanding of the optical properties of the breast has been ongoing. In this chapter we provided an overview of the relevant structural, physiological, and metabolic properties of the human female breast that affect the absorption and scattering tissue signatures that are the basis of optical mammography.

As clinical optical mammography matures, its potential impact on cancer management becomes more clearly defined. The three main applications emerging as the most likely to benefit cancer patients, as proposed by the Network for Translational Research: Optical Imaging (NTROI), are monitoring of neoadjuvant chemotherapy response, screening for subpopulations of women in which mammography does not work well, and imaging tool as an adjunct to mammography [61]. However, multicenter clinical trials with standardized imaging platforms are still required to truly establish optical mammography as a clinical tool.

## REFERENCES

1. Intes, X., and Azar, F., Introduction to clinical optical imaging, in *Translational Multimodality Optical Imaging*, Chap. 1, F. Azar and X. Intes (eds.), Artech House, Norwood, MA, 2008.
2. Thomsen, S., and Tatman, D., Physiological and pathological factors of human breast disease that can influence optical diagnosis, *Ann. N.Y. Acad. Sci.*, Vol. 838, 1998, pp. 171–193.
3. Welch, A.G., and Van Germert, M.J.C. (eds.), *Optical–Thermal Response of Laser-Irradiated tissue*, Plenum Press, New York, 1995.
4. Cheong, W.F., Prahl, S.A., and Welch, A.J., A review of the optical properties of biological tissues, *IEEE J. Quantum Electron.*, Vol. 26, 1990, pp. 2166–2185.
5. Braverman, I.M., Ultrastructure and organization of the cutaneous microvasculature in normal and pathological states, *J. Invest. Dermatol.*, Vol. 93, 1989, pp. 2S–9S.
6. Going, J.J., Ductal-lobar organisation of human breast tissue, its relevance in disease and a research objective: vector mapping of parenchyma in complete breasts (the Astley Cooper project), *Breast Cancer Res.*, Vol. 8, 2006, p. 107.
7. Rosen, P.P., *Breast Pathology*, Lippincott-Raven, Philadelphia, 1996.
8. Fowler, P.A., et al., Cyclic changes in composition and volume of the breast during the menstrual cycle, measured by magnetic resonance imaging, *Br. J. Obstet. Gynaecol.*, Vol. 97, 1990, pp. 595–602.
9. Graham, S.J., et al., Changes in fibroglandular volume and water content of breast tissue during the menstrual cycle observed by MR imaging at 1.5T, *J. Magn. Reson. Imaging*, Vol. 5, 1995, pp. 695–701.

10. Drife, J.O., Breast modifications during the menstrual cycle, *Int. J. Gynecol. Obstet*., Vol. 1, 1989, pp. 19–24.
11. Page, D., and Anderson, T.J., *Diagnostic Histopathology of the Breast*, Churchill Livingstone, New York, 1987.
12. Woodward, H.Q., and White, D.R., The composition of body tissues, *Br. J. Radiol*., Vol. 59, 1986, pp. 1209–1219.
13. Boulnois, J.L., Photophysical processes in recent medical laser developments: a review, *Lasers Med. Sci*., Vol. 1, 1986, pp. 47–66.
14. Vogel, A., and Venugopalan, V., Mechanisms of pulsed laser ablation of biological tissues, *Chem. Rev*., Vol. 103, No. 2, 2003, pp. 577–644.
15. Cerussi, A.E., et al., Sources of absorption and scattering contrast for near-infrared optical mammography, *Acad. Radiol*., Vol. 8, 2001, pp. 211–218.
16. European Standard EN 60825, 5th ed., European Commission, Berlin, 1997.
17. Ghadially, F.N., *Ultrastructural Pathology of the Cell and Matrix*, 3rd ed., Vols. 1 and 2, Butterworth, Boston, 1996.
18. Backman, V., et al., Polarized light scattering spectroscopy for quantitative measurement of epithelial structures in situ, *IEEE J. Sel. Top. Quantum Electron*., Vol. 5, 1999, pp. 1019–1026.
19. Beuthan, J., et al., The spatial variation of the refractive index in biological cells, *Phys. Med. Biol*., Vol. 41, 1996, pp. 369–382.
20. Beauvoit, B., et al., Correlation between the light scattering and the mitochondrial content of normal tissues and transplantable rodent tumors, *Anal. Biochem*., Vol. 226, 1995, pp. 167–174.
21. Doornbos, R.M.P., et al., The determination of in vivo human tissue optical properties and absolute chromophore concentrations using spatially resolved steady-state diffuse reflectance spectroscopy, *Phys. Med. Biol*., Vol. 44, 1999, pp. 967–981.
22. Troy, T.L., and Thennadil, S.N., Optical properties of human skin in the near infrared wavelength range of 1000 to 2200 nm, *J. Biomed. Opt*., Vol. 6, 2001, pp. 167–176.
23. Cutler, M., Transillumination as an aid in the diagnosis of breast lesions, *Surg. Gynecol. Obstet*., Vol. 48, 1929, pp. 721–728.
24. Curling, T.B., *A Practical Treatise on the Diseases of the Testis and of the Spermatic Cord and Scrotum*, pp. 125–181, Samuel Highley, London, 1843.
25. Bright, R., *Diseases of the Brain and Nervous System*, Longman, London, 1831.
26. Millikan, G.A., Photometric methods of measuring the velocity of rapid reactions: III. A portable microapparatus applicable to an extended range of reactions, *Proc. R. Soc. A*, Vol. 155, 1936, pp. 277–292.
27. Hartridge, H., and Roughton, F.J., The rate of distribution of dissolved gases between the red blood corpuscle and its fluid environment: I. Preliminary experiments on the rate of uptake of oxygen and carbon monoxide by sheep's corpuscles, *J. Physiol*., Vol. 62, 1927, pp. 232–242.
28. Severinghaus, J.W., and Astrup, P.B., The history of blood-gas analysis, *Int. Anesthiol. Clin*., Vol. 25, 1987, pp. 1–224.
29. Millikan, G.A., The oxymeter: an instrument for measuring continuously oxygen-saturation of arterial blood in man, *Rev. Sci. Instrum*., Vol. 13, 1942, pp. 434–444.
30. Gros, C.M., Quenneville, Y., and Hummel, Y., Diaphanologie mammaire, *J. Radiol. Electrol. Med. Nucl*., Vol. 53, 1972, pp. 297.

31. Profio, A.E., Sartorius, O.W., and Navarro, G.A., Scientific basis of breast diaphanography, *Med. Phys.*, Vol. 16, 1989, pp. 60–65.
32. Carlsen, E., *Diagnostic Imaging*, p. 28, Spectrascan, Inc., South Windsor, CT, 1982.
33. Monsees, B., Destouet, J.M., and Totty, W.G., Light scanning versus mammography in breast cancer detection, *Radiology*, Vol. 163, 1987, pp. 463–465.
34. Monsees, B., Destouet, J.M., and Gresell, D., Light scan evaluation of non palpable breast lesions, *Radiology*, Vol. 163, 1987, pp. 467–470.
35. Summary minutes of the 45th meeting of the Obstetrics and Gynecological Devices Panel, Food and Drug Administration, U.S. Public Health Service, Jan. 11, 1991.
36. Intes, X., and Chance, B., Non-PET functional imaging techniques optical, *Radiol. Clin. North Am.*, Vol. 43, 2005, pp. 221–234.
37. Knoll, G.F., *Radiation Detection and Measurements*, 3rd ed., Wiley, New York, 1999.
38. Lin, Y., et al., Noninvasive, low-noise, fast imaging of blood volume and deoxygenation changes in muscles using light-emitting diode continuous-wave imager, *Rev. Sci. Instrum.*, Vol. 73, 2002, pp. 3065–3074.
39. Xu, R.X., et al., Development of a handheld near-infrared imager for dynamic characterization of in vivo biological tissue systems, *Appl. Opt.*, Vol. 46, 2007, pp. 7442–7451.
40. Culver, J.P., et al., Three dimensional diffuse optical tomography in the parallel plane transmission geometry: evaluation of a hybrid frequency domain/continuous wave clinical system for breast imaging, *Med. Phys.*, Vol. 30, 2003, pp. 235–247.
41. Grable, R.J., et al., Optical computed tomography for imaging the breast: first look, *Proc. SPIE*, Vol. 4082, 2000, pp. 40–45.
42. Colak, S.B., et al., Clinical optical tomography and NIR spectroscopy for breast cancer detection, *IEEE J. Quantum Electron.*, Vol. 5, 1999, pp. 1143–1158.
43. Van der Mark, M.B., et al., Clinical study of the female breast using spectroscopic diffuse optical tomography, presented at the Optical Society of America Biomedical Topical Meeting, Apr. 2000.
44. Grable, R.J., Rohler, D.P., and Sastry, K.L.A., Optical tomography breast imaging, *Proc. SPIE*, Vol. 2979, 2004, pp. 197–210.
45. Schmitz, C.H., et al., Instrumentation for fast functional optical tomography, *Rev. Sci. Instrum.*, Vol. 73, 2002, pp. 429–439.
46. Arridge, S.R., and Lionheart, W.R.B., Nonuniqueness in diffusion-based optical tomography, *Opt. Lett.*, Vol. 23, 1998, pp. 882–884.
47. Corlu, A., et al., Uniqueness and wavelength optimization in continuous-wave multispectral diffuse optical tomography, *Opt. Lett.*, Vol. 28, 2003, pp. 2339–2431.
48. Boas, D.A., Gaudette, T., and Arridge, S.R., Simultaneous imaging and optode calibration with diffuse optical tomography, *Opt. Express*, Vol. 8, 2001, pp. 263–273.
49. Intes, X., et al., CW-optical breast imaging enhanced with Indocyanine green, *Med. Phys.*, Vol. 30, 2003, pp. 1039–1047.
50. Chance, B., et al., Phase measurement of light absorption and scatter in human tissue, *Rev. Sci. Instrum.*, Vol. 69, 1998, pp. 3457–3481.
51. Yao, Y., et al., Frequency domain optical imaging of absorption and scattering distributions by a Born iterative method, *J. Opt. Soc. Am. A*, Vol. 14, 1997, pp. 325–342.

52. Intes, X., and Chance, B., Multi-frequency diffuse optical tomography, *J. Mod. Opt.*, Vol. 52, 2005, pp. 2139–2159.
53. Nissila, I., et al., Instrumentation for the accurate measurement of phase and amplitude in optical tomography, *Rev. Sci. Instrum.*, Vol. 73, 2002, pp. 3306–3312.
54. Kaschke, M., et al., Transillumination imaging of tissue by phase modulation techniques, *Proc. OSA Adv. Opt. Imaging Photon Migration*, Vol. 21, 1994, pp. 88–92.
55. Moesta, K.T., et al., Lasermammografie der Brustdruse-Sensitivitatssteigerung durch Hochfrequenzmodulation, *Langenbeck's Arch. Chir. Suppl.*, Vol. 1, 1996, pp. 543–548.
56. Gotz, L., et al., Optische Mammographie an praoperativen Patientinnen, *Akt. Radiol.*, Vol. 8, 1998, pp. 31–33.
57. Franceschini, M.A., et al., Frequency-domain techniques enhance optical mammography: initial clinical results, *Proc. Natl. Acad. Sci. USA*, Vol. 94, 1997, pp. 6468–6473.
58. Fantini, S., et al., Assessment of the size, position and optical properties of breast tumors in vivo by noninvasive optical methods, *Appl. Opt.*, Vol. 37, 1998, pp. 1982–1989.
59. Bevilacqua, F., et al., Broadband absorption spectroscopy in turbid media by combined frequency-domain and steady-state methods, *Appl. Opt.*, Vol. 39, 2000, pp. 6498–6507.
60. Tromberg, B.J., et al., Assessing the future of diffuse optical imaging technologies for breast cancer management, *Med. Phys.*, Vol. 35, 2008, pp. 2443–2451.
61. McBride, T.O., et al., A parallel-detection frequency-domain near-infrared tomography system for hemoglobin imaging of the breast in vivo, *Rev. Sci. Instrum.*, Vol. 72, 2001, pp. 1817–1824.
62. Culver, J.P., et al., Three-dimensional diffuse optical tomography in the parallel plane transmission geometry: evaluation of a hybrid frequency domain/continuous wave clinical system for breast imaging, *Med. Phys.*, Vol. 30, 2003, pp. 235–247.
63. Corlu, A., et al., Diffuse optical tomography with spectral constraints and wavelength optimization, *Appl. Opt.*, Vol. 44, 2005, pp. 2082–2093.
64. Hebden, J.C., Arridge, S.R., and Delpy, D.T., Optical imaging in medicine: I. Experimental techniques, *Phys. Med. Biol.*, Vol. 42, 1997, pp. 825–840.
65. Schweiger, M., and Arridge, S.R., Application of temporal filters to time-resolved data in optical tomography, *Phys. Med. Biol.*, Vol. 44, 1999, pp. 1699–1717.
66. Hebden, J.C., Kruger, R.A., and Wong, K.S., Time resolved imaging through a highly scattering medium, *Appl. Opt.*, Vol. 30, 1991, pp. 788–794.
67. Grosenick, D., et al., Development of a time-domain optical mammograph and first in vivo applications, *Appl. Opt.*, Vol. 38, 1999, pp. 2927–2943.
68. Pifferi, A., et al., Four-wavelength time-resolved optical mammography in the 680–980 nm range, *Opt. Lett.*, Vol. 28, 2003, pp. 1138–1140.
69. Schmidt, F.E.W., et al., A 32-channel time-resolved instrument for medical optical tomography, *Rev. Sci. Instrum.*, Vol. 71, 2000, pp. 256–265.
70. Intes, X., et al., Development and evaluation of a multi wavelength–multi channel time resolved optical instrument for NIR/MRI mammography co-registration, *IEEE–EMBS NEBE 2002: Defining the Future for Biomedical Engineering*, Philadelphia, Apr. 2002.

71. Alveryd, A., et al., Light scanning versus mammography for the detection of breast cancer in screening and clinical practice, *Cancer*, Vol. 65, 1990, pp. 1671–1677.
72. Arridge, S.R., and Hebden, J.C., Optical imaging in medicine: II. Modelling and reconstruction, *Phys. Med. Biol*., Vol. 42, 1997, pp. 841–853.
73. Arridge, S.R., Optical tomography in medical imaging, *Inverse Problems*, Vol. 15, 1999, pp. R41–R93.
74. Gibson, A.P., Hebden, J.C., and Arridge, S.R., Recent advances in diffuse optical imaging, *Phys. Med. Biol*., Vol. 50, 2005, pp. R1–R43.
75. Born, M., and Wolf, E., *Principles of Optics*, Cambridge University Press, Cambridge, UK, 1999.
76. Bouguer, P., *Essai d'optique sur la gradation de la lumière*, Claude Jombert, Paris, 1729.
77. Case, K.M., and Zweifel, P.F., *Linear Transport Theory*, Addison-Wesley, Reading, MA, 1967.
78. Chandrasekhar, S., *Radiative Transfer*, Dover, New York, 1960.
79. Morse, P.M., and Feschbach, H., *Methods of Theoretical Physics*, McGraw-Hill, New York, 1953.
80. Klose, A.D., and Hielscher, A.H., Iterative reconstruction scheme for optical tomography based on the equation of radiative transfer, *Med. Phys*., Vol. 26, 1999, pp. 1698–1707.
81. Jobsis, F., Noninvasive infrared monitoring of cerebral and myocardial sufficiency and circulatory parameters, *Science*, Vol. 198, 1977, pp. 1264–1267.
82. Boas, D., et al., The accuracy of near infrared spectroscopy and imaging during focal changes in cerebral hemodynamics, *Neuroimage*, Vol. 13, 2001, pp. 76–90.
83. Boas, D., Gaudette, T., and Arridge, S.R., Simultaneous imaging and optode calibration with diffuse optical tomography, *Opt. Express*, Vol. 8, 2001, pp. 263–270.
84. Boas, D., et al. Imaging the body with diffuse optical tomography, *IEEE Signal Process. Mag*., Vol. 18, 2001, pp. 57–74.
85. Arridge, S.R., Optical tomography in medical imaging, *Inverse Problems*, Vol. 15, 1999, pp. R41–R93.
86. Peters, V.G., et al., Optical properties of normal and diseased human breast tissues in the visible and near infrared, *Phys. Med. Biol*., Vol. 35, No. 9, 1990, pp. 1317–1334.
87. Welch, A.G., and Van Germert, M.J.C. (eds.), *Optical–Thermal Response of Laser-Irradiated Tissue*, Plenum Press, New York, 1995.
88. Cheong, W.F., Prahl, S.A., and Welch, A.J., A review of the optical properties of biological tissues, *IEEE J. Quantum Electron*., Vol. 26, 1990, pp. 2166–2185.
89. Thomsen, S., and Tatman, D., Physiological and pathological factors of human breast disease that can influence optical diagnosis, *Ann. N.Y. Acad. Sci*., Vol. 838, 1998, pp. 171–193.
90. Shah, N., et al., Noninvasive functional optical spectroscopy of human breast tissue, *Proc. Natl. Acad. Sci. USA*, Vol. 98, 2001, pp. 4420–4425.
91. Pogue, B.W., et al., Characterization of hemoglobin, water, and NIR scattering in breast tissue: analysis of intersubject variability and menstrual cycle changes, *J. Biomed. Opt*., Vol. 9, 2004, pp. 541–552.
92. Durduran, T., et al., Bulk optical properties of healthy female breast tissue, *Phys. Med. Biol*., Vol. 47, 2002, pp. 2847–2861.

93. Spinelli, L., et al., Bulk optical properties and tissue components in the female breast from multiwavelength time-resolved optical mammography, *J. Biomed. Opt*., Vol. 9, 2004, pp. 1137–1142.
94. Suzuki, K., et al., Quantitative measurements of optical parameters in normal breasts using time-resolved spectroscopy: in vivo results of 30 Japanese women, *J. Biomed. Opt*., Vol. 1, 1996, pp. 330–334.
95. Intes, X., Time-domain optical mammography initial results, *Acad. Radiol*., Vol. 12, 2005, pp. 934–947.
96. Grosenick, D., et al., Time-domain optical mammography: initial clinical results on detection and characterization of breast tumors, *Appl. Opt*., Vol. 42, 2003, pp. 3170–3186.
97. Grosenick, D., et al., Time-domain scanning optical mammography: I. Recording and assessment of mammograms of 154 patients, *Phys. Med. Biol*., Vol. 50, 2005, pp. 2429–2449.
98. Yates, T., et al., Optical tomography of the breast using a multi-channel time-resolved imager, *Phys. Med. Biol*., Vol. 50, 2005, pp. 2503–2517.
99. Taroni, P., et al., Time-resolved optical mammography between 637 and 985 nm: clinical study on the detection and identification of breast lesions, *Phys. Med. Biol*., Vol. 50, 2005, pp. 2469–2488.
100. Taroni, P., et al., Clinical trial of time-resolved scanning optical mammography at 4 wavelengths between 683 and 975nm, *J. Biomed. Opt*., Vol. 9, 2004, pp. 464–473.
101. Leff, D.R., et al., Diffuse optical imaging of the healthy and diseased breast: a systematic review, *Breast Cancer Res. Treat*., Vol. 108, 2008, pp. 9–22.
102. Cerussi, A., et al., Sources of absorption and scattering contrast for near-infrared optical mammography, *Acad. Radiol*., Vol. 8, 2001, pp. 211–218.
103. Pogue, B.W., et al., Quantitative hemoglobin tomography with diffuse near-infrared spectroscopy: pilot results in the breast, *Radiology*, Vol. 218, 2001, pp. 261–266.
104. Srinivasan, S., et al., Near-infrared characterization of breast tumors in vivo using spectrally constrained reconstruction, *Technol. Cancer Res. Treat*., Vol. 4, 2005, pp. 513–526.
105. Grosenick, D., et al., Time-domain optical mammography: initial clinical results on detection and characterization of breast tumors, *Appl. Opt*., Vol. 42, 2003, pp. 3170–3186.
106. Spinelli, L., et al., Characterization of female breast lesions from multi-wavelength time-resolved optical mammography, *Phys. Med. Biol*., Vol. 50, 2005, pp. 2489–2502.
107. Taroni, P., et al., Clinical trial of time-resolved scanning optical mammography at 4 wavelengths between 683 and 975nm, *J. Biomed. Opt*., Vol. 9, 2004, pp. 464–473.
108. Chance, B., et al., Breast cancer detection based on incremental biochemical and physiological properties of breast cancers: a six-year, two-site study, *Acad. Radiol*., Vol. 12, 2005, pp. 925–933.
109. Grosenick, D., et al., Time-domain scanning optical mammography: I. Recording and assessment of mammograms of 154 patients, *Phys. Med. Biol*., Vol. 50, 2005, pp. 2429–2449.
110. Durduran, T., et al., Bulk optical properties of healthy female breast tissue, *Phys. Med. Biol*., Vol. 47, 2002, pp. 2847–2861.

111. Spinelli, L., et al., Bulk optical properties and tissue components in the female breast from multi-wavelength time-resolved optical mammography, *J. Biomed. Opt.*, Vol. 9, 2004, pp. 1137–1142.

112. Pogue, B.W., et al., Characterization of hemoglobin, water, and NIR scattering in breast tissue: analysis of inter-subject variability and menstrual cycle changes, *J. Biomed. Opt.*, Vol. 9, 2004, pp. 541–552.

113. Pifferi, A., et al., Spectroscopic time-resolved diffuse reflectance and transmittance measurements of the female breast at different interfiber distances, *J. Biomed. Opt.*, Vol. 9, 2004, pp. 1143–1151.

114. Srinivasan, S., et al., Interpreting hemoglobin and water concentration, oxygen saturation, and scattering measured in vivo by near-infrared breast tomography, *Proc. Natl. Acad. Sci. USA*, Vol. 100, 2003, pp. 12349–12354.

115. Cerussi, A.E., et al., Sources of absorption and scattering contrast for near-infrared optical mammography, *Acad. Radiol.*, Vol. 8, 2001, pp. 211–218.

116. Shah, N., et al., Spatial variations in optical and physiological properties of healthy breast tissue, *J. Biomed. Opt.*, Vol. 9, 2004, pp. 534–540.

117. Cerussi, A.E., et al., Spectroscopy enhances the information content of optical mammography, *J. Biomed. Opt.*, Vol. 7, 2002, pp. 60–71.

118. Poplack, S.P., et al., Electromagnetic breast imaging: average tissue property values in women with negative clinical findings, *Radiology*, Vol. 231, 2004, pp. 571–580.

119. Karellas, A., and Vedantham, S., Breast cancer imaging: a perspective for the next decade, *Med. Phys.*, Vol. 35, 2008, pp. 4878–4897.

120. Tromberg, B., et al., Noninvasive in vivo characterization of breast tumors using photon migration spectroscopy, *Neoplasia*, Vol. 2, 2000, pp. 26–40.

121. Grosenick, D., et al., Time-domain optical mammography: initial clinical results on detection and characterization of breast tumors, *Appl. Opt.*, Vol. 42, 2003, pp. 3170–3186.

122. Grosenick, D., et al., Concentration and oxygen saturation of haemoglobin of 50 breast tumours determined by time-domain optical mammography, *Phys. Med. Biol.*, Vol. 49, 2004, pp. 1165–1181.

123. Grosenick, D., et al., Time-domain scanning optical mammography: I. Recording and assessment of mammograms of 154 patients, *Phys. Med. Biol.*, Vol. 50, 2005, pp. 2429–2444.

124. Yates, T., et al., Optical tomography of the breast using a multi-channel time-resolved imager, *Phys. Med. Biol.*, Vol. 50, 2005, pp. 2503–2517.

125. Taroni, P., et al., Time-resolved optical mammography between 637 and 985 nm: clinical study on the detection and identification of breast lesions, *Phys. Med. Biol.*, Vol. 50, 2005, pp. 2469–2488.

126. Rinnerberg, H., et al., Detection and characterization of breast tumours by time-domain scanning optical mammography, *Opto-Electron. Rev.*, Vol. 16, 2008, pp. 147–162.

127. Taroni, P., et al., Do shorter wavelengths improve contrast in optical mammography? *Phys. Med. Biol.*, Vol. 49, 2004, pp. 1203–1215.

128. Khayat, M., Clinical studies in optical imaging: an industry perspective, in *Translational Multimodality Optical Imaging*, Chap. 14, F. Azar and X. Intes (eds.), Artech House, Norwood, MA, 2008.

129. AHRQ, *Effectiveness of Noninvasive Diagnostic Tests for Breast Abnormalities: Executive Summary*, No. 2 (Publ. 06-EHC055-1), Agency for Healthcare Research and Quality, Rockville, MD, Feb. 2006; http://effectivehealthcare.ahrq.gov/healthInfo.cfm?infotype=rr&DocID=37&ProcessID=3.
130. Tromberg, B.J., et al., Assessing the future of diffuse optical imaging technologies for breast cancer management, *Med. Phys.*, Vol. 35, 2008, pp. 2443–2451.
131. Esserman, L., Neoadjuvant chemotherapy for primary breast cancer: lessons learned and opportunities to optimize therapy, *Ann. Surg. Oncol.*, Vol. 11, 2004, pp. 3S–8S.
132. Jakuboswki, D.B., et al., Monitoring neoadjuvant chemotherapy in breast cancer using quantitative diffuse optical spectroscopy: a case study, *J. Biomed. Opt.*, Vol. 9, 2004, pp. 230–238.
133. Choe, R., et al., Diffuse optical tomography of breast cancer during noeadjuvant chemotherapy: a case study with comparison to MRI, *Med. Phys.*, Vol. 32, 2005, pp. 1128–1139.
134. Cerussi, A., et al., Predicting response to breast cancer neoadjuvant chemotherapy using diffuse optical spectroscopy, *Proc. Natl. Acad. Sci. USA*, Vol. 104, 2007, pp. 4014–4019.
135. Bushberg, J.T., et al., *The Essential Physics of Medical Imaging*, Lippincott Williams & Wilkins, Philadlephia, 2002.
136. Laking, G.R., Price, P.M., and Sculpher, M.J., Assessment of the technology for functional imaging in cancer, *Eur. J. Cancer*, Vol. 38, 2002, pp. 2194–2199.
137. Townsend, D.W., Multimodality imaging of structure and function, *Phys. Med. Biol.*, Vol. 53, 2008, pp. R1–R39.
138. Levin, D.N., et al., Retrospective geometric correlation of MR, CT and PET images, *Radiology*, Vol. 169, 1988, pp. 817–836.
139. Hawkes, D.J., et al., *Coregistration of Structural and Functional Images, Positron Emission Tomography: Basic Science and Clinical Practice*, pp. 181–198, Springer-Verlag, New York. 2004.
140. Slomka, P.J., Software approach to merging molecular with anatomic information, *J. Nucl. Med.*, Vol. 45, 2004, pp. 36S–45S.
141. Christensen, N.L., et al., Positron emission tomography within a magnetic field using photomultiplier tubes and light guides, *Phys. Med. Biol.*, Vol. 40, 1995, pp. 691–697.
142. Ohlsson, B., Gundersen, J., and Nilsson, D.-M., Diaphanography: a method for evaluation of the female breast, *World J. Surg.*, Vol. 4, 1980, pp. 701–707.
143. Li, A., et al., Tomographic optical breast imaging guided by three-dimensional mammography, *Appl. Opt.*, Vol. 42, 2003, pp. 5181–5190.
144. Guven, M., et al., Diffuse optical tomography with a priori anatomical information, *Phys. Med. Biol.*, Vol. 50, 2005, pp. 2837–2858.
145. Zhu, Q., Chen, N.G., and Kurtzman, S.H., Imaging tumor angiogenesis using combined near infrared diffusive light and ultrasound, *Opt. Lett.*, Vol. 28, 2003, pp. 337–339.
146. Intes, X., et al., Diffuse optical tomography with physiological and spatial a-priori constraints, *Phys. Med. Biol.*, Vol. 49, 2004, pp. 155–164.
147. Zhu, Q., et al., Imager that combines near-infrared diffusive light and ultrasound, *Opt. Lett.*, Vol. 24, 1999, pp. 1050–1052.

148. Brooksby, B., et al., Combining near-infrared tomography and magnetic resonance imaging to study in vivo breast tissue: implementation of a Laplacian-type regularization to incorporate magnetic resonance structure, *J. Biomed. Opt*., Vol. 10, 2005, 051504.
149. Ntziachristos, V., et al., MRI-guided diffuse optical spectroscopy of malignant and benign breast lesions, *Neoplasia*, Vol. 4, 2002, pp. 347–354.
150. Choe, R., et al., Diffuse optical tomography of breast cancer during neoadjuvant chemotherapy: a case study with comparison to MRI, *Med. Phys*., Vol. 32, 2005, pp. 1128–1139.
151. Klifa, C.S., et al., Combination of magnetic resonance imaging and diffuse optical spectroscopy to predict radiation response in the breast: an exploratory pilot study, *Breast Cancer Res. Treat*., Vol. 100, 2006, pp. S202–S202.
152. Wolmark, N., et al., Preoperative chemotherapy in patients with operable breast cancer: nine-year results from National Surgical Adjuvant Breast and Bowel Project B-18, *J. Natl. Cancer Inst. Monogr*., Vol. 30, 2001, pp. 96–102.
153. Tromberg, B.J., et al., Imaging in breast cancer—diffuse optics in breast cancer: detecting tumors in pre-menopausal women and monitoring neoadjuvant chemotherapy, *Breast Cancer Res*., Vol. 7, 2005, pp. 279–285.
154. Cerussi, A.E., et al., Can diffuse optical spectroscopy predict the final pathological response of neoadjuvant chemotherapy? A retrospective pilot study, *Breast Cancer Res. Treat*., Vol. 94, 2005, pp. S50–S50.
155. Shah, N., et al., Combined diffuse optical spectroscopy and contrast-enhanced magnetic resonance imaging for monitoring breast cancer neoadjuvant chemotherapy: a case study, *J. Biomed. Opt*., Vol. 10, 2005, 051503.
156. Fang, Q., et al., Combined optical and x-ray tomosynthesis breast imaging, *Radiology*, 2008. submitted.
157. Konecky, S.D., et al., Comparison of diffuse optical tomography of human breast with whole-body and breast-only positron emission tomography, *Med. Phys*., Vol. 35, 2008, pp. 446–455.

# 12

# PHOTOACOUSTIC TOMOGRAPHY

Huabei Jiang and Zhen Yuan
*University of Florida, Gainesville, Florida*

12.1 Introduction 337
12.2 Photoacoustic theory 339
12.3 PAT imaging methods 342
12.4 Photoacoustic wave equations 342
12.5 Finite-element and model-based PAT reconstruction methods 343
  12.5.1 Frequency-domain PAT reconstruction algorithm 344
  12.5.2 Time-domain PAT aeconstruction algorithm 352
12.6 Quantitative PAT 356
  12.6.1 Algorithm 1 356
  12.6.2 Algorithm 2 357
  12.6.3 Algorithm 3 359
12.7 PAT imaging instrumentation 362
12.8 In vivo applications 362
References 365

## 12.1 INTRODUCTION

Biomedical *photoacoustic tomography* (PAT), also called *optoacoustic tomography* or *thermoacoustic tomography*, is based on the photoacoustic (PA) effect, first described in 1880 by Alexander Graham Bell. In PAT, a short-pulsed laser source is typically used to irradiate the tissue of interest. The absorption of laser pulses gives rise to a rapid temperature rise and subsequent thermoelastic expansion of

---

*Advances in Optical Imaging for Clinical Medicine*, Edited by Nicusor Iftimia, William R. Brugge, and Daniel X. Hammer
Copyright © 2011 John Wiley & Sons, Inc.

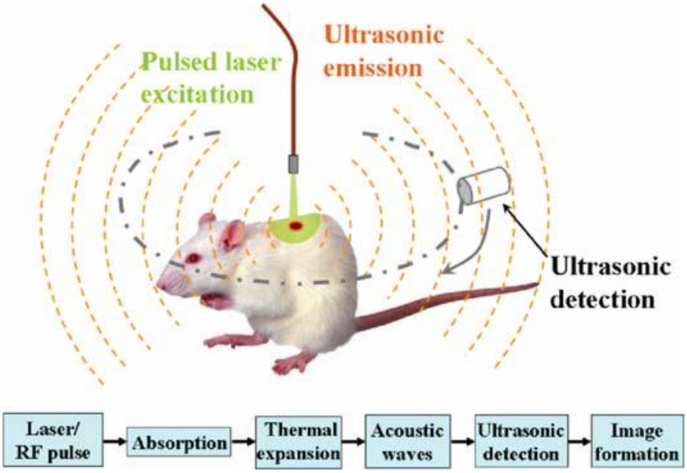

**FIGURE 12.1** PAT imaging. (After http://en.wikipedia.org/wiki/Photoacoustic_imaging_in_biomedicine.)

the irradiated tissue volume. The pressure distribution induced by tissue expansion prompts acoustic wave propagation toward tissue surfaces, where they are detected by one or an array of ultrasound transducers (see Figure 12.1). The acquired acoustic data by ultrasound transducers are then used to recover the PA images qualitatively or quantitatively. PAT can capture tissue mechanical properties such as ultrasound velocity, optical properties such as absorption and scattering coefficients, and physiological or functional parameters such as deoxyhemoglobin (HbR), oxyhemoglobin ($HbO_2$), and water ($H_2O$).

Research interest in laser-induced PAT is rapidly growing, largely because of its unique capability of combining high optical contrast and high ultrasound resolution in a single modality. Recent in vivo studies have shown that the optical absorption contrast between tumor and normal tissues in the breast can be as high as 3 : 1 in the near-infrared region, due to the significantly increased vascularity in the tumors [1–3]. However, optical imaging has low spatial resolution, due to strong light scattering. Ultrasound imaging can provide better resolution than optical imaging, due to less scattering of acoustic wave. However, the contrast for ultrasound imaging is low, making it often incapable of revealing diseases at early stages. In addition, ultrasound imaging cannot provide functional parameters, including HbR, $HbO_2$, and $H_2O$ concentrations. PAT combines the advantages of optical and ultrasound imaging in a single modality, yet overcomes the limitations associated with optical and ultrasound.

Hence, PAT can be regarded as a hybrid imaging modality that provides the high contrast and specificity of optical imaging along with the high spatial resolution of ultrasound. The latter is depth dependent, being limited by the frequency-dependent nature of acoustic attenuation in tissue. For centimeter penetration depths, submillimeter spatial resolution is possible. For example, PAT imaging can reach a depth of about 1 cm at a wavelength of 580 nm with an axial resolution of less than 100 μm. PAT has shown the potential to detect breast cancer, to probe brain functioning in small animals, and to assess vascular and skin diseases.

In addition to the high-resolution anatomical imaging offered by PAT, several recent studies have suggested that it is possible to recover optical absorption and scattering coefficient maps when conventional PAT is combined with a light transport model [4–8]. This allows PAT to provide spatially resolved quantitative physiological and molecular information by exploiting the known spectral characteristics of specific chromophores. For example, by obtaining optical absorption images at multiple wavelengths, it is possible to quantify the local concentrations of spectrally distinct endogenous chromophores, such as $HbO_2$ and HbR, which also allow for the calculation of absolute blood oxygen saturation ($SO_2$). Such quantitative physiological parameters may become critical for accurate diagnostic decision making.

Recent advances in PAT have also shown that the images of both acoustic velocity and optical absorption can be recovered simultaneously [9]. This ability to recover both optical and acoustic properties not only provides more accurate reconstruction of optical property over conventional PAT because of the elimination of the assumption of homogeneous acoustic velocity built into conventional PAT methods, but also adds the potential to better differentiate benign from malignant lesions, as it is known that there exist significant differences in acoustic properties between normal and tumor tissues [10].

## 12.2 PHOTOACOUSTIC THEORY

The major challenge for photoacoustic (PA) studies is that photoacoustics involves two historically separate fields, optics and ultrasound. This complicates notation and makes it difficult to find experts who are competent in both fields [11]. The basic physical principle behind PA can be demonstrated using some empirical equations.

A three-dimensional model using lateral dimensions $x$ and $y$ and depth $z$ is the basis for PA. In PA, biological tissue is irradiated homogeneously with a short laser pulse of energy $E$ (J) on an area $A$ ($m^2$), and the approximate photon density or radiant exposure ($J/m^2$) on the surface is written

$$\Phi(x, y, 0) = \frac{E}{A} \tag{12.1}$$

The radiant exposure for large depth $z$ is estimated by

$$\Phi(x, y, 0) \propto \Phi_0 e^{-\mu_{\text{eff}} z} \tag{12.2}$$

where $\mu_{\text{eff}}$ is the effective optical attenuation coefficient, which is a function of the optical absorption coefficient $\mu_a$ and reduced scattering coefficient $\mu_s'$:

$$\mu_{\text{eff}} = \sqrt{3\mu_a(\mu_a + \mu_s')} \tag{12.3}$$

It should be noted that the photon density can be calculated accurately using the photon diffusion equation with any type of source distribution. In PA, the stress generation depends on the locally absorbed light energy density $\Psi$, which is the product of the optical absorption coefficient $\mu_a$ and photon density $\Phi$:

$$\Psi = \mu_a \Phi \tag{12.4}$$

With the density $\rho$ (kg/m$^3$) and specific heat $C_p$ [J/(kg · °C)], the absorbed light energy leads to a temperature increase (°C):

$$\Delta T(x, y, z) = \frac{\Psi(x, y, z)}{\rho C_p} \tag{12.5}$$

Additionally, due to laser excitation, the absorbed light energy also gives rise to a fractional volume expansion $dV/V$:

$$\frac{dV}{V} = -\kappa p + \beta\, \Delta T \tag{12.6}$$

where $\kappa$ denotes the isothermal compressibility and $\beta$ is the thermal coefficient of volume expansion; $\Delta T$ and $p$ are the changes in temperature (K) and pressure (Pa), respectively. The isothermal compressibility $\kappa$ can be expressed as

$$\kappa = \frac{C_p}{\rho v_s^2 C_v} \tag{12.7}$$

where $C_p$ and $C_v$ are, respectively, the specific heat capacities at constant pressure and volume, and $v_s$ is the ultrasound velocity. If the laser excitation is in both the thermal and stress confinements, the fractional volume expansion is negligible and the local pressure rise can be obtained from equation (12.6):

$$p_0 = \frac{\beta\, \Delta T}{\kappa} \tag{12.8}$$

If we define a set of coefficients as the Grueneisen parameter $\Gamma$,

$$\Gamma = \frac{\beta}{\kappa \rho C_v} = \frac{\beta v_s^2}{C_p} \tag{12.9}$$

equation (12.8) is rewritten in consideration of (12.4), (12.5), and (12.9) as

$$p_0 = \frac{\beta \mu_a \Phi}{\kappa \rho C_v} = \Gamma \mu_a \Phi \tag{12.10}$$

For water and diluted aqueous solution, $\Gamma$ can be estimated by the empirical equation

$$\Gamma(T_0) = 0.0043 + 0.0053 T_0 \tag{12.11}$$

in which $T_0$ is the temperature in degrees Celsius. $p_0$ is often specified as the initial pressure for a temporal PA wave equation. These sets of empirical equations for the calculation of $p_0$ should satisfy the stress confinement and thermal confinement conditions. Efficient direct conversion to pressure is possible if the acoustic transient does not leave the heated region during the heating process. This condition, called *stress confinement*, is satisfied if the pulse duration $t_p$ is smaller than the propagation time of the acoustic transient through region $d$ with acoustic velocity $v_s$:

$$\tau_p < \frac{d}{v_s} \tag{12.12}$$

If the laser pulse width is much shorter than the thermal relaxation time $\tau_{\text{th}}$, the excitation is said to be in thermal confinement, and the heat conduction is negligible during the laser pulse. The thermal confinement condition is written

$$\tau_{\text{th}} < \frac{d^2}{\alpha_{\text{th}}} \tag{12.13}$$

in which $\alpha_{\text{th}}$ is the thermal diffusivity (m$^2$/s) and $d_c \approx 1/\mu_{\text{eff}}$.

**Example** A laser pulse with energy $E = 30$ mJ, pulse length = 10 ns, beam radius $r = 1$ cm, and wavelength 550 nm irradiates a human blood vessel. The radiant exposure is

$$\Phi_0 = \frac{E}{\pi r^2} = \frac{30\ \text{mJ}}{3.14\ \text{cm}^2} = 9.55\ \text{mJ/cm}^2$$

Assuming that $\mu_a = 25\ \text{cm}^{-1}$, the absorbed light energy density is calculated as

$$\begin{aligned}\Psi &= 25 \times 9.55 = 238.75\ \text{mJ/cm}^3 = 2.38 \times 10^5\ \text{J/m}^3\\ &= 2.38 \times 10^5\ \text{Pa} = 2.38\ \text{bar}\end{aligned}$$

Then we can get the temperature increase and initial pressure generated:

$$\Delta T(x, y, z) = \frac{\Psi(x, y, z)}{\rho C_p} = \frac{238.75\ \text{mJ/cm}^3}{(1\ \text{g/cm}^3 \times 4\ \text{J g}^{-1}\ \text{K}^{-1})} = 59.7\ \text{mK}$$

$$p_0 = \Gamma\Psi = 0.2 \times 2.38\ \text{bar} = 0.476\ \text{bar}$$

To get this pressure, stress confinement with a region $d = 1/\mu_a = 400\ \mu$m and sound velocity $v_s = 1.5\ \mu$m/ns needs to be satisfied:

$$\tau_p = 10\ \text{ns} < \frac{d}{v_s} = 266\ \ \text{ns}$$

## 12.3 PAT IMAGING METHODS

Two typical PA techniques are currently being used for PAT imaging: time-resolved and frequency-domain methods. Based on the two techniques, several imaging schemes have been developed for tissue PAT imaging, such as the Fourier transform, P-transport, statistical approach, and back-projection methods [12–17]. However, most of these imaging methods have been focused on direct image formulation from the acoustical data measured, which may not fully exploit all the information provided. In consideration of the advantages over direct imaging methods, increasing attention has been paid to model-based PAT reconstruction methods, in which the Helmholtz-like PA wave equation has commonly been used as an accurate model for image reconstruction. Due to the use of an effective reconstruction algorithm, PAT is able to improve the resolution limitation and to realize quantitative imaging. Phantom and in vivo experiments have shown that model-based reconstruction methods, including *k*-space and finite element based, are able to recover both structural and functional information on biological tissues [18–22].

## 12.4 PHOTOACOUSTIC WAVE EQUATIONS

PA wave generation and propagation in an inviscid acoustic medium are described by a Helmholtz-like wave equation. To derive the PA equation, three general elastic mechanical and fluid dynamic equations are responsible for the PA generation and propagation. The acoustic waves are governed by the basic Newton's law of motion equation,

$$\rho(r)\frac{\partial}{\partial t}V(r,t) = -\nabla p(r,t) \tag{12.14}$$

$$\nabla \cdot V(r,t) = -\frac{1}{\rho(r)v_s^2(r)}\frac{\partial}{\partial t}p(r,t) + \beta\frac{\partial}{\partial t}T(r,t) \tag{12.15}$$

and the equation of continuity, where $V$ is particle velocity and $v_s$ is the acoustic velocity. In thermal confinement, the thermal elastic equation becomes

$$\rho(r)C_p\frac{\partial}{\partial t}T(r,t) = H(r,t) \tag{12.16}$$

where $H$ is the source term, which can be written as $H = \Psi I(t)$, and $I(t)$ is the temporal illumination function. Considering (12.14)–(12.16) and eliminating $V$, we obtain

$$\rho(r)\nabla \cdot \left(\frac{1}{\rho(r)}\nabla p(r,t)\right) - \frac{1}{v_s^2(r)}\frac{\partial^2}{\partial t^2}p(r,t) = -\frac{\beta}{C_p}\frac{\partial}{\partial t}H(r,t) \tag{12.17}$$

If a homogeneous elastic medium is assumed, equation (12.17) is written

$$\nabla^2 p(r,t) - \frac{1}{v_s^2(r)}\frac{\partial^2}{\partial t^2} p(r,t) = -\frac{\beta}{C_p}\frac{\partial}{\partial t} H(r,t) \tag{12.18}$$

which is the general PA equation. If a homogeneous acoustic field is also assumed, (12.18) is written

$$\nabla^2 p(r,t) - \frac{\partial^2}{v_0^2\,\partial t^2} p(r,t) = -\frac{\beta}{C_p}\frac{\partial}{\partial t} H(r,t) \tag{12.19}$$

where $v_0$ is the uniform velocity within the entire acoustic field. Denoting the following Fourier transform form for acoustic pressure,

$$P(r,\omega) = \int_{-\infty}^{+\infty} p(r,t)\,\exp(-i\omega t)\,dt \tag{12.20}$$

and taking the Fourier transform on the variable $t$ of (12.18), one gets

$$\nabla^2 P(r,\omega) + k_0^2(1+O)P(r,\omega) = \frac{ik_0 v_0 \beta \Psi(r)}{C_p} \tag{12.21}$$

where $P$ is the pressure wave in the frequency domain, $k_0 = \omega/v_0$ is the wave number described by the angular frequency $\omega$ and the speed of the acoustic wave in a reference or coupling medium $v_0$, and $O$ is a coefficient that depends on both acoustic speed and attenuation:

$$O = \frac{v_0^2}{v^2} - 1 + \frac{iAv_0}{k_0 v^2} \tag{12.22}$$

where $v$ is the speed of acoustic wave in the scattering medium or tissue and $A$ is the acoustic attenuation coefficient. We can get the following PA equation in the frequency domain if a homogeneous acoustic field without attenuation is considered:

$$\nabla^2 P(r,\omega) + k_0^2 P(r,\omega) = \frac{ik_0 v_0 \beta \Psi(r)}{C_p} \tag{12.23}$$

## 12.5 FINITE-ELEMENT AND MODEL-BASED PAT RECONSTRUCTION METHODS

Clearly, an effective reconstruction algorithm is critical in model-based PAT. Thus far, several algorithms have been implemented [23–27], most of which have been tested successfully using phantom and in vivo data. However, these algorithms almost all rely on analytical solutions to the PA wave equation in a regularly shaped imaging domain without appropriate boundary conditions applied. The major assumption made in these linear algorithms is that biological tissues are acoustically homogeneous, which may not be true in reality. Thus, this assumption may affect the quality of optical absorption reconstruction, especially for low-contrast cases. In particular, acoustic properties cannot be reconstructed because of this assumption.

We have developed a nonlinear reconstruction algorithm, which is based on the finite-element (FE) solution to the full PA wave equation without the homogeneous acoustic property assumption made thus far in the literature [20,21]. The finite-element method (FEM) has been a powerful numerical method for solving the Helmholtz wave equation because of its computational efficiency and unrivaled ability to accommodate tissue heterogeneity and geometrical irregularity as well as to allow complex boundary conditions and source representations. The FE-based reconstruction algorithm is implemented based on a dual meshing method, which allows us to use a large mesh for accurate forward solution of the PA wave equation, subject to the well-known radiation or absorbing boundary conditions, while a much smaller mesh is used for the inverse solution. This reconstruction approach in PAT is an iterative Newton method with combined Marquardt and Tikhonov regularizations that can provide stable inverse solutions. The approach uses the hybrid regularizations-based Newton method to update an initial optical and acoustic property distribution iteratively in order to minimize an object function composed of a weighted sum of the squared difference between computed and measured data. In addition, the adjoint sensitivity method has also been incorporated in the algorithm, which is able to reduce the computational cost dramatically for calculating the Jacobian matrix involved in nonlinear inverse procedures. Together with an iterative Newton method, this nonlinear algorithm is able to solve the Helmholtz wave equation precisely and to fulfill reliable inverse computation for an arbitrary measurement configuration.

### 12.5.1 Frequency-Domain PAT Reconstruction Algorithm

***Forward Model and Inverse Computation*** Expanding acoustic pressure $P$ as the sum of coefficients multiplied by a set of basis functions, $\psi_j : P = \sum P_j \psi_j$, the finite element discretization of Helmholtz wave equation (12.21) can be written

$$\sum_{j=1}^{N} P_j \left[ \langle \nabla\psi_j \cdot \nabla\psi_i \rangle - \langle k_0^2(1+O)\psi_j\psi_i \rangle - \oint \left( \eta\psi_j + \gamma \frac{\partial^2\psi_j}{\partial\varphi^2} \right) \psi_i \, ds \right]$$

$$= -\langle \frac{ik_0 c_0 \beta \Psi}{C_p \psi_i} \rangle \tag{12.24}$$

where $\eta = (-ik_0 - 3/2\rho + i3/8k_0\rho^2)/(1 - i/k_0\rho)$, $\gamma = (-i/2k_0\rho^2)/(1 - i/k_0 \rho)$, $N$ is the total number of nodes of the finite element mesh, $\langle \cdot \rangle$ indicates integration over the problem domain, $\oint$ expresses integration over the boundary, and the following second-order absorbing boundary conditions have been applied [28]:

$$\nabla P \cdot \hat{n} = \eta P + \gamma \frac{\partial^2 P}{\partial \varphi^2} \tag{12.25}$$

In both the forward and inverse calculations, the unknown coefficients $O$ and $\Psi$ need to be separated into real ($O_R$ and $\Psi_R$) and imaginary ($O_I$ and $\Psi_I$) parts, both of which are expanded in a similar fashion to $P$ as a sum of unknown parameters multiplied by a known spatially varying basis function. The matrix form of (12.24) is expressed as follows:

$$[A]\{P\} = \{B\} \tag{12.26}$$

where

$$\begin{aligned}
A_{ij} &= \langle \nabla\psi_j \cdot \nabla\psi_i \rangle - k_0^2 \langle \psi_j \psi_i \rangle - k_0^2 \left\langle \sum_k O_{R,k} \psi_k \psi_j \psi_i \right\rangle \\
&\quad - ik_0^2 \left\langle \sum_l O_{I,l} \psi_l \psi_j \psi_i \right\rangle - \oint \left( \eta\psi_j + \gamma \frac{\partial^2 \psi_j}{\partial \varphi^2} \right) \psi_i \, ds \\
B_i &= -\frac{I k_0 c_0 \beta \left\langle \sum_k \Psi_{R,k} \psi_k \psi_i \right\rangle}{C_p} + \frac{k_0 c_0 \beta \left\langle \sum_l \Psi_{I,l} \psi_l \psi_i \right\rangle}{C_p} \\
\{P\} &= \{P_1, P_2, \ldots, P_N\}^{\mathrm{T}}
\end{aligned}$$

To form an image from a presumably uniform initial guess of the optical and acoustic property distribution, we use iterative Newton's method to update $O_R$, $O_I$, $\Psi_R$, and $\Psi_I$ from their starting values. In this method, we Taylor-expand $P$ about an assumed $(O_R, O_{I,} \Psi_R, \Psi_I)$ distribution, which is a perturbation away from some other distribution, $(\tilde{O}_R, \tilde{O}_I, \tilde{\Psi}_R, \tilde{\Psi}_I)$, such that a discrete set of $P$ values can be expressed as

$$\begin{aligned}
P(\tilde{O}_R, \tilde{O}_I, \tilde{\Psi}_R, \tilde{\Psi}_I) &= P(O_R, O_I, \Psi_R, \Psi_I) + \frac{\partial P}{\partial O_R} \Delta O_R + \frac{\partial P}{\partial O_I} \Delta O_I \\
&\quad + \frac{\partial P}{\partial \Psi_R} \Delta \Psi_R + \frac{\partial P}{\partial \Psi_I} \Delta \Psi_I + \cdots
\end{aligned} \tag{12.27}$$

where $\Delta O_R = \tilde{O}_R - O_R$, $\Delta O_I = \tilde{O}_I - O_I$, $\Delta \Psi_R = \tilde{\Psi}_R - \Phi_R$, and $\Delta \Psi_I = \tilde{\Psi}_I - \Phi_I$. If the assumed optical and acoustic property distribution is close to the true profile, the left-hand side of (12.27) can be considered as true data (observed or measured), and the relationship can be truncated to yield

$$\boldsymbol{J}\,\Delta\chi = \boldsymbol{P}^o - \boldsymbol{P}^c \tag{12.28}$$

where

$$\boldsymbol{J} = \begin{bmatrix} \partial P_1/\partial O_{R,1} & \cdots & \partial P_1/\partial O_{R,K} & \partial P_1/\partial O_{I,1} & \cdots & \partial P_1/\partial O_{I,L} & \partial P_1/\partial \Psi_{R,1} & \cdots & \partial P_1/\partial \Psi_{R,K} & \partial P_1/\partial \Psi_{I,1} & \cdots & \partial P_1/\partial \Psi_{I,L} \\ \partial P_2/\partial O_{R,1} & \cdots & \partial P_2/\partial O_{R,K} & \partial P_2/\partial O_{I,1} & \cdots & \partial P_2/\partial O_{I,L} & \partial P_2/\partial \Psi_{R,1} & \cdots & \partial P_2/\partial \Psi_{R,K} & \partial P_2/\partial \Psi_{I,1} & \cdots & \partial P_2/\partial \Psi_{I,L} \\ \vdots & \ddots & \vdots & \vdots & \ddots & \vdots & \vdots & \ddots & \vdots & \vdots & \ddots & \vdots \\ \partial P_M/\partial O_{R,1} & \cdots & \partial P_M/\partial O_{R,K} & \partial P_M/\partial O_{I,1} & \cdots & \partial P_M/\partial O_{I,L} & \partial P_M/\partial \Psi_{R,1} & \cdots & \partial P_M/\partial \Psi_{R,K} & \partial P_M/\partial \Psi_{I,1} & \cdots & \partial P_M/\partial \Psi_{I,L} \end{bmatrix}$$

$$\Delta\chi = (\Delta O_{R,1}, \Delta O_{R,2}, \ldots, \Delta O_{R,K}, \Delta O_{I,1}, \Delta O_{I,2}, \ldots, \Delta O_{I,L}, \Delta\Psi_{R,1}, \Delta\Psi_{R,2}, \ldots, \Delta\Psi_{R,K}, \Delta\Psi_{I,1}, \Delta\Psi_{I,2}, \ldots, \Delta\Psi_{I,L})^{\mathrm{T}}$$

$$\boldsymbol{P}^o = (P_1^o, P_2^o, \ldots, P_M^o)^{\mathrm{T}}$$
$$\boldsymbol{P}^c = (P_1^c, P_2^c, \ldots, P_M^c)^{\mathrm{T}}$$

and $P_i^o$ and $P_i^c$ are measured and calculated based on the assumed $(O_R, O_I, \Psi_R, \Psi_I)$ distribution data for $i = 1, 2, \ldots, M$ locations. $O_{R,k}$ $(k = 1, 2, \ldots, K)$ and $O_{i,l}$ $(l = 1, 2, \ldots, L)$ are the reconstruction parameters for the acoustic property profile, while $\Psi_{R,k}$ $(k = 1, 2, \ldots, K)$ and $\Psi_{I,l}$ $(l = 1, 2, \ldots, L)$ are the reconstruction parameters for the optical property profile. In order to realize an invertible system of equations for $\Delta\chi$, (12.28) is left-multiplied by the transpose of $\boldsymbol{J}$ to produce

$$(\boldsymbol{J}^{\mathrm{T}}\boldsymbol{J} + \lambda\boldsymbol{I})\,\Delta\chi = \boldsymbol{J}^{\mathrm{T}}(\boldsymbol{P}^o - \boldsymbol{P}^c) \tag{12.29}$$

where regularization schemes are invoked to stabilize the decomposition of $\boldsymbol{J}^{\mathrm{T}}\boldsymbol{J}$; $\boldsymbol{I}$ is the identity matrix and $\lambda$ is the regularization parameter determined by combined Marquardt and Tikhonov regularization schemes. We have found that when $\lambda = (\boldsymbol{P}^o - \boldsymbol{P}^c) \times \text{trace}\,[\boldsymbol{J}^{\mathrm{T}}\boldsymbol{J}]$, the reconstruction algorithm generates the best results for PAT image reconstruction. The process now involves determining the calculated scattering field data and Jacobian matrix using a dual meshing scheme coupled with an adjoint sensitivity method. The reconstruction algorithm here uses the hybrid regularization-based Newton method to update an initial (guess) optical and acoustic property distribution iteratively via the solution of (12.26) and (12.29) so that an object function composed of a weighted sum of the squared difference between computed and measured acoustic pressures for all acoustic frequencies and optical wavelengths can be minimized.

If an acoustic homogeneous medium is assumed, the discrete matrix equations for the forward and inverse solutions can be simplified as follows:

$$[A]\{P\} = \{B\}, \qquad (\boldsymbol{J}^{\mathrm{T}}\boldsymbol{J} + \lambda\boldsymbol{I})\,\Delta\chi = \boldsymbol{J}^{\mathrm{T}}(\boldsymbol{P}^o - \boldsymbol{P}^c) \tag{12.30}$$

in which the elements of matrix $\boldsymbol{A}$, $\boldsymbol{B}$, and $\Delta\chi$ are written

$$A_{ij} = \langle \nabla\psi_j \cdot \nabla\psi_i \rangle - k_0^2 \langle \psi_j \psi_i \rangle - \oint \left( \eta\psi_j + \gamma \frac{\partial^2 \psi_j}{\partial \varphi^2} \right) \psi_i \, ds \tag{12.31}$$

$$B_i = -\frac{I k_0 c_0 \beta \left\langle \sum_k \Phi_{R,k} \psi_k \psi_i \right\rangle}{C_p} + \frac{k_0 c_0 \beta \left\langle \sum_l \Psi_{I,l} \psi_l \psi_i \right\rangle}{C_p} \tag{12.32}$$

$$\Delta\chi = (\Delta\Psi_{r,1}, \Delta\Psi_{r,2}, \ldots, \Delta\Psi_{r,nn}, \Delta\Psi_{i,1}, \Delta\Psi_{i,2}, \ldots, \Delta\Psi_{i,nn})^{\mathrm{T}} \tag{12.33}$$

The Jacobian matrix formed by $\partial P/\partial \Psi$ along the boundary measurement sites can be computed using the following matrix equations:

$$\begin{bmatrix} A_r & -A_i \\ A_i & A_r \end{bmatrix} \begin{bmatrix} \partial P_r/\partial \Psi_r \\ \partial P_i/\partial \Psi_r \end{bmatrix} = \begin{bmatrix} 0 & -\partial B_i/\partial \Psi_r \\ \partial B_i/\partial \Psi_r & 0 \end{bmatrix} \begin{bmatrix} 1 \\ 0 \end{bmatrix} \tag{12.34}$$

$$\begin{bmatrix} A_r & -A_i \\ A_i & A_r \end{bmatrix} \begin{bmatrix} \partial P_r/\partial \Psi_i \\ \partial P_i/\partial \Psi_i \end{bmatrix} = \begin{bmatrix} 0 & -\partial B_i/\partial \Psi_i \\ \partial B_i/\partial \Psi_i & 0 \end{bmatrix} \begin{bmatrix} 0 \\ 1 \end{bmatrix} \tag{12.35}$$

where the symbols $r$ and $i$ denote the real and imagery part of the matrix.

### *Numerical Strategies*

*Dual-Meshing Scheme* Realizing the fact that acoustic fields at megahertz frequencies change rapidly while tissue optical and acoustic property distributions are usually relatively uniform, we have implemented a dual-meshing method for fast, yet accurate inverse computation. The dual-meshing scheme exploits two separate meshes: one fine mesh for accurate wave propagation and one coarse mesh for parameter recovery. This dual-meshing scheme allows a significant reduction of the problem size during the reconstruction, thus increasing overall computational efficiency. In fact, the idea of dual meshing has been implemented in optical image reconstruction, where this method has proved to be able to significantly enhance the quality of image reconstruction [29]. Here we present the implementation of this method in PAT reconstruction.

Implementation of the dual-meshing scheme affects two components of the reconstruction algorithm: (1) the forward solution at each iteration for the scattering pressure field, where the acoustic and optical property profiles are defined on the coarse mesh while the forward solution calculation is based on the fine mesh, and (2) calculation of the Jacobian matrix, which is used to update the acoustic and optical property profile estimates during the inverse solution procedure. Thus, for the forward solution, the inner product, $\langle\cdot\rangle$, in (12.26) is performed over the elements of the fine mesh, while $O_R$, $O_I$, $\Psi_R$, and $\Psi_I$ need to be expanded in the basis functions that are defined over the coarse mesh. For example, for an arbitrary node $i$ of the fine mesh which is embedded in a coarse mesh element with nodes $L_1$, $L_2$, and $L_3$, the values of $O_R$ and $O_I$ at node $i$ become

$$\begin{aligned} O_R(x_i, y_i) &= \sum_{n=1}^{3} O_{R,Ln}\phi_{Ln}(x, y) \\ O_I(x_i, y_i) &= \sum_{n=1}^{3} O_{I,Ln}\phi_{Ln}(x, y) \end{aligned} \tag{12.36}$$

where $\phi_{Ln}$ is the Lagrangian basis function over the coarse mesh.

The second impact of the dual-meshing method appears during the construction of Jacobian matrix, $\boldsymbol{J}$, which is used to update the object profile values. The elements of $\boldsymbol{J}$ are composed of the partial derivatives of the scattering field at the observation sites with respect to the values of $O_R$, $O_I$, $\Psi_R$, and $\Psi_I$ at each node within the coarse mesh. Considering the impact of the dual meshing, the elements of Jacobian matrix can be written

$$\begin{aligned} &\frac{\partial A_{ij}}{\partial O_{R,k}} = \langle -k_0^2\phi_k\psi_i\psi_j\rangle \qquad &&\frac{\partial A_{ij}}{\partial O_{I,l}} = \langle -ik_0^2\phi_l\psi_i\psi_j\rangle \\ &\frac{\partial A_{ij}}{\partial \Psi_{R,k}} = \left\langle \frac{-ik_0c_0\beta\phi_k\psi_i}{C_p}\right\rangle \qquad &&\frac{\partial A_{ij}}{\partial \Psi_{I,l}} = \left\langle \frac{k_0c_0\beta\phi_l\psi_i}{C_p}\right\rangle \end{aligned} \tag{12.37}$$

where $k$ and $\ell$ are the nodes on the coarse mesh, $\phi_k$ and $\phi_\ell$ are the basis functions centered on nodes $k$ and $\ell$ in this mesh, and the inner products are still performed over the elements in the fine mesh. Since $\phi_k$ and $\psi_i$ are defined on the coarse and fine mesh, respectively, evaluating these inner products can be quite involved. A way to simplify these integrations is to generate the fine mesh from the coarse mesh by splitting the coarse elements into fine elements.

*Adjoint Sensitivity Method* The coupled complex adjoint sensitivity method can be utilized to efficiently determine the Jacobian matrix [30]. Direct differentiation of both sides of (12.26) with respect to $O_R$ and $\Psi_R$ gives, respectively,

$$[A]\left\{\frac{\partial P}{\partial O_R}\right\} = -\left[\frac{\partial A}{\partial O_R}\right]\{P\} \tag{12.38b}$$

$$[A]\left\{\frac{\partial P}{\partial \Psi_R}\right\} = \left\{\frac{\partial B}{\partial \Psi_R}\right\} - \left[\frac{\partial A}{\partial \Psi_R}\right]\{P\} \tag{12.38c}$$

An equivalent set of equations can be obtained for differentiation with respect to $O_I$ and $\Psi_I$ by replacing $O_R$ with $O_I$ in (12.38a) and $\Psi_R$ with $\Psi_I$ in (12.38b). The Jacobian matrix can be calculated through several steps. First, we define a $N \times M$ matrix $\Xi$, and let $\Xi$ satisfy the following relationship:

$$[A]^{\mathrm{T}}[\Xi] = [\Delta_d] \tag{12.39}$$

where the vector $\Delta_d$ has the unit value at the measurement sites or nodes and zero at other nodes. Then we left multiply (12.38a) and (12.38b) with the transpose of $[\Xi]$,

$$[\Xi]^{\mathrm{T}}[A]\left\{\frac{\partial P}{\partial O_R}\right\} = -[\Xi]^{\mathrm{T}}\left[\frac{\partial A}{\partial O_R}\right]\{P\}$$

$$[\Xi]^{\mathrm{T}}[A]\left\{\frac{\partial P}{\partial \Psi_R}\right\} = [\Xi]^{\mathrm{T}}\left\{\frac{\partial B}{\partial \Psi_R}\right\} - [\Xi]^{\mathrm{T}}\left[\frac{\partial A}{\partial \Psi_R}\right]\{P\} \tag{12.40}$$

Equations (12.40a) and (12.40b) can be written further:

$$\left\{\frac{\partial P}{\partial O_R}\right\}^{\mathrm{T}}[A]^{\mathrm{T}}[\Xi] = -\{P\}^{\mathrm{T}}\left[\frac{\partial A}{\partial O_R}\right]^{\mathrm{T}}[\Xi]$$

$$\left\{\frac{\partial P}{\partial \Psi_R}\right\}^{\mathrm{T}}[A]^{\mathrm{T}}[\Xi] = \left\{\frac{\partial B}{\partial \Psi_R}\right\}^{\mathrm{T}}[\Xi] - \{P\}^{\mathrm{T}}\left[\frac{\partial A}{\partial \Psi_R}\right]^{\mathrm{T}}[\Xi] \tag{12.41}$$

Inserting (12.39) into (12.41a) and (12.41b), we get

$$\left\{\frac{\partial P}{\partial O_R}\right\}^{\mathrm{T}} = -\{P\}^{\mathrm{T}}\left[\frac{\partial A}{\partial O_R}\right]^{\mathrm{T}}[\Xi], \left\{\frac{\partial P}{\partial \Psi_R}\right\}^{\mathrm{T}}$$

$$= \left\{\frac{\partial B}{\partial \Psi_R}\right\}^{\mathrm{T}}[\Xi] - \{P\}^{\mathrm{T}}\left[\frac{\partial A}{\partial \Psi_R}\right]^{\mathrm{T}}[\Xi] \tag{12.42}$$

Now we can tell immediately that the left-hand side of the equations above actually gives the corresponding elements in the relative Jacobian matrix based on the adjoint sensitivity method:

$$\left\{\frac{\partial P}{\partial O_R}\right\} = -[\Xi]^{\mathrm{T}}\left[\frac{\partial A}{\partial O_R}\right]\{P\}, \quad \left\{\frac{\partial P}{\partial \Psi_R}\right\} = [\Xi]^{\mathrm{T}}\left\{\frac{\partial B}{\partial \Psi_R}\right\} - [\Xi]^{\mathrm{T}}\left[\frac{\partial A}{\partial \Psi_R}\right]\{P\} \tag{12.43}$$

*Multifrequency Strategy* Since PA signals contain a wide range of frequencies, multifrequency acoustic data can be used to increase the amount of data measured for image enhancement. In this approach, (12.29) is first computed for each frequency, and we get

$$(\boldsymbol{J}_{\omega}^{\mathrm{T}}\boldsymbol{J}_{\omega} + \lambda \boldsymbol{I})\,\Delta\chi = \boldsymbol{J}_{\omega}^{\mathrm{T}}(\boldsymbol{P}_{\omega}^{o} - \boldsymbol{P}_{\omega}^{c}) \tag{12.44}$$

where $\boldsymbol{J}_{\omega}$ is the frequency-dependent Jacobian matrix formed by $\frac{\partial P}{\partial O_{R,I}}$ and $\frac{\partial P}{\partial \Psi_{R,I}}$ at each frequency, and $P_{\omega}^{o}$ and $P_{\omega}^{c}$ are the frequency-dependent measured and calculated acoustic pressures. Then the submatrix of the Jacobian for each frequency is assembled to form the full Jacobian matrix.

### *Reconstructed Results*

**Example 1: Chicken Bone Phantom Experiments** Chicken bone phantom experiments were first performed to evaluate our reconstruction algorithms using the PAT imaging system described in Section 12.7. A homogeneous acoustic field was assumed for our reconstructions. We performed the experiments using two different pairs of chicken bones of different shapes and sizes (see Figure 12.2a and 12.2c for the geometry of the chicken bone experiments). In the tests we embedded the bones in a 25-mm-diameter solid cylindrical phantom (1% Intralipid + india ink + distilled water + agar powder). We then immersed the object-bearing solid phantom in a 110-mm-diameter water background. The acoustic data were taken at 120 positions when the receiver was scanned circularly over 360°. All reconstructions were performed with a fine mesh of 20,081 nodes and 39,680 triangular elements for the forward computation and a coarse mesh of 1301 nodes and 2480 triangular elements for the inverse calculation. Figure 12.2b and 12.2d display the reconstructed PA images for two different pairs of chicken bones. We see that the arbitrary shape and size of the bones are

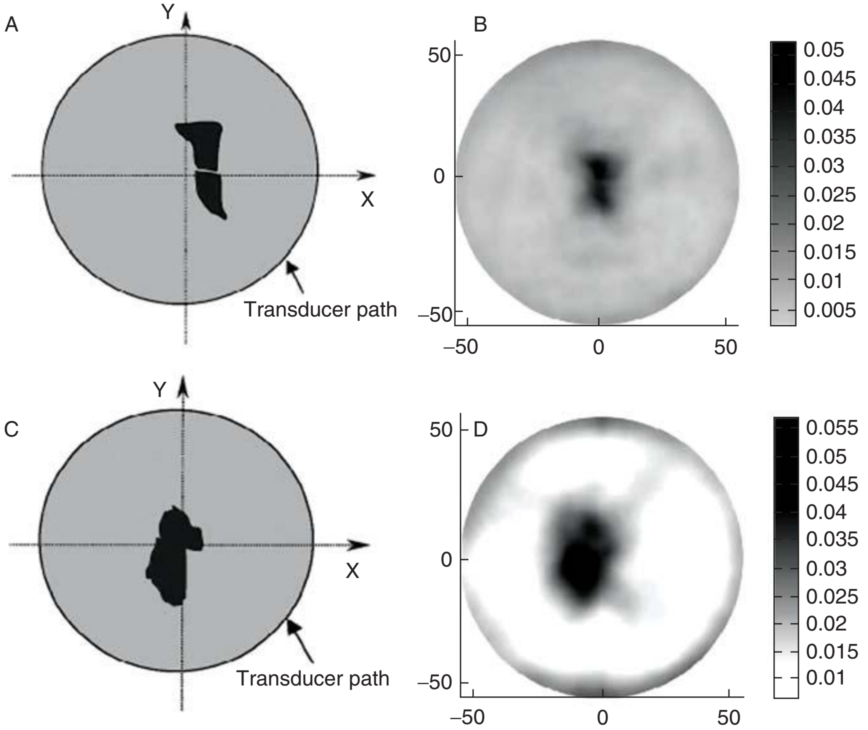

FIGURE 12.2 (a,c) Test geometry of the chicken bone experiments; (b,d) reconstructed absorbed energy density images for two pairs of chicken bones. (From [18], with permission.)

imaged correctly. We also note that the joint between the two bones is detectable for both cases.

**Example 2: Nanoparticles Phantom Experiments** In this example we first embedded one or two nanoparticle-containing objects in a 10- or 25-mm-diameter solid cylindrical Intralipid/ink phantom. For a two-target case, each target contained 0.5-nM nanoparticles. For a one-target case, the target had only 0.25-nM nanoparticles. We then immersed the object-bearing solid phantom in a 110-mm-diameter water background. The gold nanoparticles had an average diameter of 20 nm. These gold nanoparticles exhibit a strong plasma resonance peak around 530 nm. The molar extinction coefficient of the nanoparticles was determined to be $1 \times 10^9$ $M^{-1}$ $cm^{-1}$, about three orders of magnitude larger than that of a typical organic molecule. The nanoparticle concentration used in our experiments ranged from 0.25 to 0.5 nM, which gave an absorption coefficient of the object of 0.025 to 0.05 $mm^{-1}$. While we used these nanoparticles for this phantom study, we believe that they are excellent candidates as contrast agent for PAT. Figure 12.3a and 12.3b present the reconstructed absorbed energy density and

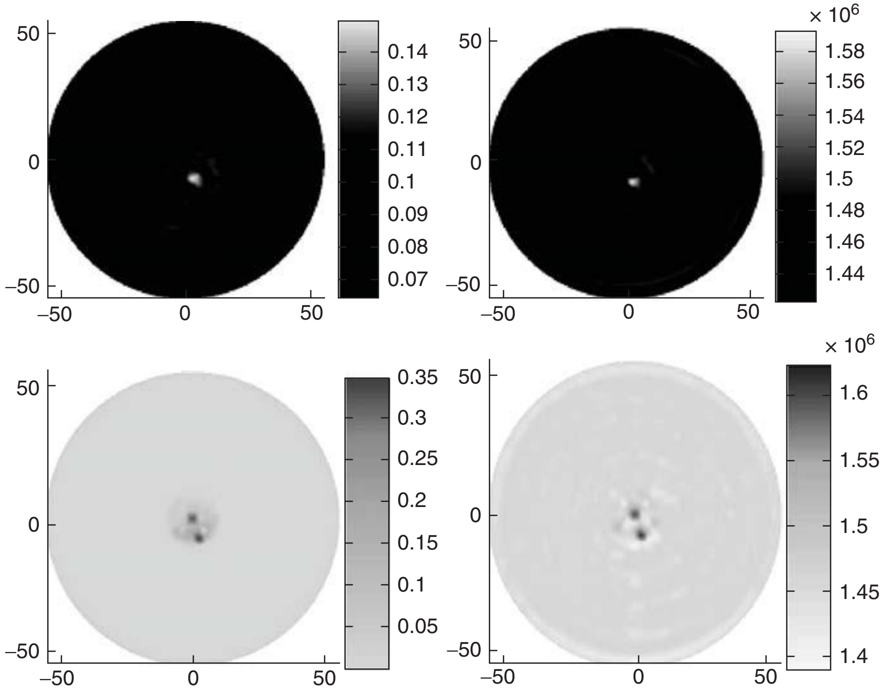

**FIGURE 12.3** Reconstructed absorbed light energy density (the first column) and acoustic speed (the second column) images. The axes (left and bottom) illustrate the spatial scale, in millimeters, whereas the gray scale (right) records the acoustic speed, in mm/s, or absorbed optical energy density, in a relative unit. (a) One-target test case; (b) two-target test case. (After [21], with permission.)

acoustic speed for one- and two-target cases, respectively. By estimating the full width half maximum (FWHM) of the acoustic speed, we found that the recovered diameter size of these objects ranges from 2.8 to 3.3 mm, in good agreement with the actual object size of 3 mm. The images were recovered using measured acoustic data at one optical wavelength.

### 12.5.2 Time-Domain PAT Aeconstruction Algorithm

***Forward Model and Inverse Computation*** In the time domain, the PA wave equation in tissue can be described by the following Helmoholtz-like equation for an acoustically homogeneous medium:

$$\nabla^2 p(\boldsymbol{r}, t) - \frac{1}{v_0^2}\frac{\partial^2 p(\boldsymbol{r}, t)}{\partial t^2} = -\frac{\beta}{C_p}\frac{\partial \Theta(\boldsymbol{r}, t)}{\partial t} \tag{12.45}$$

where $\Theta$ is the time- and space-dependent light intensity and is written

$$\Theta(\boldsymbol{r}, t) = \Psi(\boldsymbol{r}) I(t) \tag{12.46}$$

where $\Psi(\boldsymbol{r})$ and $I(t)$ are, respectively, the space- and time-related parts of the incident pulsed laser source. The wave equation (12.45) then becomes

$$\nabla^2 p(\boldsymbol{r}, t) - \frac{1}{v_0^2}\frac{\partial^2 p(\boldsymbol{r}, t)}{\partial t^2} = -\frac{\beta \Psi(\boldsymbol{r})}{C_p}\frac{\partial I(t)}{\partial t} \tag{12.47}$$

Expanding $p$ as the sum of coefficients multiplied by a set of basis function $\psi_j$, $p = \sum \psi_j p_j$, the finite-element discretization of (12.47) is written

$$\sum_{j=1}^{N} p_j \left[\int_S \nabla\psi_i \cdot \nabla\psi_j \, dS\right] + \sum_{j=1}^{N} \frac{\partial^2 p_j}{\partial^2 t}\left[\int_S \frac{1}{v_0^2}\psi_i \psi_j \, dS\right] - \oint_l \psi_i \nabla p \cdot \hat{n} \, dl = \int_S \frac{\beta\Psi}{C_P}\frac{\partial I}{\partial t}\psi_i \, dS \tag{12.48}$$

The Bayliss–Turkel radiation boundary conditions are employed here:

$$B_m p = 0 \tag{12.49}$$

where $B_m$ is a sequence of linear differential operators,

$$B_m = \prod_{l=1}^{m}\left(\frac{1}{v_0}\frac{\partial}{\partial t} + \frac{\partial}{\partial r} + \frac{4l-3}{2r}\right) \tag{12.50}$$

and $B_m$ is subject to the accuracy

$$B_m = O\left(\frac{1}{r^{2m+1+1/2}}\right) \tag{12.51}$$

This method provides an even more accurate approximation of the Sommerfeld radiation condition by annihilating higher-order terms in $1/r$. However, the higher-order (i.e., $m > 2$) boundary operators are not recommended for numerical implementation since they tend to spoil the sparsity of the finite element matrix. As such, the first-order absorbing boundary operator method is written

$$B_1 p = \frac{\partial p}{\partial r} + \frac{1}{v_0}\frac{\partial p}{\partial t} + \frac{p}{2r} = 0 \tag{12.52}$$

The boundary term based on (12.52) is rewritten

$$\nabla p \cdot \hat{n} = -\frac{1}{v_0}\frac{\partial p}{\partial t} - \frac{p}{2r} \tag{12.53}$$

In both the forward and inverse calculations, the unknown coefficients $\Psi$ need to be expanded in a similar fashion to $p$ as a sum of unknown parameters multiplied by a known spatially varying basis function. Thus, Eq. (12.48) can be expressed as the following matrix form in consideration of Eq. (12.53),

$$[K]\{p\} + [C]\{\dot{p}\} + [M]\{\ddot{p}\} = [B] \tag{12.54}$$

where the elements of the matrix are written

$$\begin{aligned}
K_{ij} &= \int_S \nabla\psi_i \cdot \nabla\psi_j \, dS + \frac{1}{2r}\oint_l \psi_i\psi_j \, dl \\
C_{ij} &= \frac{1}{v_0}\oint_l \psi_i\psi_j \, dl \\
M_{ij} &= \frac{1}{v_0^2}\int_S \psi_i\psi_j \, dS \\
B_i &= \frac{\beta}{C_p}\int_S \psi_i \left(\sum_k \psi_k\Psi_k\right) dS \cdot \frac{\partial I}{\partial t} \\
\{p\} &= \{p_1, p_2, \cdots, p_N\}^{\mathrm{T}} \\
\{\dot{p}\} &= \left\{\frac{\partial p_1}{\partial t}, \frac{\partial p_2}{\partial t}, \cdots, \frac{\partial p_n}{\partial t}\right\}^{\mathrm{T}} \\
\{\ddot{p}\} &= \left\{\frac{\partial^2 p_1}{\partial^2 t}, \frac{\partial^2 p_2}{\partial^2 t}, \cdots, \frac{\partial^2 p_n}{\partial^2 t}\right\}^{\mathrm{T}}
\end{aligned}$$

The time-dependent finite-element matrix equation (12.54) is discretized in time by Newmark's time-stepping scheme.

As to the inverse computation, the iterative Newton's method is used to update the initial value $\Psi_0$. In this method we Taylor-expand $p$ about an assumed $\Psi$

distribution, which is a perturbation away from another distribution $\tilde{\Psi}$, such that a discrete set of $p$ values can be expressed as

$$p_i(\tilde{\Psi}_1, \tilde{\Psi}_2, \cdots, \tilde{\Psi}_N) = p_i(\Psi_1, \Psi_2, \cdots, \Psi_N) + \frac{\partial p_i}{\partial \Psi_1}\Delta\Psi_1 + \frac{\partial p_i}{\partial \Psi_2}\Delta\Psi_2 + \cdots + \frac{\partial p_i}{\partial \Psi_N}\Delta\Psi_N \tag{12.55}$$

where $\Delta\Psi_j = \tilde{\Psi}_j - \Psi_j$, $j = 1, 2, \cdots, N$. If the assumed acoustic pressure distribution is close to the true profile (observed or measured), the relationship can be truncated to yield

$$\boldsymbol{J}\,\Delta\chi = \boldsymbol{P}^o - \boldsymbol{P}^c \tag{12.56}$$

where

$$\boldsymbol{J} = \begin{bmatrix} \frac{\partial p_1}{\partial \Psi_1} & \frac{\partial p_1}{\partial \Psi_2} \cdots & \frac{\partial p_1}{\partial \Psi_N} \\ \frac{\partial p_2}{\partial \Psi_1} & \frac{\partial p_2}{\partial \Psi_2} \cdots & \frac{\partial p_2}{\partial \Psi_N} \\ \vdots & \vdots & \\ \frac{\partial p_N}{\partial \Psi_1} & \frac{\partial p_N}{\partial \Psi_2} \cdots & \frac{\partial p_N}{\partial \Psi_N} \end{bmatrix}$$

$$\Delta\Psi = (\Delta\Psi_1, \Delta\Psi_2, \cdots, \Delta\Psi_N)^{\mathrm{T}}$$

$$\boldsymbol{p}^o = (p_1^o, p_2^o, \cdots, p_M^o)^{\mathrm{T}}$$

$$\boldsymbol{p}^c = (p_1^c, p_2^c, \cdots, p_M^c)^{\mathrm{T}}$$

and $p_i^o$ and $p_i^c$ are the real data measured and calculated for $i = 1, 2, \ldots, M$ boundary measurement locations, while $\Psi_k (k = 1, 2, \ldots, N)$ are the reconstruction parameters for the absorbed energy density profile. To realize an invertible system of equations for $\Delta\chi$, (12.56) is left-multiplied by the transpose of $\boldsymbol{J}$ to produce

$$(\boldsymbol{J}^{\mathrm{T}}\boldsymbol{J} + \lambda\boldsymbol{I})\Delta\chi = \boldsymbol{J}^{\mathrm{T}}(\boldsymbol{p}^o - \boldsymbol{p}^c) \tag{12.57}$$

where regularization schemes are invoked to stabilize the decomposition of $\boldsymbol{J}^{\mathrm{T}}\boldsymbol{J}$, $\boldsymbol{I}$ is the identity matrix, and $\lambda$ is the regularization parameter determined by combined Marquardt and Tikhonov regularization schemes.

The reconstruction algorithm here uses the hybrid regularization-based Newton method to update an initial optical property distribution iteratively via the solution of (12.54) and (12.57) so that an object function composed of a weighted sum of the squared difference between computed and measured acoustic pressures for all time steps can be minimized. In this algorithm, multiple time-sequence measurements are used to increase the amount of data measured for image enhancement. For each time sequence, Eq. (12.57) is computed and is rewritten

$$(\boldsymbol{J}_t^{\mathrm{T}}\boldsymbol{J}_t + \lambda \boldsymbol{I})\Delta\chi = \boldsymbol{J}_t^{\mathrm{T}}(\boldsymbol{p}_t^o - \boldsymbol{p}_t^c) \tag{12.58}$$

where $\boldsymbol{J}_t$ is the time-dependent Jacobian matrix formed by $\partial p/\partial\Psi$ at each time sequence, and $p_t^{o,c}$ are the time-dependent measured and calculated acoustic fields. Here the submatrix of the Jacobian for each time sequence is assembled to form the full Jacobian matrix for all time steps. Thus, we just need to solve (12.58) one time per iteration for the entire time range of interest.

***Reconstructed Results*** For the phantom experiments in the time domain, we embedded one or two objects ranging from 1 to 3 mm in diameter in a 50-mm-diameter solid cylindrical Intralipid/ink phantom. We then immersed the object-bearing solid phantom into the water tank. A total of 120 receivers were distributed equally along the transducer scanning surface. We chose $J(t) = \delta(t - t_0)$ as the time-dependent light intensity. The fine mesh used for forward calculations consisted of 23,665 nodes and 46,848 triangular elements, while the coarse mesh used for inverse calculations had 1525 nodes and 2928 triangular elements. Figure 12.4a and 12.4b present the reconstructed absorbed energy density

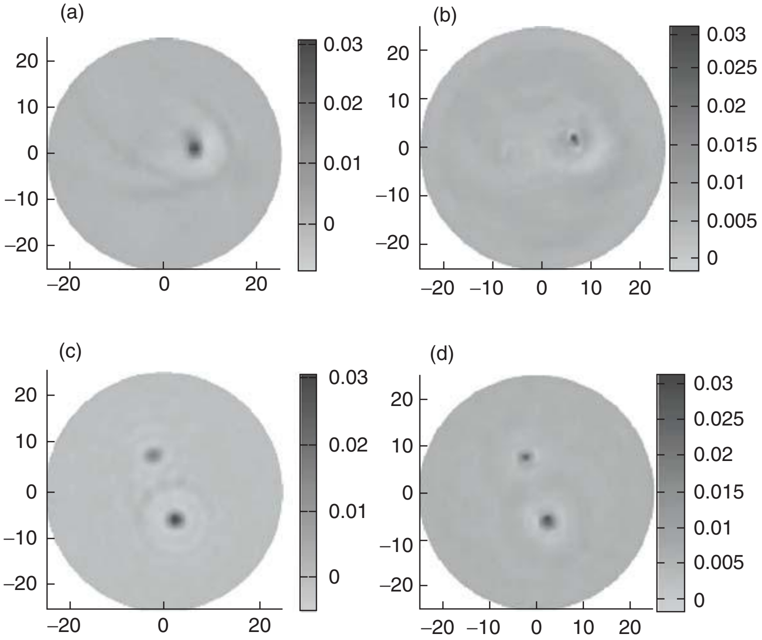

**FIGURE 12.4** Reconstructed absorbed energy density images in the frequency domain (left column) and the time domain (right column). (a,b) One-target case; (c,d) two-target case. (From [5], with permission.)

images of one object having a size of 1.0 mm in the frequency and time domains, respectively, while Figure 12.4c and 12.4d display the images for a two-target case (target diameter in 2 or 3 mm).

## 12.6 QUANTITATIVE PAT

Although conventional PAT can image tissues with high spatial resolution, it provides only the distribution of absorbed light energy density that is the product of both the *intrinsic* optical absorption coefficient and the *extrinsic* optical fluence distribution. Thus, the imaging parameter of conventional PAT is clearly not an intrinsic property of tissue. It is well known, however, that it is the tissue absorption coefficient that correlates directly with tissue physiological and functional information. These physiological parameters, including hemoglobin concentration, blood oxygenation, and water content, are critical for accurate diagnostic decision making. We have described the model-based reconstruction algorithms for PAT in Section 12.5 and validated them using phantom experiments. The algorithms use finite element solutions to the PA wave equation subject to the radiation or absorbing boundary conditions (BCs). Together with regularization techniques, these algorithms are able to offer more accurate inverse solutions to the distribution of absorbed light energy density.

The goal of quantitative PAT is to recover the optical absorption distribution from the absorbed energy density available from conventional PAT. We have developed three algorithms that allow quantitative PAT possible. These algorithms are based on the finite-element solution to the PA wave equation coupled with the photon diffusion equation [4,5,7].

### 12.6.1 Algorithm 1

It is well known that the nonlinear relation between the optical fluence and optical absorption coefficient can be approximated by the photon diffusion equation and type III BCs:

$$\nabla \cdot D(r)\nabla\Phi(r) - \mu_\alpha(r)\Phi(r) = -S(r) \qquad - D\nabla\Phi \cdot n = \alpha\Phi \tag{12.59}$$

where $D(r)$ is the diffusion coefficient and can be stated as $D = 1/[3(\mu_a + \mu')]$, where $\mu'$ is the reduced scattering coefficient. $S$ is the distributed source due to pulsed excitation and $S =$ pulse energy/$\int_{V_1} dV_1$, where $V_1$ is the attenuation volume integrated by the illumination area over penetration depth $1/\mu_{\text{eff}}$ across the subsurface where $\mu_{\text{eff}} = \sqrt{3\mu_a(\mu_a + \mu')}$. As such, if the incident laser source, boundary coefficient $\alpha$, absolute absorbed energy density $\Psi$, and realistic scattering distribution are known in advance, $\mu_a$ can be determined by the following iterative solution procedure using the finite-element method:

1. Choose an initial value for $\mu_a$ (e.g., $\mu_a = 0.0001\ \text{mm}^{-1}$).
2. Compute the optical fluence $\Phi$ using the diffusion equation.

3. Calculate the absorbed energy density by $\Psi^c = \mu_a \Phi$.
4. Compute the error between $\Psi$ and $\Psi^c$, and $\mu_a$ is updated using $\mu_a = \Psi / \Phi$.
5. If the error is sufficiently small, the iterative calculation stops; otherwise, repeat steps 2 to 4 until a small error is reached.

To reduce the boundary noise effect, the absorption coefficient within the boundary domain needs to be assumed.

***Experimental Tests*** Phantom data from the nanoparticle experiments described in Section 12.5 were used to validate Algorithm 1. Figure 12.5a, 12.5b, and 12.5c present the reconstructed absorption coefficient images of two objects having 0.5-, 0.25-, and 0.125-nM nanoparticles in each of the objects, respectively. We see that the object(s) in each case are clearly detected. By estimating the FWHM of the absorption coefficient profiles shown in Figure 12.5, we found that the recovered object size ranged from 2.8 to 3.3 mm, which is in good agreement with the actual object size of 3 mm. Moreover, the nanoparticle concentration used in our experiments (0.125, 0.25, and 0.5 nM) gave an absorption coefficient of the object of 0.01, 0.025, and 0.05 mm$^{-1}$, respectively. As can be seen from Figure 12.5, we are able to obtain quantitatively resolved images in terms of the size as well as the absorption coefficient of the objects.

### 12.6.2 Algorithm 2

The second algorithm also includes two steps. The first is to obtain the map of absorbed light energy density using conventional PAT. The second step is to obtain the distribution of optical fluence using diffusing light measurements along the boundary coupled with a photon diffusion equation–based optimization procedure and to recover the distribution of optical absorption coefficient from the optical fluence and the absorbed energy density obtained from the first step.

The second step is based on the iterative solution of the diffusion equation in (12.59) and the following $\chi^2$ calculation:

$$\chi^2 = \sum_{i=1}^{M} (\Phi_i^{(m)} - \Phi_i^{(c)})^2 \tag{12.60}$$

where $\Phi_i^{(m)}$ and $\Phi_i^{(c)}$ are the measured and calculated optical fluence for $i = 1, 2, \cdots, M$ boundary locations. The goal of the second step is to obtain the distribution of optical fluence within the entire imaging domain through an optimization procedure based on (12.59) and (12.60). This simple least-squares minimization scheme can be explained as follows. Given a range of values of $\mu'$, $\mu_a$, and $S$ (always available empirically), we compute the $\chi^2$ error as a function of $\mu'$, $\mu_a$, and $S$, where $\Phi_i^{(m)}$ is from the measured optical data and $\Phi_i^{(c)}$ is calculated from (12.59). The rationale of this scheme is based on the argument that the minimum of $\chi^2$ corresponds to the effective values of $\mu_s$, $\mu_a$, and $S$

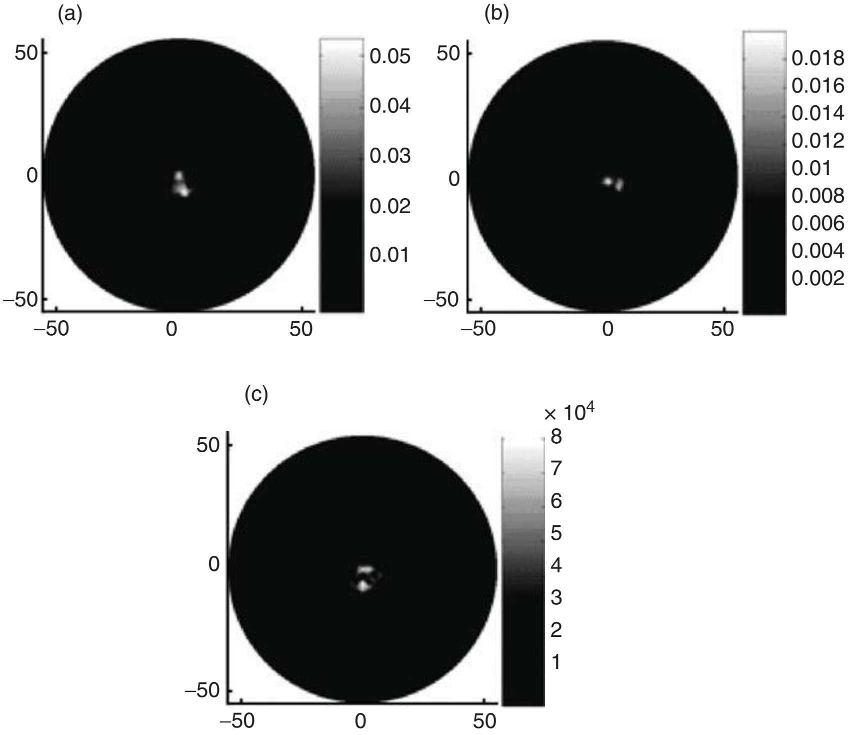

**FIGURE 12.5** Reconstructed optical absorption coefficient images from three experiments; two targets containing (a) 0.5-, (b) 0.25-, and (c) 0.125-nM nanoparticles. The axes (left and bottom) give the spatial scale in millimeters, where the gray scale (right) indicates the optical absorption coefficients in inverse millimeters. (From [5], with permission.)

associated with the medium of interest. The desired distribution of optical fluence, $\Phi$, is calculated from (12.59) with the optimized set of $\mu'$, $\mu_a$, and $S$ in place. Thus, the final distribution of $\mu_a$ is calculated using $\mu_a = \Psi/\Phi$, where $\Psi$ is obtained from the conventional PAT (the first step discussed above).

***Experimental Tests*** Three experiments were conducted to test Algorithm 2. In the experiments we embedded one or two objects ranging from 1 to 3 mm in a 50-mm-diameter solid cylindrical Intralipid/ink phantom. We then immersed the object-bearing solid phantom into the water tank. The absorption coefficient of the background phantom was 0.01 $\text{mm}^{-1}$, while the absorption coefficient of the target(s) was 0.03 $\text{mm}^{-1}$.

Diffusing light was collected along the surface of the phantom using a 2-mm-diameter fiber optic bundle coupled with a 2-GHz-bandwidth high-speed photodetector and recorded by a 2.5-GHz-bandwidth digital oscilloscope. A computer controlled the scanning of the fiber bundle, and 120 optical measurements were conducted and used in the calculation.

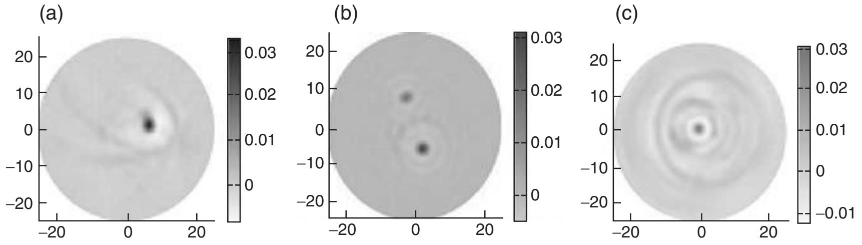

**FIGURE 12.6** Reconstructed optical absorption coefficient images ($\text{mm}^{-1}$); (a) 1-mm-diameter target; (b) two targets (2 and 3 mm in diameter, respectively); (c) 0.5-mm-diameter target. (From [4], with permission.)

Figures 12.6 present the reconstructed optical absorption images of one or two objects of 1.0 (Figure 12.6a), 2.0, and 3.0 mm (Figure 12.6b), and 0.5 mm (Figure 12.6c) in diameter. We see that the object(s) in each case are clearly detected. By estimating the FWHM of the optical absorption property profiles, the recovered objects were 1.1, 1.7, 3.2, and 0.7 mm, which is in good agreement with the actual object size of 1.0, 2.0, 3.0, and 0.5 mm. We also note from Figure 12.6 that the reconstructed images are quantitative in terms of the recovered absorption coefficient value of the objects.

### 12.6.3 Algorithm 3

Although Algorithms 1 and 2 are very effective in recovering optical absorption coefficient, there are certain limitations associated with these approaches. For example, for Algorithm 1, one has to know the exact boundary reflection coefficients as well as the exact strength and distribution of an incident light source, which require careful experimental calibration procedures. It is often difficult to obtain these initial parameters accurately. The use of Algorithm 2 requires diffusing light measurements, making the hardware implementation complicated. In addition, the recovered results for both Algorithms 1 and 2 depend strongly on the accuracy of the distribution of absolute absorbed energy density from conventional PAT. To overcome these limitations, a novel reconstruction approach that combines conventional PAT with a diffusion equation–based regularized Newton method for accurate recovery of optical properties is proposed. This approach is based on the following photon diffusion equation as well as the Robin boundary conditions, in consideration of the absorbed energy density, $\Psi = \mu_a \Phi$:

$$\nabla \cdot D(r)\nabla(E(r)\Psi(r)) - \Psi(r) = -S(r) \tag{12.61}$$

$$-D\nabla(E(r)\Psi) \cdot n = E(r)\alpha\Psi \tag{12.62}$$

where $E(r) = 1/\mu_a(r)$, and $S(r)$ is the incident point or distributed source term. For the inverse computation, the Tikhonov regularization sets up a weighted term as well as a penalty term in order to minimize the squared differences between computed and measured absorbed energy density values,

$$\min_{\chi} \|\boldsymbol{\Psi}^c - \boldsymbol{\Psi}^o\|^2 + \beta\|\boldsymbol{L}[\boldsymbol{E} - \boldsymbol{E}_0]\|^2 \tag{12.63}$$

where **L** is the regularization matrix or filter matrix and β is the regularization parameter. $\Psi^o = (\Psi_1^o, \Psi_2^o, \ldots, \Psi_N^o)^{\mathrm{T}}$ and $\Psi^c = (\Psi_1^c, \Psi_2^c, \ldots, \Psi_N^c)^{\mathrm{T}}$, where $\Psi_i^o$ is the absorbed energy density obtained from PAT, and $\Psi_i^c$ is the absorbed energy density computed from (12.61) and (12.62) for $i = 1, 2\ldots, N$ locations within the entire PAT reconstruction domain. The initial estimate of absorption coefficient can be updated based on the iterative Newton method as follows:

$$\delta\boldsymbol{E} = (\boldsymbol{J}^{\mathrm{T}}\boldsymbol{J} + \lambda\boldsymbol{I} + \beta\boldsymbol{L}^{\mathrm{T}}\boldsymbol{L})^{-1}[\boldsymbol{J}^{\mathrm{T}}(\boldsymbol{\Psi}^o - \boldsymbol{\Psi}^c) - \beta\boldsymbol{L}^{\mathrm{T}}\boldsymbol{L}\boldsymbol{E}] \tag{12.64}$$

where **J** is the Jacobian matrix formed by $\partial\Psi/\partial\mathrm{E}$ inside the entire reconstruction domain, including the boundary zone. The practical update equation resulting from (12.64) is utilized with $\beta = 1$,

$$\Delta(\boldsymbol{E}) = (\boldsymbol{J}^{\mathrm{T}}\boldsymbol{J} + \lambda\boldsymbol{I} + \boldsymbol{L}^{\mathrm{T}}\boldsymbol{L})^{-1}[\boldsymbol{J}^{\mathrm{T}}(\boldsymbol{\Psi}^o - \boldsymbol{\Psi}^c)] \tag{12.65}$$

In addition to the usual Tikhonov regularization, the PAT image (absorbed energy density map) is used both as input data and as prior structural information to regularize the solution so that the ill-posedness associated with such inversion can be reduced. In our reconstruction scheme, the PAT image is first segmented into different regions according to different heterogeneities or tissue types using commercial software. We then employ both the distribution of absorbed energy density in the entire imaging domain and segmented prior structural information for optical inversion. The segmented prior spatial information can be incorporated into the iterative process using the regularization filter matrix **L** shown in (12.65). Laplacian-type filter matrix is employed and constructed according to the region or tissue type with which it is associated based on derived priors. This filter matrix is able to relax the smoothness constraints at the interface between different regions or tissues, in directions normal to their common boundary, so that the covariance of nodes within a region is basically realized. As such, the elements of matrix **L**, $L_{ij}$, is specified as follows [31]:

$$L_{ij} = \begin{cases} 1 & \text{if } i = j \\ -1/NN & \text{if } i, j \subset \text{ one region} \\ 0 & \text{if } i, j \subset \text{ different region} \end{cases} \tag{12.66}$$

where *NN* is the total node number within one region or tissue. It is noted from (12.65) that a hybrid regularization scheme that combines both Levenberg–Marquardt and Tikhonov regularizations are utilized. The optical absorption coefficient distribution is reconstructed through the iterative procedures described by (12.61) and (12.65).

***Experimental Tests*** Two phantom experiments were used to validate Algorithm 3. In the experiments we embedded two objects with a size ranging from 2.0 to 5.5 mm in diameter in a 50-mm-diameter solid cylindrical Intralipid/ink phantom. We then immersed the object-bearing solid phantom into a 110.6-mm-diameter water background. The background phantom had $\mu_a = 0.01$ mm$^{-1}$ and $P\mu' = 1.0$ mm$^{-1}$, while the two targets had $\mu_a = 0.03$ mm$^{-1}$ and $\mu' = 2.0$ mm$^{-1}$ for test 1 and $\mu_a = 0.07$ mm$^{-1}$ and $\mu' = 3.0$ mm$^{-1}$ for test 2. The results from the two sets of experiments are shown in Figure 12.7a and 12.7b, which present the reconstructed absorption coefficient images of two objects 2.0 and 3.0 mm (test 1) and 5.5 mm (test 2) in diameter, respectively, while the recovered absorbed energy density maps for tests 1 and 2 are plotted in Figure 12.7c and 12.7d for comparison. We see that the objects in each case are clearly detected. By estimating the FWHM of the absorption coefficient profiles, the recovered object size was found to be 1.8, 2.7, and 5.0 mm, which is also in good agreement with the actual object size of 2.0, 3.0, and 5.5 mm for tests 1 and 2.

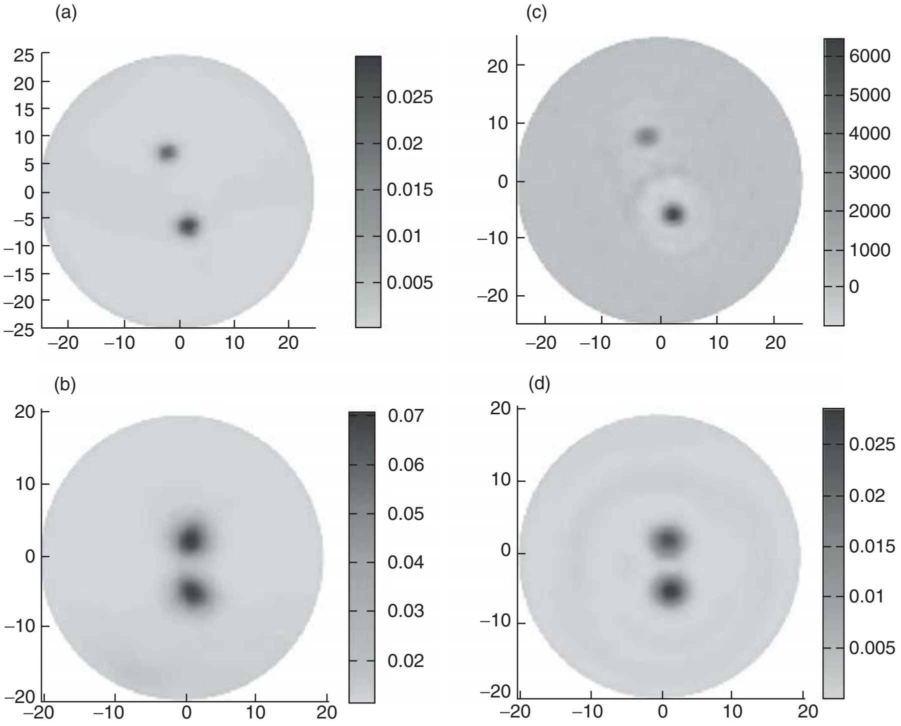
(a)
25
20
15
10
5
0
−5
−10
−15
−20
−25
−20
−10
0
10
20
0.025
0.02
0.015
0.01
0.005
(c)
20
10
0
−10
−20
−20
−10
0
10
20
6000
5000
4000
3000
2000
1000
0
(b)
20
10
0
−10
−20
−20
−10
0
10
20
0.07
0.06
0.05
0.04
0.03
0.02
(d)
20
10
0
−10
−20
−20
−10
0
10
20
0.025
0.02
0.015
0.01
0.005

**FIGURE 12.7** (a,b) Reconstructed absorption coefficient images and (c,d) absorbed light energy density images for tests 1 and 2. Images (a) and (c) are for test 1, and (b) and (d) are for test 2. The axes (left and bottom) illustrate the spatial scale, in millimeters, whereas the gray scale (right) records the absorption coefficient in mm$^{-1}$ or absorbed light energy density in relative units. (From [7], with permission.)

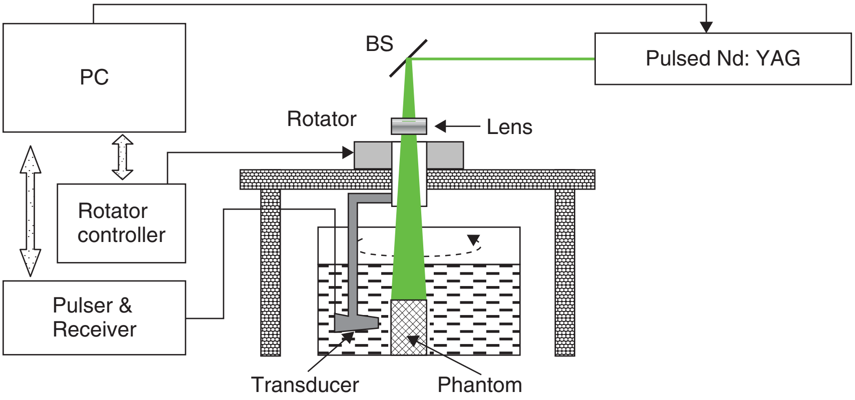

**FIGURE 12.8** Typical PAT system. BS, beamsplitter; PC, personal computer.

## 12.7 PAT IMAGING INSTRUMENTATION

A typical PAT system consists of a pulsed laser source, a singe transducer scanning subsystem or a transducer array, and an acoustic signal detection subsystem (see Figure 12.8). In this system, pulsed light from a Nd:YAG, Ti:sapphire, or diode laser are coupled into the phantom via an optical subsystem and generate acoustic pressure wave. A transducer (1 MHz or higher central frequency) is used to receive the acoustic signals. The transducer and the phantom or tissues are immersed in a water tank. A rotary stage rotates the receiver relative to the center of the tank. One set of data is taken at 120/360 positions when the receiver is scanned circularly over 360°. The complex wavefield signal is first amplified by a preamplifier and then amplified further by a pulser/receiver. A data acquisition board converts it into digital board that is fed to a computer. The entire data acquisition is realized through C programming. In this system, data collection for a total of 120 measurements requires about 2 minutes.

In the typical PAT setup shown above, the mechanical scanning reduces the speed of data acquisition significantly. The use of a transducer array has clear acquisition time advantages over a mechanically scanned system, making real-time data acquisition possible. In addition, a transducer array–based system eliminates the use of a water tank and allows the direct contact of the array with the skin (of course, ultrasound gel needs to be applied as coupling medium). The major drawback of an array-based system, however, is its significantly added cost.

## 12.8 IN VIVO APPLICATIONS

Thus far, PAT has been applied for breast cancer detection, brain imaging, and detection of skin diseases [24,27,32–34]. Here we demonstrate its application in epilepsy imaging, a new application developed in our laboratory [35]. The

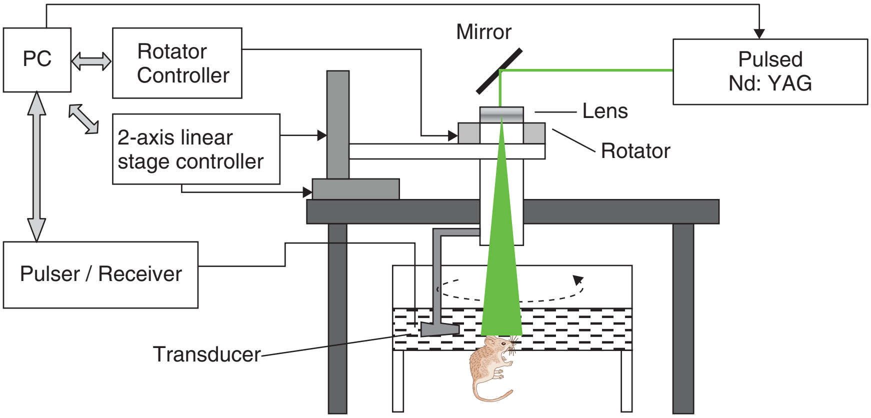

**FIGURE 12.9** In vivo PAT system. (After [35], with permission.)

in vivo results show that PAT can “visualize” seizures accurately in a simple rat model of a focal seizure induced by microinjection of GABA-A antagonist bicucullin methiodide (BMI). For the in vivo experiments, we have modified the laboratory system described above, especially on the animal–transdcer interface. Figure 12.9 shows the schematic of the in vivo system. The light source was a pulsed Nd:YAG laser (Altos, Bozeman, Montana) with a pulse duration of 4 ns and up to 360 mJ of pulse power at a wavelength of 532 nm. The diameter of laser beam was expanded to 30 mm by a lens. The light power was 15 mJ/cm$^2$ at the surface of the rat head. An immersion acoustic transducer with a 1-MHz nominal frequency (Valpey Fisher, Hopkinton, Massachusetts) was driven by a motorized rotator to receive acoustic signals over 360° at an interval of 3°, and thus a total of 120 measurements were performed for one planar scanning. Scanning along the $z$-axis was accomplished by mounting the rotator and the transducer on a platform driven by a linear stage. The acoustic transducer was immersed into the water tank, and the rat head was placed into the imaging region through an opening covered with a piece of polyethylene membrane at the bottom of the tank. The complex wavefield signal was amplified by a pulser/receiver (GE Panametrics, Waltham, Massachusetts) and then was acquired at 100 Ms/s by a high-speed PCI data acquisition board (Gage Applied Tech., Canada). A LabView program controlled the entire system.

Experiments were performed on several rats. In a typical experiment, a 20-day-old male Sprague–Dawley rat was anesthetized with urethane 1 g/kg via intraperitoneal injection. Following anesthesia the rat was place on the PAT testing system. Focal seizure was induced by microinjection of 10 μL of 1.9-mM BMI. EEG measurements (the current gold standard) were conducted to confirm the occurrence of seizure. Two EEG electrodes were placed 2.5 mm away from the location of BMI injection on the surface of the rat brain. The robust high-voltage spike and wave discharge shown in Figure 12.10b confirmed the induced acute seizures (appeared 3 minutes after the injection). Because the animals were

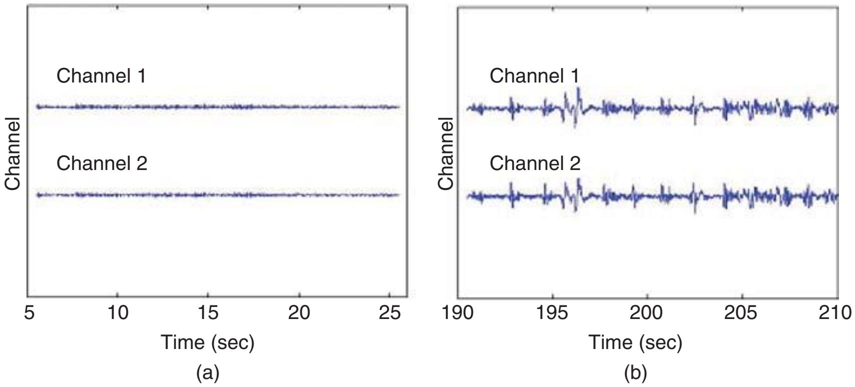

**FIGURE 12.10** EEG signals measured at two different times after BMI injection: (a) 0 minutes; (b) 3 minutes. (After [35], with permission.)

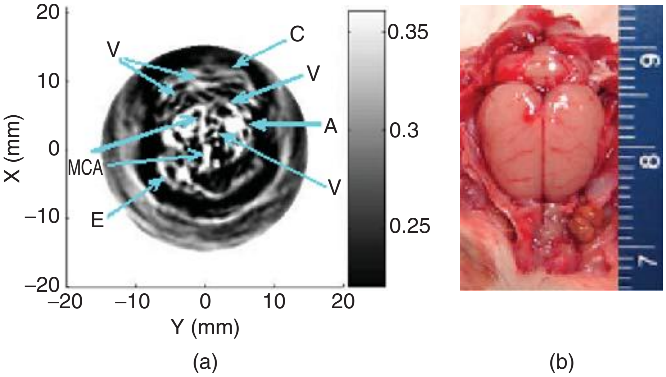

**FIGURE 12.11** (a) Typical PAT image of the rat brain with seizure induced (acquired with the skin and skull intact). A, increased absorption caused by seizure; C, cerebellum; E, the eye; MCA, middle cerebral artery; V, blood vessel. The BMI injection was applied over the left parietal cortex 5.0 mm posterior to bregma and 3.5 mm lateral to the sagittal sinus. (b) Open-skull photograph of the rat brain surface obtained after the PAT experiment for comparison. (After [35], with permission.)

anesthetized, no focal motor seizures could be observed in these animals despite the clear electrographic seizures.

Figure 12.11a shows a typical PAT image of the rat brain 6 minutes after the BI injection (the gray scale shows the optical absorption where lighter regions indicate greater absorption). Various soft tissues in the brain were visible because of their different optical absorption compared to the open-skull photograph after the PAT imaging (Figure 12.11b). Most important, the seizure onset region (ca. 3 mm in size) was clearly detected (indicated by arrow A in Figure 12.11a). The contrast between the seizure onset and surroundings was striking, which

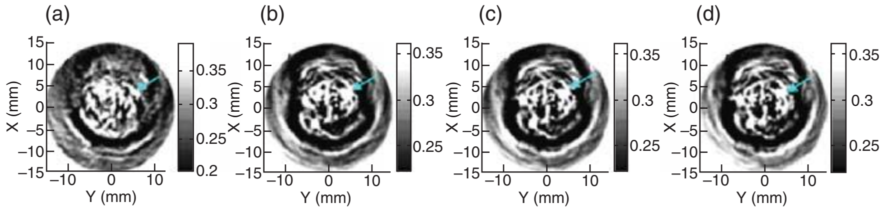

**FIGURE 12.12** PAT images obtained at different times after the BMI injection: (a) 0–5 minutes; (b) 6–10 minutes; (c) 11–15 minutes; (d) 16–20 minutes. (After [35], with permission.)

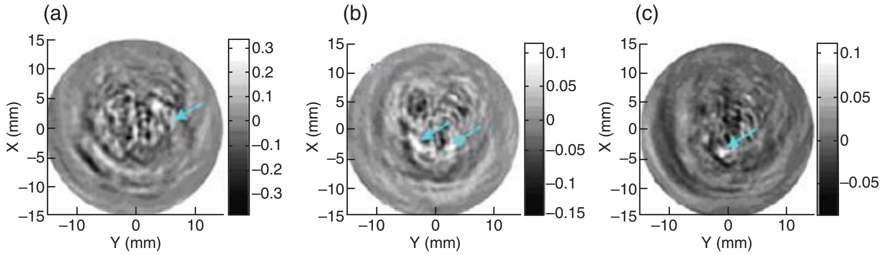

**FIGURE 12.13** Subtraction images from the images shown in Figure 12.12: (a): Figure 12.12a − 12.12b; (b) Figure 12.12b − 12.12c; (c) Figure12c − 12.12d (After [35], with permission.)

was believed to be caused by the increased blood oxygenation and blood volume associated with seizure onset. To make sure that this contrast was indeed due to the seizure onset (not because of the injection of a liquid or physical contractions), we have performed controlled measurements where the rats were injected with 10 μL of saline: no significant increase in absorption was observed at the location of the injection. Figure 12.12 presents PAT images of the rat brain obtained at a series of times after the bmi injection. Again, the seizure onset was clearly visible at each time period (indicated by the arrow). Interestingly, the propagation of the seizure activity was observable by subtracting the images at two different time periods after the seizure onset (see Figure 12.13: The propagation was indicated by arrows). This suggests that it is possible to image the dynamic of seizure activity with PAT.

## REFERENCES

1. Jiang, H., et al., Near-infrared optical imaging of the breast with model-based reconstruction, *Acad. Radiol.*, Vol. 9, 2002, pp. 186–194.
2. Pogue, B.W., et al., Quantitative hemoglobin tomography with diffuse near-infrared spectroscopy: pilot results in the breast, *Radiology*, Vol. 218, 2001, pp. 261–266.
3. Cerussi, A.E., et al., Sources of absorption and scattering contrast for near-infrared optical mammography, *Acad. Radiol.*, Vol. 8, 2001, pp. 211–218.

4. Yin, L., et al., Tomographic imaging of absolute optical absorption coefficient in turbid medium using combing photoacoustic and diffusing light measurements, *Opt. Lett*., Vol. 32, 2007, pp. 2556–2558.
5. Yuan, Z., and Jiang, H., Quantitative photoacoustic tomography: recovery of optical absorption coefficient map of heterogeneous medium, *Appl. Phys. Lett*., Vol. 88, 2006, p. 231101.
6. Cox, B., et al., 2D quantitative photoacoustic image reconstruction of absorption distributions in scattering medium using a simple iterative method, *Appl. Opt*., Vol. 45, 2006, pp. 1866–1875.
7. Yuan, Z., Wang, Q., and Jiang, H., Reconstruction of optical absorption coefficient maps of heterogeneous medium by photoacoustic tomography coupled with diffusion equation based regularized Newton method, *Opt. Express*, Vol. 15, 2007, pp. 18078–18081.
8. Ripoll, J., and Ntziachristos, V., Quantitative point source photoacoustic inversion formulas for scattering and absorbing medium, *Phys. Rev. E,* Vol. 71, 2005, p. 031912.
9. Yuan, Z., Zhang, Q., and Jiang, H., Simultaneously reconstruction of acoustic and optical properties of heterogeneous medium by quantitative photoacoustic tomography, *Opt. Express*, Vol. 14, 2006, pp. 6749–6753.
10. Greenleaf, J.F., and Bahn, R.C., Clinical imaging with transmissive ultrasound computerized tomography, *IEEE Trans. Biomed. Eng*., Vol. 28, 1981, pp. 177–185.
11. Niederhauser, J.J., Real-Time Biomedical Optoacoustic Imaging, Ph.D. dissertation, No. 15572, Swiss Federal Institute of Technology, Zurich, Switzerland,
12. Karabutov, A.A., Savateeva, E., and Oraevsky, A., Imaging of layered structures in biological tissues with opto-acoustic front surface transducer, *Proc. SPIE*, Vol. 3601, 1999, pp. 284–295.
13. Kruger, R.A., Reinecke, D., and Kruger, G., Thermoacoustic computed tomography: technical considerations, *Med. Phys*., Vol. 26, 1999, pp. 1832–1837.
14. Liu, P., The P-transform and photoacoustic image reconstruction, *Phys. Med. Biol*., Vol. 43, 1998, pp. 667–674.
15. Kostli, K.P., et al., Optoacoustic imaging using a three-dimensional reconstruction algorithm, *IEEE J. Sel. Top. Quantum Electron*., Vol. 7, 2001, pp. 918–923.
16. Zhulina, Y.V., Optical statistical approach to optoacoustic image reconstruction, *Appl. Opt*., Vol. 39, 2000, pp. 5971–5977.
17. Chen, Z., Tang, Z., and Wan, W., Photoacoustic tomography imaging based on a 4f acoustic lens imaging systems, *Opt. Express*, Vol. 15, 2007, pp. 4966–4976.
18. Yuan, Z., et al., Finite element-based photoacoustic tomography: phantom and chicken bone experiments, *Appl. Opt*., Vol. 45, 2006, pp. 3177–3183.
19. Yuan, Z., and Jiang, H., Three-dimensional finite element-based photoacoustic tomography: reconstruction algorithm and simulations, *Med. Phys*., Vol. 34, 2007, pp. 538–546.
20. Jiang, H., Yuan, Z., and Gu, X., Spatially varying optical and acoustic property reconstruction using finite element-based photoacoustic tomography, *J. Opt. Soc. Am. A*, Vol. 23, 2006, pp. 878–888.
21. Yuan, Z., et al., Imaging of small nanoparticle-containing objects using finite element–based photoacoustic tomography, *Opt. Lett*., Vol. 30, 2005, pp. 3054–3056.

22. Cox, B.T., Arridge, S.R., and Beard, P.C., $K$-space propagation models for acoustically heterogeneous media: application to biomedical photoacoustics, *J. Acoust. Soc. Am.*, Vol. 121, 2007, pp. 3453–3464.
23. Hoelen, C.G.A., et al., Three-dimensional photoacoustic imaging of blood vessls in tissue, *Opt. Lett.*, Vol. 23, 1998, pp. 648–650.
24. Viator, J.A., et al., Clinical testing of a photoacoustic probe for port wine stain depth determination, *Lasers Surg. Med.*, Vol. 30, 2002, pp. 141–148.
25. Paltauf, G., et al., Iterative reconstruction algorithm for optoacoustic imaging, *J. Acoust. Soc. Am.*, Vol. 112, 2002, pp. 1536–1544.
26. Wang, X., et al., Photoacoustic tomography of biological tissues with high cross-section resolution: reconstruction and experiment, *Med. Phys.*, Vol. 29, 2002, pp. 2799–2805.
27. Yin, B., et al., Fast photoacoustic imaging system based on 320-element linear transducer array, *Phys. Med. Biol.*, Vol. 49, 2004, pp. 1339–1346.
28. Jin, J.M., *The Finite Element Method in Electromagnetics*, Wiley, New York, 2002.
29. Gu, X., Xu, Y., and Jiang, H., Mesh-based enhancement schemes in diffuse optical tomography, *Med. Phys.*, Vol. 30, 2003, pp. 861–869.
30. Fedele, F., Laible, J.P., and Eppstein, M.J., Coupled complex adjoint sensitivities for frequency-domain fluorescence tomography: theory and vectorized implement, *J. Comp. Phys.*, Vol. 187, 2003, pp. 597–619.
31. Brooksby, B., et al., Near infrared (NIR) tomography breast reconstruction with a prior structural information from MRI: algorithm development reconstruction heterogeneities, *IEEE J. Sel. Top. Quantum Electron.*, Vol. 9, 2003, pp. 199–209.
32. Oraevsky, A.A., et al., Laser opto-acoustic imaging of the breast: detection of cancer angiogensis, *Proc. SPIE*, Vol. 3597, 1999, pp. 352–363.
33. Siphanto, R.I., et al., Serial noninvasive photoacoustic imaging of neovascularization in tumor angiogenesis, *Opt. Express*, Vol. 13, 2005, pp. 89–95.
34. Niederhauser, J.J., et al., Combined ultrasound and optoacoustic system for real-time high-contrast vascular imaging in vivo, *IEEE Trans. Biomed. Eng.*, Vol. 24, 2005, pp. 436–440.
35. Zhang, Q., et al., Noninvasive imaging of epileptic seizure in vivo using photoacoustic tomography, *Phys. Med. Biol.*, Vol. 53, 2008, pp. 1921–1931.

# 13

# OPTICAL IMAGING AND MEASUREMENT OF ANGIOGENESIS

Brian S. Sorg
*University of Florida, Gainesville, Florida*

13.1 Introduction 370
13.2 Angiogenesis: a brief overview 370
  13.2.1 Biology of angiogenesis 371
  13.2.2 Measurement of angiogenesis 373
13.3 Potential clinical applications 376
  13.3.1 Cancer and other diseases 377
  13.3.2 Plastic and reconstructive surgery 379
  13.3.3 Ophthalmology 379
13.4 Optical techniques to image angiogenesis 380
  13.4.1 Molecular imaging 381
  13.4.2 Planar fluorescence imaging 382
  13.4.3 Spectral imaging 384
  13.4.4 Laser doppler and speckle contrast imaging 386
  13.4.5 Optical coherence tomography 388
  13.4.6 Multiphoton microscopy 390
  13.4.7 Optoacoustic imaging 392
  13.4.8 Diffuse spectroscopy and optical tomography 393
13.5 Other modalities 396
  13.5.1 X-ray CT 396
  13.5.2 MRI 396
  13.5.3 Nuclear imaging 398
  13.5.4 Ultrasound 398
13.6 Conclusions 399
References 400

---

*Advances in Optical Imaging for Clinical Medicine*, Edited by Nicusor Iftimia, William R. Brugge, and Daniel X. Hammer
Copyright © 2011 John Wiley & Sons, Inc.

## 13.1 INTRODUCTION

Angiogenesis is a process fundamental to several normal tissue physiological functions and responses, and also many pathological conditions. The ability to monitor and quantify angiogenesis clinically could aid in the management of certain diseases, healing responses, and therapies. Although several methods for measurement of angiogenesis are in development and being implemented using conventional medical imaging modalities, optical techniques also have the potential to make a contribution in this area. To properly design and evaluate optical techniques to measure angiogenesis, an appreciation of the complex physiology of the process is needed. Also needed is an understanding of methods to quantify angiogenesis and independent means to test the optical measurements. The purpose of this chapter is to briefly review some of the fundamental aspects of angiogenesis and angiogenesis measurement methods and to examine the current state of some optical techniques that have been employed to measure various aspects of the angiogenesis process.

## 13.2 ANGIOGENESIS: A BRIEF OVERVIEW

*Angiogenesis* is defined as the addition of new blood vessel segments primarily from postcapillary venules to existing vascular networks [1,2]. The process of angiogenesis generally refers to vessels on the relative order of the size of capillaries [3]. The result of angiogenesis is local expansion of the capillary network, resulting in an increased local microvessel density [4]. The increased microvessel density due to angiogenesis improves local oxygen and nutrient transport by reducing the diffusion distance between a tissue region and a blood vessel [4]. The process of angiogenesis is distinguished from *vasculogenesis*, which is classically defined as the embryonic development of the vascular system and de novo formation of blood vessels directly from progenitor cells [1,2]; *arteriogenesis*, which is the modification of the arteriolar network [5]; and *remodeling*, which is a change in the shape and structure of existing vasculature [1].

In a healthy normal adult there is generally little endothelial cell proliferation [6,7]. Specific physiologic conditions in which angiogenesis occurs regularly include growth and development, wound healing, and menstruation and reproduction [3,7]. Angiogenesis can also occur during functional changes accompanying tissue and muscular growth, due to athletic training and conditioning [1]. Similarly, arteriogenesis can occur in response to increased metabolic demand from a tissue or organ, or adaptation to a vascular occlusion to maintain homeostasis [5]. Blood vessels can respond to ambient stimuli, such as levels of metabolites and physical forces [1]. For example, oxygen and glucose are important metabolites, and local tissue hypoxia and hypoglycemia can stimulate angiogenesis to form neovasculature from existing capillary networks [6]. Increased fluid shear stress can stimulate arteriogenesis from existing arterioarteriolar anastomoses [4]. Angiogenesis can also occur in an inflammatory response [1] as a number of immune cells (leukocytes) secrete angiogenic factors [6]. For example, antigen-presenting dendritic cells can secrete both pro- and antiangiogenic factors [8].

In addition to certain normal physiological processes, there are a number of pathological conditions in which angiogenesis occurs. Angiogenesis is a key feature of numerous diseases, such as cancer, in which angiogenesis is a prominent characteristic of solid tumors and also of some nonneoplastic diseases such as diabetic retinopathy, Crohn's disease, and autoimmune diseases such as rheumatoid arthritis [3]. In terms of time scales, a normal nonpathological angiogenesis response tends to occur over a period of days to months, while pathological angiogenesis as part of a disease process can occur over a period of years [3].

The process of angiogenesis from a molecular and cell biology perspective is quite complex. In the next section, the biology of angiogenesis is reviewed very briefly. Interested readers are encouraged to consult the scientific literature to explore the subject further.

### 13.2.1 Biology of Angiogenesis

There are two major distinct modes of angiogenesis by which new blood vessels arise [1]. In one mode, termed *sprouting*, endothelial cells from an existing vessel form a bud on the vessel exterior wall. The bud then develops into a tubular sprout that grows and eventually connects to an adjacent vessel, thereby forming a new patent vessel with blood flow. Recruitment of pericytes, smooth muscle cells, fibroblasts, and secretion of extracellular matrix ensures proper stabilization and function of the new vessel [5,9]. *Pericyte* is the collective name given to a specific group of blood vessel support cells. While the biology of pericytes is not understood completely at this time, it is known that these cells help stabilize blood vessels by providing mechanical support and through secretion of various signaling factors [10]. Pericytes also play a role in angiogenesis by guiding migrating endothelial cell sprouts to help form new vascular connections [10]. In summary, sprouting requires proliferation and invasion of endothelial cells and thus is a relatively slow process [11]. In the second mode, termed *intussusception*, endothelial cells migrate to protrude into the vessel lumen from opposite sides to form a partition in the form of a pillar that divides the lumen [11]. The endothelial cell partition grows along the vessel axis and eventually splits the vessel into separate structures that will become new individual blood vessels [1,9]. Intussusception can be a fast process that takes place in hours or minutes, because endothelial cell proliferation is not required [9]. Rather, endothelial cells migrate and rearrange their formation within the existing vessel to form the pillar and separate into new vessels. Other cells, such as pericytes and fibroblasts, assist in this process [11]. Once the new vessels have formed and stabilized by either mode of angiogenesis, changes in phenotype can occur such that the vessels mature into new arterioles, venules, or capillaries. Figure 13.1 depicts the two previously mentioned modes of angiogenesis.

The process of angiogenesis is very complex and is regulated by a large number of molecular factors. These factors include diffusible regulatory molecules

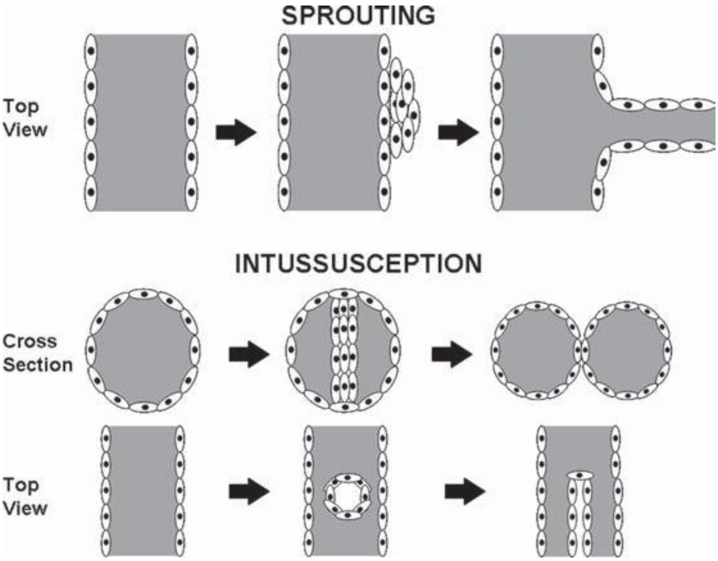

**FIGURE 13.1** Angiogenesis adds new vessels from existing vasculature by sprouting or intussusception. In sprouting, endothelial cells first form buds, then tubular sprouts that connect with adjacent vessels. In intussusception, endothelial cells form a partition that divides the lumen of a vessel prior to the creation of two separate structures. Support cells are omitted from the figure for clarity.

that are released from various tissue components, including blood and endothelial cells, tissue stroma, and extracellular matrix [6,9]. Some pathological cells, in particular cancer cells, can also release angiogenic factors. Other angiogenic regulatory factors are cell membrane–bound and bound to the extracellular matrix [12]. Angiogenesis is regulated on the molecular level by a balance between pro- and antiangiogenic factors. Stimulation of angiogenesis involves an increase in the effect of proangiogenic factors compared to antiangiogenic factors [6] that results in various coordinated cell–matrix and cell–cell interactions involved in the angiogenesis process [12].

In normal nonpathological angiogenesis, a specific sequence of steps takes place that is tightly controlled and regulated by a variety of molecular factors [5]. In a simplified form these steps are (1) up-or/down-regulation of pro-or antiangiogenic factors; (2) disruption of vessels, basement membrane dissolution, and invasion of the extracellular matrix; and (3) endothelial cell proliferation and/or migration, and vessel formation. Some important pro-angiogenic factors involved in this sequence of steps include the following [5,6,9,12]:

1. *Vascular endothelial growth factor* (VEGF). VEGF is a family of diffusible proangiogenic molecules that have varying degrees of structural similarities [13,14]. VEGF can also be found bound in the extracellular matrix and

can be released by matrix degradation. VEGF is currently the most potent proangiogenic molecule known, and is one of many factors up-regulated by hypoxia inducible factor-1 (HIF-1) activation [15,16]. So important is VEGF to angiogenesis that the deletion of VEGF receptors in knockout mice is lethal to developing embryos [2,14]. The HIF-1 pathway is one of the most sensitive pathways for detection of tissue oxygenation. There are a number of different cell membrane receptors for VEGF that can be found on hematopoietic stem cells among other cells, and the combination of specific receptor and ligand determines the cellular response. VEGF increases vascular permeability; induces endothelial cell proliferation, migration, and tube formation during sprouting; and signals endothelial progenitor cells to enter the bloodstream from the bone marrow [13]. VEGF also helps to up-regulate urokinase and tissue plasminogen inhibitors which initiate degradation of the extracellular matrix to assist endothelial cell migration.

2. *Angiopoietins.* Angiopoietins are a family of proteins that bind to the Tie family of cell membrane receptors. This diffusible proangiogenic factor is generally responsible for the maintenance and stabilization of blood vessels and the survival of endothelial cells. Angiopoietins can also stimulate endothelial cell sprouting. The stable vessel structure must be broken down for the budding and sprouting of new vessels, and the angiopoietin Ang-2 in the presence of VEGF helps to disrupt the structural integrity of endothelial cell connections to surrounding pericytes. Ang-2 also stimulates endothelial cell production of matrix metalloproteinases which break down the extracellular matrix to allow cell migration.
3. *Platelet-derived growth factor* (PDGF). The influence of the diffusible molecule PDGF on angiogenesis is only beginning to be understood, but research indicates that PDGF is a factor in proliferation and recruitment of pericytes and helps contribute to endothelial cell differentiation.
4. *Fibroblast growth factor* (FGF). FGF exists in both acidic and basic forms (aFGF and bFGF, respectively). FGF stimulates endothelial cell growth and proliferation and stimulates endothelial cells to produce factors such as matrix metalloproteinases that break down the extracellular matrix to assist with migration.

In contrast to the proangiogenic factors, many antiangiogenic factors function by inhibiting endothelial cell proliferation and migration, favoring endothelial cell apoptosis over cell survival, and binding to membrane receptors that promote angiogenesis, thereby blocking their function [5]. Angiogenesis inhibitors include various cytokines produced by immune cells such as interleukins and interferons, endostatin produced by platelets, as well as molecules in the extracellular matrix such as fibronectin and thrombospondin-1 [7].

### 13.2.2 Measurement of Angiogenesis

Angiogenesis is a complex process that involves many different molecular factors and cell types acting together to induce structural and functional changes to existing vasculature. Thus, any assessment of angiogenesis will probably measure only one or a few aspects of this process. It should also be kept in mind that angiogenesis is a dynamic process, so any measurement represents a condition of some part of the angiogenesis process at a particular point in space and time [17]. Several methods used to measure angiogenesis are discussed briefly in this section, and interested readers are directed to the references for more details.

Measurements of angiogenesis can be classified as *direct* or *indirect*. Direct measurements of angiogenesis can in theory give the least ambiguous measurements of angiogenesis. Direct measurements involve imaging of the microvasculature and comparisons of various metrics of the amount of microvasculature in a particular region to surrounding reference regions or to previous time points of the same region. Direct measurements also include quantification of structural changes in existing vasculature due to the angiogenesis process, although this is not as straightforward a result as the quantification of blood vessels in a region of interest. With indirect methods, an attempt is made to measure parameters associated with physiological consequences of angiogenesis. Indirect measurements of angiogenesis generally involve measurements of some characteristic of microvascular function in order to correlate changes in these functional values with the process of angiogenesis and the appearance of neovasculature. Some indirect parameters that can be measured include blood flow and perfusion, blood volume, vascular permeability, vessel oxygenation, hypoxia, and various angiogenesis molecular factors, such as VEGF and its receptors, integrins, endothelial cell surface markers, and extracellular matrix angiogenesis molecules [18,19]. Indirect measurements, especially those that correspond to hemodynamic parameters, currently are used more commonly in clinical practice in vivo, as these measurements can be performed in a minimally or noninvasive fashion with standard medical imaging techniques [20].

Quantification of the density of microvessels in an image region or volume is an example of a direct method of angiogenesis measurement. *Vascular length density*, also commonly referred to in the literature as *microvessel density*, is one such method of angiogenesis measurement that has been used in vitro in histology sections and can also be employed in vivo in some circumstances. These measurements have been shown to have correlations with various angiogenic parameters, including growth factor expression (VEGF and bFGF) [17]. Vascular length density measurements are based on a stereoscopic technique to measure the length of linear structures within a volume by counting the number of intersections of the linear structures within a two-dimensional plane section of the volume [21]. In one implementation of the technique, the number of intersections between blood vessels and a sampling grid is used to calculate the vascular length density [22,23]. The vascular length density computed in this manner is generally reported in units of $\mathrm{mm/mm^3}$ or $\mathrm{mm^{-2}}$. An alternative method to measure vascular length density can be performed in situations where blood vessels grow predominantly in two-dimensional planes. In this case, the total length of the vasculature per image area is computed and the units are generally reported as $\mathrm{mm/mm^2}$ but may also appear as $\mathrm{mm^{-1}}$ [24]. Vascular volume fraction, in a manner analogous to two-dimensional microvessel density measurements, can be used with three-dimensional image data to measure angiogenesis [25]. This technique can be used to measure angiogenesis compared to baseline images by tracking an increase in the volume fraction of blood vessels. Accuracy can be improved if a distinguishing vascular feature can be identified in the image area such that the same region of interest can be imaged over time [25]. A vascular volume fraction is expressed as a percentage or as a dimensionless fraction. Microvessel density measurements are currently considered a standard technique for the measurement of angiogenesis; however, there is currently no standard protocol for performing the measurements, thus, there is great variability in the reported materials and methods used to perform the technique [26]. The lack of a standard protocol for performing microvessel density measurements can make comparison of results from different laboratories difficult and lead to ambiguous conclusions.

Quantification of blood vessel structure and morphology is another direct measurement technique for angiogenesis in the sense that it involves direct imaging of microvasculature. Techniques for quantification of blood vessel structure and morphology can be used to characterize structural changes in microvessels that occur as a result of stimulation by proangiogenic factors. Various methods exist for measurement of the morphological changes that occur to established vasculature prior to the formation of functional neovasculature [27]. Tortuosity is a commonly used example of one such measurement. The tortuosity of a vessel or vessel segment in the simplest sense is the ratio of the actual pathlength of a blood vessel between two points to the straight-line distance between the two points. Other definitions are also possible [28]. Tortuosity is a dimensionless parameter or is expressed as a percentage, depending on how it is defined. Automated measurements are generally made using images processed to skeletonize the blood vessels in order to identify the blood vessel centerline [27,29].

Techniques to calculate tortuosity can include additional processing to smooth noisy data and employ models for calculating the arc length of curved vessel segments [29]. Tortuosity measurements can be performed on two-dimensional images provided that the vessels lie in the imaging plane. Tortuosity measurements can also be performed on three-dimensional data sets. Besides tortuosity, other methods exist for measurement of vascular morphology and structure. For example, a morphological model of a normal blood vessel can be established, and measurements of vessel characteristic deviations from the vessel model can be quantified [27]. Fractal dimension is another technique to measure angiogenesis in terms of vascular branching patterns and space filling of the microvasculature [30].

As mentioned previously, commonly applied indirect measurements of angiogenesis generally involve measurements of some aspect of microvascular function that presumably correlates with the angiogenesis process. The use of intravenously injected tracer molecules is a common technique for measuring vascular function parameters. The parameters that can be measured include blood flow, vascular permeability to the tracer molecule, and the relative amount of the tracer molecule that is exchanged with the tissue due to the circulating blood (fractional extraction). These quantities are related, and generally a pharmacokinetic compartmental model of tracer exchange is needed to derive these parameters from measured signals [31]. Laking et al. review a number of quantitative methods and models to measure vascular physiology [32]. One such commonly derived parameter is the plasma transfer constant ($K^{\text{trans}}$, units of $\text{min}^{-1}$), which is a measure of tracer transport from the plasma into the extracellular space [33]. The actual interpretation of $K^{\text{trans}}$ is dependent on whether blood flow to the tissue region of interest or vascular permeability are limiting factors in the rate of exchange [32,33]. It was mentioned previously that VEGF increases vascular permeability; thus, measurements of $K^{\text{trans}}$ can provide an indication of the VEGF levels in a measured region, which would suggest increased angiogenesis; however, there are some examples in which measured vascular permeability was not correlated with VEGF levels [34]. A problem with the use of models for indirect assessment of vascular function is that the actual vascular functional parameter of interest is not directly measured but, instead, must be computed from the model. The models usually contain assumptions that may not be completely valid for a given situation, thus limiting the accuracy of the calculation [32]. Caution should be used when interpreting indirect signals of angiogenesis, as some parameters may have multiple causes; thus, measurements of parameters such as perfusion and permeability may not accurately quantify the actual degree of angiogenesis [35].

Molecular imaging is another indirect method for measurement of angiogenesis. In this method, a contrast agent conjugated to a ligand for a molecular factor associated with angiogenesis provides contrast to identify regions of active angiogenesis and quantify the degree of angiogenesis based on the signal amplitude from the contrast agent. Molecular imaging is discussed in more detail in Section 13.4.1.

From the previous discussion it can be seen that there are numerous ways to attempt to measure and quantify angiogenesis. Ultimately, it is up to the investigator to determine how a particular measurement of angiogenesis correlates to a tissue function, disease state, or prognosis for a given condition, and if indirect markers of angiogenesis are used, how well these markers reflect the actual angiogenesis processes in the tissue of interest [20]. The choice of parameter to be measured may be dictated and limited by the tissue of interest to be measured, and the measurement or imaging modality available to the investigator.

## 13.3 POTENTIAL CLINICAL APPLICATIONS

Dysregulated angiogenesis is a characteristic of many diseases and can perpetuate or worsen the disease state [12]. Cancer is a prototypical example [36]. In addition to cancer there are a number of diseases in which abnormal angiogenesis or vascular remodeling is a prominent feature [6]. For example, most skin diseases and pathologies are characterized by hypervascularity [37]. One of the triggers of angiogenesis mentioned previously is hypoxia. Inadequate oxygen delivery resulting in hypoxia that can lead to angiogenesis can be caused by anomalous extracellular matrix deposition [6]. This process occurs in Alzheimer's disease and diabetes, among others. In the following sections, examples of clinical motivations for measurement of angiogenesis are discussed briefly.

### 13.3.1 Cancer and Other Diseases

Solid tumors require the formation of neovasculature to proliferate and grow beyond a certain size (ca. 1 to 2 mm) [38,39], and almost all solid tumors express some amount of VEGF [5]. However, the microvasculature of tumors is structurally abnormal, with poor to no differentiation into proper arterioles and venules, chaotic branching, little or no smooth muscle or innervation, gaps in the endothelial lining and basement membrane, arteriovenous shunts, larger-than-normal diameters, increased tortuosity, and large intervessel distances [36,40]. Improper balance of proangiogenic factors is a suspected cause of abnormal tumor microvasculature [6]. The irregular morphology leads to aberrant perfusion compared to normal tissue, hypotension which can lead to vessel collapse, and increased flow resistance, among other abnormalities [36,41]. As a result, the mass transport functions of the microvasculature are compromised in tumors, with inadequate delivery of nutrients and oxygen and poor metabolic waste removal [42].

The combination of abnormal microvasculature and compromised mass transport functionality results in various peculiarities of oxygen delivery in tumors compared to normal tissue. For example, large intervessel distances in some tumor regions result in radial oxygen gradients that create chronically hypoxic areas, due to diffusion limits of oxygen in metabolically active tissue [36,43]. Increased flow resistance and hypotension can result in complete cessation of flow and vessel collapse, which will lead to hypoxia [36,41]. Increased vascular tortuosity and distance from a well-oxygenated feeding vessel can result in a longitudinal oxygen gradient in the afferent direction along the vessel, with the effect that a well perfused region can still be hypoxic due to deoxygenated blood [44,45]. Hypoxia can cause red blood cells to stiffen and increase flow resistance, with a consequence of even more hypoxia [41,43].

Motivation for measuring angiogenesis in tumors is due in part to tumor dependence on angiogenesis for growth and development. Additionally, in some cancers, angiogenesis is present in premalignant lesions and may precede metaplasia and hyperplasia in the developmental process of carcinogenesis, thus angiogenesis may have potential as an early biomarker for some types of cancer [46]. Increased VEGF expression has been found in most types of cancer [47]. In some types of cancer it has been demonstrated that angiogenesis can be an independent prognostic indicator of disease progression and response to therapy [35]. Using microvessel density measurements in histology sections, a connection between tumor vascularity, disease progression, and patient prognosis has been established for breast cancer, prostate cancer, and non-small-cell lung carcinomas, among others [48]. Thus, tumor vasculature presents a target common to most solid tumors [49]. Significant research effort has been focused on drugs that inhibit angiogenesis and thus halt tumor growth [3,6]. Several drugs have already been approved for clinical use and there are a large number of antiangiogenic agents currently in clinical trials [3]. Anti-angiogenic agents target one or more of the molecules or receptors associated with the stages of angiogenesis [50]. For example, bevacizumab (sold under the name Avastin by Genentech) is an antibody that targets VEGF and reduces its angiogenic effect in tumors. Vascular targeting drugs may have several benefits, including enhancement of cytotoxic effects to endothelial cells from conventional chemotherapeutic agents and inhibition of tumor repopulation during breaks in drug administrations throughout the course of chemotherapy treatment [49]. The ability to image and measure angiogenesis preclinically in laboratory animals can be useful for the development and comparison of antiangiogenic drugs. Clinically, angiogenesis quantification may help to monitor therapy and assess treatment results. Since angiogenesis is part of the tumor development process, quantification of angiogenesis and microvascular function may be useful in cancer diagnostics and monitoring of changes in suspicious lesions. Surgery is an angiogenesis-promoting event that can affect the treatment of cancer [51]. Angiogenesis as part of the wound-healing process from surgery for the removal of tumors can stimulate dormant clinically undetectable metastases to proliferate. Use of antiangiogenic agents after surgery to prevent this effect may impair the healing process from the surgical procedure; thus, monitoring of angiogenesis may help with clinical diagnostic and therapeutic aspects of cancer treatment after surgical procedures.

Aberrant angiogenesis is also a component of a variety of other diseases, and dysregulated VEGF expression is an important factor in many cases. Diabetes mellitus is one such example. Diabetes is complex in that abnormally excessive angiogenesis can occur in the retina (diabetic retinopathy) and kidney (diabetic nephropathy), yet in other tissues, angiogenesis is impaired, leading to complications such as ulcerations on the foot and rejection of transplants and grafts due to poor vascularization [52,53]. VEGF present in excessive or insufficient levels is one of the many contributing factors of pathological angiogenesis in diabetes. Techniques to measure and image angiogenesis may provide information on the progression of a healing wound and aid in the development and testing of new therapies to improve wound healing in diabetic patients. Autoimmune and inflammatory diseases are frequently characterized by pathological angiogenesis. Psoriasis is primarily a chronic inflammatory disease of the skin, and abnormal vascularization of affected regions is due in part to aberrant angiogenesis, which is necessary to sustain psoriasis skin lesions characterized by epidermal hyperplasia [54]. Increased VEGF levels are often seen in patients with psoriasis, and immune cells recruited to the lesion sites support local angiogenesis by secretion of VEGF. Increased VEGF levels are also seen in patients with some systemic autoimmune diseases such as lupus and rheumatoid arthritis [55]. Angiogenesis that results in abnormal microvasculature helps to sustain inflammation in rheumatoid arthritis [55,56]. Antiangiogenic therapies developed for cancer treatment have been proposed as a therapeutic modality for the treatment of rheumatoid arthritis [56]. Techniques to monitor angiogenesis in arthritic joints may help in clinical management of antiangiogenic therapies for treatment of this disease.

### 13.3.2 Plastic and Reconstructive Surgery

Angiogenesis associated with wound healing is particularly important in plastic and reconstructive surgery. Measuring angiogenesis clinically can be useful for monitoring the health of skin flaps in reconstructive surgery and potentially in the future for tissue constructs that may ultimately replace skin flaps and grafts [57]. Measurement of angiogenesis can also be useful to monitor the progress of angiogenesis that has been clinically induced as part of a treatment protocol. Therapeutic angiogenesis has been proposed as a component of treatments for wound healing, nerve growth, and skin flap vascularization [7].

In plastic and reconstructive surgery involving vascularized flaps and free grafts, angiogenesis in the transplanted tissue subsequent to surgery can be a determining factor in the survival of the tissue and success of the surgery [58]. Inadequate microcirculatory perfusion of healing tissue that results in insufficient oxygen delivery can slow or halt the wound-healing process [59]. Oxygen is a crucial component of the wound-healing process, as the functional activity of certain enzymes that participate in collagen synthesis requires oxygen to be present in the tissue [59] (a lower bound of oxygen for collagen production has been estimated at a $pO_2$ of 20 mmHg [60]). Adequate tissue oxygenation is also required to fight infection, as immune cells generate reactive oxygen species to destroy invading bacteria in a healing wound [61]. Monitoring of angiogenesis may help assess the health of healing flaps and grafts after surgery.

In tissue engineering applications a new vascular network is required to support implanted cells or tissues created and constructed ex vivo; however, there are oxygen transport limitations that hinder practical implementation of engineered tissue constructs. Oxygen supplied by microvessels sufficient for support of cell metabolism is limited by diffusion and consumption typically to a distance of about 150 to 200 $\mu$m radially from a supply vessel [57]. The ability to measure angiogenesis serially in vivo may help monitor how effectively a particular vascular carrier construct helps to establish a network of vessels in a tissue graft. There is a need for this type of assessment in the evaluation of new engineering tissue constructs [62], as the development of neovasculature can be slow and this may not be sufficient for support of cells implanted in a tissue scaffold or construct, thus limiting the ultimate success of the implant.

### 13.3.3 Ophthalmology

Angiogenic diseases of the eye are a common cause of visual impairment and blindness [63,64]. For example, diabetic retinopathy is a common vision-threatening complication associated with diabetes mellitus [65]. Senile macular degeneration is another common angiogenic pathologic condition of the eye [63]. Pathological angiogenesis in the retina is caused in some cases by ischemia, and VEGF plays an important role in retinal neovascularization [64,66,67]. Laser treatments are a standard course of therapy for angiogenic retinopathies, but there are a number of emerging alternative approaches, including systemic administration of drugs, local injection of antiangiogenic agents, gene therapy, and stem cell therapy [63,67]. A variety of antiangiogenic agents are being investigated as alternative treatments for angiogenic ocular pathologies [64]. Antiangiogenic agents originally developed as anticancer therapies may also benefit the treatment of nonneoplastic angiogenesis-dependent ocular diseases. For example, the anti-VEGF antibody bevacizumab, which first received approval for treatment of colorectal cancer, has also been shown to help treat age-related macular degeneration [3]. Monitoring and measurement of angiogenesis in the retina and choroid can benefit the monitoring and evaluation of alternative therapies for treatment of angiogenic ocular pathologies, in particular antiangiogenic agents.

Angiography in the retina and choroid is well established and can be accomplished by several different optical methods. Spatial resolution on the order of 25 μm can be achieved which is sufficient for directly imaging angiogenic vessels [68]. However, it has been noted that in retinal vessels, measurable changes in established vasculature precede the appearance of detectable neovasculature, thus forecasting subsequent angiogenesis [29]. Thus, new technologies that can detect subtle changes that occur prior to the appearance of neovasculature may help with earlier detection of the onset of disease and may bring new insights into the evaluation of alternative treatments.

## 13.4 OPTICAL TECHNIQUES TO IMAGE ANGIOGENESIS

Optical techniques to image angiogenesis are attractive because some methods have sufficient spatial resolution and imaging depth to capture features characteristic of the process of angiogenesis, particularly pathological angiogenesis, including abnormal and irregular vascular morphology, high vascular permeability, and abnormal blood flow [69]. While the scattering nature of tissue imposes restrictions on the depth and spatial resolution for tissue optical imaging and measurement techniques, there are still a variety of situations and circumstances where optical imaging is well suited. For example, optical imaging for endoscopic examination of the gastrointestinal tract is a standard procedure for the detection of colon cancer. Microvascular alterations due to angiogenesis are some of the earliest signs of neoplasia formation in the colon [69], and optical techniques can potentially be designed to image and measure these changes.

In the following sections, a number of optical techniques for detection and measurement of angiogenesis are discussed. It is not our intent to provide a tutorial or extensive review of the various imaging techniques, and prior knowledge or familiarity with the subject matter is assumed. Rather, each technique is discussed in the context of the ability to measure angiogenesis, and particular emphasis is placed on clinical uses or demonstrations of the technique in this regard if applicable. For comparison to the optical techniques discussed, a number of standard medical imaging methods and how they are currently being applied to measurement of angiogenesis are also discussed briefly.

### 13.4.1 Molecular Imaging

Conjugation of contrast agents to molecules with an affinity to specific biomarkers of angiogenesis can be used to highlight regions actively undergoing angiogenesis. The following discussion in general is applicable to most of the other imaging modalities discussed in this section since the only factor required to change from one modality to another is the appropriate choice of contrast agent. Several examples related to various optical modalities are discussed.

Cancer research has driven much of the effort to find molecular targets of angiogenesis for the purpose of targeting tumor microvasculature. Molecular factors associated with tumor angiogenesis can provide a more stable common target to many types of cancer, compared to targeting ligands on the tumor cell surface that are specific to particular types of cancer [70]. A major difficulty in molecular targeting of angiogenic vessels is finding a marker that is highly expressed in angiogenic tissues with insignificant expression in normal nonangiogenic tissues. Most markers identified thus far have this problem to some extent [70]. Some endothelial cell membrane surface markers, such as CD31, CD34, and von Willebrand factor (vWF), are fairly ubiquitous throughout the vasculature in many different tissues and can serve as general markers of vascular endothelium [71]. Other cell surface proteins are expressed more specifically on endothelial cells undergoing angiogenesis. One such marker is CD105, a receptor for transforming growth factor (TGF) -β 1 and TGF-β 3 [71,72]. CD105 is up-regulated by hypoxia and its expression has been documented on endothelial cells undergoing angiogenesis, including in tumor microvasculature [72,73]. CD-105 expression has also been documented in normal tissues, although to a lesser extent than in tissues undergoing angiogenesis [70]. Ligands used for contrast agent binding to molecular targets of interest include relatively small molecules such as peptides up to larger molecules such as antibodies. Work toward antibody targeting of angiogenic vessels has been performed [70]. Some markers for angiogenesis are actually located on the abluminal surface of the endothelial cells, which requires extravasation of the targeting agent for efficacy [70]. There are a number of relevant reviews related to general optical molecular imaging [74–77].

Birchler et al. conjugated the near-infrared fluorescent dye Cy7 to an antibody to a particular domain of fibronectin that appears in tissue undergoing angiogenesis [78]. Reflectance fluorescence imaging was used to highlight regions of angiogenesis due to contrast agent localization in a mouse with angiogenesis induced by subcutaneously implanted F9 teratocarcinoma cells and in a rabbit corneal pocket assay. Cai et al. used RGD-peptide-labeled NIR quantum dots to target angiogenesis in U87MG human glioblastoma tumors grown subcutaneously in athymic nude mice [79]. Signal could be measured 20 minutes after intravenous injection of quantum dots with peak signal achieved 6 hours postinjection. There was little nonspecific accumulation of quantum dots without the RGD-peptide. Jin et al. used a similar technique with RGD-peptide conjugated to a fluorescent dye [80]. IGROV1 human ovarian adenocarcinoma tumors were grown in athymic nude mice as subcutaneous flank tumors or as intraperitoneal disseminated nodules. Peak fluorescence reflectance signal was reached within 3 to 6 hours postinjection of contrast agent and imaging was still possible up to 48 hours later. Hsu et al., using U87MG orthotopically implanted human glioblastoma tumors in nude mice, demonstrated specificity of a Cy5.5 RGD-peptide conjugated fluorescence contrast agent as an unlabeled RGD-peptide ligand-blocked contrast agent binding when administered prior to the Cy5.5 contrast agent, while the nonconjugated dye exhibited nonspecific binding [81]. Von Wallbrunn et al. used a CD13/APN-targeted NGR-peptide conjugated with Cy5.5 to target metalloexopeptidase CD13/aminopeptidase N (APN) expression in HT-1080 human fibrosarcomas and MCF-7 human mammary adenocarcinomas grown in nude mice [82]. APN is an enzyme that plays a role in cancer angiogenesis and metastasis. Peak fluorescence signal measured by fluorescence tomography was reached within about 5 hours after contrast agent administration.

Molecular imaging can provide selective contrast for specific molecular factors associated with angiogenesis. High signal/noise ratios can be achieved, allowing early detection of angiogenesis.

### 13.4.2 Planar Fluorescence Imaging

One of the simplest methods for measurement of angiogenesis in terms of instrumentation and equipment is fluorescence reflectance imaging with near-infrared (NIR) contrast agents used as blood pool contrast agents and for measurements of vascular permeability. While direct imaging of microvasculature with this technique is severely depth limited due to tissue scattering even with NIR contrast agents, measurements of angiogenesis are still possible in accessible relatively superficial tissue regions. Tomographic fluorescence imaging of angiogenesis is covered in Section 13.4.8.

NIR fluorescent dyes have been used as microcirculation contrast agents to highlight the microvasculature for measurements of angiogenesis. Angiography with intravenous injection of the small-molecule dye sodium fluorescein has been used clinically for many years for evaluation of the microcirculation, most notably in the eye and also to a lesser extent in the skin [83]. Bolus injection of sodium fluorescein temporarily highlights the microcirculation before rapidly exchanging and equilibrating with extravascular extracellular space within minutes, at which point it is difficult to distinguish microvessels from background extracellular space fluorescence. Mellor et al. used fluorescein angiography of the skin to investigate dermal angiogenesis in human patients with breast cancer–related lymphedema [84]. A bolus injection of sodium fluorescein was administered intravenously to breast cancer patients with symptoms of breast cancer–related lymphedema, which included a swollen arm on the treated side of the body where the breast cancer was located (the ipsilateral arm). Simultaneous NIR fluorescence video microscopy imaging was performed on the ipsilateral arm and the asymptomatic contralateral arm which was used as a control. Microvessel density, defined in this study as the number of microvessels/mm$^2$, was determined from the images by counting the number of vessels with a diameter $\leq 16$ μm in each field of view. The authors found no difference in microvessel density between the ipsilateral and contralateral arms, and this finding was interpreted as evidence of angiogenesis given that the swelling-induced increase in skin surface area of the ipsilateral arm was expected to have a lower microvessel density in the absence of angiogenesis (i.e., angiogenesis must have taken place to preserve the microvessel density in the swollen arm). Stanton et al. used similar methods to clinically measure angiogenesis in human skin basal cell carcinomas [85]. In this study, the authors quantified angiogenesis in terms of the fractional area of blood vessels and blood vessel length density (length of blood vessels per unit imaged area, reported as cm$^{-1}$ in this paper). In each case, a sampling grid technique was used. For fractional area measurements the number of vessels that intersected a grid of sampling points was counted, while for vessel length density measurements the number of blood vessel intersections with a grid of parallel lines was counted and normalized to the total line length of the sampling grid and multiplied by a stereological correction factor. Higher values of both measurements were seen in skin basal cell carcinomas than in normal tissue.

The pharmacokinetics of macromolecular fluorescent contrast agents have been used for fluorescence reflectance imaging measurements of changes in vascular permeability associated with angiogenesis. Gurfinkel et al. used indocyanine green dye and carotene-conjugated 2-devinyl-2-(1-hexyloxyethyl) pyropheophorbide (HPPH-car) as contrast agents for NIR fluorescence reflectance imaging of tumors in a spontaneous canine mammary adenocarcinoma [86]. While indocyanine green is a small molecule with a molecular weight of 775, it readily binds to albumin and other plasma proteins upon intravenous injection [87]; thus, for permeability studies, indocyanine green bound to plasma proteins behaves essentially like a macromolecule. The contrast agents used by Gurfinkel et al. had different tissue uptake parameters, so pharmacokinetic models were tailored to each agent, including a biexponential model to account for the rapid uptake and washout of ICG, and a single exponential model to reflect tissue uptake and retention without washout of HPPH-car. Measurements such as these can be useful for determination of parameters related to angiogenesis, such as tissue vascular fraction and vascular permeability. Any such calculated parameters will be a bulk average for the imaged tissue volume. SIDAG (1,1′-bis[4-sulfobutyl]indotricarbocyanine-5,5′-dicarboxylic acid diglucamide monosodium) was used by Wall et al. as a perfusion fluorescence contrast agent in athymic nude mice with several human tumor xenografts that have different angiogenic activity [88]. Local tumor contrast agent concentrations were determined from fluorescence reflectance and tomography measurements and compared to MRI vascular volume fraction measurements employing an MRI contrast agent and to immunohistochemistry microvessel density measurements made with a sampling grid technique. The level of VEGF expression by cell cultures of each tumor type was also compared. In this study, the authors found that the fluorescence contrast agent concentration correlated well with the other measurements and thus demonstrated that use of perfusion optical contrast agents can potentially be used for angiogenesis measurements.

NIR fluorescence reflectance imaging may be useful as a relatively simple and inexpensive method for clinical measurement of angiogenesis. The requirement of injectable contrast agents for implantation of the method could be a drawback in some applications.

### 13.4.3 Spectral Imaging

Spectral imaging enables the acquisition of an optical spectrum (absorption, fluorescence, etc.) for every pixel in an image, resulting in a three-dimensional data set: two spatial dimensions and one wavelength dimension [89–93]. The spectral data can be processed in a number of ways to accomplish different goals. Pixel classification is performed for assignment of pixels to distinct classes based on known pure reference spectra or spectra mathematically determined to be distinct based on the spectral content of the data set, while spectral unmixing is performed to determine the relative or absolute amount of a number of different spectrally distinct substances present at each pixel location using either a linear or a nonlinear combination of the spectra [94–102]. The processed spectral information can then be placed into a spatial context in an image.

With regard to microvasculature, oxy- and deoxyhemoglobin and their derivatives have unique optical spectra [103], and hemoglobin has a distinct optical spectrum compared to other tissue chromophores; thus, spectral imaging can be used to measure tissue microvascular functional information, such as blood oxygenation, based on hemoglobin absorption spectra. Several researchers have used spectral imaging for measurements of microvascular oxygenation in terms of hemoglobin saturation with microvessel resolution [104–111]. These measurements, however, were performed on laboratory animal preparations designed to enable high-resolution imaging of microvessels, or in retinal vessels which are readily accessible for imaging. In general, spectral imaging of tissue will involve reflectance imaging. In some anatomical locations, such as various regions of the gastrointestinal tract, it may be possible to directly image superficial microvessels; however, in most situations microvascular function will need to be inferred from bulk tissue measurements. Accurate determination of values such as hemoglobin saturation and total hemoglobin concentration from bulk tissue measurements will probably require a model of light propagation in tissue to account for tissue scattering effects which can result in wavelength-dependent crosstalk between adjacent pixels due to differences in the pathlength and exit angles of photons emanating from neighboring tissue regions [112]. Some researchers have employed tissue light propagation model–based processing of reflectance spectral imaging data, which range from relatively simple to detailed and complex for different tissues such as colon and skin [113–115].

A number of different investigators have employed spectral imaging of hemoglobin absorption to help enhance the contrast of tissue microvasculature and infer microvascular function. Muto et al., in a clinical setting, used a simple modification of a video endoscope system with a monochrome CCD camera by replacing the normal red, green, and blue color filters used on the illumination lamp to produce color images with narrowband (30-nm) filters at 415, 445, and 500 nm [116]. This simple change improved the image contrast for superficial microvasculature of pharyngeal tissue and improved the detection of head and neck cancers at the carcinoma in situ stage by visual inspection of abnormal microvasculature in the neoplastic epithelium. Roblyer et al. also used a narrowband spectral imaging technique to enhance microvascular contrast in developing oral neoplasia in human patients [117]. Others have used spectral imaging to highlight changes in microvascular function following systemic or local perturbations. For example, Zuzak et al. examined tissue oxygen delivery clinically in sickle cell patients following administration of inspired nitric oxide [118]. Kostenicha et al. imaged changes in normal and tumor local tissue hemoglobin oxygenation during photodynamic therapy in mice due to consumption of oxygen by the photochemical activation process and subsequent microvascular damage in the tumor [119].

In terms of spectral imaging applications to the measurement of angiogenesis, there is currently a lack of literature dedicated explicitly to detailed spectral imaging angiogenesis measurements with confirmation and quantification of the degree of angiogenesis by independent means. The difficulty in interpretation of bulk tissue hemoglobin signals when microvessels cannot be imaged directly may be a factor in the limited attempts to apply spectral imaging to measurements of angiogenesis to date, although some efforts have been made. For example, Vogel et al. used NIR spectral imaging with human patients to infer changes in the microvasculature of Kaposi's sarcoma lesions which are highly vascularized [114]. Images were acquired using bandpass filters with 40-nm bandwidths at 700, 750, 800, 850, 900, and 1000 nm. Some of the patients in the study were undergoing therapy with an experimental drug, while others only had retroviral therapy for treatment of AIDS. Spectral imaging measurements consistently indicated an increased blood volume compared to adjacent lesion-free normal tissue which reflects the angiogenic and highly vascular nature of the lesions compared to normal tissue. However, measurements of hemoglobin saturation were inconsistent; some lesions had higher than normal oxygenation, whereas others had lower than normal oxygenation. It was hypothesized that an inflammatory response associated with the lesions caused higher oxygenation in some cases. This is a reasonable interpretation given that Stamatas and Kollias showed that inflammation can cause changes in oxyhemoglobin due to erythema that can be measured by spectral imaging [120]. Kotz et al. highlighted the abnormal oxygen transport function of tumor microvasculature by systemic perturbation with inspired oxygen to contrast bulk tissue hemoglobin saturation measurements in normal and tumor tissue in a preclinical model [121]. Hemoglobin saturation measurements in tumors are expected to differ from normal tissue with inspired oxygen breathing due to the presence of arteriovenous anastomoses or functionally similar such structures that help shunt highly oxygenated blood due to inspired oxygen from tumor-feeding arterioles to tumor-draining venules [108]. While contrast between tumor and normal tissue may be improved, quantification of the degree of angiogenesis from bulk tissue signals using this method may be very difficult.

In summary, spectral imaging may have some application to measurements of angiogenesis, but there have not yet been a significant number of detailed studies that explore this possibility. In addition, a number of obstacles may hinder this application of spectral imaging. In general, spectral imaging is limited to relatively superficial tissue measurements. Difficulty in processing spectral imaging data from bulk turbid tissue measurements is another potential problem, and model-based methods of processing may be required. Interpretation of microvascular functional information obtained from spectral imaging data for quantification of the degree of angiogenesis is another problem, given that other factors can influence microvascular functional parameters measurable with spectral imaging besides angiogenesis.

### 13.4.4 Laser Doppler and Speckle Contrast Imaging

Laser Doppler and laser speckle contrast imaging are mathematically equivalent techniques for measuring the relative velocity of moving light-scattering particles [122,123]. Laser Doppler measurements are typically single-point measurements made with a laser beam, but imaging can be accomplished by scanning the laser beam across a region of interest. Imaging measurements have advantages over single-point measurements in terms of reproducibility and repeatable spatial localization of the tissue region of interest at multiple time points [124]. Laser speckle contrast imaging is by nature a full-field imaging technique. Both techniques can be performed endoscopically [125].

Laser Doppler and speckle contrast techniques can be used to assess tissue perfusion by measuring the movement of red blood cells in the tissue microcirculation. It has been shown in skin, for example, that the origins of the Doppler signal is blood perfusion in capillaries, arterioles, and venules in the dermis [126]. In cases where microvasculature cannot be imaged directly, the signal from within a probed tissue volume represents a complex integration of the signals from randomly oriented vessels with varying blood flow directions and velocities [127]. Laser Doppler and speckle contrast imaging provide semiquantitative measurements of perfusion in the sense that the perfusion measurements are relative, with arbitrary units rather than absolute with units in terms of blood velocity or volume rate [126,127]; however, it has been shown that the perfusion signal varies in a linear fashion with tissue blood perfusion [124]. Although progress has been made toward achieving true velocity measurements with laser Doppler and speckle contrast techniques, limitations remain and more work needs to be done [128].

In clinical use, laser Doppler and speckle contrast techniques can be particularly effective at providing immediate real-time information on perfusion changes in response to some treatment or therapy, such as laser treatment of blood vessels in port wine stains [129]. Tissue perfusion measurements can also be performed chronically as laser Doppler flowmetry has been used for clinical assessment of skin wound healing [130]. A comparison of laser Doppler and laser speckle contrast imaging of perfusion in human burn scars has clinically shown equivalence in the measurements produced by both techniques [131]. The sensitivity of the perfusion measurements is such that in skin, Doppler measurements can detect perfusion fluctuations due to respiration, heartbeat, and natural cyclical contractions of vascular smooth muscle [126].

With regard to measurements of angiogenesis, laser Doppler and speckle contrast methods are indirect measurement techniques since they measure microvascular function in terms of perfusion. In some studies that explicitly examined the relation between the perfusion signal measured by laser Doppler techniques and angiogenesis, a correlation was found between the laser Doppler measurements and other measurements of angiogenesis. For example, in several studies employing a rat model of hind limb ischemia, laser Doppler perfusion imaging detected a trend in limb perfusion that was consistent with x-ray angiography and immunohistochemical microvessel density measurements of angiogenesis [132,133]. A positive trend in the correlation between laser Doppler measurements of perfusion in human laryngeal tumors and microvessel density measurements from biopsies of the interrogated tissue has been demonstrated, although the correlation was weak [134]. In general, however, laser Doppler and speckle imaging techniques can have significant limitations for monitoring of angiogenesis. There are a number of confounding variables that can cause changes in perfusion signals unrelated to angiogenesis in the tissue. Tissue optical properties changes that occur as part of the wound-healing process can obliterate or alter the perfusion signal such that tissue blood flow either cannot be monitored at all or interpretation of the signal is difficult [135,136]. The laser Doppler signal in blood vessels varies as a function of red blood cell concentration (vessel microhematocrit) and velocity; therefore, a change in any of these functional parameters unrelated to angiogenesis will cause a change in the measured perfusion signal [137]. Variations in blood velocity and microhematocrit can be induced by changes in local temperature, vasomotor tone, pain, and inflammatory response of the tissue region of interest at the time of measurement [124]. Changes in perfusion can also be caused by mechanical factors such as physical compression or stretching of tissue [138]. In a study of human skin cancer that included malignant melanomas, basal cell carcinomas, and benign melanocytic nevi, it was demonstrated that increases in the perfusion signal were caused by both increased microvessel density and increased blood perfusion due to enlarged microvessel diameters [139]. Thus, interpretations of the laser Doppler signal with regard to the appearance of neovasculature can be confounded by similar changes to the signal induced by morphological changes in blood vessels which result in increased blood flow without the appearance of neovasculature. A more subtle complicating factor is that the perfusion signal measured by laser Doppler and speckle contrast techniques may not necessarily correlate with the oxygen transport function of the microcirculation, as has been demonstrated in skin [138]. The many factors that can cause a change in tissue perfusion make it difficult to attribute changes in the laser Doppler and speckle contrast perfusion signal exclusively to angiogenic processes, and similarly, some alterations in microvascular function due to angiogenesis may not be detected.

In summary, while measurements of angiogenesis have been demonstrated with laser Doppler and speckle contrast imaging, clinical utility appears to be severely limited at present and may only be applicable to very specific conditions and applications. Further research leading to absolute measurements of tissue perfusion may enhance the prospects for clinical adoption of these techniques to measurements of angiogenesis [127].

### 13.4.5 Optical Coherence Tomography

Optical coherence tomography (OCT) can generate three-dimensional images of tissue morphology in vivo through imaging of backscattered light, with optical sectioning ability to tissue depths in the range 1 to 2 mm achieved through the use of low-coherence interferometry [140–142]. Optical coherence microscopy (OCM), a variant of OCT, combines the high transverse resolution of confocal microscopy with the high axial resolution of OCT to achieve spatial resolution in the range 1 to 10 μm in three-dimensions [143]. OCT imaging of microvessel morphology can be achieved with a variety of methods, most of which use contrast generated by moving scatterers due to blood vessel perfusion. Doppler OCT, a variant of OCT, can provide blood velocity information [144–146]. Fourier- or spectral-domain approaches to OCT have vastly increased data acquisition speed and the range of Doppler measurements [147–149] such that accurate mapping of low velocities is possible. Other methods for blood vessel contrast with OCT include molecular imaging of endogenous hemoglobin contrast or exogenous intravascular absorbing dyes, and exogenous intravascular OCT scattering contrast agents such as gold nanoparticles and microbubbles [150–153]. Blood vessel function can also be measured in terms of oxygen transport based on hemoglobin saturation with spectroscopic OCT methods [154–157] and hematocrit measured by scattering attenuation by red blood cells [158]. Thus, potentially, OCT can be used for both direct and indirect measurements of angiogenesis with high spatial resolution in relatively superficial tissue layers. There are hundreds of examples in the literature of numerous variations of OCT being used to image and measure microvasculature, with ophthalmology as the dominant application area. Brief descriptions of some examples of OCT imaging of microvasculature follow.

Kagemann et al. used Fourier-domain OCT to measure hemoglobin saturation in retinal blood vessels of human subjects [157]. Relative measurement of blood oxygenation was accomplished through the use of an optical density ratio, with optical densities signals from blood vessels calculated based on Beer's law attenuation of the signal from a blood vessel with surrounding tissue used as a reference, and a ratio calculated for two different wavelengths of light available from their superluminescent diode light source: 805 nm, an isobestic wavelength, and 855 nm, a wavelength with differential absorption for oxy- and deoxyhemoglobin. Optical density ratio differences were observed between arterioles and venules, which indicated increased oxygenation of arterioles, as expected. Previous blood flow measurements with Fourier-domain OCT quantified blood flow in terms of velocity (mm/s). Wang et al. demonstrated that blood flow measurements could be made with flow rates measured in terms of absolute blood volumes (μL/min) in retinal microvessels using a dual-plane scanning technique [159]. Flow volumes of less than 3 μL/min were measured in the smallest-diameter vessels. Michaely et al. demonstrated full three-dimensional retinal vessel network blood flow measurements [146], and Makita et al. used a similar but simplified technique to obtain two-dimensional blood flow information from *en face* images of retinal vessels [160]. Mariampillai et al. used high-frame-rate imaging (>370 kHz) with speckle variance processing to provide contrast to microvessels imaged in mouse dorsal skin fold window chambers [161]. Vessels with a diameter on the order of about 25 μm were able to be resolved (Figure 13.2).

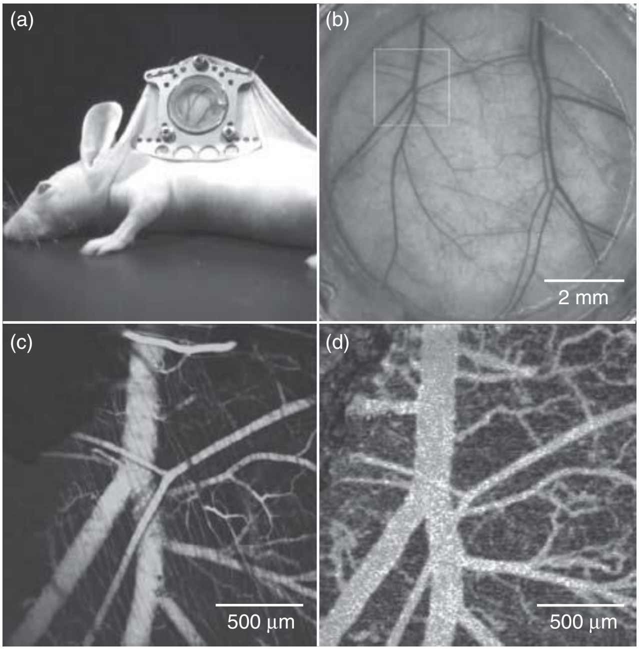

**FIGURE 13.2** OCT images of microvasculaure obtained by variance speckle contrast detection: (a,b) mouse dorsal skin fold window chamber model; (c) confocal fluorescence image of the microvascular region indicated by the box in (b); (d) OCT image of the same region. (From [161], with permission.)

OCT is a versatile imaging modality capable of both direct and indirect measurements of angiogenesis with the same instrumentation. OCT is already being applied to ophthalmology and may find other applications for angiogenesis measurement.

### 13.4.6 Multiphoton Microscopy

Nonlinear multiphoton excitation of fluorescence can enable three-dimensional imaging of structures to depths on the order of 500 to 600 μm in turbid media with minimal photobleaching or damage to living cells and tissue and with spatial resolution sufficient to detect neovasculature [162–166]; thus, angiogenesis in tissue and organ surfaces can be measured. Endogenous chromophores and exogenous contrast agents can be targeted. Multiphoton microscopy has been used to directly image blood vessels, primarily through the use of exogenous intravascular fluorescent optical contrast agents (dyes, quantum dots, etc.) [167]. As a direct imaging method, measurement of angiogenesis from three-dimensional data sets is relatively straightforward with multiphoton microscopy. Measurements of the number of vessels per unit volume, vessel surface area per unit volume, total vessel length per unit volume, tortuosity, fractal dimension, and others can be derived from multiphoton microscopy data sets of microvasculature, and these measurements can be useful for the measurement of angiogenesis [28].

In addition to vessel numbers, structure, and morphology, some measurements of vascular function can be assessed with multiphoton microscopy. This may potentially be useful for early detection of angiogenesis or measurements of some aspect of the angiogenesis process other than the appearance of neovasculature. For example, in retinal vessels it has been noted that measurable changes in established vasculature precede the appearance of detectable neovasculature, thus forecasting subsequent angiogenesis [29]. Blood velocity in vessel segments can be determined with multiphoton microscopy and the use of an exogenous fluorescent contrast agent that labels the plasma fraction of the blood. This is accomplished by performing rapid sequential line scans in vessel segments, with the line scan parallel to the vessel axis and thus the blood flow in the vessel [168]. Nonfluorescent red blood cells give dark contrast to the fluorescence from the plasma marker and appear as dark spots in the line scan. Blood flow causes the dark spots from the moving red blood cells to appear at different positions in the line scan. If the sequential line scans are arranged to form an $x$ (position) $\times$ $t$ (time) image, the red blood cell dark spots appear as streaks in the resulting image, and the slope of the streaks $(x/t)$ gives the velocity and the direction of flow relative to the scan direction [168]. With sufficient spatial resolution a velocity profile can be obtained in the vessel by moving the position of the scan line to different positions off the vessel axis midline. In addition to blood velocity, multiphoton microscopy can be used for measurements of vascular permeability [28,169]. This can be accomplished by comparing the signal from intravascular and extravascular spaces over time, following intravenous administration of a fluorescent contrast agent that can exchange with the tissue. The optical sectioning ability of multiphoton microscopy can enable more accurate determinations of vascular permeability than fluorescence reflectance imaging methods discussed in a previous section [28], and the permeability of individual vessels can be measured [25], thus highlighting any regional heterogeneities; however, measurement of a bulk permeability is not practical.

Intriguing new developments demonstrate that the potential exists for multiphoton microscopy imaging of microvessel morphology from endogenous hemoglobin contrast without the need for fluorescent contrast agents, and that blood oxygenation may also be measured [170,171]. Using an excited-state absorption (sequential two-photon absorption) two-color pump–probe technique, Fu et al. [171] demonstrated that three-dimensional blood vessel morphology images can be obtained from microvasculature in a mouse ear based on endogenous absorption contrast from hemoglobin as shown in Figure 13.3.

Using the same technique, it is even possible to discriminate between oxy- and deoxyhemoglobin and thus differentiate between arterioles and venules based on differences in the excited-state absorption signals between oxy- and deoxyhemoglobin [170]. With further development, it may be possible to perform absolute measurements of microvascular hemoglobin saturation in a three-dimensional microvessel network from endogenous signals.

With spatial resolution sufficient to image neovasculature, multiphoton microscopy can be used for direct measurements of angiogenesis in the surface regions of accessible tissues and organs. The availability of endoscopic multiphoton instruments and devices can extend these capabilities to body cavities and internal organs [172–175]. The potential ability to image microvessel structure and morphology with endoscopic probes and without the administration of exogenous contrast agents may foster clinical application of multiphoton microscopy for angiogenesis measurements.

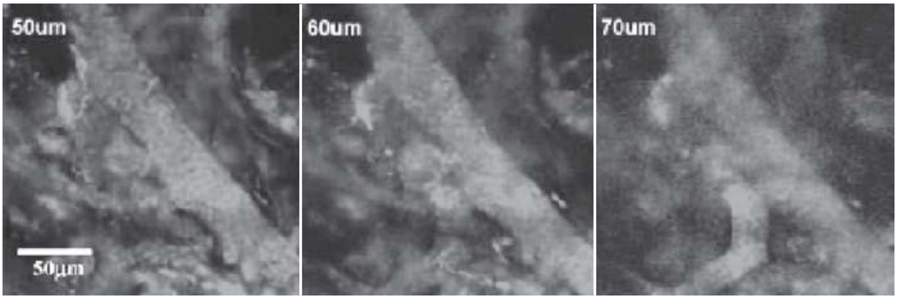

**FIGURE 13.3** Multiphoton microscopy images of microvasculature in a mouse ear at various depths obtained by an excited-state absorption two-color pump–probe technique based on hemoglobin absorption without addition of exogenous fluorescent contrast agents. (After [171], with permission.)

### 13.4.7 Optoacoustic Imaging

Optoacoustic (photoacoustic) imaging employs ultrasound detection of acoustic waves due to brief, rapid thermal expansion generated by short-pulsed lasers [176]. This combination of optical contrast by selective targeting of endogenous or exogenous chromophores with detection of deeply penetrating acoustic waves makes imaging possible several times greater than the optical penetration depth of the wavelength of light used. Endogenous chromophores such as hemoglobin and exogenous contrast agents such as nanoparticles, indocyanine green, and Evans Blue have been employed, and various configurations, such as handheld probes, tomographic scanning, and acoustic microscopy, have been used [177–189].

There are several examples in the literature where optoacoustic methods are used for imaging of tissue microvasculature and angiogenesis [180,183–189]. Depending on the instrument design, the spatial resolution of optoacoustic imaging can be sufficient to resolve microvasculature; thus, direct measurements of angiogenesis are possible. In addition, by using differential optical absorption of oxy- and deoxyhemoglobin, functional measurements of microvascular hemoglobin saturation are possible. Using a tomographic scanning configuration, Wang et al. demonstrated optoacoustic imaging of rat brain vasculature through intact skulls [183]. A tunable pulsed dye laser delivered two different wavelengths to provide absorption contrast between oxy- and deoxyhemoglobin for the generation of acoustic waves. Functional imaging was demonstrated by changing the breathing gas from hyperoxic to hypoxic oxygen concentrations and imaging the brain vascular hemoglobin saturation with optoacoustic imaging. Ku et al. imaged tumor-initiated angiogenesis in rat brains through intact skulls [184]. Metastatic mammary tumors were either implanted in the cortex directly or metastasized to the brain following cardiac left ventricular inoculation of tumor cells. Angiogenesis was identified by the abnormal microvasculature induced by the developing tumor. Xiang et al. imaged tumor neovasculature development in a chicken chorioallantoic membrane model following implantation of C8161 metastatic human melanoma tumor cells [190]. In addition, microvascular damage due to photodynamic therapy with protoporphyrin IX photosensitizer could be imaged. Maslov et al. used an acoustic microscopy configuration to achieve high spatial resolution such that microvascular structures as small as capillaries could be resolved in a mouse ear, as shown in Figure 13.4 [180]. A trade-off in imaging depth was required to achieve this high spatial resolution, since a high-frequency ultrasound transducer was required (>300 MHz) and the acoustic wave attenuation at this frequency limited the acoustic penetration depth to about 100 μm. In the examples above and the optoacoustic tomography literature to date, there has not yet been a detailed quantitative investigation of angiogenesis measurements validated by an independent means, especially in a clinical situation.

Optoacoustic tomography can potentially enable imaging of microvasculature and angiogenesis with spatial resolution sufficient to image microvascular morphology at depths greater then many other optical techniques. This ability may

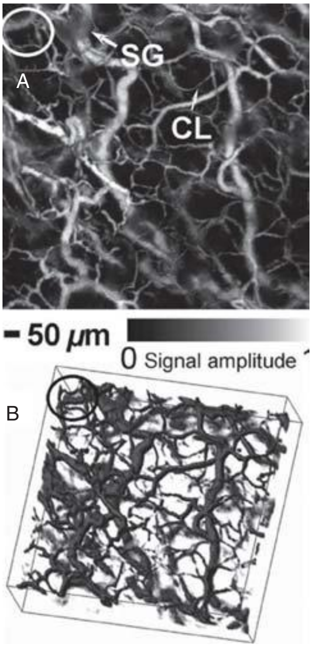

**FIGURE 13.4** Optoacoustic microscopy images of microvasculature in a mouse ear using hemoglobin absorption as an endogenous optical contrast agent. Microvessels on the order of 5-μm diameter can be resolved. (From [180], with permission.)

extend to challenging anatomical locations, as evidenced by the imaging of rat brain vasculature through intact skulls, as described previously. Thus, optoacoustic imaging may have a potential for direct measurements of angiogenesis in various accessible tissues and organs accessible to the instrumentation required for the technique. More research is currently required to demonstrate this potential.

### 13.4.8 Diffuse Spectroscopy and Optical Tomography

Diffuse optical spectroscopic and tomographic techniques employ approximations to the optical radiative transport equation based on photon diffusion for measurements and imaging of tissue optical properties, spectra of endogenous tissue chromophores, and distribution of exogenous optical contrast agents [191–199]. The use of wavelengths in the near infrared, where scattering dominates absorption and the diffusion approximation is valid, enables measurements of angiogenesis relatively deep within the body, such as within breast tissue or the brain. However, since the spatial resolution of diffuse optical spectroscopy and tomography is not sufficient to resolve neovasculature arising from angiogenesis, indirect measurement methods must be used. Signals related to microvascular volume fraction or oxygen transport function can be derived from endogenous absorption by hemoglobin. Steady-state and dynamic signals from fluorescent contrast agents can provide information on vascular volume fraction from steady-state signals, or vascular permeability from dynamic signals. In other cases, a change in a measured signal can implicate angiogenesis as the underlying cause, but this must be validated by an independent means, as these measurements are subject to misinterpretation if other factors can cause similar changes.

Instruments have been designed for use as stand-alone devices or for incorporation with ultrasound, x-ray tomography, and MRI systems. Diffuse optical spectroscopy and tomography methods have been employed to measure functional parameters related to tumor physiology, including angiogenesis, based on intrinsic optical absorption contrast of hemoglobin, water, and lipids, as well as tissue scattering properties [200–202]. Using human glioblastoma xenografts in athymic nude mice, Saxena et al. used steady-state diffuse spectroscopy to measure oxyhemoglobin and deoxyhemoglobin concentration in the tumor location at various times during tumor growth [203]. These measurements were then compared to histological assessment of microvascular density measurements in the tumor (number of vessels per unit area). The authors found that an increase in microvessel density followed a trend with an increase in deoxyhemoglobin concentration and thus concluded that deoxyhemoglobin concentration could potentially be used as a marker of tumor angiogenesis in growing tumors. One area of significant research for applications of diffuse spectroscopy and optical tomography is breast cancer diagnosis and monitoring of therapy [197]. Zhu et al. performed a comparison similar to that of Sazena et al. in human breast cancer patients [204]. Optical tomographic imaging was used to compare total hemoglobin concentration to microvessel density measurements made from tissue obtained from biopsies or surgical resections. In contrast to the measurements of Saxena et al., the authors found a statistically significant correlation between total hemoglobin concentration and microvessel density. Carpenter et al. combined breast tissue optical tomographic imaging data with MRI data that were acquired simultaneously using a custom-designed MRI-compatible optical tomography apparatus [205]. In a case study of a patient with an infiltrating ductal carcinoma, the authors found a higher total hemoglobin concentration in the tumor compared to the surrounding tissue. Additionally, decreased hemoglobin saturation was found in the tumor compared to the surrounding tissue. While the optical data were not compared explicitly to an independent method for assessment of the microvasculature, the trends in the data appear to be consistent with an angiogenic tumor that has abnormal oxygen transport. Cuccia et al. developed a technique that could effectively enable a combination of spectral imaging with spatially modulated light and a diffusion model of photon propagation in tissue that may be a useful method to measure bulk tissue microvascular function (hemoglobin concentration and saturation) with optical sectioning ability to a limited depth in tissue [206]. A detailed examination of angiogenesis measurements with this technique has not yet been published.

A number of different investigators have employed intravenous injection of optical contrast agents to measure vascular volume fraction or vascular permeability [207–211]. Montet et al. used macromolecule fluorescent microvascular contrast agents to measure the vascular volume fraction of tumors in mice by fluorescence tomography [212]. The contrast agents were high-molecular-weight polymers labeled with long-wavelength-emission fluorescent dyes. The authors showed a correlation between vascular volume fraction calculated with fluorescence tomography to immunohistochemistry microvascular density measurements after treatment of the tumors with the antiangiogenic agent bevacizumab (anti-VEGF antibody) [212]. Cuccia et al. used diffuse reflectance spectroscopy in rats to measure the pharmacokinetics properties of indocyanine green and methylene blue in rat mammary adenocarcinomas [210]. These measurements were correlated to MRI pharmacokinetic measurements using a gadolinium contrast agent in the same tumors. A two-compartment pharmacokinetic model was fit to the tumor optical contrast agent concentration over time data to extract capillary permeability surface area product and plasma volume fraction among other pharmacokinetic parameters. The fast-clearing methylene blue provided estimates of the arterial input function, while the indocyanine green, which binds to albumin in plasma, provided information about macromolecular pharmacokinetics in the tumor. The parameters calculated from the optical measurements were in good agreement with those from MRI measurements. Alacam et al. performed indocyanine green pharmacokinetics measurements similar to those of Cuccia et al., but these authors used diffuse optical tomography with human breast cancer patients to obtain spatially resolved pharmacokinetic measurements [209]. A two-compartment model was employed to calculate the pharmacokinetics parameters. The spatially resolved measurements revealed some intratumoral heterogeneity in the indocyanine green pharmacokinetics-rate parameters that bulk measurements could not reveal. Figure 13.5 is an example of pharmacokinetic-rate parameters in a breast tumor from a human patient.

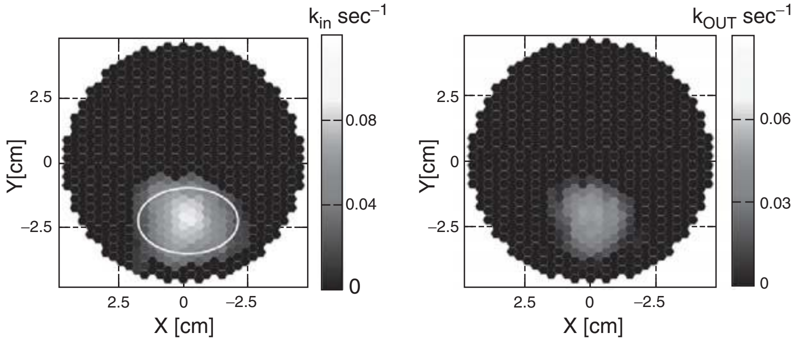

**FIGURE 13.5** Pharmacokinetic-rate parameters for ICG in a human patient with an invasive breast ductal carcinoma. The circled region in the left image indicates the approximate tumor location and size. The parameters $k_{\text{in}}$ and $k_{\text{out}}$ are rate parameters with units of $s^{-1}$ that reflect the leakage of ICG into and out of the extravascular extracellular space, respectively. (From [209], with permission.)

Diffuse spectroscopy and optical tomography methods may be promising techniques for clinical measurement of angiogenesis. Methods that rely on endogenous hemoglobin absorption signals for assessment of angiogenesis may require validation of angiogenesis by independent means to avoid misinterpretation of the signals. Pharmacokinetics measurements may be comparable to MRI measurements, and thus optical techniques for these measurements may in some cases be an acceptable alternative to MRI.

## 13.5 OTHER MODALITIES

A number of techniques with conventional medical imaging modalities have been used to detect and image angiogenesis. X-ray computed tomography (x-ray CT), magnetic resonance imaging (MRI), nuclear imaging, and ultrasound are discussed briefly below.

### 13.5.1 X-ray CT

Imaging blood vessels with x-ray CT requires administration of an x-ray contrast agent to highlight vascular morphology and function [213,214]. Larger vessels on the order of 100 μm can be directly imaged using this technique, but this spatial resolution is not sufficient to directly image angiogenic vessels [68]. Vascular function can be assessed using dynamic contrast techniques. By using appropriate timing of image capture pre- and postadministration of a contrast agent, blood flow and volume, fluid transit times, and vascular permeability can be measured [213,214]. In x-ray CT the signal due to the presence of contrast agent is directly related to the contrast agent concentration in the tissue; thus, calculation of various parameters related to microvessel function from contrast signal intensities is relatively straightforward [213–215]. Two-compartment models are generally sufficient to describe the pharmacokinetics of current clinically available x-ray contrast agents [215]. This technique can highlight differences in tissue regions that may indicate increased angiogenesis. A drawback to this method is the use of ionizing radiation; thus, cumulative exposure restrictions may limit serial observations.

### 13.5.2 MRI

Blood flow, vascular permeability, blood vessel morphology, and water diffusion can be assessed with MRI, and some of these signals can be used for angiogenesis measurement [213,214]. Contrast agents can be used with MRI imaging to highlight blood vessel morphology and function. Blood vessel function is assessed by measuring the pharmacokinetic behavior of the contrast agents [216]. Contrast agents for MRI vascular imaging include paramagnetic liposomes and iron nanoparticles [5]. For measurement of vascular function with MRI contrast agents, techniques such as dynamic susceptibility contrast MRI (DSC-MRI) and dynamic relaxivity contrast-enhanced MRI (DCE-MRI) have been employed [35,213,217]. Both of these methods can be used to measure blood volume and flow, and DCE-MRI can also be used to measure permeability (to the contrast agent). Contrast agents complexed with larger molecules, such as proteins (e.g., Gd-albumin), can enable measurements of blood volume and vessel hyperpermeabilty (permeability to macromolecules) [68,216]. $T_1$-weighted DCE-MRI can be used to measure various transport parameters related to passage of contrast agent through the extravascular space, while $T_2^*$-weighted DCE-MRI can be used to measure the transit of a bolus of contrast agent through the vasculature to calculate parameters related to blood volume and flow [18,214,217]. Molecular imaging is possible if the contrast agents are labeled with antibodies against cell surface proteins found on proliferating endothelial cells [5,19]. Molecular factors in general are expressed in the pico- to micromolar range; thus, molecular detection with MRI is challenging [20]. Nuclear imaging techniques are generally more sensitive at measuring low concentrations of radiolabeled markers [20].

A nontrivial challenge in the quantification of vascular functional parameters with the use of MRI contrast agents is that unlike x-ray CT, there is not a direct relation between the MRI signal intensity and tissue contrast agent concentration [213,216]. This is because the signal detected is from MRI is from water, so the signal that is measured is actually due to the contrast agent effect on the water signal. This effect is complex and not all variables are known for a given condition, so calculation of the information desired requires a model [213]. MRI measurements of angiogenesis are often made relative to tissue areas selected as normal tissue, due to the difficulty in interpreting changes in MRI signal magnitude [19].

MRI techniques for measuring blood vessel function also exist that do not require the use of traditional MRI contrast agents. Deoxyhemoglobin is paramagnetic, whereas oxyhemoglobin is diamagnetic. These differences in magnetization can be sensed in the $T_2^*$ decay time as the decay time decreases with an increased amount of deoxyhemoglobin present to distort the regional magnetic field. Inspired oxygen can be used with blood oxygen level–dependent (BOLD) MRI imaging to measure blood perfusion, with oxygen acting effectively as a contrast agent. However, since the BOLD MRI signal depends on both oxygenation and blood flow, it can be difficult to interpret [217]. Arterial spin tag labeling can be used to measure blood perfusion without the administration of exogenous contrast agents [217]. In this imaging technique, arterial blood is spin-tagged at a regional point just before the feeding arteriole supplies blood to a tissue region of interest. A potential limitation of arterial spin tag labeling is measurement artifacts created due to loss of the tagging signal if an arterial feeding vessel is far from a region of interest and the tagged blood has a long transit time to reach this region [217].

DCE-MRI is currently considered one of the more promising clinical techniques for measuring angiogenesis [217]. Some studies have shown a positive correlation between microvessel density measurements from histology and prognosis for several types of cancer; however, in other studies, angiogenesis measurements from MRI have had an even stronger correlation with cancer prognosis than have microvessel density measurements [19].

### 13.5.3 Nuclear Imaging

Nuclear imaging techniques do not provide true anatomical images and thus cannot directly resolve angiogenic vessels [218]. However, perfusion can be assessed by nuclear imaging techniques and can be quantified in absolute terms [18]. In positron emission tomography (PET) imaging, [$^{15}$O]water, [$^{15}$O]carbon monoxide, and [$^{13}$N]ammonia are among some of the agents that can be used to measure perfusion [5,20,219]. [$^{15}$O]water can exchange between plasma and the tissue extravascular space; thus, models are required to interpret the signals from this type of imaging. As noted in the review by Laking et al. [32], the models currently used most often are based on work by Kety and Schmidt. Since the spatial resolution of PET imaging is on the order of several millimeters, the functional signals represent an average of many different vessels in an imaging region [68].

Nuclear imaging techniques are very sensitive and capable of measuring low concentrations of radiolabeled markers [20]. This capability makes nuclear imaging a good candidate for molecular imaging with appropriately tagged markers. Antibodies or peptides with binding affinity for cell surface proteins found on proliferating endothelial cells can be labeled with radionuclides [5,20,219]. One such example is [$^{18}$F]galacto-RGD, which is a vascular tracer that tags $\alpha_v\beta_3$ integrin. In another example, radiolabeled VEGF has been used with single photon emission computed tomography (SPECT) and PET imaging to identify angiogenic vessels via targeting of the VEGF receptor [218,220].

Among some of the limitations of nuclear imaging are high cost and spatial resolution that is poor compared to other standard clinical imaging modalities. In addition, there is the need for on-site production of some radiochemicals with a cyclotron due to the short half-lives of the radioisotopes [213]. For example, [$^{15}$O]water has a half-life of only 2 minutes [32].

### 13.5.4 Ultrasound

Ultrasound can provide indirect measurements of angiogenesis from bulk tissue Doppler measurements of tissue perfusion with about 1-mm resolution [213]. Doppler ultrasound can highlight some of the abnormal morphology of tumor vessels [216]. Doppler ultrasound can also be used to measure microvascular volume fraction in terms of the volume of tissue with a velocity greater than zero [32]. One problem with this technique is that it captures measurements from all blood vessels, not just the small angiogenic vessels [32].

Ultrasound contrast agents can be used to provide microvascular contrast and increase spatial resolution. Microbubbles (gas-filled shells composed of lipids, polymers, or other matierals) can be used as ultrasound vascular contrast agents and improve spatial resolution such that vessels with diameters in the range 50 to 100 μm can be imaged, but detailed validations of ultrasound with standard histology measurements of angiogenesis are currently lacking [213,214]. Contrast agents can also help improve vascular volume fraction ultrasound measurements [214]. Ultrasound molecular imaging can be accomplished with the use of contrast agents. Microbubbles conjugated with anti-VEGF antibodies or RGD peptides that target $\alpha_v\beta_3$ integrins have been used to highlight proliferating neovasculature induced by tumor angiogenesis [220]. One problem with any clinical ultrasound technique is that the quality of the resulting images and data are operator dependent [19].

## 13.6 CONCLUSIONS

Angiogenesis is a complex process orchestrated by a host of molecular factors that induce a number of different morphological and functional changes in the microvasculature from which neovasculature arises. Imbalances in the molecular factors that control the formation of neovasculature in pathological conditions result in dysregulated angiogenesis. For pathologies in which angiogenesis is a key component of the disease process or normal physiological responses in which angiogenesis is a desired outcome, accurate quantitative measurement, monitoring, and imaging of angiogenesis can benefit clinical management of these conditions.

There are a number of ways to quantify angiogenesis, and the particular method employed will depend on the capabilities of the instrumentation for direct imaging of microvessels or indirect measurement of microvessel function or molecular factors associated with the angiogenesis process. Also, the anatomical region to be measured must be factored into the decision regarding the capabilities of the measurement/imaging modality chosen to measure the desired signal. An understanding of the biology of the physiological response or pathological condition can be helpful in choosing the optimal signal to monitor to achieve the most meaningful measurements to maximize clinical benefit. It is up to the investigator to achieve an appropriate balance in the choice of measurement method, measurement modalilty, and angiogenesis signal to measure within constraints provided by the particular case under investigation.

Optical methods may play a role in clinical quantitative measurement and imaging of angiogenesis. Several different angiogenesis measurement methods are also being developed and implemented using established conventional imaging modalities. However, optical methods may have advantages in some situations in terms of instrumentation cost, resolution, functional measurements, potential for small portable devices, and other factors. With a conscientious application to the development and testing of existing and new optical modalities of the concepts described previously, optical methods for quantitative angiogenesis measurement may become established clinical modalities in their own right.

## REFERENCES

1. Zakrzewicz, A., et al., Angioadaptation: keeping the vascular system in shape, *News Physiol. Sci*., Vol. 17, 2002, pp. 197–201.
2. Tirziu, D., and Simons, M., Angiogenesis in the human heart: gene and cell therapy, *Angiogenesis*, Vol. 8, 2005, pp. 241–251.
3. Folkman, J., Angiogenesis: an organizing principle for drug discovery? *Nat. Rev. Drug Discov*., Vol. 6, 2007, pp. 273–286.
4. Heil, M., et al., Arteriogenesis versus angiogenesis: similarities and differences, *J. Cell. Mol. Med*., Vol. 10, 2006, pp. 45–55.
5. Jouanneau, E., Angiogenesis and gliomas: current issues and development of surrogate markers, *Neurosurgery*, Vol. 62, 2008, pp. 31–52.
6. Carmeliet, P., and Jain, R.K., Angiogenesis in cancer and other diseases, *Nature*, Vol. 407, 2000, pp. 249–257.
7. Li, W.W., et al., The role of therapeutic angiogenesis in tissue repair and regeneration, *Adv. Skin Wound Care*, Vol. 18, 2005, pp. 491–500.
8. Sozzani, S., et al., Dendritic cell–endothelial cell cross-talk in angiogenesis, *Trends Immunol*., Vol. 28, 2007, pp. 385–392.
9. Hillen, F., and Griffioen, A.W., Tumour vascularization: sprouting angiogenesis and beyond, *Cancer Metastasis Rev*., Vol. 26, 2007, pp. 489–502.
10. Bergers, G., and Song, S., The role of pericytes in blood-vessel formation and maintenance, *Neuro-Oncol*., Vol. 7, 2005, pp. 452–464.
11. Burri, P.H., et al., Intussusceptive angiogenesis: its emergence, its characteristics, and its significance, *Dev. Dyn*., Vol. 231, 2004, pp. 474–488.
12. Otrock, Z.K., et al., Understanding the biology of angiogenesis: review of the most important molecular mechanisms, *Blood Cells Mol. Dis*., Vol. 39, 2007, pp. 212–220.
13. Hicklin, D.J., and Ellis, L.M., Role of the vascular endothelial growth factor pathway in tumor growth and angiogenesis, *J. Clin. Oncol*., Vol. 23, 2005, pp. 1011–1027.
14. Otrock, Z.K., et al., Vascular endothelial growth factor family of ligands and receptors: review, *Blood Cells Mol. Dis*., Vol. 38, 2007, pp. 258–268.
15. Harris, A.L., Hypoxia: a key regulatory factor in tumor growth, *Nat. Rev. Cancer*, Vol. 2, 2001, pp. 38–47.
16. Maxwell, P.H., and Ratcliffe, P.J., Oxygen sensors and angiogenesis, *Cell Dev. Biol*., Vol. 13, 2002, pp. 29–37.
17. Hasan, J., et al., Intra-tumoural microvessel density in human solid tumours, *Br. J. Cancer*, Vol. 86, 2002, pp. 1566–1577.
18. Sinusas, A.J., Imaging of angiogenesis, *J. Nucl. Cardiol*., Vol. 11, 2004, pp. 617–633.
19. Miller, J.C., et al., Imaging angiogenesis: applications and potential for drug development, *J. Natl. Cancer Inst*., Vol. 97, 2005, pp. 172–187.
20. Provenzale, J.M., Imaging of angiogenesis: clinical techniques and novel imaging methods, *Am. J. Roentgenol*., Vol. 188, 2007, pp. 11–23.
21. Russ, J.C., and Dehoff, R.T., *Practical Stereology*, 2nd ed., pp. 39–70, Plenum Press, New York, 1999.

22. Dewhirst, M.W., et al., Effects of bradykinin on the hemodynamics of tumor and granulating normal tissue microvasculature, *Radiat. Res.*, Vol. 130, 1992, pp. 345–354.
23. Chen, I.I., et al., Microvascular rarefaction in spontaneously hypertensive rat cremaster muscle, *Am. J. Physiol.*, Vol. 241, 1981, pp. H306–H310.
24. Sarraf-Yazdi, S., et al., Inhibition of in vivo tumor angiogenesis and growth via systemic delivery of an angiopoietin 2-specific RNA aptamer, *J. Surg. Res.*, Vol. 146, 2008, pp. 16–23.
25. Brown, E.B., et al., In vivo measurement of gene expression, angiogenesis and physiological function in tumors using multiphoton laser scanning microscopy, *Nat. Med.*, Vol. 7, 2001, pp. 864–868.
26. Nico, B., et al., Evaluation of microvascular density in tumors: pro and contra, *Histol. Histopathol.*, Vol. 23, 2008, pp. 601–607.
27. Tyrrell, J.A., et al., A 2-D/3-D model-based method to quantify the complexity of microvasculature imaged by in vivo multiphoton microscopy, *Microvasc. Res.*, Vol. 70, 2005, pp. 165–178.
28. Tozer, G.M., et al., Intravital imaging of tumour vascular networks using multiphoton fluorescence microscopy, *Adv. Drug Deliv. Rev.*, Vol. 57, 2005, pp. 135–152.
29. Hart, W.E., et al., Measurement and classification of retinal vascular tortuosity, *Int. J. Med. Inf.*, Vol. 53, 1999, pp. 239–252.
30. Parsons-Wingerter, P., et al., A novel assay of angiogenesis in the quail chorioallantoic membrane: stimulation by bFGF and inhibition by angiostatin according to fractal dimension and grid intersection, *Microvasc. Res.*, Vol. 55, 1998, pp. 201–214.
31. Kiessling, F., et al., Non-invasive assessment of vessel morphology and function in tumors by magnetic resonance imaging, *Eur. Radiol.*, Vol. 17, 2007, pp. 2136–2148.
32. Laking, G.R., et al., Imaging vascular physiology to monitor cancer treatment, *Crit. Rev. Oncol. Hematol.*, Vol. 58, 2006, pp. 95–113.
33. Neves, A.A., and Brindle, K.M., Assessing responses to cancer therapy using molecular imaging, *Biochim. Biophys. Acta*, Vol. 1766, 2006, pp. 242–261.
34. Jordan, B.F., et al., Dynamic contrast-enhanced and diffusion MRI show rapid and dramatic changes in tumor microenvironment in response to inhibition of HIF-1alpha using PX-478, *Neoplasia*, Vol. 7, 2005, pp. 475–485.
35. Rajendran, J.G., and Krohn, K.A., Imaging hypoxia and angiogenesis in tumors, *Radiol. Clin. North Am.*, Vol. 43, 2005, pp. 169–187.
36. Dewhirst, M.W., Angiogenesis and blood flow in solid tumors, in *Drug Resistance in Oncology*, pp. 3–23, B.A. Teicher (ed.), Marcel Dekker, New York, 1993.
37. Perry, B.N., and Arbiser, J.L., The duality of angiogenesis: implications for therapy of human disease, *J. Invest. Dermatol.*, Vol. 126, 2006, pp. 2160–2166.
38. Gimbrone, M.A., et al., Tumor dormancy in vivo by prevention of neovascularization, *J. Exp. Med.*, Vol. 136, 1972, pp. 261–276.
39. Warren, B.A., Tumor angiogenesis, in *Tumor Blood Circulation: Angiogenesis, Vascular Morphology and Blood Flow of Experimental and Human Tumors*, pp. 49–75, H.-I. Peterson (ed.), CRC Press, Boca Raton, FL, 1979.

40. Warren, B.A., The vascular morphology of tumors, in *Tumor Blood Circulation: Angiogenesis, Vascular Morphology and Blood Flow of Experimental and Human Tumors*, pp. 1–47, H.-I. Peterson (ed.), CRC Press, Boca Raton, FL, 1979.
41. Jain, R.K., Determinents of tumor blood flow: a review, *Cancer Res.*, Vol. 48, 1988, pp. 2641–2658.
42. Endrich, B., and Vaupel, P., The role of the microcirculation in the treatment of malignant tumors: facts and fiction, in *Blood Perfusion and Microenvironment of Human Tumors*, pp. 19–39, M. Molls and P. Vaupel (eds.), Springer-Verlag, New York, 1998.
43. Vaupel, P., Oxygen supply to malignant tumors, in *Tumor Blood Circulation: Angiogenesis, Vascular Morphology and Blood Flow of Experimental and Human Tumors*, pp. 143–168, H.-I. Peterson (ed.), CRC Press, Boca Raton, FL, 1979.
44. Dewhirst, M.W., et al., Quantification of longitudinal tissue pO2 gradients in window chamber tumours: impact on tumour hypoxia, *Br. J. Cancer*, Vol. 79, 1999, pp. 1717–1722.
45. Dewhirst, M.W., Concepts of oxygen transport at the microcirculatory level, *Semin. Radiat. Oncol.*, Vol. 8, 1998, pp. 143–150.
46. Sharma, R.A., et al., Angiogenesis as a biomarker and target in cancer chemoprevention, *Lancet Oncol.*, Vol. 2, 2001, pp. 726–732.
47. Ferrara, N., Vascular endothelial growth factor as a target for anticancer therapy, *Oncologist*, Vol. 9, Suppl. 1, 2004, pp. 2–10.
48. Weidner, N., Tumor vascularity as a prognostic factor in cancer patients: the evidence continues to grow, *J. Pathol.*, Vol. 184, 1998, pp. 119–122.
49. Kerbel, R.S., Antiangiogenic therapy: a universal chemosensitization strategy for cancer? *Science*, Vol. 312, 2006, pp. 1171–1175.
50. Siemann, D.W., et al., Differentiation and definition of vascular-targeted therapies, *Clin. Cancer Res.*, Vol. 11, 2005, pp. 416–420.
51. van der Bilt, J.D.W., and Rinkes, I.H.M.B., Surgery and angiogenesis, *Biochim. Biophys. Acta*, Vol. 1654, 2004, pp. 95–104.
52. Simons, M., Angiogenesis, arteriogenesis, and diabetes: Paradigm reassessed? *J. Am. Coll. Cardiol.*, Vol. 46, 2005, pp. 835–837.
53. Martin, A., et al., Abnormal angiogenesis in diabetes mellitus, *Med. Res. Rev.*, Vol. 23, 2003, pp. 117–145.
54. Azfar, R.S., and Gelfand, J.M., Psoriasis and metabolic disease: epidemiology and pathophysiology, *Curr. Opin. Rheumatol.*, Vol. 20, 2008, pp. 416–422.
55. Carvalho, J.F., et al., Vascular endothelial growth factor (VEGF) in autoimmune diseases, *J. Clin. Immunol.*, Vol. 27, 2007, pp. 246–256.
56. Bainbridge, J., et al., Angiogenesis as a therapeutic target in arthritis: lessons from oncology, *Curr. Pharm. Des.*, Vol. 12, 2006, pp. 2631–2644.
57. Laschke, M.W., et al., Angiogenesis in tissue engineering: breathing life into constructed tissue substitutes, *Tissue Eng.*, Vol. 12, 2006, pp. 1–12.
58. Kambouri, K., et al., Comparison of angiogenic activity after urethral reconstruction using free grafts and pedicle flap: an experimental study, *Eur. J. Pediatr. Surg.*, Vol. 16, 2006, pp. 323–328.
59. Gottrup, F., Oxygen in wound healing and infection, *World J. Surg.*, Vol. 28, 2004, pp. 312–315.

60. Hunt, T.K., and Pai, M.P., The effect of varying ambient oxygen tensions on wound metabolism and collagen synthesis, *Surg. Gynecol. Obstet.*, Vol. 135, 1972, pp. 561–567.
61. Hopf, H.W., et al., Wound tissue oxygen tension predicts the risk of wound infection in surgical patients, *Arch. Surg.*, Vol. 132, 1997, pp. 997–1004.
62. Tanaka, Y., et al., Tissue engineering skin flaps: Which vascular carrier, arteriovenous shunt loop or arteriovenous bundle, has more potential for angiogenesis and tissue generation ? *Plast. Reconstr. Surg.*, Vol. 112, 2003, pp. 1636–1644.
63. Wegewitz, U., et al., Novel approaches in the treatment of angiogenic eye disease, *Curr. Pharm. Des.*, Vol. 11, 2005, pp. 2311–2330.
64. Afzal, A., et al., Retinal and choroidal microangiopathies: therapeutic opportunities, *Microvasc. Res.*, Vol. 74, 2007, pp. 131–144.
65. Gargiulo, P., et al., Diabetes mellitus and retinopathy, *Dig. Liver Dis.*, Vol. 36, Suppl. 1, 2004, pp. S101–S105.
66. Gariano, R.F., and Gardner, T.W., Retinal angiogenesis in development and disease, *Nature*, Vol. 438, 2005, pp. 960–966.
67. Campochiaro, P.A., Gene therapy for ocular neovascularization, *Curr. Gene Ther.*, Vol. 7, 2007, pp. 25–33.
68. McDonald, D.M., and Choyke, P.L., Imaging of angiogenesis: from microscope to clinic, *Nat. Med.*, Vol. 9, 2003, pp. 713–725.
69. Meining, A., and Wallace, M.B., Endoscopic imaging of angiogenesis in vivo, *Gastroentrology*, Vol. 134, 2008, pp. 915–918.
70. Alessi, P., et al., Molecular targeting of angiogenesis, *Biochim. Biophys. Acta*, Vol. 1654, 2004, pp. 39–49.
71. Zhang, E.G., et al., Expression of CD105 (endoglin) in arteriolar endothelial cells of human endometrium throughout the menstrual cycle, *Reproduction*, Vol. 124, 2002, pp. 703–711.
72. Duff, S.E., et al., CD105 is important for angiogenesis: evidence and potential applications, *FASEB J.*, Vol. 17, 2003, pp. 984–992.
73. Behrem, S., et al., Endoglin is a better marker than CD31 in evaluation of angiogenesis in glioblastoma, *Croat. Med. J.*, Vol. 46, 2005, pp. 417–422.
74. Sokolov, K., et al., Molecular optical imaging of therapeutic targets of cancer, *Adv. Cancer Res.*, Vol. 96, 2007, pp. 299–344.
75. Boppart, S.A., et al., Optical probes and techniques for molecular contrast enhancement in coherence imaging, *J. Biomed. Opt.*, Vol. 10, 2005, p. 041208.
76. Licha, K., and Olbrich, C., Optical imaging in drug discovery and diagnostic applications, *Adv. Drug Deliv. Rev.*, Vol. 57, 2005, pp. 1087–1108.
77. Bremer, C., et al., Optical-based molecular imaging: contrast agents and potential medical applications, *Eur. Radiol.*, Vol. 13, 2003, pp. 231–243.
78. Birchler, M., et al., Infrared photodetection for the in vivo localisation of phage-derived antibodies directed against angiogenic markers, *J. Immunol. Methods*, Vol. 231, 1999, pp. 239–248.
79. Cai, W., et al., Peptide-labeled near-infrared quantum dots for imaging tumor vasculature in living subjects, *Nano Lett.*, Vol. 6, 2006, pp. 669–676.
80. Jin, Z.-H., et al., Noninvasive optical imaging of ovarian metastases using Cy5-labeled RAFT-c(-RGDfK-)$_4$, *Mol. Imaging*, Vol. 5, 2006, pp. 188–197.

81. Hsu, A.R., et al., In vivo near-infrared fluorescence imaging of integrin $\alpha_v\beta_3$ in an orthotopic glioblastoma model, *Mol. Imaging Biol.*, Vol. 8, 2006, pp. 315–323.
82. von Wallbrunn, A., et al., In vivo optical imaging of CD13/APN-expression in tumor xenografts, *J. Biomed. Opt.*, Vol. 13, 2008, p. 001007.
83. O'goshi, K.-I., and Serup, J., Safety of sodium fluorescein for in vivo study of skin, *Skin Res. Technol.*, Vol. 12, 2006, pp. 155–161.
84. Mellor, R.H., et al., Evidence for dermal angiogenesis in breast cancer related lymphedema demonstrated using dual-site fluorescence angiography, *Microcirculation*, Vol. 9, 2002, pp. 207–219.
85. Stanton, A.W.B., et al., Expansion of microvascular bed and increased solute flux in human basal cell carcinoma in vivo, measured by fluorescein video angiography, *Cancer Res.*, Vol. 63, 2003, pp. 3969–3979.
86. Gurfinkel, M., et al., Pharmacokinetics of ICG and HPPH-car for the detection of normal and tumor tissue using fluorescence, near-infrared reflectance imaging: a case study, *Photochem. Photobiol.*, Vol. 72, 2000, pp. 94–102.
87. Desmettre, T., et al., Fluorescence properties and metabolic features of indocyanine green (ICG) as related to angiography, *Surv. Ophthalmol.*, Vol. 45, 2000, pp. 15–27.
88. Wall, A., et al., Differentiation of angiogenic burden in human cancer xenografts using a perfusion-type optical contrast agent (SIDAG), *Breast Cancer Res.*, Vol. 10, 2008, p. R23.
89. Garini, Y., et al., Spectral imaging: principles and applications, *Cytometry A*, Vol. 69A, 2006, pp. 735–747.
90. Bearman, G., and Levenson, R., Biological imaging spectroscopy, in *Biomedical Photonics Handbook*, pp. 1–26, T. Vo-dinh (ed.), CRC Press, Boca Raton, FL, 2003.
91. Schultz, R.A., et al., Hyperspectral imaging: a novel approach for microscopic analysis, *Cytometry*, Vol. 43, 2001, pp. 239–247.
92. Zimmermann, T., et al., Spectral imaging and its applications in live cell microscopy, *FEBS Lett.*, Vol. 546, 2003, pp. 87–92.
93. Harris, A.T., Spectral mapping tools from the earth sciences applied to spectral microscopy data, *Cytometry A*, Vol. 69A, 2006, pp. 872–879.
94. Manolakis, D., and Shaw, G., Detection algorithms for hyperspectral imaging applications, *IEEE Signal Process. Mag.*, Vol. 19, 2002, pp. 29–43.
95. Keshava, N., and Mustard, J.F., Spectral unmixing, *IEEE Signal Process. Mag.*, Vol. 19, 2002, pp. 44–57.
96. Landgrebe, D., Hyperspectral image data analysis, *IEEE Signal Process. Mag.*, Vol. 19, 2002, pp. 17–28.
97. Chang, C.-I., and Brumbley, C., Kalman filtering approach to multispectral/hyperspectral image classification, *IEEE Trans. Aerosp. Electron. Syst.*, Vol. 35, 1999, pp. 319–330.
98. Schwartzkopf, W.C., et al., Maximum-likelihood techniques for joint segmentation-classification of multispectral chromosome images, *IEEE Trans. Med. Imaging*, Vol. 24, 2005, pp. 1593–1610.
99. Du, Y., et al., New hyperspectral discrimination measure for spectral characterization, *Opt. Eng.*, Vol. 43, 2004, pp. 1777–1786.

100. Lansford, R., et al., Resolution of multiple green fluorescent protein color variants and dyes using two-photon microscopy and imaging spectroscopy, *J. Biomed. Opt.*, Vol. 6, 2001, pp. 311–318.

101. Nielsen, A.A., Spectral mixture analysis: linear and semi-parametric full and iterated partial unmixing in multi- and hyperspectral image data, *Int. J. Compu. Vis.*, Vol. 42, 2001, pp. 17–37.

102. Kuan, C.-Y., and Healey, G., Using independent component analysis for material estimation in hyperspectral images, *J. Opt. Soc. Am. A*, Vol. 21, 2004, pp. 1026–1034.

103. Assendelft, O.W.V., *Spectrophotometry of Haemoglobin Derivatives*, pp. 1–152, Charles C Thomas, Springfield, IL, 1970.

104. Dunn, A.K., et al., Simultaneous imaging of total cerebral hemoglobin concentration, oxygenation, and blood flow during functional activation, *Opt. Lett.*, Vol. 28, 2003, pp. 28–30.

105. Ellsworth, M.L., et al., Measurement of hemoglobin oxygen saturation in capillaries, *Am. J. Physiol.*, Vol. 252, 1987, pp. H1031–H1040.

106. Kobayashi, H., and Takizawa, N., Imaging of oxygen transfer among microvessels of rat cremaster muscle, *Circulation*, Vol. 105, 2002, pp. 1713–1719.

107. Shonat, R.D., et al., Near-simultaneous hemoglobin saturation and oxygen tension maps in mouse brain using an AOTF microscope, *Biophys. J.*, Vol. 73, 1997, pp. 1223–1231.

108. Sorg, B.S., et al., Spectral imaging facilitates visualization and measurements of unstable and abnormal microvascular oxygen transport in tumors, *J. Biomed. Opt.*, Vol. 13, 2008, p. 014026.

109. Sorg, B.S., et al., Hyperspectral imaging of hemoglobin saturation in tumor microvasculature and tumor hypoxia development, *J. Biomed. Opt.*, Vol. 10, 2005, p. 044004.

110. Styp-Rekowska, B., et al., An imaging spectroscopy approach for measurement of oxygen saturation and hematocrit during intravital microscopy, *Microcirculation*, Vol. 14, 2007, pp. 207–221.

111. Khoobehi, B., et al., Hyperspectral imaging for measurement of oxygen saturation in the optic nerve head, *Invest. Ophthalmol. Vis. Sci.*, Vol. 45, 2004, pp. 1464–1472.

112. Arnoldussen, M.E., et al., Consequences of scattering for spectral imaging of turbid biologic tissue, *J. Biomed. Opt.*, Vol. 5, 2000, pp. 300–306.

113. Englmeier, K.-H., et al., A method for the estimation of the hemoglobin distribution in gastroscopic images, *Int. J. Bio-Med. Comput.*, Vol. 41, 1996, pp. 153–165.

114. Vogel, A., et al., Using noninvasive multispectral imaging to quantitatively assess tissue vasculature, *J. Biomed. Opt.*, Vol. 12, 2007, p. 051604.

115. Hidović-Rowe, D., and Claridge, E., Modelling and validation of spectral reflectance for the colon, *Phys. Med. Biol.*, Vol. 50, 2005, pp. 1071–1093.

116. Muto, M., et al., Narrow band imaging: a new diagnostic approach to visualize angiogenesis in superficial neoplasia, *Clin. Gastroenterol. Hepatol.*, Vol. 3, 2005, pp. S16–S20.

117. Roblyer, D., et al., Multispectral optical imaging device for in vivo detection of oral neoplasia, *J. Biomed. Opt.*, Vol. 13, 2008, p. 024019.

118. Zuzak, K.J., et al., Imaging hemoglobin oxygen saturation in sickle cell disease patients using noninvasive visible reflectance hyperspectral techniques: effects of nitric oxide, *Am. J. Physiol. Heart Circ. Physiol*., Vol. 285, 2003, pp. H1183–H1189.
119. Kostenicha, G., et al., Monitoring PDT-induced damage using spectrally resolved reflectance imaging of tissue oxygenation, *Cancer Lett*., Vol. 219, 2005, pp. 169–175.
120. Stamatas, G.N., and Kollias, N., In vivo documentation of cutaneous inflammation using spectral imaging, *J. Biomed. Opt*., Vol. 12, 2007, p. 051603.
121. Kotz, K.T., et al., Inspiratory contrast for in vivo optical imaging, *Opt. Express*, Vol. 16, 2008, pp. 19–31.
122. Briers, J.D., Laser Doppler and time-varying speckle: a reconciliation, *J. Opt. Soc. Am. A*, Vol. 13, 1996, pp. 345–350.
123. Briers, J.D., et al., Capillary blood flow monitoring using laser speckle contrast analysis (LASCA), *J. Biomed. Opt*., Vol. 4, 1999, pp. 164–175.
124. Wårdell, K., et al., Laser Doppler perfusion imaging by dynamic light scattering, *IEEE Trans. Biomed. Eng*., Vol. 40, 1993, pp. 309–316.
125. Forrester, K.R., et al., Endoscopic laser imaging of tissue perfusion: new instrumentation and technique, *Lasers Surg. Med*., Vol. 33, 2003, pp. 151–157.
126. Kvandal, P., et al., Low-frequency oscillations of the laser Doppler perfusion signal in human skin, *Microvasc. Res*., Vol. 72, 2006, pp. 120–127.
127. Fredriksson, I., et al., Optical microcirculatory skin model: assessed by Monte Carlo simulations paired with in vivo laser Doppler flowmetry, *J. Biomed. Opt*., Vol. 13, 2008, p. 014015.
128. Rajan, V., et al., Review of methodological developments in laser Doppler flowmetry, *Lasers Med. Sci*., Vol. 24, 2009, pp. 269–283.
129. Huang, Y.-C., et al., Noninvasive blood flow imaging for real-time feedback during laser therapy of port wine stain birthmarks, *Lasers Surg. Med*., Vol. 40, 2008, pp. 167–173.
130. Iabichella, M.L., et al., A review of microvascular measurements in wound healing, *Lower Extremity Wounds*, Vol. 5, 2004, pp. 181–199.
131. Stewart, C.J., et al., A comparison of two laser-based methods for determination of burn scar perfusion: laser Doppler versus laser speckle imaging, *Burns*, Vol. 31, 2005, pp. 744–752.
132. Duan, J., et al., Hypercholesterolemia inhibits angiogenesis in response to hindlimb ischemia–nitric oxide–dependent mechanism, *Circulation*, Vol. 102, Suppl. III, 2000, pp. III-370 to III-376.
133. Hamano, K., et al., The induction of angiogenesis by the implantation of autologous bone marrow cells: a novel and simple therapeutic method, *Surgery*, Vol. 130, 2001, pp. 44–54.
134. Jacob, A., et al., Validation of laser Doppler fluxmetry as a method of assessing neoangiogenesis in laryngeal tumours, *Eur. Arch. Otorhinolaryngol*., Vol. 263, 2006, pp. 444–448.
135. Stewart, C.J., et al., Kinetics of blood flow during healing of excisional full-thickness skin wounds in pigs as monitored by laser speckle perfusion imaging, *Skin Res. Technol*., Vol. 12, 2006, pp. 247–253.

136. Rajan, V., et al., Influence of tissue optical properties on laser Doppler perfusion imaging, accounting for photon penetration depth and the laser speckle phenomenon, *J. Biomed. Opt.*, Vol. 13, 2008, p. 024001.
137. Sheikh, A.Y., et al., Hyperoxia improves microvascular perfusion in a murine wound model, *Wound Repair Regen.*, Vol. 13, 2005, pp. 303–308.
138. Melis, P., et al., Oxygenation and microcirculation during skin stretching in undermined and nonundermined skin, *Plast. Reconstr. Surg.*, Vol. 112, 2003, pp. 1295–1301.
139. Stücker, M., et al., Increased laser Doppler flow in skin tumors corresponds to elevated vessel density and reactive hyperemia, *Skin Res. Technol.*, Vol. 12, 2006, pp. 1–6.
140. Boppart, S.A., et al., In vivo cellular optical coherence tomography imaging, *Nat. Med.*, Vol. 4, 1998, pp. 861–865.
141. Fujimoto, J.G., et al., Optical biopsy and imaging using optical coherence tomography, *Nat. Med.*, Vol. 1, 1995, pp. 970–972.
142. Huang, D., et al., Optical coherence tomography, *Science*, Vol. 254, 1991, pp. 1178–1181.
143. Izatt, J.A., et al., Optical coherence microscopy in scattering media, *Opt. Lett.*, Vol. 19, 1994, pp. 590–592.
144. Hitzenberger, C.K., et al., Three-dimensional imaging of the human retina by high-speed optical coherence tomography, *Opt. Express*, Vol. 11, 2003, pp. 2753–2761.
145. Izatt, J.A., et al., In vivo bidirectional color Doppler flow imaging of picoliter blood volumes using optical coherence tomography, *Opt. Lett.*, Vol. 22, 1997, pp. 1439–1441.
146. Michaely, R., et al., Vectorial reconstruction of retinal blood flow in three dimensions measured with high resolution resonant Doppler Fourier domain optical coherence tomography, *J. Biomed. Opt.*, Vol. 12, 2007, p. 041213.
147. Leitgeb, R., et al., Performance of Fourier domain vs. time domain optical coherence tomography, *Opt. Express*, Vol. 11, 2003, pp. 889–894.
148. White, B., et al., In vivo dynamic human retinal blood flow imaging using ultra-high-speed spectral domain optical coherence tomography, *Opt. Express*, Vol. 11, 2003, pp. 3490–3497.
149. Yun, S.H., et al., High-speed optical frequency-domain imaging, *Opt. Express*, Vol. 11, 2003, pp. 2953–2963.
150. Troutman, T.S., et al., Optical coherence tomography with plasmon resonant nanorods of gold, *Opt. Lett.*, Vol. 32, 2007, pp. 1438–1440.
151. Cang, H., et al., Gold nanocages as contrast agents for spectroscopic optical coherence tomography, *Opt. Lett.*, Vol. 30, 2005, pp. 3048–3050.
152. Yang, C., Molecular contrast optical coherence tomography: a review, *Photochem. Photobiol.*, Vol. 81, 2005, pp. 215–237.
153. Barton, J.K., et al., Use of microbubbles as an optical coherence tomography contrast agent, *Acad. Radiol.*, Vol. 9, Suppl. 1, 2002, pp. S52–S55.
154. Faber, D.J., et al., Toward assessment of blood oxygen saturation by spectroscopic optical coherence tomography, *Opt. Lett.*, Vol. 30, 2005, pp. 1015–1017.
155. Faber, D.J., et al., Light absorption of (oxy-)hemoglobin assessed by spectroscopic optical coherence tomography, *Opt. Lett.*, Vol. 28, 2003, pp. 1436–1438.

156. Lu, C.-W., et al., Measurement of the hemoglobin oxygen saturation level with spectroscopic spectral-domain optical coherence tomography, *Opt. Lett*., Vol. 33, 2008, pp. 416–418.

157. Kagemann, L., et al., Spectral oximetry assessed with high-speed ultra-high resolution optical coherence tomography, *J. Biomed. Opt*., Vol. 12, 2007, p. 041212.

158. Iftimia, N.V., et al., Toward noninvasive measurement of blood hematocrit using spectral domain low coherence interferometry and retinal tracking, *Opt. Express*, Vol. 14, 2006, pp. 3377–3388.

159. Wang, Y., et al., In vivo total retinal blood flow measurement by Fourier domain Doppler optical coherence tomography, *J. Biomed. Opt*., Vol. 12, 2007, p. 041215.

160. Makita, S., et al., Quantitative retinal-blood flow measurement with three-dimensional vessel geometry determination using ultrahigh-resolution Doppler optical coherence angiography, *Opt. Lett*., Vol. 33, 2008, pp. 836–838.

161. Mariampillai, A., et al., Speckle variance detection of microvasculature using swept-source optical coherence tomography, *Opt. Lett*., Vol. 33, 2008, pp. 1530–1532.

162. Denk, W., et al., Two-photon laser scanning fluorescence microscopy, *Science*, Vol. 2448, 1990, pp. 73–76.

163. Dunn, K.W., and Young, P.A., Principles of multiphoton microscopy, *Nephron Exp Nephrol*., Vol. 103, 2006, pp. e33–e40.

164. Helmchen, F., and Denk, W., Deep tissue two-photon microscopy, *Nat. Methods*, Vol. 2, 2005, pp. 932–940.

165. Diaspro, A., et al., Two-photon fluorescence excitation and related techniques in biological microscopy, *Q. Rev. Biophys*., Vol. 38, 2005, pp. 96–166.

166. Williams, R.M., et al., Multiphoton microscopy in biological research, *Curr. Opin. Chem. Biol*., Vol. 5, 2001, pp. 603–608.

167. Werkmeister, E., et al., Multiphoton microscopy for blood vessel imaging: new non-invasive tools (Spectral, SHG, FLIM), *Clin. Hemorheol. Microcirc*., Vol. 37, 2007, pp. 77–88.

168. Schaffer, C.B., et al., Two-photon imaging of cortical surface microvessels reveals a robust redistribution in blood flow after vascular occlusion, *PLoS Biol*., Vol. 4, 2006, p. e22.

169. Reyes-Aldasoro, C.C., et al., Estimation of apparent tumor vascular permeability from multiphoton fluorescence microscopic images of P22 rat sarcomas in vivo, *Microcirculation*, Vol. 15, 2008, pp. 65–79.

170. Fu, D., et al., Label-free in vivo optical imaging of microvasculature and oxygenation level, *J. Biomed. Opt*., Vol. 13, 2008, p. 040503.

171. Fu, D., et al., High-resolution in vivo imaging of blood vessels without labeling, *Opt. Lett*., Vol. 32, 2007, pp. 2641–2643.

172. Myaing, M.T., et al., Fiber-optic scanning two-photon fluorescence endoscope, *Opt. Lett*., Vol. 31, 2006, pp. 1076–1078.

173. König, K., et al., Clinical two-photon microendoscopy, *Microsc. Res. Tech*., Vol. 70, 2007, pp. 398–402.

174. Kim, P., et al., In vivo confocal and multiphoton microendoscopy, *J. Biomed. Opt*., Vol. 13, 2008, p. 010501.

175. Göbel, W., et al., Miniaturized two-photon microscope based on a flexible coherent fiber bundle and a gradient-index lens objective, *Opt. Lett*., Vol. 29, 2004, pp. 2521–2523.
176. Wang, L.V., and Wu, H.-S., Photoacoustic tomography, in *Biomedical Optics: Prinicples and Imaging*, pp. 283–321, J Wiley, Hoboken, NJ, 2007.
177. Yuan, Z., et al., Imaging of small nanoparticle-containing objects by finite-element-based photoacoustic tomography, *Opt. Lett*., Vol. 30, 2005, pp. 3054–3056.
178. Ku, G., and Wang, L.V., Deeply penetrating photoacoustic tomography in biological tissues enhanced with an optical contrast agent, *Opt. Lett*., Vol. 30, 2005, pp. 507–509.
179. Wang, X., et al., Noninvasive laser-induced photoacoustic tomography for structural and functional in vivo imaging of the brain, *Nat. Biotechnol*., Vol. 21, 2003, pp. 803–806.
180. Maslov, K., et al., Optical-resolution photoacoustic microscopy for in vivo imaging of single capillaries, *Opt. Lett*., Vol. 33, 2008, pp. 929–931.
181. Niederhauser, J.J., et al., Combined ultrasound and optoacoustic system for real-time high-contrast vascular imaging in vivo, *IEEE Trans. Med. Imaging*, Vol. 24, 2005, pp. 436–440.
182. Petrova, I.Y., et al., Optoacoustic monitoring of blood hemoglobin concentration: a pilot clinical study, *Opt. Lett*., Vol. 30, 2005, pp. 1677–1679.
183. Wang, X., et al., Noninvasive imaging of hemoglobin concentration and oxygenation in the rat brain using high-resolution photoacoustic tomography, *J. Biomed. Opt*., Vol. 11, 2006, p. 024015.
184. Ku, G., et al., Imaging of tumor angiogenesis in rat brains in vivo by photoacoustic tomography, *Appl. Opt*., Vol. 44, 2005, pp. 770–775.
185. Kolkman, R.G.M., et al., In vivo photoacoustic imaging of blood vessels with a pulsed laser diode, *Lasers Med. Sci*., Vol. 21, 2006, pp. 134–139.
186. Wang, X., et al., Noninvasive photoacoustic angiography of animal brains in vivo with near-infrared light and an optical contrast agent, *Opt. Lett*., Vol. 29, 2004, pp. 730–732.
187. Kolkman, R.G.M., et al., Photoacoustic determination of blood vessel diameter, *Phys. Med. Biol*., Vol. 49, 2004, pp. 4745–4756.
188. Pilatou, M.C., et al., Photoacoustic imaging of brain perfusion on albino rats by using Evans Blue as contrast agent, *Arch. Physiol. Biochem*., Vol. 111, 2003, pp. 389–397.
189. Sivaramakrishnan, M., et al., Limitations of quantitative photoacoustic measurements of blood oxygenation in small vessels, *Phys. Med. Biol*., Vol. 52, 2007, pp. 1349–1361.
190. Xiang, L., et al., Real-time optoacoustic monitoring of vascular damage during photodynamic therapy treatment of tumor, *J. Biomed. Opt*., Vol. 12, 2007, p. 014001.
191. Gibson, A.P., et al., Recent advances in diffuse optical imaging, *Phys. Med. Biol*., Vol. 50, 2005, pp. R1–R43.
192. Hielscher, A.H., Optical tomographic imaging of small animals, *Curr. Opin. Biotechnol*., Vol. 16, 2005, pp. 79–88.
193. Boas, D.A., et al., Imaging the body with diffuse optical tomography, *IEEE Signal Process. Mag*., Nov. 2001, pp. 57–75.

194. Venugopalan, V., et al., Radiative transport in the diffusion approximation: an extension for highly absorbing media and small source-detector separations, *Phys. Rev. E*, Vol. 52, 1998, pp. 2395–2407.
195. Tan, Y., and Jiang, H., Diffuse optical tomography guided quantitative fluorescence molecular tomography, *Appl. Opt.*, Vol. 47, 2008, pp. 2011–2016.
196. Rasmussen, J.C., et al., Radiative transport in fluorescence-enhanced frequency domain photon migration, *Med. Phys.*, Vol. 33, 2006, pp. 4685–4700.
197. Tromberg, B.J., et al., Assessing the future of diffuse optical imaging technologies for breast cancer management, *Med. Phys.*, Vol. 35, 2008, pp. 2443–2451.
198. Cerussi, A.E., et al., Spectroscopy enhances the information content of optical mammography, *J. Biomed. Opt.*, Vol. 7, 2002, pp. 60–71.
199. Jakubowski, D.B., et al., Monitoring neoadjuvant chemotherapy in breast cancer using quantitative diffuse optical spectroscopy: a case study, *J. Biomed. Opt.*, Vol. 9, 2004, pp. 230–238.
200. Zhou, C., et al., Diffuse optical monitoring of blood flow and oxygenation in human breast cancer during early stages of neoadjuvant chemotherapy, *J. Biomed. Opt.*, Vol. 12, 2007, p. 051903.
201. Jiang, H.B., et al., Near-infrared optical imaging of the breast with model based reconstruction, *Acad. Radiol.*, Vol. 9, 2002, pp. 186–194.
202. Yates, T., et al., Optical tomography of the breast using a multi-channel time-resolved imager, *Phys. Med. Biol.*, Vol. 50, 2005, pp. 2503–2518.
203. Saxena, V., et al., A noninvasive multimodal technique to monitor brain tumor vascularization, *Phys. Med. Biol.*, Vol. 52, 2007, pp. 5295–5308.
204. Zhu, Q., et al., Utilizing optical tomography with ultrasound localization to image heterogeneous hemoglobin distribution in large breast cancers, *Neoplasia*, Vol. 7, 2005, pp. 263–270.
205. Carpenter, C.M., et al., Image-guided optical spectroscopy provides molecular-specific information in vivo: MRI-guided spectroscopy of breast cancer hemoglobin, water, and scatterer size, *Opt. Lett.*, Vol. 32, 2007, pp. 933–935.
206. Cuccia, D.J., et al., Modulated imaging: quantitative analysis and tomography of turbid media in the spatial-frequency domain, *Opt. Lett.*, Vol. 30, 2005, pp. 1354–1356.
207. Weersink, R.A., et al., Accuracy of noninvasive in vivo measurements of photosensitizer uptake based on a diffusion model of reflectance spectroscopy, *Photochem. Photobiol.*, Vol. 66, 1997, pp. 326–335.
208. Ntziachristos, V., et al., Concurrent MRI and diffuse optical tomography of breast after indocyanine green enhancement, *Proc. Natl. Acad. Sci.*, Vol. 97, 2000, pp. 2767–2772.
209. Alacam, B., et al., Pharmacokinetic-rate images of indocyanine green for breast tumors using near-infrared optical methods, *Phys. Med. Biol.*, Vol. 53, 2008, pp. 837–859.
210. Cuccia, D.J., et al., In vivo quantification of optical contrast agent dynamics in rat tumors by use of diffuse optical spectroscopy with magnetic resonance imaging coregistration, *Appl. Opt.*, Vol. 42, 2003, pp. 2940–2950.
211. Intes, X., et al., In vivo continuous-wave optical breast imaging enhanced with indocyanine green, *Med. Phys.*, Vol. 30, 2003, pp. 1039–1047.

212. Montet, X., et al., Tomographic fluorescence imaging of tumor vascular volume in mice, *Radiology*, Vol. 242, 2007, pp. 751–758.

213. Jeswani, T., and Padhani, A.R., Imaging tumour angiogenesis, *Cancer Imaging*, Vol. 5, 2005, pp. 131–138.

214. Goh, V., et al., Functional imaging of colorectal cancer angiogenesis, *Lancet Oncol*., Vol. 8, 2007, pp. 245–255.

215. Dawson, P., Functional imaging in CT, *Eur. J. Radiol*., Vol. 60, 2006, pp. 331–340.

216. Daldrup-Link, H.E., et al., Imaging of tumor angiogenesis: current approaches and future prospects, *Curr. Pharm. Des*., Vol. 12, 2006, pp. 2661–2672.

217. Barrett, T., et al., MRI of tumor angiogenesis, *J. Magn. Reson. Imaging*, Vol. 26, 2007, pp. 235–249.

218. Dobrucki, L.W., and Sinusas, A.J., Imaging angiogenesis, *Curr. Opin. Biotechnol*., Vol. 18, 2007, pp. 90–96.

219. Higuchi, T., et al., Imaging of angiogenesis in cardiology, *Eur. J. Nucl. Med. Mol. Imaging*, Vol. 34, 2007, pp. S9–S19.

220. Cai, W., and Chen, X., Multimodality molecular imaging of tumor angiogenesis, *J. Nucl. Med*., Vol. 49, 2008, pp. 113S–128S.

# 14

# HIGH-RESOLUTION PHASE-CONTRAST OPTICAL COHERENCE TOMOGRAPHY FOR FUNCTIONAL BIOMEDICAL IMAGING

Taner Akkin
*University of Minnesota, Minneapolis, Minnesota*
Digant P. Davé
*University of Texas–Arlington, Arlington, Texas*

14.1 Introduction 414
14.2 Time-domain phase-sensitive interferometry 414
  14.2.1 Importance of differential phase operation 416
  14.2.2 System description 417
14.3 Spectral-domain phase-sensitive interferometry 419
14.4 Applications of differential phase-contrast imaging 421
  14.4.1 Surface profilometry 421
  14.4.2 Quantitative phase-contrast microscopy 423
  14.4.3 Optical detection of neural action potentials 425
14.5 Comparison of time- and spectral-domain phase-sensitive systems 428
14.6 Conclusions 429
References 429

*Advances in Optical Imaging for Clinical Medicine*, Edited by Nicusor Iftimia, William R. Brugge, and Daniel X. Hammer
Copyright © 2011 John Wiley & Sons, Inc.

## 14.1 INTRODUCTION

By measuring the phase on an interference signal, subwavelength changes in optical pathlength (OPL) can be measured. Although phase information is readily available in any interferometric setup, environmental perturbations corrupt the phase, rendering it difficult to interpret. For a reliable phase measurement, the interferometer design should enable cancellation of phase noise via implementation of a common-mode phase noise rejection scheme. This can be achieved in a common path interferometric setup or dual-channel interferometer. For example, time-domain dual-channel phase-sensitive interferometers utilizing either two polarization [1–3] or wavelength [4] channels, and common path spectral domain [5–7] interferometers can provide excellent phase sensitivity. Because common path and differential phase interferometric implementations enable common-mode noise cancellation, measurement of depth-resolved subwavelength changes in OPL is possible and allows novel optical imaging applications. In this chapter, phase-sensitive implementations of low-coherence interferometry in the time and spectral domains are described for biomedical applications.

## 14.2 TIME-DOMAIN PHASE-SENSITIVE INTERFEROMETRY

Conventional time-domain optical coherence tomography (OCT) [8] is typically used as a single-channel instrument that can generate depth-resolved images of a sample utilizing only amplitude information from the interferometric signals acquired. Figure 14.1a illustrates a basic fiber-based time-domain OCT system and its coherence function. Interference occurs when the difference between the optical pathlengths in the reference and sample arms is within the coherence length of the low-coherent light source. By scanning the beam in axial and lateral directions, depth-resolved tissue microstructures can be reconstructed by the amplitude demodulation of interferometric signal (Figure 14.1b). The imaging depth for OCT systems is typically a few millimeters in scattering tissue. The axial resolution $\Delta z$ (ca. 2 to 20 $\mu$m) is determined by the center wavelength $\lambda_0$ and the spectral bandwidth $\Delta\lambda$ of the light source. For light sources with a Gaussian-shaped power spectral density, it is given by $\Delta z = [(2\ln 2)/\pi](\lambda_0^2/\Delta\lambda)$, where $\Delta z$ and $\Delta\lambda$ represent the values for the full width at half maximum (FWHM). Therefore, OCT systems operating at shorter wavelengths and utilizing broad-bandwidth optical sources provide better axial resolution. The lateral resolution depends on the sample path optics, which focuses the beam on the sample and is given by $\Delta x \approx 1.22(f_L\lambda_0/d)$, where $d$ is the spot size on the lens with the focal length $f_L$. High lateral resolution requires a lens with high numerical aperture, resulting in a small beam spot at the focus.

In interferometry, both the amplitude and phase of the fringes carry physical information about the sample. To make use of the phase information, common path interferometers or differential measurement of dual-channel interferometers can be utilized. Assume an interferometric system similar to time-domain OCT,

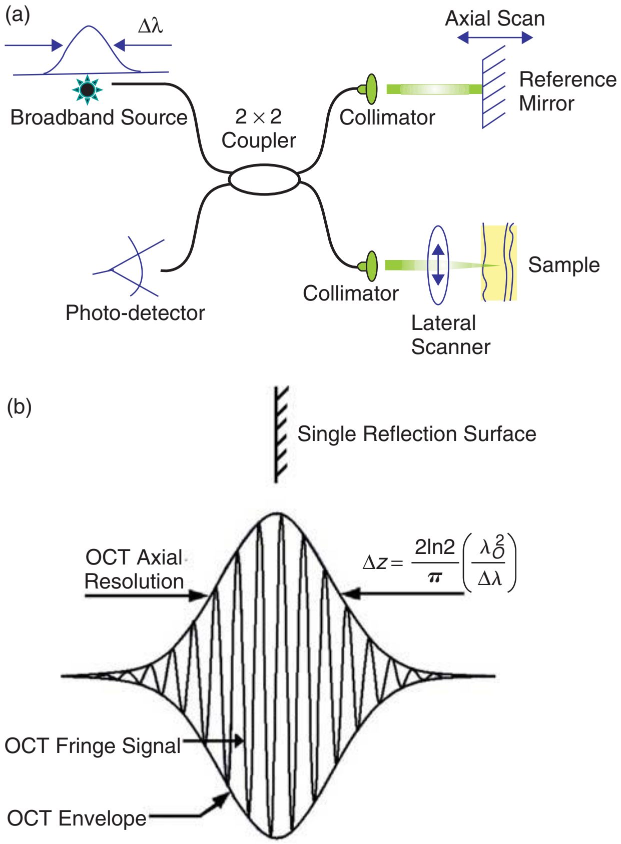
(a)
Δλ
Axial Scan
Reference Mirror
Broadband Source
2 × 2 Coupler
Collimator
Sample
Photo-detector
Collimator
Lateral Scanner
(b)
Single Reflection Surface
OCT Axial Resolution
$\Delta z = \frac{2\ln 2}{\pi}\left(\frac{\lambda_0^2}{\Delta\lambda}\right)$
OCT Fringe Signal
OCT Envelope

**FIGURE 14.1** (a) Fiber-based time-domain OCT; (b) OCT coherence function.

but with two uncorrelated channels. When the spectral density of the low-coherent light source is Gaussian with angular optical frequency width $\Delta\omega$, the interference term on each channel is proportional to

$$I_m(\tau) \propto e^{-(\tau/4a)^2} \cos(2\pi f \tau + \varphi_m + \phi_N) \tag{14.1}$$

where $m$ stands for the individual channels, $a = (\ln 2)^{1/2}/\Delta\omega$, $f$ is the modulation frequency, $\phi_N$ is the phase noise in the interferometer due to environmental perturbations, and $\varphi$ is the phase factor that carries physically relevant information about a specimen. In these channels $\varphi$ is proportional to the optical pathlength difference between reference and respective sample paths, which change due to changes in refractive index or geometrical size of the sample. Since $\phi_N$ is present in both channels, noise is canceled by computing the phase difference between the two channels ($\Delta\varphi = \varphi_1 - \varphi_2$). The OPL change between these channels ($\Delta p$)

is calculated from the phase difference and yields subwavelength sensitivity:

$$\Delta p = \frac{\lambda}{4\pi}\Delta\varphi \tag{14.2}$$

### 14.2.1 Importance of Differential Phase Operation

To demonstrate the efficacy of the differential phase approach in rejecting common-mode noise, a time-domain phase-sensitive system with two orthogonal polarization channels (described in the next section) is used to measure the temporal response of a liquid-crystal variable retarder. Figure 14.2 shows the fluctuations in each channel ($\varphi_1$ and $\varphi_2$) due to environmental perturbations such as vibration and temperature drift. This noise is the main obstacle for using single-channel conventional OCT systems for phase-sensitive measurements, making them inadequate for applications, which require detection of subwavelength changes in OPL. Figure 14.2 also shows the common-mode noise rejection of the differential phase operation ($\Delta\varphi$), which reveals the temporal response of the variable retarder in detail.

The differential phase system is sensitive to subnanometer changes in OPL. Using the same setup, very small pathlength changes are induced by slightly altering the amplitude of the variable retarder's drive signal. The measurement is divided into four stages, each of which is 10 ms in duration. The first and last stages are driven by the same voltage amplitude; hence, the same phase

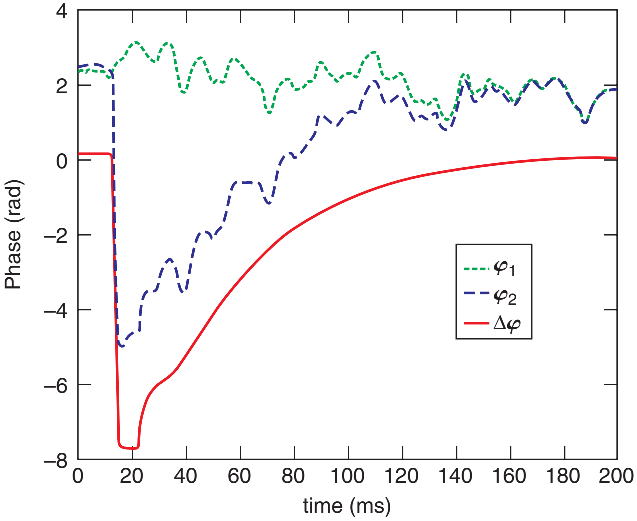

**FIGURE 14.2** Temporal response of a liquid-crystal variable retarder measured by a time-domain differential phase system. As shown, noise on individual channels ($\varphi_1$ and $\varphi_2$) is removed from the differential phase signal ($\Delta\varphi$). The drive signal is applied to the variable retarder between 10 and 20 ms.

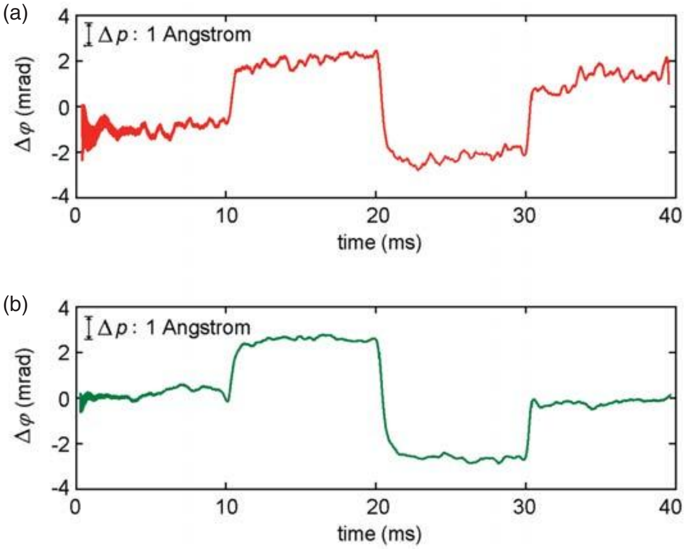

**FIGURE 14.3** Differential phase measurement allows subnanometer sensitivity to OPL changes: (a) single record; (b) average of 10 records. Traces have a 3-kHz bandwidth.

levels are expected. The OPL difference between these channels is altered in opposite directions in the second and third stages. Figure 14.3a shows that the phase sensitivity of an individual record is as low as 1 mrad, which corresponds to an OPL change of nearly 1 Å (0.1 nm) when the source wavelength is centered at 1.31 μm [equation (14.2)]. Assuming that the environmentally induced single-channel phase noise is 1.5 rad (Figure 14.2), the differential measurement improves the phase sensitivity by at least three orders of magnitude (>30 dB) compared to single-channel performance. Such a high common-mode rejection allows subnanometer-sensitive measurements. Furthermore, averaging over multiple records improves the minimum detectable signal. Averaging $N$ records should improve the signal/noise ratio by a factor of $N^{1/2}$. Figure 14.3b shows noise reduction and removal of a slow drift by averaging.

### 14.2.2 System Description

The results above are produced by a dual-channel differential phase-contrast interferometer (DPC-OCT) that allows time- and depth-resolved measurement of angstrom/nanometer-scale OPL changes. Figure 14.4 illustrates a schematic diagram of the DPC-OCT whose channels correspond to orthogonal polarization modes of polarization-maintaining (PM) fiber. Light from a low-coherence source ($\lambda_0 = 1.31$ μm and $\Delta\lambda \approx 60$ nm) propagates toward the 2 × 2 PM coupler, and two decorrelated orthogonal polarization states (fast and slow) are created by the birefringent of the PM fiber. After splitting, phase modulation is achieved in the reference arm using a lithium niobate ($LiNbO_3$) electrooptic waveguide

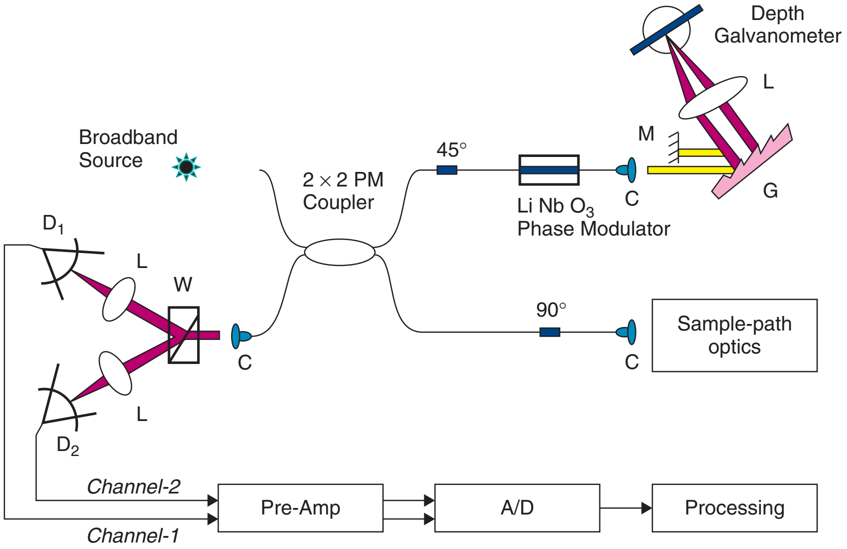

**FIGURE 14.4** Differential phase-contrast OCT (DPC-OCT). A/D, analog-to-digital converter; C, collimator; D, detector; G, diffraction grating; L, lens; M, mirror; W, Wollaston prism.

phase modulator, which allows propagation of the slow channel only; therefore, a 45° splice ensures coupling of both modes equally into the modulator. A rapid-scanning optical delay line in the bulk portion of the reference arm is configured to compensate for the dispersion imbalance between the reference and sample arms of the interferometer by adjusting the grating-lens separation, which minimizes the width of coherence functions. To locate both coherence functions at the same position, a 90° splice in the sample path is used. Configuration of sample path optics depends on the specific application. The basic configuration, which only focuses light on a sample (Figure 14.5a), is used for the results presented above. This configuration can be used for OCT imaging as well. Figure 14.5 illustrates the other two main configurations to record differential phase measurements from laterally and longitudinally separated points.

When OPLs of reference and sample arms match, light backscattered from these arms interferes in the PM coupler. A Wollaston prism in the detection path separates the two polarization channels for detection. The output of each photodetector is amplified and bandpass-filtered in the analog domain prior to digitization and processing. Depth-resolved intensity images of tissues, as in OCT imaging, can be obtained by an envelope detection algorithm that uses low-pass filtering of the squared channels (incoherent detection, or amplitude demodulation). However, extraction of the phase difference between the interferometric fringes in the two polarization channels is sufficient in many applications. In these cases, instead of scanning tissue in depth over many coherence lengths, stable sinusoidal fringes are obtained by phase modulation, which scans only

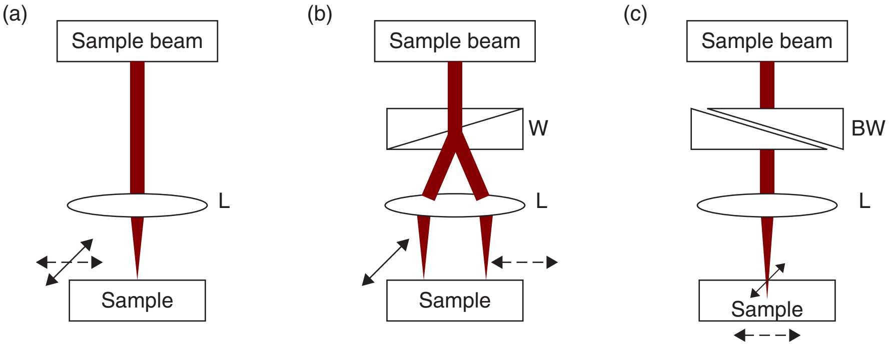

**FIGURE 14.5** Sample path configurations: probing single point (a), and two (b) lateral or (c) longitudinal points with orthogonal polarization channels. BW, birefringent wedges; L, lens; W, Wollaston prism.

one fringe repeatedly. Since information is contained in the computed phase, zero-phase digital bandpass filters may be implemented to suppress noise further, provided that the filters must be sufficiently wide to cover the bandwidth of the phase signal. The phase of fringes in each channel is calculated by computing the angle between the signal and its Hilbert transform. The phases are unwrapped to remove phase jumps, and the subsequent subtraction yields the phase difference, $\Delta\varphi$, which is then converted to change in OPL using equation (14.2).

Applications of DPC-OCT include high-resolution intensity and phase imaging, determination of refractive index and birefringence, surface profilometry, measurement of tissue response to external stimuli, measurement of transient changes in surface displacement, birefringence and optical pathlength, cellular imaging, and endoscopic and microfluidic biosensing. Some of the applications are introduced in Section 14.4.

## 14.3 SPECTRAL-DOMAIN PHASE-SENSITIVE INTERFEROMETRY

Consider an optical setup in which after traveling through two optical paths (reference and sample), light from a low-coherence light source is recombined and the spectrum is measured. The spectrum recorded is not only the superposition of the spectrum of light from the sample and the reference path but it has an additional term that is present due to the nonzero cross-correlation of reference and sample spectrums. This nonzero cross-correlation term modulates the spectrum, giving rise to spectral interference. The modulation frequency is proportional to the optical pathlength difference between the reference and sample paths. The recorded spectral interference, $S(k)$, due to the mixing of light from the reference and sample paths, can be written

$$S(k) = S_{\mathrm{ref}}(k) + S_{\mathrm{samp}}(k) + 2\sqrt{S_{\mathrm{ref}}(k)S_{\mathrm{samp}}(k)}\mu(k)\cos(2\pi k\,\Delta p + \varphi_0) \quad (14.3)$$

where $k$ is the wave vector, $\mu(k)$ is the spectral coherence function, and $\Delta p$ is the optical pathlength difference between the reference and sample paths. $S_{\text{ref}}(k)$ and $S_{\text{samp}}(k)$ are the spectrum of light from the reference and sample paths, respectively. $\Delta p$ is a product of the geometrical pathlength difference ($\Delta z$) and refractive index of the medium separating the reference and sample paths, which can be calculated by Fourier transformation of (14.3). It should be noted that $\mu(k)$ is not a Fourier transform of the temporal coherence function. Depth-resolved subwavelength changes in $\Delta p$ can be measured by detecting the change in phase of the frequency component of interest in the modulation term in (14.3):

$$\varphi|_{z=n\Delta z} = \tan^{-1}\frac{\text{Im}[F(S(k)]}{\text{Re}[F(S(k)]} = \frac{4\pi n\,\Delta z}{\lambda_0} \tag{14.4}$$

SD-OCT, also known as Fourier-domain OCT, measures cross-spectral density using a spectrometer at the detection path of the interferometer [9]. Fiber-based implementation of a common-path SD-OCT is shown in Figure 14.6. The system can be constructed with commercially available components and minimal effort in optical alignment.

In the interferometer setup, light from a broadband light source is coupled into a 2 × 2 single-mode fiber (SMF) splitter. Any low-coherence broadband light source can be used as long as the spectrum of the light source is stable and sufficient light can be coupled into a single-mode fiber to maintain the signal/noise ratio necessary to detect a desired phase change in the spectral interference fringes. Fiber-coupled superluminescent diodes (SLDs) are an excellent choice. These compact sources have a stable spectral and power output. Given the potential of damage to an SLD due to backreflection from the optical setup, an optical isolator is inserted between the SLD source and the input port of the 2 × 2 SMF coupler.

In the common-path configuration, only one output port of the coupler is used. The port that is not used should be angle polished or angle cleaved to avoid any backreflection from the fiber–air interface into the coupler. As an alternative, the fiber can be dipped in 60 to 80% glycerol solution to avoid backreflection. This backreflection will reduce the signal/noise ratio of the interferometric signal and hence the sensitivity of the measured phase. An alternative for the coupler in the common-path configuration is to use a circulator, which is a three-port optical

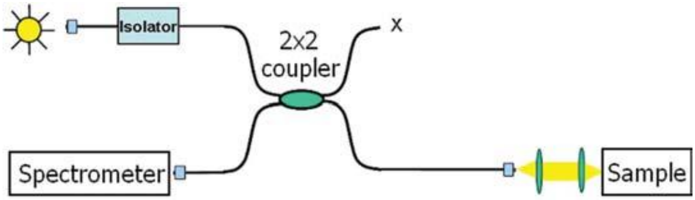

**FIGURE 14.6** Setup of a common-path fiber-based spectral-domain phase-sensitive interferometer.

component. When there is a semitransparent surface such as a glass–air interface along the path, light backreflected from this surface can be utilized for the reference light. Therefore, it interferes with the light backreflected or backscattered from the sample located along the same path. The other configuration makes use of differential phase measurement and includes a reference arm. Unlike in time-domain systems, the reference arm of spectral-domain systems has a very simple design that may only include a reflecting surface. The standard deviation of the phase noise, when autointerference of glass surfaces is used in our setup, corresponds to about 50-pm noise on OPL. This means that the phase sensitivity of SD-OCT systems allows measurement of subnanometer changes in OPL at multiple depths. The noise level depends on the signal/noise ratio; therefore, probing tissues may increase the noise level due to a reduction in the light level collected from the tissue. Another factor affecting the noise level is vibration. Although vibrations in the axial direction can be eliminated by differential measurement, vibrations in the lateral direction may degrade the phase signal for tissues, which are known to have rough surfaces.

## 14.4 APPLICATIONS OF DIFFERENTIAL PHASE-CONTRAST IMAGING

In the following sections we present the use of phase-sensitive detection for surface profilometry, quantitative phase-contrast microscopy, and optical detection of neural action potentials.

### 14.4.1 Surface Profilometry

The shape and quality of the optical surfaces, including the cornea and lens in the eye, are crucial for better performance. To acquire nanometer-scale information about surfaces, phase-sensitive interferometry can be utilized for noncontact characterization of surfaces and surface structures. Noncontact techniques for measuring surface roughness include the scanning electron microscope, light scattering, light sectioning, and various interferometric techniques, such as fringes of equal chromatic order, Nomarski and differential interference contrast, Tolansky multiple-beam interferometry, and two-beam interferometry based on Michelson, Linnik, and Mirau (see the article by Bhusnan et al. [10] for a survey of these techniques).

To demonstrate and compare the accuracy and capability of DPC-OCT and SD-OCT methods, a sample consisting of two chromium film layers is prepared. Three-dimensional images of the surface topography are recorded for both cases and shown in Figure 14.7. The insets illustrate the beams scanned over the sample. The separation of laterally displaced DPC-OCT beams was 1.1 mm (Figure 14.7a), and only one of the beams passed over the step by using a galvanometer-based scanning setup while a motorized stage under the sample was moving slowly (ca. 100 μm/s) in the other direction. The interference fringe

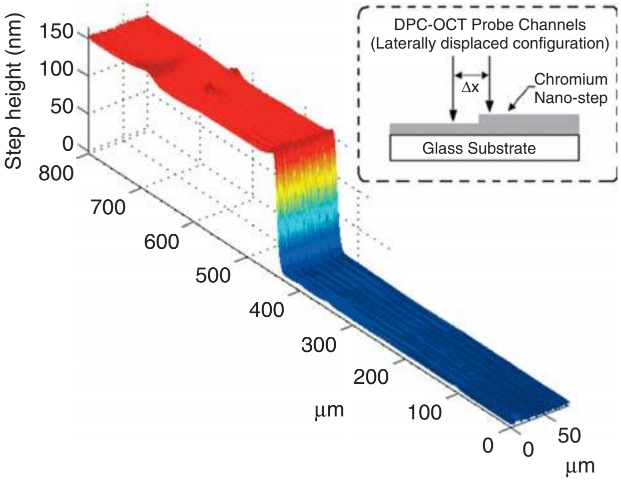

(a)

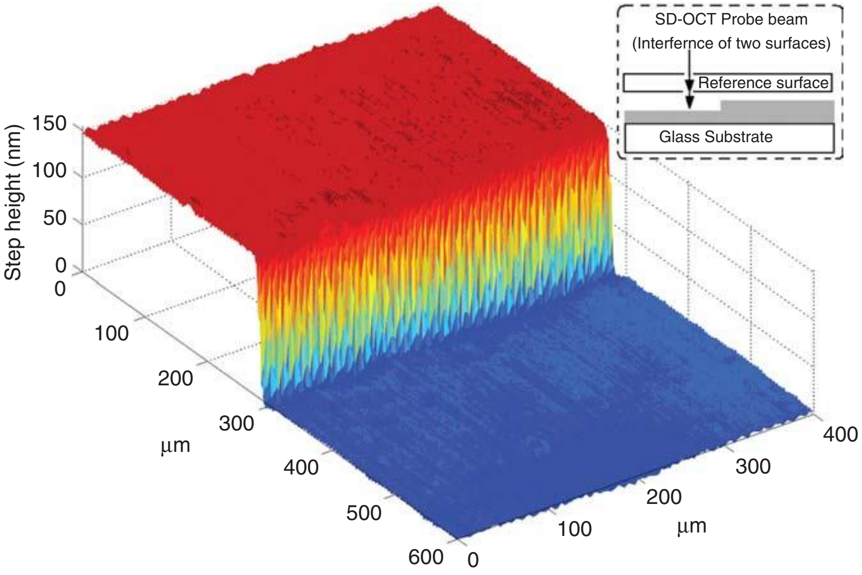

(b)

**FIGURE 14.7** Imaging a chromium nanostep by (a) DPC-OCT and (b) SD-OCT systems. With the inclusion of a reference surface, longitudinally displaced channels of DPC-OCM can also be used for the image.

frequency as a result of $LiNbO_3$ phase modulation was 50 kHz, and the channels were acquired at a 5-MS/s sampling rate. Figure 14.7b shows the differential phase imaging across the chromium step compared with a stationary reference in the SD-OCT setup. The scanning was performed by galvanometer-based scanners, and CCD integration time of the spectrometer was 34 $\mu$s. Not only the step height (ca. 150 nm), but also smaller surface features on the order of 10 nm are visible in Figure 14.7. An atomic force microscope confirmed the measured step height and the existence of smaller surface features. The measurements are in excellent agreement with each other.

The differential phase approach is useful for imaging surface or subsurface tissue response to certain stimuli for diagnostic purposes [11]. These include surface displacement of cartilage tissue in response to electrical stimulation, laser-induced photothermal changes inside arterial tissue, and transient structural changes due to neural action potentials. The latter is described in Section 14.4.3.

### 14.4.2 Quantitative Phase-Contrast Microscopy

Phase-contrast techniques are ideally suited to image specimens with spatial variation in OPL. The phase of the light revealed by an interferometer conveys information on the optical properties and/or geometrical features of a specimen, which cannot be accessed by intensity measurement. Addition of phase-contrast methods (e.g., Zernike phase contrast and differential interference contrast) to conventional bright-field microscopy allows clear visualization of unstained cells and tissue specimens. For example, unstained human epithelial cheek cells are not visible using bright-field microscopy but are clearly visible with microscopic detail of cell structure when viewed under a phase-contrast microscope. Similarly, phase detection of OCT interference fringe intensity signals has the potential to dramatically improve phase-contrast resolution of conventional OCT images, especially in biological specimens where the reflectivity contrast is poor or refractive index variations are small. More importantly, quantification of precise and direct quantification of measured phase is possible. Three different resolution parameters (lateral, longitudinal, and contrast) define the ultimate resolution of an OCT image. Lateral resolution can be improved by using focusing optics of higher numerical aperture (NA). It is the longitudinal resolution and, more importantly, the lack of phase-contrast resolution that limit the ability of a conventional OCT instrument to image unstained biological specimen such as tissue with subcellular resolution. Phase resolution defines the ability to resolve spatial changes in OPL, whereas the longitudinal resolution defines the ability to resolve two reflectors in depth. In conventional OCT the coherence length of the broadband light source limits the phase contrast and longitudinal resolution. Tissue constituents are distinguished optically by spatial variation in refractive index. Connective tissue fibers (bundles of elastin and collagen), cell walls, cytoplasmic organelles, and cell nuclei contribute most to local refractive index variations $[\Delta n(x, y, z)]$. It is the combination of spatial variation in the refractive index and geometric size of tissue constituents that contributes to the total phase contrast (i.e., spatial variation in OPL). Subwavelength changes in OPL in cells and tissues can be detected if the phase of the recorded interference fringe intensity signal is measured. In structural imaging of tissue with conventional OCT, only the envelope of the interference fringe intensity signal is detected.

Quantitative phase-contrast imaging of live cells using a prototype differential phase-contrast optical coherence microscope (DPC-OCM) [12] which includes human epithelial cheek cells, skeletal muscle cells, and malignant kidney cells is described below. Cell lines (skeletal muscle cell line L6) were maintained in Dulbecco's modified Eagle medium (DMEM, Life Technologies) supplemented with 5% fetal bovine serum (FBS) and 1% penicillin–streptomycin–antimycotic (PSA, Life Technologies). Cells were grown at 37°C in a humidified air atmosphere with 5% $CO_2$ for 72 hours on No. 0 glass coverslips. Human epithelial cheek cells were prepared by gently swabbing the inner cheek of a volunteer with a cotton tip and placing the specimen on a glass coverslip.

The sample holder was mounted on a computer-controlled linear motorized XY translation stage. Cells to be imaged with DPC-OCM are first visualized with an inverted microscope placed underneath the sample holder (Figure 14.8). A 40× objective lens was used to focus DPC-OCM sample beams to a spot diameter of 3.5 μm. In these experiments, lateral and collinear configurations were used for *en face* DPC-OCM imaging of cells, as shown in Figure 14.8. Synchronous movement of motorized linear translation stages in the $XY$-plane does *en face* imaging of the specimen. Interference fringe intensity signal in each channel is recorded while the specimen is translated along the $X$-direction, which constitutes a single line scan. Stacking processed individual line scans gives an *en face* DPC-OCM image of the cell layer.

*En face* DPC-OCM images of single epithelial cheek cells and corresponding bright-field images are shown in Figure 14.9. *En face* DPC-OCM images quantitatively map the variation of optical pathlength in cells. A DPC-OCM image

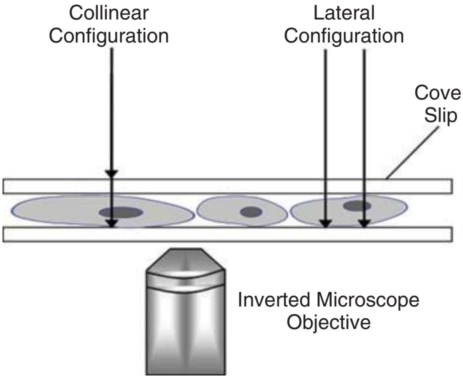

**FIGURE 14.8** Sample path configuration for recording bright-field and *en face* DPC-OCM images.

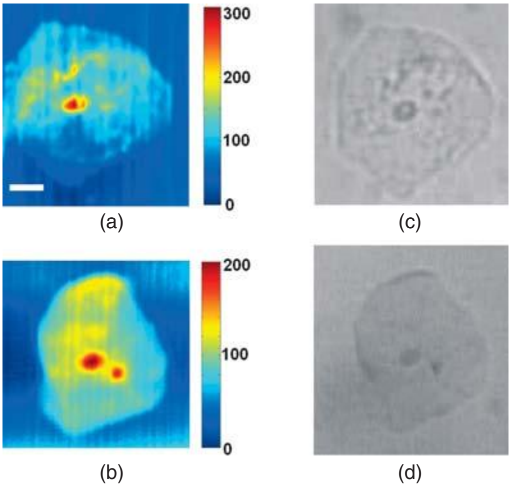

**FIGURE 14.9** (a,b) DPC-OCM and (c,d) bright-field microscope images of single human epithelial cheek cells. Lateral (a) and collinear (b) probe beam configurations were used to record DPC-OCM images. The color bar denotes the optical pathlength in nanometers. Scale bar, 10 μm.

of multiple epithelial cheek cells is compared with a phase-contrast microscope image of similar epithelial cheek cells (Figure 14.10a and 14.10d). Shown in Figure 14.10 are images of epithelial cheek cells, skeletal muscle, and malignant kidney cells. In DPC-OCM images, despite the relatively coarse lateral resolution (3.5 μm), cell boundaries and cell nucleus are distinct and other subcellular features are visible. Additional subcellular features are visible in DPC-OCM images of epithelial cheek cells (Figures 14.9 and 14.10) which are larger in size. In DPC-OCM images, contrast arises entirely due to refractive index variation ($\Delta n$) or thickness of subcellular structures. Importantly, DPC-OCM phase-contrast images provide a *quantitative measure* of changes in optical pathlength within the cell—an important analytical feature that can potentially be very useful in studying function-related cellular and subcellular morphological changes with nanometer resolution.

### 14.4.3 Optical Detection of Neural Action Potentials

Imaging neural structure and function has been the focus of significant research. Depth-resolved optical methods such as OCT produce high-resolution cross-sectional images of neural microstructure and allow noninvasive or minimally invasive investigations in clinics. For instance, imaging of retinal nerve fiber layers, owing to transparent structures in the eye, is the most successful OCT application that is clinically available for diagnostic purposes.

In neural diseases, nerve fibers can lose their functionality before cell death occurs, and therefore any diagnostic tool that provides a measure of functionality

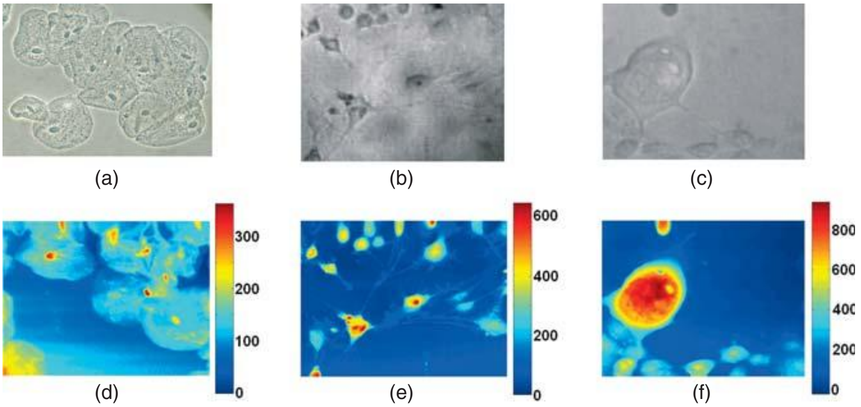

**FIGURE 14.10** Microscope images (top row) and false-color DPC-OCM images (bottom row): (a) phase-contrast microscope and (d) DPC-OCM images of human epithelial cheek cells; (b) bright-field microscope and (e) DPC-OCM images of human skeletal muscle cells; (c) bright-field microscope and (f) DPC-OCM images of malignant human kidney cells. Dimensions of all images are 150 × 200 μm. The color bar units in DPC-OCM images indicate the optical pathlength in nanometers.

is vital. Electrical action potentials are studied widely for neural function, but use of intra- or extracellular electrodes is not feasible in many applications. Such electrodes can easily induce irreversible damage to nerve fibers as well. A noninvasive method to assess local function, if developed successfully, would revolutionize the functional neural imaging field. Optical methods are promising to address this need, since they provide high temporal and spatial resolutions.

To observe functional changes associated with action potential (AP) propagation, a number of optical methods have been implemented for nearly six decades. Signs of neural function include changes in absorption, birefringence, optical rotation, fluorescence, and light scattering, as well as swelling, shrinkage, and shortening [13]. These signals indicate structural changes in the functioning nerve. Unfortunately, there is not a single noninvasive/noncontact device that can measure individual AP propagation in a clinical setting. Nonetheless, research in the optical imaging field is ongoing and the results suggest further investigations.

Interferometric differential phase measurements have the potential to study depth-resolved neural function with nanometer scale sensitivity to motion or optical pathlength change. Using DPC-OCT, noncontact optical measurement of transient displacements (swelling and/or shrinkage) associated with AP propagation has been recorded from a single point on crayfish [14] and lobster [15] nerves. Such transient changes have also been reported for crayfish axon, squid axon, and lobster nerve models using reflecting surfaces on the sample [16–18]. SD-OCT technology allows us to observe and image all points in a depth profile simultaneously with adequate temporal resolution (<50 μs) for probing millisecond-duration fast neural signals at multiple depths. Therefore,

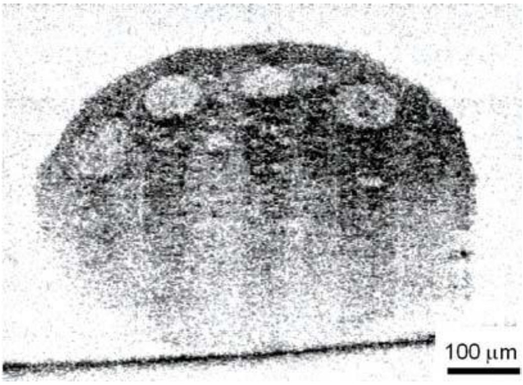

**FIGURE 14.11** Cross-sectional image of a crayfish ventral nerve cord. Two lateral and two medial giant axons are visible in the top portion of the nerve.

SD-OCT extends the use of differential phase measurements for function at a single point to function along a full depth profile. Transient phase changes using SD-OCT has been demonstrated on crayfish and lobster nerve models [19]. If the transient structural changes during AP propagation indicate functional and dysfunctional neural regions selectively, the optical method will contribute to our understanding of neural mechanisms during excitation and may lead to early detection of neural diseases in the future.

SD-OCT's real-time cross-sectional images is used to select a particular region of neural tissue for functional interrogation. Figure 14.11 shows a frame indicating two lateral and two medial giant axons in the top portion of a crayfish ventral nerve cord. Two superluminescent diodes were combined to obtain 75 nm (FWHM) spectral bandwidth centered at 835 nm, which resulted in a measured axial resolution of 4.9 μm in air (ca. 3.5 μm in neural tissue). Temporal resolution was 34 μs for a depth profile (A-line). By scanning the beam over the sample laterally using LabVIEW, images are acquired at 29 frames/s. The real-time display rate is about 3 frames/s when a cross-sectional image (B-scan) contains 1000 A-lines.

SD-OCT without lateral scanning produces what is known as M-mode imaging, in which a same-depth profile (A-line) is monitored over time. AP propagates during M-mode imaging and creates transient changes that may be detectable by the optical system. The intensity and phase of the interference signal can be utilized for investigations. To demonstrate the capability of SD-OCT phase measurements to detect nanometer-range transient changes due to AP propagation, a crayfish ventral nerve cord was dissected. For this particular experiment, one side of the nerve was squeezed in an attempt to increase internal axonal pressure, and both sides of the nerve were tied with sutures. Then the nerve was placed in a nerve chamber. The SD-OCT system was used to visualize the cross section of the nerve. A particular depth profile (Figure 14.12) was selected for functional investigation. The reference arm was

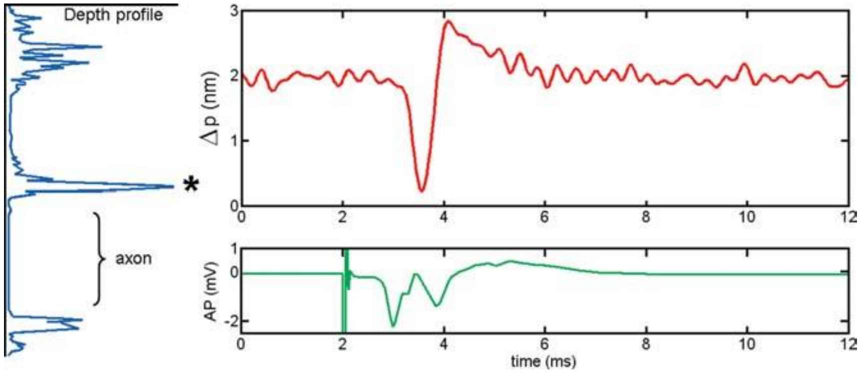

**FIGURE 14.12** Single depth profile of a crayfish ventral nerve cord (left panel) monitored during AP propagation. The asterisk indicates the point whose phase analysis revealed the optical signal ($\Delta p$) to the right. To show details of the optical signal, 100 responses are averaged for each trace. Stimulus is presented at 2 ms as an artifact in electrical AP is visible.

included in the optical setup; therefore, a glass–saline interface above the nerve was used as a reference for the differential phase measurement.

APs were created electrically, and electrical compound AP was recorded differentially around the optical measurement site for comparison. Stimulus, a 50–μs current pulse, was presented at 2 ms and resulted in an artifact in the electrical measurement. When the AP arrived at the optical measurement area, the top surface of a giant axon, as indicated by an asterisk, produced a nanometer-scale change in OPL ($\Delta p$). The downward signal corresponds to a change in the shrinkage direction, and it is followed by a change in the swelling direction. The result indicates biphasic behavior. To reveal the details of the optical signal, 100 responses are averaged for each trace. The bottom surface of the axon also produced a signal, which was in the shrinkage direction. Therefore, differential phase measurement from these two surfaces can be used, and the reference glass–saline interface may not be needed. Displacements in swelling and shrinkage directions have been reported in the literature (see [14] for details). Our new study on single squid giant axons, which will appear elsewhere, also produced millisecond-duration OPL changes. The biphasic behavior was dominant, but the initial direction of the change depended on lateral location. Research on understanding the mechanisms of these signals and the relations to other optical signals (e.g., cross-polarized intensity change, known as retardance or birefringence change; scattering change) is in progress.

## 14.5 COMPARISON OF TIME- AND SPECTRAL-DOMAIN PHASE-SENSITIVE SYSTEMS

Phase-sensitive measurements in the time domain (TD) and the spectral domain (SD) yield subnanometer-range sensitivity to changes in OPL and allow novel biomedical applications. If only two depth-resolved points (reference and probing points) are needed, TD systems (i.e., DPC-OCT or DP-OCM) are adequate. Indeed, TD systems with phase modulation produce better temporal resolution than their SD relatives, whose temporal resolution is limited by the CCD integration time of the spectrometer. Furthermore, the amount of data saved by TD systems can be much less than that saved by SD systems. On the other hand, SD systems have a clear advantage over TD systems when it is necessary to probe a full-depth profile simultaneously. The temporal resolution of SD systems, which is currently on the order of 30 μs, is sufficient for many applications.

## 14.6 CONCLUSIONS

As described here, phase-sensitive low-coherence interferometry has many applications where refractive index or physical changes in structure exist. Common-mode noise cancellation and high temporal and spatial resolution are the important attributes that are required by novel applications. The measurements are depth resolved and in reflection mode. This allows noncontact, noninvasive, or minimally invasive applications by its nature. Since the optical systems can be built with fibers, endoscopic applications are feasible.

## REFERENCES

1. Hitzenberger, C.K., and Fercher, A.F., Differential phase contrast in optical coherence tomography, *Opt. Lett*., Vol. 24, 1999, pp. 622–624.
2. Davé, D.P., and Milner, T.E., Optical low-coherence reflectometer for differential phase measurement, *Opt. Lett*., Vol. 25, 2000, pp. 227–229.
3. Davé, D.P., et al., Phase-sensitive frequency-multiplexed optical low-coherence reflectometry, *Opt. Commun*., Vol. 193, 2001, pp. 39–43.
4. Yang, C., et al., Interferometric phase-dispersion microscopy, *Opt. Lett*., Vol. 25, 2000, pp. 1526–1528.
5. White, B.R., et al., In vivo dynamic human retinal blood flow imaging using ultra-high-speed spectral domain optical Doppler tomography, *Opt. Express*, Vol. 11, 2003, pp. 3490–3497.
6. Choma, M.A., et al., Spectral-domain phase microscopy, *Opt. Lett*., Vol. 30, 2005, pp. 1162–1164.
7. Joo, C., et al. Spectral-domain optical coherence phase microscopy for quantitative phase-contrast imaging, *Opt. Lett*., Vol. 30, 2005, pp. 2131–2133.
8. Huang, D., et al., Optical coherence tomography, *Science*, Vol. 254, 1991, pp. 1178–1181.
9. Fercher, A.F., et al., Measurement of intraocular distances by backscattering spectral interferometry, *Opt. Commun*., Vol. 117, 1995, pp. 43–48.
10. Bhusnan, B., Wyant, J.C., and Koliopoulus, C.L., Measurement of surface topography of magnetic tapes by Mirau interferometry, *Appl. Opt*., Vol. 24, 1985, pp. 1489–1497.

11. Akkin, T., et al. Imaging tissue response to electrical and photothermal stimulation with nanometer sensitivity, *Lasers Surg. Med*., Vol. 33, 2003, pp. 219–225.
12. Rylander, C.G., et al., Quantitative phase contrast imaging of cells with phase sensitive optical coherence microscopy, *Opt. Lett*., Vol. 29, 2004, pp. 1509–1511.
13. Cohen, L.B., Changes in neuron structure during action potential propagation and synaptic transmission, *Physiol. Rev*., Vol. 53, 1973, pp. 373–418.
14. Akkin, T., et al., Detection of neural activity using phase-sensitive optical low-coherence reflectometry, *Opt. Express*, Vol. 12, 2004, pp. 2377–2386.
15. Fang-Yen, C., et al., Noncontact measurement of nerve displacement during action potential with a dual-beam low-coherence interferometer, *Opt. Lett*., Vol. 29, 2004, pp. 2028–2030.
16. Hill, B.C., et al., Laser interferometer measurement of changes in crayfish axon diameter concurrent with action potential, *Science*, Vol. 196, 1977, pp. 426–428.
17. Iwasa, K., and Tasaki, I., Mechanical changes in squid giant axons associated with production of action potentials, *Biochem. Biophys. Res. Commun*., Vol. 95, 1980, pp. 1328–1331.
18. Yao, X., Rector, D.M., and George, J.S., Optical lever recording of displacements from activated lobster nerve bundles and *Nitella* internodes, *Appl. Opt*., Vol. 42, 2003, pp. 2972–2978.
19. Akkin, T., Joo, C., and de Boer, J.F., Depth resolved measurement of transient structural changes during action potential propagation, *Biophys. J*., Vol. 93, 2007, pp. 1347–1353.

# 15

# POLARIZATION IMAGING

MIRCEA MUJAT
*Physical Sciences, Inc., Andover, Massachusetts*

15.1 Introduction 431
15.2 Polarization analysis 433
15.3 Polarization microscopy 436
15.4 Other polarization-sensitive techniques 441
  15.4.1 Polarization-sensitive optical coherence tomography 441
  15.4.2 Polarized light scattering 441
15.5 Biomedical applications 444
  15.5.1 Cancer detection 444
  15.5.2 Optical medical diagnostics 444
  15.5.3 Biomechanics and tissue engineering 445
  15.5.4 Biology 446
15.6 Other polarization imaging applications 446
  15.6.1 Remote sensing 446
  15.6.2 Industry and research 447
15.7 Conclusions 448
References 449

## 15.1 INTRODUCTION

Polarization is a fundamental property of light, and its measurement is one of the effective means of investigating light–matter interaction. In recent years there has been increased interest in the propagation of polarized light in random scattering

---

*Advances in Optical Imaging for Clinical Medicine*, Edited by Nicusor Iftimia, William R. Brugge, and Daniel X. Hammer
Copyright © 2011 John Wiley & Sons, Inc.

media both for media characterization and for imaging purposes. Optical imaging is used in medicine to study tissue from the organelle to organ level to help detect, diagnose, and treat pathological processes.

Polarization imaging provides additional contrast mechanisms as compared to traditional intensity imaging, without having to stain or label the sample. Tissue properties probed by polarization are the anisotropic real and imaginary parts of the refractive index that modify the polarization. Subsequently, linear and circular birefringence and dichroism measured through polarimetric techniques could be used to differentiate between normal and diseased tissue with the purpose of noninvasive optical diagnosis. Currently, the most targeted property is the linear birefringence specific to the highly organized structure of collagen, whereas circular birefringence and linear and circular dichroism are generally not explored. These additional properties are also related to structural and chemical anisotropies and they can reveal characteristics currently not visible with standard intensity imaging. Scattering of polarized light on microscopic particles, such as nuclei and fibers, also changes the polarization. The advantage of polarized light scattering over traditional light-scattering techniques is that polarization is sensitive to shape, orientation, internal structure of the particles, and structural characteristics of the global system in addition to size distribution and concentration normally probed with traditional techniques. There are numerous and very important applications of this research in biomedicine, military field, materials science, and industry as we will see below.

The most complete spatial polarimetric characterization of biological tissue is provided by Mueller matrix imaging. In addition to the classical intensity image, the Mueller matrix [1] contains information on birefringent, dichroic, or depolarization properties of the tissue. In particular cases when there is a priori knowledge regarding the tissue investigated (i.e., target composition or expected structure, degree of alignment, etc.), measurement of subsets of the Muller matrix elements could provide useful information. Various techniques, such as orthogonal polarization or differential polarization, have been used successfully for differentiating between normal and diseased tissue.

Collagen provides an extracellular matrix and gives mechanical strength to skin, tendons, cartilage, and intervertebral disks. Anisotropies within the chemical structure of collagen fibers generate intrinsic birefringence, and the fibers' highly organized shape and alignment generate form birefringence, both of which can be measured for tissue structural characterization only by polarimetric techniques. Alteration of collagen's physical properties, and therefore loss of both types of birefringence, is generated by heating in burns [2,3], by cancer or other degenerative diseases, or by trauma in the lamina propria of the human vocal folds [4], and may underlie pathological processes such as scar tissue formation, osteoarthritis, and back pain. Polarimetric imaging has the potential to reveal the spatial distribution of birefringence and dichroism as opposed to standard imaging, being of significant interest for medical diagnostics.

## 15.2 POLARIZATION ANALYSIS

The state of polarization or light polarization refers to the way in which the electric field of the light wave oscillates during propagation. The electric field vector generally oscillates perpendicular to the propagation direction of the wave. Most polarization phenomena can be treated considering only the electric field components in a plane perpendicular to the propagation direction; however, in cases of very tight focus, as in high-resolution microscopy, an axial component of the electric field might need to be considered. The light beam can in general be partially polarized, meaning that the electric field can have a deterministic component (polarized part) and a random component (unpolarized part). Natural light is unpolarized, whereas light that passes through a polarizer is fully polarized (pure state of polarization). The polarization is called *linear* when the electric field oscillates in a plane while propagating, it is called *circular* when the electric field vector traces a spiral, and it is called *elliptical* when the tip of the electric field vector follows an ellipse in a plane perpendicular to the direction of propagation. The electric field vector can always be decomposed into a horizontal ($x$) and a vertical ($y$) component, and the direction of propagation is $z$. Both components have amplitude ($a$) and phase ($\varphi$). The phase difference $\delta = \varphi_x - \varphi_y$ is called *retardance* or *phase delay*. A polarizer allows only one component of the electric field to pass, along the direction of the polarizer, while absorbing the field component perpendicular to the polarizer's direction. A retarder or wave plate introduces a phase delay. A quarter-wave plate, for example, introduces 90° phase delay, transforming linear polarization into circular polarization if the incident light polarization is at 45° with respect to the axis of the wave plate. A wave plate can be made of a (birefringent) crystal that has an anisotropic refractive index (i.e., the wave experiences different refractive index values for different orthogonal polarizations).

Several mathematical formalisms are used to represent the state of polarization and the polarimetric properties of a system altering the light polarization. The Jones formalism [5] deals with fully polarized light and nondepolarizing systems and is very useful for interference phenomena and fiber optic propagation. Stokes–Mueller [1,6] formalism accounts for partially polarized light and depolarizing systems and can be used in most practical applications. It employs directly measurable light intensity but cannot describe interference phenomena. The cross-spectral density formalism [7] was recently developed to unify the polarimetric and coherent properties of light and is capable of describing partially polarized light and polarization propagation, but its use in describing depolarizing systems is rather difficult. Several excellent monograms treat these formalisms in detail [7–14].

The most common representation of the polarization state is the Stokes vector [6], which fully describes partially polarized light. The Stokes vector is a real $4 \times 1$ column vector: $S = [\mathrm{I\ Q\ U\ V}]^{\mathrm{T}}$, where $^{\mathrm{T}}$ represents the transpose. The Stokes vector components represent combinations of intensities. A polarizer oriented horizontally ($x$), vertically ($y$), or at ±45° would let light of intensity

$I_{x/y}$ or $I_{45^\circ/-45^\circ}$ pass through as components of linear polarization along the $x$, $y$, or ±45° directions, while a quarter-wave plate followed by a polarizer oriented at ±45° with respect to the slow axis of the wave plate would transmit $I_{\mathrm{l/r}}$ as the intensities of the left and right components of circular polarization. The Stokes vector components are defined as $I = I_x + I_y, Q = I_x - I_y, U = I_{45^\circ} - I_{-45^\circ}, V = I_l - I_r$. The degree of polarization $P$, which represents the ratio between the intensity of the deterministic component and the total intensity of the beam, can be calculated as $P = \sqrt{Q^2 + U^2 + V^2}/I$. $P = 1$ represents pure state of polarization, $P = 0$ corresponds to natural, unpolarized light, and $0 < P < 1$ describes partially polarized light. The Stokes vector cannot be made of any combination of four numbers; only those combinations of four real numbers that satisfy the *Stokes criterion*, $0 \leq P \leq 1$, can be associated with a state of polarization of light.

Biological samples, optical components, reflection, and scattering can change the light polarization. As the light is described by the Stokes vector, we need a representation for the altering process, the sample, and this is called the *Mueller matrix* (M). The Mueller matrix is a real 4 × 4 matrix that transforms a Stokes vector ($S_{\mathrm{in}}$) into another Stokes vector ($S_{\mathrm{out}}$), as the sample changes one state of polarization into another. Mathematically, this can be written

$$S_{\mathrm{out}} = \begin{bmatrix} I_{\mathrm{out}} \\ Q_{\mathrm{out}} \\ U_{\mathrm{out}} \\ Q_{\mathrm{out}} \end{bmatrix} = MS_{\mathrm{in}} = M_{11} \begin{bmatrix} 1 & m_{12} & m_{13} & m_{14} \\ m_{21} & m_{22} & m_{23} & m_{24} \\ m_{31} & m_{32} & m_{33} & m_{34} \\ m_{41} & m_{42} & m_{43} & m_{44} \end{bmatrix} \begin{bmatrix} I_{\mathrm{in}} \\ Q_{\mathrm{in}} \\ U_{\mathrm{in}} \\ V_{\mathrm{in}} \end{bmatrix} \tag{15.1}$$

where the Mueller matrix $M$ was normalized to the first element $M_{11}$. $M_{11}$ is generally interpreted as transmission of unpolarized light, as in conventional microscopy. The normalized matrix elements can vary only between $-1$ and $+1$. The Mueller matrix is the most complete representation of the optical properties of a sample, which are typically described in terms of the complex refractive index. The real part of the refractive index is given by the ratio between the speed of light in that medium and the speed of light in vacuum. The imaginary part of the refractive index is given by the absorption coefficient, how much the light is attenuated while passing through the sample. *In anisotropic media, both the real and imaginary parts of the refractive index could be different for different states of polarization and for different propagation directions*; orthogonal linear or circular polarization components can travel with different speeds (birefringence) or can be attenuated differently (dichroism). The birefringence, which is the refractive index difference for orthogonal polarizations, $\Delta n = n_e - n_o$, generates phase retardance $\delta = (2\pi/\lambda)\Delta nt$, where $t$ is the thickness of the sample. Similarly, dichroism, which is the differential attenuation for orthogonal polarizations, $\Delta k = k_e - k_o$, generates diattenuation $d = (2\pi/\lambda)\Delta kt$. The phase retardance and diattenuation can be retrieved from the Mueller matrix and are generally different for linear and circular polarizations. The optical properties of the sample, the birefringence and the dichroism (also different for linear and circular polarizations), can then be determined for a known thickness *t* of the sample. They can be the result of structural and/or chemical anisotropies.

Actin, tubulin, cytoskeleton, microfilaments, microtubules, elongated macromolecules, proteins, biopolymers, nerve fibers, and collagen fibrils are anisotropic microstructures that alter the light polarization. In addition to linear birefringence, other optical effects, such as dichroism and optical activity, may be used for characterizing these microstructures. These optical properties can be spatially mapped using Mueller matrix imaging, and can potentially be of diagnostic value; they are, however, missed and generally not explored, due in part to the experimental and analytical complexity of extracting them.

There are many techniques for measuring the Stokes vector or the Mueller matrix, some of which have been reviewed previously [15–17]. In addition to measuring combinations of intensities, as is usually done, one can derive helpful polarization information by monitoring intensity fluctuations [18] or by performing interferometric measurements [19] in particular circumstances. The proper measurement technique for a specific experiment is selected based on a priori knowledge about the target, partial measurements sometimes being sufficient. The time frame of the process affecting the incident polarization or the process dynamics needs to be considered when choosing the measuring technique.

For proper interpretation of the measurements, decomposition procedures applied to the experimental results allow for quantitative evaluation of the depolarization, retardance, and diattenuation introduced by different parts of the sample. Complete polarimetric analysis by Mueller matrix imaging is desired for understanding multiple overlapping effects and for correct analysis of the sample and of the processes affecting light polarization. Individual polarization properties of the sample need to be extracted explicitly from the Mueller matrix measured and need to be related to the chemical and structural properties of the sample. Decomposition procedures [20–22] to identify and illustrate polarization-dependent properties of a sample are still under development and present significant interest. Phenomenological interpretation of the decomposition results is necessary for taking advantage of the full potential of polarization imaging. The first published decomposition scheme [21] separates a measured Mueller matrix in a series of three Mueller matrices: a diattenuator followed by a retarder and a depolarizer. A more recent decomposition [22] separates a measured Mueller matrix in two retarders that have between them a sandwich composed of a partial polarizer and a retarder. A detailed description of these algorithms is beyond the scope of this chapter; most importantly to mention here are the practical results of these procedures: depolarization, diattenuation, and retardance, which can be linked to different structural and physical properties of the sample and are extracted and mapped for quantitative identification of refractive index anisotropies.

## 15.3 POLARIZATION MICROSCOPY

A novel technique for imaging biological tissue without labeling or staining, called *Mueller matrix polarization microscopy*, is exploited for visualizing the distribution of the anisotropic complex refractive index, an intrinsic property of the internal cellular and tissue microstructure. In addition to linear birefringence (the only polarization property currently investigated in microscopy) biological tissue (cells) also exhibits circular birefringence (optical activity in chiral media) and linear and circular dichroism (differential absorption for orthogonal polarizations) that can potentially be identified only from a complete Mueller matrix. Precise measurement of these properties will open a new window into the structural organization of complex biological entities. The new capabilities will provide fundamental insight into the microstructure of cells and living tissue, their transformations and interactions, studied in developmental and structural biology, leading to improved diagnosis, prognosis, and treatment of cancer and degenerative diseases.

It is essential to analyze the microstructure and the dynamics of live cells to fully understand, detect, and diagnose early pathological processes. Polarimetric techniques can be used in microscopy for noninvasive live cell imaging by taking advantage of polarization sensitivity to the birefringence, dichroism, and shape of such anisotropic microstructures as nerve fibers, microtubules, microfilaments, and collagen fibrils. Polarization microscopy can provide unprecedented details in biophysical measurement of cell functions, in analyzing the effects of electric or magnetic fields, photoactivation, testing of drugs or biocompatible polymers on live tissue, and in longitudinal studies on interacting cellular structures during cell division, motility, and apoptosis.

Polarizing microscopes are extremely useful for specialized medical and industrial applications, such as identifying crystals or fibers suspended in liquid and detecting defects in semiconductors or finding stress distributions in metal or glass. Polarized light is used for contrast enhancement with birefringent materials in techniques such as dark- or bright-field polarized light microscopy, or differential interference contrast (DIC). Polarized light microscopy has been applied to the study of minerals in rock thin sections. Also, identification of asbestos fibers is possible using polarized light microscopy. Asbestos is the name of a group of natural mineral fibers. When breathed in, asbestos fibers are a health hazard [23,24]. Scanning electron microscopy and x-ray microanalysis are used typically for sample screening; however, polarization microscopy gives a faster and easier alternative that can be utilized to differentiate between asbestos and other fibers and between the major asbestos types [24]. These techniques, used for contrast enhancement, are, however, only qualitative, doing partial polarimetry; a great deal of a priori knowledge is needed about the sample for correct interpretation of the result.

It is worth mentioning here that polarizing microscopes are slightly more sophisticated than regular optical microscopes. They are similar to regular microscopes in terms of imaging capabilities: magnification, image size, depth of focus, and transmission or reflection configurations. In addition to regular microscopes, polarizing microscopes have the ability to alter the state of polarization in both the illumination and imaging path by insertion of polarizers and wave plates. A special type of microscope objective, the strain-free objective, is used for polarization analysis. Regular microscope objectives might have residual strains in the lenses that induce nonuniform strain birefringence, which creates polarization artifacts in the images obtained using such objectives.

The extraordinary work of Oldenbourg and collaborators [25,26] has pushed the field of polarization microscopy toward quantitative estimation of polarimetric properties of microstructures. A universal compensator made of two liquid-crystal variable retarders (LCVRs) and a polarizer was used either in the illumination or in the imaging path, with a circular analyzer or polarizer used in the other path [27]. Retardance magnitude and orientation images were obtained for a large range of microstructures and dynamic processes of living cells, including microtubules, spindle fibers, mitosis, filamentous actin, and helical flagella filaments [28–31]. All these measurements are, however, based on the assumption that biological microstructures exhibit only linear birefringence and no dichroism, an *assumption that might not always be correct*. The system can measure phase retardance in transmission in only one wavelength range (546 nm). Doing only partial polarimetry, not the full Mueller matrix, the method cannot differentiate between overlapping linear or circular birefringence or dichroism effects, and a great deal of a priori knowledge is needed about the sample for correct interpretation of the result. Circularly polarized light can be transformed into elliptically polarized light by either differential absorption (dichroism) or phase retardance (birefringence), and this system would wrongly interpret dichroism as birefringence. The Stokes vector describes the light and not the process transforming it as the Mueller matrix does. Complete polarimetric analysis by Mueller matrix imaging is desired for understanding multiple overlapping effects and for correct quantitative analysis of the sample and of the processes affecting light polarization.

A simple test instrument, a Mueller matrix microscope, is shown schematically in Figure 15.1. The system, developed by Physical Sciences Inc. (Andover, Massachusetts), is capable of performing complete Mueller matrix imaging in both transmission and reflection configurations. The system is based on two polarizers ($P_1$ and $P_2$) and four liquid-crystal variable retarders (LCVRs 1 to 4; Meadowlark Optics, Frederick, Colorado), easily controlled by a computer. For generation of the state of polarization, the polarizer $P_1$ and a combination of two LCVRs (1 and 2) are used as shown in Figure 15.1. Similar to the universal compensator [27], LCVR1 is rotated 45° with respect to the axis of the polarizer, while LCVR2 has one axis parallel to $P_1$. Both variable retarders are controlled from a computer through a National Instruments' data acquisition board (DAQ). The desired retardation is introduced by each of the two retarders when a specific voltage is applied on the retarder from the computer. Any state of polarization can be generated in this way [15,32]. The polarization analyzer is similar to the generator but in reverse order [33].

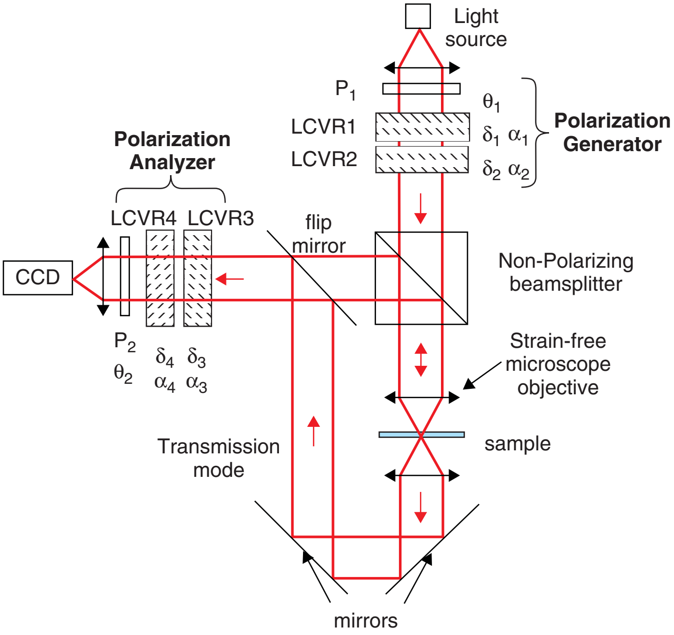
Light source
P$_1$
θ$_1$
LCVR1
δ$_1$ α$_1$
LCVR2
δ$_2$ α$_2$
Polarization Generator
Polarization Analyzer
LCVR4 LCVR3
flip mirror
CCD
Non-Polarizing beamsplitter
P$_2$
θ$_2$
δ$_4$ δ$_3$
α$_4$ α$_3$
Strain-free microscope objective
sample
Transmission mode
mirrors

**FIGURE 15.1** Mueller matrix microscope.

Sixteen sequential images are acquired for different combinations of retardances ($\delta_1$ to $\delta_4$) generated by the four LCVRs. The CCD, which is polarization insensitive, records only intensity information, as in any regular imaging system. However, the intensity distribution in the recorded images changes from image to image as the polarization generator and the polarization analyzer change their properties. Since the polarization characteristics vary across the sample, the transmission and reflection also vary across the sample and with the input polarization. Therefore, the recorded intensity images depend on the sample's polarization properties (expressed through the Mueller matrix elements) and the retardances ($\delta_1$ to $\delta_4$) generated by the four LCVRs. Mathematically, this can be expressed by writing the recorded intensity image as a linear combination of the 16 Mueller matrix elements with coefficients related to the retardances $\delta_1$ to $\delta_4$ and other polarization properties of the microscope (orientation of polarizers and LCVRs). One needs a system of 16 equations to solve for the 16 unknowns (the Mueller matrix elements) given the recorded 16 intensity images. All the coefficients in this system of equations can be found theoretically, at least in principle; however, they can easily be obtained experimentally by performing a system calibration. To simplify the analysis without any loss of generality, one can consider that the Mueller matrix elements for a given sample are linearly related to the 16 intensity images through a calibration matrix. Therefore, to obtain the Mueller matrix for any sample one needs to perform the system calibration (just once), and then record 16 intensity images while varying retardances $\delta_1$ to $\delta_4$. In our case, the calibration matrix was determined experimentally using standard targets such as a polarizer, a wave plate and air. The measurement error was estimated at 0.004 per normalized matrix element (the maximum element value is 1).

The acquisition time for a complete Mueller matrix depends on the available power of light incident on the sample, on the frame rate of the CCD, and on the LCVRs' switching time. The light source used for these tests was a fiber-coupled Xe arc lamp filtered with a green bandpass filter (532 nm) with a 10-nm bandwidth. Measurements can be done at other wavelength simply by changing the filter in front of the light source.

The system was tested on mica (Figure 15.2a), and natural quartz (Figure 15.2b) pieces embedded in index matching oil ($n = 1.560$ for mica and $n = 1.544$ for quartz). The index matching was used to reduce the refractive index contrast as much as possible. The microscope objectives used here (4× magnification) were developed by Meiji Techno in Japan as strain-free objectives for their polarization microscopes. The image size is 500 μm (1024 pixels).

The first image (11, top left corner) represents the transmission of unpolarized light, obtained typically with a regular microscope. One can barely distinguish that there are multiple mica or quartz pieces; however, other matrix elements clearly identify several pieces with different birefringent properties. The effect is relatively small for mica but is quite substantial for quartz. As expected, mica shows only retardance, as illustrated by the $3 \times 3$ bottom right part of the Mueller matrix. The elements 12, 13, 21, and 31 are basically zero. This is not the case for the quartz crystals, which are also known to exhibit diattenuation, as seen in elements 12, 13, 21, and 31. Figure 15.2 is a clear example that partial polarimetry for measuring only phase retardance will produce incorrect results, by ignoring additional optical properties.

The bending structure (alternation of black and white) in most of the matrix elements in Figure 15.2b indicates a very strong effect generating phase wrapping. Quartz birefringence at about 500 nm is 0.009, about twice mica birefringence (0.00460) and the quartz crystals were probably thicker than the mica sheets. Biological samples are expected to exhibit smaller effects than those of crystalline quartz, and are less likely to show phase wrapping.

Figure 15.3a shows the Mueller matrix images of a sample collected from a dusty spider web. The polarimetric properties of a thread from the sample make it stand out in most of the matrix elements, but it is basically indistinguishable from the rest of the sample in the first element (11), which is the regular microscope-type image. Figure 15.3b shows the Mueller matrix images of a part of a zebrafish, illustrating tremendous differences among different parts of the fish body that are indistinguishable in the regular microscope image (11). *These biological samples also clearly exhibit diattenuation*, as seen in nonzero elements 12, 13, 21, and 31. It should also be noted that the retardance properties of the thread in Figure 15.3a vary along the thread as seen in matrix elements 24 and 42, due to either thickness variations or birefringence variations. Different parts of the fish body (i.e., the aorta, the notochord, the muscles, and the gut) can be clearly identified in Figure 15.3b. Structural variations across each of these body

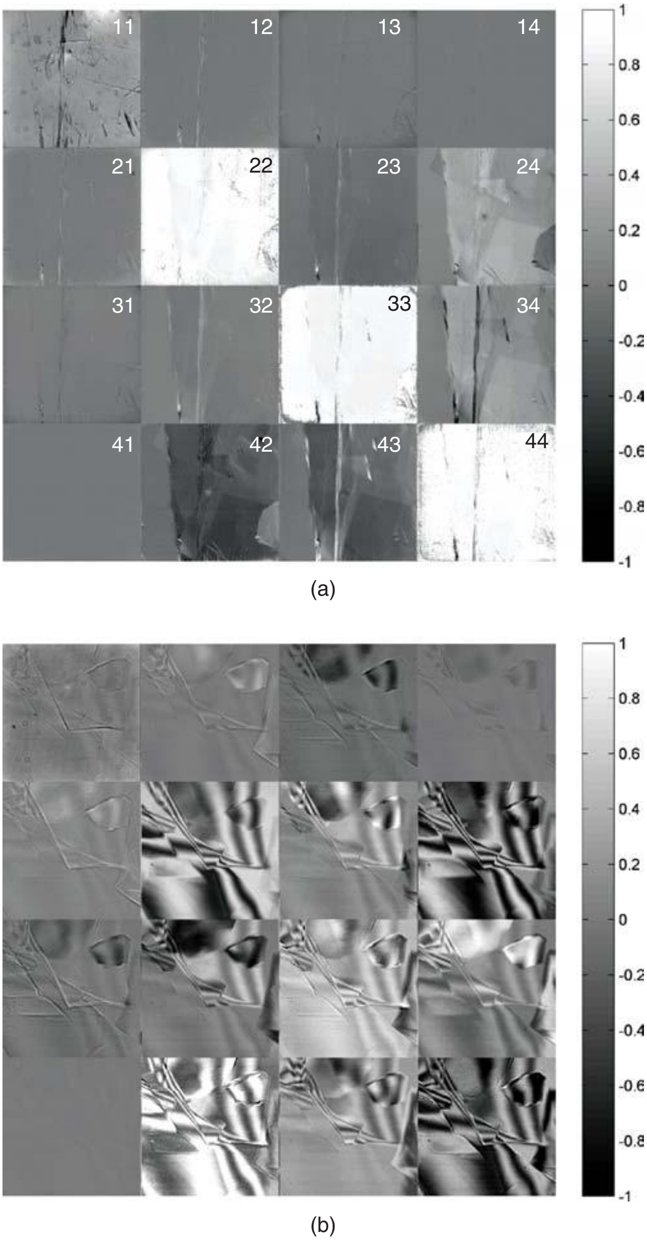
11
12
13
14
21
22
23
24
31
32
33
34
41
42
43
44
1
0.8
0.6
0.4
0.2
0
-0.2
-0.4
-0.6
-0.8
-1
(a)
1
0.8
0.6
0.4
0.2
0
-0.2
-0.4
-0.6
-0.8
-1
(b)

**FIGURE 15.2** Mueller matrix images of (a) mica and (b) quartz pieces embedded in index matching oil.

parts can be identified in the matrix elements, but they are not noticeable in the intensity image 11. The thin lines across the notochord are intersegmental vessels. Figure 15.3c and 15.3d show the Mueller matrix for silk (c) and synthetic and wool (d) fibers pulled from clothing. These fibers clearly exhibit different structural properties among different fibers, as well as along the same fiber, while the inhomogeneity is not apparent in matrix element 11. Worth noting here is the general symmetry of the Mueller matrix with respect to the main diagonal, some elements having opposite signs ($24 = -42$, $34 = -43$), as expected.

The examples illustrated in Figures 15.2 and 15.3 clearly demonstrate the potential of polarization microscopy for imaging microscopic structures relevant for both material science and biomedical research and illustrate anisotropies not visible in the regular microscopy images. Polarization analysis exploits the intrinsic anisotropy of the complex refractive index, providing label-free imaging, and is expected to provide additional insight into the internal structural organization and transformations of biological tissue.

## 15.4 OTHER POLARIZATION-SENSITIVE TECHNIQUES

### 15.4.1 Polarization-Sensitive Optical Coherence Tomography

The most successful application of optical coherence tomography (OCT) [34–37] is perhaps in ophthalmology. One of its functional extensions, polarization-sensitive OCT (PS-OCT) [38–42], combines the sensitivity of interferometric techniques with polarimetric capabilities providing depth sectioning of polarization-dependent tissue properties. Birefringent structures in the eye include the cornea and the retinal nerve fiber layer (RNFL). The RNFL exhibits birefringence due to the orderly arrangement of axons and microtubules within the RNFL. PS-OCT measures the RNFL thickness and phase retardation introduced by the RNFL simultaneously, therefore providing direct access to the RNFL birefringence [phase retardation = $(2\pi/\lambda)$ × birefringence × RNFL thickness, where $\lambda$ is the light wavelength]. A quantitative birefringence map of in vivo human RNFL was recently demonstrated [43], showing clearly that the RNFL birefringence varies across the retina, with larger values superior and inferior to the optic nerve head (ONH) and smaller values nasal and temporal to the ONH. The standard clinical methods for diagnosing glaucoma (i.e., visual field testing) can diagnose glaucomatous vision loss only after up to 40% of the nerve tissue is lost irreversibly [44–46], whereas it is expected that RNFL thickness and birefringence measurements can detect structural changes before nerve tissue is lost. In addition to ophthalmic applications, PS-OCT was used for noninvasive assessment of burn depth [41,47] based on collagen thermal denaturizing.

### 15.4.2 Polarized Light Scattering

The polarimetric signature of tissue also depends on the cellular architecture, which can be used for detecting abnormalities in addition to the changes observed

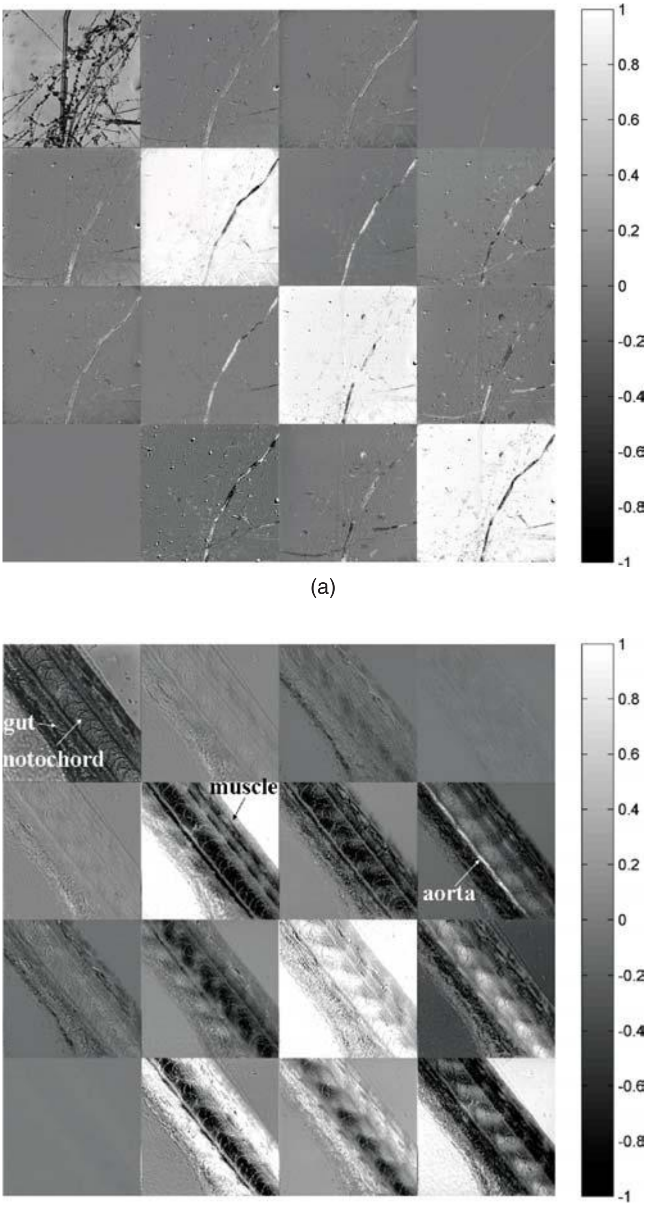
1
0.8
0.6
0.4
0.2
0
-0.2
-0.4
-0.6
-0.8
-1
gut
notochord
muscle
aorta

(a)

(b)

**FIGURE 15.3** Mueller matrix images of (a) dusty spider web, (b) zebrafish trunk, (c) silk fibers, and (d) synthetic (tilted) and wool (vertical) fibers.

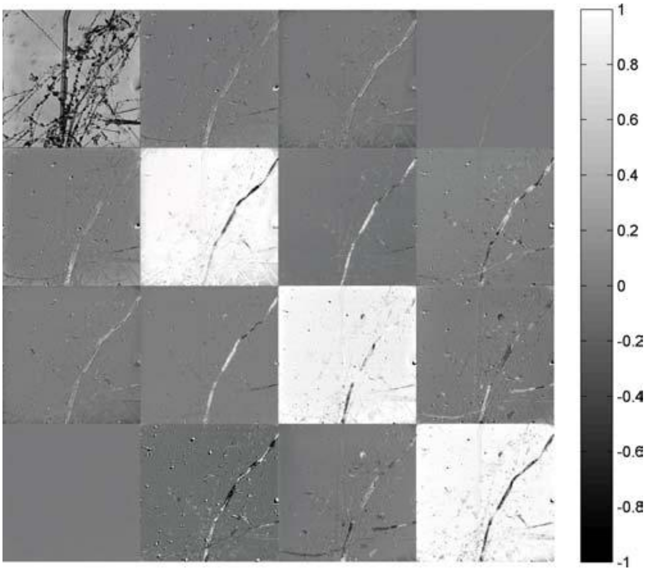
1
0.8
0.6
0.4
0.2
0
-0.2
-0.4
-0.6
-0.8
-1

(c)

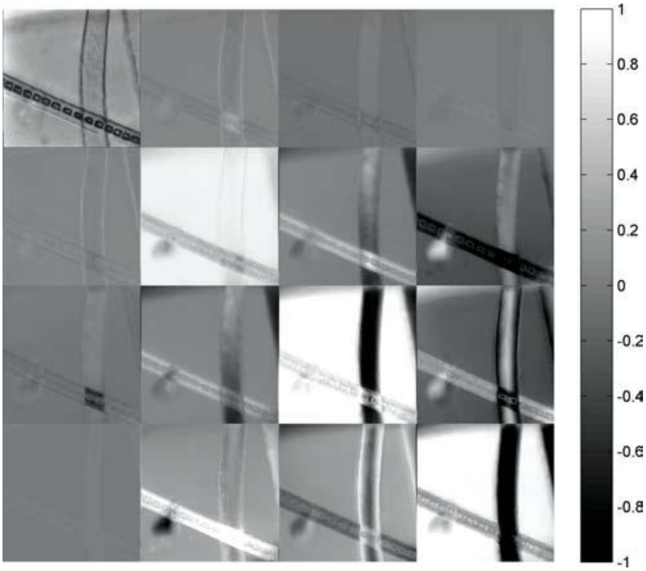
1
0.8
0.6
0.4
0.2
0
-0.2
-0.4
-0.6
-0.8
-1

(d)

**FIGURE 15.3** (*Continued*)

in tissue birefringence. For example, nuclei and internal cellular organelles act as scattering structures that affect the polarization, depending on their distribution within the tissue, and their size, concentration, or geometry. It is well known that cancerous cells exhibit enlarged nuclei and increased mitochondria content compared to normal cells; therefore, normal and cancerous tissue will have different polarization signatures, due to different scattering properties. *Imaging the superficial layers of biological tissue can provide screening and early detection of cancer* [48,49].

## 15.5 BIOMEDICAL APPLICATIONS

### 15.5.1 Cancer Detection

Melanoma, a superficial cancer that occurs in the epithelial layers of skin, is one of the deadliest types of superficial cancer in the world (one person dies of melanoma every hour in the United States [50]). Cancer results in denaturizing of collagen and therefore in a loss of birefringence due to deformation of the regular molecular binding structure and even the damage to the helixlike molecules. Based on these effects, cancerous structures can be differentiated from benign or normal structure through a spatial characterization of tissue birefringence. In addition to linear birefringence, other optical effects, such as dichroism and optical activity, may be used for differentiating normal and cancerous tissue. These optical properties can be spatially mapped using Mueller matrix imaging and can be of potential diagnostic value; they are, however, generally not explored or ignored, since their measurement might be more challenging in scattering tissues. *Assessment of these properties as markers for cancer could be valuable since they provide intrinsic contrast mechanisms in addition to the current markers*. Polarimetric endoscopic techniques could be used for imaging where conventional biopsy is hazardous, for early detection of superficial cancers in internal organs accessible by endoscopes, and for guided surgical interventions or therapy.

A simple system was developed and used in clinics to image skin cancer [48,49]. The tissue is illuminated with linearly polarized light, and two images are acquired in parallel and orthogonal polarization channels. A polarization image is computed by dividing the difference image by the sum image. The system was used to identify the borders of skin cancer. This technique does not offer a quantitative assessment of the refractive index anisotropy but seems to provide enough contrast enhancement to guide surgeons in identifying the true boundaries of cancerous tissue.

### 15.5.2 Optical Medical Diagnostics

Polarization-based optical properties of tissue are very important in noninvasive medical diagnostics. In dermatology, detection of skin lesions [48,49,51,52], as well as discrimination between normal and cancerous tissue (moles) and identification of lupus lesions [53,54], is possible using Mueller matrix imaging polarimetry. Currently, the only method available to diagnose suspected cancerous tissue (skin cancer) is surgical biopsy [52]. Real-time measurement of skin stretch and estimation of stresses are required in wound closure, healing, and scar tissue formation [55] as well as in plastic surgery. A noninvasive investigation method is desired. Methods currently available are direct contact and ultrasonic imaging [56]. Tissue-structure changes under strain are visible as birefringence variations in polarimetric images.

Birefringence is related to various biological components, such as collagen fibers, muscle fibers, keratin, and glucose. Measurement of birefringence helps in structural characterization of retina [43] and other tissues. Retinal polarization imaging reveals valuable information about diabetes and other diseases that could lead to blindness. The spatial distribution of the complex index of refraction can be determined from diattenuation and retardance images [53], providing a new contrast mechanism for medical imaging [57,58]. Significant efforts have been made to develop a noninvasive blood glucose sensor by use of optical approaches, including near-infrared absorption spectroscopy, near-infrared scattering measurements, Raman spectroscopy, photoacoustics, OCT [59], and polarimetry [60–62].

Orthogonal polarization spectral imaging [63] was used to visualize human microcirculation. The sample is illuminated with linear polarization, and the imaging is performed in the orthogonal polarization channel. The contrast is provided by spectral absorption, while the orthogonal polarization configuration is used to select multiple scattered photons that penetrate deep into the tissue and to reject the specular reflection at the tissue surface, which is mainly nondepolarizing.

### 15.5.3 Biomechanics and Tissue Engineering

The engineering of new biomaterials requires a thorough understanding of the structure and function of the natural tissue. The relationship between tissue microstructure and its function is of significant interest in biomechanics and tissue engineering. Mechanical properties of biological tissue depend on its structural organization at various scale levels. Histological methods can provide some microstructural information; they are, however, destructive and can alter the relationship between tissue components. Polarization imaging can be used to investigate the structure of healthy tissue and its response to stress, to provide tissue engineers with a better understanding of tissue functions, and to characterize new engineered tissue and evaluate its performance.

Cartilage is a highly anisotropic and inhomogeneous tissue in which collagen fibers form a complex three-dimensional network. Polarimetric imaging techniques are capable of cartilage structural characterization, of finding links between cartilage structure and function, and of investigating the biomechanics of articular cartilage that covers the sliding surfaces of bones in joints [64,65]. Osteoarthritis is associated with irreversible degradation of the cartilage and consequent disruption of the normal collagen structure that can be assessed by birefringence measurements [38,66].

### 15.5.4 Biology

Optical activity measurements have been performed routinely by chemists and biologists for more that a century, but only on clear solutions. Measurements on optically active particles are still to be done. Glucose is the major carbohydrate energy source that is utilized by living organisms. The ability to detect glucose concentrations in biological media noninvasively provides fascinating possibilities in the field of analytical chemistry and biosensing in areas such as cell culture bioreactors (used in tissue engineering). However, scattering cannot be neglected for bioparticles such as red blood cell membranes, virus nuclei, mitochondria, and ribosomes. One cannot dilute such media without destroying their structural elements [67]. Noninvasive measurement of optical activity effects in such systems is very important [62].

Microbiologists are concerned with rapid and unambiguous identification of a variety of microorganisms [68]. Conventional methods are time consuming and expensive. Several researchers have found that unique signatures can be gathered for particular microorganisms from polarized scattering measurements [69–71]. There is also increasing interest in microbiology used to determine how bacteria are able to adjust their physical parameters rapidly to changing growth conditions. Size distribution for a population of rod-shaped cells can be measured in real time and in vivo [72]. Routine use of structural investigations is desired in clinical bacteriology.

The marine environment contains very diverse types of particles, such as marine chlorella and phytoplankton, with interesting characteristics (core–shell structure, nonspherical, optically active) that can be retrieved from polarized light scattering [73]. Honeybees, anthropoids, squids, and octopuses have eyes sensitive to polarized light. They use it either for orientation or for better visualization of the environment through polarization difference imaging (cross-polarized channels) [74].

## 15.6 OTHER POLARIZATION IMAGING APPLICATIONS

### 15.6.1 Remote Sensing

Some of the most important remote sensing applications of Mueller matrix imaging polarimetry are target identification, discrimination between natural and human-made targets based on depolarization characteristics [74,75], shape and orientation determination of a target [76], detection of biological contamination, target acquisition, and mine detection in the infrared [77]. Polarization imaging techniques offer the distinct possibility of yielding images with higher inherent visual contrast than that obtainable using normal techniques [78]. The performance of a polarization imager can be improved by using active illumination. Recent research on linear polarization difference imaging [79] demonstrated that ranges two to three times greater than in conventional intensity imaging in scattering suspensions could be achieved. In astronomy and astrophysics, a great deal of knowledge can be obtained by analyzing the radiation scattered by particles in the atmosphere of planets and satellites, planetary ring systems, interplanetary dust clouds, circumstellar matter, and interstellar media [80].

### 15.6.2 Industry and Research

The shape of particles and their orientation in space are of importance in the manufacture of aerosols, pharmaceuticals, paints, and coatings, and to applications in remote sensing and imaging through obscuring random media [81]. Nondestructive, noninvasive, and fast light-scattering techniques have been used in quality control for defect identification. These techniques give excellent results for monodisperse, homogeneous, and dilute suspensions of spheres. However, if the particles become nonspherical, have a complex size distribution, are composed of different layers, or are in concentrated solutions, the mean size calculated by commercial particle-sizing instruments can be very different from the real mean size. Several scattering geometries can give the same intensity pattern [82], and therefore polarization sensitivity is required to extract the correct information from scattering measurements.

Optical rotation and circular dichroism measurements on transparent and weakly absorbing samples have been employed to provide information on the identity, electronic structure, stereochemistry, and concentration of constituent chiral molecules. There is much current interest in chiral systems for which standard transmission methods are not appropriate, as, for example, chiral thin films, strongly absorbing chiral materials, inhomogeneous chiral media, and chiral materials with surface roughness [83].

Flow birefringence occurs when a fluid becomes optically anisotropic in flows with a velocity gradient and is particularly significant in polymer solutions [84]. By measuring flow birefringence directly, polarimetry serves as a unique experimental tool in studying the static and dynamic properties of polymers.

The size distribution of spherical $SiO_2$ particles on a silicon wafer has been obtained from Mueller matrix measurements [85], with important applications in the semiconductor industry. Imaging the Mueller matrix has been used for measuring the polarization aberration matrices due to strain birefringence of a plastic lens, the point-spread matrix of a LCTV, and characterization of spatial light modulators, polarizing beamsplitters [86], and optoelectronic devices [54].

Investigation of phase and structural transformations for rapidly pulse-heated metallic materials, thin-film characterization and monitoring, and measurement of optical properties of pure liquid metals can be done by measuring the ellipsometric parameters [32,87]. The effect of surface roughness and observation angle on the degree of polarization of thermal radiation is also of interest for imaging purposes in the 10- to 11-μm band [88]. Heterodyne polarimetry can be used to measure the Faraday rotation for far-infrared laser radiation transmitted through tokamak plasma, to determine the poloidal field distribution, and subsequently to determine the current density profile, which plays a crucial role in plasma equilibrium and stability [89].

Short-versus long-path photons (ballistic vs. diffuse background) emerging from a scattering medium can be discriminated by means of polarization techniques [90]. Other techniques that demonstrated similar capabilities, with the purpose of improving imaging quality and depth penetration in turbid media are time-of-flight spectrophotometry [91], time-gated imaging employing delayed coincidence [92], optical heterodyne [93], and second-harmonic-generation cross-correlation techniques [94]. These imaging systems are expensive and complex, and are limited by the response time of the detectors.

All these applications have in common the fact that the main goal is the determination of inhomogeneities of the complex refractive index, which is polarization sensitive in the form of linear or circular birefringence or dichroism. Structural characteristics of scattering media are subsequently related to physical properties of interest in the biomedical field, remote sensing, industry, and research. Noninvasive, sensitive, and fast measurement methods are needed for analyzing inhomogeneous media in different scattering regimes and geometries, relevant for applications such as the ones listed above.

## 15.7 CONCLUSIONS

Polarization imaging has the tremendous potential to provide stain- and label-free structural and functional characteristics of biological tissue and microstructures that are not visible with regular imaging. Anisotropies of the complex refractive index can be assessed and visualized quantitatively using polarimetric techniques and can be related to tissue properties for the purpose of noninvasive diagnosis. The targets for biomedical applications of polarization imaging range from cellular microstructures to large tissue areas.

Compared to other imaging techniques based only on intensity information, polarization imaging exploits refractive index anisotropies as intrinsic contrast mechanisms. Chemical anisotropies can be imaged with other imaging techniques, such as fluorescence imaging using contrast agents that specifically label targeted properties. Fluorescence is insensitive to structural anisotropies such as alignment of fibers or nonspherical scatterers. Randomly oriented or parallel fibers will give the same fluorescence signal, but they will have different polarization signatures. Polarization imaging, on the other hand, is not specific on chemical composition; different chemical compounds can have the same birefringence or dichroism. A combined polarization–fluorescence imaging technique could benefit from the advantages of each technique in identifying the chemical and structural anisotropies.

Confocal imaging is polarization insensitive, and polarization imaging has no axial discrimination. A combined confocal–polarization imaging technique could provide both axial and polarization discrimination, with potential applications in imaging layered structures. An initial demonstration of such a technique has been presented and tested on a stack of linear retarders and glass plates [95], but its application to samples of practical interest such as biomedical tissue is yet to be tested. Similarly, PS-OCT is a combination of interferometric and polarization techniques, as mentioned earlier, that provides both axial and polarization discrimination.

While polarization imaging by itself has a remarkable potential to image anisotropies at both the microscopic and macroscopic levels, its combination with other imaging techniques can become extremely powerful in providing structural and functional characteristics of biological tissue.

## REFERENCES

1. Mueller, H., The foundation of optics, *J. Opt. Soc. Am.*, Vol. 38, 1948, p. 661.
2. Maitland, D.J., and Walsh, J.T., Quantitative measurements of linear birefringence during heating of native collagen, *Lasers Surg. Med.*, Vol. 20, No. 3, 1997, pp. 310–318.
3. Sankaran, V., and Walsh, J.T., Jr., Optical real-time measurement of collagen denaturation, *Proc. SPIE*, Vol. 2975, 1997, p. 34.
4. Madruga de Melo, E.C., et al., Distribution of collagen in the lamina propria of the human vocal fold, *Laryngoscope*, Vol. 113, No. 12, 2003, pp. 2187–2191.
5. Jones, R.C., A new calculus for the treatment of optical systems: IV, *J. Opt. Soc. Am.*, Vol. 32, No. 8, 1942, pp. 486–493.
6. Stokes, G.C., On the composition and resolution of sreams of polarized light from different sources, *Trans. Cambr. Philos. Soc.*, Vol. 9, 1852, pp. 399–416.
7. Wolf, E., Unified theory of coherence and polarization of random electromagnetic beams, *Phys. Lett. A*, Vol. 312, No. 5–6, 2003, pp. 263–267.
8. Born, M., and Wolf, E., *Principles of Optics*, 7th ed., Harvard University Press, Cambridge, MA, 1999.
9. Brosseau, C., *Fundamentals of Polarized Light: A Statistical Approach*. Wiley, New York, 1998.
10. Chipman, R.A., Polarimetry, in *Handbook of Optics*, pp. 22.1–22.37, M. Bass (ed.), McGraw-Hill, New York, 1994.
11. Collett, E., *Polarized Light: Fundamentals and Applications*. Marcel Dekker, New York, 1993.
12. Mandel, L., and Wolf, E., *Optical Coherence and Quantum Optics*. Cambridge University Press, Cambridge, UK, 1995.
13. Shurcliff, W.A., *Polarized Light*. Harvard University Press, Cambridge, MA, 1966.
14. Wolf, E., *Introduction to the Theory of Coherence and Polarization of Light*, Cambridge University Press, Cambridge, UK, 2007.
15. Mujat, M., Polarimetric Characterization of Random Electromagnetic Beams and Applications, Ph.D. dissertation, University of Central Florida, Orlando, FL, 2004.
16. Mujat, M., and Dogariu, A., Real-time measurement of the polarization transfer function, *Appl. Opt.*, Vol. 40, No. 1, 2001, pp. 34–44.
17. Tyo, J.S., et al., Review of passive imaging polarimetry for remote sensing applications, *Appl. Opt.*, Vol. 45, No. 22, 2006, pp. 5453–5469.

18. Mujat, M., Dogariu, A., and Agarwal, G.S., Interferometric measurement of the degree of polarization and control of the contrast of intensity fluctuations, *Opt. Lett.*, Vol. 29, No. 13, 2004, pp. 1539–1541.
19. Mujat, M., Baleine, E., and Dogariu, A., Interferometric imaging polarimeter, *J. Opt. Soc. Am. A*, Vol. 21, No. 11, 2004, pp. 2244–2249.
20. LeRoyBrehonnet, F., et al., Optical media and target characterization by Mueller matrix decomposition, *J. Phys. D*, Vol. 29, No. 1, 1996, pp. 34–38.
21. Lu, S.Y., and Chipman, R.A., Interpretation of Mueller matrices based on polar decomposition, *J. Opt. Soc. Am. A*, Vol. 13, No. 5, 1996, pp. 1106–1113.
22. Ossikovski, R., Interpretation of nondepolarizing Mueller matrices based on singular-value decomposition, *J. Opt. Soc. Am. A*, Vol. 25, No. 2, 2008, pp. 473–482.
23. Wikipedia, http://en.wikipedia.org/wiki/Asbestos, 2009.
24. OSHA, *Polarized Light Microscopy of Asbestos—Non-mandatory*, 1910.1001 App. J, Occupational Safety and Health Administration, U.S. Department of Labor, Washington, DC, http://www.osha.gov/pls/oshaweb/owadisp.show_document?p_table=STANDARDS&p_id=10005.
25. Oldenbourg, R., A new view on polarization microscopy, *Nature*, Vol. 381, No. 6585, 1996, pp. 811–812.
26. Oldenbourg, R., and Mei, G., New polarized-light microscope with precision universal compensator, *J. Microsc. Oxford*, Vol. 180, 1995, pp. 140–147.
27. Shribak, M., and Oldenbourg, R., Techniques for fast and sensitive measurements of two-dimensional birefringence distributions, *Appl. Opt.*, Vol. 42, No. 16, 2003, pp. 3009–3017.
28. Barry, E., et al., Entropy-driven formation of a chiral liquid-crystalline phase of helical filaments, *Phys. Rev. Lett.*, Vol. 96, No. 1, 2006, pp. 018305.
29. Oldenbourg, R., Polarized light microscopy of spindles, *Methods Cell Biol.*, Vol. 61, 1999, pp. 175–208.
30. Oldenbourg, R., Dynamic views of living cell fine structure revealed by electro-optically modulated polarization microscopy, *J. Gen. Physiol.*, Vol. 114, No. 1, 1999, p. 1A.
31. Katoh, K., et al., Birefringence imaging directly reveals architectural dynamics of filamentous actin in living growth cones, *Mol. Biol. Cell*, Vol. 10, No. 1, 1999, pp. 197–210.
32. Krishnan, S., and Nordine, P.C., Fast ellipsometry and Mueller matrix ellipsometry using the division-of-amplitude photopolarimeter, *Proc. SPIE*, Vol. 2873, 1996, pp. 152–156.
33. Laude-Boulesteix, B., et al., Mueller polarimetric imaging system with liquid crystals, *Appl. Opt.*, Vol. 43, No. 14, 2004, pp. 2824–2832.
34. Fercher, A.F., et al., Measurement of intraocular distances by backscattering spectral interferometry, *Opt. Commun.*, Vol. 117, No. 1–2, 1995, pp. 43–48.
35. Huang, D., et al., Optical coherence tomography, *Science*, Vol. 254, No. 5035, 1991, pp. 1178–1181.
36. Wojtkowski, M., et al., Ultrahigh-resolution, high-speed, Fourier domain optical coherence tomography and methods for dispersion compensation, *Opt. Express*, Vol. 12, No. 11, 2004, pp. 2404–2422.

37. Yun, S.H., et al., High-speed optical frequency-domain imaging, *Opt. Express*, Vol. 11, No. 22, 2003, pp. 2953–2963.
38. Nassif, N.A., et al., Evaluation of osteoarthritis progression using polarization-sensitive optical coherence tomography, *Proc. SPIE*, Vol. 5318, 2004, p. 170.
39. de Boer, J.F., and Milner, T.E., Review of polarization sensitive optical coherence tomography and Stokes vector determination, *J. Biomed. Opt*., Vol. 7, No. 3, 2002, pp. 359–371.
40. de Boer, J.F., et al., Polarization-sensitive optical coherence tomography, in *Handbook of Optical Coherence Tomography*, pp. 237–274, B.E. Bouma and G.J. Tearney (eds.), Marcel Dekker, New York, 2002.
41. de Boer, J.F., et al., Two-dimensional birefringence imaging in biological tissue by polarization-sensitive optical coherence tomography, *Opt. Lett*., Vol. 22, No. 12, 1997, pp. 934–936.
42. Hitzenberger, C.K., et al., Measurement and imaging of birefringence and optic axis orientation by phase resolved polarization sensitive optical coherence tomography, *Opt. Express*, Vol. 9, No. 13, 2001, pp. 780–790.
43. Mujat, M., et al., Auto-calibration of spectral-domain optical coherence tomography spectrometers for in-vivo quantitative retinal nerve fiber layer birefringence determination, *J. Biomed. Opt*., Vol. 12, No. 4, 2007, p. 041205.
44. Kerrigan-Baumrind, L.A., et al., Number of ganglion cells in glaucoma eyes compared with threshold visual field tests in the same persons, *Invest. Ophthalmol. Vis. Sci*., Vol. 41, No. 3, 2000, pp. 741–748.
45. Quigley, H.A., Addicks, E.M., and Green, W.R., Optic-nerve damage in human glaucoma: 3. Quantitative correlation of nerve-fiber loss and visual-field defect in glaucoma, ischemic neuropathy, papilledema, and toxic neuropathy, *Arch. Ophthalmol*., Vol. 100, No. 1, 1982, pp. 135–146.
46. Sommer, A., et al., Clinically detectable nerve-fiber atrophy precedes the onset of glaucomatous field loss, *Arch. Ophthalmol*., Vol. 109, No. 1, 1991, pp. 77–83.
47. de Boer, J.F., et al., Imaging thermally damaged tissue by polarization sensitive optical coherence tomography, *Opt. Express*, Vol. 3, No. 6, 1998, pp. 212–218.
48. Jacques, S.L., Ramella-Roman, J.C., and Lee, K., Imaging skin pathology with polarized light, *J. Biomed. Opt*., Vol. 7, No. 3, 2002, pp. 329–340.
49. Ramella-Roman, J.C., et al., Design, testing, and clinical studies of a handheld polarized light camera, *J. Biomed. Opt*., Vol. 9, No. 6, 2004, pp. 1305–1310.
50. American Melanoma Foundation, Statistics, http://www.melanomafoundation.org/facts/statistics.htm, 2005.
51. Jacques, S.L., Video imaging of superficial biological tissue layers using polarized light, U.S. patent 6,177,984, Jan. 23, 2001.
52. Hill, A.R., et al., Development and calibration of an automated Mueller matrix polarization system for skin lesion differentiation, *Proc. SPIE*, Vol. 4250, 2001, pp. 449–454.
53. Smith, M.H., Interpreting Mueller matrix images of tissues, *Proc. SPIE*, Vol. 4257, 2001, p. 82.
54. Smith, M.H., et al., Mueller matrix imaging of GaAs/AlGaAs self-imaging beam-splitting waveguides, *Proc. SPIE*, Vol. 3121, 1997, pp. 47–54.

55. Federici, J.F., et al., Noninvasive light-reflection technique for measuring soft-tissue stretch, *Appl. Opt*., Vol. 38, No. 31, 1999, pp. 6653–6660.
56. Odonnell, M., et al., Internal displacement and strain imaging using ultrasonic speckle tracking, *IEEE Trans. Ultrason. Ferroelectr. Freq. Control*, Vol. 41, No. 3, 1994, pp. 314–325.
57. Jiao, S.L., and Wang, L.H.V., Two-dimensional depth-resolved Mueller matrix of biological tissue measured with double-beam polarization-sensitive optical coherence tomography, *Opt. Lett*., Vol. 27, No. 2, 2002, pp. 101–103.
58. Lompado, A., Smith, M.H., and Krishnaswamy, V., Measurement of the transmission and reflection Mueller matrices of a thin blood column, *Proc. SPIE*, Vol. 4263, 2001, pp. 161–169.
59. Esenaliev, R.O., et al., Noninvasive monitoring of glucose concentration with optical coherence tomography, *Opt. Lett*., Vol. 26, No. 13, 2001, pp. 992–994.
60. Timothy, W.K., et al., Multispectral polarimetric glucose detection using a single Pockels cell, *Opt. Eng*., Vol. 33, No. 8, 1994, pp. 2746–2753.
61. Cameron, B.D., and Cote, G.L., Polarimetric detection of glucose in biologically based fluids, *Proc. SPIE*, Vol. 2982, 1997, p. 308.
62. Ghosh, N., Wood, M.F.G., and Vitkin, I.A., Mueller matrix decomposition for extraction of individual polarization parameters from complex turbid media exhibiting multiple scattering, optical activity, and linear birefringence, *J. Biomed. Opt*., Vol. 13, No. 4, 2008, p. 044036.
63. Groner, W., et al., Orthogonal polarization spectral imaging: a new method for study of the microcirculation, *Nat. Med*., Vol. 5, No. 10, 1999, pp. 1209–1213.
64. Ugryumova, N., et al., The collagen structure of equine articular cartilage, characterized using polarization-sensitive optical coherence tomography, *J. Phys. D*, Vol. 38, No. 15, 2005, pp. 2612–2619.
65. Drexler, W., et al., Correlation of collagen organization with polarization sensitive imaging of in vitro cartilage: implications for osteoarthritis, *J. Rheumatol*., Vol. 28, No. 6, 2001, pp. 1311–1318.
66. Li, X., et al., OCT imaging of osteoarthritic cartilage: structure, polarization sensitivity, and clinical feasibility, *Proc. SPIE*, Vol. 3598, 1999, pp. 152–157.
67. Kokhanovsky, A.A., Radiative transfer in chiral random media, *Phys. Rev. E*, Vol. 60, No. 4, 1999, pp. 4899–4907.
68. Diaspro, A., Radicchi, G., and Nicolini, C., Polarized-light scattering: a biophysical method for studying bacterial-cells, *IEEE Trans. Biomed. Eng*., Vol. 42, No. 10, 1995, pp. 1038–1043.
69. Bickel, W.S., and Stafford, M.E., Polarized light scattering from biological systems: a technique for cell differentiation, *J. Biol. Phys*., Vol. 9, No. 2, 1981, pp. 53–66.
70. DeVolk, B., et al., Particle identifying apparatus, U.S. patent 4,953,980, Sept. 4, 1990.
71. Salzman, G.C., et al., Biological particle identification, U.S. patent 4,884,886, Dec. 5, 1989.
72. Bronk, B.V., et al., Measuring diameters of rod-shaped bacteria in-vivo with polarized-light scattering, *Biophys. J*., Vol. 69, No. 3, 1995, pp. 1170–1177.
73. Kouzoubov, A., Brennan, M.J., and Thomas, J.C., Treatment of polarization in laser remote sensing of ocean water, *Appl. Opt*., Vol. 37, No. 18, 1998, pp. 3873–3885.

74. Kattawar, G.W., Virtues of Mueller matrix detection of objects embedded in random media, *Proc. SPIE*, Vol. 3914, 2000, p. 478.
75. Walraven, R., Polarization imagery, *Opt. Eng*., Vol. 20, No. 1, 1981, pp. 14–18.
76. Gerligand, P.Y., Smith, M.H., and Chipman, R.A., Polarimetric images of a cone, *Opt. Express*, Vol. 4, No. 10, 1999, pp. 420–430.
77. Howe, J.D., et al., Polarization sensing for target acquisition and mine detection, *Proc. SPIE*, Vol. 4133, 2000, p. 202.
78. Solomon, J.E., Polarization imaging, *Appl. Opt*., Vol. 20, No. 9, 1981, pp. 1537–1544.
79. Tyo, J.S., et al., Target detection in optically scattering media by polarization-difference imaging, *Appl. Opt*., Vol. 35, No. 11, 1996, pp. 1855–1870.
80. Hovenier, J.W., Vandehulst, H.C., and Vandermee, C.V.M., Conditions for the elements of the scattering matrix, *Astron. Astrophys*., Vol. 157, No. 2, 1986, pp. 301–310.
81. Bates, A.P., Hopcraft, K.I., and Jakeman, E., Particle shape determination from polarization fluctuations of scattered radiation, *J. Opt. Soc. Am. A*, Vol. 14, No. 12, 1997, pp. 3372–3378.
82. Delplancke, F., Automated high-speed Mueller matrix scatterometer, *Appl. Opt*., Vol. 36, No. 22, 1997, pp. 5388–5395.
83. Silverman, M.P., et al., Enhanced optical rotation and diminished depolarization in diffusive scattering from a chiral liquid, *Opt. Commun*., Vol. 132, No. 5–6, 1996, pp. 410–416.
84. Onuki, A., and Doi, M., Flow birefringence and dichroism of polymers: 1. General-theory and application to the dilute case, *J. Chem. Phys*., Vol. 85, No. 2, 1986, pp. 1190–1197.
85. Kaplan, B., Compain, E., and Drevillon, B., Phase-modulated Mueller ellipsometry characterization of scattering by latex sphere suspensions, *Appl. Opt*., Vol. 39, No. 4, 2000, pp. 629–636.
86. Chipman, R.A., Sornsin, E.A., and Pezzaniti, J.L., Mueller matrix imaging polarimetry: an overview, *Proc. SPIE*, Vol. 2873, 1996, pp. 5–12.
87. Krishnan, S., Yugawa, K.J., and Nordine, P.C., Optical properties of liquid nickel and iron, *Phys. Rev. B*, Vol. 55, No. 13, 1997, pp. 8201–8206.
88. Jordan, D.L., Lewis, G.D., and Jakeman, E., Emission polarization of roughened glass and aluminum surfaces, *Appl. Opt*., Vol. 35, No. 19, 1996, pp. 3583–3590.
89. Rommers, J.H., and Howard, J., A new scheme for heterodyne polarimetry with high temporal resolution, *Plasma Phys. Control. Fusion*, Vol. 38, No. 10, 1996, pp. 1805–1816.
90. Schmitt, J.M., Gandjbakhche, A.H., and Bonner, R.F., Use of polarized-light to discriminate short-path photons in a multiply scattering medium, *Appl. Opt*., Vol. 31, No. 30, 1992, pp. 6535–6546.
91. Shimizu, K., et al., Backscattering of a picosecond pulse from densely distributed scatterers, *Appl. Opt*., Vol. 18, No. 20, 1979, pp. 3484–3488.
92. Hebden, J.C., Kruger, R.A., and Wong, K.S., Time resolved imaging through a highly scattering medium, *Appl. Opt*., Vol. 30, No. 7, 1991, pp. 788–794.

93. Toida, M., et al., 2-Dimensional coherent detection imaging in multiple-scattering media based on the directional resolution capability of the optical heterodyne method, *Appl. Phys. B*, Vol. 52, No. 6, 1991, pp. 391–394.
94. Yoo, K.M., Xing, Q.R., and Alfano, R.R., Imaging objects hidden in highly scattering media using femtosecond 2nd-harmonic-generation cross-correlation time gating, *Opt. Lett*., Vol. 16, No. 13, 1991, pp. 1019–1021.
95. Lara, D., and Dainty, C., Double-pass axially resolved confocal Mueller matrix imaging polarimetry, *Opt. Lett*., Vol. 30, No. 21, 2005, pp. 2879–2881.

# 16

# NANOTECHNOLOGY APPROACHES TO CONTRAST ENHANCEMENT IN OPTICAL IMAGING AND DISEASE-TARGETED THERAPY

NICUSOR IFTIMIA
*Physical Sciences, Inc., Andover, Massachusetts*

LARA MILANE
*School of Pharmacy, Northeastern University, Boston, Massachusetts*

AMY OLDENBURG
*University of North Carolina at Chapel Hill, Chapel Hill, North Carolina*

MANSOOR AMIJI
*School of Pharmacy, Northeastern University, Boston, Massachusetts*

16.1 Introduction 456
16.2 Nanotechnology-based contrast agents for optical imaging and targeted therapy 458
  16.2.1 Superparamagnetic iron oxide nanoparticles 459
  16.2.2 Gold nanoparticles 461
  16.2.3 Quantum dots 465
16.3 Enhanced-contrast optical imaging using functionalized nanoprobes 467
  16.3.1 Fluorescence imaging 468
  16.3.2 Optical coherence tomography 470
  16.3.3 Combined imaging modalities 474
16.4 Nanotechnology-based drug delivery systems for disease-targeted therapy and tissue regeneration 480
  16.4.1 Fundamental requirements for drug delivery systems 481
  16.4.2 Disease-targeted therapy 486

---

*Advances in Optical Imaging for Clinical Medicine*, Edited by Nicusor Iftimia, William R. Brugge, and Daniel X. Hammer
Copyright © 2011 John Wiley & Sons, Inc.

16.4.3 Tissue regeneration 491
16.5 Conclusions 494
References 494

## 16.1 INTRODUCTION

As shown in previous chapters, imaging plays a fundamental role in early diagnosis and prognosis of various diseases, mainly through the detection of anatomically defined abnormalities. Optical imaging at both the macroscopic and microscopic levels is used intensively by clinicians as a tool to aid in establishing a diagnosis. New advances in optics, data acquisition, and image processing made possible the development of novel optical imaging technologies, including diffuse tomography, confocal microscopy, fluorescence microscopy, optical coherence tomography, and multiphoton microscopy, which can be used to image tissue or biological entities with enhanced contrast and resolution [1–10]. Optical imaging technologies are more affordable than the traditional radiological technologies and provide both structural and functional information with enhanced resolution. However, they still lack sensitivity and specificity for cancer detection. Therefore, within the past several years, there has been increasing interest in improving clinical effectiveness of optical imaging by combining emerging optical technologies with novel exogenous contrast agents, including several types of nanovectors (e.g., nanoparticles, ligands, quantum dots), which can be functionalized with various agents (such as antibodies or peptides) that are highly expressed by cancer receptors [11–15]. In this way, in addition to improved sensitivity and specificity, it becomes possible to label proteins in live cells and obtain a clearer understanding of the dynamics of intracellular networks, signal transduction, and cell–cell interactions [16–20].

The use of the enhanced sensitivity and specificity molecular imaging approaches in medicine has the potential to affect positively the prevention, diagnosis, and treatment of various diseases, including cancer [12,19–23]. Synthetic nanostructures, such as nanoparticles and nanodevices, being of the same size as biological entities, can readily interact with biomolecules on both the cell surface and within the cell. If functionalized to recognize cancer receptors, they have the potential to increase diagnostic effectiveness substantially [21,23–25]. Ultimately, the combination of these new molecular and nanotechnology approaches with new developments in microscopic and spectroscopic techniques toward high spatial resolution, such as optical coherence tomography, optical fluorescence microscopy, scanning probe microscopy, electron microscopy, and mass spectrometry imaging, can offer molecular resolution and high sensitivity, allowing for a better understanding of the cell's complex "machinery" in basic research. The resulting accelerated progress could pave the way to more inventive and powerful in vivo diagnostic tools.

Recent work performed by various research groups demonstrates the benefit of molecular probes for contrast and specificity enhancement in optical imaging. For example, Sokolov et al. [25] have reported real-time optical imaging of precancer using antiepidermal growth factor receptor antibodies conjugated to gold nanoparticles. Aaron et al. [26] have reported the use of plasmon resonance coupling of metal nanoparticles for molecular imaging of carcinogenesis in vivo. Oldenburg et al. [27] have reported the use of magnetic particles for magnetomotive contrast enhancement in optical coherence tomography. Also, Loo et al. [28] have reported the use of gold nanoshell bioconjugates for molecular imaging in living cells.

Besides contrast enhancement in medical diagnostics, these highly specific contrast agents also represent a promising alternative for cancer treatment. They are the best candidates for the next generation of drug delivery methods. Therefore, research has recently been concentrated in the creation of nanotechnology-based platform technologies that can couple molecular-specific early detection strategies with appropriate therapeutic intervention and monitoring capabilities. The appeal for using nanoagents in selective tumor targeting is also favored by the potential to deliver a concentrated dose of drug in the vicinity of (or even inside) the target tissue, reducing the drug exposure of healthy cells. The nanoagents can be engineered to bind to drugs, proteins, enzymes, antibodies, or nucleotides and can be directed to an organ, tissue, or tumor. Recent work by El-Sayed et al. [29], Ito et al. [30], Amiji et al. [31], Torchilin et al. [32], and O'Neal et al. [33] demonstrates the potential of nanoagents for both cancer diagnosis and therapy. However, besides tumor specificity, they also need to be engineered to maximize their systemic circulation and reach the tumor in sufficiently high concentration [34].

The emergence of nanotechnology will also have a significant impact on the drug delivery sector, affecting just about every route of administration from oral to injectable. Novel, highly engineered nanodevices will constitute platforms capable of hosting several components that could actively perform specific tasks of diagnostic and therapeutic functions at the cellular scale. It is well known that drugs with a narrow *therapeutic index* (also known as the *therapeutic ratio*, which is a comparison of the amount of a therapeutic agent that causes the therapeutic effect to the amount that causes toxic effect) creates a major challenge for pharmaceutical scientists. The use of nanotechnology for the delivery of such drugs could overcome this problem. However, several key processes are still to be tailored before molecular specificity levels can be attained, such as the way in which the drug is stored in the nanoagents, the mechanism that drives them toward the target, and the biological barriers that need to be overcome. Each of these developments has its own technical challenges and involves different research fields; thus, each solution must be considered from specific viewpoints before they can be all integrated into a single outcome.

## 16.2 NANOTECHNOLOGY-BASED CONTRAST AGENTS FOR OPTICAL IMAGING AND TARGETED THERAPY

A wide range of nanoparticles and single-molecule targeting and/or contrast enhancement agents are currently used in biology and medicine [19,35–40]. These include iron oxide–based nanoparticles, gold nanoparticles, quantum dots, dendrimers, and liposomes, among others. As discussed above, these nanoagents can be highly engineered to perform multiple functions. However, several steps should be carefully taken during synthesis to produce nanoagents suitable for medical imaging and therapy applications, as follows:

1. *Synthesis of the optical core.* The first fabrication step is the synthesis of the nanocore, which may encapsulate a fluorochrome or a therapeutic agent [41,42]. The most popular system for nanoparticle preparation is the water-in-oil (w/o) microemulsion system, also commonly referred to as reverse micelles. The use of w/o microemulsions for nanoparticle preparation has attracted a lot of attention for its simplicity and for the full control provided over the particle size.
2. *Synthesis of the shell.* The shell serves several purposes: protecting the optical core from the external environment, thus improving its photostability (e.g., for organic dyes), enhancing the optical properties, and providing further ability to bind and/or adhere to molecules for surface stability and bioconjugation. Various shell materials are used, including gold or silver nanocomposites, depending on the specific application and desired optical signal [41–44].
3. *Surface modification.* There is a natural tendency for the particles to coagulate and aggregate, depending on their surface chemistry. However, it is important that the nanoparticles remain suitably dispersed, preferably in an aqueous environment of ionic strength similar to that of the bioenvironment of the biomedical application. This may be achieved by modifying the surface of the nanoparticles by employing various dispersing agents (e.g., surfactants, polymers, and chelating groups). Surface treatments are also performed for covalent bounding of antibodies or other functionalization agents [11,26,29].
4. *Bioconjugation and targeting.* For targeted delivery of the nanoparticles to the desired site of action and specific binding, it is necessary to attach suitable biomolecules on their surface, such as antibodies, peptides, and enzymes. These molecules can also act to promote or maintain adequate dispersion of the nanoparticles. The conjugation of the nanoparticles for specific targeting of cancer cells has been described in detail in many reports [30,40–45].

A brief presentation of the fabrication/functionalization approaches for several types of nanoparticles follows.

### 16.2.1 Superparamagnetic Iron Oxide Nanoparticles

Superparamagnetic iron oxide (SPIO) nanoparticles have a variety of applications in molecular and cellular imaging [46,47]. They have been investigated for cellular imaging of in vivo macrophage activity, for detection of liver metastases, metastatic lymph nodes, inflammatory and/or degenerative diseases, stem cell migration, and immune cell trafficking, as well as for molecular imaging studies. SPIOs are based on iron oxide colloids (ca. 1 to 20 nm), which may be prepared by coprecipitation of ferrous and ferric salts in water in the presence of citric acid and sodium hydroxide. The iron oxide colloids are washed to remove excess sodium hydroxide and then oxidized to $\gamma$-$Fe_2O$ by suspension in nitric acid and subsequent stirring at moderate temperatures.

As shown in Figure 16.1, the iron oxide colloids may be embedded in poly(ethylene oxide)–modified poly($\epsilon$-caprolactone) (PEO-PCL) materials. The resulting nanoparticles, a few hundred nanometers in size, can be labeled with various dyes, functionalized with peptides or antibodies for specific targeting of cancer cells, and also used as carrier vehicles for cytotoxic drugs (e.g., paclitaxel). The nanoparticles can release the treatment drug when an external magnetic field is applied. They can be also heated in alternating magnetic fields to induce tissue hyperthermia [48–50].

Such nanoparticles are currently being fabricated in several academic laboratories and biotech companies. Scanning electron microscopy (SEM) images of iron oxide colloids entrapped in 200-nm PEO-PCL nanoparticles fabricated in Mansoor Amiji's lab at Northeastern University are shown in Figure 16.2.

SPIO nanoparticles with appropriate surface chemistry are being widely used experimentally for numerous in vivo applications, such as magnetic resonance imaging contrast enhancement, tissue repair, immunoassay, detoxification of biological fluids, hyperthermia, drug delivery, and cell separation. They are also usually labeled with dyes to provide contrast enhancement for both MR and fluorescence imaging. This approach seems to be very attractive for the detection of

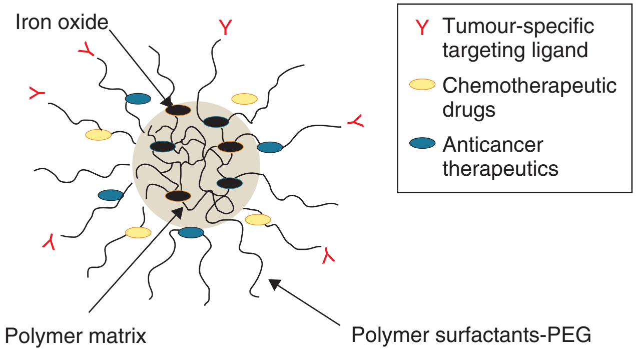

**FIGURE 16.1** PCL iron oxide–core nanoparticle with PEG surfactants and attached anticancer and chemotherapeutic drugs.

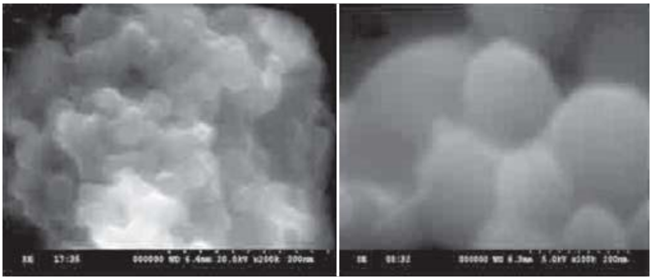

(a) (b)

**FIGURE 16.2** Scanning electron microscopy images of the $Fe_2O_3$ colloids (a) used for PCL iron oxide nanoparticle fabrication (b) in Mansoor Amiji's laboratory at Northeastern University's School of Pharmacy. The mean size of the colloids is about 20 nm, and the mean size of the PCL nanoparticles is about 200 nm.

surgical margins. For example, precise determination of brain tumor margins is very important for the successful outcome of patients undergoing surgery. Kircher et al. [51] recently reported the use of a multimodal nanoparticle contrast agent consisting of an optically detectable NIR fluorochrome conjugated to an MRI-detectable iron oxide core for brain tumor margins delineation in a rat animal model. They found that the multimodal nanoparticle probe Cy5.5-cross-linked iron oxide (CLIO) permitted the preoperative visualization of brain tumors by serving as an MRI contrast agent and afforded an intraoperative discrimination of tumors from brain tissue because of its near-IR fluorescence (see Figure 16.3).

The ability to track the same probe by both preoperative MR and intraoperative optical imaging seems to be very useful for the intraoperative visualization and accurate resection of tumors (see Figure 16.4).

The superparamagnetic nanoparticles can also be designed to act as transducers that capture external electromagnetic energy at 350 to 400 kHz, a frequency that is not significantly absorbed by tissue, but is sufficiently absorbed by SPIOs to trigger the release of various pharmacological agents. Therefore, the multifunctional nanoparticles were used to demonstrate remote, pulsatile release of single or multiple species in vitro, as well as to provide imaging contrast enhancement and remote actuation upon implantation in vivo [52–55]. Release of agents from either the surface or core when triggered by an external stimulus (electric current, magnetic fields, temperature, light, or ultrasound) has been studied extensively. For example, recent work of Derfus et al. [56] shows that dextran-coated iron oxide nanoparticles conjugated with a fluorophore release the fluorophore in the presence of electromagnetic pulses. They also performed an in vivo mouse experiment that showed the controlled release of drugs in the presence of an electromagnetic field (see Figure 16.5). Similarly, magnetic nanoparticles were used as heat generators to induce localized cell death [55].

Once more, these studies suggest that the targeted delivery of "smart" nanoparticles is the next step toward improved medical diagnosis and more efficient

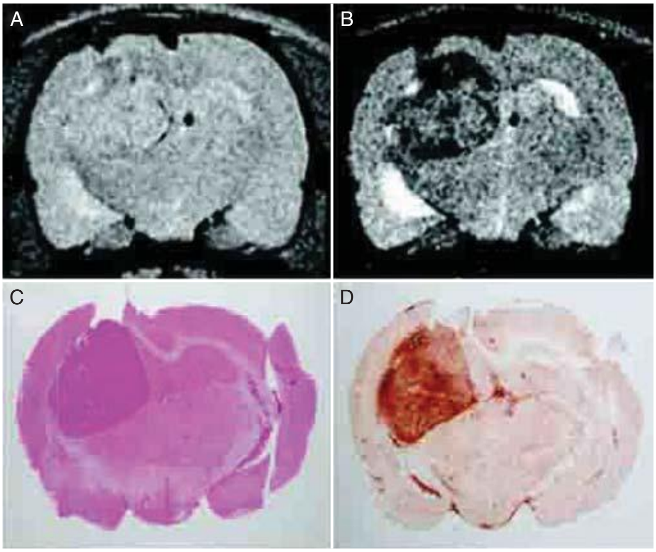

**FIGURE 16.3** Cy5.5-CLIO nanoparticle as a preoperative MRI contrast agent. (A, B) Proton density and $T_2$-weighted images. Tumor uptake of iron is evident on $T_2$-weighted images as regions of low signal intensity, whereas tumor is isointense to surrounding tissue using proton density images. (C) H&E staining of histological section corresponding to MRI slices in parts A and B. (D) DAB-amplified Prussian Blue staining of histological section corresponding to MRI slices in parts A and B. (From [51], with permission.)

oncologic therapies. Current improvements in this field rely on (1) particle functionalization with specific ligands for targeting cell membrane receptors and (2) loading of the nanoparticles onto cells (e.g., dendritic cells, T-cells, and macrophages) that have an active role in tumor growth.

### 16.2.2 Gold Nanoparticles

Gold nanoparticles are another class of metal nanoparticles that have found a niche in the biomedical field. They are versatile agents with a variety of biomedical applications, including use in highly sensitive diagnostic assays, thermal ablation, and radiotherapy enhancement, as well as drug and gene delivery [57–59]. They offer additional advantages, such as the ability to be easily manufactured into a variety of particle sizes ranging from 2 to 200 nm in diameter, surface modification using thiol chemistry, and high electron density of the metal, allowing for visualization of the nanoparticles by electron microscopy and x-ray analytical techniques.

Gold colloids were used initially in biological applications in 1971 when Faulk and Taylor invented the immunogold staining procedure [57]. Since then, the labeling of targeting molecules, especially proteins, with gold nanoparticles has revolutionized the visualization of cellular or tissue components by electron

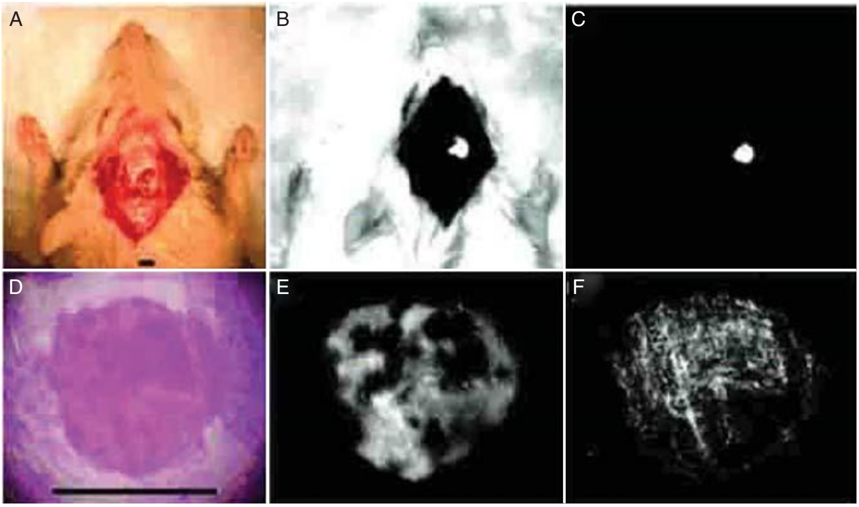

**FIGURE 16.4** Delineation of a GFP-expressing 9L glioma tumor by optical imaging in an intraoperative setting. Craniotomy was performed on a Fischer 344 rat bearing a 3-mm-diameter 9L glioma tumor. The brain tissue overlying the tumor was removed and optical imaging performed. (A) White light image; (B) GFP channel; (C) Cy5.5-channel; (D–F) histological processing and microscopy of the tumor shown in parts A to C (D, H&E stain; E, GFP channel; F, Cy5.5 channel). 20-μm sections, 2.5× original magnification, scale bar, = 5 mm. (From [51], with permission.)

microscopy. The optical and electron-beam contrast qualities of gold colloid have provided excellent detection qualities for immunoblotting, flow cytometry, hybridization assays, and other techniques. The vast prior history of gold colloid–based materials has greatly facilitated the development of biomedical applications of newer gold-based nanoparticles.

One of the most important advantages of the gold nanoparticles is that they can be functionally “tailored” by surface modification using thiol chemistry to produce a variety of probes for specific applications [59,60]. Surface functionalization is essential in biomedical applications. It allows for specific tissue targeting by selective interaction with cells or biomolecules. Additionally, surface modification procedures are applied to provide long circulation of the nanoparticles within the body. In this way, passive targeting of tumors and inflammatory sites has higher efficacy. The systemic circulation can be increased from minutes to hours or even days by use of poly(ethylene glycol) (PEG) stealth shielding. PEG modification is often referred to as *PEGylation*, a term that implies the covalent binding or noncovalent entrapment or adsorption of PEG onto an object. PEG modification of the nanoparticles provides long-circulating properties by evading macrophage-mediated uptake and removal from the systemic circulation [61].

Gold nanoparticles seem to be very well suited for enhanced-contrast optical imaging. Their optical properties make them very attractive for imaging

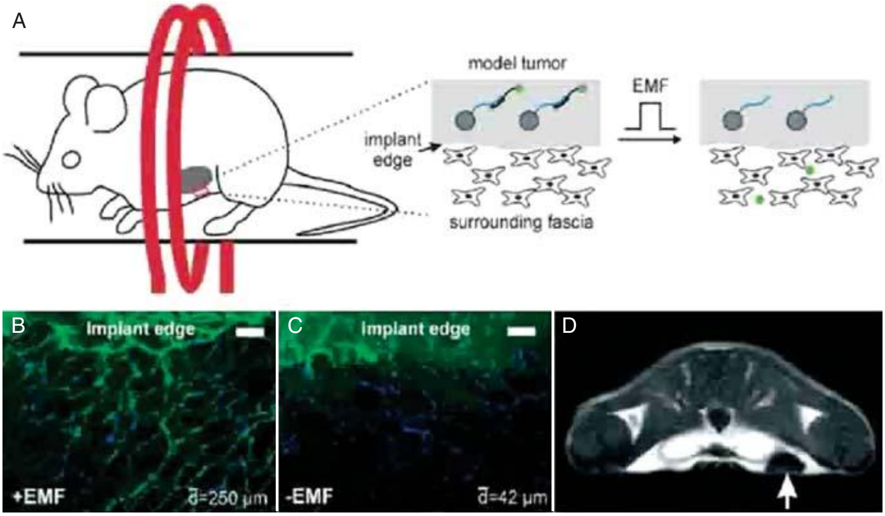

**FIGURE 16.5** Remotely triggered release from nanoparticles in vivo. Nanoparticles were mixed with matrigel and injected subcutaneously near the posterior mammary fat pad of mice, forming model tumors. (A) Application of EMF to implants containing 18-bp tethers resulted in release of model drugs and penetration far into surrounding tissue (B) compared to unexposed controls (C; scale bar, 100 μm). These mice were imaged with a 7T MRI scanner, and transverse section (D) depicts image contrast due to the presence of nanoparticles (arrow). (From [56], with permission.)

of biological samples. For example, Sokolov et al. have used molecular specific gold nanoparticles to differentiate between normal and tumor cells in reflectance mode. Rahman et al. [62] have used the anti-EGFR conjugated gold particles to increase the confocal imaging contrast of cancer cervical tissue phantoms.

Among gold nanoparticles, gold nanoshells and gold nanorods are special classes that offer additional advantages over those of simple gold colloids. Their absorbance peak can be tuned to a wavelength of interest. The nanoshells are composed of a dielectric core, such as silica, coated with an ultrathin metallic layer, typically gold. Gold nanoshells have physical properties similar to those of gold colloids, particularly strong optical absorption, due to gold's collective electronic response to light.

The nanoshells can be engineered to interact with specific wavelengths of light. This special property enables applications in both cancer diagnosis and therapy. By controlling the physical parameters of the nanoshells (varying the relative thicknesses of the core and shell), it is possible to engineer nanoshells that primarily scatter light, which is desirable for many imaging applications, or alternatively, to design nanoshells that are strong absorbers. An illustrative example is shown in Figure 16.6 Nanoshells with a silica core of 60 nm and a 20-nm gold shell have two plasmonic absorption bands, at 525 and 730 nm,

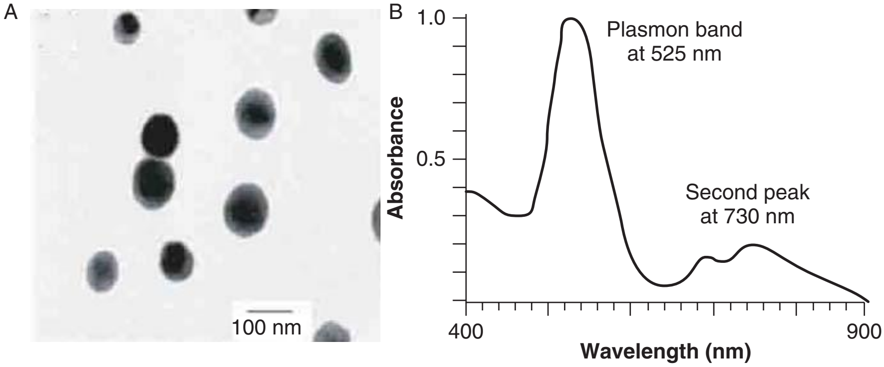

**FIGURE 16.6** Resonance wavelength tuning of gold nanoshells. (Courtesy of Mansoor Amiji's laboratory at Northeastern University.)

respectively. By changing the shell thickness, these bands can be tuned to lower or higher wavelengths.

The extremely agile "tunability" of optical resonance is a property unique to plasmon-resonant nanostructures such as nanoshells, naocages, and nanorods. No other molecule or nanoparticle structure can be designed to have as systematically tunable optical absorption resonance. The extremely high near-infrared absorption cross section (on the order of $10^{-15}$ m$^2$ for nanoshells and $10^{-14}$ m$^2$ for nanorods) of these nanostructures make them very well suited for photothermal-based therapy applications [63–65]. Wang and colleagues [64] have completed a comprehensive investigation of the optical properties of metal nanoshells and achieved quantitative agreement between Mie scattering theory and the experimentally observed optical-resonant properties. As a result, it is now possible to design gold nanoshells predictively with the desired optical-resonant properties and then to fabricate the nanoshell with the dimensions and nanoscale tolerances necessary to achieve these properties.

Several research groups have performed successful studies proving that nanoshells can be used to create high-contrast images of tissue, enhance cancer presence, and provide precise tumor therapy [29,63–65]. For example, El-Sayed et al. [29] have conjugated gold nanorods with an aspect ratio of 3.9 to antiepidermal growth factor receptor (anti-EGFR) antibodies for selective photothermal therapy in the NIR region. The gold nanorods were incubated in cell cultures with a nonmalignant epithelial cell line (HaCaT) and two malignant oral epithelial cell lines (HOC 313 clone 8 and HSC 3). The malignant cell death occurred with less than half the laser energy required to kill normal cells, due to the photothermal effect of the EGFR-labeled gold nanorods that were overexpressed by the malignant cells. Hirsch et al. [65] have also tested the photothermal destruction of carcinoma cells by NIR-absorbing gold nanoshells. With the same laser fluence, only gold nanoshell–treated samples underwent photothermal destruction (see Figure 16.7).

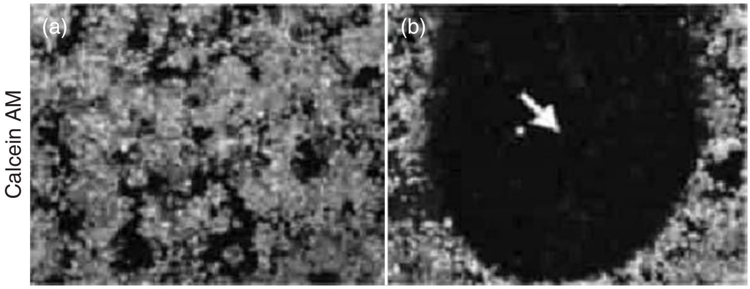

**FIGURE 16.7** Localized photothermal destruction of carcinoma cells by NIR-absorbing gold nanoshells: (a) laser irradiation of carcinoma cells; (b) laser irradiation of carcinoma cells incubated with functionalized gold nanoshels. Calcein AM viability staining reveals that only gold nanoshell–treated samples underwent photothermal destruction within the laser spot (b). (From [65], with permission.)

Although a much longer list of examples showing the potential benefit of the gold nanoparticles for both imaging contrast enhancement and cancer therapy could be presented, our goal was to provide readers with an introduction to this topic and stimulate more interest for further studies.

### 16.2.3 Quantum Dots

Recently, rare earth–doped nanocrystals and quantum dot nanocrystals (Qdots) have also been used as contrast enhancement agents in optical imaging [66–69]. Depending on their coating and their physical and chemical properties, they can target a specific tissue or cell and can be made to fluoresce for imaging purposes. Colloidal semiconductor quantum dots are single crystals with a few nanometers in diameter whose size and shape can be controlled precisely by the duration, temperature, and ligand molecules used in the synthesis. By strictly controlling the synthesis process, Qdots that have composition- and size-dependent absorption and emission can be manufactured (Figure 16.8).

The absorption and emission process of the Qdots is explained briefly next. Absorption of a photon with energy above the semiconductor bandgap energy results in the creation of an electron–hole pair (or exciton). The absorption has an increased probability at higher energies (i.e., shorter wavelengths) and results in a broadband absorption spectrum, in marked contrast to standard fluorophores. For nanocrystals smaller than the Bohr exciton radius (a few nanometers), energy levels are quantized, with values directly related to the Qdot size (an effect called *quantum confinement*, hence the name *quantum dots*). The radiative recombination of an exciton, characterized by a long lifetime, usually >10 ns, leads to the emission of a photon in a narrow, symmetric energy band. The long fluorescence lifetime of Qdots enables the use of time-gated detection [71] to separate their signal from that of shorter-lived species (such as the background autofluorescence encountered in cells).

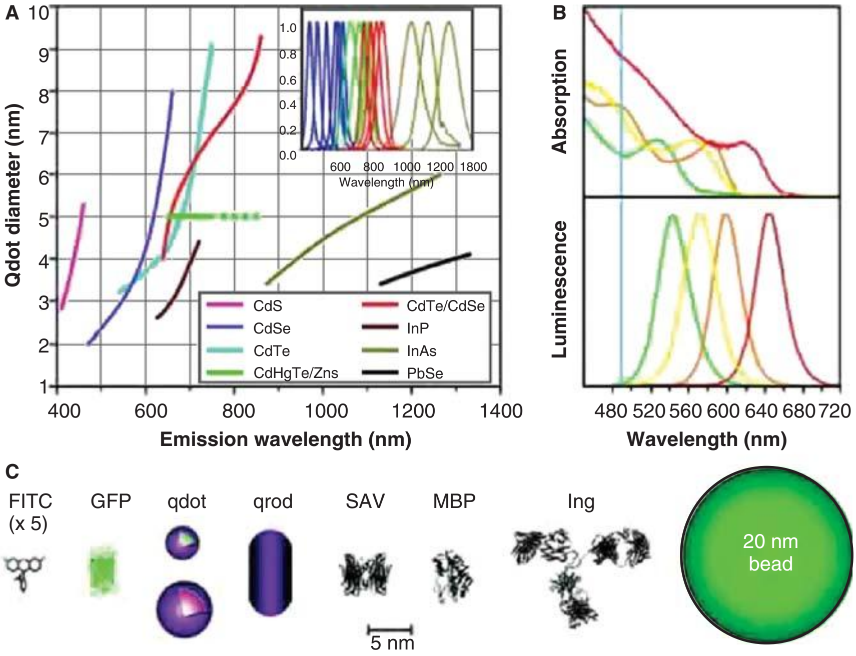

**FIGURE 16.8** (A) Emission maxima of quantum dots of different composition. (B) Absorption (upper curves) and emission (lower curves) spectra of four CdSe/ZnS Qdot samples. The blue vertical line indicates the 488-nm line of an argon-ion laser, which can be used efficiently to excite all four types of Qdots simultaneously. (C) Size comparison of Qdots and comparable objects: FITC, fluorescein isothiocyanate; GFP, green fluorescent protein; Qdot, green (4 nm, top) and red (6.5 nm, bottom) CdSe/ZnS Qdot; Qrod, rod-shaped Qdot; SAV, streptavidin; MBP, maltose binding protein; IgG, immunoglobulin G. (From [70], with permission.)

Using appropriate material composition and size, Qdots with emission in visible, NIR, and even far-IR spectra can be obtained. This is a very useful benefit, especially if one wants to cover the NIR spectrum, where only a few high-quantum-yield dyes exist. Because Qdots have a broad excitation spectrum, a combination of nanocrystals can be excited with a certain laser wavelength and detected concurrently in different color channels, so the multiplexing capabilities are greater than those of conventional materials. This property facilitates the Qdots for use in complex surroundings such as living cells. They are brighter than conventional dyes, offering a more intense fluorescent light emission, which means that even a small number of Qdots is enough to produce an adequate signal. They also are more photostable, so the acquisition time can be longer.

Qdots are also excellent probes for two-photon confocal microscopy because they are characterized by a very large two-photon absorption cross section [72]. They also have a largely untapped potential as customizable donors for fluorescence resonance energy transfer (FRET) [69].

Qdots are expected to be particularly useful for imaging in living tissues, where signals can be obscured by scattering. Chemical groups with different functionalities can be attached to the surface of a Qdot, producing a multimodality probe. The Qdots have already demonstrated their potential application in medical imaging, such as for lymph-node surgery and tracking metastatic tumors [73–75]. However, Qdots cytotoxicity is a major problem and for the moment is their major limitation for clinical use. Biodistribution and toxicological studies are currently being undertaken by different research groups [76,77] to study precisely their impact on humans, animals, and the environment. In the vent that the cytotoxicity problem will be solved in the future, it will enable Qdots use in medicine and biology.

## 16.3 ENHANCED-CONTRAST OPTICAL IMAGING USING FUNCTIONALIZED NANOPROBES

Most of the optical techniques currently used for in vivo medical imaging suffer from low contrast between neoplastic and normal tissue and are unable to image early biomolecular changes associated with carcinogenesis, thus limiting their clinical value. Therefore, various technologies for contrast enhancement are being developed. Among them, nanoparticle-based technologies have generated much interest due to their enhanced absorption or scattering optical capabilities and ease of functionalization by adding surface fluorophores and cell targeting agents (i.e., antibodies, peptides, etc.). Optical techniques combined with molecular contrast agents show a real promise for high-resolution noninvasive functional imaging of tissue with improved sensitivity, specificity, and cost-effectiveness relative to current approaches. Numerous studies have shown the viability of scattering-based optical approaches, including spectroscopy, confocal microscopy, and optical coherence tomography (OCT) [76–80]. For example, Lee et al. [78] have developed oil-filled encapsulating protein microspheres that can incorporate various particles such as gold and carbon to alter backscattering optical signatures for OCT. Rajadhyaksha et al. have has used polystyrene microspheres to enhance imaging of skin and microcirculation under confocal reflectance microscopy [79]. Recent work by Sokolov et al. [59] demonstrated that the detection of precancerous cells using confocal reflectance imaging can be enhanced with gold nanoparticles bioconjugated with antiepidermal growth factor receptor antibodies.

Besides contrast enhancement, due to either absorption or scattering enhanced cross sections, the nanoparticles can be functionalized to selectively target cancer cells only. Therefore, their use in medicine enables both selective therapy and imaging with enhanced sensitivity and specificity. Many in vitro and in vivo demonstrations have shown the practicality of various nanoparticles for both imaging contrast enhancement and selective therapy [14,19,24,26,33,41,48]. However, more efforts are necessary for clinical translation of the various nanotechnologies. Recent studies show that various optical technologies, such as

OCT, reflectance microscopy, and fluorescence microscopy, can be adapted to take benefit of the enhanced-contrast capabilities offered by various nanoagents. For example, several microscopy and coherence imaging approaches, such as Raman fluorescence microscopy [80], spectrosopic OCT [81,82], magnetotomotive OCT [83], and CARS microscopy [84,85], have shown contrast enhancement when used in correlation with optical probes. By careful design of both optical systems and nanoagents, it is possible to generate multiple-order-of-magnitude improvements in optical contrast enhancement, which could potentially lead to higher sensitivity and specificity detection of early stage cancer lesions. A more detailed description of some of the current research efforts in this area is presented below.

### 16.3.1 Fluorescence Imaging

Whereas reflectance-based optical techniques for in vivo imaging often suffer from low contrast between neoplastic and normal tissue and are unable to image early biomolecular changes associated with carcinogenesis, thus limiting their clinical value, fluorescence labeling of molecular markers has made possible significant contrast enhancement. As shown before, various fluorochromes can be attached to markers or nanoagents to increase the contrast between neoplastic and normal tissue. The nanoagents can be functionalized to target various cancer receptors, such as epithelial growth factor receptors (EGFR) or integrins, which exist on a cell's surface. The EGFR receptor is one of four receptors in the HER (human epidermal growth factor receptor) signaling pathway. The pathway consists of at least four cellular receptors: EGFR/HER1, HER2, HER3, and HER4. Approximately 11 different factors are known to bind and activate these receptors in certain patterns. EGFR is activated by binding of its specific ligands, including epidermal growth factor and transforming growth factor $\alpha$ (TGF$\alpha$). Integrins are heterodimeric cell surface receptors that were found in early studies to mediate the adhesion between cells and the extracellular matrix (ECM), by binding to ligands with an exposed arginine–glycineaspartate (RGD) sequence [86]. They play key roles in tumor invasion, metastasis, and neovascularization. These proteins associate as $\alpha\beta$ heterodimers in the native environment, where the $\alpha$ and $\beta$ subunits control distinct but complementary physiological functions [87]. Currently, 18 $\alpha$ and eight $\beta$ integrin subunits have been identified, with each $\beta$ subunit associating with different $\alpha$ proteins.

A lot of interest has recently been directed toward the development of various antiangiogenic drugs and tumor imaging agents, labeled with fluorochromes, that can target the $\alpha_v\beta$ integrin receptors (ABIR) because of their association with a number of cancers, including colon [88], cervical [89], prostate [90], and breast [91]. Particularly, expression of ABIR in tumor cells undergoing angiogenesis and on the epithelium of tumor-induced neovasculature alters the interaction of cells with the extracellular matrix, thereby increasing tumorigenicity and invasiveness of cancers. These receptors also stimulate intracellular signaling and gene expression involved in cell growth, migration, and survival. These same processes, if not regulated properly, can lead to thrombosis, inflammation, and cancer. In fact, integrins have been demonstrated to be participants in these diseases and can also act as disease markers. Therefore, research has focused on developing RGD peptides that could mimic cell adhesion proteins and bind to integrins. For example, Achilefu's group at Washington University of St. Louis has developed a novel RGD peptide that binds to epithelial cancers with high affinity [86]. They have also attached a cypate dye, similar to indocyanine green (ICG), to the RGD peptide. This dye is approved by the U.S. Food and Drug Administration (FDA) for use in humans and was chosen as the optical molecular probe because it fluoresces in the near-infrared (NIR) region of the spectrum. Recent work performed by researchers at Physical Sciences, Andover, Massachusetts, also demonstrates the highly selective binding of RGD-based contrast agents. An example of the selective binding of the RGD peptide to HT29 colon cells is shown in Figure 16.9.

The integrin or EGFR binding contrast agents can also be attached to nanoparticles that can be engineered to enhance the MR or reflectance optical imaging contrast. The development of nanoparticulate contrast agents provides an increasing contribution to the field of diagnostic and molecular imaging. Such agents provide several advantages over traditional compounds. First, they may contain a high payload of contrast-generating material, which greatly improves their detectability. Second, multiple properties may easily be integrated within one nanoparticle to allow its detection with several imaging techniques or to include therapeutic qualities. Finally, the surface of such nanoparticles may be modified to improve circulation half-lives or to attach targeting groups. Several groups have shown the utility of various nanotechnologies for fluorescence imaging contrast enhancement and cancer delineation [21,24,72,92].

Although there has been much progress in molecular imaging with fluorescent probes, some critical aspects that need to be addressed before these (fluorophores) can be employed for clinical translation are:

1. Detection of the fluorescent signals generated from deeply located targets at the tissue surface.

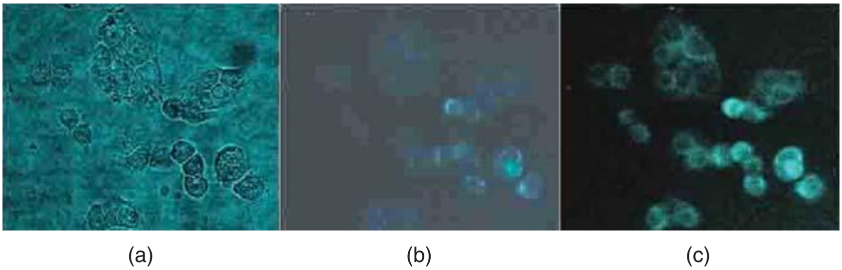
(a) (b) (c)

**FIGURE 16.9** Binding of the PCL-$\alpha_v\beta_3$-cypate agent (from Achilefu's group at Washington University of St. Louis) to HT29 cancer cells: (a) VIS reflectance image; (b) negative (PCL-cypate only) control NIR image; (c) PCL-$\alpha_v\beta_3$-cypate NIR image. Magnification, 40×.

2. Optimization of loading of encapsulated dye for optimum detection.
3. Sufficient photostability for in vivo applications.
4. Synthesis of a range of NIR dyes with fluorescence in the NIR window, 650 to 900 nm, for application to varied biological samples.
5. Ideal probes for multicolor experiments. They should have a narrow symmetric emission spectrum (in contrast to conventional dyes with a broad emission spectrum and a long tail at red wavelengths), and the entire group of probes should ideally be excitable at a single wavelength.

### 16.3.2 Optical Coherence Tomography

Optical coherence tomography (OCT) is the optical analog of ultrasound. It performs cross-sectional imaging by measuring the magnitude and echo time delay of backscattered light. Image resolutions of 1 to 10 μm can be achieved, and imaging can be performed in situ and in real time. OCT was first demonstrated in 1991 [93]. Since that time, numerous applications of OCT for biomedical imaging have been demonstrated in areas including ophthalmology, cardiology, gastroenterology, and oncology [94–100].

A typical OCT system is comprised of a Michelson interferometer, which is formed by a beamsplitter or 2 × 2 coupler, a moving mirror for optical delay in the reference arm, and a focusing lens in the sample arm. A typical fiber optic version of an OCT system is shown in Figure 16.10. A short temporal coherence-length light source such as a superluminescent diode is used to provide optical depth ranging. Interference fringes corresponding to different depths within the sample are demodulated and used to build up the depth reflectivity profile. The sample arm light beam is scanned in one or both of the transverse directions, and rapid successive axial measurements are performed. The result is a two- or three-dimensional data set, which represents the optical backscattering in a cross-sectional plane or volume of the material or tissue.

In the time-domain implementation of OCT (TD-OCT) shown in Figure 16.10, a scanning mechanism is used in the reference arm of the interferometer to build up the depth reflectivity profile. The limited speed of the scanning mechanism

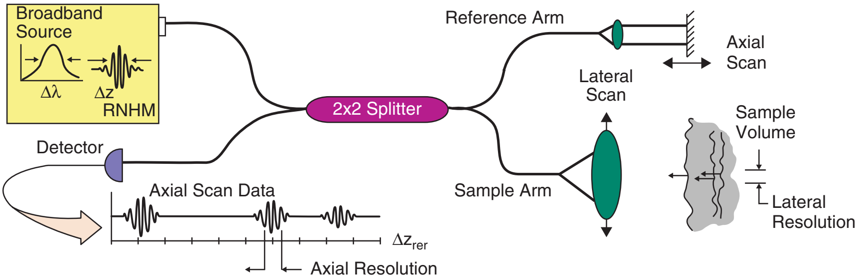

**FIGURE 16.10** Fiber optic–based OCT system.

limits the imaging speed of OCT and therefore precludes its use for real-time screening of large tissue volumes. Recently, a new paradigm of performing OCT has been adopted from spectral radar. In this new method, called *spectral-domain OCT* or *Fourier-domain OCT* (SD-OCT), individual spectral components of low-coherence light are detected separately by use of a spectrometer consisting of a charge-coupled device (CCD) array [101]. The fast readout speed of CCD arrays and the signal/noise ratio (SNR) advantage of SD-OCT make it promising for certain high-speed and low-power applications. This new method enables a nominal three-order-of-magnitude increase in either imaging speed or sensitivity (or a balance of each), thus overcoming the sensitivity limitations inherent in TD-OCT [102]. Another implementation of Fourier-domain OCT is based on the use of a wavelength swept source and a single element detector, easing requirements on data throughput and optical alignment compared to those of spectrometer CCDs [103]. Swept-source OCT can also be performed with full-field illumination to acquire an entire three-dimensional OCT image during each sweep [104].

OCT is very attractive for medical diagnostics because it provides images of tissue structure at the micrometer scale in situ and in real time with a resolution that is at least one order of magnitude higher than that of conventional ultrasound. OCT functions as a type of optical biopsy, and unlike conventional histopathology, does not require removal of tissue specimens for microscopic examination. It has shown great promise in disease diagnosis, including various cancers [94–100]. However, OCT in its basic form suffers from low contrast between neoplastic and normal tissue and is unable to image early biomolecular changes associated with carcinogenesis. This severely limits its clinical value. To address this shortcoming, there has been much interest in developing mechanisms for endogenous molecular imaging (without adding contrast agents) and molecular contrast imaging (using contrast agents) with OCT, as it would significantly extend its diagnostic capabilities. The ability to directly contrast biomolecules endogenous to the tissue would be very powerful.

Various OCT modalities are being developed to exploit endogenous contrast mechanisms. Spectroscopic OCT has been used to image tissue absorption from endogenous chromophores such as melanin [81], to analyze wavelength-dependent scattering [105–108], or to size cellular nuclei, which is of interest because nuclear enlargement in epithelial cells is associated with cancer [109]. Polarization-sensitive OCT is used to measure phase retardation in birefringent tissue which has application in retinal imaging [110], burn-depth determination [111], atherosclerosis imaging [112], muscular dystrophy [113], and detection of basal cell carcinomas [114]. Pump–probe OCT [115,116] and nonlinear interferometric vibrational imaging [117] are also promising methods to sense endogenous biomolecules based on their nonlinear optical susceptibilities. Although these endogenous methods are attractive as they do not require the addition of exogenous agents for contrast, they may be limited in scope because many diagnostic markers do not exhibit a detectible optical signal.

The introduction of exogenous contrast agents targeted to biomolecules in tissue has the potential to substantially increase the versatility of molecular OCT, analogous to histological stains in optical microscopy [118]. The first type of OCT contrast agents studied were based on protein microbubbles [119] and microspheres [120], which provide high optical scattering (positive contrast) in OCT images. Given the large size of these agents, they are appropriate for intravascular targeting, and may be designed to carry therapeutic payloads. Near-infrared (NIR) dyes with their absorption band tuned to one side of the OCT light source spectrum can be contrasted using spectroscopic OCT to sense the associated reduction in the optical scattering signal [121,122]. A dye of particular interest is indocyanine green, which has been FDA approved for human use in other applications. However, the utility of absorbing dyes is currently limited by the relatively high concentration (typically micromolars) necessary to provide OCT contrast enhancement in tissue.

In comparison to the foregoing approaches, nanotechnology-based contrast agents for OCT may provide greater optical cross sections with nanoscale dimensions to enhance their pharmacokinetics [123]. Nanoparticle OCT contrast agents that have low cytotoxicity for biomedical applications fall into two main categories: plasmon-resonant gold and magnetic iron oxides. We note that the safety of any of the nanoparticles discussed below remain to be proven, and may be highly dependent on the surface coating and surface electrical charge.

Gold nanoparticles exhibit optical resonances due to surface plasmon waves (called *surface plasmon resonance*); these resonances may be tuned to the near-infrared (NIR) wavelengths used for OCT imaging by appropriate shaping of the nanoparticles. Many of the properties and applications of plasmon-resonant nanoparticles were detailed earlier in the chapter; here we review how they have been used as OCT contrast agents. Several geometries of NIR-resonant gold nanoparticles have been investigated for OCT contrast. For gold nanoshells, the relative thicknesses of the gold layer to silica core determine the resonance wavelength, and the overall nanoshell diameter determines whether it will predominantly absorb or scatter light at the resonance, resulting in negative or positive OCT contrast, respectively [124]. In one study, nanoshells of 291-nm core and 25-nm shell thickness provided the highest backscattering for positive OCT contrast at 1310-nm wavelength [125]. Multifunctional imaging and therapeutic nanoshells of 119-nm core and 12-nm shell were shown to collect within mouse tumors via the EPR (enhanced permeation and retention) effect; nanoshell-contrasted OCT images of the tumors was consistent with subsequent histology, and concomitant photothermal treatment resulted in increased survival [126]. Smaller in comparison, gold nanocages are hollowed-out cube structures nominally 30 nm on a side which have been tuned to absorb near 800 nm for negative OCT contrast [127,128]. Gold nanorods may be generated over a large range of sizes (tens to hundreds of nanometers), and exhibit longitudinal plasmon resonances that are tuned by adjusting the aspect (length/width) ratio of the rod. Aspect ratios larger than about 3 shift these resonances into the NIR, where they have been used for positive or negative OCT contrast, depending on their size [129,130]. While plasmon-resonant nanoparticles may be engineered with specific optical properties, it is not clear which properties will provide the best contrast against a tissue optical background.

While one analysis of contrasted OCT signals indicated the used of highly scattering agents [125], another analysis and experiments in tissue phantoms suggested the use of absorbing agents while using a backscattering albedo metric; this method is based on the premise that the small intrinsic absorption of tissue is easier to contrast than the relatively large intrinsic scattering of tissue [129]. Another consideration is that optically scattering plasmon-resonant particles in general need to be of dimensions >100 nm, in comparison to absorbing nanoparticles nominally <50 nm. Thus, absorbing nanoparticles may be desired in applications where particle pharmacokinetics are affected adversely by larger particle sizes. Also, as mentioned above, absorbing nanoparticles can be used concomitantly for selective heating of cancer cells (hyperthermic therapy) using higher-powered light sources than are used for nondestructive imaging [131,132].

Spectroscopic OCT has also been employed with nanocages and nanorods because it can sense a plasmon resonance peak if it is sharper than the OCT imaging band (see Figure 16.11) [127,129]. If the spectroscopic variability of the native tissue is relatively low, spectroscopic OCT may also increase the contrast sensitivity and predicates the use of nanoparticles with high-quality factor resonances.

Another promising method for OCT contrast is to exploit the photothermal properties of absorbing gold nanoparticles; because the tissue refractive index is temperature dependent, there is a temperature-dependent optical path change that

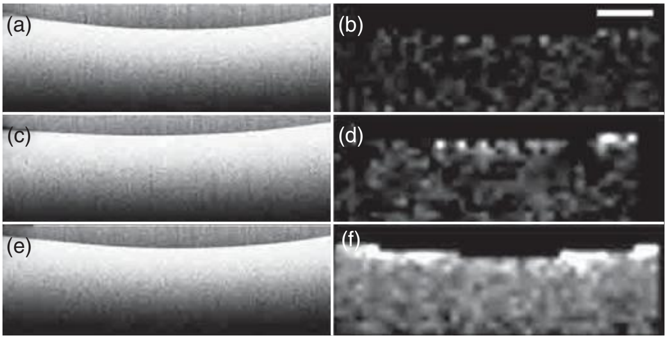

**FIGURE 16.11** OCT images of tissue phantoms with varying concentrations of plasmon-resonant nanorods, as described in [115,119]. Left and right columns are the structural OCT and their associated spectroscopically contrasted nanorod OCT images, respectively. (a, b) control phantoms; (c, d) phantoms with nanorods added at a concentration of 7.2-cm$^{-1}$ peak attenuation; (e, f) phantoms with nanorods added at a concentration of 18-cm$^{-1}$ peak attenuation. Spectroscopic OCT allows for the differentiation of nanorod-dosed phantoms (right column) in comparison to the standard structural OCT image (left column).

can be sensed by phase-resolved OCT [132,133]. The particular advantage of this contrast method is that it can be modulated by using a different absorption band than the OCT imaging light, and can modulate the photothermal light source while imaging with OCT. The ability to modulate signals externally can greatly enhance sensitivity against the tissue background, as explored in more detail below.

Magnetomotive OCT is a method developed to contrast magnetic nanoparticles in OCT [27,83,134]. Of particular interest are magnetic iron oxides, as they are currently used as liver contrast agents in MR imaging [18,135] and have been molecularly targeted to cancer in an in vivo animal model [136]. They are typically composed of a maghemite ($\gamma$-$Fe_2O_3$) and/or magnetite ($Fe_3O_4$) core exhibiting a large magnetic susceptibility (ca. $10^5$ larger than that of tissue). An applied magnetic field gradient will pull on magnetic nanoparticles with a force proportional to their susceptibility, and the cells in contact with the magnetic nanoparticles will deform and displace in response to this force. Because the nanoparticles no not have a detectible optical signal, OCT senses the resulting deformation of the light-scattering cells in mechanical contact with the magnetic nanoparticles. OCT is particularly well suited for detecting these induced nanoscale (subwavelength) displacements via monitoring the optical phase of the interferogram [137]. Magnetomotive OCT is performed by employing a programmable electromagnet to apply a modulated magnetic field (typically, 10 to 1000 Hz) onto the tissue during OCT imaging [27]. The induced displacement of magnetic nanoparticles in the tissue gives rise to a modulated amplitude or phase signal that can be detected with high specificity against a highly dynamic tissue background [134–140], as shown in Figure 16.12.

The primary consideration for in vivo imaging using modulated techniques (including photothermal contrast) is that the modulation rate must be faster than the speckle decorrelation rate of the tissue arising from respiration, cardiac function, and Brownian motion [83,132]. In particular, magnetomotive OCT has been used to contrast individual macrophage cells in a tissue scaffold [27], image nanoparticles in an in vivo tadpole [83], monitor diffusion of nanoparticles into an ex vivo rat mammary tumor [134], monitor uptake of nanoparticles in liver [138], and monitor blood flow [139].

Magnetic nanoparticles may also be heated using radio-frequency electromagnetic fields to provide selective heating of cancer sites, called *hyperthermic therapy* [141]. Both plasmon-resonant and magnetic nanoparticles provide OCT contrast at nanomolar concentrations [129,134], which is highly promising toward molecular imaging, and specifically, the ability to target and image cell surface receptors. However, to date, OCT imaging of site-directed contrast agents have not yet been demonstrated in vivo, and future progress in both nanoparticle design and OCT imaging techniques is needed to achieve this goal.

### 16.3.3 Combined Imaging Modalities

Multiple modality imaging approaches are taken in many clinical situations to better differentiate tissue structures and enhance the diagnostic yield of the screening

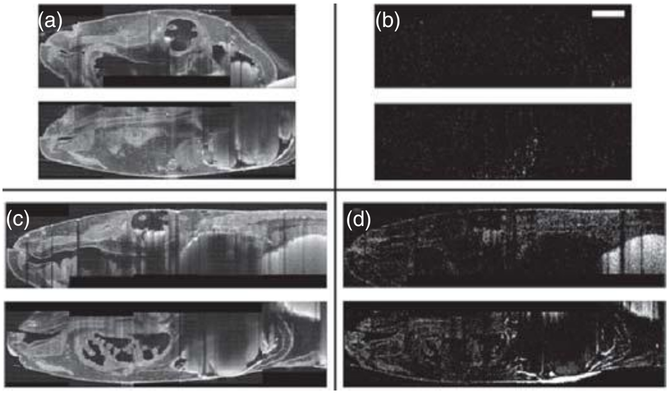

**FIGURE 16.12** OCT images of in vivo African frog tadpoles acquired dorsally and ventrally as described by Oh et al. [134]. Left and right columns are the structural OCT and their associated magnetomotive OCT images, respectively. (a, b) Control tadpole, showing background in the magnetomotive image due to motion of the beating heart; (c, d) tadpole exposed to magnetic nanoparticles overnight, showing contrast in the intestinal tract (ventral region) as well as excreted nanoparticles embedded in the mounting clay. Scale bar, 500 µm.

procedure. For example, MR imaging is frequently combined with fluorescence imaging or diffuse optical imaging [51,142]. Usually, these imaging technologies are combined within the same instrument [143–146]. Again, to enhance cancer specificity, various molecular markers are used in combination with these dual- or multiple-modality imaging approaches. For example, functionalized nanoparticles are used to enhance the contrast of MR and fluorescence imaging simultaneously. Here we discuss two representative examples of enhanced-contrast dual-modality imaging: combined MR–fluorescence imaging and combined fluorescence–OCT imaging.

***Fluorescence–MR Imaging*** Magnetic resonance imaging (MRI) and optical techniques are highly complementary imaging methods. Combining these techniques would therefore have significant advantages in clinical medicine. Highly engineered contrast agents can be fabricated to enhance imaging resolution for multiple imaging modalities simultaneously. In the field of MR imaging, for example, and especially in the emerging field of cellular and molecular MR imaging, flexible strategies to synthesize contrast agents that can be manipulated in terms of size and composition and that can be easily conjugated with targeting ligands are being developed. These agents can also be engineered to provide contrast enhancement for fluorescence imaging. Many research groups are developing such contrast agents that are suitable for multimodal imaging. As an example, Tréhin et al. [146] have developed a multimodal nanoparticle CLIO-Cy5.5, which is detectable by both magnetic resonance imaging and fluorescence, to assist in intraoperatively visualizing tumor boundaries. These nanoparticles allow for preoperative MRI contrast enhancement and intraoperative fluorescence contrast enhancement. To demonstrate this dual capability, they performed both MR and fluorescence imaging measurements. They examined the accuracy of tumor margin determination of orthotopic tumors implanted in hosts with differing immune responses to the tumor. The true tumor margin determined by GFP tumor fluorescence was compared against the tumor margin indicated by Cy5.5 fluorescence. To resolve which cells internalized the nanoparticle and to quantitate degree of uptake, tumors were disaggregated and cells were analyzed by flow cytometry and fluorescence microscopy (see Figure 16.13). It can be observed that the Cy5.5 loaded nanoparticles slightly overestimate the brain tumor, due to nanoparticle localization around the tumor inside microglia/macrophages. However, the overall tumor localization was very good.

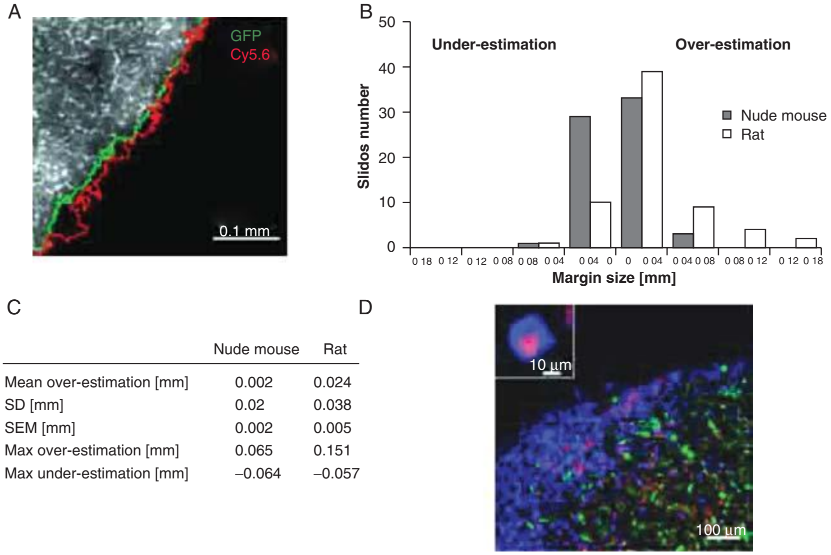

| | Nude mouse | Rat |
|---|---|---|
| Mean over-estimation [mm] | 0.002 | 0.024 |
| SD [mm] | 0.02 | 0.038 |
| SEM [mm] | 0.002 | 0.005 |
| Max over-estimation [mm] | 0.065 | 0.151 |
| Max under-estimation [mm] | –0.064 | –0.057 |

**FIGURE 16.13** Tumor border determination using CLIO-Cy5.5. (A) Tumor border determined using signal intensity measurements. The border was determined using GFP fluorescence (green boundary) and CLIO-Cy5.5 fluorescence (red boundary). GFP fluorescence is shown in gray. (B) Accuracy of tumor border by CLIO-Cy5.5 fluorescence. The Cy5.5 border extension beyond the GFP border is defined as overestimation; the reverse is defined as underestimation. The majority of measurements between the two borders were close to zero for both rat and nude mouse models. (C) Accuracy of border determination by CLIO-Cy5.5 fluorescence. The standard deviation (SD), standard error of the mean (SEM), maximum overestimation, and maximum underestimation are given. (D) Etiology of slight differences in margin determination between models. Fluorescent microscopy micrograph of a 20-µm-thick brain slice labeled with anti-CD11b antibody for microglia/macrophage staining (blue); tumor cells are in green, CLIO-Cy5.5 is in red, and normal brain is in black. Inset: Accumulation of CLIO-Cy5.5 inside $CD11b^+$ cells (microglia/macrophages). (From [146], with permission.)

Beside magnetic nanoparticles, lipid-based nanoparticles, such as liposomes or micelles, are also being used extensively in recent decades as drug carrier vehicles. A relatively new and promising application of lipidic nanoparticles is their use as multimodal MR contrast agents [147]. MR-detectable and fluorescent amphiphilic molecules can easily be incorporated in lipidic nanoparticles. Furthermore, targeting ligands can be conjugated to lipidic particles by incorporating lipids with a functional moiety to allow a specific interaction with molecular markers and to achieve accumulation of the particles at disease sites.

The development of various nanoparticulate contrast agents is a rapidly growing area of research that seems to provide an increasing contribution to the field of diagnostic and molecular imaging. Such agents provide several advantages over traditional compounds. First, they may contain a high payload of the contrast-generating material, which greatly improves their detectability. Second, multiple properties may easily be integrated within one nanoparticle to allow its detection with several imaging techniques or to include therapeutic qualities. Finally, the surface of such nanoparticles may be modified to improve circulation half-lives or to attach targeting groups.

***OCT/Laser-Induced Fluorescence Imaging*** Optical coherence tomography (OCT) and laser-induced fluorescence (LIF) are promising modalities for tissue characterization in human patients and animal models [148]. OCT detects coherently backscattered light, whereas LIF detects fluorescence emission of endogenous biochemicals such as reduced nicotinamide adenine dinucleotide (NADH), flavin adenine dinucleotide (FAD), collagen, and fluorescent proteins, or exogenous substances such as cyanine dyes. Given the complementary mechanisms of contrast for OCT and LIF, the combination of the two modalities could potentially provide more sensitive and specific detection of disease than can either modality alone.

Although OCT offers a tremendous potential as a diagnostic tool for detection and characterization of epithelial cancer, it is associated with a limited field of view, on the order of millimeters, and thus scanning of large organs is not very practical because it involves the time-consuming analysis of very large data sets. The use of a guidance tool such as fluorescence imaging can more efficiently highlight the presence of suspicious lesions and perform OCT imaging only on those lesions as a confirmatory tool. Dual-modality probes for both OCT and LIF can be implemented using small-diameter optical fibers, suggesting a particular synergy for endoscopic applications. However, although endogenous and exogenous fluorescence have shown to be relatively sensitive to cancer, fluorescence specificity is still limited when no targeting contrast agents are used [149]. Also, it provides poor delineation of tumor margins. Fluorescence imaging provides enhanced sensitivity and specificity for cancer when tissues are labeled with tumor-specific fluorescence agents [150]. Therefore, a combined OCT–fluorescence imaging technique in conjunction with tumor-targeted delivery of contrast agents seems to be a more attractive approach for large organ cancer screening [151].

While contrast-enhancement methods for either one of these two imaging modalities have been used before [59,72,92], simultaneous contrast enhancement with a single contrast agent has not yet been demonstrated. Recently, Physical Sciences in Andover, Massachusetts, in collaboration with Northeastern University's School of Pharmacy, has developed a technology that can provide contrast enhancement for both fluorescence and OCT imaging. This technology is based on the use of polycaprolactone (PCL) microparticles coated with gold nanospheres and labeled with an RGD cypate conjugated peptide. The RGD peptide recognizes the $\alpha_v\beta_3$ integrin receptor (ABIR), which is overexpressed by epithelial cancer cells. The RGD cypate was provided by Achilefu's group at the Washington University School of Medicine in St. Louis, Missouri [152]. The cypate dye enhances the fluorescence imaging contrast, while the highly scattering PCL microparticles provide OCT contrast enhancement. Enhanced-contrast fluorescence imaging serves better for OCT guidance, while enhanced-contrast OCT imaging allows for better differentiation of various cancer lesions and thus serves for biopsy guidance. This approach also provides the net advantage of enhancing the capabilities of both imaging techniques while minimizing the quantity of the drug administered and therefore the overall toxicity effects. Initially, the PCL microparticles were coated with gold nanoparticles (AuNPs) with a diameter of 10 to 20 nm (see Figure 16.14), which were attached on the thiol groups of the surface-modified gelatin micropheres. However, gold nanorods or nanoshells can be used to enhance the absorption cross section of the microparticles and make them suitable for targeted therapy. The functionalized AuNP-coated PCL microparticles can be fabricated in various sizes and either applied topically or delivered intravenously.

The size of the microparticles was optimized to provide enhanced scattering at 1310 nm, which is one of the typical wavelengths for OCT imaging. Particles with a mean size of about 1.5 to 2.0 μm provided the best scattering performance at 1300-nm illumination. These microparticles also have a very high absorption cross section at slightly lower wavelengths (600 to 900 nm), which make them very attractive for therapy.

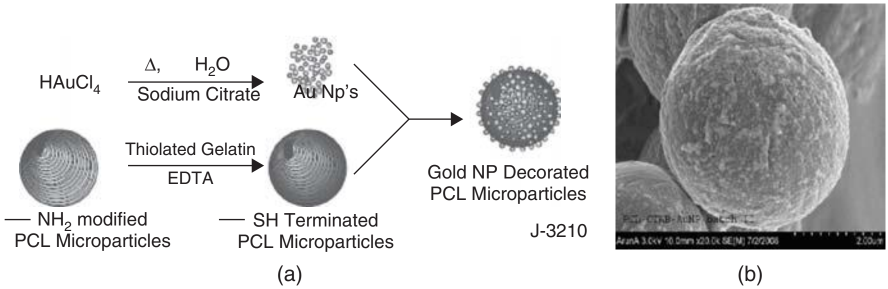
HAuCl$_4$
Δ, H$_2$O
Sodium Citrate
Au Np's
Thiolated Gelatin
EDTA
Gold NP Decorated PCL Microparticles
NH$_2$ modified PCL Microparticles
SH Terminated PCL Microparticles
J-3210

(a) (b)

**FIGURE 16.14** (a) AuNP-coated PCL microparticles fabrication process; (b) ESM photograph of the microparticles.

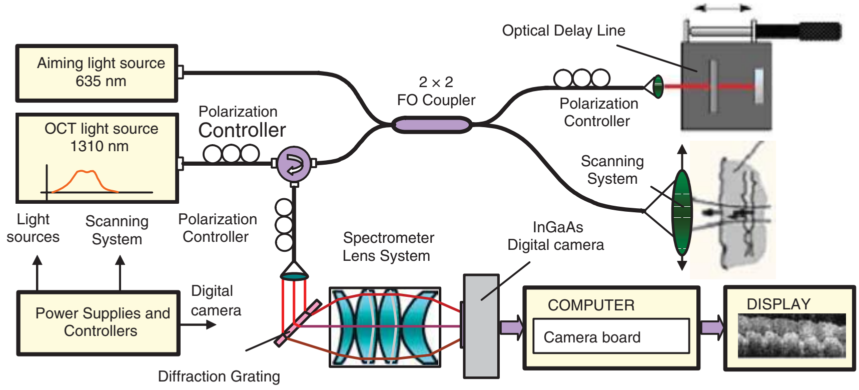
Optical Delay Line
Aiming light source
635 nm
2 × 2
FO Coupler
Polarization
Controller
Polarization
Controller
OCT light source
1310 nm
Scanning
System
Light
sources
Scanning
System
Polarization
Controller
Spectrometer
Lens System
InGaAs
Digital camera
Digital
camera
Power Supplies and
Controllers
COMPUTER
Camera board
DISPLAY
Diffraction Grating

**FIGURE 16.15** SD-OCT system.

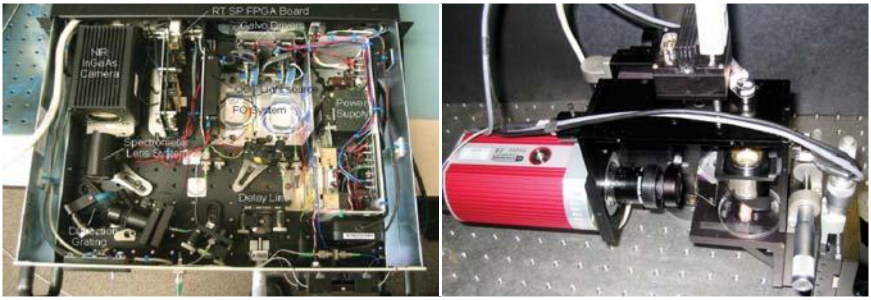
RT SP FPGA Board
Galvo Drivers
NIR
InGaAs
Camera
OCT Light Source
FO System
Power
Supply
Spectrometer
Lens System
Delay Line
Diffraction
Grating

(a) (b)

**FIGURE 16.16** (a) SD-OCT system; (b) OCT/laser-induced fluorescence imaging probe.

A dual-modality fluorescence–OCT imaging instrument was used to ex vivo test the efficacy of the microparticles for both OCT and fluorescence imaging contrast enhancement. A schematic of the OCT system is shown in Figure 16.15, while photographs of the OCT instrumentation box and combined OCT–fluorescence imaging probe are shown in Figure 16.16. The OCT system, based on the spectral domain approach, uses a light source with a central wavelength of 1312 nm and a bandwidth of about 100 nm, which provides an axial resolution of about 8 μm (in air). A high-speed InGaAs (Sensors Unlimited) and a custom digital signal processing board make possible a 40-frame/s imaging rate.

The OCT/laser-induced fluorescence imaging probe uses a laser diode (785 nm/50 mW) to excite NIR cypate dye from nanoparticles. An NIR enhanced-response camera (Rolera XR, QImaging) is used for fluorescence imaging. The benchtop imaging probe can collect large OCT raster images (10 × 10 mm) and fluorescence images over an area of 25 × 25 mm.

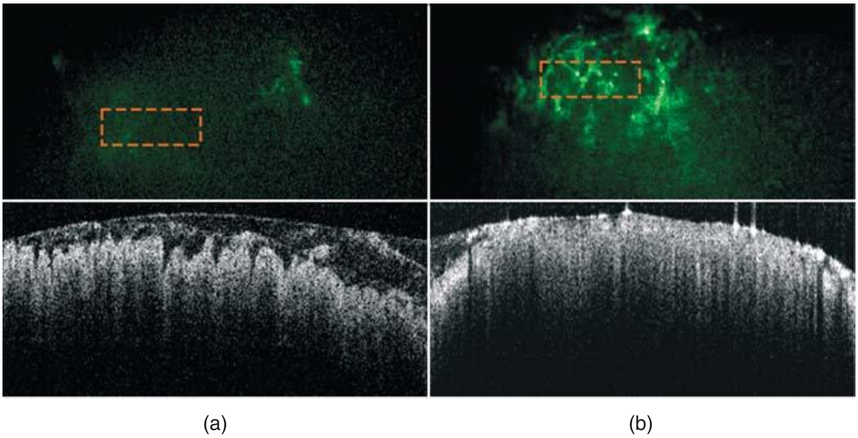

**FIGURE 16.17** Fluorescence–OCT imaging of human colon tissue: (a) normal colon; (b) cancerous colon tissue. The red rectangles in the floorescence images indicate the OCT imaging areas. OCT scale bar, 500 μm.

Preliminary testing on human colon tissue samples of the dual-modality enhanced-contrast imaging approach has shown promising results [151]. Both normal and cancer colon samples were used. A microparticle solution ($10^{10}$ microparticles per 500 μL of phosphate buffer solution or PBS) was topically applied on the colon tissue and left to incubate for 1 hour. After incubation, the colon sample was washed three to five times with saline solution. OCT and fluorescence images were taken before and after incubation on both normal and carcinogenic tissue samples. The OCT image showed increased scattering of the cancer sample after particle incubation, while the fluorescence image showed increased fluorescence only on the cancer sample (see Figure 16.17). This demonstrates the preferential binding of the microparticles to the cancer sample.

The enhanced-contrast dual-modality imaging approach seems to be very promising for better differentiation of tissue structures and might help to provide diagnostic yield enhancement during cancer screening procedures. However, in vivo testing of this approach will require further progress on both nanoparticle design and development of a suitable OCT/fluorescence imaging probe.

## 16.4 NANOTECHNOLOGY-BASED DRUG DELIVERY SYSTEMS FOR DISEASE-TARGETED THERAPY AND TISSUE REGENERATION

The merger between pharmaceutical science and nanotechnology is continually expanding and has undoubtedly led to the development of many intersecting subdisciplines, such as nanomedicine. In recent years, nanomedicine has emerged at the forefront of trends in medicine and therapeutics. Nanomedicine is holding ground with the development of drug delivery, medical, and diagnostic

**TABLE 16.1 PubMed Search**[a]

| Search Term | Number of Hits |
|---|---|
| Drug delivery system | 65,398 |
| Nanotechnology | 14,279 |
| Nanotechnology drug delivery system | 1,220 |
| Nanomedicine | 828 |
| Nanocarrier | 96 |
| Nanoparticle | 20,886 |

[a] Search conducted on December 19, 2008.

applications. Nanomaterials are being perfected to improve biological and subsurface imaging, as biological sensors for the detection of pathogens and mutations, as tools for tissue engineering and nanosurgery, as probes for molecular structure, and as agents of drug and gene delivery [153,154].

As indicated in Table 16.1, a survey of the literature reveals the tremendous interest in and the great diversity of nanotechnology-based drug delivery systems. These systems range from simple homogeneous nanocarriers to complex core–shell organic/inorganic hybrid nanoparticles.

The clinical promise of nanocarriers is verified by the success of currently approved formulations such as Doxil. Doxil was approved by the FDA in 1995; the formulation consists of doxorubicin encapsulated in PEG-modified liposomes. Doxorubicin is a common chemotherapeutic agent that prevents DNA replication by intercalating between base pairs and by inhibiting topoisomerase II. Doxil reduces the required dose of doxorubicin and the residual side effects such as cardiotoxicity [155]. More recently developed nanotechnology-based drug delivery systems include Abraxane (approved in 2005), which consists of albumin-bound paclitaxel particles (paclitaxel hyperstabilizes microtubules, preventing cell division and is also a common chemotherapeutic agent). Nanotechnology-based drug delivery systems will undoubtedly continue to evolve from the laboratory to the clinic, expanding the discipline of nanomedicine.

### 16.4.1 Fundamental Requirements for Drug Delivery Systems

As many existing pharmaceutics are less than ideal with respect to parameters such as toxicity and therapeutic index, there is a recognized need to improve these pharmacological features through the design of effective drug delivery systems. The fundamental intent of drug delivery systems is to improve the therapeutic index (ratio of lethal dose to minimum effective dose) of biologically active agents [155]. The inherent properties of nanotechnology-based drug delivery systems make them ideal platforms for achieving this basic aim of drug delivery. As mentioned previously, the small size of nanocarriers permits cell uptake and subcellular interactions. The shape of a nanocarrier is a second important characteristic. The shape of a nanocarrier contributes to the fate of a nanocarrier and can dictate cellular uptake kinetics of the formulation. For example, a recent study conducted by J. M. DeSimone and fellow researchers revealed that high-aspect-ratio (150 nm diameter, 450 nm height) rod-shaped nanoparticles are internalized more rapidly and to a greater extent than are comparable formulations with alternative shapes and lower aspect ratios [156]. Another significant property of nanotechnology-based drug delivery systems is their very large surface area/volume ratio [157–160]. This large ratio increases frictional forces and enables nanoparticles to be held in colloidal suspension [157–160]. This property also confers high loading capability and a large surface area for modification and multifunctionalization. The size, shape, and the area/volume ratio are three physical properties of nanocarriers. As indicated in Table 16.2, there are physical, design, and functional parameters that define a nanocarrier system.

Although there are a multitude of different nanotechnology-based drug delivery system designs, nanocarriers share three basic design requirements: core platform material, a therapeutic agent, and surface properties. The core material can be inorganic, organic, or a hybrid combination. Inorganic-based systems include gold, silver, iron, and silica nanoparticles as well as quantum dots. Organic-based systems include liposomes, nanoemulsions, fullerenes, carbon nanotubes, dendrimers, micelles, and polymeric nanocarriers. Depending on the fundamental design of the system, the selection of platform materials, and the properties of the biologically active agent, the agent can be encapsulated [as in paclitaxel loaded poly(lactic-*co*-glycolic acid) nanoparticles], adsorbed onto the core material (such as anionic siRNA interacting with cationic liposomes), or chemically attached to the platform material and further entrapped or associated with the particle surface [155]. The size, lipophilicity, charge, and the innate properties of the therapeutic agent selected largely dictate the type of interaction that will occur with the

**TABLE 16.2 Defining Parameters of Nanocarriers**

| Physical Parameters | Design Parameters | Functional Parameters |
|---|---|---|
| Size | Core platform material | Essential<br>High loading efficiency<br>Avoiding RES clearance<br>Biocompatible materials |
| Shape | Biologically active agent | Overcoming biological barriers<br>Low off-target effects (low toxicity)<br>Appreciable drug release at target site (therapeutic effect) |
| Surface area/volume ratio | Surface properties | Nonessential<br>Active targeting<br>Multifunctional/dual-acting |

platform material. The third design parameter that defines a nanocarrier system are the surface properties, including charge, modification density, and type of modification (e.g., PEGylation or targeting ligands). Surface properties can have dramatic effects. For example, it is well established that for the majority of cell types, cationic nanocarriers have better uptake kinetics than those of anionic and neutral carriers, as most cell membranes have an excessive negative charge (ca. 70 mV) [156]. The utility of this effect is evident when evaluating the plethora of cationic lipids and cationic polymers that have emerged and have been used in nanocarrier formulations.

The functional parameters that define a nanocarrier system are compound parameters that are determined by the physical and design specifications. There are essential and nonessential functional parameters. A high loading efficiency is required for the nanocarrier to improve the therapeutic index of a compound in comparison to the free drug in solution. A nanocarrier formulation with a low loading efficiency may require a high dose to elicit a therapeutic response, which could lead to increased residual toxicity. A second essential functional parameter of nanocarriers is the ability of the system to overcome biological barriers. There are barriers to drug delivery at every level of biological organization (the biological levels being organism, organ system, organ, tissue, cell, organelle, molecular assemblies, macromolecules, and small molecules). The organism level of organization may be considered a biological barrier that is overcome by the route of administration. For the delivery system to reach its target cell population, it must escape recognition by the immune system and maintain circulating blood concentrations high enough and long enough for the system to transverse the organ system, organ, and tissue levels of organization. Once at the site of the target cell population, the system must penetrate the cell membrane (molecular assembly) to reach a subcellular target such as an organelle (e.g., nucleus) or macromolecule target (e.g., a protein or enzyme). The system may need to further penetrate an organelle membrane (such as the nuclear envelope) to reach the macromolecular or small-molecule target (e.g., nucleotides). Once inside the cell, endosomal escape is perhaps the most challenging barrier for a therapeutic to overcome. The ability of a nanocarrier to overcome these biological barriers is essential for the system to have a therapeutic effect [161].

An additional essential functional parameter of nanocarriers is the ability to avoid eliciting an immune response and subsequent clearance by the reticuloendothelial system (RES) [162]. The RES consists of immune-responsive phagocytotic cells (macrophages and monocytes in the spleen, lungs, and lymph nodes; Kupffer cells in the liver). A well-established approach to decreasing RES clearance and increasing circulating plasma concentration and residence time of the nanocarrier is to modify the surface of the nanocarrier with poly(ethylene glycol) (PEG) chains [163]. Depending on the platform material and design schema of the formulation, PEG can be integrated with the platform material during nanoparticle synthesis, adsorbed to the nanocarrier surface, or attached covalently [163]. The molecular weight (MW) of the PEG required to suppress protein adsorption, again, depends on the formulation design schema but generally requires a minimum MW of 2000 [163]. The term *PEGylation* has been coined to refer to this common surface modification technique. For a nanocarrier to be effective, it must avoid eliciting an appreciable immune response and avoid being cleared by the RES system.

A fourth functional parameter that must be considered in formulating nanocarriers is the use of biocompatible materials [164,165]. This is both a design parameter (when considering the core platform material) and a functional parameter (when considering subsequent modifications and the synergy of coadministrating multiple chemical entities). It is important to use platform and modification materials that are FDA approved or are GRAS (generally regarded as safe). Not doing so can increase the clinical translation time and cost. For example, quantum dots are composed of a highly toxic core material such as cadmium selenide surrounded by a more inert substance such as zinc sulfide; when considered for clinical applications it is likely that quantum dots would be considered for applications only in nonresponsive, end-stage diseases, due to the cost–benefit analysis of therapeutic benefit versus toxic burden [166]. An important consideration in regard to biocompatibility is how chemical modification, physical modification, or coadministration with various other entities can affect biocompatibility. For example, conjugating a peptide to a biocompatible polymer may decrease the degradation of the polymer. Similarly, coadministration of two biologically active agents may significantly alter the pharmacokinetic and pharmacodynamic behavior of an agent. For example, administering the P-glycoprotein (P-gp) substrate paclitaxel alone will have a dramatically different effect than if it is coadministered with verapamil, a P-gp inhibitor; coadministration of verapamil with paclitaxel will increase the cellular retention and hence the cellular toxicity of paclitaxel [167]. Additional safety concerns surround biologics such as recombinant proteins and viral vectors [168]. Innate properties, biological source/propagation, postmodification, and combined administration are important considerations in selecting biocompatible materials.

An essential requirement for nanocarriers to achieve is low toxicity. The nanocarrier must not have a higher preference for an off-target cell type. Like most parameters, the toxicity of a nanocarrier formulation is subjected to cost–benefit analysis—the clinical application of the system must be justifiable. This is a return to the primary objective of drug delivery systems: to improve the therapeutic index of an agent. Toxicity can also be regarded as a compound trait that results from the collective interactions of the physical, design, and functional characteristics of the system. As such, avoiding RES clearance through PEGylation can greatly reduce the hepatotoxicity of a therapeutic [163]. It is important to optimize all functional parameters to achieve the lowest residual toxicity for a particular formulation. The parameter with the most compound character is undoubtedly the therapeutic effect. As demonstrated in Figure 16.18, the therapeutic effect is a composite characteristic that is determined by the other essential functional parameters and can be enhanced by the nonessential parameters.

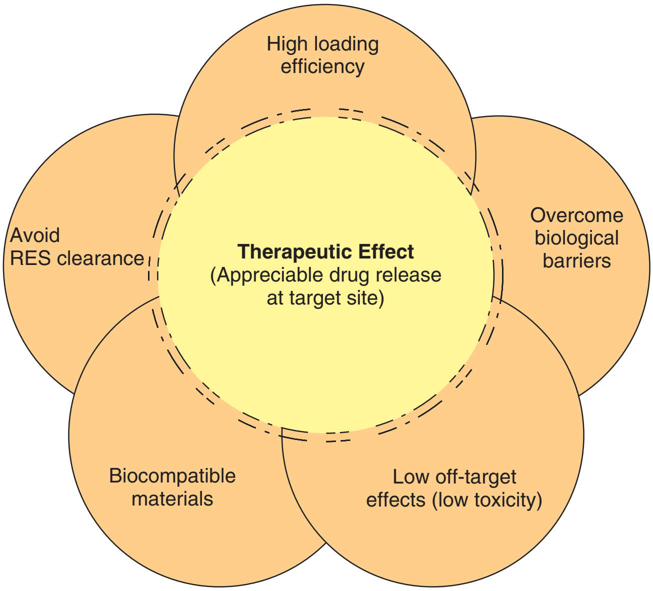
High loading efficiency
Avoid RES clearance
Therapeutic Effect
(Appreciable drug release at target site)
Overcome biological barriers
Biocompatible materials
Low off-target effects (low toxicity)

**FIGURE 16.18** Essential functional requirements for drug delivery systems.

As illustrated, the therapeutic effect is a composite trait that results from the synergy of the five other parameters. For example, a formulation that has high cellular uptake by facilitated or active transport (overcome biological barrier) maintains high plasma concentrations, due to PEGylation (avoids RES clearance), and contains a therapeutically relevant dose (high loading efficiency) could have a high therapeutic effect due to this combination of traits. This effect could be enhanced further by modifying the surface of the formulation with a disease-specific targeting ligand or by adding a co-therapeutic that increases the cellular retention of the primary agent (nonessential active targeting and multifunctionalization).

Developing the nonessential functional parameters of a nanocarrier system can greatly increase the therapeutic potential of the system. Active targeting (detailed in the next section) can help a system to overcome biological barriers (active transport verses nonspecific endocytosis), decrease the residual toxicity of a system, and increase the therapeutic effect [169]. The potential to multifunctionalize nanocarriers is a clear benefit of the pharmaceutical science/nanotechnology intersection, which holds great clinical promise and has the potential to revolutionize traditional medicine. As illustrated in Figure 16.19, multifunctionalization expands the capability of a nanocarrier system where PEGylation, active targeting, multiple therapeutics, and imaging modalities can be combined [164]. Various multifunctional formulations are discussed in subsequent sections. As there is great variability in the selection of materials and tailored parameters, there are innumerable possible combinations and strategies for multifunctionalization.

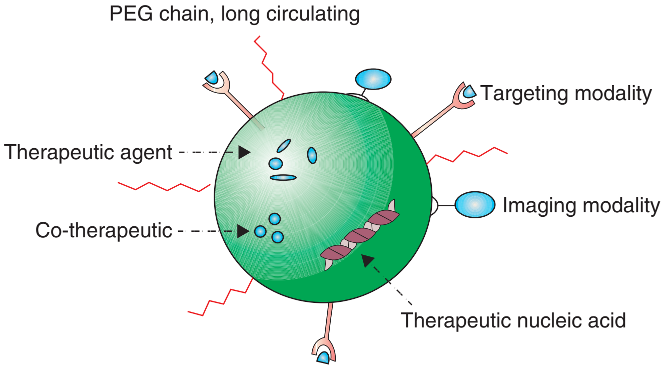

**FIGURE 16.19** Multifunctional potential of nanocarriers. (From [164], with permission.)

Although there are a plethora of therapeutic agents, targeting moieties, and imaging agents, there are some guiding parameters for selecting ideal combinations of therapeutic agents. For example, multifunctional nanocarriers that are loaded with two therapeutic agents designed to treat cancer are often evaluated by the same process as standard combination chemotherapy, through use of the combination index [170,171]. The combination index is equal to the concentration of drug A required to achieve 50% cell kill efficiency when used in combination with drug B divided by the $IC_{50}$ of drug A when used alone, plus the concentration of drug B required to achieve 50% cell kill efficiency when used in combination with drug A divided by the $IC_{50}$ of drug B when used alone [170,171].

$$\begin{aligned}\text{combination index} &= \frac{\begin{array}{c}IC_{50}\text{ concentration of drug A}\\ \text{when administered with drug B}\end{array}}{IC_{50}\text{ of drug A alone}}\\ &\quad+\frac{\begin{array}{c}IC_{50}\text{ concentration of drug B}\\ \text{when administered with drug A}\end{array}}{IC_{50}\text{ of drug B alone}}\end{aligned} \tag{16.1}$$

A combination index value of less than 1 is indicative of a synergistic combination, a value equal to 1 represents an additive combination, and a value of more than 1 indicates antagonism [170,171]. Using the combination index to assess the relationship of combination therapy can be helpful in optimizing the design parameters of the formulation (drug selection).

### 16.4.2 Disease-Targeted Therapy

The mechanisms of targeting nanocarriers to a particular disease are generally categorized as either active or passive targeting strategies [169]. Passive targeting strategies include general administration that leads to nonlocalized systemic availability and the local application of an agent, such as intratumor injection [169]. Passively targeting cancer by a general route of administration that leads to nonlocalized systemic availability also takes advantage of the microenvironment of the tumor. For example, nanocarriers that passively target cancer exploit the enhanced permeability and retention (EPR) effect [169,172]. The EPR effect in tumors is the result of abnormal (more discontinuous) vasculature, angiogenesis and excessive vasculature density, increased permeability from an overproduction of factors such as VEGF/VPF and MMPs (vascular endothelial growth factor/vascular permeability factor, matrix metalloproteinase), and deficient lymphatic/RES drainage [20]. This combination leads to a higher accumulation of therapeutics in the tumor tissue relative to normal tissue (due to the "leaky" tumor vasculature) [169,172]. It also leads to increased retention in the tumor tissue, due to poor lymphatic drainage [34,169,172]. Conversely, active targeting involves the use of disease-specific targeting ligands such as antibodies (antigen targeting), lectins (carbohydrate targeting), and peptides (receptor targeting) [169]. This strategy exploits the phenotypic changes that characterize a particular disease. Many disease cells will overexpress certain factors and receptors to increase survival and maintain homeostasis [173]. Overexpression of these receptors leads to membrane clustering; for example, certain types of cancer such as ovarian cancer have been shown to overexpress the EGFR receptor [173,174]. Overexpression of EGFR leads to a higher number of EGFR receptors and increased receptor density (clustering) in the cell membrane, which potentiates the effects of EGF [173,174]. As such, surface modification of nanocarriers with an EGFR-specific peptide or antibody are successful strategies for targeting these types of cancer. For example, gelatin nanoparticles loaded with reporter plasmid DNA [encoding enhanced green fluorescent protein (eGFP)] and surface-modified with an EGFR targeting peptide have been shown to increase the transfection efficiency of the system relative to nontargeted nanoparticles in pancreatic cancer cells that overexpress EGFR (Panc-1) [175].

A common targeting approach is to selectively conjugate the Fab′ fragments (antigen binding regions) of a monoclonal antibody to the surface of a nanocarrier. One such system that was recently developed used the Fab′ fragments of a humanized anti-HER2 monoclonal antibody [176]. HER2, like EGFR, is a member of the ErbB family of tyrosine kinase receptors. The researchers covalently linked the Fab′ fragments to the surface of NHS-activated PLGA nanoparticles loaded with PE38KDEL, a protein toxin [176]. Cytotoxicity studies and cell trafficking using FITC-labeled nanoparticles demonstrated higher cell kill and internalization relative to a nontargeted formulation and free drug in HER2-overexpressing breast cancer cells (BT-474 and MDA-MB-231) [176]. This increased efficacy was not evident in HER2-negative MCF-7 cells [24]. The $IC_{50}$ values for HER2-targeted PLGA nanoparticles loaded with PE38KDEL was 46 pM for BT-474 cells, 265 pM for MDA-MB-231 cells, and over 1000 pM for MCF-7 cells, while the $IC_{50}$ value for the nontargeted drug-loaded nanoparticles alone and for the free drug alone was over 1000 pM for all three cell lines [176]. The in vivo data supported the in vitro results. At a dose of 0.9 mg/kg, the HER2-targeted drug-loaded nanoparticles decreased tumor volume more rapidly and more dramatically in BALB/c nude mice with BT-474 breast cancer xenografts than in controls and nontargeted drug-loaded nanoparticles [176]. The mean tumor volume (eight mice each) after treatment with HER2-targeted drug-loaded nanoparticles was 13 $\mathrm{mm}^3$, 598 $\mathrm{mm}^3$ for PBS-treated mice, 579 $\mathrm{mm}^3$ for PE38KDEL-treated mice, 536 $\mathrm{mm}^3$ for mice treated with nontargeted drug-loaded nanoparticles combined with anti-HER2 Fab′ solution, and 529 $\mathrm{mm}^3$ for drug-loaded nanoparticles conjugated with anti-CD25 [176]. The HER2-targeted drug-loaded nanoparticles also had reduced nonspecific hepatotoxicity compared to the free drug and to free drug modified with anti-HER2 Fab′ [176].

Although most targeted formulations appear to be more effective in vitro, an increase in target cell accumulation does not necessarily decrease off-target effects. Since these targets (receptors, antigens, and carbohydrates) are endogenous, they are also expressed on the surface of nondisease cells. When designing a targeted system and selecting a disease target, it is important to consider the ratio of basal target expression in nondisease tissue to the overexpression levels in disease tissue. As evident from a review of the literature, there has been much reported success with targeting the ErbB family of receptors. Although the anti-HER2 Fab′ conjugated PLGA nanoparticles were very successful in treating HER2-positive breast cancer xenografts, it would be interesting to assess the formulation in HER2-negative xenografts to further support the in vitro data. The dependence of active targeting on expression levels, which may vary greatly from one patient to another, raises an important clinical concern. It will become necessary to parallel the progress in developing targeted drug delivery formulations with clinical methods for determining the target expression levels in nondiseased and diseased tissue. This personalized medicine may become a future standard. The scenario of prescreening a patient's disease phenotype and customizing treatment based on the results may become conventional practice.

In the research and development of antigen-targeted nanocarriers, the importance of epitope specificity and selection has been illustrated. Silvia Muro and fellow researchers recently demonstrated the significance of epitope selection in targeting PECAM-1 (platelet–endothelial cell adhesion molecule; also known as CD-31) [177]. PECAM-1 is a glycoprotein belonging to the immunoglobulin superfamily; it is involved in cell signaling, inflammation, migration, and angiogenesis [177,178]. PECAM-1 is an attractive vascular target, as it is expressed constitutively at very high levels in endothelial cells (and this expression is maintained in most disease states), whereas PECAM-1 expression is absent or low in epithelial cells and nonvascular cells [177,178]. Muro's study evaluated five monoclonal antibodies (mAb) that each recognize a different epitope of PECAM-1 [177]. The antibodies were absorbed to the surface of 130-nm FITC-labeled polystyrene particles [25]. Surface binding and cell-uptake studies were conducted in human umbilical vein endothelial cells (HUVECs); the targeted nanocarrier formulations were incubated with cells for 1 hour at 37°C [177]. When conjugated to the 130-nm polystyrene nanoparticles, the mAb (mAb4G6) specific for the most membrane proximal region of PECAM-1 did not bind endothelial cells, although high binding was observed for the antibody alone [177]. The researchers speculate that this lack of binding is due to spatial inaccessibility of the antibody to the membrane-proximal region of PECAM-1 due to the added bulkiness of the nanocarrier (i.e., binding may occur if the antibody distance from the surface of the nanocarrier was increased) [177]. Also in support of this theory, lower (but not absent) binding was observed for nanocarriers conjugated to a mAb (mAbGi34) specific for an epitope located in the mid-extracellular region of PECAM-1, whereas the polystyrene nanoparticles conjugated with the three mAb (mAb62, mAb35, mAb37) specific for membrane-distal regions of PECAM-1 displayed the highest degree of binding to HUVECs [177].

Interestingly, the degree of targeted nanoparticle internalization did not parallel the degree of nanocarrier/mAb binding to the surface of PECAM-1-positive cells [25]. The researchers suggest that the epitope of the targeting antibody determines the specific cellular localization of the nanocarrier complex (sustained association with the cell surface or cellular internalization) [177]. The highest cell uptake occurred with nanocarriers conjugated with the mAb (mAbGi34) specific for an epitope in the mid-extracellular region of PECAM-1 (the adhesion effect of this mAb is unknown) [177]. Even though cell surface binding of mAb37-nanocarriers was appreciable, no cell uptake was demonstrated for nanocarriers conjugated to mAb37 (mAb37 is specific for an epitope in the membrane-distal region of PECAM-1; the adhesion effect of this antibody is also unknown) [177]. Nanocarriers conjugated with mAb62 and mAb35 were both internalized to an appreciable extent (both antibodies target epitopes in the membrane-distal region of PECAM-1; mAb62 has been shown to have an inhibitory effect on PECAM-1 adhesion, whereas mAb35 has been shown to activate PECAM-1 adhesion) [177].

Although the researchers convey that the epitope specificity is responsible for determining the cellular fate of the nanocarrier (extracellular or intracellular), it would be interesting to assess additional time points, as the degree of uptake of the different epitope-targeted nanocarriers may normalize over time. Cell-uptake kinetics can be cell-type specific, and many nontargeted nanocarriers require a minimum of 3 hours before there can be appreciable detection inside the cell. Showing that these same results are maintained over longer incubation times would solidify this demonstration of epitope specificity. Nevertheless, this study suggests the importance of selecting the most advantageous macromolecular target and subsequently optimizing the intramolecular targeting schema of the system. Other common targeting techniques include the use of cell-penetrating peptides (such as the HIV-derived TAT peptide), biotin receptor targeting, integrin targeting, mitochondrial targeting, and hyaluronan/CD44 targeting, to name a few [179–182]. Optimizing the intramolecular targeting strategies for these and other targets could increase the level of subcellular specificity that is achieved by directing nanocarriers to specific cellular locations via epitope targeting.

Many multifunctional, multitargeted nanocarriers are being developed. Dual-targeting strategies can decrease the off-target accumulation (decrease toxicity) and increase the effectiveness of a system, as most disease cells simultaneously overexpress multiple factors, increasing their distinction from nondiseased cells. One such dual-targeting system was designed to target doxorubicin-loaded liposomes to the folate receptor and to the EGFR receptor, both of which are overexpressed in certain types of cancer [183]. Folate was incorporated by synthesizing a lipid–PEG–folate construct that was post-inserted into the doxorubicin-loaded liposomes; the construct was 1,2-distearoyl-*sn*-glycerophosphoethanolamine (DSPE)-PEG3350-folate [183]. A monoclonal antibody specific for EGFR (mAb225) was thiolated and conjugated to malemide residues on DSPE-PEG2000 incorporated in the liposomes [183]. The design scheme is illustrated in Figure 16.20.

KB cells were used to evaluate this dual-targeting nanocarrier system; KB cells are human papillomavirus 18 (HPV-18)–infected HeLa cervical cancer

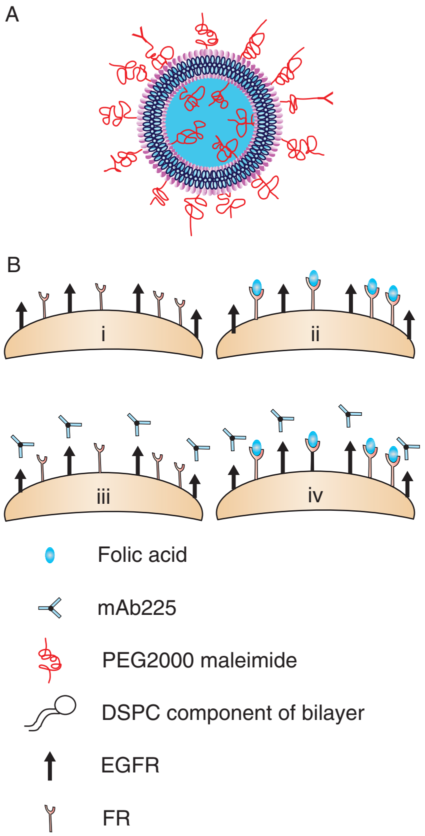

**FIGURE 16.20** Dual-targeting liposome schematic: (A) liposomal preparation with DSPE-PEG3350-folate, PEG, and mAb225 (targeting EGFR); (B) available receptors of target KB cells (i), nontarget cells with only one type of receptor available (ii and iii), and cells with no receptors available (iv). (From [183], with permission.)

cells. Cells were incubated with singly targeted formulations, nontargeting formulations, and dual-targeting formulations for 2 hours at 37°C, washed three times with medium, and either fixed for imaging studies or reincubated in fresh medium for 72 hours for cytotoxicity assessments [183]. Confocal imaging revealed that the cellular localization of doxorubicin was the same for all formulations (nuclear localization), indicating that the mechanism of uptake and cellular processing of doxorubicin is the same regardless of the surface modification on the nanocarrier [183]. The researchers defined targeting selectivity as the ratio of nontarget cell $LC_{50}$ values (with one or both receptors blocked by excessive added ligand) to target cell $LC_{50}$ values (no blocked receptors) [183]. As such, the dual-targeting liposomes demonstrated a 10-fold enhancement in folate receptor selectivity and a fourfold enhancement in EGFR selectivity [183]. The true virtue of this dual-targeting system is the potential to decrease off-target toxicity. Using a dual-targeting approach could greatly decrease the threat of toxicity, decrease the need to develop personalized medicine to increase the safety of active targeting approaches, simplify the large-scale production of multifunctional nanocarriers, and decrease the time and cost for clinical translation.

### 16.4.3 Tissue Regeneration

Nanotechnology-based drug delivery systems are ideal for tissue regeneration, due to three attributes; (1) one may tailor and control the release kinetics of multiple therapeutics; (2) nanoscale patterns promote tissue growth; and (3) nanoscale patterns hinder infection and bacterial growth [184–186]. Perhaps the most vital requirement for tissue regeneration is the high demand of growth factors [184–186]. Until the merger of nanotechnology, drug delivery, and tissue engineering, the major challenge in tissue regeneration was preventing burst release of growth factors and achieving sustained release [184–186]. Combining the sustained and controlled delivery of growth factors and proteins with the benefits of nanopatterning is transforming tissue engineering [184–186].

Tissue engineering strategies can be classified as in vitro–or in vivo–based and depend on the regenerative ability of the target tissue (some tissues will actively engage in repair, whereas others, such as the heart and central nervous system, do not have this ability) [185]. In vitro–based engineering centers around the use of a three-dimensional scaffold that promotes cell growth for subsequent implantation (currently used clinically for artificial skin). There is a dual focus of in vivo–based engineering: to provide mechanical support and to create a microenvironment that enhances growth [185]. Most of the defining parameters of nanocarriers apply to nanoscaffolds for tissue regeneration, yet also of importance is the porosity to allow extensive cell seeding (analogous to the relevance of the surface area/volume ratio of nanocarriers) [185]. As demonstrated in Figure 16.21, cells adhere and respond to nanopatterns, probably because the extracellular matrix (site of endogenous adhesion) is a protein-rich, nanoscale structure [186]. Pore size, depth, and patterning can have extreme effects on cell

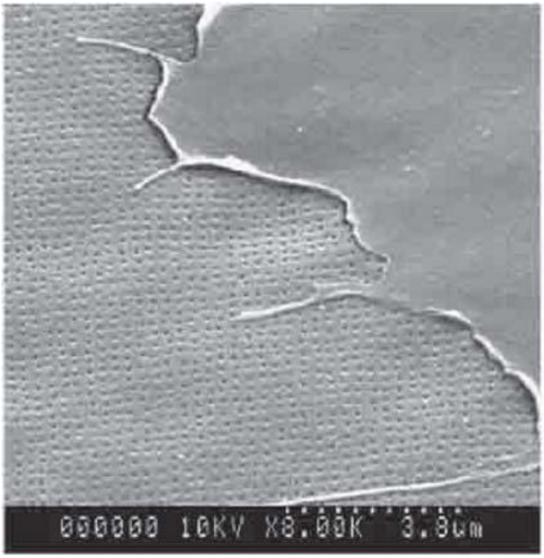

**FIGURE 16.21** Nanopatterns promote cell growth. This SEM micrograph shows the filopodia of a fibroblast exploring a nanopatterned surface. (From [185], with permission.)

adhesion and propagation; factors such as sheer stress must also be considered when designing a scaffold [186].

As demonstrated in Figure 16.22, there are many different strategies for producing nanopatterns [34]. Phase separation is a very popular technique for nanofabrication. A recently developed nanoscaffold used phase separation combined with sugar leaching to produce a poly(L-lactic acid) (PLLA) nanoscaffold for an intricate drug delivery/tissue regeneration platform [184]. The objective of the system was to provide a biodegradable platform capable of controlled and sustained delivery of platelet-derived growth factor-BB (PDGF-BB) [184]. To achieve this, PDGF-BB was encapsulated in PLGA microspheres, which were then seeded into the PLLA nanofibrous scaffold by suspending the microspheres in hexane, depositing them on the scaffold, and immobilizing the microspheres via vacuum drying [184].

The researchers varied the amount of PDGF-BB loading from 10- to 3000-ng/mg microspheres and evaluated the release by placing the scaffold in PBS/SDS buffer at 37°C while orbital-shaking at 60 rpm [184]. Two different microsphere formulations were incorporated in the nanofibrous scaffolds and evaluated based on the MW of the PLGA; a 6.5- and a 64-kDa PLGA [184]. The microspheres made with the low-molecular-weight PLGA released 54% of PDGF-BB within the first 72 hours, with subsequent slow release of 40% over 40 days; the higher-MW PLGA microspheres demonstrated a much lower (less than 3%) burst release, with a gradual incline in release accelerating at day 35 [184]. This system allows for the tailoring of release kinetics based on the MW of the PLGA,

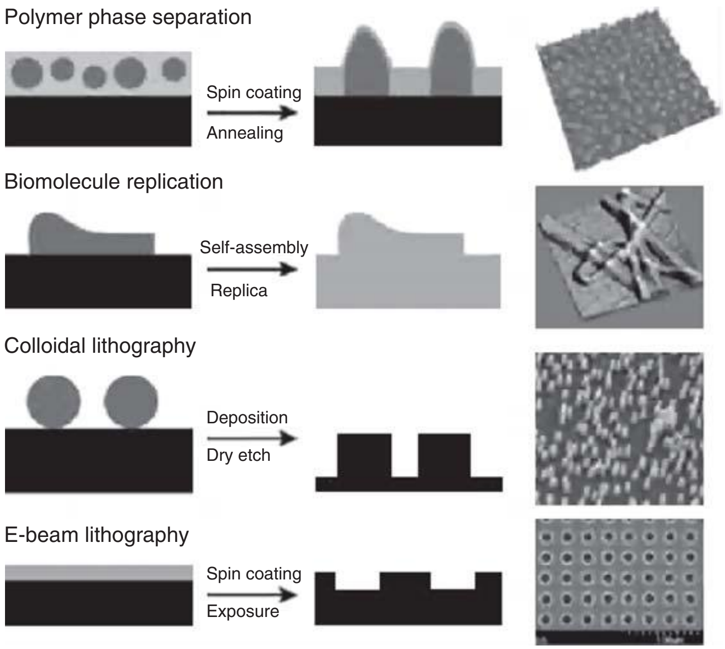
Polymer phase separation
Spin coating
Annealing
Biomolecule replication
Self-assembly
Replica
Colloidal lithography
Deposition
Dry etch
E-beam lithography
Spin coating
Exposure

**FIGURE 16.22** Nanopatterning techniques. (From [185], with permission.)

drug loading in the microspheres, and degree of PLLA scaffold modification with the microspheres [184]. Further testing of this delivery system may lead to tissue regeneration scaffolds that are capable of controlled and extended release in vivo [184].

In vivo–based tissue engineering scaffolds are inherently multifunctional, as they must establish temporary mechanical stability that can degrade and give way to endogenous tissue that is regenerated while also providing a microenvironment that promotes and sustains cell growth. As there are countless combinations of multifunctional nanocarriers for disease-targeted therapy, there are also endless combinations of multifunctional tissue regeneration formulations. Many of these formulations have demonstrated success in animal models. For example, a formulation aimed at bone regeneration used a hydrogel system loaded with bone morphogenetic protein-2 (BMP-2) and demonstrated that protein delivery can be slowly sustained over 20 days, after which 90% of protein was released [187]. This study used dual-energy x-ray absorptometry (DEXA) to evaluate bone formation and density in a rat model [187]. Other approaches include the use of thermal-responsive polymers, the use of supercritical fluid processing to form foamed scaffolds, and the use of uniform layer–layer nanoscaffolds [188,189]. The intersection of nanoscience with tissue regeneration and drug delivery formulation will undoubtedly continue to deepen and lead to new advances in emerging subdisciplines.

## 16.5 CONCLUSIONS

The combination of the various optical techniques with innovative molecular markers seems to be a powerful new approach for molecular imaging and disease-targeted therapy. Researchers have developed new optical methods for imaging a variety of cellular and molecular processes in vivo, including protein interactions, protein degradation, and protease activity. Whereas optical imaging has been used primarily for research in small-animal models, there are several areas in which optical molecular imaging shows high promise to translate rapidly to clinical medicine.

The focus on optical imaging techniques for molecular imaging is driven in large part by the sensitivity for imaging optical contrast agents and reporter molecules in vivo. The lower limits of detection for optical imaging may reach picomolar or even femtomolar concentrations of an optical reporter or contrast agent. Combined with the minimal background of techniques such as bioluminescence imaging and fluorescence imaging in the near-infrared spectrum, the signal/background ratio for detecting specific molecular signals equals or exceeds that which can be achieved with other molecular imaging modalities.

Nano-enabled delivery systems for imaging contrast enhancement and cancer targeting are the fastest-growing form of nanotechnology among major pharmaceutical companies. Optical imaging tags will help to identify diseases earlier and may avoid the need for expensive technologies and equipment. Diagnostic imaging of this type is being applied increasingly to animals in preclinical dosing studies. Regulatory authorities are supporting nanotechnologies that can improve the development of pharmaceuticals and diagnostic agents. Many regulatory policies are currently being reassessed to ensure innovation and safety when utilizing nanotechnologies. However, many questions must be answered before large-scale clinical implementation of these nanotechnologies.

## REFERENCES

1. Laurence, P.C., Baker, H., and Kelloff, G., Foreword: Potential of optical imaging for early cancer detection, screening, diagnosis and image guided treatment, *Technol. Cancer Res. Treat*., Vol. 2, No. 6, 2003, pp. 487–489.
2. Gibson, A., Hebden, J., and Arridge, S., Recent advances in diffuse optical imaging, *Phys. Med. Biol*., Vol. 50, 2005, pp. R1–R43.
3. Boas, D.A., et al., Imaging the body with diffuse optical tomography, *IEEE Signal Process. Mag*., Vol. 18, 2001, pp. 57–75.
4. Basilion, J.P., Current and future technologies for breast cancer imaging, *Breast Cancer Res*., Vol. 3, 2001, pp. 14–16.
5. Anderson-Engels, S., et al., In vivo fluorescence imaging for tissue diagnostics, *Phys. Med. Biol*., Vol. 42, 1997, pp. 815–822.
6. Pawley, J., *Handbook of Biological Confocal Microscopy*, 2nd ed., Springer Science and Business Media, New York, 1995.

7. Huang, D., et al., Optical coherence tomography, *Science*, Vol. 254, No. 5035, 1991, pp. 1178–1181.
8. Tearney, G.J., et al., In vivo endoscopic optical biopsy with optical coherence tomography, *Science*, Vol. 276, 1997, 2037–2039.
9. Vakoc, B.J., et al., Comprehensive esophageal microscopy by using optical frequency-domain imaging, *Gastrointest. Endosc.*, Vol. 65, No. 6, 2007, pp. 898–905.
10. Zipfel, W.R., Williams, R.M., and Webb, W.W., Nonlinear magic: multiphoton microscopy in the biosciences, *Nat. Biotechnol.*, Vol. 11, 2003, pp. 1369–1377.
11. Pomper, M.G., Molecular imaging: an overview, *Acad. Radiol.*, Vol. 8, 2001, pp. 1141–1153.
12. Moffmann, H.J., and Menkens, A.E., Molecular imaging in cancer: future directions and goals of the National Cancer Institute, *Acad. Radiol.*, Vol. 7, 2000, pp. 905–907.
13. Li, K.C.P., et al., Molecular imaging applications in nanomedicine, *Biomed. Microdevices*, Vol. 6, 2004, pp. 113–116.
14. Srinivas, P. R, Barker, P., and Srivastava, S., Nanotechnology in early detection of cancer, *Lab. Invest.*, Vol. 82, 2002, pp. 657–662.
15. Medintz, I.L., et al., Quantum dot bioconjugates for imaging, labelling and sensing, *Nat. Mater.*, Vol. 4, 2005, pp. 435–446.
16. Zhang, L., et al., Molecular imaging of AKT kinase activity, *Nat. Med.*, Vol. 13, 2007, pp. 1114–1119.
17. Verma, M., and Srivastava, S., New cancer biomarkers deriving from NCI early detection research, *Recent Results Cancer Res.*, Vol. 163, 2003, pp. 72–84.
18. Josephson, L., et al., High-efficiency intracellular magnetic labeling with novel superparamagnetic-TAT peptide conjugate, *Bioconjug. Chem.*, Vol. 10, 1999, pp. 186–191.
19. Sipkins, D.A., et al., Detection of tumor angiogenesis in vivo by alphavbeta3-targeted magnetic resonance imaging, *Nat. Med.*, Vol. 4, 1998, pp. 623–630.
20. Bogdanov, A.A., Jr., et al., Cellular activation of the self-quenched fluorescent reporter probe in tumor microenvironment, *Neoplasia*, Vol. 4, 2002, pp. 228–236.
21. Moon, W.K., et al., Enhanced tumor detection using a folate receptor-targeted near-infrared fluorochrome conjugate, *Bioconjug. Chem.*, Vol. 14, 2003, pp. 539–545.
22. Wang, H.Z., et al., Detection of tumor marker CAA125 in ovarian carcinoma using quantum dots, *Acta Biochim. Biophys. Sin.*, Vol. 36, No. 10, 2004, pp. 681–686.
23. Kumar, S., and Richards-Kortum, R., Optical molecular imaging agents for cancer diagnostics and therapeutics, *Nanomedicine*, Vol. 1, 2006, pp. 23–30.
24. Kim, J.S., et al., Self-assembled hybrid nanoparticles for cancer-specific multimodal imaging, *J. Am. Chem. Soc.*, Vol. 129, No. 29, 2007, pp. 8962–8963.
25. Sokolov, K., et al., Real-time vital optical imaging of precancer using anti-epidermal growth factor receptor antibodies conjugated to gold nanoparticles, *Cancer Res.*, Vol. 63, 2003, pp. 1999–2004.
26. Aaron, J., et al., Plasmon resonance coupling of metal nanoparticles for molecular imaging of carcinogenesis in vivo, *J. Biomed. Opt.*, Vol. 12, 2007, p. 034007.
27. Oldenburg, A.L., Gunther, J.R., and Boppart, S.A., Imaging magnetically labeled cells with magnetomotive optical coherence tomography, *Opt. Lett.*, Vol. 30, 2005, pp. 747–749.

28. Loo, C., et al., Nanoshell-enabled photonics-based imaging and therapy of cancer, *Technol. Cancer Res. Treat.*, Vol. 3, 2004, pp. 33–40.
29. El-Sayed, I., et al., Selective laser photo-thermal therapy of epithelial carcinoma using Anti-EGFR antibody conjugated gold nanoparticles, *Cancer Lett.*, Vol. 239, No. 1, 2006, pp. 129–135.
30. Ito, A., et al., Magnetite nanoparticle-loaded anti-HER2 immunoliposomes for combination of antibody therapy with hyperthermia, *Cancer Lett.*, Vol. 212, No. 2, 2004, pp. 167–175.
31. Amiji, M., et al., Intratumoral administration of paclitaxel in a thermogelling PluronIC® F-127 formulation, *Proceedings of the American Association of Pharmaceutical Scientists, Pharmaceutical Congress of the Americas*, Vol. 1, 2001, p. 129.
32. Torchilin, V.P., et al., Immunomicelles: targeted pharmaceutical carrier for poorly soluble drugs, *Proc. Natl. Acad. Sci. USA*, Vol. 100, 2003, pp. 6039–6044.
33. O'Neal, D.P., et al., Photo-thermal tumor ablation in mice using near infrared-absorbing nanoparticles, *Cancer Lett.*, Vol. 209, 2004, pp. 171–176.
34. Maeda, H., et al., Tumor vascular permeability and the EPR effect in macromolecular therapeutics: a review, *J. Control. Release*, Vol. 65, 2000, pp. 271–284.
35. Pomper, M.G., Molecular imaging: an overview, *Acad. Radiol.*, Vol. 8, 2001, pp. 1141–1153.
36. Hoffmann, J.M., and Menkens, A.E., Molecular imaging in cancer: future directions and goals of the National Cancer Institute, *Acad. Radiol.*, Vol. 7, 2000, pp. 905–907.
37. Bok Lee, S., Focus on nanoparticles for cancer diagnosis and therapeutics, *Nanomedicine*, Vol. 2, No. 5, 2007, pp. 647–648.
38. Brigger, I., Dubernet, C., and Couvreur, P., Nanoparticles in cancer therapy and diagnosis, *Adv. Drug Deliv. Rev.*, Vol. 54, 2002, pp. 631–665.
39. Wickline, S.A., and Lanza, G.M., Molecular imaging, targeted therapeutics, and nanoscience, *J. Cell. Biochem. Suppl.*, Vol. 39, 2002, pp. 90–97.
40. Achilefu, S., Lighting up tumors with receptor-specific optical molecular probes, *Technol. Cancer Res. Treat.*, Vol. 3, No. 4, 2004, pp. 393–409.
41. Gao, X.H., et al., In vivo cancer targeting and imaging with semiconductor quantum dots, *Nat. Biotechnol.*, Vol. 22, 2004, pp. 969–976.
42. Weisleder, R., et al., Cell-specific targeting of nanoparticles by multivalent attachment of small molecules, *Nat. Biotechnol.*, Vol. 23, 2005, pp. 1418–1423.
43. Caplan, M.R., and Rosca, E.V., Targeting drugs to combinations of acceptors: a modeling analysis of potential specificity, *Ann. Biomed. Eng.*, Vol. 33, 2005, pp. 1113–1124.
44. Vu, T.O., et al., Peptide-conjugated quantum dots activate neuronal receptors and initiate downstream signalling of neurite grown, *Nano Lett.*, Vol. 5, 2005, pp. 603–607.
45. Brigger, I., Dubernet, C., and Couvreur, P., Nanoparticles in cancer therapy and diagnosis, *Adv. Drug Deliv. Rev.*, Vol. 54, 2002, pp. 631–665.
46. Kim, D., Superparamagnetic iron oxide nanoparticles for bio-medical applications, *Scr. Mater.*, Vol. 44, No. 8–9, 2001, pp. 1713–1717.
47. Saiyed, Z.M., Telang, S.D., and Ramchand, C.N., Application of magnetic techniques in the field of drug discovery and biomedicine, *Biomagn. Res. Technol.*, Vol. 1, 2003, p. 2.

48. Shinkai, M., et al., Intracellular hyperthermia for cancer using magnetite cationic liposomes: in vitro study, *Jpn. J. Cancer Res.*, Vol. 87, 1996, pp. 1179–1183.
49. Chan, D.C.F., Kirpotin, D.B., and Bunn, P. A, Jr., Synthesis and evaluation of colloidal magnetic iron oxides for the site-specific radiofrequency-induced hyperthermia of cancer, *J. Magn. Magn. Mater.*, Vol. 122, 1993, pp. 374–378.
50. Ito, A., et al., Tumor regression by combined immunotherapy and hyperthermia using magnetic nanoparticles in an experimental subcutaneous murine melanoma, *Cancer Sci.*, Vol. 94, 2003, pp. 308–311.
51. Kircher, M.F., et al., A multimodal nanoparticle for preoperative magnetic resonance imaging and intraoperative optical brain tumor delineation, *Cancer Res.*, Vol. 63, 2001, pp. 8122–8125.
52. Hergt, R., et al., Physical limits of hyperthermia using magnetite fine particles, *IEEE Trans. Magn.*, Vol. 34, No. 5, 1998, pp. 3745–3754.
53. Ito, A., Honda, H., and Kobayashi, T., Cancer immunotherapy based on intracellular hyperthermia using magnetite nanoparticles: a novel approach of heat-controlled necrosis with heat shock protein expression, *Cancer Immunol. Immunother.*, Vol. 55, 2006, pp. 320–328.
54. Hilger, I., Hergt, R., and Kaiser, W.A., Use of magnetic nanoparticle heating in the treatment of breast cancer, *IEE Proc. Nanobiotechnol.*, Vol. 152, No. 1, 2005, pp. 33–39.
55. Tanaka, K., et al., Intratumoral injection of immature dendritic cells enhances antitumor effect of hyperthermia using magnetic nanoparticles, *Int. J. Cancer*, Vol. 116, No. 4, 2005, pp. 624–633.
56. Derfus, A.M., et al., Remotely triggered release from magnetic nanoparticles, *Adv. Mater.*, Vol. 19, 2007, pp. 3932–3936.
57. Faulk, W.P., and Taylor, G.M., An immunocolloid method for the electron microscope, *Immunochemistry*, Vol. 8, 1971, pp. 1081–1083.
58. Hainfeld, J.F., Slatkin, D.N., and Smilowitz, H.M., The use of gold nanoparticles to enhance radiotherapy in mice, *Phys. Med. Biol.*, Vol. 49, 2004, pp. 309–315.
59. Sokolov, K., et al., Real-time vital optical imaging of precancer using anti-epidermal growth factor receptor antibodies conjugated to gold nanoparticles, *Cancer Res.*, Vol. 63, 2003, pp. 1999–2004.
60. Kommareddy, S., and Amiji, M., Targeted drug delivery to tumor cells using colloidal carriers, *Cellular Drug Delivery: Principles and Practice*, pp. 181–215, in D.R. Lu and S. Oie (eds.), Humana Press, Totowa, NJ, 2004.
61. Kaul, G., and Amiji, M., Long-circulating poly(ethylene glycol)-modified gelatin nanoparticles for intracellular delivery, *Pharm. Res.*, Vol. 19, 2002, pp. 1062–1068.
62. Rahman, M., et al., Optical imaging of cervical pre-cancers with structured illumination: an integrated approach, *Gynecol. Oncol.*, Vol. 99, No. 3, Suppl. 1, 2005, pp. 112–115.
63. Loo, C., et al., Gold nanoshell bioconjugates for molecular imaging in living cells, *Opt. Lett.*, Vol. 30, 2005, pp. 1012–1014.
64. Wang, H., et al., Controlled texturing modifies the surface topography and plasmonic properties of Au nanoshells, *J. Phys. Chem. B*, Vol. 9, 2005, p. 2.
65. Hirsch, L.R., Stafford, R.J., and Bankson, J.A., Nanoshell-mediated near-infrared thermal therapy of tumors under magnetic resonance guidance, *Proc. Natl. Acad. Sci. USA*, Vol. 100, No. 23, 2003, pp. 13549–13554.

66. Bruches, M., et al., Semiconductor nanocrystals as fluorescent biological labels, *Science*, Vol. 281, 1998, pp. 2013–2016.
67. Chan, W.C.W., and Nie, S.M., Quantum dot bioconjugates for ultrasensitive non-isotopic detection, *Science*, Vol. 281, 1998, pp. 2016–2018.
68. Michel, C.M., et al., Discrete nanostructures of quantum dots/Au with DNA, *J. Am. Chem. Soc*., Vol. 126, 2004, pp. 10832–10833.
69. Medintz, I.L., et al., Quantum dot bioconjugates for imaging, labelling and sensing, *Nat. Mater*., Vol. 4, 2005, pp. 435–446.
70. Michalet, X., et al., Quantum dots for live cells, in vivo imaging, and diagnostics, *Science*, Vol. 307, No. 5709, 2005, pp. 538–544.
71. Dahan, M., et al., Time-gated biological imaging by use of colloidal quantum dots, *Opt. Lett*., Vol. 26, 2001, pp. 825–827.
72. Larson, D., et al., Water-soluble quantum dots for multiphoton fluorescence imaging in vivo, *Science*, Vol. 300, 2003, pp. 1434–1436.
73. Iga, A.M., et al., Clinical potential of quantum dots, *J. Biomed. Biotechnol*., 2007, p. 76087.
74. Gao, X., et al., In vivo cancer targeting and imaging with semiconductor quantum dots, *Nat. Biotechnol*., Vol. 22, No. 8, 2004, pp. 969–976.
75. Parungo, C.P., et al., Intraoperative identification of esophageal sentinel lymph nodes with near-infrared fluorescence imaging, *J. Thorac. Cardiovasc. Surg*., Vol. 129, No. 4, 2005, pp. 844–850.
76. Tsay, J.M., and Michalet, X., New light on quantum dot cytotoxicity, *Chem. Biol*., Vol. 12, No. 1, 2005, pp. 1159–1161.
77. Lovríc, J., et al., Unmodified cadmium telluride quantum dots induce reactive oxygen species formation leading to multiple organelle damage and cell death, *Chem. Biol*., Vol. 12, No. 11, 2005, pp. 1227–1234.
78. Lee, T.M., et al., Engineered microsphere contrast agents for optical coherence tomography, *Opt. Lett*., Vol. 28, No. 17, 2003, pp. 1546–1548.
79. Rajadhyaksha, M., Gonzalez, S., and Zavislan, J.M., Detectability of contrast agents for confocal reflectance imaging of skin and microcirculation, *J. Biomed. Opt*., Vol. 9, No. 2, 2004, pp. 323–331.
80. Van Manen, H.J., and Otto, C., Hybrid confocal Raman fluorescence microscopy on single cells using semiconductor quantum dots, *Nano Lett*., Vol. 7, No. 6, 2007, pp. 1631–1636.
81. Morgner, U., et al., Spectroscopic optical coherence tomography, *Opt. Lett*., Vol. 25, 2000, pp. 111–113.
82. Boppart, S.A., et al., Optical probes and techniques for molecular contrast enhancement in coherence imaging, *J. Biomed. Opt*., Vol. 10, 2005, p. 041208-1-14.
83. Oldenburg, A.L., et al., Magnetomotive contrast for in vivo optical coherence tomography, *Opt. Express*, Vol. 13, 2005, pp. 6597–6614.
84. Potma, E.O., Evans, C.L., and Xie, X.S., Heterodyne coherent anti-Stokes Raman scattering (CARS) imaging, *Opt. Lett*., Vol. 31, No. 2, 2006, pp. 241–243.
85. Cheng, J.-X., Potma, E.O., and Xie, S.X., Coherent anti-Stokes Raman scattering correlation spectroscopy: probing dynamical processes with chemical selectivity, *J. Phys. Chem. B*, Vol. 108, No. 3, 2004, pp. 827–840.

86. Achilefu, S., et al., Novel receptor-targeted fluorescent contrast agents for in vivo tumor imaging, *Invest. Radiol.*, Vol. 35, 2000, pp. 479–485.
87. Brooks, P.C., et al., Integrin Alpha(V)Beta(3) antagonists promote tumor-regression by inducing apoptosis of angiogenic blood-vessels, *Cell*, Vol. 79, 1994, pp. 1157–1164.
88. Bruns, C.J., et al., Vascular endothelial growth factor is an in vivo survival factor for tumor endothelium in a murine model of colorectal carcinoma liver metastases, *Cancer*, Vol. 89, 2000, pp. 488–499.
89. Gruber, G., et al., Correlation between the tumoral expression of beta 3-integrin and outcome in cervical cancer patients who had undergone radiotherapy, *Br. J. Cancer*, Vol. 92, 2005, pp. 41–46.
90. Wang, X., et al., Beta3 integrins facilitate matrix interactions during transendothelial migration of PC3 prostate tumor cells, *Prostate*, Vol. 63, 2005, pp. 65–80.
91. Schulz, S., et al., True positive somatostatin receptor scintigraphy in primary breast cancer correlates with expression of sst2A and sst5, *Breast Cancer Res. Treat.*, Vol. 72, 2002, pp. 221–226.
92. Mulder, W.J.M., et al., Magnetic and fluorescent nanoparticles for multimodality imaging, *Nanomedicine*, Vol. 2, No. 3, 2007, pp. 307–324.
93. Huang, D., et al., Optical coherence tomography, *Science*, Vol. 254, 1991, p. 1178.
94. Sampson, D.D., Trends and prospects for optical coherence tomography, in *2nd European Workshop on Optical Fiber Sensors*, J.M. López-Higuera and B. Culshaw (eds.), *Proc. SPIE*, Vol. 5502, 2004, pp. 51–58.
95. Fujimoto, J.G., et al., Optical biopsy and imaging using optical coherence tomography, *Nat. Med.*, Vol. 1, 1995, pp. 970–972.
96. Kobayashi, K., et al., High-resolution cross-sectional imaging of the gastrointestinal tract using optical coherence tomography: preliminary results, *Gastrointest. Endosc.*, Vol. 47, 1998, pp. 515–523.
97. Hsiung, P.L., et al., Benign and malignant lesions in the human breast depicted with ultrahigh resolution and three-dimensional optical coherence tomography, *Radiology*, Vol. 244, No. 3, 2007, pp. 865–874.
98. Bouma, B.E., et al., High-resolution imaging of the human esophagus and stomach in vivo using optical coherence tomography, *Gastrointest. Endosc.*, Vol. 51, 2000, pp. 464–474.
99. Pitris, C., et al., High-resolution imaging of gynecologic neoplasms using optical coherence tomography, *Obstet. Gynecol.*, Vol. 93, 1999, pp. 135–139.
100. Poneros, J.M., et al., Diagnosis of dysplasia in Barrett's esophagus using optical coherence tomography, AB113, in *Digestive Disease Week*, American Gastroenterological Association, San Francisco, CA, 2001.
101. Fercher, A.F., et al., Optical coherence tomography: principles and applications, *Rep. Prog. Phys.*, Vol. 66, 2003, pp. 239–303.
102. Leitgeb, R., Hitzenberger, C.K., and Fercher, A.F., Performance of Fourier domain vs. time domain optical coherence tomography, *Opt. Express*, Vol. 11, 2003, pp. 889–894.
103. Chinn, S.R., Swanson, E.A., and Fujimoto, J.G., Optical coherence tomography using a frequency-tunable optical source, *Opt. Lett.*, Vol. 22, 1997, pp. 340–342.

104. Sarunic, M.V., Weinberg, S., and Izatt, J.A., Full-field swept-source phase microscopy, *Opt. Lett*., Vol. 31, 2006, p. 1462.
105. Oldenburg, A.L., Xu, C., Boppart, S.A., Spectroscopic optical coherence tomography and microscopy, *IEEE J. Sel. Top. Quant. Electron*., Vol. 13, 2007, pp. 1629–1640.
106. Adler, D.C., et al., Optical coherence tomography contrast enhancement using spectroscopic analysis with spectral autocorrelation, *Opt. Express*, Vol. 12, 2004, p. 5487.
107. Xu, C., Carney, P.S., and Boppart, S.A., Wavelength-dependent scattering in spectroscopic optical coherence tomography, *Opt. Express*, Vol. 13, 2005, pp. 5450–5462.
108. Dyer, S.D., et al., Spectroscopic phase-dispersion optical coherence tomography measurements of scattering phantoms, *Opt. Express*, Vol. 14, 2006, pp. 8138–8153.
109. V. Backman, et al., Detection of preinvasive cancer cells, *Nature*, Vol. 406(6791), 2000, pp. 35–36.
110. Michels, S., et al., Value of polarisation-sensitive optical coherence tomography in diseases affecting the retinal pigment epithelium, *Br. J. Ophthalmo*., Vol. 92, 2008, pp. 204–209.
111. Srinivas, S.M., et al., Determination of burn depth by polarization-sensitive optical coherence tomography, *J. Biomed. Opt*., Vol. 9, 2004, p. 207.
112. Kuo, W.-C., et al., Polarization-sensitive optical coherence tomography for imaging human atherosclerosis, *Appl. Opt*., Vol. 46, 2007, p. 2520.
113. Pasquesi, J.J., et al., In vivo detection of exercise-induced ultrastructural changes in genetically-altered murine skeletal muscle using polarization-sensitive optical coherence tomography, *Opt. Express*, Vol. 14, 2006, p. 1547.
114. Strasswimmer, J., et al., Polarization-sensitive optical coherence tomography of invasive basal cell carcinoma, *J. Biomed. Opt*., Vol. 9, 2004, p. 292.
115. Yaqoob, Z., et al., Molecular contrast optical coherence tomography: a pump–probe scheme using indocyanine green as a contrast agent, *J. Biomed. Opt*., Vol. 11, No. 5, 2006, p. 054017.
116. Applegate, B.E., and Izatt, J.A., Molecular imaging of endogenous and exogenous chromophores using ground state recovery pump–probe optical coherence tomography, *Opt. Express*, Vol. 14, 2006, p. 9142.
117. Marks, D.L., and Boppart, S.A., Nonlinear interferometric vibrational imaging, *Phys. Rev. Lett*., Vol. 92, No. 12, 2004, p. 123905.
118. Gambichler, T., et al., Epidermal thickness assessed by optical coherence tomography and routine histology: preliminary results of method comparison, *J. Eur. Acad. Dermatol. Venereol*., Vol. 20, No. 7, 2006, pp. 791–795.
119. Barton, J.K., Hoying, J.B., and Sullivan, C.J., Use of microbubbles as an optical coherence tomography contrast agent, *Acad. Radiol*., Vol. 9, No. 1, 2002, pp. 52–55.
120. Lee, T.M., et al., Engineered microsphere contrast agents for optical coherence tomography, *Opt. Lett*., Vol. 28, 2003, pp. 1546–1548.
121. Yang, C., et al., Spectral triangulation molecular contrast optical coherence tomography with indocyanine green as the contrast agent, *Opt. Lett*., Vol. 29, No. 17, 2004, pp. 2016–2018.
122. Xu, C., et al., Near-infrared dyes as contrast-enhancing agents for spectroscopic optical coherence tomography, *Opt. Lett*., Vol. 29, No. 14, 2004, pp. 1647–1649.
123. Boppart, S.A., et al., Optical molecular imaging probes and techniques for optical coherence tomography, *J. Biomed. Opt*., Vol. 10, No. 4, 2005, p. 041208-1-14.

124. Lin, A.W.H., et al., Optically tunable nanoparticle contrast agents for early cancer detection: model-based analysis of gold nanoshells, *J. Biomed. Opt*., Vol. 10, 2005, p. 064035.
125. Agrawal, A., et al., Quantitative evaluation of optical coherence tomography signal enhancement with gold nanoshells, *J. Biomed. Opt*., Vol. 11, 2006, p. 041121.
126. Gobin, A.M., et al., Near-infrared resonant nanoshells for combined optical imaging and photothermal cancer therapy, *Nano Lett*., Vol. 7, 2007, p. 1929.
127. Cang, H., et al., Gold nanocages as contrast agents for spectroscopic optical coherence tomography, *Opt. Lett*., Vol. 30, 2005, pp. 3048–3050.
128. Chen, J.Y., et al., Gold nanocages: bioconjugation and their potential use as optical imaging contrast agents, *Nano Lett*., Vol. 5, 2005, pp. 473–477.
129. Oldenburg, A.L., et al., Plasmon-resonant gold nanorods as low backscattering albedo contrast agents for optical coherence tomography, *Opt. Express*, Vol. 14, 2006, pp. 6724–6738.
130. Troutman, T.S., Barton, J.K., and Romanowski, M., Optical coherence tomography with plasmon resonant nanorods of gold, *Opt. Lett*., Vol. 32, 2007, pp. 1438–1440.
131. Huang, X., et al., Cancer cell imaging and photothermal therapy in the near-infrared region by using gold nanorods, *J. Am. Chem. Soc*., Vol. 128, 2006, p. 2115.
132. Adler, D.C., et al., Photothermal detection of gold nanoparticles using phase-sensitive optical coherence tomography, *Opt. Express*, Vol. 16, 2008, pp. 4376–4393.
133. Skala, M.C., et al., Photothermal optical coherence tomography of epidermal growth factor receptor in live cells using immunotargeted gold nanospheres, Nano Lett., Vol. 8, 2008, p. 3461.
134. Oh, J., et al., Magneto-motive detection of tissue-based macrophages by differential phase optical coherence tomography, *Laser Surg. Med*., Vol. 39, 2007, pp. 266–272.
135. Lee, J.H., et al., Artificially engineered magnetic nanoparticles for ultra-sensitive molecular imaging, *Nat. Med*., Vol. 13, 2007, pp. 95–99.
136. Choma, M.A., et al., Spectral-domain phase microscopy, *Opt. Lett*., Vol. 30, 2005, pp. 1162–1164.
137. Arruebo, M., et al., Magnetic nanoparticles for drug delivery, *Nano Today*, Vol. 2, 2007, pp. 22–32.
138. Kim, J., et al., Imaging nanoparticle flow using magneto-motive optical Doppler tomography, *Nanotechnology*, Vol. 18, 2007, p. 035504.
139. Oldenburg, A.L., Gunther, J.R., and Boppart, S.A., Imaging magnetically labeled cells with magnetomotive optical coherence tomography, *Opt. Lett*., Vol. 30, 2005 pp. 747–749.
140. Ito, A., et al., Medical application of functionalized magnetic nanoparticles, *J. Biosci. Bioeng*., Vol. 100, 2005, pp. 1–11.
141. Josephson, L., et al., Near-infrared fluorescent nanoparticles as combined MR/optical imaging probes, *Bioconjug. Chem*., Vol. 13, No. 3, 2002, pp. 554–560.
142. Beaurepaire, E., et al., Combined scanning optical coherence and two-photon-excited fluorescence microscopy, *Opt. Lett*., Vol. 24, No. 14, 1999.
143. Barton, J.K., Tumlinson, A.R., and Utzinger, U., Combined endoscopic optical coherence tomography and laser induced fluorescence, in *Optical Coherence Tomography Technology and Applications*, W. Drexler and J.G. Fujimoto (eds.), Springer-Verlag, Berlin, 2008.

144. Yeh, A.T., et al., Selective corneal imaging using combined second harmonic generation and two-photon excited fluorescence, *Opt. Lett*., Vol. 27, 2002, pp. 2082–2084.
145. Sun, J., et al., In vivo multimodal nonlinear optical imaging of mucosal tissue, *Opt. Express*, Vol. 12, No. 11, 2004, pp. 2478–2486.
146. Tréhin, R., et al., Fluorescent nanoparticle uptake for brain tumor visualization, *Neoplasia*, Vol. 8, No. 4, 2006, pp. 302–311.
147. Mulder, W.J.M., et al., Lipid-based nanoparticles for contrast-enhanced MRI and molecular imaging, *NMR Biomed*., Vol. 19, No. 1, 2006, pp. 142–164.
148. Hariri, L.P., et al., Ex vivo optical coherence tomography and laser-induced fluorescence spectroscopy imaging of murine gastrointestinal tract, *Comp. Med*., Vol. 57, No. 2, 2007, pp. 175–185.
149. Nakamura, H., et al., Quantitative detection of lung cancer cells by fluorescence in situ hybridization: Comparison with conventional cytology, *Chest*, Vol. 128, 2005, pp. 906–911.
150. Miller, J., Clinical molecular imaging, *J. Am. Coll. Radiol*., Vol. 1, No. 1, 2004, pp. 4–23.
151. Iftimia, N., et al, A combined OCT-nanotechnology approach for epithelial cancer screening and therapy, in *Reporters, Markers, Dyes, Nanoparticles, and Molecular Probes for Biomedical Applications*, Conference 7190, *Proc. SPIE*, Vol. 7190, 2009.
152. Jain, K.K., Nanotechnology-based drug delivery for cancer, *Technol. Cancer Res. Treat*., Vol. 4, No. 4, 2005, pp. 407–416.
153. Salata, O., Applications of nanoparticles in biology and medicine, *J. Nanobiotechnol*., Vol. 2, No. 1, 2003, p. 3.
154. Kingsley, J.D., et al., Nanotechnology: a focus on nanoparticles as a drug delivery system, *J. Neuroimmune Pharmacol*., Vol. 1, No. 3, 2006, pp. 340–350.
155. Gratton, S.E., et al., The effect of particle design on cellular internalization pathways, *Proc. Natl. Acad. Sci. USA*, Vol. 105, No. 33, 2008, pp. 11613–11618.
156. Hede, S., and Huilgol, N., Nano: the new nemesis of cancer, *J. Cancer Res. Ther*., Vol. 2, No. 4, 2006, pp. 186–195.
157. Moghimi, S.M., Hunter, A.C., and Murray, J.C., Nanomedicine: current status and future prospects, *FASEB J*., Vol. 19, No. 3, 2005, pp. 311–330.
158. Pokropivny, V., and Skorokhod, V., New dimensionality classifications of nanostructures, *Physica E*, Vol. 40, No. 6, 2008, pp. 2521–2525.
159. Thornton, G., Materials science: watching nanoparticles grow, *Science*, Vol. 300, No. 5624, 2003, pp. 1378–1379.
160. Alexis, F., et al., Factors affecting the clearance and biodistribution of polymeric nanoparticles, *Mol. Pharmacol*., Vol. 5, No. 4, 2008, pp. 505–515.
161. Batrakova, E.V., and Kabanov, A.V., Pluronic block copolymers: evolution of drug delivery concept from inert nanocarriers to biological response modifiers, *J. Control. Release*, Vol. 130, No. 2, 2008, pp. 98–106.
162. Moghimi, S.M., Hunter, A.C., and Murray, J.C., Long-circulating and target-specific nanoparticles: theory to practice, *Pharmacol. Rev*., Vol. 53, No. 2, 2001, pp. 283–318.
163. Jabr-Milane, L.S., et al., Multi-functional nanocarriers to overcome tumor drug resistance, *Cancer Treat. Rev*., Vol. 34, No. 7, 2008, pp. 592–602.

164. Jabr-Milane, L.S., et al., Multi-functional nanocarriers for targeted delivery of drugs and genes, *J. Control. Release*, Vol. 130, No. 2, 2008, pp. 121–128.

165. Geys, J., et al., Acute toxicity and prothrombotic effects of quantum dots: impact of surface charge, *Environ. Health Perspect*., Vol. 116, No. 12, 2008, pp. 1607–1613.

166. Berg, S.L., et al., Effect of R-verapamil on the pharmacokinetics of paclitaxel in women with breast cancer, *J. Clin. Oncol*., Vol. 13, No. 8, 1995, pp. 2039–2042.

167. Greenough, T.C., et al., Safety and immunogenicity of recombinant poxvirus HIV-1 vaccines in young adults on highly active antiretroviral therapy, *Vaccine*, Vol. 26, No. 52, 2008, pp. 6883–6893.

168. Sinha, R., et al., Nanotechnology in cancer therapeutics: bioconjugated nanoparticles for drug delivery, *Mol. Cancer Ther*., Vol. 5, No. 8, 2006, pp. 1909–1917.

169. Zhao, L., Wientjes, M.G., and Au, J.L., Evaluation of combination chemotherapy: integration of nonlinear regression, curve shift, isobologram, and combination index analyses, *Clin. Cancer Res*., Vol. 10, No. 23, 2004, pp. 7994–8004.

170. Devalapally, H., et al., Modulation of drug resistance in ovarian adenocarcinoma by enhancing intracellular ceramide using tamoxifen-loaded biodegradable polymeric nanoparticles, *Clin. Cancer Res*., Vol. 4, No. 10, 2008, pp. 3193–3203.

171. Monsky, W.L., et al., Augmentation of transvascular transport of macromolecules and nanoparticles in tumors using vascular endothelial growth factor, *Cancer Res*., Vol. 59, 1999, pp. 4129–4135.

172. Rojo, F., et al., Targeted therapies in breast cancer, *Semin. Diagn. Pathol*., Vol. 25, No. 4, 2008, pp. 245–261.

173. Hsieh, M.Y., et al., Stochastic simulations of ErbB homo and heterodimerisation: potential impacts of receptor conformational state and spatial segregation, *IET Syst. Biol*., Vol. 2, No. 5, 2008, pp. 256–272.

174. Magadala, P., and Amiji, M., Epidermal growth factor receptor-targeted gelatin-based engineered nanocarriers for DNA delivery and transfection in human pancreatic cells, *AAPS J*., Vol. 10, No. 4, 2008, pp. 565–576.

175. Chen, H., et al., Preparation and characterization of PE38KDEL-loaded anti-HER2 nanoparticles for targeted cancer therapy, *J. Control. Release*, Vol. 128, No. 3, 2008, pp. 209–216.

176. Garnacho, C., et al., Differential intra-endothelial delivery of polymer nanocarriers targeted to distinct PECAM-1 epitopes, *J. Control. Release*, Vol. 130, No. 3, 2008, pp. 226–233.

177. Newman, P.J., The biology of PECAM-1, *J. Clin. Invest*., Vol. 99, No. 1, 1997, pp. 3–8.

178. Yang, W., et al., Targeting cancer cells with biotin-dendrimer conjugates, *Eur. J. Med. Chem*., Vol. 44, No. 2, 2009, pp. 862–868.

179. Platt, V.M., and Szoka, F.C., Jr., Anticancer therapeutics: targeting macromolecules and nanocarriers to hyaluronan or CD44, a hyaluronan receptor, *Mol. Pharmacol*., Vol. 5, No. 4, 2008, pp. 474–486.

180. Garg, A., et al., Targeting colon cancer cells using PEGylated liposomes modified with a fibronectin-mimetic peptide, Pub. Med. 18835580, *Int. J. Pharmacol*., 2008.

181. Galluzzi, L., et al., Mitochondria as therapeutic targets for cancer chemotherapy, *Oncogene*, Vol. 25, No. 34, 2006, pp. 4812–4830.

182. Saul, J. M, Annapragada, A.V., and Bellamkonda, R.V., A dual-ligand approach for enhancing targeting selectivity of therapeutic nanocarriers, *J. Control. Release*, Vol. 114, No. 3, 2006, pp. 277–287.

183. Wei, G., et al., Nano-fibrous scaffold for controlled delivery of recombinant human PDGF-BB, *J. Control. Release*, Vol. 112, No. 1, 2006, pp. 103–110.

184. Quaglia, F., Bioinspired tissue engineering: the great promise of protein delivery technologies, *Int. J. Pharm*., Vol. 364, No. 2, 2008, pp. 281–297.

185. Gadegaard, N., et al., Applications of nano-patterning to tissue engineering, *Microelectron. Eng*., Vol. 83, 2006, pp. 1577–1581.

186. Hosseinkhani, H., et al., Bone regeneration through controlled release of bone morphogenetic protein-2 from 3-D tissue engineered nano-scaffold, *J. Control. Release*, Vol. 117, No. 3, 2007, pp. 380–386.

187. Xiaoyan, A., et al., Preparation of chitosan-gelatin scaffold containing tetrandrine-loaded nano-aggregates and its controlled release behavior, *Int. J. Pharm*., Vol. 350, No. 1–2, 2008, pp. 257–264.

188. Tai, H., et al., Control of pore size and structure of tissue engineering scaffolds produced by supercritical fluid processing, *Eur. Cell Mater*., Vol. 14, 2007, pp. 64–77.

189. Kikuchi, A., and Okano, T., Nanostructured designs of biomedical materials: applications of cell sheet engineering to functional regenerative tissues and organs, *J. Control. Release*, Vol. 101, No. 1–3, 2005, pp. 69–84.

# 17

# MOLECULAR PROBES FOR OPTICAL CONTRAST ENHANCEMENT OF GASTROINTESTINAL CANCERS

Jonathan W. Hardy
*Stanford University School of Medicine, Stanford, California*
Jonathan T. C. Liu
*State University of New York at Stony Brook, Stony Brook, New York*
Anson W. Lowe and Christopher H. Contag
*Stanford University School of Medicine, Stanford, California*

17.1 Introduction 506
17.2 DNA microarrays for target identification 507
17.3 Phage display 511
17.4 Potential targets and possible pitfalls 516
  17.4.1 Mucins 516
  17.4.2 Wnt receptors 517
  17.4.3 Tight junction probes 519
  17.4.4 Integrins 520
  17.4.5 Enzymes 521
  17.4.6 Pitfalls 522
17.5 Probe design 523
17.6 Conclusions 525
References 525

---

*Advances in Optical Imaging for Clinical Medicine*, Edited by Nicusor Iftimia, William R. Brugge, and Daniel X. Hammer
Copyright © 2011 John Wiley & Sons, Inc.

## 17.1 INTRODUCTION

The gastrointestinal (GI) tract, being a system of hollow organs that is accessible via endoscopy, is more amenable to the optical detection of cancer than many other tissues, and optical technologies are rapidly advancing with the purpose of early detection of cancer as a primary objective. The surface of the GI tract is accessible to direct examination via endoscopy, and the most common GI cancers originate in the superficial mucosa (mucous membrane), where unscattered ballistic photons can penetrate to depths that are relevant for interrogating tissue properties and detecting cellular markers. Improvements in instrumentation now permit the detection of these photons to depths that were not possible employing previous methods. High-resolution microscopy, which relies largely on the diffraction-limited focusing of ballistic photons, would be very useful for imaging of cancer-associated morphology or the detection of specific molecular probes, because it can be used to examine the thin mucosal layer of less than 1 mm thickness in which most GI cancers arise. In addition, molecular probes whose binding characteristics are verified by microscopy could facilitate rapid wide-field detection of precancerous lesions over large areas, followed by closer inspection with endomicroscopy. Probes that detect GI cancer have been identified using several methods [1–4] and the clinical application of both contrast-enhancing agents and specific molecular diagnostic reagents capable of revealing early disease markers is on the horizon.

The development of detection reagents may also be followed by image-guided or targeted therapy based on the binding specificity of the compounds: however, not one such reagent is in current clinical use for detection of GI malignancies or any other pathology of the GI tract. Although some antigens associated with cancer progression are known, it is safe to say that much more is unknown, and the molecular details of precancer processes and early malignant transformation are still largely obscure despite decades of analyses. New tools brought to bear on this problem have and will continue to alter profoundly the understanding of the pathogenic events as well as aid in the early detection of cancer. The identification of molecular targets on the surfaces of cancer cells that are amenable to optical detection is only one aspect of an unprecedented effort in multifaceted molecular analyses of malignancy. These studies include multiparametric analyses of gene expression patterns and molecular dissection of disease mechanisms that have led to a greater understanding of the cause and to the identification of risk factors that may comprise the basis of early detection and prevention. Thus, despite the current lack of specific optical detection reagents for use by the endoscopist, there is considerable hope that these molecular approaches will lead to better diagnostic tools, improved prognoses, and more effective therapies. In this chapter we cover the development of imaging reagents based on the molecular biology of GI cancers and the opportunities for their use as diagnostics and therapeutics. The development of confocal endomicroscopes for in vivo detection of disease is described in Chapter 7, and the reagents being developed will serve as a means of enhancing contrast for these instruments and creating functional assays for disease detection. Integration of these two areas of technology is necessary to achieve the benefits that will be realized in the clinic.

In the early phases of cancer development, the molecular and cellular changes are quite subtle compared to the drastically altered properties of full malignancy. While frank cancer of the colon is readily visible with common endoscopes, low-grade dysplasia (abnormal growth) and precancerous cells and lesions are often difficult for the endoscopist, or even the pathologist, to recognize. Furthermore, the molecular differences associated with early stages of cancer are not well defined, possibly because of the difficulty in identifying and isolating definitive samples that represent the functional spectrum of disease progression. For example, some of these lesions are not associated with polyps or other obvious structures, or anatomical changes, that facilitate identification and precise excision for histopathological evaluation. These and other problems have made the development of specific reagents difficult using standard techniques such as the identification of antigens by immunization or protein purification. With the postgenomic era and the availability of microarray and proteomic analyses performed on very small samples, the rational design of probes that bind targets identified by these methods becomes more practical. However, even with many years of accumulated knowledge regarding the appearance of individual antigens, few specific probes have been developed. As the extensive list of cancer antigens grows, reagent development must advance for the information to be useful for the detection of GI dysplasia in order for the full promise of specific and early detection to be realized [5–7].

## 17.2 DNA MICROARRAYS FOR TARGET IDENTIFICATION

Microarrays are designed to screen biological samples such as biopsies for the expression of thousands of genes at once [8–10]. Typically, DNA fragments corresponding to each gene are arrayed on glass microscope slides by an array printer that places tiny volumes in precise patterns on the slide. To determine which genes are expressed, the sample of choice is processed to prepare a fluorescent probe derived from its RNA. The extraction of RNA for the purposes of array analysis is not trivial, and RNA quality affects the outcome of the process. RNA can be extracted from tissue or cells using a variety of methods designed to avoid exposure of the sample to RNAses, the enzymes that degrade RNA. These enzymes are among the most stable of proteins and require protein-destroying reagents such as phenol or isothiocyanate to be employed. Commercial kits are now available that provide clean RNA for making a fluorescently labeled probe. This probe is hybridized to the microarray, and the slide is scanned by a laser [10]. The level of hybridization to each of the DNA fragments on the slide is then used to determine the expression level of the corresponding gene. Array technology is exploding and has revolutionized biology by enabling multiplexed assays of different types of biological molecules, including RNA, proteins, and glycans (sugars).

As an example of the postgenomic analysis of GI cancer, the gene expression patterns of Barrett's esophagus and associated malignancy have been determined [11]. The data have contributed important information pertaining to cancer progression and have revealed possible targets for the development of molecular probes. Barrett's esophagus, a pathological condition caused by acid reflux, is one of the most common GI conditions, and millions of people suffer from this condition. The alterations in the mucosa of the esophagus due to constant exposure to gastric acids include a transition from normal esophageal cell morphology to a cell morphology resembling that of intestinal tissue (Figure 17.1).

This transformation, referred to as *metaplasia*, is readily apparent upon endoscopy and is characterized by a salmon-colored section of mucosa at the distal esophagus near the stomach. This process alters the epithelial morphology from the "squamous" (from the Greek "fish scale") appearance of the normal esophagus to a columnar appearance, characterized by the long cells generally found in the intestine. People with Barrett's esophagus have an increased risk of developing esophageal cancer. Cancer is thought to result from the abnormal growth of this tissue during the process of rebuilding the mucosa, as abnormal or hyperactive growth often produces transformed cells.

The specific detection of precancerous lesions in Barrett's is especially important due to the difficulty of treatment of this disorder. Unlike the intestine, the esophagus is not amenable to resection, and surgeries that remove tissue from this organ cause considerable morbidity. The detection of early cancer in

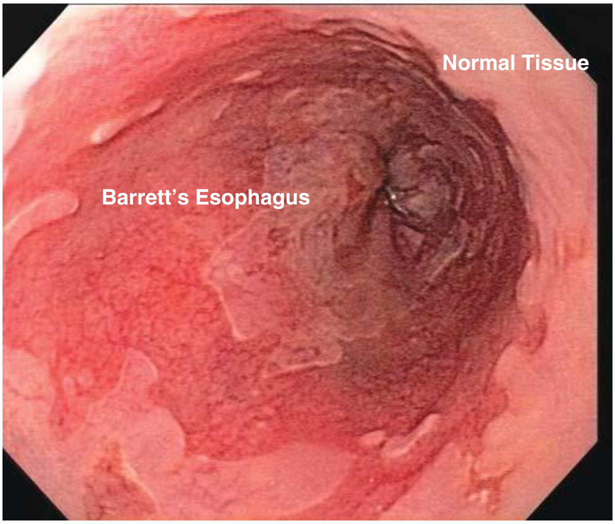

**FIGURE 17.1** Altered appearance of mucosal surface in Barrett's esophagus. The normal squamous epithelium is replaced in the region proximal to the stomach by columnar cells reminiscent of the intestine. The alteration is due to the effects of bile and acid on the lining of the esophagus, the result of acid reflux. Normal light pink tissue and darker Barrett's tissue are indicated. (From [2], with permission.)

Barrett's patients is complicated by the abnormal appearance of the tissue and the lack of an obvious structure such as a polyp that is associated with cancer progression in other regions of the GI tract. Dysplasia, or abnormal growth, affects 1% of Barrett's patients and is often indistinguishable from nondysplastic Barrett's tissue upon endoscopy. Thus, for screening of these patients, many random four-quadrant biopsies are performed, in which tissue samples are removed from four areas distributed evenly around the circumference of the esophagus, and this process is repeated along the length of the organ. These biopsies are not only costly and time consuming but can also easily miss early lesions. A probe that could differentiate early cancer from Barrett's tissue would therefore be of great use in early detection.

Hao et al. have performed microarray analysis of Barrett's tissues [11] and have identified a gene set that can accurately distinguish precancerous tissue from Barrett's esophagus in terms of gene expression. For the experiment, 48 biopsy samples from 17 patients were analyzed. Normal esophageal tissues as well as samples from the duodenum were compared to Barrett's tissue as well as adenoma (a type of dysplasia of glands such as those that secrete mucus, which may progress to adenocarcinoma, cancer derived from glands). One sample of high-grade dysplasia was also included in this study. The microarray data from samples clustered well as an indication of shared gene expression profiles, and these profiles correlated with progression of Barrett's esophagus to cancer and led to the identification proteins as possible targets for the development of optical imaging probes.

Interestingly, two samples classified using microarray data were determined by pathology as distinct from their classification by gene expression profile. One sample was obtained adjacent to an adenoma of a patient, and it clustered with adenoma. The other sample determined by pathology to be poorly differentiated invasive adenoma clustered with Barrett's. Although the first sample could have been adenoma rather than Barrett's tissue adjacent to the cancer, the misidentification of the second sample, whether by the array or by the pathologist, is more difficult to explain. However, the samples analyzed by array methods were not identical to the biopsies submitted for pathology, and the many variants exhibited in Barrett's esophagus can be difficult to classify even by an experienced pathologist. Gene expression profiles will aid in the study of this cancer by contributing to our understanding of disease progression and identifying markers that delineate steps in this progression.

The study of Hao et al. provides an excellent example of the complexities of correlating data from arrays with the observations of pathologists, and how this process should be undertaken carefully so as to avoid conflicting results, which may be more misleading than informative. In the study by Hao et al., the investigators took great care in obtaining the biopsies by employing an experienced endoscopist, and the biopsies were encoded rather than described so as not to bias the pathology. Also, the tissues were processed rapidly to avoid RNA degradation, and poor spot signals on the arrays were eliminated from analysis. The results showed excellent correlation between arrays, and the evaluation of the pathologists and nonheirarchical clustering readily classified the samples. In addition, advanced algorithms of array analysis were used, including significance analysis of microarrays (SAM), which determines the statistical significance of data, and prediction analysis of microarrays (PAM), which identifies genes capable of discriminating samples.

It must be stressed that array data can be deceptive in that even when the RNA is degraded, results are obtained because the probes hybridize and signals are generated. Thus, samples must be carefully evaluated for RNA quality before the hybridization is performed, especially in the case of archival tissues. In addition, the choice of samples for RNA preparation in relation to the biopsies evaluated by pathologists must be made carefully. The evaluation must proceed in a double-blind manner so that the assessment of the pathologist is independent of that of the physician obtaining the biopsy. In the end, the ability to discriminate among cancer, dysplasia, and normal tissue is dependent on keeping the process free of bias. There is no means of determining the validity of the analysis if such bias is introduced inadvertently, because the data will appear to correlate well when in fact they are flawed. Thus, the onus falls on the investigator to impose a rigorous protocol and carefully avoid even unconscious errors, particularly when the subjective evaluation of a pathologist is a critical component. In addition, in the study of Hao et al., array observations were correlated with RT-PCR (reverse transcriptase–polymerase chain reaction, which amplifies and quantifies a given mRNA sequence) in order to validate the expression levels of several genes, and immunohistochemistry was employed to determine where expression was occurring within the tissues sampled. In addressing these concerns properly, Hao et al. have demonstrated the power of such a procedure to reveal fundamental processes of cancer progression as well as to identify possible targets of diagnosis and intervention.

This study revealed many differences between adenoma and Barrett's tissue regarding the expression of genes encoding surface proteins, some of which may be exploited for probe design. Of particular prominence in the data was the increased expression of many genes in the stromal tissues early in the progression. Stromal cells surround and support the tumor but are not tumor cells. Genes of several types of collagen, for example, were found to be highly overexpressed in stroma. Collagen is not expected to be produced in large amounts by cancer cells, and the increased expression of collagen genes is likely to be stromal in origin. Stromal involvement in the progression of cancer is now understood to be critical. Alteration of stromal and matrix proteins could prove to be important for the early detection of cancer, but these targets may not be amenable to endomicroscopy because of their depth in the tissue. The abundance and altered distribution of some stromal proteins may facilitate imaging, but they will probably not be detectable using topically applied reagents. When specific probes are designed, the location and abundance of the target must be considered carefully.

Specific genes that are found to be up-regulated during the progression from abnormal growth to life-threatening cancer will be useful as diagnostics only if they display characteristics amenable to the development of imaging reagents.

Not only must the target be more abundant in the lesion, but it must be accessible for probe binding in a manner that facilitates imaging. For a topically applied probe, these requirements would seem to require that the target be a surface-associated structure, as access to the cytoplasm or deeper tissue is assumed to be limited. When arrays or other gene expression technologies are used to identify targets, the results indicate RNA expression levels of the thousands of genes arrayed on the slide. The most straightforward approach is to identify differentially expressed genes encoding membrane-associated surface proteins and to develop reagents that bind to the proteins. However, there are instances in which probes could conceivably bind in a specific and useful manner if the target were not up-regulated. For example, if a masking substance such as mucus is produced in lower abundance in a precancerous lesion, the binding of a probe may be enhanced in this location because of increased availability rather than target overexpression. Also, target proteins not exhibiting differential expression may be modified by enzymes that do. Thus, the identification of targets not associated with overt changes in gene expression and the development of probes that bind to such targets may be more successful when employing a less directed approach.

## 17.3 PHAGE DISPLAY

Phage (or bacteriophage formally) are viruses that infect bacteria. These viruses are readily manipulated by well-established recombinant DNA techniques and have been exploited for many years for gene transfer, DNA sequencing, and protein expression [12,13]. The technique of phage display refers to expressing libraries of peptides or small proteins on the surfaces of phage particles and using the binding of these modified particles to select for specific peptide reagents. This technique provides a means of identifying probes, from vast libraries, based on the binding of recombinant phage to specific molecular targets. Phage display is a very powerful method of generating peptide-based reagents that bind to a chosen substance, cell, or tissue. This method has proven valuable in a remarkably diverse set of circumstances. This process takes advantage of the huge combinatorial complexity of protein sequences and the ability to propagate the phage biologically in bacteria. For these purposes, a phage display library is produced by inserting small synthetic pieces of DNA into the genome of the virus. Each piece of the inserted synthetic DNA codes for a different protein sequence and the sequences are randomized during synthesis to provide for a large pool of different sequences, each in a different viral particle. Because the DNA pieces are inserted into a part of the viral genome that encodes a surface-exposed protein, each phage displays a unique peptide on its surface that is available for binding to given target molecule.

A large library of distinct phage can be produced, and because 20 amino acids are naturally employed in proteins by bacteria, the number of different sequences possible is truly vast. The entire library can consist of billions of different and unique phage, or clones, that can be isolated and replicated separately. Such libraries are now available commercially and are readily screened for binding to tissues. For this procedure, the entire library of billions of different clones is incubated with the target molecule, cell, or tissue. The weak binding phage are washed away, and the tightest-binding clones, whose inserted DNA fragment encodes a peptide that binds to the tissue, are removed from the sample with acid, a process termed *elution*. The entire screening procedure is referred to as *panning*. The resulting phage are then applied to a smooth layer of bacteria (called a *bacterial lawn*) on a petri dish, where individual phage clones infect the bacteria and form a small zone of clearance or plaque. Each plaque is derived from a single phage particle and is therefore clonal. The phage plaques are picked from the bacterial lawn and grown separately, resulting in a huge amount of phage that have the same insert. One then collects many such clones, verifies the binding properties of each clone separately, and determines the sequence of each DNA insert. From this sequence, a corresponding synthetic polypeptide (protein fragment) can be prepared. If the process is successful, the peptide will bind specifically to the molecular target and can be conjugated to a tracer for imaging. Although it seems highly unlikely that any given phage will contain a specific and useful insert, the sheer number of available clones provides much in terms of possible specific molecular interactions if the selection is carefully done. Phage display has proven successful in a wide range of circumstances.

In the study by Hsiung et al., biopsied tissues from the colon were used as the target [2]. This approach of using the tissue directly as opposed to specific molecules avoids the potential pitfalls of directed screening against a preselected target by reducing the biases associated with the selection of specific molecular targets. By panning phage libraries on the target tissues themselves in conditions that are close to how the probe will ultimately be used enables the study of a myriad of molecular targets, including complex carbohydrates, extracellular matrix components, and secreted proteins as well as other elements that may not fall out of gene expression analyses but may be extremely useful targets. The use of intact biopsy tissue, not dissociated cells from these tissues, selects for phage that bind to the exposed surfaces, and when developing probes for topical application to the gut mucosa, this is an important selection step in the screening procedure.

Because a phage library contains so many different clones, the process of isolating the correct ones is fraught with difficulty. For every cancer-specific phage clone, literally hundreds of millions must be discarded. Some of these irrelevant clones will contain inserts that bind tightly to all tissues and cells and will thus be useless for specific detection but still may get through the panning process. These clones probably outnumber by orders of magnitude the specific clones desired. There are many variations of panning that avoid such problems. The first is to pre-clear the library with appropriate substances, cells, or tissues that will absorb the irrelevant phage and leave the desired clones available for binding the relevant target. Hsiung et al. performed this step using the human epithelial cell line CRL7869, which is considered to be nontumorigenic. The resulting cleared library was then panned repeatedly with fresh colon biopsies (Figure 17.2).

The clearing of the library presumably removes clones that bind nonspecifically to common cell surface components such as those comprising the lipid bilayer and the many proteins found on many cells of the body. In the study by Hsiung et al. the panning of the cleared library was performed in a manner that selected for phage that bound to the desired target: that is, the surface of dysplastic tissue. By retaining both the bound and unbound phage from a given biopsy, the choice of which sample to pan further could be delayed until after the pathology of the biopsy was determined. If the biopsy was normal, the unbound phage was retained for further panning, and if the biopsy was dysplastic, the bound and eluted phage was retained. Hsiung et al. repeated this process until there were but a few hundred phage clones remaining. This strategy also permitted the panning of the library against biopsies from many different patients, to select phage clones

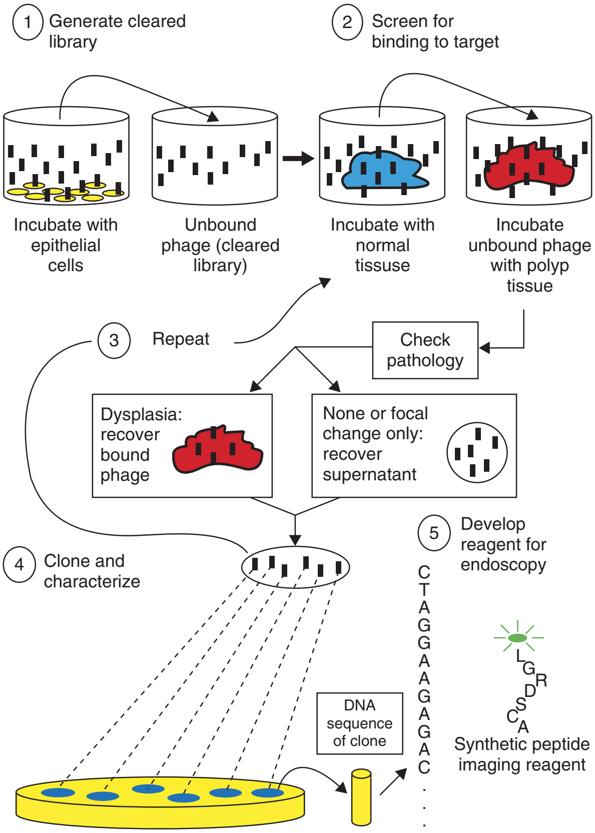
1 Generate cleared library
2 Screen for binding to target
Incubate with epithelial cells
Unbound phage (cleared library)
Incubate with normal tissuse
Incubate unbound phage with polyp tissue
3 Repeat
Check pathology
Dysplasia: recover bound phage
None or focal change only: recover supernatant
4 Clone and characterize
5 Develop reagent for endoscopy
DNA sequence of clone
C T A G G A A G A G A C . . .
L G R D S C A
Synthetic peptide imaging reagent

**FIGURE 17.2** Panning procedure of Hsiung et al. used for the identification of a peptide probe for colon cancer. The method involves the delayed selection of either bound or unbound phage subsequent to pathology. (From [2], with permission.)

that bind to dysplastic lesions from different individuals, an obviously vital property for any imaging reagent.

These clones were then screened for specific binding, a critical step that represents a bottleneck in the system in that the screening assays are often very laborious, and high-throughput approaches have yet to be perfected. The first assay employed involved comparative binding to a colon cancer cell line, HT29, and the nontumorigenic CRL7869 cells. As a screen for dysplasia, this assay is less than optimal, because the cancer cell line may exhibit many properties that are different from dysplasia in a patient. Nonetheless, several clones exhibited increased binding to the cancer cells, which may be indicative of specificity, whereas control phage lacking inserts did not show differential binding in this assay. The inserts of these clones were sequenced and peptides derived from one of the insert sequences was synthesized and used for imaging in patients. Although not ideal, this procedure was successful, as demonstrated by specific binding to dysplastic crypts in patients as observed with an endoscope equipped with a fiber optic–based miniaturized microscope (Figure 17.3). The results were confirmed in several other patients.

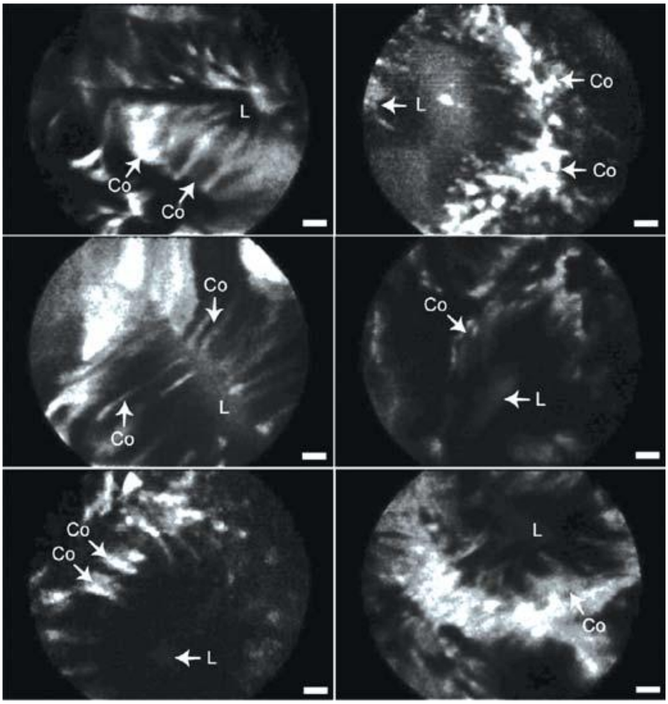

**FIGURE 17.3** Fluorescence detection of dysplasia using a peptide identified by phage display. Hsiung et al. panned a commercial phage library with fresh biopsies and identified the insert sequence of a promising candidate. A corresponding peptide-fluorescein conjugate was synthesized and used as a probe for endomicroscopy. The Cellvisio instrument from Mauna Kea Technologies was used for endomicroscopy. (From [2], with permission.)

No doubt the success of this effort was due to the panning process, which not only facilitated binding to the desired tissue but also imposed the requirement of specific binding in successive rounds of panning on many biopsies. The procedure also selected for phage that bind to the surface of the cells of the tissue, because they were eluted using acid, which will not release internally bound phage particles. Although this method was successful, there are many difficulties associated with the procedure. Because the biopsies contain exposed portions of deeper tissue and not just the surface, phage could bind the internal (basolateral) part of the biopsy rather than the surface that was exposed in the lumen of the intestine in the patient. In addition, the screening of peptides in patients is not feasible for large numbers of peptides. Currently, the best method of screening the phage is using microscopy on excised tissues, and this is quite laborious. In addition, the binding of phage to the actual luminal surface in such samples is difficult to ascertain, because the tissues are typically sectioned, exposing internal cellular structures not accessible to the probe during endomicroscopy. Therefore, although successful for Hsiung et al., the screening method employed here would require a large clinical organization and also technical staff in order to produce many probes. Nonetheless, initial results have been promising.

Once peptides are identified that appear to bind dysplasic tissues, determining the actual molecular target that they bind is not trivial. One might suppose that homology to known ligands may be useful in this regard, but that may not be the case. It would be unlikely that specific binding of a given phage is mediated in a manner identical to a known and well-described interaction such that it could be identified by homology. Far more likely would be the binding of the phage to some part of a target that is not involved in ligand recognition. However, some molecules, such as integrins and cell–cell contact mediators, exhibit extensive contact surfaces, which might be mimicked in part by a selected peptide. Homology of a selected peptide with human or murine ligands can easily be analyzed using current algorithms and should certainly be performed when peptides with good imaging capabilities are identified, but it is fair to say that one would be very fortunate to happen upon a direct hit using this approach. In any case, finding homology to a ligand would only provide a good guidepost for initial investigation as to the identity of a target; further evidence of specificity would be necessary for verification.

Alternative approaches for target identification include direct binding assays, such as Western blots as well as a variety of techniques employing mass spectrometry. To the knowledge of the authors, none of these have been employed for the purpose of identifying an unknown target for a given peptide. Alternatively, it may be possible to employ cross-linking for this purpose using a moiety such as benzophenone attached to the end of the peptide and a detectable and retrievable moiety such as biotin attached to the other end. One would then bind the labeled peptide to target cells and expose them to ultraviolet light in order to cross-link the benzophenone to the bound molecular target. Then the cells could be lysed and the lysate passed over a streptavidin column to trap the bound peptide–target conjugate and to determine the identity using mass spectrometry. Such a procedure is entirely speculative at this point, and the identification of molecular targets may not be straightforward.

## 17.4 POTENTIAL TARGETS AND POSSIBLE PITFALLS

In this section we discuss some of possible molecular targets for the optical detection of cancer in the GI tract. These targets have been selected from among many hundreds of possible candidates to illustrate the opportunities and challenges of detection based on specific molecules. Although optical methods are those discussed here, many modalities of molecular cancer detection share common problems associated with the individual targets. These hurdles include expression patterns, abundance, and accessibility, among other difficulties. To overcome these obstacles, a thorough understanding of the idiosyncrasies of each molecule will be required. Nevertheless, specific detection of targets such as those discussed here could revolutionize the field of cancer diagnosis.

### 17.4.1 Mucins

The entire GI tract is covered in a layer of mucus. This substance, although seemingly homogeneous, is actually highly complex and produced by a large number of genes encoding both the mucin proteins and enzymes responsible for the elaborate decoration of mucins with polysaccharides. The MUC genes (Muc for the mouse) encode mucins and have been found to be regulated differentially throughout the body. They are also expressed in many cancers, where studies indicate that patterns of MUC gene expression are altered during the progression of some tissues to malignancy [14]. Part of the MUC protein typically consists of up to several hundred repeated amino acid residue motifs that serve as substrates for glycosylation (the addition of carbohydrates, sugar molecules, usually in large chains). Over 50% of the molecular mass of the MUC proteins consist of carbohydrate, and the composition and sequence of the carbohydrate can be widely different even on the same MUC protein in the same animal. In the pancreas, MUC proteins can be 80% carbohydrate and have a molecular weight of over 1 million kDa. MUC1 has been well characterized by Gendler et al., who have written an excellent review of tethered mucins [15]. At first thought to have merely antiadhesive properties, these proteins have now been demonstrated to have signal transduction capabilities and to interfere with toll-like receptor (TLR) signaling, a critical component of the innate immune response [16]. TLR ligands such as bacterial flagellin bind to MUC1. Elegant studies performed on Muc1$^{-/-}$ knockout mice as well as mice expressing transgenic human MUC1 have demonstrated multiple functions of this mucin and are revealing an active and important protein [17,18].

A highly variable structure such as MUC1 might seem like a poor candidate for specific imaging, in which consistency from person to person is a necessity. However, MUC1 has a relatively invariant core that has been shown to be amenable to peptide binding [19]. A peptide derived from the sequence of the combining site of an antibody directed to the core of MUC1 binds the target with good affinity and specificity [20]. This peptide has been linked to imaging agents and shown to function as a contrast agent for tumors in animals. Because

MUC1 is not highly expressed in the colon but is associated with colon cancer progression, it may represent a good target for imaging early dysplasia.

There are several reasons to attempt to target mucins specifically. First, they are abundant. The cells of the GI mucosa produce large amounts of these proteins. Second, many of the mucins, including the MUC1 protein, are found on the surfaces of cells. Finally, as mentioned above, the mucins can be expressed differentially in cancer progression. Hao et al. identified MUC1 as a differentially expressed protein that was up-regulated in Barrett's cancer samples. The structure of MUC1 makes probe design for imaging directed toward this target a complex problem, but there are several possible solutions. Splice variants of MUC1 are commonly expressed in both normal and cancerous tissue, and these variants have been shown to remove the central and heavily glycosylated portion of the protein. This isoform, MUC1Y, has been shown to be expressed on many tumors and could be selected for as metastasis develops [19]. In addition, a secreted isoform is apparently released from the cell surface by proteolysis. The molecular functions of MUC1 with regard to tumors are unknown, but mice deficient in the Muc1 (mouse) gene produce tumors that grow slowly and metastasize less frequently than those from wild-type animals [18]. This protein is therefore of interest for intervention as well as imaging.

### 17.4.2 Wnt Receptors

Expression of the Frizzled (FZ in humans) homolog 4, a Wnt receptor, was found to be increased in cancer progression in Barrett's esophagus as well as in colon cancer [11,21]. Wnt (wingless in *Drosophila*) is a secreted factor involved in early development that regulates cell interactions and is implicated in carcinogenesis. There are many Wnt proteins and FZ receptors in mammals, and these proteins are responsible for the alteration of gene expression involved in cell proliferation. The Wnt pathway is highly complex and conserved across huge evolutionary distances and is involved in many processes regulating cell function and cell interactions, such that mutations in Wnt affect a wide variety of properties in the tissues of many animals, from worms to humans.

Neural development, stem cell activity, and wound healing are all regulated by Wnt signaling. Many Wnt proteins are apparently expressed in normal as well as malignant tissue in the colon, whereas others are up-regulated in cancer. FZ receptors bind Wnt and are implicated in the increased Wnt signaling observed in cancer progression. The expression of some FZ homologs was found to be highly differential in the progression to colon cancer, and Hao et al. [11] found a 4.9-fold increase in FZ4 expression in adenomatous tissue versus Barrett's esophagus. FZ receptors are expressed in the colonocytes and at the base of the crypt, which may facilitate imaging. As the expression increases greatly during cancer progression, perhaps the degree to which specific probes bind to this target could indicate the stage of cancer. Because the FZ receptors are homologous, careful techniques would have to be employed to develop specific imaging reagents that would bind only the FZ protein chosen, but because their expression is highly correlated with cancer progression, such an effort may produce a very useful set of reagents. In addition, the lack of expression of some FZ proteins in normal tissue may facilitate directed therapy. These proteins may someday prove to be important tools for optical detection as well as possible specific intervention based on subverting or inhibiting the Wnt pathway.

Infiltrating cells may present problems in the identification of molecular targets. Many of the surface proteins found to be up-regulated in the transition from Barrett's esophagus to adenoma are associated with lymphocytes or other cells of the immune system. This result raises interesting questions and has implications for optical imaging. Inflammation is commonly associated with many cancers, and the immune response to cancer progression is well known, although nonspecific. Possible targets for optical imaging may reside in the immune component rather than the cancer cells themselves, but this could lead to nonspecific reagents that cross-react with other inflammatory conditions. The immune response may not be sufficiently specific as to allow only for detection of processes associated with cancer progression. It is likely that the components of immunity are similar in many conditions and that specificity will be poor. Also, the cells of the immune system are generally not exposed to the lumen of the esophagus, stomach or intestine, limiting access to surface markers. Nonetheless, there may be systemic delivery methods that permit the optical detection of inflammation associated with premalignant lesions. An intravenously administered probe may have access to the layers of the colon in which the inflammatory cells can be found. Similarly, certain substances secreted by immune cells could be detected by intravenous administration.

Perhaps the most troubling aspect of the discovery that many up-regulated genes are associated with immune responses is that it confounds the analysis of array data and proteomic discovery of molecular targets. This result necessitates the validation of all possible targets by in situ hybridization, immunohistochemistry, or other methods that can determine which cells are expressing a given target in relevant tissue specimens. Such methods, although commonly employed, are not always informative with regard to expression on lumenal surfaces, because the lumenal surface is usually cut through in tissue sections and is seen only as a layer. Particularly with invaginated tissues such as the colon, this lack of exposure can be a problem. In the case of Hao et al., hybridization to the stromal tissues was used to demonstrate the differential expression of cancer-related molecules, but these were not surface associated and would not provide utility as imaging reagents.

Optical imaging is poised to play a decisive role in the next generation of reagents for early detection of cancer. It is clear that miniaturized microscopes in endoscopes will be extremely useful for imaging reagent binding, in that they can provide subcellular resolution. Hsiung et al. [2] demonstrated this technique using a fiber optic–based microscope. This device can be used to visualize fluorescien, GFP, and other fluorophores that excite with 488-nm light. The microscope was critical in the study by Hsiung et al. and revealed startling images of the peptide probe binding specifically to dysplastic crypts in patients undergoing endoscopy.

In this case, the staining of colonocytes in the walls of the crypt was clearly evident and demonstrated the utility of endoscopic microscopy for cancer detection. The use of topically administered peptides in the GI tract is direct and will enable the endoscopist to identify cancers through increased contrast and may enable them to molecularly type tissues within the patient. Such strategies will benefit from the combination of wide-field detection and microscopy such that binding of the agent can be localized globally and evaluated locally for morphological details of disease. The intent is to screen the large surface area of the gut with confidence and to facilitate cellular analyses such that early detection of dysplasia in the GI tract and monitoring and therapeutic outcomes are improved.

### 17.4.3 Tight Junction Probes

Tight junctions (TJs) are complexes of proteins that help epithelial cells to adhere to each other and form the strong barriers necessary for specific exclusion and absorption of substances by the mucosa. These complexes form between the cells and are therefore not expected to be present in high concentration on the lumenal side of the mucosal surface. However, there is strong evidence that some pathogens gain access to the submucosal compartment by binding to TJ proteins. In addition, the subcellular localization of some proteins is affected during the process of cancer development. Cancer cells are abnormal, and TJ proteins may be overexpressed in cancer cells and not necessarily always part of the complete TJ complex. Malignant invasive cancers would not be expected to form TJ complexes, as these would restrict metastasis and form ordered structures not usually observed in tumors, yet many TJ proteins are overexpressed in cancer cells. Thus, the normal subcellular localization of TJ proteins should not be taken as evidence that these proteins will all be useless for imaging purposes and cancer detection. If pathogens can access these proteins for invasion of normal tissue, perhaps molecular probes can access them for detection.

Certain members of the claudin family, which are TJ proteins, have been found to be overexpressed in the progression of GI cancer. Claudin 18 was revealed to be expressed in adenomatous tissue at nearly six times the level of Barrett's esophagus in the study of Hao et al., and claudins have been implicated in malignancy and invasive phenotype [22]. Several claudins are either overexpressed or repressed in diverse cancers. The claudin gene family is large, and many members exhibit tissue-specific expression patterns in normal tissues. An excellent review of these interesting proteins is available [23]. In this review, the important point is made that one would expect reduction in the expression of TJ proteins to occur in cancer, because the TJ restricts cells and reduces nutrient availability, and the dissolution of intracellular contacts is a hallmark of malignancy. The apparently paradoxical overexpression of some claudins and other TJ proteins in cancer cells is thus another example of the complex nature of cancer and the problems faced in cancer detection. Nonetheless, if certain claudins are found to be up-regulated in tumor progression, specific reagents designed for their detection could be extremely valuable, because these proteins are structural in nature and therefore may be highly expressed.

Similar to the claudin gene family are other surface proteins that exhibit subcellular localization which would probably preclude their utility as imaging targets if the localization were identical to that of normal cells. We must not assume that such proteins in cancer cells are localized normally; cancer is by nature a deregulated and undifferentiated state in which many normal processes are subverted or otherwise abnormal. Specific probe design must factor in these alterations to achieve maximum success because the many complex patterns of target expression obviously affect the efficacy of detection. Although these factors greatly complicate the problem of specificity, one may hope that by being forced to confront them directly in the initial stages, a more effective reagent will result from the effort.

### 17.4.4 Integrins

Integrins are members of a family of heterodimeric proteins whose function is to serve as communication conduits that link extracellular components to appropriate intracellular responses. These proteins connect the extracellular matrix (ECM) and surface structures of other cells to the intracellular machinery of signal transduction and the cytoskeleton. Integrin-expressing cells may thus sense the ECM or other cells and react in a highly specific manner, such as to form tissues or react to stimuli. For example, integrins transduce information regarding contact with the ECM protein fibronectin to the intracellular reorganization of actin, which is directly responsible for cell shape and motility. Integrins also transduce signals that affect cell proliferation and the avoidance of apoptosis and are thus often critical for the development of cancer. The malignant phenotype, being invasive, depends on either suppressing or subverting normal contact with cells or the ECM. Migration of cancer cells has been linked to up-regulation of some integrins, and this process is attributed to intracellular signaling occurring subsequent to integrin ligand binding. The presence of 24 distinct integrin heterodimer combinations in humans would seem to greatly complicate the development of imaging reagents based on these proteins. However, highly specific peptides that bind to integrins have been developed using phage display.

Many integrins bind the arginine–glycine–aspartic acid (RGD) moiety of their ligands, particularly the $\alpha_v\beta_3$ integrin expressed by newly forming vasculature, a characteristic component of tumors. Thus, imaging reagents based on RGD are in current use as radiological and optical tumor detection agents [24]. The efficacy of optical reagents based on this principle is unclear but is certainly not beyond reason. Because RGD-based reagents target vasculature that is deeper than can be accessed by some optical modalities, the utility of these probes will be limited to regions that are accessible to optical probes. The binding of integrins to RGD complicates the identification of peptides that bind to integrins by phage display, because any phage containing the RGD sequence in its insert will bind to many intergrins without the fine specificity that is the real advantage of phage display. One method of avoiding this problem during probe selection would be to pretreat the cells expressing the chosen integrin target with a peptide containing the RGD sequence, to attempt to block binding by RGD containing phage. The relatively simple methods of panning and phage recovery are amenable to many such alterations that increase the odds of success.

### 17.4.5 Enzymes

Certain targets provide imaging potential based on specific properties of the protein other than a reagent that binds its general structure. Enzymes that are up-regulated in cancer may bind substrates that could be modified to serve as specific imaging probes for cancer. However, intracellular targets suffer from the problems of delivery common to many molecular agents designed to cross the cell membrane. The delivery problem has plagued both detection methods as well as therapies for decades, and only marginal progress toward its resolution has been accomplished. Certain peptides derived from the HIV tat protein, which mediates cell entry, and peptides based on the same principle composed of polyarginine, have been employed to induce the passage of drugs and imaging agents across the cell membrane [25]. These hybrid molecules have yet to reach their full potential but have shown promising results to date. Some enzyme substrates may pass into the cell without additional moieties, and these have been exploited for detection and treatment. To develop such substances as optical reagents, however, a fluorescent or otherwise optically detectable entity must be conjugated to the substrate, which may impede or abrogate its transport or binding to the target.

Matrix metalloproteases (MMPs) are enzymes that degrade the collagen that forms a large part of the ECM. MMPs are up-regulated by cancer cells, which employ these enzymes in the invasion of tissues. MMP-2 is a member of this enzyme family that is expressed by many cancers. In glioma, a very aggressive and deadly brain tumor, MMP-2, was found to be highly up-regulated. MMP-2 is linked to binding of the peptide, chlorotoxin, a venom protein made by scorpions that is not poisonous to mammals [26]. Chlorotoxin is an unusual protein of 36 amino acid residues among which are eight cysteine residues, implying several intramolecular disulfide bonds. This protein has been linked to a Cy5.5 dye for fluorescence imaging, in order to detect tumors [4]. This method is an exciting innovation that has proven highly effective in the detection of tumors in animal models. Because GI cancers up-regulate MMP-2, chlorotoxin may serve as a valuable imaging agent for endomicroscopy.

Another protein whose endogenous properties have been exploited for imaging is cyclo-oxygenase. The cyclo-oxygenase-2 (COX-2) enzyme is responsible for the synthesis of prostaglandin, which stimulates inflammation and affects many other processes of the body. Inhibitors of the COX enzymes reduce inflammation and have been used to treat arthritis and pain. These substances are highly effective but can increase the risk of heart attack. Because COX-2 is up-regulated in GI cancers and expression in normal tissues is very low, this enzyme could conceivably be used as a target for specific detection by optical means, provided that the probe can be made to cross the cell membrane. COX-2 inhibitors readily gain access to the cytosol, but a compound that is optically detectable would presumably require the conjugation of a fluorophore or other agent to the basic structure [27]. Such extra moieties can greatly affect the transport or diffusion of a given compound. The development of imaging reagents based on cytoplasmic targets thus becomes a problem of chemistry and delivery, in addition to the identification of the target. Although several means of such delivery have been proposed, they have yet to affect the problem significantly. If and when solutions are found, new horizons of detection and treatment will unfold.

### 17.4.6 Pitfalls

Some expression data may be misleading with regard to possible imaging targets. One gene exhibiting differential expression arising from array data is the neurexin-3 (NRXN3) gene, which is up-regulated in Barrett's adenoma. Some neurexins are among the largest of human genes at 1.8 megabases in length, and exhibit extensive alternate splicing variation [28]. The number of possible splice variants of these genes is truly staggering. Hundreds of possible alternatively spliced NXNR3 messages are possible, leading to a plethora of possible proteins, including both surface and secreted forms. Thus, the mere identification of this gene as overexpressed in cancer through mRNA analysis is not useful. Before any type of effort would be made to develop an imaging agent directed toward such a protein, the exact forms of all of the proteins would have to be determined as well as their relative abundance in the target tissue of many individuals. The NRXN3 gene therefore exemplifies one of the profound challenges to the development of imaging tools based on array data: differential expression.

Many mammalian genes exhibit splicing variants that could greatly confound the effort to develop imaging reagents. Whereas it is now relatively straightforward to extract RNA and hybridize it to an array, this information provides only expression levels based on the DNA present in the chip and therefore represents only part of the picture. Certainly such data are very useful as an indication and are essential in the screening of thousands of genes. However, careful consideration must be taken in the actual decision as to which genes to pursue. The data from many individuals must be interrogated before a reagent with dependable characteristics can be developed. In addition, within any individual, many forms of a protein can be expressed, so that when the chosen gene is transfected in cell culture or cells expressing the gene are employed for the purposes of phage screening or other methods to develop the reagent, differential expression must be considered carefully. These problems suggest that proteomic methods may sometimes be more useful than gene arrays for probe development. In any case, selection of the target must be careful, and many complications of the procedure may arise.

The process of specific expression of target genes and the development of probes directed against the desired proteins involves standard recombinant DNA methods. However, the actual practice often belies the simple design of constructs on paper. To express genes appropriately for techniques such as phage display, skilled attention to detail and a sound knowledge of cell culture and transfection are necessary. The optimal method for such a procedure would be to express the protein of interest in a mammalian cell line that is readily amenable to transfection, such as COS cells, which are monkey kidney cells that are easy to grow as well as transfect. COS-1 through COS-7 cell clones express the large T antigen and therefore support the replication to a high copy number of vectors that contain the SV40 origin of replication. These vectors replicate to thousands of copies per cell and can contain SV40-based promoters that express genes at very high levels. Such systems provide for good expression levels that greatly enhance the chances of procedures such as phage display to identify reagents specific to the protein of interest.

Another quite significant hurdle is the creation of the actual construct itself. Although simple in concept, this step can actually comprise the most difficult and time-consuming challenge in the entire process. In the past, one would design oligonucleotide primers for polymerase chain reaction (PCR) amplification of the target gene from cells or tissues known to express the protein of interest. This gene would be amplified and cloned into an expression vector using specific restriction enzyme sites designed into the primers. Careful choice of which portions of the expressed mRNA molecule is required for the success of this procedure, and even then it may simply fail for a number of reasons, such as message stability and abundance. In addition, the amplified insert must be accurately sequenced to assure authenticity and to avoid common errors due to fidelity of the polymerases used for PCR. Fortunately, the explosion of commercial molecular biology now permits the avoidance of many of these steps, because full-length, sequenced cDNA clones are now available for purchase from a variety of sources, some of which actually offer reasonable prices. These clones are often available in expression vectors ready for immediate use or convenient transfer to the vector of choice.

## 17.5 PROBE DESIGN

The detection of GI cancer by optical means generally requires fluorescence or contrast enhancement of some kind. Although reflectance imaging is useful, the problems associated with using this modality in depth in tissues outweigh the lack of need for an exogenous agent. In addition, the optical detection of specific targets is greatly facilitated by fluorescence. The use of fluorescein conjugates such as the peptide employed by Hsiung et al. permits 488-nm excitation, commonly used by many instruments, including some with utility in vivo. Fluorescein is well studied chemically and approved by the U.S. Food and Drug Administration for a number of indications. One major drawback of this compound is that it is excited by blue light and emits in the green region of the spectrum. Light of these wavelengths does not penetrate tissues very deeply, and as many molecules in mammalian tissues fluoresce at these wavelengths, probes in this region of the spectrum suffer from high background and, consequently, poor signal/noise ratios. Fluorescent substances that excite with wavelengths near the red end of the visible spectrum, such as CY5 and the Alexa-Fluor dyes, as well as indocyanine green (ICG) and LICOR IRDye 800CW, have been explored recently with promising results [29]. These compounds not only permit deeper tissue imaging but also fluoresce at wavelengths that exhibit much less autofluorescent background. However, the chemistry of these substances and many of the newer fluorophores is not as well developed as fluorescein, and the conjugation process has not been perfected. One can expect rapid progress in this area of investigation and the synthesis of a wide variety of new compounds and new conjugation chemistries that will result in a range of new optical probes.

In addition to fluorescent dyes, a number of other substances for optical detection have recently come into play. Quantum dots, which are nanoparticles commonly made of colloidal cadmium, are being used in very diverse circumstances [30]. These particles are highly fluorescent and do not suffer from photodegradation, the breakdown of molecules by light. The wavelengths absorbed and emitted by quantum dots depend on the size of the dot, with larger dots having an emission that is "redder." A range of quantum dots that excite at one wavelength but emit over a wide range is possible, and these are providing opportunities for unprecedented flexibility in optical detection of molecular targets in cancer. In addition to these probes, nanotechnology has produced several new methods of enhancing optical signals, such as nanoshells and nanorods, which enhance fluorescence by employing plasmon resonance imparted by gold and other metals [31,32]. Although the future use of these remarkable tools is open, there remain some concerns about toxicity, and because they are relatively new, integrating them into current system procedures will take time.

Optical coherence tomography (OCT) is a reflectance technique that produces images based on interference of incident and reference beams. This method can image structures 1 to 2 mm beneath the surface of tissue, deeper than can confocal microscopy. Because only coherent reflected light is detected, fluorescence, which emits incoherent signals, cannot be employed for OCT. The reason for this limitation is that the incoherent light of fluorescence cannot be recombined with the reference beam for interference. Thus, the design of specific probes for OCT is not as straightforward as that for confocal or other fluorescence systems. Contrast agents for OCT have been devised that detect changes in blood flow and other properties of tissue, but these are not specific to given molecular targets. However, many aspects of OCT have been manipulated such that this method shows great potential for screening the GI tract [33]. Because this chapter is focused on specific probes, OCT is not discussed here in depth.

Molecules altered in disease states can be detected by techniques such as Raman spectroscopy. For example, during the progression of colon cancer, the nuclei of cells increase in number and size and a layer of nuclear staining becomes more pronounced in the crypts. This alteration is one of the most important clues employed by the pathologist. Nuclei, which contain DNA and RNA in large amounts, may have a distinctive Raman spectrum that could change with the progression to malignancy. In addition, other changes, such as those associated with increased proliferation, may have distinctive features in the Raman spectrum. New instruments to detect such features, particularly those employing surface-enhanced Raman scattering (SERS), have been produced, and this method shows great promise for specific diagnosis [34]. In addition, the technique of Fourier transform infrared (FTIR) spectroscopy may reveal spectral features of premalignant lesions [35]. One problem associated with spectral information is that no image is produced and the clinician must trust the spectral processing algorithm rather than an image. Presumably, should the methods prove accurate, physicians would learn to trust such data, but it is safe to say that this process will be slow. It would probably be much easier for the clinical community to accept modalities that provide images such as those from endomicroscopy, which allow for evaluation and judgment. A remaining challenge is to improve the ability to quantify images and to link the information to large databases in order to reduce human bias and make interpretation less subjective.

## 17.6 CONCLUSIONS

In summary, the tools of the molecular biologist have revealed many avenues of progress that can be exploited for optical imaging, and together with outstanding efforts in instrumentation, a new future is dawning for this field. With the unprecedented information now available regarding cancer and other diseases and the increasing ability to analyze this wealth of data, the specific detection of disease by optical methods cannot be far. However, the challenges are significant. Although methods such as phage display are being employed with great success, the targets are limited in number and the development of specific reagents is complicated by problems of structure and expression. Every target has unique problems that must be overcome before a specific and accurate detection reagent can be identified. The assays for specificity must be greatly improved before significant progress can be made. Staining of ex vivo samples is clearly difficult and the results will always be suspect until the reagent is employed in human subjects. Even when such a probe is in hand, problems of delivery and toxicity must be addressed, making the process of production lengthy and expensive. Perhaps the most significant hurdle to the development of new probes is the primary evaluation of a given probe in a clinical setting, and clearly these issues need to be addressed.

## REFERENCES

1. Keller, R., et al., Fluorescence endoscopy using a fluorescein-labeled monoclonal antibody against carcinoembryonic antigen in patients with colorectal carcinoma and adenoma, *Endoscopy*, Vol. 34, No. 10, 2002, pp. 801–807.
2. Hsiung, P.L., et al., Detection of colonic dysplasia in vivo using a targeted heptapeptide and confocal microendoscopy, *Nat. Med.*, Vol. 14, No. 5, 2008, pp. 454–458.

3. Kelly, K.A., Waterman, P., and Weissleder, R., In Vivo imaging of molecularly targeted phage, *Neoplasia*, Vol. 8, No. 12, 2006, pp. 1011–1018.
4. Veiseh, M., et al., Tumor paint: a chlorotoxin:Cy5.5 bioconjugate for intraoperative visualization of cancer foci, *Cancer Res*., Vol. 67, No. 14, 2007, pp. 6882–6888.
5. Margolis, D.J., et al., Molecular imaging techniques in body imaging, *Radiology*, Vol. 245, No. 2, 2007, pp. 333–356.
6. Blasberg, R.G., and Gelovani, J., Molecular-genetic imaging: a nuclear medicine-based perspective, *Mol. Imaging*, Vol. 1, No. 3, 2002, pp. 280–300.
7. Endres, P.J., et al., Cell-permeable MR contrast agents with increased intracellular retention, *Bioconjug. Chem*., Vol. 19, No. 10, 2008, pp. 2049–2059.
8. Halbleib, J.M., et al., Transcriptional modulation of genes encoding structural characteristics of differentiating enterocytes during development of a polarized epithelium in vitro, *Mol. Biol. Cell*, Vol. 18, No. 11, 2007, pp. 4261–4278.
9. Saaf, A.M., et al., Parallels between global transcriptional programs of polarizing Caco-2 intestinal epithelial cells in vitro and gene expression programs in normal colon and colon cancer, *Mol. Biol. Cell*, Vol. 18, No. 11, 2007, pp. 4245–4260.
10. Schena, M., et al., Quantitative monitoring of gene expression patterns with a complementary DNA microarray, *Science*, Vol. 270, No. 5235, 1995, pp. 467–470.
11. Hao, Y., et al., Gene expression profiling reveals stromal genes expressed in common between Barrett's esophagus and adenocarcinoma, *Gastroenterology*, Vol. 131, No. 3, 2006, pp. 925–933.
12. Brissette, R., and Goldstein, N.I., The use of phage display peptide libraries for basic and translational research, *Methods Mol. Biol*., Vol. 383, 2007, pp. 203–213.
13. Smith, G.P., Filamentous fusion phage: novel expression vectors that display cloned antigens on the virion surface, *Science*, Vol. 228, No. 4705, 1985, pp. 1315–1317.
14. Labouvie, C., et al., Differential expression of mucins and trefoil peptides in native epithelium, Barrett's metaplasia and squamous cell carcinoma of the oesophagus, *J. Cancer Res. Clin. Oncol*., Vol. 125, No. 2, 1999, pp. 71–76.
15. Hattrup, C.L., and Gendler, S.J., Structure and function of the cell surface (tethered) mucins, *Annu. Rev. Physiol*., Vol. 70, 2008, pp. 431–457.
16. Ueno, K., et al., MUC1 mucin is a negative regulator of toll-like receptor signaling, *Am. J. Respir. Cell Mol. Biol*., Vol. 38, No. 3, 2008, pp. 263–268.
17. Schroeder, J.A., et al., MUC1 overexpression results in mammary gland tumorigenesis and prolonged alveolar differentiation, *Oncogene*, Vol. 23, No. 34, 2004, pp. 5739–5747.
18. Spicer, A.P., et al., Delayed mammary tumor progression in Muc-1 null mice, *J. Biol. Chem*., Vol. 270, No. 50, 1995, pp. 30093–30101.
19. Zrihan-Licht, S., et al., Characterization and molecular cloning of a novel MUC1 protein, devoid of tandem repeats, expressed in human breast cancer tissue, *Eur. J. Biochem*., Vol. 224, No. 2, 1994, pp. 787–795.
20. Medarova, Z., et al., In Vivo imaging of tumor response to therapy using a dual-modality imaging strategy, *Int. J. Cancer*, Vol. 118, No. 11, 2006, pp. 2796–2802.
21. Holcombe, R.F., et al., Expression of Wnt ligands and frizzled receptors in colonic mucosa and in colon carcinoma, *Mol. Pathol*., Vol. 55, No. 4, 2002, pp. 220–226.

22. Wu, Y.L., et al., Expression transformation of claudin-1 in the process of gastric adenocarcinoma invasion, *World J. Gastroenterol.*, Vol. 14, No. 31, 2008, pp. 4943–4948.
23. Morin, P.J., Claudin proteins in human cancer: promising new targets for diagnosis and therapy, *Cancer Res.*, Vol. 65, No. 21, 2005, pp. 9603–9606.
24. Beer, A.J., et al., [$^{18}$F]galacto-RGD positron emission tomography for imaging of alphavbeta3 expression on the neovasculature in patients with squamous cell carcinoma of the head and neck, *Clin. Cancer Res.*, Vol. 13, No. 22, Pt. 1, 2007, pp. 6610–6616.
25. Wender, P.A., et al., The design, synthesis, and evaluation of molecules that enable or enhance cellular uptake: peptoid molecular transporters, *Proc. Natl. Acad. Sci. USA*, Vol. 97, No. 24, 2000, pp. 13003–13008.
26. DeBin, J.A., Maggio, J.E., and Strichartz, G.R., Purification and characterization of chlorotoxin, a chloride channel ligand from the venom of the scorpion, *Am. J. Physiol.*, Vol. 264, No. 2, Pt. 1, 1993, pp. C361–C369.
27. Uddin, J., et al., Selective visualization of cyclooxygenase-2 in inflammation and cancer by targeted fluorescent imaging agents, *Cancer Res.*, Vol. 70, 2010, pp. 3618–3627.
28. Rowen, L., et al., Analysis of the human neurexin genes: alternative splicing and the generation of protein diversity, *Genomics*, Vol. 79, No. 4, 2002, pp. 587–597.
29. Rasmussen, J.C., et al., Lymphatic imaging in humans with near-infrared fluorescence, *Curr. Opin. Biotechnol.*, Vol. 20, No. 1, 2009, pp. 74–82.
30. Smith, B.R., et al., Real-time intravital imaging of RGD-quantum dot binding to luminal endothelium in mouse tumor neovasculature, *Nano Lett.*, Vol. 8, No. 9, 2008, pp. 2599–2606.
31. Bardhan, R., et al., Fluorescence enhancement by Au nanostructures: nanoshells and nanorods, *Am. Chem. Soc. Nano*, Vol. 3, No. 3, 2009, pp. 744–752.
32. Loo, C., et al., Nanoshell-enabled photonics-based imaging and therapy of cancer, *Technol. Cancer Res. Treat.*, Vol. 3, No. 1, 2004, pp. 33–40.
33. Adler, D.C., et al., Three-dimensional endomicroscopy of the human colon using optical coherence tomography, *Opt. Express*, Vol. 17, No. 2, 2009, pp. 784–796.
34. Stokes, D.L., and Vo-Dinh, T., Development of an integrated single-fiber SERS sensor, *Sensors Actuators B*, Vol. 69, No. 1, 2000, pp. 28–36.
35. Wang, T.D., et al. Detection of endogenous biomolecules in Barrett's esophagus by Fourier transform infrared spectroscopy, *Proc. Natl. Acad. Sci. USA*, Vol. 104, No. 40, 2007, pp. 15864–15869.

# INDEX

5-Aminolevulnic acid (5-Ala), 272
A2E, 97,105, 111
Absorption
  coefficient, 290, 339, 340, 351, 356–61
  length, 290
  light, 288–89
Absorption spectra, 310
Acoustic wave, 338, 342, 343
Acoustic velocity, 339, 341–42
Action potential(s), 413, 421, 423, 425–26
Adaptive optics, 118, 124–133
Adaptive optics, types
  AOSLO, 128, 131–33
  AO-FDOCT, 128–30
  AO fluorescence, 129–31
  AO fundus imager, 128
Adenocarcinoma, 192, 199
Adenoma, 509
Adjoint sensitivity method, 348
AKs, *see* Keratosis, actinic
Angioblastic meningioma, 271
Angiogenesis
  arteriogenesis, 370
  biology, 371–73
  intussusception, 371–72
  marker, 374, 376–77, 381, 394, 397–98
  measurement types, 373–76
  pericyte, 371–73
  remodeling, 370, 376
  sprouting, 371–73
  vasculogenesis, 370
Angiopoietins, 370
Anisotropy factor, 290
Anthracene 263
Atherosclerotic, 267–71, 278
  arteries, 263
  cardiovascular disease, 264
  fibrotic, 267–70
  high-risk, 265, 269, 278
  plaque(s), 264–265, 268–269, 272–273, 275, 277
Aorta, 266–67
Aromatic amino acids, 256
Arterial wall(s)
  diseased, 265
  normal, 267, 269
Astrocytoma, 271, 273
Autofluorescence emission, 269
Average fluorescence lifetime, 266
Axon, 423–26

---

*Advances in Optical Imaging for Clinical Medicine*, Edited by Nicusor Iftimia, William R. Brugge, and Daniel X. Hammer

Copyright © 2011 John Wiley & Sons, Inc.

Back-projection, 342
Barett's esophagus, 192–198, 507–11
BCC, *see* Carcinoma, basal cell
Benign, 318, 323–24
  meningioma, 271
Biexponential deconvolution, 269
Billiary, 188, 199–201
Bioluminescence imaging, 77
Biopsy, 207, 208, 271–72, 278
Birefringence, 432, 434–37, 439, 441, 444–45, 447–48
  circular birefringence, 432, 436–37, 448
Blood oxygen saturation, 291
Body mass index, 320–21
Boundary condition, 344–45, 352
Brain monitoring
  motor tasks, 295
  verbal fluence tasks, 296
Brain tumors, 77, 256, 272–74, 278–79
  glioma, 271–73, 275–78
  malignant, 271
  meningioma, 271, 273, 275–78
  primary, 271–72, 278
Breast
  cancer, 311, 321,323
  functional parameters, 309, 319, 321, 323
  lesion optical properties, 323
  optical properties, 318–20
Bruch's membrane, 96–98, 107, 123

Cancer, 371–372, 376–78, 380–83, 385, 389, 394–95, 398, 432, 436, 444–45. *See also* Tumor
  adenocarcinoma, 382–83, 395
  carcinoma, 377, 381–83, 395
  delineation, 469
  sarcoma, 382–85
Carcinoma
  basal cell (BCC), 168, 170, 175, 177, 181
  metastatic, 273
  squamous cell (SCC), 170–71, 175, 178, 181
Cardio imaging and diagnosis
  angioscopy, 234, 236, 238–39, 248
  intracoronary MRI, 234, 237
  intravascular ultrasound, 234–35, 241, 248
  near-infrared (NIR) spectroscopy, 234, 237–39
  OCT, 234, 238–51
  thermography, 234, 237–39
Carotid
  artery, 268
  plaque(s), 268–69
Catheters, 189–91, 264–65, 269
  balloon, 190–211, 194,196–98
  cirfumferential scanning, 199–201
  helical scanning, 191
  linear scanning, 190–91, 194, 196
  longitudinal scanning, *see* Catheters, linear scanning
Cell(s), 423–26
Cerebral perfusion, 297
Chemotherapy, 324–25
Cholangiocarcinoma, 199–201
Chromophores, 289, 309
Choriocapillaris, 89–90, 96–97, 105, 107–10, 135
Choroid, 89–90, 95–99, 104–05, 107, 109–10, 130, 134–35, 141
Choroidal neovascularization, 95–96, 98, 109–10, 141
Coherence range gate, 106, 114, 119, 137
Collagen, 256, 263, 265, 268–69, 432, 435–36, 441, 444–45
  reach lesions, 270
  type I, 267
  type II, 263, 266–67
  type III, 266–67
  type IV, 266–67
  type V, 266–67
Colon, 188, 190, 198–99
Color vision, 103, 127–28, 138
Commercial ophthalmic imagers
  Carl Zeiss Meditec Inc. Stratus OCT, 116–17
  Carl Zeiss Meditec Inc. Cirrus OCT, 120
  Heidelberg Retinal Angiographer (HRA), 95, 110–11, 113
  Heidelberg Retinal Tomographer (HRT), 113
  Heidelberg Spectralis, 110, 137
  Laser Diagnostic Technologies GDx, 113
  TopCon fundus imager, 107
Complement factor H, 96
Computed/computerized tomography, 19, 52, 58, 72–73, 75, 264, 272, 327
  axial and helical scanning, 19–20
  cardiac CT angiography, 22
  CT scanner, 19
  image artifacts, 20–21
  medical applications, 21–22
Cone density, 91, 133
Confocal endoscopic microscopy, 60
  myocardial infarction, 235, 237, 241–42, 248
  plaque rupture, 234–35, 238, 250
  stenosis, 234–35, 239
  thrombosis, 236–37, 243, 246–48

Confocal microscopy, types, 205–31
  conventional, 212–15
  dual axis, 220–23
  single axis, 212–15
Confocal range gate, 94, 106, 112, 137
Contrast
  agents, 211–12, 297, 376, 381–84, 388, 390–99
  autofluorescence, 211–12
  endogenous, 211–12
  enhanced MRI, 265
  exogenous, 211–12
  fluorescence, 210–12, 225
  reflectance, 211–12, 225–26
Convolution, 261–63
  equation, 262, 264
Coronary events, 234, 241
  acute myocardial infarction (AMI), 237, 247
  myocardial infarction, 235, 237, 241–42, 248
  plaque rupture, 234–35, 238, 250
  stenosis, 234–35, 239
  thrombosis, 236–37, 243, 246–48
C-reactive protein, 265
CT, *see* Computed/computerized tomography
Cyst, 323

Decay
  associated spectra, 266
  constant values, 263
  dynamics, 257
Deconvolution
  algorithm, 260
  biexponential, 269
  Laguerre, 262–64, 266–69
  method, 261
Deformable mirror, types, 127
DEJ, *see* Skin
Deoxyhemoglobin, *see* Hemoglobin
Depolarization, 432, 435, 446
Depth resolution, 293
Dermascopy, 168, 170–171, 181
Diaphanography, 311
Diattenuation, 434, 435, 439, 445
Dichroism, 432, 434–37, 444, 447–48
  circular dichroism, 432, 436, 447
Diffraction theory, 214, 215, 222–23
Diffuse
  optical tomography, 317
  reflectance, 274, 279
  spectra, 274
  spectroscopy, 273–74, 279
Diffusion equation, 356–61
Direct ophthalmoscopy, 106
Discrete Laguerre functions (DLFs), 261–64
Discrete time Laguerre functions (DLFs), 262–64
Disease, 371, 376–80
Disease targeted therapy, 480, 486, 493
  antigen-targeted nanocarriers, 488
  vascular endothelial growth, 487
  vascular permeability factor, 487
Doppler, 386–88, 398
  flowery, 118, 133–35
  OCT, *see* Optical coherence tomography, Doppler
DPC-OCM, 422, 424–26
Drug delivery, 457, 459, 480–85, 488, 491–93
  fundamental requirements, 481
  parameters, 481–86, 491
  residence time, 483
  therapeutic index, 457, 481, 483–84
    toxicity, 457, 459, 467, 472, 478, 481–85, 487–89, 491
Dual beam registration, 129
Dual mesh, 34, 346–47
Duodenum, 199
Dynamic (time resolved) autofluorescence, 273
Dysplasia, 192–198, 507

Early lesions, 268–69
ECM, 520–21
Elastin, 256, 263, 265, 269
Electroencephalography (EEG), 298
Electroretinography (ERG), 138–39
Elution, 512, 515
Emission spectra, 256, 266, 268, 275–77
Endogenous fluorophores, 258, 261, 263, 269
Endomicroscopy, 506
Endoscope
  instrument channel, 209–10, 225
  Optiscan, 208–09
  Pentax, 208–09
Enzyme(s)
  cofactor, 275–76. *See also* NADH
  cyclooxygenase-2, 521–22
  matrix metalloproteases, 521
  metabolic cofactors, 256
Epithelium
  biopsy of, 509
  columnar, 508
  mucous membrane, 506
  squamous, 508
Esophagus, 192–98
Esophagus, Barretts, *see* Barrett's esophagus
Expansive (positive) remodeling, 271
Extracellular matrix, *see* ECM

f/#, 105
Fast-gated cameras, 257
FGF, 373–74
Fibroblast growth factor, *see* FGF
Fiber bundle, 216–17
Fibroblastic meningioma, 271
Fibrocalcified plaque, 268
Fibrotic cap(s), 268, 270
Fibrous
  lesions, 267
  plaque, 268
  thick-cap atheroma, 271
  thin cap, 265
  tissue, 271
Finger tapping, 294
Finite element method, 343–61
Flavins, 256, 273, 279
FLIM, *see* Fluorescence lifetime imaging microscopy
Fluence, 356–58
Fluorescence, 381–84, 389–91, 395
  decay, 257
  decay data, 261
  decay dynamics, 257
  decay emission, 269
  emission spectra, 257
  impulse response function (IRF), 261–64
  intensity decay, 257–58
  intensity pulse, 261
  lifetime, 256–58
  lifetime imaging microscopy (FLIM), 258
  spectra, 260
  spectroscopy, 273
Fluorescence measurements, 256–57, 261
  steady-state, 256, 273–75
  time-resolved, 256–59, 261, 263, 266–70, 275–77
Fluorescence lifetime imaging microscopy (FLIM), 258
Fluorescein angiography (FA), 97, 99, 105, 107–10, 137
Fluoroscopy, 18
  absorbed dose rate, 19
  medical applications, 19
  technique description, 18
fNIRS, 289–300
Fovea, 89, 91
Foveal avascular zone (FAZ), 91, 127, 131–32
Fourier transform, 293, 342, 343
Frequency domain, 292–93, 314–15, 342, 344
Frizzled (FZ), 517–18
Functionalization, 458, 461–62, 467, 482, 485
Functional magnetic resonance imaging (fMRI), 288, 298
Functional near-infrared spectroscopy, *see* fNIRS
  continuous-wave (CW), 291, 294–95
  frequency-domain (FD), 292, 294–95
  null distance approach, 298–99
  time domain (TD), 292–99
Functional parameters, 309
Fundus photography, 91, 105, 107–08, 112, 118, 124

Ganglion cells, 90, 131, 138–41
Gastric cardia, 192–98
Gastroenterology, 187–202
Gastro imaging modalities, 65–69
  endomicroscopy, 67–69
  fluorescein-guided, endomicroscopy, 67–68
  OCT, 65, 69
  white-light endoscopy, 60, 62, 64, 68
Gene therapies, 98, 128, 142
Geographic atrophy (GA), 96–97
Glaucoma, 48–53, 56, 58
Glioblastoma, 271, 273
  multiforme (GBM), 271, 274
Gliomas, 271–73
  high-grade, 272–73, 275, 277
  low-grade, 272
  malignant, 272
Gold nanoparticles, 457–58, 461–63, 465, 467, 472–73, 478
  applications, 461–64
  nanorods, 463–64, 472–73, 478
  nanoshells, 463–65, 472, 478
  plasmon resonance, 457, 472–73
  photothermal therapy, 464
  size, 456, 458, 461, 472–73, 478, 481–82, 491
  tunability, 464
Gradient index (GRIN) optics, 215
Group velocity dispersion, 115

Hartmann-Shack wavefront sensor, 125
HbO2, *see* Hemoglobin, oxygenated
Hemodynamic (s), 288, 295, 296, 298
Hemoglobin, 384–85, 388–89, 391–94, 396–97
  deoxygenated, 288, 290
  oxygenated, 288, 290, 293, 296
  total, 291
Heterodyne detection, 105
HIF-1, 373
Histology, architectural, 188
Histopathology, *see* Pathology
Homogeneous acoustic, 339, 343–44, 350
Hypoxia, 370, 373–74, 376–77, 381
Hypoxia-inducible factor-1, *see* HIF-1

Image-guided radiation therapy, 38
  CBCT, 41–42
  detectors used in IGRT, 41
  kV-kV match, 41, 43
Imaging catheters, 189–91
Imaging contrast enhancement, 459–60, 465, 467, 469, 479, 494
  enhanced scattering, 478
  fluorescence, 456, 459–60, 465–66, 468–70, 475–80, 494
  magnetomotive OCT, 457, 474
Imaging, cross-sectional, 187
Imaging, in vivo, 188, 192–201
Imaging, non-contact, 188
Imaging, non-excisional, 188
Imaging, optical coherence tomography, *see* Optical coherence tomography
Imaging, volumetric
Imaging of gastrointestinal conditions, 61–65
  adenocarcinoma, 58, 62–63, 65–66
  adenomatous polyps, 65
  Barrett's Esophagus (BE), 61, 66–68
  Crohn's disease, 64
  dysplastic polyps, 65
Imaging for radiation therapy planning, 32
  CT, 32–36, 38–39
  MR, 33,35–36,38,40
  PET, 36,38, 40
  US, 32–33
Imaging method, 342
Image reconstruction, 342, 346–47
Imaging system(s), 350
Immunoscintigraphy, 265
Indirect ophthalmoscopy, 106
Indocyanine green (ICG), angiography (ICGA), 105, 107–10, 297
Instrument response function, 261
Integrins, 520–21
Intensified CCD (ICCD), 294
Interferometry, 188
Interventional cardiology, 70–71
Intraocular pressure (IOP), 91, 94
Intraoperative diagnosis, 272
In vivo, 338, 342, 344, 362
In vivo imaging, *see* Imaging, in vivo
  Lodopsin (photopsin), 89
IRF, *see* Instrument response function
Iron oxide nanoparticles, 459–60
  applications, 459
  carrier vehicles, 459, 477
  controlled release of drugs, 460
  size, 456, 458–60, 481–82, 491
  transducers, 460
Isobestic point(s), 291

Keratosis, actinic (AKs), 170–71, 177
$K^{trans}$376

Laguerre
  deconvolution, 263–64
  deconvolution method, 262–64
  deconvolution technique, 262
  expansion coefficient(s) (LEC(s)), 262–64
  expansion of the kernel technique (LET), 261–64
  functions, 261–263
Lambert–Beer law, 291
Laser microsurgery, 140–41
Lateral geniculate nucleus, 131
Layers of the retina
  Bruch's membrane, 88–89, 96–98, 107, 123
  choriocapillaris, 88–90, 96–97, 105, 107–110, 135
  choroid, 88–89, 97, 105, 107, 109, 130, 135
  connecting cilia, 89
  external limiting membrane, 88–89
  ganglion cell layer, 88–89, 130–31, 138–40
  Henle fibers, 88–89
  inner limiting membrane, 88–89, 98, 105
  inner plexiform layer, 88–89
  inner nuclear layer, 88–89, 110, 129–30
  nerve fiber layer (NFL or RNFL), 88–89, 91, 94–95, 113, 119, 130, 133, 136
  outer plexiform layer, 88–89, 98, 130
  outer nuclear layer, 88–91
  photoreceptor layer, 88–89
  retinal pigment epithelium, 88–89
  sclera, 88, 104–105
LDR and HDR brachytherapy, 32–33
Least-squares
  analytical solution, 263
  fitting, 264
  iterative reconvolution (LSIR), 261
  minimization, 263
  nonlinear optimization, 261
  optimization, 261
Lesions
  atherosclerotic, 266–67
  collagen-rich, 270
  early, 268–69
  fibrotic, 267
  fibrous, 267
  inflamed, 269
  lipid-rich, 265
  necrotic, 269
Light propagation model, 317
Light-scattering spectroscopy, 211

LINAC, 35–37
  energy range, 36
  fractionation, 36
Linear algorithm, 344
Lipid(s), 288, 309
Lipofuscin, 97, 105, 109–12, 118, 129
Low coherence interferometry, 106, 114–15, 118, 123

Macrophage, 234, 265, 268, 239–42
  fibrous cap disruption, 235, 242–43, 247–48
Macula, 89
Malignant, 318, 323–24
Manua Kea Technologies, 208–09, 212, 225, 226
Magnetic resonance imaging (MRI), 22, 265, 326–27, 383, 394–398
  medical applications, 24, 27, 28
  MR contrast agents, 25
  MR pulse sequences, 25
  MRI scanner construction, 23
  T1 and T2 weighted images, 24
Marker, angiogenesis, *see* Angiogenesis, marker
Maximum permissible exposure (MPE), 310
Melanoma, 164, 171, 174, 177, 178,181
MEMS, 218–19, 223–24
Meningioma(s)
  angioblastic, 271
  benign, 271
  fibroblastic, 271
  meningothelial, 271
  psammonmatous, 271
Menopause, 320
Metaplasia, 508
Metastatic carcinoma, 273
Michelson interferometer, 114–15
Microarray, 507–11
Microchannel plate photomultiplier (MCP-PMT), 294
Microelectromechanical systems, *see* MEMS
Microvessel density, *see* Vascular length density
Microscopy, confocal, 164, 168, 175, 182
  confocal mosaicing microscopy, 175
Mohs micrographic Surgery, 175, 177
Monte Carlo simulations, 215, 221, 223
Molecular imaging, 376, 381–82, 388, 397–99
Motion equation, 342
MRI contrast enhancement, 476
Mucins, 516, 517
Mucosa, 506
Mueller matrix, 432, 434–42, 444
Multianode microchannel plate (MCP), 297
Multiexponential
  components, 261
  expressions, 261
  function, 263
  IRF, 261
  LSIR, 264
  model, 261
  parameters, 269
Multi-focal ERG, 102–03, 132, 138–39
Multiphoton, microscopy, 142, 390–391
Multimodal, imaging, 325–27, 475
  fluorescence-MR, 475
  OCT/laser-induced, fluorescence imaging, 477, 479
  retinal imaging, 136–37
Multispectral imaging, 211, 227

NADH, 256, 273–76, 279
Nanoagent preparation, 458, 490
  bioconjugation, 457–58, 467
  surface modification, 458, 461–62, 478, 484, 487, 491
Nanoparticles, 351, 456–65, 467, 469, 472–83, 487–89
  gold, 457–58, 461–63, 465, 467, 472–73, 478
  iron oxide, 459–60
  quantum dots, 456, 458, 465–66, 482, 484
Nanotechnologies, 456–57, 467, 469, 472, 480–82, 485, 491, 494
  cancer targeting, 494
  specific binding, 458
Near-infrared, 309
  spectroscopy, 265, 317
Necrosis, 269, 272, 276
Necrotic
  core, 268–69
  lesion, 269
  plaques, 268
Neoplastic, tissue(s), 274, 278–79
Nicotinamide adenine dinucleotide, *see* NADH
Neurexins, 522
Neuroimaging, 72–77
  computed tomography (CT), 72–73, 75
  diffusion-weighted MRI, 74
  functional MRI (fMRI), 74, 76
  magnetic resonance, angiogram MRA, 74
  magnetic resonance imaging-MRI, 52, 73–74, 77
  magnetic resonance venogram, MRV, 74
  MRI spectroscopy, 75
  optical imaging, 77
  positron emission tomography (PET), 75
Neurovascular coupling, 288
Newton's method, 344, 346, 354, 359, 360
Nonlinear reconstruction, 344
NTROI, 328
Nuclear imaging, 397–98

Nuclear medicine, 26
  PET-CT scanners, 29
  PET medical applications, 29–31
  PET scanner operation, principle, 26, 28,29
  positron emission tomography, -PET, 26, 271–72, 288, 298, 326–27
  radioisotopes used for SPECT, 30
  radionuclides used for PET, 26, 28
  single photon emission computed tomography-SPECT, 30, 326
  SPECT medical applications, 32
  SPECT scanner operation, principle, 31
Numerical aperture, 105–06, 137

Ocular examination, 48, 50
Ocular melanoma, 49, 52
Ocular pathologies, 48, 52
OCT, *see* Optical coherence tomography
Oncology, 321
Ophthalmic optical imaging
  confocal scanning laser, ophthalmoscopy (CSLO), 56–57
  fundus photography, 50–51
  OCT, 52–54
  scanning laser polarimetry (SLP), 50, 56, 58
  slit lamp, 48, 50
Ophthalmoscopy, 50, 56–57
Optical activity, 435–36, 444, 446
Optical biopsy, 207–08
Optical pathlength, 414–15, 419–20, 424–26
Optical coherence tomography (OCT), 52–54, 60–65, 69, 71, 77, 187–202, 265, 271, 388–90, 414–29
  axial resolution, 53–54, 56, 60
  diagnostic criteria, 195–96
  Doppler, 61, 65, 202
  Fourier domain, 118–124
  Fourier domain mode-locking, 122–23
  line field, 123–24
  optical frequency domain imaging (OFDI), 119, 189, 191, 195–98
  parallel, 122–23
  principles, 188–89
  scanning speed, 53–54
  spectral-domain OCT (SD-OCT), 53–55, 118–24, 420–23, 426–27, 471, 479
  swept source, 119–122
  time-domain OCT (TD-OCT), 53–54, 113–17, 470–71
Optical Doppler tomography, 121, 133
Optical imaging, 187–202
Optic nerve head, 89
Optical sectioning, 213
OPTIMAMM, 322
Optoacoustic, 392–93
Optophysiology, 139–40
Oxyhemoglobin, *see* Hemoglobin, oxygenated

Pancreas, 199–201
Pancreatobiliary ductal system, 199–201
Panning, 512–14
Panretinal photocoagulation, 99–101, 107
Pathology
  biopsy, 168, 178, 181, 182
  histopathology, 164–65, 168–70, 178, 181
  gastrointestinal, 188, 192, 196, 199
  gold standard, 206
  in vivo, 205–31
  interobserver variability, 207
  telepathology, 226
PDGF, 373
Peptides, 456, 458–59, 467, 469, 478, 484, 487, 489
Permeability, vascular, 373–76, 380, 382–83, 390–91, 394–97. *See also* Pharmacokinetics
Phage display, 511–516
Pharmacokinetics, 383, 395–96
Phase-contrast, 413–30
  differential, 413, 417, 418, 421, 424
  microscopy, 413, 421, 423
Phase noise, 414–15, 417, 421
Phase sensitive, 413–30
  interferometer, 414, 420
  interferometry, 413–14, 419, 421
Photoacoustic wave, 342
Photodynamic therapy (PDT), 107–08
Photon density, 339, 340
Photon migration, 289, 290, 292
  absorption coefficient, 290
  reduced scattering coefficient, 290
Phototransduction, 90
Plaque(s), characterization, 238, 243, 250
  atherosclerotic, 264–65, 268–69, 272–73, 275, 277
  calcific, 240
  disruption, 265
  fibro-calcific, 240, 268
  fibrous, 238, 240, 268
  lipid-rich, 237–38, 240, 242–43, 267
  rupure, 264
  thin-capped fibroatheroma (TCFA), 234–35, 241
  vulnerable, 234–36, 238, 241, 248, 250–51, 264–65, 271
Plasma transfer constant, *see* $K^{trans}$, Pharmacokinetics
Platelet-derived growth factor, *see* PDGF

Polarization imaging, 432, 435, 445–46, 448, 449
Polarization-maintaining (PM) fiber, 417
Polarization microscopy, 436–37, 441
Polarization sensitive OCT, 136
Polarizer, 433–34, 437–39, 445
Positron emission tomography, *see* Nuclear medicine
Prediction analysis of microarrays (PAM), 510
Pre-market approval (PMA), 312
Presbyopia, 89
Primary brain tumors, 271–272
Psammomatous meningioma, 271

Quantum dots, 381–82, 390, 456, 458, 465–66, 482, 484, 524
  applications, 467
  cross-section, 466
  cytotoxicity, 467
  lifetime, 465
  size, 465–66

Raman spectroscopy, 265
Receptors, 456–57, 461, 464, 467, 468, 474, 478, 487–91
  epidermal/antiepidermal, growth factor, 457, 464, 467, 468
  integrins, 468–69, 478, 489
Reflectance spectroscopy, 265
Relative oxygen saturation, 309, 323
Retardance, 433–35, 437–39, 445
Retarder, 433, 435, 437, 448
Retinal autofluorescence (AF), 97, 105, 110–12, 129, 137
Retinal blood flow, 90
Retinal diseases age-related macular, degeneration (AMD or ARMD), 96–97
  angioid streaks, 98
  arterial and venous, obstructions, 100
  Best's disease, 98
  central serous, chorioretinopathy (CSC), 97–98
  cystoid macular edema, 98
  diabetic retinopathy (DR), 99–100
  epiretinal membranes, 98
  inflammatory diseases, 104
  infectious diseases, 104
  macular holes, 98
  macular dystrophy, 98
  optic nerve head disorders, 95
  papilledema, 95
  primary open angle glaucoma, 92–93, 104
  retinal detachments, 104
  retinopathy of prematurity (ROP), 101–02
  retinitis pigmentosa, 103
  rod-cone and cone-rod, dystrophy, 103
  Stargardt's disease, 98
  tumors, 104
  trauma, 104
Retinal development, 90–91
Retinal pigment epithelium (RPE), 89–90, 96–98, 103–05, 107–12, 128–29, 131, 135–36, 141
Retinal stimulation, 140–41
Retinal tissue absorption, 105
Reverse transcriptase polymerase chain reaction (RT-PCR), 510
Rhodopsin, 89
Rod density, 91
Rupture-prone plaque, 264

Sampling error, 202
Scanning laser ophthalmoscopy, 104, 112, 128
  adaptive optics, 128
  flying-spot, 112
  line-scanning, 112
Scattering, 310–11, 318–19
  center, 290
  coefficient, 288, 290–91
  length, 290
  light, 288–89
SCC, *see* Carcinoma, squamous cell
Schlemm's canal, 94
Scintilation, 128, 140
SD-OCT, *see* OCT
Seizure, 363
Scanning
  Lissajous, 219–20
  post-objective, 220–21
  raster, 219
Signal-to-noise ratio, 118, 121, 128
Simultaneous time- and wavelength-resolved fluorescence spectroscopy (STWRFS), 260–61
Single photon emission computed tomography, *see* Nuclear imaging
Significance analysis of microarrays (SAM), 510
Single-photon avalanche diode (SPAD) detectors, 299
Skin
  dermal–epidermal junction (DEJ), 165–68, 174, 178, 181
  dermis- papillary dermis, reticular, dermis, skin appendages, 167–68

  epidermis- tratum corneum, granular layer, spinous layer, basal, layer, keratinocytes, 166–67
  cancer, 164, 168, 171, 177, 181
Slit lamp biomicroscopy, 104, 106–07
Small animal imaging, 141–42
Sound velocity, 340–41
Space-resolved spectroscopy (SRS), 291
Spatial light modulator, 219
Specialized intestinal metaplasia (SIM), 61–62, 192–98
Speckle, 386–89
SPECT, *see* Nuclear imaging
Spectral imaging, 384–86,394
Spectroscopic OCT, 471–73
Spectroscopic techniques
  diffuse reflectance, 273–274
  reflectance, 265
  steady-state fluorescence, 273
  systems for point measurements, 258
  time-resolved laser-induced fluorescence, 256
Simultaneous time- and wavelength-resolved fluorescence, 260–261
Spectroscopy, diffuse, 393–96
Stable/unstable angina, 237, 241
Standard error mapping, 132
Static (steady-state) autofluorescence, 273
Stents, 241–48
  drug-eluting stents (DES), 243, 246–47
  restenosis, 243, 247
  strut apposition, 247–48
Stiles-Crawford effect, 127
Stress confinement, 340–41
Stokes vector, 433–35, 437
Stomach, 192–193
Surface modification, 458, 461–62, 478, 484, 487, 491
  PEGylation, 462, 483–85
  thiol chemistry, 461, 462, 478, 490
Superluminiscent diode, 115
Surface profilometry, 413, 419, 421
Surgery, 378–79
Suspicious lesions, 322

TD-OCT, *see* OCT
Therapeutic window, 309
Thermoelastic expansion, 337
Tight junctions, 519–20
Time-correlated single-photon counting (TCSPC), 258, 293–94, 297
Time domain, 315–16, 352, 355
  functional near infrared, spectroscopy (fNIRS), 292–300
Time-gated, 259
Time-resolved laser-induced fluorescence spectroscopy, 256, 258–71, 273, 278
Tissue oxygenation index, 293
Tissue regeneration, 480, 491–93
  scaffolds, 474, 491–93
  tissue regeneration platform, 492
Tomography
  diffuse optical, 393–96
  fluorescence, 382–83, 395
  optical coherence, *see* OCT
  positron emission, *see* Nuclear imaging
  single photon emission computed, *see* Nuclear imaging
TR-LIFS, see Time-resolved laser-induced fluorescence spectroscopy

Ultrasound, 12, 49, 52–53, 58, 60, 65–66, 70, 77, 326–27
  acoustic impedance, 13
  attenuation, 13
  axial and lateral resolution, 15
  characteristics, 13
  endoscopic, 65–66
  intravascular ultrasound (IVUS), 70–71
  medical applications, 15–17
  transducer, 338, 350, 355, 362, 363

Vascular endothelial growth factor, *see* VEGF
Vascular length density, 374, 383
Vascular permeability, *see* Permeability, vascular
Vascular volume fraction, 374–75, 383, 393–95, 398–99
VEGF, 372–74, 376–78, 380, 384, 395, 398–99
Velocity, blood, 386–90, 398
Visibility scores, 322
Visibility grading criteria, 322
Visual psychophysics, 141
Vulnerable plaque, 264–65, 271

Water, 288, 309
Wavelength-resolved fluorescence spectroscopy, 260
Wound, 370, 378–79, 387
White matter, 274–77

X-ray(s), 17, 394, 396–97
  medical applications, 18
  technique description, 17
  tomography, *see* Tomography